AN EXPERIMENTAL INVESTIGATION OF ROLL COATING PHENOMENA

Barry Malone

Department of Mechanical Engineering

University of Leeds

Leeds, LS2 9JT

Submitted in accordance with the requirements for the degree of

Doctor of Philosophy

June, 1992

To Fiona, Dan & Ellen

Abstract

This thesis gives an account of an extensive experimental investigation of the operation of a twin roll coater. Two distinct modes of operation are identified: Classical (fully-flooded inlet) and Meniscus (ultra-starved inlet). The former has been the subject of investigation for a number of years; the latter is less well known and would appear to have escaped the attention of the Coating Community at large prior to the research work reported here being carried out.

A detailed description of how the key features of an industrial roll coater can be reproduced using a piece of simple but well designed experimental apparatus, which encapsulates all the necessary elements for an in-depth study of the flow, is presented. Various methods are used to visualise the flow. These include dye injection and novel computerised particle tracking techniques, coupled with state-of-the-art image processing and High Speed Video photography.

Experiments reveal that the flow associated with the Classical mode of operation is essentially one-dimensional throughout the nip; Meniscus coating flow, on the other hand, is uniquely two-dimensional, containing large vortical structures. Also the pressure distributions are found to be quite distinct. A fully-flooded nip results in a pressure profile which exhibits a characteristic maximum and minimum, while an ultra-starved nip produces one which is linear and entirely sub-ambient.

The transformation of the flow from one mode of operation to the other is then considered, a key feature of which is the behaviour of the upstream free surface which moves

in to a minimum point and then out again as the flux is reduced, giving a non-singular result, that is, there are two non-dimensional values of the flux for each free surface position.

Finally, the subject of instability in roll coating is addressed, for both the Classical and Meniscus regimes. A number of new instabilities were observed using High Speed Video photography and tentative explanations for their occurrence are given.

Acknowledgements

I would like to express my sincere thanks to those people who made this study possible:

Mr. R.T. Harding, Mr. L. Bellon, and Mr. B. Randhawa for their technical assistance in the design and manufacture of the experimental apparatus. Also, Mr. S. Cail and Mr. P. Oates for their help and advice in the electronics applications.

A special thankyou to Mr. S. Burridge for his advice and expertise in all aspects of the photographic, video, and High speed video applications.

Dr. S. Howe for his advice and technical support, and ICI Imagedata for sponsoring the project in the form of a C.A.S.E. studentship.

Mr. H.M. Thompson for allowing me to use a number of his results, and for his support and advice on the theoretical aspects of roll coating. I am also grateful to him for many stimulating discussions on anything but roll coating.

I would particularly like to thank my supervisors Dr. P.H. Gaskell and Dr. M.D. Savage for their enthusiasm, support and advice on all aspects of this work, as well as Dr. T. David for his early involvement.

Finally, a very special thankyou to my wife, Fiona, for her patience, support and encouragement throughout.

Nomenclature

In some cases the use of certain notation is local to a particular section and is defined when introduced; such symbols are not listed here. With regard to images of the flow field etc., roll surfaces always move from right to left unless otherwise stated.

Ca	Capillary Number
c	Position of the fluid-air interface
H_0	Minimum gap size in a two-roll or plate-roll geometry
$h(x)$	Local roll separation
$h(c)$	Roll separation at fluid-air interface
h_1, h_2	Average film thickness on upper and lower rolls respectively
h_0	Inlet thickness in roll coating
h^∞	Asymptotic film thickness
L_0	Length of fluid bead in roll coating
p	Fluid pressure
P	Atmospheric pressure
Q	Volume flow rate
Q_0	Inlet volume flow rate
Q_1	Outlet volume flow rate on upper roll
Q_2	Outlet volume flow rate on lower roll
R_1, R_2	Radii of upper and lower rolls respectively
R	Average roll radius ($2/R = 1/R_1 + 1/R_2$)

r	Radius of curvature of fluid-air interface
Re	Reynolds number
S	Roll speed ratio (U_1/U_2)
s	Position of downstream film-splitting point
T	Surface Tension
u, w	Velocities of flow in x, z directions respectively
U_1, U_2	Peripheral speeds of upper and lower rolls respectively
V_c	Critical air entrainment velocity
W_0	Width of fluid bead in Meniscus coating
x, z	global coordinates
X_S	Position of downstream film-splitting stagnation line
X_I	Position of upstream film-splitting stagnation line
Z_L	Location of top of lower vortex in forward meniscus coating
Z_U	Location of bottom of lower vortex in forward Meniscus coating
β	Modified capillary number
ϵ	Dimensionless flow rate through the nip (Q/UH_0)
η	Dynamic viscosity
μ	Kinematic viscosity
θ	Angle of fluid film on a rotating roll
ρ	Fluid density
ψ	Streamfunction

Contents

Chapter 1

Introduction

1.1 Coating Processes

Perhaps the simplest and most easily identifiable example of a coating process is that associated with the application of paint using a brush or roller. This is not to suggest the application of a thin liquid layer onto a surface is a trivial process. Quite the opposite. At the industrial level the goals are much more exacting – namely to lay down a controlled liquid layer, of uniform thickness, at the highest possible speed and with the minimum wastage resulting from coating defects. The thickness and uniformity of the liquid layer are the critical parameters which restrict the process operating window.

Coating processes feature strongly in the manufacture of photographic film, packaging and associated film products, magnetic recording media, surgical dressings, fabrics, paper and adhesive tape, to name but a few. New applications are constantly being found such as in the production of thermal printing paper and optical recording media ('Compact Disc' technology). As the requirements of thin film coatings become more exacting, so the need to understand and predict the behaviour of the manufacturing process itself becomes paramount.

The myriad of different coater designs (Booth [1970,1990]) is testament to the practical difficulties involved in coating, and the emergence of coating technology as something of a *black art*, rather than a science. This unstructured development has been due, in part, to the wide range of coating rheologies encountered. In general, the fluid properties are specifically designed so that the finished film performs a certain function; be it as a protective layer or serving a more 'active' role such as the recording of information. Therefore the properties of the fluid are generally not adjustable for the purpose of coating.

The manufacturing process associated with a particular product, from the base web to the finished film, may involve a sequence of coating operations (e.g. forward roll coating, slot coating, and reverse roll coating performed sequentially), with intermediate drying/curing of each layer. Clearly, multiple processes such as these require compromise in terms of line speed and fluid rheology, because the success of each coating operation may depend on different parameters. In addition, when the complete coating and drying/curing process is considered, the scope for altering fluid properties to achieve the optimum coating flow is further constrained by requirements of acceptable wetting/spreading and efficient drying/curing of the wet film.

It is only in recent years that coating processes have attracted the interest of the scientific community in an attempt to bring a measure of quantitative understanding to such flows. There are two important reasons for this shift in behaviour; new industries which utilise such coating operations have evolved, such as magnetic media manufacturing (video tape, for example), together with greater productivity and uniformity requirements in relation to well established industrial coating processes – the manufacturing quality of photographic products, for example, have increased in line with increased international competitiveness. The complexity of such coating processes

presents a multitude of challenging problems for the experimentalist and theoretician alike.

Roll coating (described in §1.2) is only one of a number of thin film coating processes. In addition, there are many coating systems which use stationary dyes to direct liquid onto a substrate, or web (Figures 1.1(a), (b), (c) & (d) are examples of slot, knife, slide, and curtain coating, respectively). The term 'pre-metered coater' is often used to describe a number of coating systems. This essentially refers to those machines where all the fluid which is fed to the coating head is applied to the web, such as in slot, slide, and curtain coaters. Conversely, in classical roll coating the nip is fully-flooded, often resulting in flow-back, and the amount of fluid picked up or applied to the web is a strong function of the fluid properties, mainly viscosity, and factors such as roll speeds. Although this thesis is primarily concerned with roll coating flow, many of the techniques described here could be applied equally well to the former group of pre-metered coating systems.

A basic two-roll coater configuration is illustrated in Figures 1.2(a) & (b). A thin liquid film is laid down on a moving web. Fluid is picked up by the lower roll (often referred to as an applicator roll) in a continuous fashion from a bath and enters the small 'nip' (the position of the minimum roll separation) formed between the web and the lower roll. A fraction of the fluid is transferred onto the web of material in contact with the upper roll and the remainder is returned to the bath via the lower roll. In a typical industrial process the liquid film on the coated web is subsequently dried or cured.

Several common coating geometries are shown in Figure 1.3. Figures 1.3(a) & (b) represent simple forward (direct) and reverse roll coating systems, respectively. In

both cases the nip is supplied with fluid directly from the bath (or pan) by the viscous lifting action of the lower roll. Such systems are often referred to as pan-fed or dip roll coaters. Figures 1.3(c) & (d) are examples of the basic forward roll coater with a modified feed mechanism; 1.3(c) shows a slot-fed nip, whereby the fluid issues from a slot onto the surface of the lower roll, and the supply can be controlled by, for example, varying the pressure. Figure 1.3(d) illustrates the use of a three roll system whereby the offset roll meters the inlet film on the lower roll; this is itself a reverse roll coating configuration. Figures 1.3(e) & (f) are examples of variations on the basic two roll coater. The former, extrusion coater, can be used to coat both sides of a web simultaneously. In kiss coating the tensioned web is supported hydrodynamically above the upper roll.

Roll coating systems can be categorised into several distinct groups according to the design of the rolls themselves:

1. Rigid (non-deformable) rolls

2. Deformable (rubber-coated) rolls

3. Gravure (knurled/engraved) rolls

The first of these categories forms the focus of the present study. Although the bulk of the investigations concentrate on the forward roll coating case, several interesting features of reverse roll coating were discovered during the course of this work and are reported accordingly.

1.2 Classical (Fully-Flooded) Roll Coating

The classical roll coating flow regime is illustrated in Figure 1.4(a) where there is sufficient fluid supplied at inlet to justifiably refer to it as a 'fully-flooded' condition. The fluid flow through the roll nip can be described using hydrodynamic lubrication theory (Reynolds[1886]). Fluid is dragged into the nip region by the moving roll surfaces under the action of viscosity (see Figure 1.4(b)). Since the geometry is converging, the 'squeezing' action generates high pressures on the inlet side. Conversely, the diverging geometry downstream of the nip results in low pressures (below atmospheric). The pressure profile for such a system (see Figure 1.4(c)) has been widely reported (e.g. Floberg[1965]). Indeed, if the rolls themselves were completely submerged, the pressure profile on the downstream side of the nip would be an inverted mirror image of that on the upstream. The hydrodynamic pressure generation is governed by the geometric factor, H_0/R (where H_0 is the minimum gap width and R is the average roll radius). This geometric factor is a measure of the slope between the roll surfaces. In the nip region the flow is assumed to be one-dimensional; the fluid velocity in the z-direction is negligible compared to that in the x-direction.

Downstream of the nip the fluid splits into two films at the position $x = s$; one is transferred to the web, the other returns to the bath via the lower roll. Continuity considerations suggest that since the inlet is fully-flooded, the film thicknesses, h_1 and h_2, on the web and lower roll respectively, are of the same order of magnitude as the minimum roll separation. In the vicinity of the film-splitting fluid-air interface (or meniscus) the flow is fully two-dimensional and distinctly different from the lubrication-type flow in the central core of the nip (refer to Figure 1.4(b)). The flow in this region is bounded by the fluid-air interface and so surface tension may be important.

Historically, the similarity between the geometry of a roll coater and that of a lubricated bearing led early workers in the field to adopt a lubrication-based approach in attempting to understand this flow. Experimental investigations revealed key features of roll coating flows which subsequently motivated analysis aimed more specifically at this class of problem. Attempts to analyse the flow can be placed into three categories, ranging from simple mathematical models based on lubrication theory, to asymptotic analyses, and beyond to the full numerical solution of the governing Navier-Stokes equations of motion. More recently experiments have been used only as a secondary means of investigation; to verify theoretical predictions, or to obtain functional fits to data (e.g. see Benkreira, Edwards & Wilkinson [1981]).

1.2.1 Theoretical Modelling

Lubrication Theory

Very early analyses for special cases of the geometry shown in Figure 1.4(b) and other similar geometries were carried out by Martin[1916] (slider bearings), Jeffrey[1922] (fully immersed counter-rotating rolls), and Gatcombe[1945] (spur gears). Jeffrey, for example, solved the bi-harmonic equation $\nabla^4\psi = 0$ for the streamfunction, ψ, in an infinite two-dimensional domain to produce the first 'picture' of the flow between rotating rolls (see Figure 1.5).

The fluid flow between two converging solid surfaces, one of which is moving relative to the other, has been widely investigated using hydrodynamic lubrication theory. This theory was introduced by Reynolds[1886], the background of which can be found in any one of a number of textbooks (e.g. Cameron[1976]). It is employed in the analysis of non-contact bearings for example (Dowson & Taylor[1979]), and indeed in any such system designed to support a load.

A roll coater may be thought of as a lightly loaded bearing; it is usual to assume that the inlet fluid film completely floods the nip and that lubrication theory can be used to model the flow in this region (Savage[1982]), such that the resulting fluid flow and pressure distribution are similar to that found in hydrodynamic bearings, as discussed in § 1.2 (see Figure 1.4(c)).

Taylor[1963] was the first to suggest that the flow field associated with a roll coater might be separated into two distinct regions; a near rectilinear flow through the nip, and a two-dimensional flow downstream of the nip, in the vicinity of the film-splitting meniscus. Under a fully-flooded inlet condition (see Figure 1.4(b)) the fluid extends far upstream of the nip. For the purposes of a lubrication model it is assumed to extend to infinity; this distance being very large compared to $(RH_0)^{1/2}$ – a typical length scale in the x-direction. Therefore, lubrication theory is used to model the flow in a semi-infinite region extending from far upstream of the nip to the onset of the downstream recirculation region (Savage[1977a,b]). The normal procedure is to solve Reynolds lubrication equation for the pressure distribution $p(x, z)$, subject to appropriate boundary conditions;

$$\frac{\partial}{\partial x}\left[h^3(x)\frac{\partial p}{\partial x}\right] + \frac{\partial}{\partial z}\left[h^3(x)\frac{\partial p}{\partial z}\right] = 12\eta U\frac{\partial h}{\partial x} \tag{1.1}$$

where p is the fluid pressure, U is the average speed of the rolls, η the Newtonian viscosity, and $h(x)$ the local roll separation. Since the position, $x = c$, of the fluid-air interface is not known *a priori*, the solution requires three pressure (pressure gradient) boundary conditions instead of the usual two for a problem governed by a second order ordinary differential equation. Assuming that the pressure is atmospheric far upstream of the nip yields the first of these conditions:

$$p(-\infty) = 0 \tag{1.2}$$

Following Greener & Middleman [1975], Savage[1982, 1984], and Coyle, Macosko & Scriven [1986], the second pressure condition is formulated by a balance of the fluid pressure at $x = c$ and the surface tension pressure of the interface:

$$p(x = c) = -\frac{T}{r} \tag{1.3}$$

where T is the surface tension of the fluid and r is the effective radius of curvature of the interface at its leading edge. It is the specification of a third boundary condition that has led to different schools of thought in the analysis of roll coating flows.

Reynolds was the first to attempt to model a fluid-air cavity, from a consideration of gaseous cavitation. He suggested the following conditions at rupture of the fluid film:

$$p = 0, \quad \frac{\partial p}{\partial x} = 0 \tag{1.4}$$

Although Reynolds was the first to propose this condition, Swift[1931] and Steiber[1933] independently derived the same condition; it is therefore referred to in the literature as either the 'Reynolds' or 'Swift-Steiber' condition.

Birkhoff & Hays[1963] on the other hand suggested that it is the reverse flow eddy which provides the mechanism for the formation of a cavity and that consequently the cavity should form where the fluid separates from the stationary plate (this is equivalent to the position $x = s$ in Figure 1.4(b)), i.e. where the velocity and tangential stress are zero:

$$u = \frac{\partial u}{\partial z} = 0 \tag{1.5}$$

The equivalence of these conditions to those proposed by Prandtl[1904], for locating the position of separation in boundary layers, and the work of Hopkins[1957] was recognised by Birkhoff & Hays who named it the 'Prandtl-Hopkins Condition'. It is more commonly referred to however, as the 'Separation condition'.

Unfortunately, neither the Reynolds nor the Separation condition provide an ideal solution when applied to roll coating flow. Savage[1977] identified certain inadequacies of the Reynolds condition; experimental results of pressures in a lightly loaded plate-roll geometry show the presence of a downstream subambient pressure loop (Figure 1.4(c)) which the Reynolds condition cannot predict. In addition, the Reynolds condition does not predict the existence of an eddy upstream of the fluid-air interface which has been observed experimentally (see § 3.2). However, Floberg[1957] has shown that this condition is appropriate in highly loaded bearings where, because of the high pressures generated in the fluid, there is a limit to the sub-atmospheric pressure that can be sustained resulting in rupture of the fluid film in a region where $p = 0$ and $\partial p/\partial x = 0$. Taylor[1963] and Dowson & Taylor[1979] discuss the difference between this approach to film-splitting and that of the smooth flow-separation regime. They suggest that this boundary condition is most appropriate when the flow at the downstream meniscus shows a transition from smooth to irregular, cavitation-induced film-splitting (i.e. formation of bubbles of air and/or of liquid vapour within the liquid). Photographic evidence of this phenomenon is presented by Taylor[1963], Floberg[1964], and Myers & coworkers[1958, 1961].

In considering the predictions of the Separation condition, the pressure gradient at the cavity can be shown to be equivalent to:

$$\left[\frac{\partial p}{\partial x}\right]_{x=s} = \frac{2\eta U}{h^2(c)} \tag{1.6}$$

for an equal speed two roll coater, where $h(c)$ is the roll separation at the fluid-air interface. Since this value for the pressure gradient at the cavity is clearly positive, when combined with the assumption of zero pressure at rupture, implies the existence of sub-ambient pressures immediately upstream of the separation point which agrees

with the pressure distribution obtained experimentally. This analysis assumes that the flow separates at the first stagnation point downstream of the nip (i.e. at the position $x = s$) and that the pressure in the reverse flow region is of the order of $-(P/r)$ (where P is the atmospheric pressure and r is the radius of curvature of the fluid-air interface. Therefore, the model can only describe the flow over the region $-\infty < x < s$ and not $s < x < c$ as shown in Figure 1.4(b). Savage[1982] recognised that both the Reynolds and the Separation condition were useful but applied to different regions of parameter space, the Reynolds condition being more appropriate as the modified Capillary number, $\beta = T/\eta U\,[H_0/R]^{1/2}$, tended to zero.

Several authors have attempted to develop simple analytical models which crudely incorporate the film-split meniscus into a lubrication model of the flow (Pitts & Greiller [1961], Williamson[1972], Taylor[1974a,b,c], Greener & Middleman[1975,1979], Savage[1982]). In their attempt to model the flow near the meniscus Pitts & Greiller assumed a parabolic free surface shape (based on experimental observations) while Williamson [1972], in his study of the tearing of an adhesive layer between two flexible tapes guided by cylindrical dies, approximated the meniscus by a 6th order polynomial. Greener & Middleman[1975] addressed the simplified problem of symmetric roll coating (i.e. equal roll speeds and radii) for which there is a stagnation point midway between the rolls on the fluid-air interface and where the velocity and velocity gradient is zero, i.e. $u = \partial u/\partial z = 0$. Savage[1982] extended the work of Greener & Middleman to the general coating situation of unequal roll radii and speeds using the Separation and Reynolds condition to formulate models for the prediction of coating thickness.

The discrepancy between film thickness predictions from the Separation model described above, and more recent results obtained both experimentally and numerically (by Benkreira et al [1981] and Coyle et al [1986] - see Chapter 4), prompted Sav-

age[1992] to question the validity of the zero tangential stress asssumption i.e. that $\partial u/\partial z = 0$, when S (the roll speed ratio, U_1/U_2) $\neq 1$. This has resulted in a more rigorous mathematical model which predicts the onset of recirculation as a stagnation point $(u, w) = (0, 0)$. Predictions are in good agreement with both experimental and computational results. A fuller account of this analysis is given in Chapter 4, together with a comparison between corresponding experimental data and numerical simulations.

Coyne & Elrod[1970,1971] proposed a new cavitation boundary condition which followed from matching the volume flux in the lubrication regime to that at infinity:

$$q = \int_0^{h(x)} u \, dx = U h^{\infty} \tag{1.7}$$

where h^{∞} is the asymptotic film thickness (at infinity). This arose from a two-dimensional study of the cavity-fluid interface formed (a) when a thin viscous film separates from a stationary surface and is swept away on an opposite moving surface and (b) under symmetric rolling conditions with both surfaces moving (see Figure 1.6). They proposed the following condition be applied at the cavity:

$$\frac{\partial p}{\partial x} = \frac{6\eta U}{h^2(c)} \left[1 - \frac{2h^{\infty}}{h(c)}\right] \tag{1.8}$$

By looking at the steady flow from the meniscus to infinity they were able to determine $h^{\infty}/h(c)$ as a function of the Capillary number, thereby confirming Taylors[1963] experimental results that the volume flux is dependent on the Capillary number. Greener & Middleman[1979] showed that over the range of modified capillary numbers encountered in typical roll coating applications (i.e. $0 < \beta < 1$) the agreement between the Prandtl-Hopkins Separation condition and the Coyne-Elrod condition in predicting film thickness, for the case of symmetric roll coating, is quite remarkable.

Numerical Simulation

The intractibilty of a full two-dimensional coating flow by standard analytical tools has led to a great deal of interest in the numerical solution of such problems. In any numerical solution, the differential equations governing the flow must be converted into approximate algebraic equations in which the physical quantities required (e.g. fluid velocity and pressure) are expressed as discrete values at a number of spatial points (nodes) within the flow domain. These equations are then solved using a suitable solution algorithm. The primary difference between numerical techniques lies in the way in which the governing equations are recast in either a differential or integral form (see, for example, Chen[1991]).

The Finite Difference (F.D.) method, used extensively in Computational Fluid Dynamics, approximates the differentials arising in the governing equations by finite differences (see Roache[1972], for example). Unfortunately this method is generally unsuitable for irregular shaped flow domains, as is the case in free surface coating flows, because of the problems encountered in constructing finite difference approximations on irregular grids.

A second method which has been employed for free surface flows is the Boundary Element (B.E.) technique, used for example by Kelmanson[1983] for the 'die- swell' problem. Although this method has the topological flexibility required in the solution of free surface problems and is cost-effective, since only boundary information is evaluated, the governing equations must be linear (i.e. the method is only applicable to zero-Reynolds number or inviscid, irrotational flow). Therefore this technique is not suitable for the solution of practical free surface coating flows.

The Finite Element (F.E.) technique is the most commonly used numerical method for solving free surface flow problems. This method has great topological flexibility and it can accommodate nonlinear terms in the governing equations. It is preferable to use a 'Primitive Variable' , as opposed a Vorticity-Streamfunction, formulation (see Zienkiewicz[1977], Huebner[1975]) for the solution of free surface flows. Using the former method, free surface boundary conditions given in terms of the pressure are readily accommodated, and the velocity and pressure fields are calculated directly. A comprehensive historical review of F.E. analyses of coating and coating-related flows with particular regard to the problems encountered in dealing with free surfaces is provided by Thompson[1992].

A notable contribution to the advanced application of the F.E. technique to free surface flows was made by Ruschak[1980]. He proposed a free surface location method, which he called the 'Boundary Supports' technique. This technique was later refined by Kistler[1983] and termed the 'Spine' method. This work has led to a significant improvement in the parameterisation of free surface boundaries by the F.E. method and practically all subsequent computational studies of coating flows have been based on this approach. The techniques for tackling the free surfaces have been discussed thoroughly by Kistler & Scriven[1983].

With regard to roll coating, Ruschak[1982] seems to have been the first to seek a numerical solution of the full two-dimensional flow between a pair of partially submerged counter-rotating rolls, by formalising Taylor's[1963] proposal that the flow can be divided into a lubrication-type flow in the vicinity of the nip and a two-dimensional flow in the vicinity of the meniscus. He obtained a numerical solution for the two-dimensional free surface region, and using the method of matched asymptotic expansions this led directly to the specification of the boundary conditions on pressure and pressure gra-

dient at the point of formation of the cavity. This subsequently allowed the solution to the portion of the flow described by lubrication theory to be completed. Ruschak's analysis is however restricted to flow between a pair of rolls in the limit $H_0/R \rightarrow 0$ i.e. the limit of parallel roll surfaces in the film-splitting region.

Coyle, Macosko & Scriven [1982] developed a generally applicable F.E. analysis of the fully-flooded equal roll speed case; predictions compared well with the experimental meniscus location results of Pitts & Greiller[1961]. This was then extended to asymmetric forward roll coating of a Newtonian fluid (Coyle, Macosko & Scriven [1986]) and to non-Newtonian fluids (Coyle, Macosko & Scriven [1987]). Coyle, Macosko & Scriven [1990b] have successfully tackled the reverse roll coating case, as well as forward roll coating with deformable rolls (Coyle[1988a,b]). The F.E. formulation also lends itself well to analysis of stability; this is illustrated by the stability study of symmetric roll coating performed by Coyle et al [1990b].

This approach has produced some of the most detailed and accurate predictions of roll coating flow, including complete two-dimensional velocity and pressure fields and meniscus location. Within the last decade rapid advances in the sophistication of such techniques has been made possible by the increased speed and power of computers. The convenience of this method is clear; each of the physical system parameters, such as viscosity or Capillary number for example, can be varied to see the effect on the flow, giving detailed results throughout the flow domain. In addition, this approach can accommodate the typical nonlinear rheological behaviour of industrially coated liquids (e.g. Coyle et al [1987]).

It is apparent, from the current literature on coating processes, that there is an enormous amount of numerical modelling of such flows in progress, but relatively little

analytical modelling and even fewer recent experimental investigations. Increasingly, it seems that numerical results for particular coating systems are treated as being the physically correct ones, rather than as simply a set of theoretical predictions, subject to certain underlying assumptions. It must be said, however, that the highly advanced F.E. modelling of coating flows by the aforementioned group of authors, in particular, has aroused great interest amongst the international coating community. The full F.E. results of reverse roll coating presented by Coyle et al [1990b] are a good example of how this technique can predict unexpected behaviour in a coating flow; these findings and their implications are discussed more fully in chapter 7. In all the above analyses a fully-flooded inlet has been assumed.

Therefore, numerical modelling of this complex class of problems is a cost-effective way to explore the development of the flow in detail without the need to perform 'expensive 'and 'time-consuming' experiments at each stage. It is essential, however, not to loose sight of the importance of experimentation in 'steering' the application of such techniques.

1.2.2 Experimental Investigations

The similarity between the gear geometry investigated by Gatcombe[1945] and that of a two-roll coater led several authors to perform a series of experiments and make observations of the behaviour of liquids between rotating rolls. These include Banks & Mill[1954], Miller & Myers[1958], Myers, Miller & Zettlemoyer[1959], Myers & Hoffman[1961] and Floberg[1964]. Myers & Hoffman recognised three consecutive flow regions in the nip of a high speed disc-cone geometry; an upstream region containing a bank of fluid rejected by the nip and in 'turbulent' motion, a central laminar flow region, and a downstream region characterised by flow of liquid under tension with a serrated or filamentous free boundary.

In studying the flow in a plate-roll geometry Pitts & Greiller[1961] and Van de Bergh [1974] reported a single eddy ahead of the downstream fluid-air interface. This result is reproduced here (see Chapter 5) using the flow visualisation techniques described in Chapter 3. The presence of the downstream recirculations in forward roll coating were first reported by Pitts & Greiller[1961] using a crude flow visualisation technique, whereby small air bubbles were introduced into the flow (Figure 1.7 shows this eddy structure clearly). Their result for the flow pattern was identical to that predicted by Jeffrey's[1922] analytic solution, near to the roll surfaces.

Schneider[1962] carried out an experimental/theoretical investigation of unequal speed roll coating. In particular, he performed a flow visualisation study using transparent roll end-dams, and obtained streamline patterns and velocity profiles, by means of a manual frame-by-frame analysis of the motion of opaque particles in the flow, for various roll speed ratios. He also produced qualitative results for the pressure distribution by assuming that any positive/negative deviation in the measured velocity profile, between the rolls, from that of a linear velocity profile was indicative of a corresponding negative/positive pressure.

Much of the experimental work in roll coating has focused on the instabilities experienced in such processes, in particular the phenomenon of ribbing first reported by Chalmers & Hoare [1941]. Other notable authors in this area have included Pearson [1960], Pitts & Greiller [1961], Floberg [1965], Carter & Savage [1987], and Coyle [1984]. Carter & Savage, for example, proposed a model for the onset of ribbing, the predictions of which were verified experimentally. Coyle[1984] however, has cast some doubt on the validity of experimental observations of the onset of ribbing recorded by eye.

More recently Adachi, Tamura & Nakamura [1988] addressed coating flow instabilities using a stationary plate-roll geometry and concluded that rib disappearance can be achieved by a combination of a displacement of the downstream contact line with a change in the contact angle. In practice, there are two possible ways of achieving this; (a) make the downstream diverging flow region shorter, as seen in knife/blade coaters – see Figure 1.1(b) (the blade can be thought of as a stationary, 'truncated' roll), (b) control the dynamic contact angle, either by mechanical means, as in the case of reverse roll coating (see Figure 1.3(b)) or by modifying the surface tension of the fluid to lower the curvature of the meniscus. Chapter 7 gives a fuller account of the various instabilities observed in roll coating.

A number of authors have concentrated on the measurement of the film thicknesses/flow rate through the nip under various operating conditions, invariably using crude but effective mechanical devices, such as a scraper blade or needle micrometer (these techniques are described in Chapter 2). Pitts & Greiller[1961], Schneider[1962], and Hintermaier & White[1965] measured flow rate for an equal speed two roll coater. Pitts & Greiller found the non-dimensional flux, ϵ (here $\epsilon = 2Q/UH_0$, where Q is the volume flux of fluid per unit length of roll), to lie in the range 1.26 to 1.38. Sullivan & Middleman[1979] and Adachi et al [1988] measured flow rate for the zero speed ratio plate-roll configuration and obtained an average value of $\epsilon = 1.2$. Benkreira et al [1981] performed no less than 1500 experimental measurements of flow rate for a variable speed two-roll coater using rolls of differing radii and a Capillary number range extending from 0.03 to 15, and found $\epsilon = 1.31$ with a standard deviation of 0.4%. They concluded h_1/h_2 to be independent of Capillary number, but strongly dependent on the roll speed ratio, S. The implications of these results are discussed in Chapter 4 and a comparison is made with theoretical and numerical predictions.

In combing through the literature, it is evident that there are few recent publications on fundamental experimental studies of coating flows. This can be attributed to the extremely difficult task of making observations and obtaining physical measurements of such high speed, small-scale flows contained within highly constricted geometries. A notable exception is the flow visualisation study of slide coating made by Schweizer[1988]. This investigation illustrates the importance and power of experimental analysis. Using a combination of flow visualisation techniques, including dye tracers and the hydrogen bubble method, he obtained elegant pictures of the associated flow field; in particular the results revealed the presence of unexpected recirculations within the flow. These recirculations had not been predicted by sophisticated F.E. analysis, because not enough was known about the physical structure of the flow (e.g. contact angles/locations). Once this experimental information became available, the modified F.E. analyses produced flow field results containing the observed recirculations, i.e. they were only then able to mimic the physical system.

It is often stated that numerical simulation is akin to performing a theoretical experiment on a computer. However, the above example illustrates that this can be far removed from the physical experiment, since the foundations of the numerical model often rely upon simplifying assumptions and boundary conditions. However one can see the attraction of such techniques in light of the tremendous difficulties involved in obtaining experimental information. Much of the experimental work presented in this thesis has only been made possible by the recent advent of High Speed Video and image processing technology, for example (see Chapter 3).

1.3 Meniscus (Ultra-Starved) Roll Coating

Until recently the fluid mechanics of rigid roll coating was thought to be well understood; however a new roll coating regime is revealed, which, although used in industry for a number of decades, appears to have escaped the attention of the coating community at large. Previous roll coating analysts have assumed that the inlet is always fully-flooded, which typically results in a rolling 'bank' of fluid upstream of the nip, often with visible backflow down the roll and into the bath (see Figure 1.8). Roll coating can, however, operate over a far wider range of 'inlet flux' conditions than has previously been considered. Looking at the two extremes of this inlet condition, Figure 1.9(a) shows the fully-flooded roll coating system, for which there is in effect only one meniscus downstream of the nip where the fluid splits into two layers. This is the accepted 'Classical Roll Coating' regime addressed by previous authors. Figure 1.9(b) on the other hand shows the same coating geometry but with a much reduced inlet flux giving rise to a second meniscus upstream of the nip. The latter case is referred to in this thesis as either 'Meniscus' or 'Ultra-starved' Roll Coating. The two conditions have different areas of application. Considering the practical engineering constraints on the minimum achievable uniform gap between a pair of rigid rolls (typically 100 micrometers), the fully-flooded process produces film thicknesses of the order of the gap size, whereas the Meniscus process can generate films an order of magnitude smaller than the gap size.

When the inlet is not fully-flooded it is said to be starved; starved inlets have been widely investigated in lubrication and elastohydrodynamic lubrication (E.H.L.) systems in particular. Wolveridge, Baglin and Archard[1971], for example, studied the effect of modest fluid starvation on the lubrication of two cylinders in line contact in both the rigid and E.H.L. cases. They modelled the degree of fluid starvation by al-

tering the upstream distance from the point of minimum roll separation at which the boundary condition $p = 0$ is applied. This was considered to be the point at which the lubricant pressure builds up. Lauder[1966] proposed a zero-reverse-flow boundary condition where pressure builds up at a location in the inlet defined by the condition $u = \partial u/\partial z = 0$. Oteri[1972], however, in his study of the inlet boundary condition found that the pressure build-up depended on the amount of lubricant available, and found no evidence to support Lauders' proposition.

Saman[1974] realised that it is important to define precisely what is meant by a starved inlet and proposed that a system is starved if all the lubricant supplied at inlet passes uni-directionally through the conjunction (i.e. there is no reverse flow at inlet or in the nip; that is to say the rolling bank of fluid is no longer present). This, coupled with the Reynolds boundary condition (see §§ 1.3.1) at outlet, enables theoretical prediction of load capacity for the starved case to be made. The above situation corresponds to modest starvation only. Roll coating can however be operated under conditions where the thickness of the inlet film is substantially less than that associated with modest starvation resulting in a 'bead' of fluid suspended in the nip region, and continuity considerations suggest that flow through the nip is essentially two-dimensional (i.e. for severe starvation uni-directional flow is impossible to attain).

As outlined in § 1.3 much of the difficulty in modelling Classical roll coating flow has resulted from uncertainty about the position and boundary conditions applicable at the film-splitting free surface. In assuming a 'thick' inlet film, applying the upstream boundary condition $p(-\infty) = 0$ is adequate. The Meniscus roll coating case however, with its relatively 'thin' inlet film resulting in the formation of a second upstream free surface which meets the web at a dynamic wetting line, presents a far more challenging problem.

1.4 Additional Complications of Free Surface Coating Flows

By their very nature, coating flows are free surface flows. Free surfaces are menisci, i.e. liquid/gas interfaces. A meniscus is a layer of finite thickness in which density varies rapidly from that of the bulk liquid to that of the bulk gas. However, its' thickness is usually no more than a few tens of Angstroms and is therefore negligible in comparison with fluid mechanical length scales. It is convenient to approximate menisci as mathematical surfaces. The steep density gradient at a meniscus, which is effectively a discontinuity, gives rise to a property known as surface tension which produces an isotropic *capillary* stress within the meniscus not unlike that in a stretched rubber membrane.

Any flow which is bounded by one or more free surfaces is influenced to some degree by their very presence. As the term 'free surface' suggests this boundary is to some extent free to move, that is to translate and transform, which in turn can dramatically alter the flow domain. The flow near a coating meniscus is nearly always two dimensional as is the case in roll coating. As well as the likelihood of the flow domain being highly irregular, viscous, inertial, surface tension and gravitational effects may all be important. The requirements to model such flows accurately are largely beyond the means of classical analysis. Hence it is the Finite Element method which features largely in the modelling of these flows – see Chapter 1, §§ 1.2.1. It is here, in particular, where experimental observations can make a significant contribution by providing evidence of interface location for numerical simulation, and in validating the results from such models.

Another feature common to coating flows is that they invariably contain three-phase

contact lines, formed at the intersection of two immiscible fluids with a solid boundary. Contact lines can be either:

1. **Static**, if the *apparent* point of contact is stationary (relative to the solid surface).

2. **Dynamic**, if the *apparent* point of contact translates (relative to the solid boundary).

Dynamic contact lines are also referred to as wetting lines. Every coating flow has a wetting line; liquid must come into contact with, and displace air from, a dry web, i.e. the sheet being coated. Most coating systems also have static wetting lines, although this is not the case in a simple two-roll coater (see Figure 1.10(a)). The slot coater illustrated in Figure 1.1(a) posseses a dynamic contact line and two static contact lines. The physics of dynamic wetting is therefore of considerable importance in the study of coating flows. However, not a great deal is known about the mechanism behind this fundamental coating phenomenon. A more detailed review of contact-line problems is given by Dussan[1979].

During coating, liquid displaces air from the surface of the substrate at the three-phase contact line where air, liquid, and solid meet (Figure 1.10(b)). When this region is magnified and viewed through an optical microscope, the liquid/air interface appears to intersect the substrate at a well defined angle. This angle is termed the *apparent dynamic contact angle.* Burley & Kennedy[1976] carried out an experimental investigation of the behaviour of a dynamic contact line, with particular reference to the mechanism of air entrainment. At very low speeds (of the order of millimetres/sec) the apparent dynamic contact angle equals the static contact angle. As speed is increased the apparent dynamic contact angle monotonically increases, ultimately reaching a nominal value of 180^o. Thereafter the previously straight wetting line adopts a saw-tooth shape (i.e. the wetting line breaks into inclined, straight sections). The flow

becomes three-dimensional and possibly also unsteady. At sufficiently high speeds air bubbles are entrained from the vertices of the sawtooth wetting line which are the farthest downstream. Burley & Kennedy present an experimental correlation for the onset of air entrainment, relating the critical air entrainment velocity, V_c, and the most fundamental of the liquid properties; $V_c = 1.14(T/\eta)^{0.77}$. O'Connell[1989] gives a full account of previous work related to static/dynamic contact angles in addressing the behaviour of contact lines with regard to the mechanism of air entrainment. In coating flows, therefore, it is generally necessary to avoid this critical condition, and consequently the factors which determine the dynamic contact angle are of great interest.

Modelling of the flow near the three-phase contact line is complicated by the 'apparent breakdown' of the classical hydrodynamic equations and/or boundary conditions in this region. Huh & Scriven[1971] examined the mutual displacement of two viscous liquids along a flat solid surface and showed that the equations and boundary conditions of classical hydrodynamics predict that the liquid flowing in the neighbourhood of a dynamic contact line exerts an infinite force on the substrate. This is clearly physically incorrect. They suggest that the classical no-slip boundary condition may not be valid near the wetting line. Dussan[1976] describes the motion of the displacing fluid near the wetting line as a rolling-type flow whilst the displaced fluid (e.g. air) undergoes a more complicated motion.

Several theoretical models have been proposed with the goal of removing the force singularity at the wetting line (Hocking[1977], Dussan V[1979], Cox[1986]) which is done by postulating slip between solid and fluid close to the wetting line. This introduces a slip length scale measuring the distance from the wetting line over which slip occurs. Very few models have attempted to explain why slip occurs near the wetting line but those of Ruckenstein & Dunn[1977] and Ruckenstein & Rajora[1983] propose a

slip mechanism in terms of the gradient of a chemical potential in the fluids. However the problems remain of finding a realistic model for slip and specifying a contact angle at the contact line.

Hansen & Toong[1971] realised that hydrodynamic forces can cause the slope of the meniscus to change rapidly near the dynamic contact line, and they predicted that these significant changes occur over distances too small to be resolved with an optical microscope. They conclude that, in general, the apparent contact angle is not equal to the actual contact angle and that much, if not all, of the variation in the apparent contact angle with speed can be attributed to 'hydrodynamic bending' of the meniscus very near the substrate.

Teletzke, Davis & Scriven [1984] modified the classical hydrodynamics equations to include the effects of the fluid microstructure over distances from the substrate so small (less than 1μm) that the liquid is no longer homogeneous. They predict that above a certain speed an air film is entrained which is at first so thin that the residual air is not likely to be detected. The thickness of the air film increases with further increases in speed. Thus an interesting physical question emerges; rather than deciding whether air is entrained, investigators should be asking whether enough is being entrained to be detected. Indeed, the presence of a thin air film separating the substrate from the liquid circumvents the singularity at a three-phase contact line, and this may justify slip near a contact line in macroscopic hydrodynamic models. The wetting line problem is a clear example of how theory struggles to make any headway when experimental evidence is not available. Experimental analysis itself is made extremely difficult by the sub-microscopic scale of this mechanism.

The major problem with free surface coating processes is the susceptibility to instabili-

ties caused by the disruption in the balance of forces at the free surface. This can range from a perturbed pre- or post-coated fluid film, leading to the formation of waves and therefore a non-uniform coating, to more complex instabilties relating to the nature of the flow between the two rolls, such as ribbing.

1.5 Outline of Present Work

In Chapter 2 a detailed description is given of how the key features of the industrial roll coating process can be translated into simple experimental apparatus, while retaining all the necessary elements and combining all the necessary techniques for in-depth study of the flow. The design, development and implimentation of novel experimental techniques, together with established methods, are discussed. A comparison of the performance of a number of film thickness measurement techniques is made, and particular attention is drawn to the problem of assessing an average film thickness on a rotating roll. Suitable working fluids are selected and the techniques used to measure rheological properties are briefly described.

Chapter 3 examines various flow visualisatiom techniques, and methods suitable for a two-roll coater system are described more fully. In considering the practical difficulties of obtaining good quality results of the flow field, the methods used to record and analyse the flow are described in some detail; with particular emphasis placed on image processing and High Speed Video systems. Finally, the unique use of a computerised particle tracking system in coating flow analysis is presented.

Chapter 4 focuses on the Classical, fully-flooded, roll coating regime. A number of flow visualisation images are presented which vividly convey the structure of the flow in the nip region, including the upstream bank. Such results do not appear to have been

published in the past – only schematic diagrams have been used to describe the experimentally observed roll coating flow field. One objective of this chapter is therefore to document the Classical roll coating flow field and in so doing establish certain unique characteristics which can be compared and contrasted with the Meniscus roll coating regime, presented in Chapter 5. The mathematical roll coating film thickness model proposed by Savage[1982], which rested on an intuitive argument, is reworked (Savage[1992]) with a more realistic set of boundary conditions, leading to a more rigorous film thickness prediction model. A 'start-up jump' predicted by this model is verified with experimental flow visualisation results. The effect of gravity on film-splitting is also investigated experimentally; for an equal speed two-roll coater, the outlet thickness on the upper roll is found to be less than that on the lower roll (Benkreira et al [1981]). Finally, experimental results are compared to analytical and finite element solutions of the flow (Thompson[1992]).

The Meniscus Roll Coating process is revealed in Chapter 5, and key results are presented for the unique streamline pattern and velocity field. This regime is compared to that of the Classical case and the marked differences discussed. A simple mathematical model, developed by Thompson[1992], is presented which gives surprisingly good agreement with the experimentally observed features of the flow, and an unexpected result for pressure within the flow domain. A simplified plate-roll experimental set-up, described in Chapter 2, is developed for specifically measuring pressures. Results are contrasted with those for the Classical roll coating condition and confirm the theoretical pressure distribution for Meniscus roll coating, as well as providing the position of the pressure profile with respect to atmospheric pressure. A film thickness model is also described, based on arguments about the fluid transfer path to the upper roll and the structure of the two-dimensional flow observed. This model agrees well with experimental results, and the expression for h_1/h_2 is found to be identical to that for

the 'new' Classical roll coating film-splitting model (Savage[1992]) which is described in Chapter 4.

The transformation of the flow from a Classical condition, to a Meniscus condition is considered in Chapter 6. The pressure profile results for the two coating regimes and the transformation from one to the other are presented, together with flow visualisation results of the transforming flow field. Several key theoretical predictions of the value of ϵ at specific points during the transformation are largely confirmed experimentally by analysing pressure measurements, flow visualisation results and free surface movement. A key result is the behaviour of the upstream free surface which moves in to a minimum point and then out again as the flux, ϵ, is steadily reduced, giving a non-singular result (i.e. there are two non-dimensional values of ϵ for each free surface position). Flow field results are presented for the plate-roll and two-roll (forward and reverse) cases.

Chapter 7 briefly addresses the subject of instabilities in roll coating; those found in both the Classical and Meniscus regimes. Simple modifications to the general experimental apparatus described in Chapter 2 allow the study of the occurence of these instabilities, albeit to a limited extent. Various 'new' instabilities are observed using the High Speed Video system, and tentative explanations for such behaviour are offered. The reverse roll coating regime is discussed with regard to a number of key experimental findings. Finally the implications of all the results presented throughout this work are discussed and consolidated, together with suggestions for future work.

The underlying theme of this thesis is to present the reader with a measure of the power and significance of experimentation, not only as a means of verifying theoretical results but more importantly in breaking new ground in what may appear to be well researched and well understood physical systems. Experimental research must be car-

ried out alongside, and in many cases ahead of, other approaches to establish certain ground rules and to give continuing insight into the physics of real systems. It is vitally important not to lose sight of the physics involved. The interplay between experimental, analytical, and computational disciplines can furnish far more insight into such systems than any single approach could ever hope to do. This is indeed the case in roll coating research.

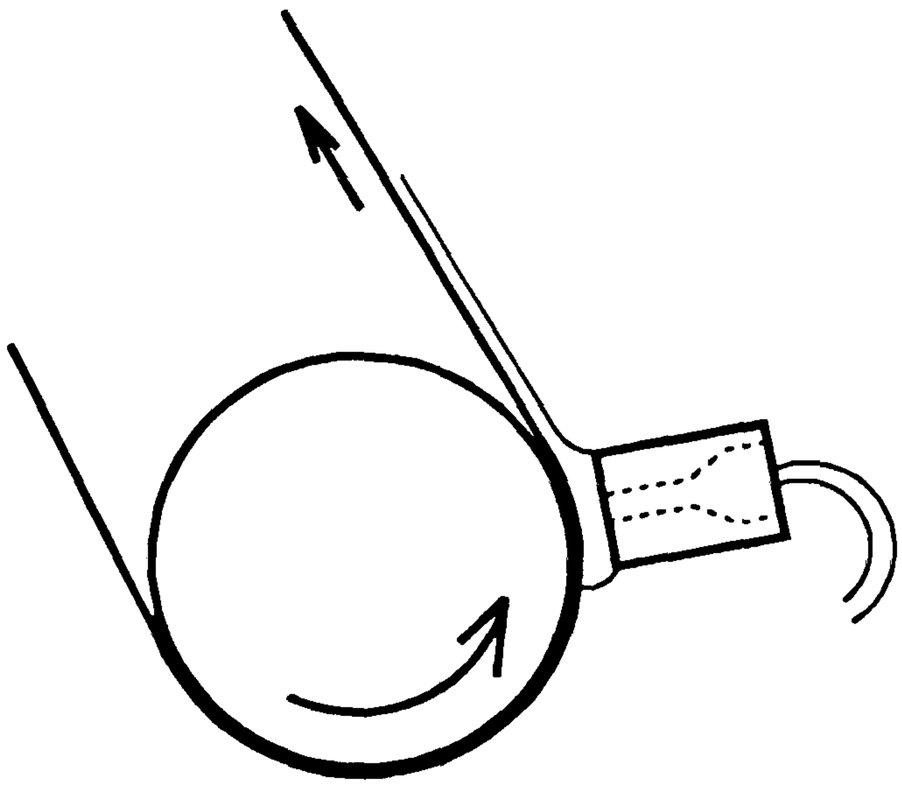

(a)

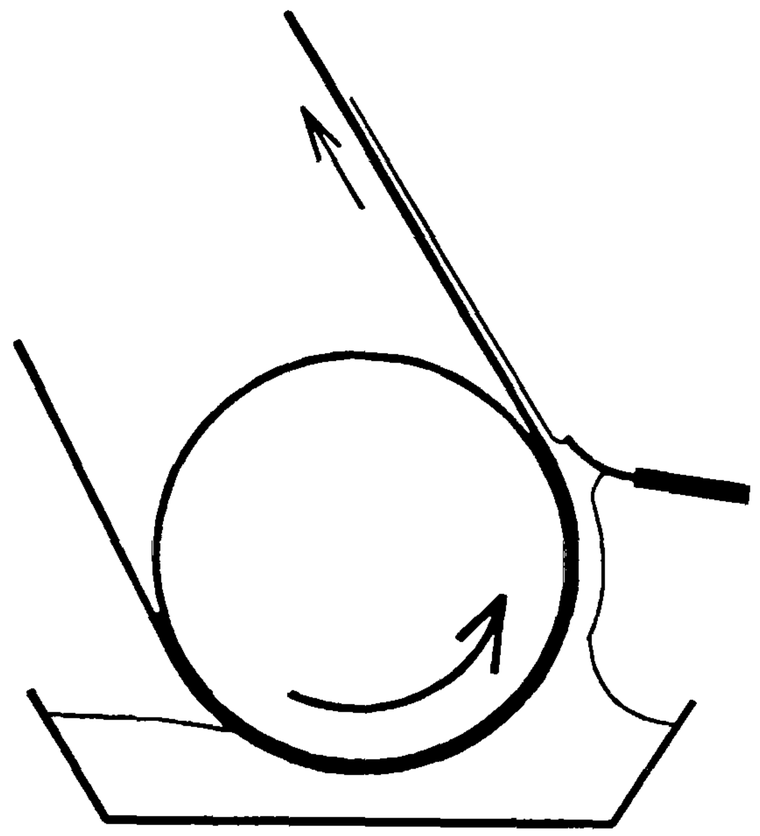

(b)

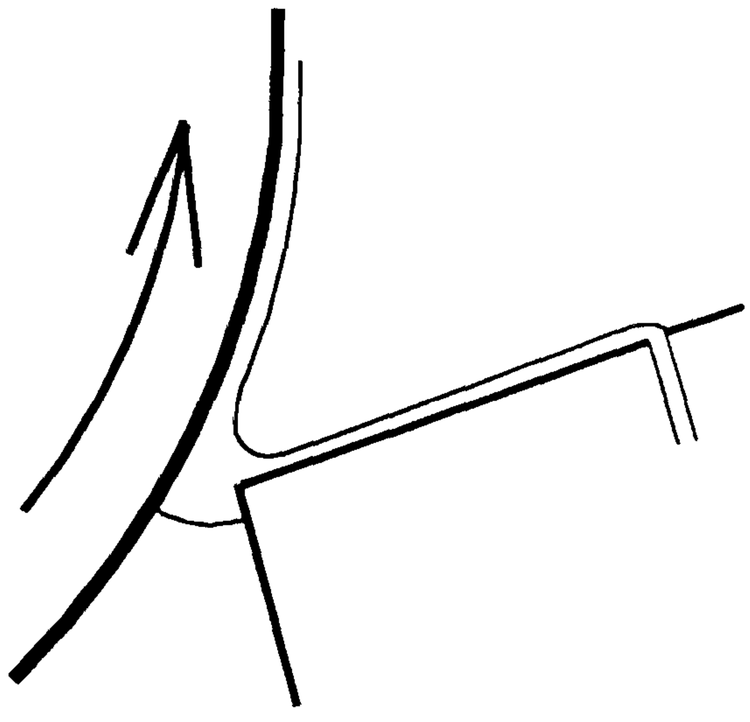

(c)

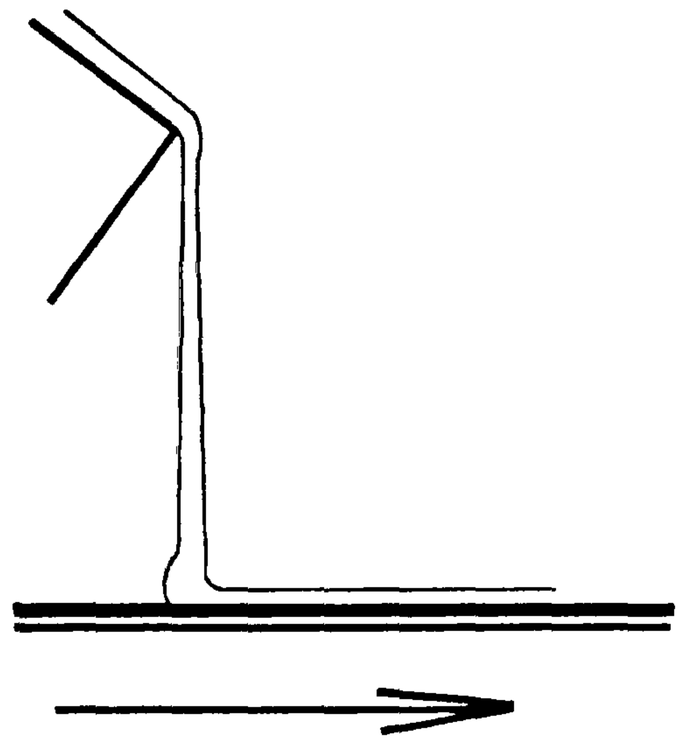

(d)

Figure 1.1: Other Common Coating Systems: (a) Slot coater, (b) Knife coater, (c) Slide coater, (d) Curtain coater.

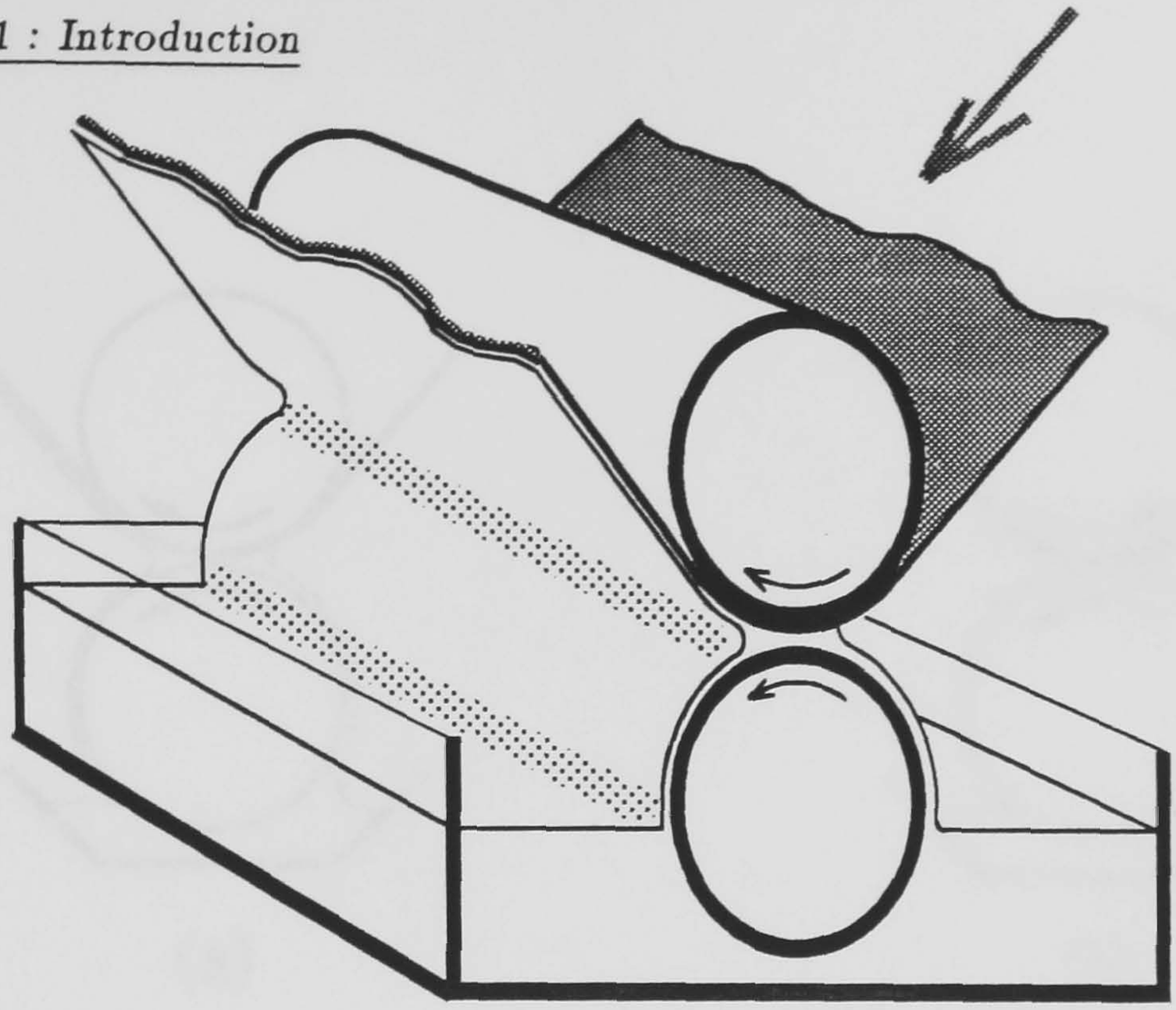

(a)

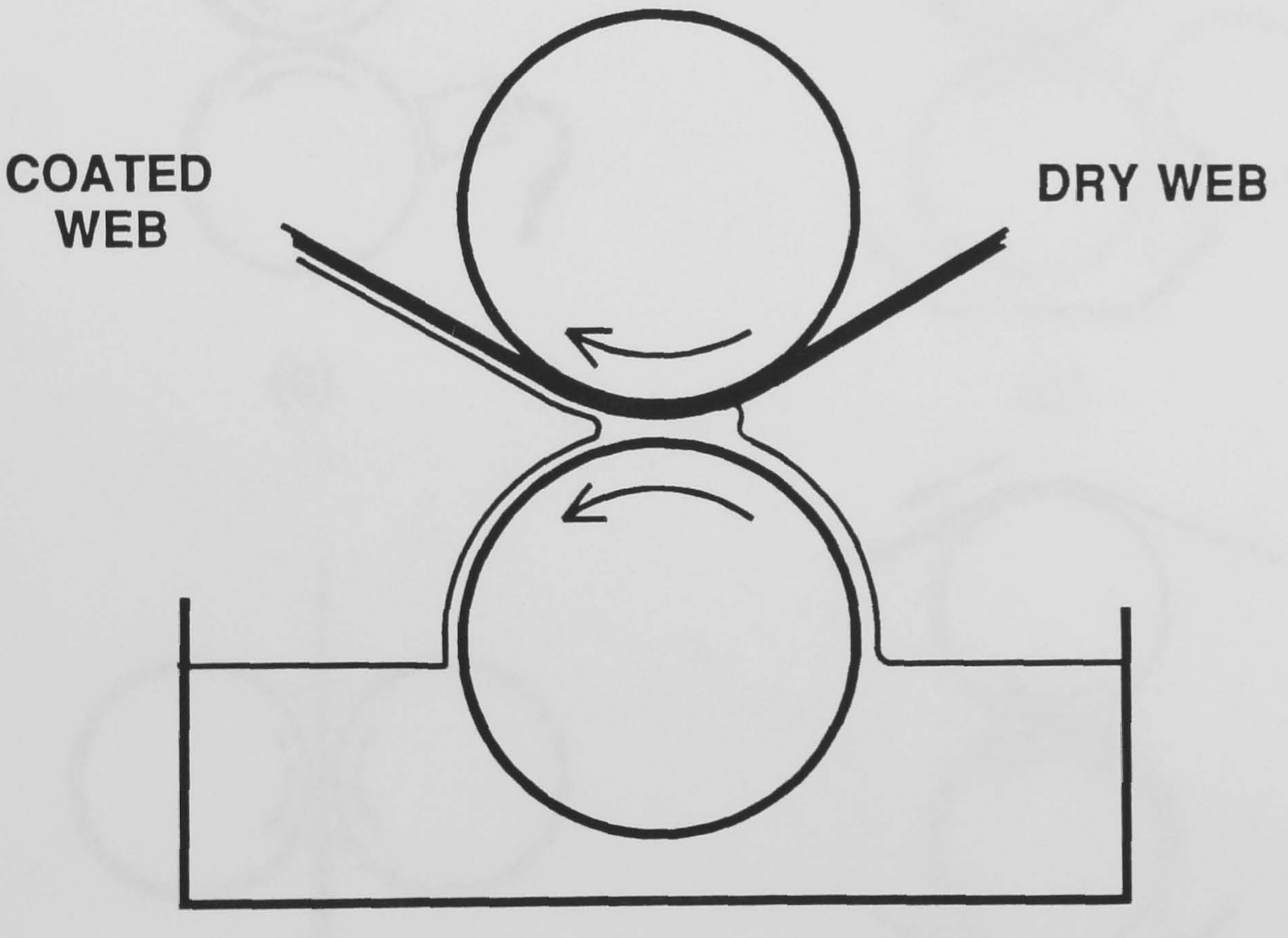

(b)

Figure 1.2: A Basic Two-Roll Coater (a) General view (b) Cross-sectional view

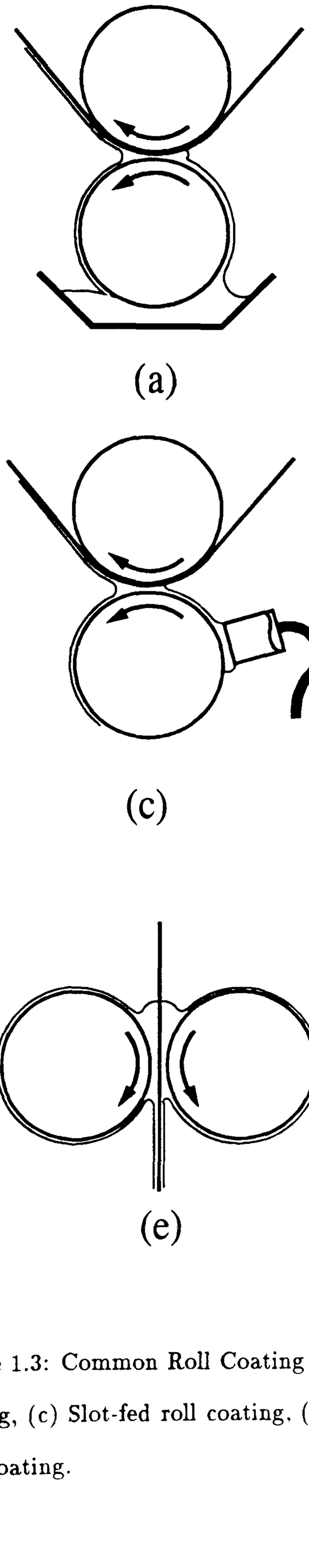

(a)

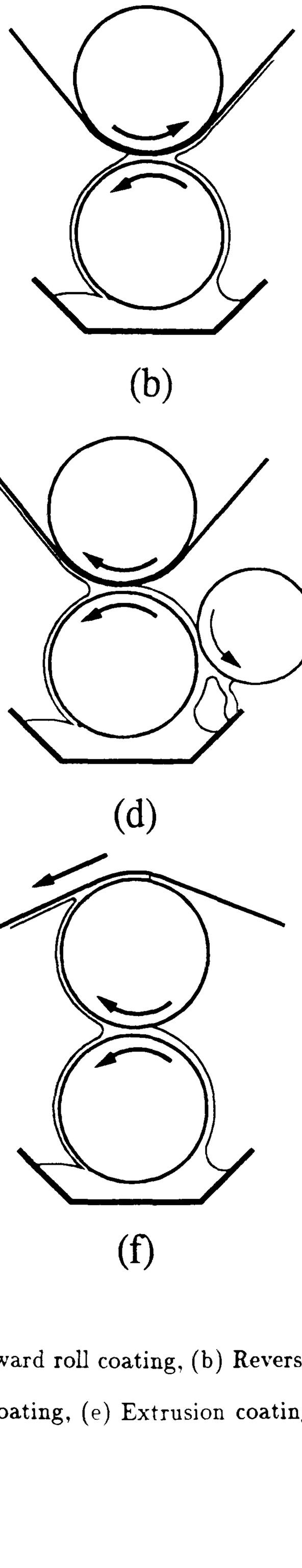

(b)

(c)

(d)

(e)

(f)

Figure 1.3: Common Roll Coating Systems: (a) Forward roll coating, (b) Reverse roll coating, (c) Slot-fed roll coating, (d) Metered roll coating, (e) Extrusion coating, (f) Kiss coating.

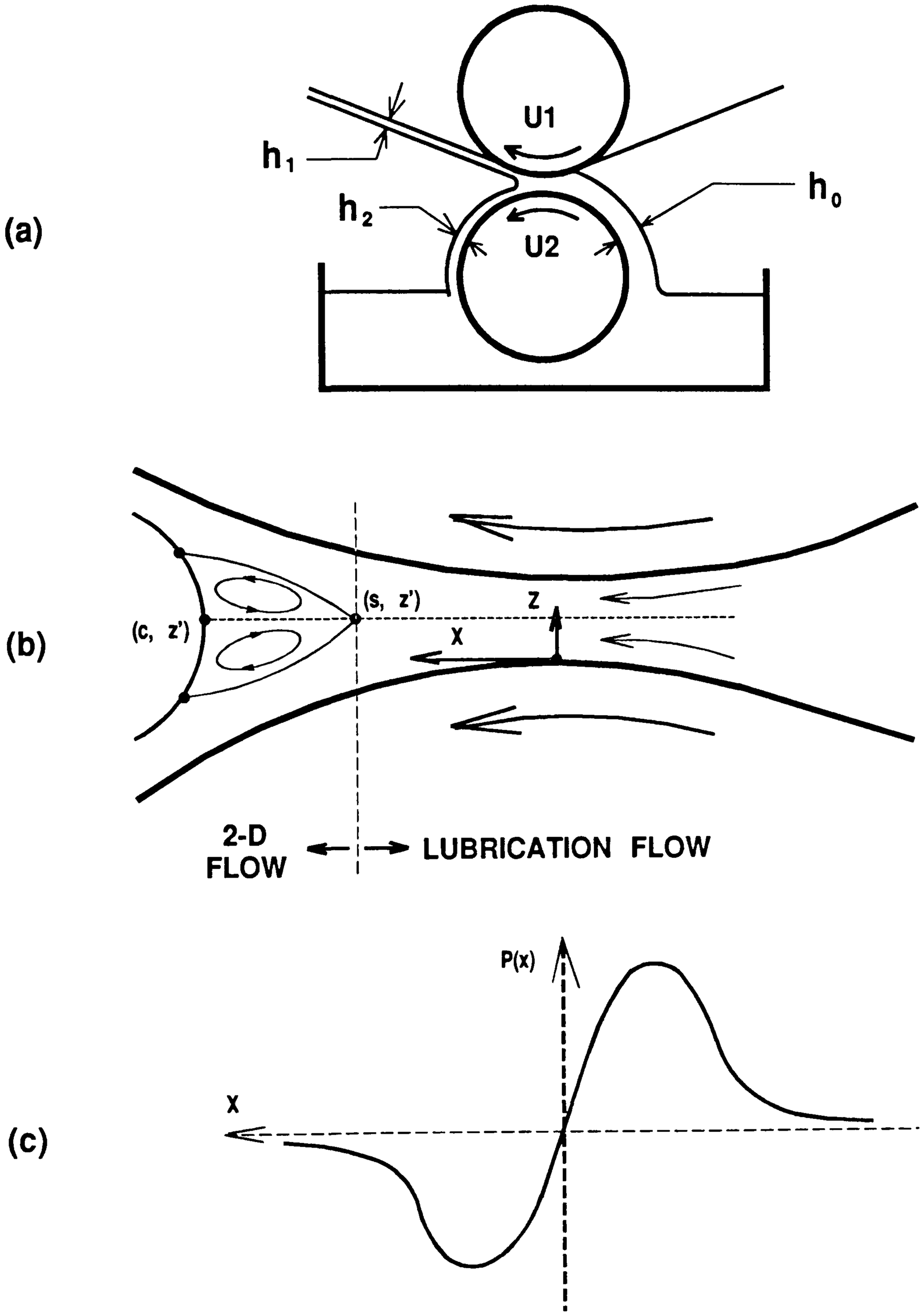

Figure 1.4: (a) Classical two-roll coater, (b) Roll nip flow, (c) Typical Pressure Profile.

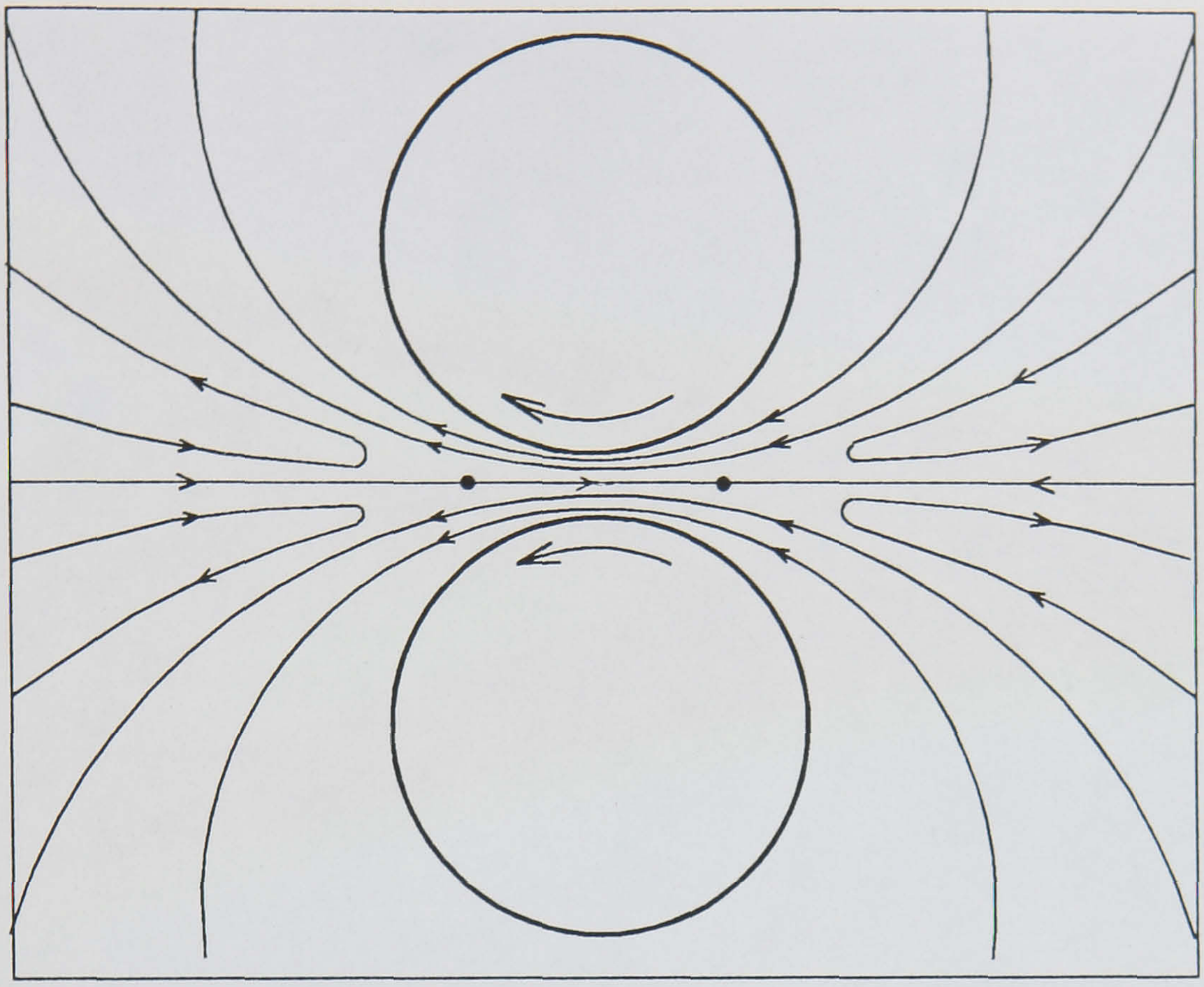

Figure 1.5: Jeffreys (1922) solution for flow between 2 counter-rotating rolls in an infinite 2-D domain

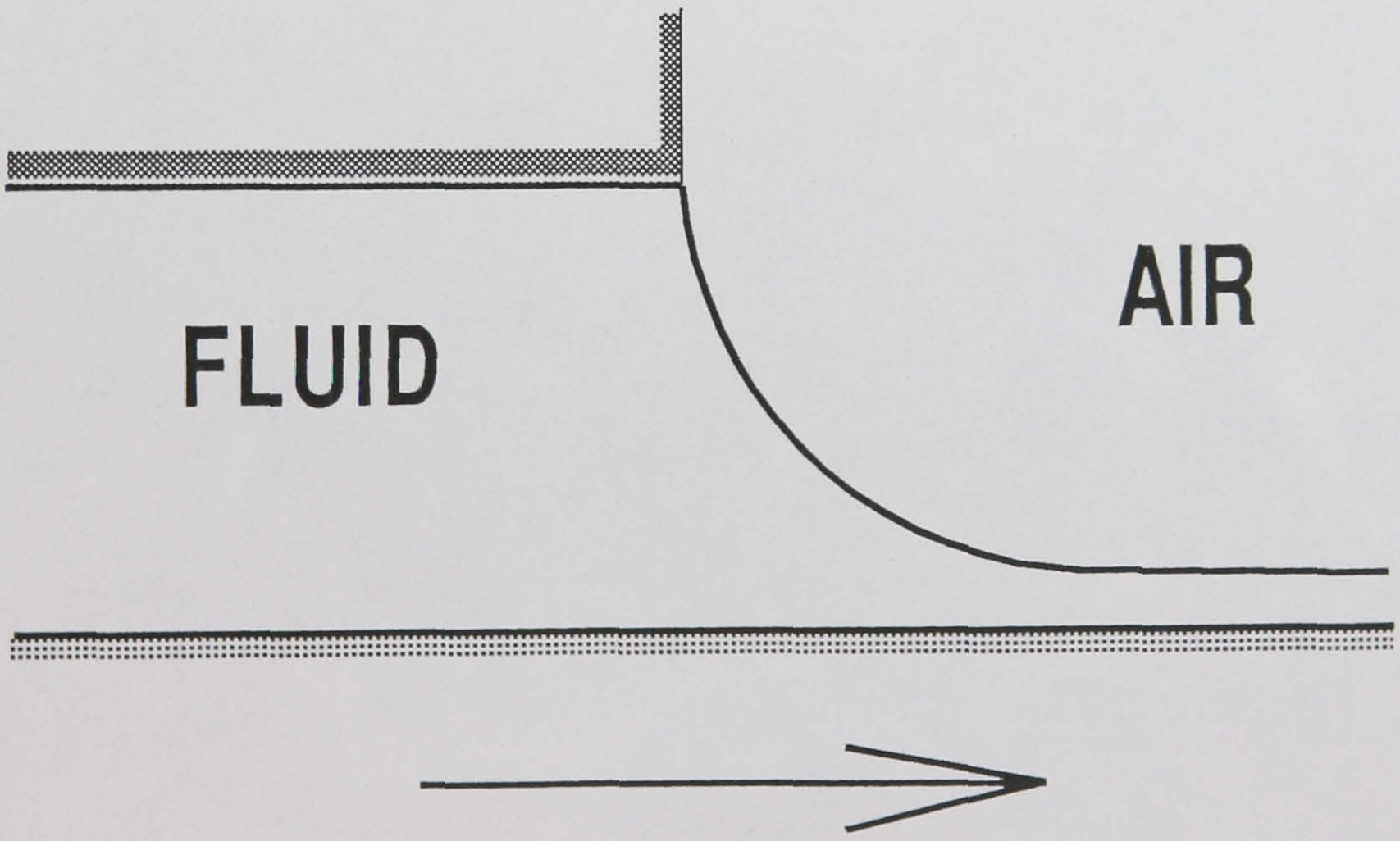

Figure 1.6: The Coyne-Elrod slider bearing geometry

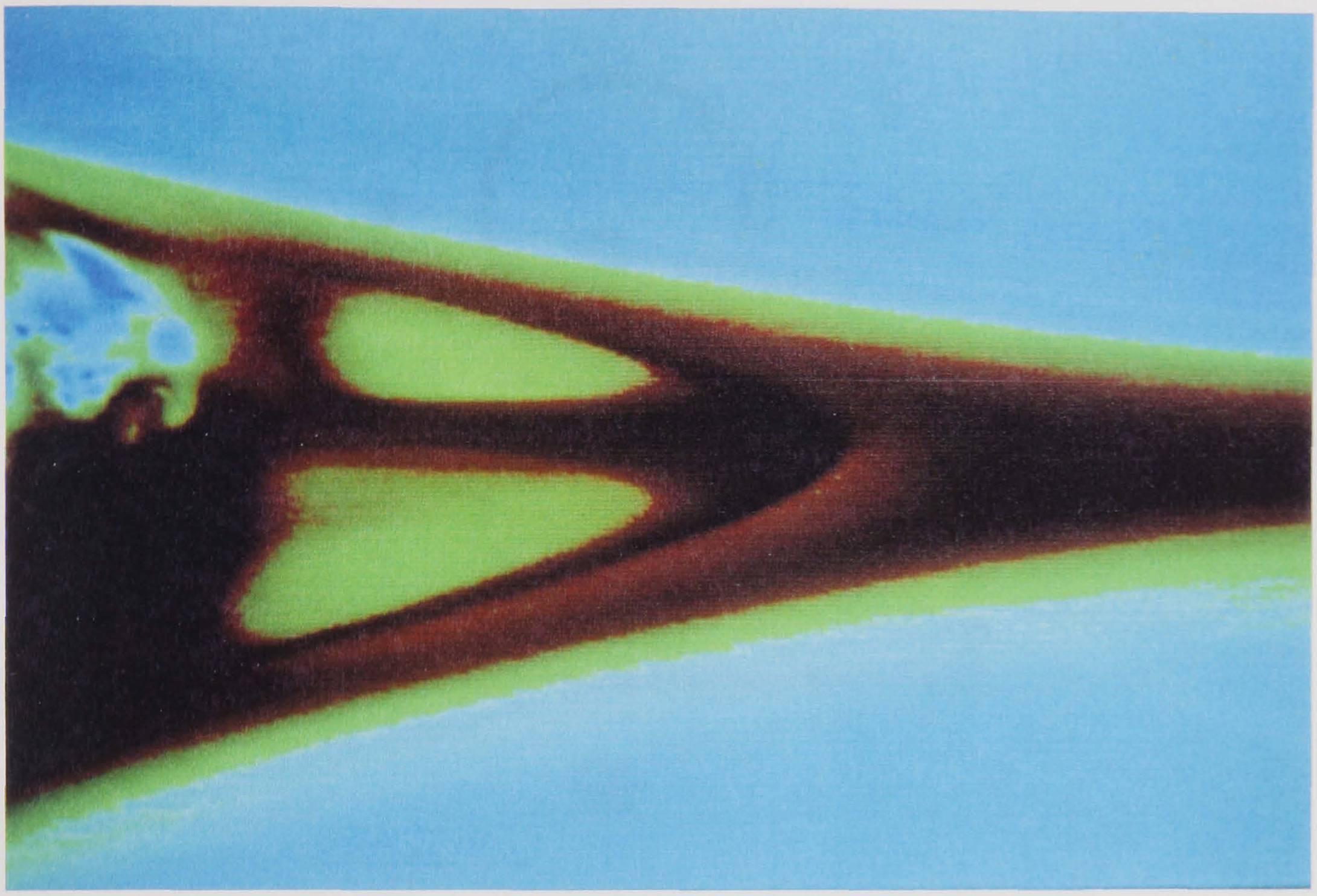

Figure 1.7: Downstream eddy flow in a two-roll coater

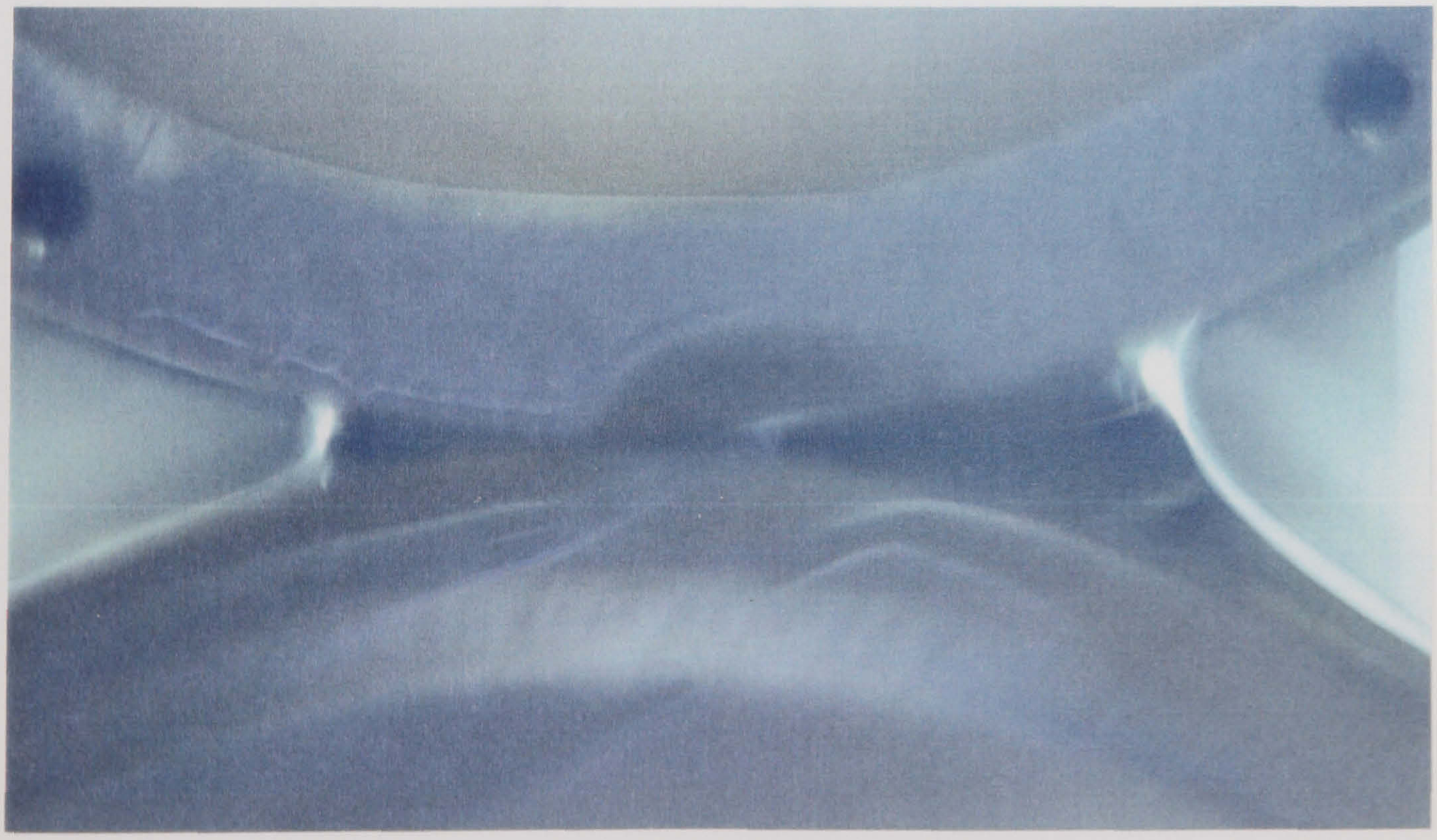

Figure 1.8: Rolling bank of fluid in Classical roll coating

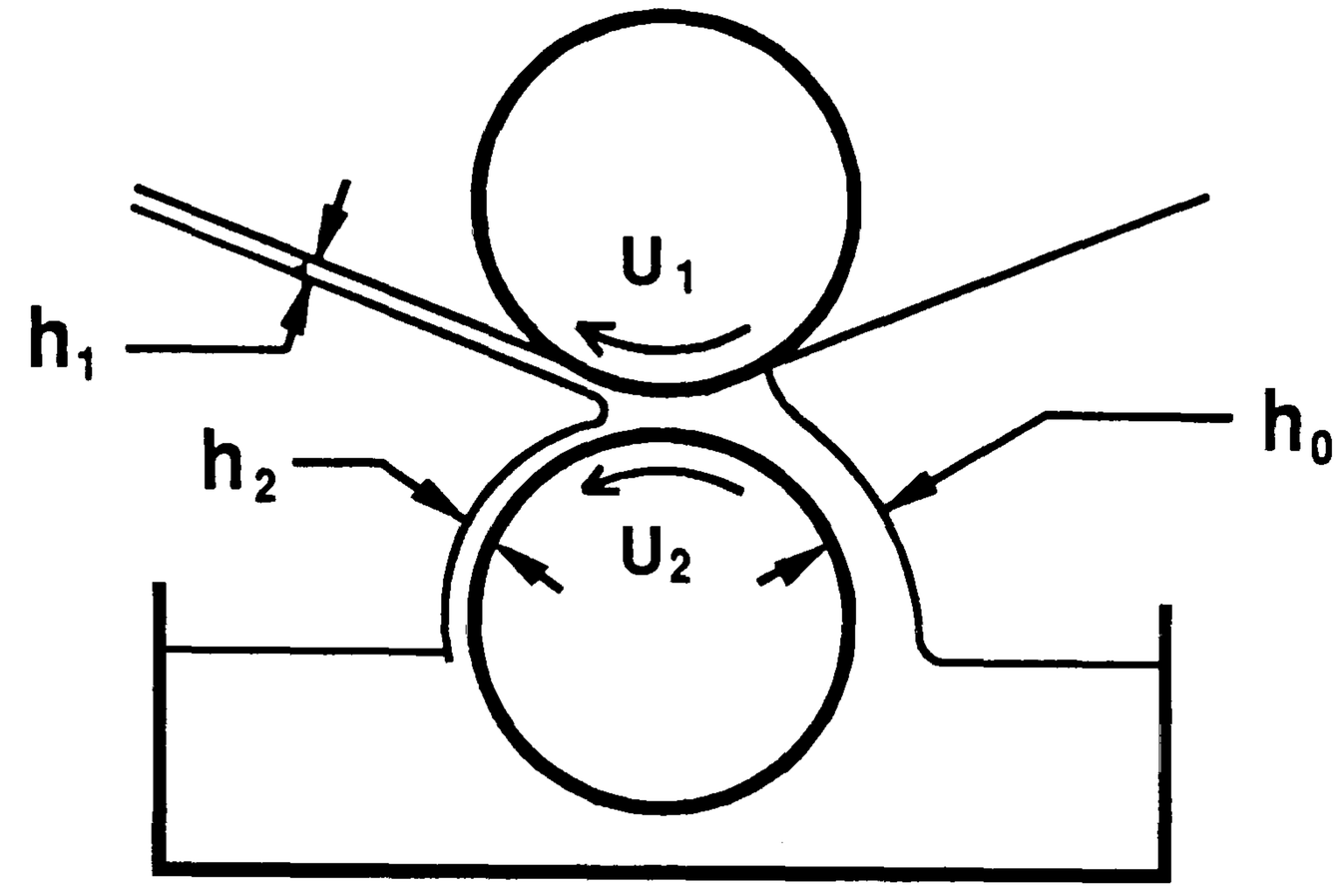

(a)

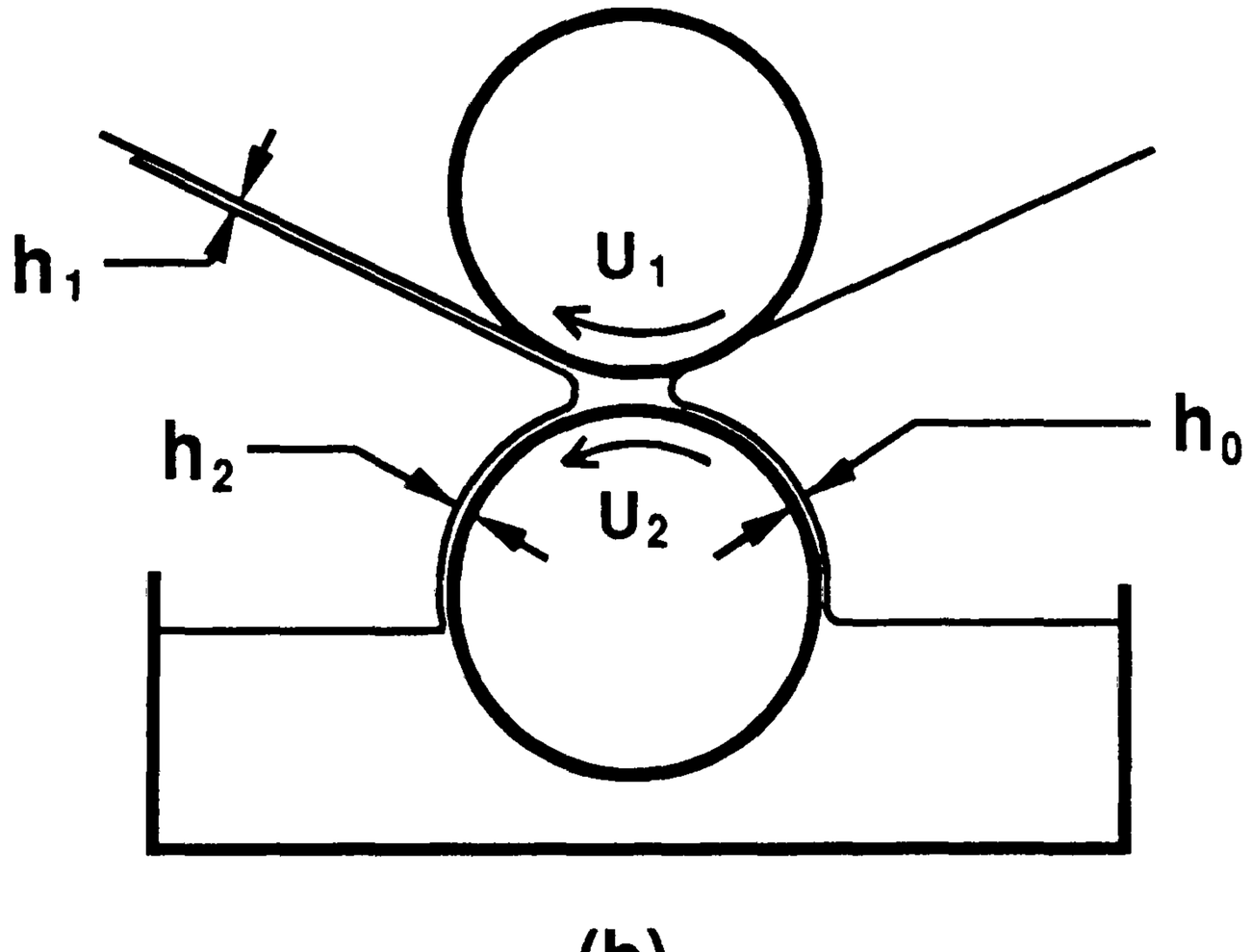

(b)

Figure 1.9: Schematic illustration of (a) Classical (Fully-Flooded) Roll Coating, (b) Meniscus (Ultra- Starved) Roll Coating.

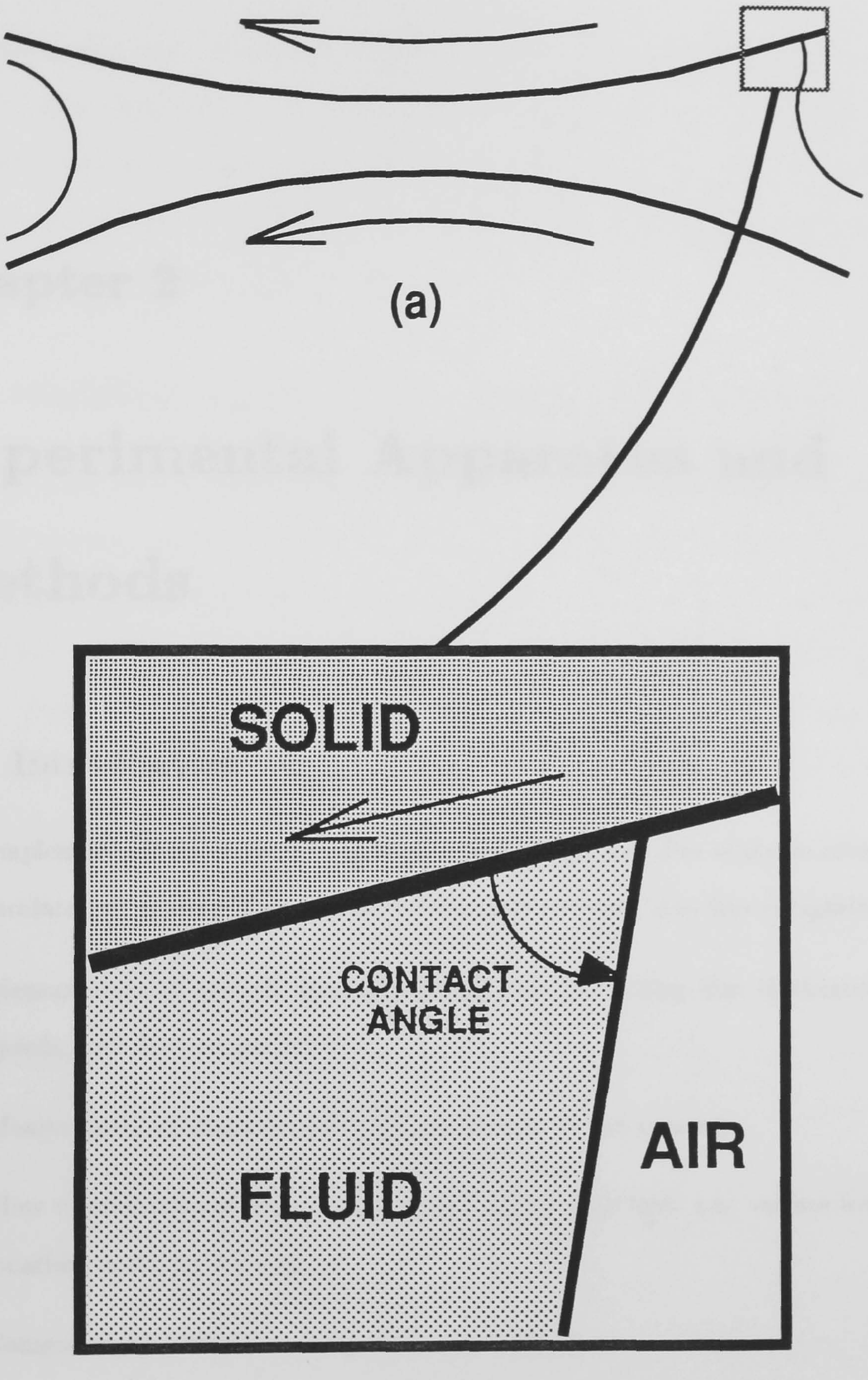

Figure 1.10: Dynamic Contact Line in A Two-Roll Coater

Chapter 2

Experimental Apparatus and Methods

2.1 Introduction

The complement of experimental techniques used throughout this study to investigate and elucidate roll coating flows can be conveniently grouped into four categories:

1. Measurement of system operating parameters (including film thicknesses, roll speeds, and fluid properties).

2. Measurement of characteristic pressure profiles in roll coating.

3. Flow visualisation of the roll nip (including dye injection, free surface form and location, and particle seeding).

4. Computerised particle tracking of the seeded flow.

To achieve meaningful, rigorous experimental results for each of the above required the design and development of specialised equipment and procedures.

The development of a general roll coating apparatus for investigating various flow regimes is now explained in some detail. The case for a second experimental system to measure pressures in such flows is made, and the subsequent design of this apparatus described. The associated flow visualisation and computerised particle tracking techniques are presented in Chapter 3.

2.2 Modelling the Industrial Roll Coating Process

In general an industrial coating machine may consist of two, three or more rolls for a particular coating operation, where the additional rolls are used for feeding and metering of fluid. To analyse such a complex system it is useful to break it down into a series of fundamental processes; in particular the flow in the nip between a single pair of rolls. Once the component processes are well understood, it is a relatively simple task to address the interaction of pairs of rolls since, for example, the predicted output from a given set of rolls will provide the input for the next set.

Fluid, which is taken onto the applicator roll by means of viscous lifting from a bath (see Figure 1.1(a), for example), is generally metered. Two examples of metering systems are doctoring (i.e. using a doctor blade as in Figure 1.3(b)) and 'three-roll reverse' (see Figure 1.2(d)). Another common method of 'feeding' the nip is to use a slotted coating head (see Figure 1.2(c)) with the subsequent removal of excess fluid by scraping. Metering is necessary, to some extent, to control the output film but also to avoid instabilities. For the purposes of the present study the fluid mechanics of such ancillary processes are not considered (although the metering roll in the three-roll-reverse system is simply an angled reverse roll coater). The thrust of this investigation is directed towards the fluid mechanics in the region of the coating nip itself.

A doctor blade is also one of several options available for use as an effective means of transforming the coating regime from a fully-flooded to ultra-starved inlet mode and vice versa, by controlling the inlet film thickness (a full account of the alternative methods is given in Chapter 6). It can also be used to maintain a particular regime when, for example, it is necessary to vary the applicator roll speed (since, for viscous lifting, the entrained film thickness is proportional to roll speed). The two-roll coater apparatus designed for the purpose of this investigation is described in subsequent sections.

2.2.1 Dimensional Considerations

There are a number of important roll coating operating parameters which must be considered as part of the process of designing a flexible experimental roll coater.

The fluid flow in a geometry such as the nip between two rigid rolls is maintained by a balance of forces. The important forces in roll coating are:

1. **Viscous Forces** – shear-driven (drag) plus pressure-driven flow in a converging/diverging geometry.

2. **Surface Tension/Capillary Forces** – the result of surface tension at a curved fluid-air interface.

Although, **Gravity** and **Inertia** forces may influence the flow to some extent.

The balance of viscous and surface tension forces, and a consideration of the roll coating geometry leads to two important dimensionless groups:

1. **Capillary Number** – $Ca = \eta U/T =$ viscous/surface tension force ratio.

2. **Geometry 'Number'** – $H_0/R =$ minimum gap size/average-roll-radius ratio.

A typical Capillary number for Classical roll coating lies in the range 0.1 to 10. In the case of Meniscus roll coating the value is generally an order of magnitude smaller due to a combination of reduced roll speeds and the use of lower viscosity fluids.

Inertia forces, on the other hand, only really become significant for ultra high speed coating operations (of the order of hundreds of metres per minute web speed). Reynolds number, Re, is a dimensionless quantity which gives an indication of the relative importance of viscous and inertia forces in a fluid system:

$$Re = \frac{INERTIA\ FORCES}{VISCOUS\ FORCES} = \frac{\rho U \frac{\partial u}{\partial x}}{\eta \frac{\partial^2 u}{\partial z^2}} = \frac{\rho U z^2}{\eta x} = \frac{\rho U H_0^2}{\eta (R H_0)^{1/2}} \qquad (2.1)$$

For the Classical roll coating regime the Reynolds number is typically of the order of 0.1.

When considering the Meniscus roll coating regime, it is not obvious which dimension to choose as a typical z-direction length scale. It might be argued that the minimum roll gap should still be taken as the characteristic length. However, the difference between Meniscus and Classical roll coating flow is the reduced inlet thickness of the former (as well as the speeds, in general) and therefore it could be argued that the inlet film thickness is an appropriate characteristic length scale bearing in mind, when considering the forces involved, that this thin layer carries the 'inertia' into the system. Therefore, taking the inlet film thickness as the typical length scale, which regardless of the above argument is the most appropriate since it distinguishes between the degree of flooding/starvation in roll coating flow, Re is found to be typically of the order of 0.005.

The above argument demonstrates clearly that it is the Capillary number which is the important nondimensional parameter in the roll coating flows of interest here. Indeed, as we shall see, the Capillary number becomes increasingly important as one moves from the Classical to the Meniscus roll coating regime.

Also, the operating speeds of roll coating processes can vary enormously. Line speeds (i.e. taking the simple two-roll coater; this is equivalent to the upper roll speed) for Classical roll coating can range from tens to hundreds of metres/minute (this is the accepted unit for describing 'throughput') with a roll speed ratio, S, typically greater than 1. For Meniscus roll coating processes, line speeds are typically of the order of tens of metres/minute with a roll speed ratio of the order of 3.

2.3 General Experimental Apparatus

2.3.1 Cantilevered roll configuration

The primary aim of this investigation was to observe the flow field within the nip of a two-roll coater and to that end a cantilevered roll system was considered to be the most appropriate design to adopt. Figure 2.1 shows the main features of this apparatus. The major advantage of such a configuration, compared to a more conventional system with the rolls supported at both ends, is far greater accessibility to the nip region. The rolls themselves can be detached from their respective steel shafts to allow ease of roll interchange. A number of rolls, manufactured from different materials were envisaged. Each roll shaft is supported in a housing by two high precision roller bearings, separated by a suitable distance so as to minimise bending and vibration of the shaft and thus the disturbance of the roll position.

2.3.2 Design of rolls

For the purposes of flow visualisation several lower/upper roll configurations could be achieved:

- Steel/Steel roll

- Steel/Hollow acrylic roll
- Acrylic/Hollow acrylic roll

The steel rolls were manufactured from stainless steel because of its excellent anti-corrosion properties. To obtain a suitable surface finish they were ground and polished. The use of acrylic rolls meant that the nip could be illuminated far more effectively. The support shafts were ground on the roll location diameter, and the rolls themselves were bored to obtain a precision H6 fit (see BS4500) in order to minimise roll runout. All roll diameters were finished on their respective support shafts to ensure concentricity. The maximum error in roll eccentricities was estimated to be 5 micrometres.

The design of a hollow acrylic top roll facilitates viewing of the fluid bead from above for the purpose of investigating instabilities (see Chapter 7 and Figure 7.2). Looking vertically down through the upper and lower 'walls' of this cylinder is equivalent to looking through two flat plates, over the very small extent of the fluid bead. Or, by using a small angled mirror, it is only necessary to look through one wall. The specified roll wall thickness must be sufficient to maintain rigidity during machining to avoid an excessive roll eccentricity. The acrylic roll surfaces were polished (including the inner surface in the case of the hollow roll) to obtain a glass-like finish. In addition the hollow upper roll was so designed to accommodate a 'viewing disc' which was necessary to visualise the flow in the nip (see Chapter 3, §§ 3.2.1). To overcome the problem of attaching a viewing disc to the hollow upper roll and in so doing distorting it to some degree, an acrylic roll was manufactured with an integral viewing 'flange' (illustrated in Figure 2.2). The upper roll support shaft was shorter to allow vertical viewing of most of the fluid bead through the hollow upper roll. For the purposes of flow visualisation, the optical quality of acrylic was found to be adequate for the present study; if this had not been the case, polycarbonate was available as an alternative.

After preliminary tests with suitable fluids, for various roll diameters, a diameter of 25mm was found to give the necessary radius of curvature to produce a reasonably low aspect ratio of bead width, W_0, to height, H_0, (see Figure 2.3) over a wide range of speeds/speed ratios for obtaining good, clear images of the flow field. Roll diameters are typically twice this size in industry. Three factors were considered in choosing the length of the rolls. Firstly, the necessary optimum viewing depth for flow visualisation (see Chapter 3). Secondly, the roll length required to model the industrial process accurately (i.e. the longitudinal aspect ratio L_0/H_0 must be large). Thirdly, a moderate roll weight to minimise deflection and vibration at high roll speeds. The chosen length of 35mm gave a more than adequate bead length/gap aspect ratio (e.g. L_0/H_0 =100, for a typical gap size of 350 micrometers) as well as a very compact design.

2.3.3 Web simulation

In a typical industrial forward roll coating process the fluid splits into two films downstream of the nip (see Figure 1.2(b)); one film returns to the fluid bath while the other is carried away on the coated web. To avoid the inclusion of a web in the present apparatus, because of the cost and complexity of associated winding equipment and the difficulties involved in controlling the web tracking (so that the web remains butted up to the back surface of the viewing plate), a scraper was employed to mimic the upper roll boundary condition. That is to say, the fluid bead 'sees' a dry boundary as it displaces air from, and coats the roll. The operation of the scraper is illustrated in Figure 2.4, whereby the fluid film on the upper roll is allowed to carry on around the roll before being removed. Figure 2.5 shows a polyester scraper in use. This technique is not 100% efficient because the roll surface is not completely dry after scraping, but the important point to note is that the fluid flux entering the bead at this 'dry' boundary is negligible. The justification for using this approach in the study of roll coating,

under smooth operating conditions, relies on the fact that industrial coating specialists strive to design a low surface tension fluid for coating onto a high surface energy web in order to achieve acceptable wetting. The fact that the 'dry' boundary in the present apparatus is actually wetted, only serves to facilitate the required goal.

The subtlety of this dry boundary condition has not been addressed previously by other workers who have used scrapers or half-submerged rolls to investigate roll coating, since it is not of prime importance in the fully-flooded case, where fluid is forced into the inlet; results of coating performance are similar for horizontal half-submerged (Greener & Middleman[1979]) and vertical two-roll systems (Benkreira et al [1981]), which dismisses any effect of a dry boundary condition. In the ultra-starved case, however, it is clear that the maintenance of the bead depends to some extent on this boundary condition; fluid is not forced to wet the 'dry' boundary as a result of imposing a 'wedge' of fluid at inlet, but rather it generates the means to do this as a result of the flow system within the bead. The effect of a dry boundary may be of crucial importance with regard to dynamic wetting; preliminary experimental studies on reverse roll coating to verify the numerical predictions of Coyle et al [1986] show a major discrepancy in the position of the 'dry' contact line (this is discussed more fully in Chapter 7).

The material from which the scraper was manufactured had to be rigid enough so as not to deform under its own weight yet be flexible enough to be clamped up against the roll, at an optimum angle, to achieve efficient removal of fluid. The performance of plastic (polyester) and metal (brass shim) scrapers was assessed. Both worked well, but the metal scraper (shim thickness – 0.3 mm) was found to remove the maximum amount of fluid. This is because metal has a higher surface energy than plastic and therefore fluid is more likely to 'attach itself' to the former. In addition, it is easier to produce

a uniform knife-edge finish on a metal blade (plastic tends to score or become fibrous). However, there is a danger that the metal scraper will scratch the roll surface, although it does appear to be lubricated. The efficiency of the scraper was determined using filter paper to absorb any excess fluid left on the roll; the paper was weighed before and after being placed on the moving roll, downstream of the scraper, for a measured time. Fluid removal for the metal scraper was found to be between 95 and 98% efficient.

2.3.4 Other Design Features

In designing the apparatus a wide range of factors were taken into account, not least of which was to make the equipment as flexible as possible – to serve not only the purpose of the present study, but future investigations also. The apparatus itself is very compact. It is bench mounted and can be levelled via adjustable screw feet in the base plate (see Figure 2.6).

Roll Drive System

Each roll is driven and controlled independently for maximum process versatility. This method has the advantage that the roll speeds/speed ratios are continuously variable. To achieve a wide range of speeds necessitates the use of a worm reduction gearbox. Therefore a motor of sufficient power to overcome the friction in the gearbox and produce an acceptable starting torque (to achieve very low speed operation) was required. In considering suitable motors, it was noted that there is very little rotational resistance from the shafts, and that the loading on the rolls during operation is negligible. A motor which fulfills the necessary requirements is the Parvalux SB 11 M (1/6 H.P.); one with an 'X' orientated gearbox, the other 'Y' orientated, to achieve a symmetrical drive system layout (see Figure 2.6). Each motor has a dedicated control unit for con-

tinuous speed variation, and is connected to the roll shaft via a 27:1 worm reduction gearbox, pulley and a toothed rubber belt. Toothed belts require very little tension for operation, and therefore loading on each roll shaft is negligible. Vibration from the drive system was also minimal.

By changing pulley sizes, the range of acheivable roll speeds can be increased further. The system is designed to run at extremely low speeds in order to gain as much information about the structure of the flow as possible. A switch was incorporated into the motor control system so that the direction of the lower roll could be reversed in order to run the apparatus as a reverse roll coater.

Precision Gap Adjustment and Roll Positioning

The lower roll bearing/shaft housing is bolted to the aluminium baseplate. Four ground steel columns are press-fitted into the lower housing onto which the upper housing is located with a precision slide fit (see Figure 2.7). There are four helical steel springs located around the columns, positioned between the upper and lower housings. The springs are able to support the weight of the upper roll/shaft/housing assembly. The control of the proximity of the upper and lower housing is achieved by a micrometer assembly (Figure 2.7); the micrometer is bolted to a plate, which in turn is fixed rigidly to the four columns. Turning the micrometer drum so as to move the shaft down forces the upper housing down against the four-spring support. Therefore, by varying the micrometer shaft position as required, the location of the upper housing can be adjusted accordingly. The precision slide fit on the columns ensures that the motion of the upper housing remains parallel. The proximity of the two housings, and thus the roll gap, can be adjusted to an accuracy of 1 micrometer. The distances from the top of the lower housing to its shaft centreline and the bottom of the upper housing to its respective shaft centreline are designed to be just less than the roll radius, so that the

gap between the rolls can effectively be reduced to zero (i.e. as the gap is reduced, the rolls will touch each other before the housings make contact).

With regard to the flow visualisation viewing plate (see §§ 2.3.3 and Chapter 3, §§ 3.2.1), it is important to align the ends of the two rolls so that side leakage is not excessive when the plate is in position (see Figure 2.8). The bearing end-caps are used to independently adjust the axial position of the shafts to facilitate alignment. In addition they are used to retain and preload the bearings via the shaft collars which reduces any internal clearance and therefore takes up any 'play' in the shaft, either axially or radially. Finally, since the end-caps are secured using four diagonally positioned screws, it is possible to make precise independent adjustments to correct any shaft/roll runout by manipulating the bearing geometry. Deep groove ball bearings (SKF 6108 grease packed) were found to be adequate and were pressed onto the roll shafts prior to assembly into the shaft housings.

Constant-level fluid bath

The thickness of fluid picked up on a rotating roll immersed in a bath is proportional to the depth of immersion (Tharmalingam & Wilkinson[1978]). To ensure that the fluid level to which the lower roll is immersed remains constant, a weir system is employed. Figure 2.9 illustrates the fluid recirculation system. Fluid is pumped from a large five litre reservoir up to a smaller header tank, which produces a constant flow into the roll bath. A deflection plate is positioned above the inlet to minimise disturbance of the bath, due to the entering fluid. Excess fluid flows over the weir and returns via the drain plug to the large reservoir (see Figure 2.10).

The bath is constructed from 6mm thick acrylic sheet. The joints are bonded and sealed using a suitable bonding agent, with the exception of the front plate which is

secured with cap screws. This allows for easy removal when interchanging rolls. The bath walls are designed to be well above the centre-line of the lower roll in order that the effect of a wide range of roll immersion heights on the lifted fluid film can be assessed, if required. The lower roll shaft enters through the rear wall of the fluid bath via a standard lip seal. The weir wall is located in guide strips on the inner walls of the bath. Therefore the height of the weir can be varied by putting various wall sizes in position. In many industrial processes the lower roll is immersed in the bath to a very small depth (the height of the fluid level is well below the roll centre-line). This in itself may be the cause of some coating instabilities (see Chapter 7).

2.3.5 Measurement of system operating parameters

Roll speed

The speeds of the rolls themselves are relatively low, therefore rapid, accurate measurement is not possible using the rotation of the rolls or the support shafts. For this reason the motors were chosen with optional extended shafts (i.e. the actual motor shaft protrudes from the motor casing). The rotational speed of this shaft can be measured; since it rotates 27 times faster than the actual roll shaft, the speed of which has been reduced through the worm gearbox, the accuracy and speed of measurement are much improved. The shaft speeds are measured using an optical tachometer. A disc is bonded to the extended shaft and reflective stickers placed equidistantly around the edge (see Figure 2.11).

Using a light source and photo cell arrangement, a pulse is registered each time a reflective sticker passes the sensor. The inputs from the two detectors (one on each motor) are fed into a tacho-ratiometer which gives the pulse rate for each sensor, the ratio of the two, and thus the roll speed ratio. The peripheral speed of a roll is given

by:

$$U = \frac{2\pi R N_P}{60 K N_S} \tag{2.2}$$

where N_S is the number of reflective stickers on the disc, N_P is the measured pulse rate per minute, K is the combined reduction ratio of the gearbox and pulleys (for equal size motor and roll shaft pulleys, $K = 27$), R is the radius of the roll and U is the speed of the roll surface.

In addition, any variation in a set motor speed (the specification of which is less than 2%) is reduced by a factor of 27 at the rolls themselves, resulting in a standard roll speed range from 5×10^{-3} m/s (0.3 metres/minute) to 0.5 m/s (30 metres/minute) [for similar pulley sizes on roll and motor shafts, i.e. a 1:1 ratio] with an accuracy of $\pm 0.1\%$. This speed range can be extended by mounting dissimilar sized pulleys on the roll input and motor output shafts.

Minimum gap size

Although the roll separation can be adjusted very accurately to within 1 micrometer using the micrometer/spring system described in §§ 2.3.4, the actual measurement of the minimum gap relies on accurate calibration of this device. The gap is calibrated using a feeler gauge. Using a 50 micrometre gauge placed in the nip, the rolls are slowly brought together until the gauge meets some resistance as it is moved in and out. In addition the optical viewing system described in Chapter 3 is employed to ensure that the feeler guage is accurately positioned horizontally; even a very small deviation can give a significant over-estimate of the gap size, since this technique relies on the operators 'feeling' of resistance. Accuracy is to within $\pm$ 25 micrometers.

In view of the magnitude of the above error (i.e. for a minimum gap size of 100

micrometres the error is ±25 %), an alternative feeler gauge material, which was tested in the latter part of the present study, is suggested. Specialised plastic wrapping film is available in thicknesses as low as 6 micrometres. The thickness of the plastic film tested was measured and found to be 12 micrometres (±1 micrometre). A strip of plastic film can be pulled through the gap whilst the gap size is decreased, until it meets with resistance, in much the same way as a conventional feeler gauge. Such flexible film has the advantage that there are no problems with ensuring horizontal alignment of the gauge. This method of gap size measurement halves the previous error.

2.4 Pressure Measurement Apparatus – Plate-Roll Geometry

The nature of the roll coating process makes the task of measuring pressures within the flow extremely difficult. The restrictive size of the nip, coupled with the fact that the roll surfaces are moving, precludes the use of standard pressure measurement techniques. Any intrusive pressure probe would certainly alter the flow system under investigation. The limitations of a surface mounted pressure transducer located within a moving roll surface are the dynamic response and operating pressure range of such a device. The simplified flat plate and roll geometry (see Figure 2.12), used by a number of authors, serves as a representative coating flow system which can accommodate the simplest fluid mechanical pressure measurement technique available – that of the manometer tube. This geometry can be treated as a two-roll coater whose upper roll is stationary and of infinite radius. The practical application of this system in the coating industry is that of a spreader bar; it is used in conjunction with a roll, wherein a flooded inlet is metered and 'spread' at outlet.

The experimental apparatus consists of a 265mm diameter, 165mm long steel roll

mounted in a bath and driven by a variable speed electric motor. A 10mm thick acrylic plate is positioned horizontally above the roll and located in a steel support frame, which is adjustable in the vertical plane to give the required plate-roll separation (see Figure 2.13). A roll with a relatively large radius of curvature is required to produce a fluid bead of sufficient width, W_0, to accommodate an adequate number of pressure tappings. Figure 2.14 illustrates the effect on the fluid bead of reducing the relative roll size; the width reduces drammatically from $W_0 = a$ to $W_0 = b$. Such an exaggerated geometry serves to 'elongate' the flow under investigation to facilitate a reasonable number of discrete pressure measurements. The geometry of the apparatus was designed to 'create' a suitably sized fluid bead covering 10 to 15 manometer tappings.

In order to measure the pressures in the fluid a series of 1.0mm diameter holes were accurately drilled, using an NC machine, at a distance of 2.0mm between centres in a line down the centre of the acrylic plate, perpendicular to the axis of the roll. The holes were then counterbored to a width of 1.35mm to accommodate 1.3mm diameter glass manometer tubes which were then bonded into position (see Figure 2.15). The tops of the manometer tubes were sealed into a vacuum chamber, the strength of which could be varied. The vacuum is an effective way to uniformly raise the zero reading in the manometer tubes in order to allow visualisation of any negative pressures generated. As the flow transforms from the Classical to Meniscus roll coating regime the cross-section of the bead decreases (as the initial semi-infinite inlet film is reduced – see Chapter 1, § 1.4), and therefore the number of pressure tappings in the bead itself decreases. Tappings which were in the fluid bead become open to the atmosphere as the transition takes place (see Figure 2.15); the effect on the vacuum was found to be negligible .

A viewing plate was located on the side of the top plate to facilitate visualisation of the flow between the plate and roll when using the dye injection technique described in Chapter 3. This set-up allows observation of fluid flow (albeit limited – the reasons for this are discussed in Chapter 6) as well as determination of the pressure profile through the bead under various operating conditions.

2.4.1 Experimental Procedure

The pressure distribution results were recorded using a Panasonic F10 video camera, or alternatively a 35mm camera. The video recording system has certain advantages over the latter which are discussed below. The zero pressure reading is first raised uniformly up the manometer tubes using the vacuum chamber connected to a variable vacuum pump. There is a slight variation in the heights of the fluid levels in each tube, due to the non-uniformity of the glass tube inner diameter. A vertical rule scale is incorporated into the image adjacent to the bank of manometer tubes for calculation of quantitative pressure measurements. Using a 35mm camera to record results requires a horizontal line in the image to serve as a reference (to take account of the zero-pressure variation in the manometer heights) in order to determine the absolute liquid height in each tube. However, using the F10 video camera coupled with a character generator allows this horizontal reference line to be placed 'on' the image as a digital overlay. The character generator can also be used to include the test conditions within the image.

Therefore a video recording/photograph is taken with the roll stationary (effectively the zero pressure profile) and again when the required operating conditions are reached. The change in the height of each pressure tapping is then calculated to provide the pressure distribution. This is done for photographic results by physically measuring the change in the liquid heights on the photographic prints. In the case of the video recording, the images are analysed using the cross-hair facility of the image processing

system (described in Chapter 3) to measure the displacement of each manometer level.

In addition, the video system has the great advantage of being able to combine and record two images simultaneously. This is achieved using two video cameras and a video mixer. One camera records the pressure profile, while the other records the dye flow within the nip (the flow visualisation technique is described in chapter 3). A Panasonic video mixer combines these two images in a split screen to provide simultaneous results (Figure 2.16(a) shows an example of a typical recording and 2.16(b) is a schematic representation for clarity). The flux, Q, passing through the nip is removed and measured using a scraper blade (the method is described in detail in the following section), and these results can be placed in the image using the character generator, together with the test operating conditions.

2.5 Measurement of Fluid Film Thickness

The purpose of a coating system is to lay down a fluid film, of a specific thickness, onto a substrate, therefore the dependence of film thickness on operational parameters is all important. It is necessary to ascertain the relationship between the inlet film thickness h_0 and the upper and lower roll outlet film thicknesses h_1 and h_2, as well as the film-splitting ratio h_1/h_2, under various operating conditions (see Figure 2.17).

The accurate on-line inspection of coating thickness, be it wet or dry, is usually a major problem in the coating industry. The measurement of dry coat thickness is often carried out by taking samples at the end of the production line; using certain properties of the finished film, its thickness can be assessed by destructive measurement techniques. It is then usually possible to estimate the wet film thickness from a knowledge of the 'solids content' of the coating fluid. The on-line measurement of wet coat thickness is a much more difficult task since a non-destructive, non-contact method has to be used in order to preserve the coat quality of the final product. Although there are devices which can monitor wet coat thickness (i.e. show a deviation in coat thickness over a given time), they cannot easily produce absolute film thickness measurements.

2.5.1 The Behaviour of a thin fluid film on a rotating roll

Yih[1960] appears to have been the first to be concerned with thin film flow in a roll coating context; he studied the behaviour of a liquid film on a roll in order to understand the fluid flow on the rolls of a paper-making machine. Moffat[1977] gives a review of previous work in this area and considers the dynamics of a viscous film on the outer surface of a horizontal roll using lubrication theory; his investigation involved an analysis of the fluid flow on a 'suspended' rotating roll. Although interested primarily in the stability of the film on a rotating roll, for which the analysis yields an instability not

unlike that of ribbing (see Chapter 7), in considering the stable problem he concludes that the fluid layer experiences substantial shear and the motion can certainly not be approximated by a rigid body rotation.

Although viscous lifting of fluid onto a rotating roll has not been widely studied, the related 'drag out' problem, whereby a thin liquid film is entrained by the steady withdrawal of a sheet from a bath of liquid, has received greater attention. The work of Landau & Levich[1942] initiated a series of detailed theoretical and experimental studies. Their work was extended to a wider capillary number range by White & Tallmadge[1965], while the effects of fluid inertia have been considered by Soroka & Tallmadge[1972] and Esmail & Hummel[1975]. Wilson[1982] consolidated the work of the previous authors and demonstrated that the Landau-Levich result is a special case of the general drag-out problem. Tharmalingam & Wilkinson[1978] adapted the aforementioned theories for predicting the film thicknesses and liquid flux on the applicator roll in a roll coating system, involving the numerical integration of the momentum equation in the dynamic meniscus region and the matching of the surface curvature with that derived for the static meniscus region near the liquid surface. The results compare well with experiment for low Capillary number (up to about 0.1), but thickness predictions for higher values are much too large because their analysis neglects inertia effects and a simplified pressure gradient approximation is employed.

Wu, Weng & Chen[1985] adopted an oblique flat plate model and, using the flow regions proposed by Landau & Levich, they included inertia force terms and more realistic two-dimensional boundary conditions for the free surface to produce reasonably accurate film thickness predictions over a wide range of Capillary number. The key result from this work is that the entrained film thickness increases with respect to increasing Capillary number up to a certain values, at which point this trend slows down and even

reverses due to inertia effects.

Even if the difficulties in the analysis of the entrainment of liquid onto the surface of a partially submerged roll are ignored, the consideration of the behaviour of the thin fluid film on a roll as it rotates is the major problem in any attempt to measure film thickness at specific points. Taking the simple case of a single rotating roll half-submerged in a reservoir (see Figure 2.18), fluid is picked up by the roll on one side and is deposited back into the reservoir on the other. At no time does the fluid film achieve an asymptotic thickness. In fact the thickness decreases as θ goes from 0 to π. The thickness of the fluid film varies as the gradient of the 'solid' surface changes. In simple terms, this can be explained by the effect of gravity on the fluid film as the orientation of the layer is changed; the fluid farthest away from the solid surface is effected the most, and this determines the velocity profile across the depth of the fluid layer.

Now consider the two roll coater configuration of the present experimental apparatus (Figure 2.4). With no web present, the surface never achieves a constant gradient and therefore the fluid film, h_1, on the upper roll never reaches an asymptotic thickness. Thus, there is no means of measuring the *actual* film thickness at a specific point. With a web present, a constant gradient (and therefore an asymptotic film thickness) is attained some time after the substrate leaves the roll surface. However, the lower roll fluid films, h_0 and h_2, can never achieve a constant thickness.

Tharmalingam & Wilkinson[1978] present results of predicted film thickness for variations of system parameters. In particular their Figure 5 shows how the film thickness varies around the roll for a range of Capillary numbers (Refer to Figure 2.18). Under Classical roll coating conditions Capillary Number can be as great as 1;

- At $Ca = 0.01$, film thickness varies over the angle shown, by 20%
- At $Ca = 0.1$, film thickness varies by 30%
- At $Ca = 0.5$, film thickness varies by 40%

Therefore, single point film thickness measurements in Classical roll coating will not give a typical average film thickness reading, unless the operator can equate the position of measurement with the velocity profile there. However, for industrial Meniscus roll coating, with less viscous fluids and the slower roll speeds necessary to maintain the bead the Capillary number is typically less than 0.01. At this value of Capillary number the variation of film thickness around the roll becomes increasingly less pronounced. Thus a single point measuring technique would seem to be plausible for this regime.

2.5.2 Alternative measurement devices

Micrometer driven needle

The micrometer driven needle device is illustrated in Figure 2.19. It is a very simple mechanical measuring technique, which has been used widely in the past (e.g. Greener & Middleman[1979]). Here the needle is machined from silver steel (for improved hardness properties) so that the end point is concentric with the micrometer shaft. A zero reading is taken on the roll surface by using a continuity circuit between the needle point and the metal surface. The needle and micrometer arrangement is electrically insulated from the stand, and therefore the rest of the apparatus. Using an Avometer (with a 1.5 volt power supply) and setting a very high resistance of the order of Megaohms results in a negligible current ($I = V/R \approx 1\text{x}10^{-6}$); therefore the capacity of the system to produce a spark across the needle-surface gap (and so give a false zero reading) is diminished. The zero reading is repeatable to within one micrometer. The eccentricity of each roll is taken into account by finding the most eccentric part of the

roll using a micrometer dial gauge. The needle micrometer is then zeroed under the assumption that the needle point will first touch the liquid layer, on the rotating roll, at this point.

Measurements of film thickness are obtained by slowly moving the needle towards the fluid film; at the moment the needle point touches the surface a large local distortion of the fluid is readily observed. There is of course always the possibility that the fluid surface will be attracted to the needle point (because of any electrostatic charge build-up there) thus giving an over-estimate for the film thickness.

Figure 2.20 shows a typical graph of film thickness against roll speed for a single roll. By taking measurements of film thickness on the upside and downside of a rotating roll (with no fluid bead present), at an angle of 45^0 to the vertical in both cases, the results confirm the theory that the film 'thins' as it travels around the roll (see Figure 2.18). The major drawback of this technique is that it is time consuming, in that each measurement must be taken manually. Results are repeatable to within 1 micrometer.

Capacitance probe

The capacitance probe technique for the measurement of wet coat thickness on a roll is based on the determination of the capacitance of the air gap between the probe and the roll surface. This arrangement acts as a parallel plate capacitor – the roll surface is one plate (the surface curvature is negligible in relation to the probe surface area) and the probe surface is the other. With no liquid between the two surfaces, the capacitance is given by:

$$C_A = \frac{E_0 E_A A}{h_A} \tag{2.3}$$

where E_0 is the dielectric constant for free space, E_A the dielectric constant for air, A is the probe surface area and h_A is the gap between the probe and roll surface. When a liquid film is coated onto the roll surface the capacitance changes and is given by:

$$C_1 = \frac{E_A E_0 A}{h_A - h_F} \tag{2.4}$$

where h_F is the liquid film thickness and C_1 the capacitance over the distance $h_A - h_F$ (see Figure 2.21). The above equation, however, only holds for a conducting fluid. With a non-conducting fluid there exists two different dielectrics between the plates, and this is equivalent to two capacitors in series. The capacitance for this system is given by:

$$C_T = \frac{C_A C_F}{C_A + C_F} \tag{2.5}$$

where C_A and C_F are the capacitance of the air gap and the fluid layer respectively, and C_T is the total capacitance of the system. From the above equations the new air gap, x, is given by:

$$x = \frac{h_F(E_A - E_F)}{E_F} + h_A \tag{2.6}$$

This technique is far more effective as a proximity probe (e.g. even a very small roll eccentricity is easily detected) than as a film thickness measurement device. This is because the metal has a far higher dielectric constant than any typical fluid; if the two were similar the technique would be far more effective, since increasing any fluid film in the capacitor gap would have the same effect as moving the plates closer together. Indeed this is the effect with liquid, however its contribution to 'closing the gap' is much lower. An added drawback of this device is that measurements are fluid specific (i.e. changing the fluid to be measured necessitates re-calibration because its' dielectric constant will inevitably differ).

Optical probes

Systems relying on the absorption of light have application in the measurement of fluid films in industry. This is particularly true in the coating industry where such liquid films are generally 'transparent', as well as the substrates onto which they are coated. Two optical probes are described below - both rely on the absorption of a quantity of light as an indication of the thickness of the film through which it has travelled. The first system is a sophisticated, commercially available device for the measurement of aqueous fluid film thickness; the second has been developed and tested in-house (with the exception of the electronic circuit itself which was supplied by ICI Engineering) for use with a wide range of non-aqueous fluids.

Professional Infra-red thickness gauge

When infra-red (IR) light passes through a water-based coating, some of it is selectively absorbed. This loss of energy is due to the vibrational excitation of the OH hydrogen radical within the solution. The peak absorption wavelength of water is 1.94 micrometres, which is far removed from the absorption wavelengths of plastic substrates (3 - 4 micrometres). By placing the light emitter on one side of the coated film (transparent) and the detector on the other, two wavelengths of light are used to determine the liquid film thickness; the first is the peak absorption wavelength, i.e. 1.94 micrometres (isolated by means of a colour filter). A second 'reference' wavelength, far outside the absorption region, is used to determine the incident energy; it follows the same path as the 'peak' wavelength and so is subjected to the same operating conditions. The wet coat thickness is calculated by measuring the change in the intensity of the two transmitted wavelengths (i.e. the energy loss due to absorption).

The absorption of the infra-red energy follows the Beer-Lambert absorption law (Lothian[1949]):

$$E_T = [E_R]^{-kh} \tag{2.7}$$

where E_T is the transmitted energy, E_R is the reference energy, h is the coating thickness and k is the absorption constant. Taking the logarithm of the above equation gives:

$$log\left[\frac{E_T}{E_R}\right] = -kh \tag{2.8}$$

Therefore the logarithm of the ratio of the two bands of radiation is directly proportional to the wet coat thickness and is easily obtained.

This method can also be operated in reflective mode (e.g. when the substrate is a highly polished metal roll) but problems can arise with alignment. The advantages of this device are that measurements are rapid and direct. This system was used by Patel[1989]. To calibrate the probe he used Meyer Bars; wire is wrapped around a rod and this is dragged over a 'thick' film of fluid; the remaining film thickness is proportional to the wire diameter. However, this method of calibration is dubious, since the operation of Meyer Bars are not well understood.

General purpose absorption probe

The principle behind this general technique is similar to that described above, except that it can be used on non-aqueous fluid films by introducing a suitable dye into the working fluid. A dye is selected with particular absorption characteristics; a 'peak' in the absorption spectrum is ideal. If, for example, 70% of the incident light is required to be absorbed in order to achieve an accurate result (that is equivalent to an absorbance of 0.7), the coefficient of extinction, γ, is calculated using the Beer-Lambert law of light

absorption:

$$\gamma = \frac{A}{C.l} \tag{2.9}$$

A = absorbance, C = concentration of dye in mols/litre and l = length of light path through fluid (equivalent to the thickness).

For a typical film thickness of 30 micrometers and a dye concentration of 1% (with a typical molecular weight of 400), so as not to affect the fluid properties, an estimate of the required coefficient of extinction can be made:

$$\gamma = \frac{0.7}{0.04 * 30 * 10^{-4}} = 90,000 \tag{2.10}$$

This is an extremely high value and it is particularly difficult to find an oil-soluble dye with this order of extinction coefficient. An example of a commercial dye with this characteristic is Waxoline dye with γ of the order of 30,000, but unfortunately it is not soluble in the silicone oils used here. Indeed, although this probe was designed to be used with a wide range of oils, its application is restricted by the limited number of oil-soluble dyes with high extinction coefficients.

A suitable dye must exhibit an absorption spectrum which peaks at the wavelength of light of the emitter or the detection wavelength of the detector (this matching can also be achieved using filters). The emitter and detector are placed side-by-side and the system works by measuring the reflected light from the highly polished roll surface (see Figure 2.22(a)) This means, however, that the amount of light being received by the detector is subject to reflections off the surface of the film, and as the film thickness changes so the angle of reflection and thus the fraction of the light falling on the detector will change. This can be overcome by using a beam-splitter to produce both a normal incident and reflected beam (see Figure 2.22(b)), although the amount of residual light reaching the detector is reduced by 75% because the light passes through

the beam-splitter twice (each time 50% is reflected and 50% transmitted).

This problem does not occur with the IR detector described earlier since it relies on the light being transmitted through the wet film and the transparent web, and the incident light is perpendicular to the film. The IR detector also has the advantage of a reference beam (it is necessary to calibrate the Dye Absorption detector). As well as the standard problem of calibration, the presence of the dye means that the fluid is 'contaminated' with regard to flow visualisation. In addition, the detector is very sensitive to the eccentricity of the roll surface unless a non-diminishing light source is used (such as a laser) .

The electronic circuit used to produce the high speed synchronous emission/detection is illustrated in Figure 2.23. The source (emitter) circuit consists of a multivibrator running at 1 KHz. This output is fed, via a current driver, into a transistor switch; the current pulse is then fed into the LED emitter. The detector circuit includes an input for a silicon detector diode working at the specified wavelength (as discussed above). As light from the LED emitter falls on the detector, the current generated is fed into a high gain amplifier. The output from the amplifier is taken into one input of a synchronous detector and compared with the multivibrator output. The output of this detector is in turn amplified, filtered, and fed to the measuring device (a digital voltmeter) to give an output range of 0 to 5V. The circuit and power supplies are housed in a self-contained unit into which the various emitters and detectors can be plugged (see Figure 2.24). The unit can be calibrated using the Full Scale Deflection (FSD) and 'Set Zero' controls.

Figures 2.25(a) & (b) show the qualitative absorption spectra for two oil-soluble dyes in silicone oil. Anthraquinone Blue (Figure 2.25(a)) has two absorption peaks in the visible region; the detector will be most effective using a matched emitter/detector

operating close to one of these maxima. Figure 2.25(b) shows the absorption spectrum for Ariavit Blue FCF; this dye exhibits a well-defined peak at around 630 nm, which is ideal for use with a laser light source. Another possibility is to match the Light Emitting Diode (LED) emission spectrum with the absorption spectrum of the dye. Figure 2.25(c) shows the emission spectra for 4 types of LED (Stanley Hi-Super Bright LEDs) and the standard eye response curve, V_λ. It can be seen that the emission spectrum of the super-red LED coincides very well with the absorption spectrum of the Ariavit Blue FCF shown in Figure 2.25(b). Therefore it is only necessary to use a general purpose spectrum-wide detector, since the emitter and dye have effectively been matched.

To obtain absolute results for absorption for particular film thicknesses, a calibration cell technique was designed (see Figure 2.26). The cells consisted of a highly polished steel lower plate (effectively the roll surface) and a perspex upper plate. To get very small and accurate step changes in cell size (and thus film thickness) 12 micrometer plastic film (described in §§ 2.3.5) was used as spacers to give cell sizes of 12, 24, 36 etc. micrometers thickness etc.. The dye was injected into the cells using a hyperdermic needle and remained there by capillary action. The disadvantages of this calibration technique were that the cells were flat compared to the curved rolls. The effect of the perspex upper plate could be measured by taking a reading for each cell with fluid but without dye present. In addition it was not possible to ascertain whether the spacers compacted flat (there was some rippling under the perspex upper plate) or alternatively whether they were 'squashed'.

By using a laser the problem of $1/r$ intensity reduction, which occurs with an incoherent light source, is eliminated (where r is the radial distance from the source). In addition, a fine point light impinging on the film minimises errors due to reflections from the free surface of the film. It is possible to use a 'laser dye', which predominantly

absorbs that wavelength of light, or alternatively a small-band filter (±5nm) for a HeNe laser which can be used with a general detector.

Scraper Collection

This simple yet effective method involves removing the liquid film from the roll surface using a scraper blade. The liquid is collected for a timed period and weighed. The average film thickness, h, can then be calculated:

$$h = \frac{W}{\rho t L U} \tag{2.11}$$

where W is the weight of liquid removed in time t, ρ is the density of the liquid, L is the length of the roll, and U is the speed of the roll surface.

Scraper blades can be mounted on the upper and lower rolls to measure both outlet film thicknesses, h_1 and h_2, simultaneously. Knowing h_1 and h_2 then, by continuity considerations, the inlet film thickness, h_0, can be calculated. The method relies on the assumption that the scraper blade removes all of the fluid film. In practice, the surface of the roll remains wetted after scraping, but this residual film is negligible (see §§ 2.3.3). It is the most time consuming of all the methods described, but it is the only approach that can give definitive results of fluid flux.

2.5.3 Discussion of measurement techniques

It soon became apparent through trials with the systems described above that for the extensive film thickness range under consideration (from fully-flooded to ultra-starved), all of the measuring techniques require calibration using the definitive scrape-off system. With such a wide range of experimental conditions envisaged, including varying inlet flux, gap size, roll speed/ratio, and fluid properties, there is no justification for assuming that the nature of the flow in the nip will be unchanged and in particular, that the

velocity profile of this flow (which eventually forms the upper and lower roll outlet films) will remain constant. To use these film thickness devices effectively would require a re-calibration for each suspected change in flow conditions, which is impractical. Therefore the scrape-off measurement technique must be applied throughout. The other devices are useful for monitoring film thickness during a constant operating routine such as is practised in industry (i.e. working as a comparator).

2.6 Consideration of Suitable Fluids

The main objective was to choose experimental fluids whose rheological properties behave in a linear manner, in order to study the simplest possible flow field. In addition, it was necessary to strike a balance between fluids which are comparable to those used in industry and fluids which accommodate the experimental techniques required to elucidate the flow field.

2.6.1 Viscosity

Viscosities of fluids for industrial applications of Meniscus roll coating, in particular, are relatively low (of the order of 1 centistoke, which is equivalent to a value of 0.001 Pa s) compared to Classical roll coating where viscosities can range from 0.05 - 500 Pa s.

For the purposes of this investigation, and in particular when considering flow visualisation, it is possible by using a higher viscosity fluid to increase the gap between a plate and roll or two-roll system to give better image definition due to the increased physical size of the flow domain. Therefore, there must be a compromise between choosing a fluid viscosity which is representative of the industrial process and a gap which is large enough to produce good quality images of the flow field. It is also desirable to be able to achieve Meniscus and Classical roll coating using the same fluid for comparison

purposes; in effect an important set of parameters remain constant.

It is true to say that in industrial applications, coated liquids are predominantly non-Newtonian (i.e. shear stress is not directly proportional to the rate of shear in a liquid). However, as a first step in attempting to understand the fundamental flow in a roll coater (Meniscus coating in particular) it is sensible to consider Newtonian fluids only. For example, a non-Newtonian shear-thinning liquid will behave differently in regions of the flow where shear stresses vary, and since the complexity of the Meniscus roll coating flow field is far from fully understood, the addition of this non-linear behaviour can only serve to complicate matters further. In addition, with non-Newtonian liquids, comparison of experimental results with simple mathematical and computational models is made more difficult.

2.6.2 Surface Tension

Surface 'tensions' and surface 'energies ' are extremely important in coating operations. The surface tension of a coating liquid must be lower than the surface energy of the substrate in order for the liquid to wet it. The origin of surface tension lies in the special state of stress that acts entirely tangential to the surface of a liquid, which forces the surface to 'contract' and to become as small as possible. This phenomenon is easily demonstrated when one considers the action of a drop of water containing washing-up liquid (low surface tension) with that of a drop of mercury (very high surface tension) on a horizontal surface; the water experiences considerable spreading, whereas the mercury drop takes on a near-spherical form to minimise its' surface area, in spite of the fact that the gravity force tending to spread it out is considerably larger.

The use of surface active agents (or surfactants) is a common method of reducing the surface tension of a liquid (as in the above example where the surfactant in washing-

up liquid lowers the surface tension of water to allow it to 'wet' surfaces for effective cleaning), a practice which is widespread in the coating industry. Surfactants have a polar, hydrophilic head and a non-polar hydrophobic tail. Once a surfactant is introduced into a 'pure' liquid, the non-polar tail is repelled by the liquid – the surfactant diffuses to the surface where the polar head remains in the liquid whilst the non-polar tail 'sticks out' into the air. The liquid then exhibits the surface tension characteristics of the non-polar tail. Since diffusion to the surface takes a finite time, then in a dynamic flow system newly created free surfaces may exhibit the surface tension of the pure liquid even when surfactant is present. The time taken for surfactant molecules to diffuse to the surface depends on the surfactant; however, even with the fastest, it usually takes more than 1 millisecond for the surface tension to start to fall. Depending on the dynamics of the flow system, this time scale may or may not be adequate. The surface tension created by a surfactant is often refered to as the *dynamic surface tension*.

As this investigation progressed it became apparent that surface tension forces were playing an important role in the mechanics of Meniscus roll coating flow. Therefore, the use of surfactants was avoided for the simple reason that this would introduce another variable into the flow system; the magnitude of dynamic surface tension (caused by the diffusion characteristics of a surfactant) is a function of localised flow conditions and as a result it is extremely difficult to quantify. It is highly desirable to use surfactants in industry, particularly in aqueous based solutions, to give good wetting of the fluid onto the coated medium. However, in this fundamental investigation, it is important to have a reasonable estimate of the surface tension force and this is far easier to assess using a 'pure' liquid.

2.6.3 Choice of fluids

A number of workers have used glycerine-water solutions in roll coating studies (e.g. Benkreira et al [1981]); viscosity can be controlled by varying the ratio of glycerine to water. Such a fluid has one major drawback with regard to the present work; attainable viscosities are too high (i.e. 0.1 Pa s minimum) to investigate Meniscus roll coating. In general, low viscosity coating fluids employed in industry (i.e. of the order of 0.001 Pa s) are highly volatile and cannot be used without specialised safety precautions and fume extraction equipment.

Silicone oils are a suitable alternative; kinematic viscosity ranges from 0.65, 1, 5, 10 centistokes and upwards (1 centistoke = $1 \times 10^{-6}\ m^2/s$). These oils are Newtonian at shear rates less than $10^4\ s^{-1}$ (shear rate = characteristic velocity/characteristic length), and optically clear. The most useful fluid, however, and the one used for the most part in this work (particularly in the flow visualisation studies), was Shell Tellus R5 oil (a light organic oil). Bearing in mind that the main strategy of this investigation was to gain a fundamental understanding of specific aspects of roll coating flow, as opposed to undertaking a statistical study of the process (with systematic variation of parameters, such as viscosity), the requirement for a universal fluid was greater than that for a series of fluids with a wider range of properties.

2.6.4 Fluid Properties

The results of measured fluid properties (using the techniques described below) are presented in Table 2.1. The values of fluid density are taken from the suppliers data sheets.

Viscosity

The glass capillary viscometer method was used to measure the viscosity of the fluids at a range of temperatures. This method relies on the resistance to motion of a liquid passing through a capillary tube. Glass capillary viscometers are designed to pass an accurately reproducible volume of liquid through a capillary by the application of an accurately reproducible force. This force is provided by the pressure of the hydrostatic head of the fluid itself in the viscometer. The time taken for the liquid to flow is, apart from a kinetic energy correction, proportional to the ratio of dynamic viscosity to density; this ratio is, by definition, the kinematic viscosity of the fluid.

Accurate temperature control and time-of-flow measurement are required. The need to apply a kinetic energy correction, particularly for the relatively low viscosity fluids used here, is avoided by choosing suitably long flow times. The glass capillary, containing the liquid to be measured is immersed in a variable-temperature oil bath for a suitable time period (approximately 20 minutes) to ensure the test liquid temperature is equal to the bath temperature before each measurement is taken. Results of viscosity versus temperature are presented in Figure 2.27 for Shell Tellus R5 and Dow Corning silicone 200/5 oils. In both cases, the variation of viscosity is negligible over the working temperature range used in this study (i.e. 20°C ±1°C).

Surface Tension

A Du Nouy 4mm platinum ring surface tensiometer was used to measure liquid surface tension. The ring was cleaned thoroughly before each measurement. The surface tension of distilled water (72.3 $\times 10^{-3}$ N/m at 25°C) was used to calibrate the surface tensiometer.

Liquid	Viscosity ($\times 10^{-6}\ m^2/s$)	Surface Tension ($\times 10^{-3}\ N/m$)	Density kg/m^3
R5 oil	8.4	43.1	839
Silicone oil 200/0.65	0.72	16.1	761
Silicone oil 200/1	1.12	17.5	818
Silicone oil 200/5	5.45	19.7	920

Table 2.1: Measured liquid properties at 20°C

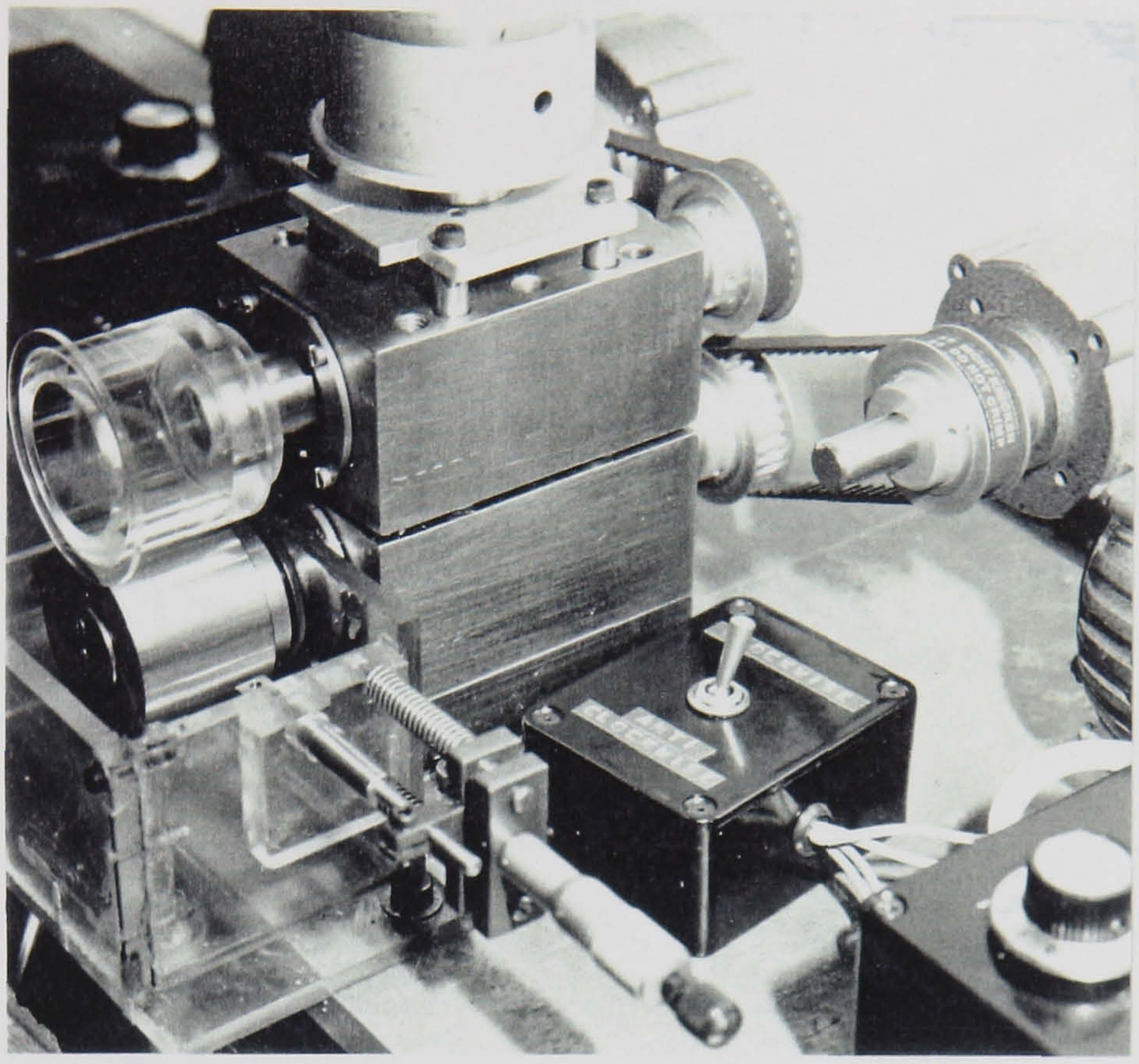

Figure 2.1: Two-roll coater configuration

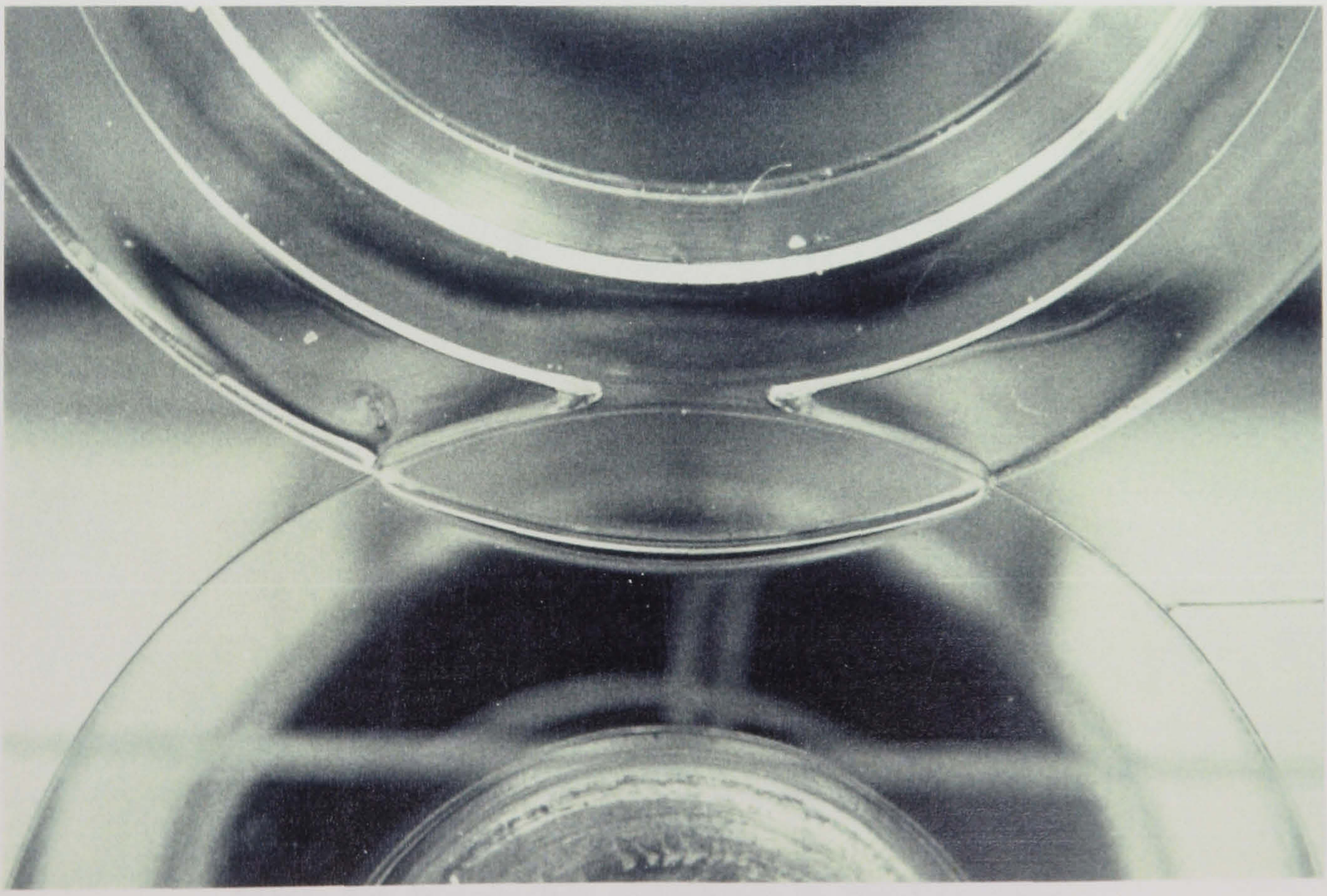

Figure 2.2: Roll with integral flange-type viewing plate

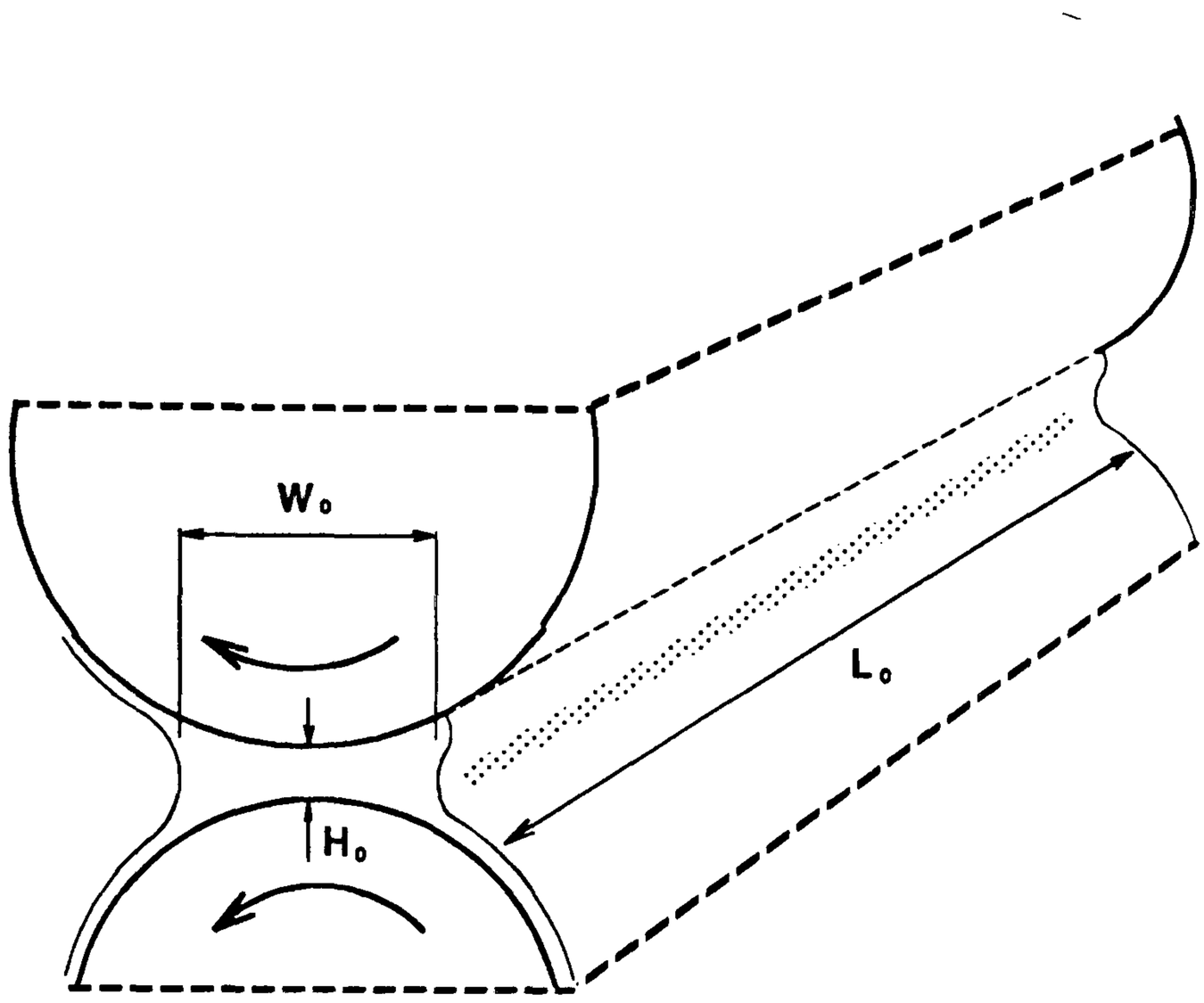

Figure 2.3: Dimensions of fluid bead in the nip

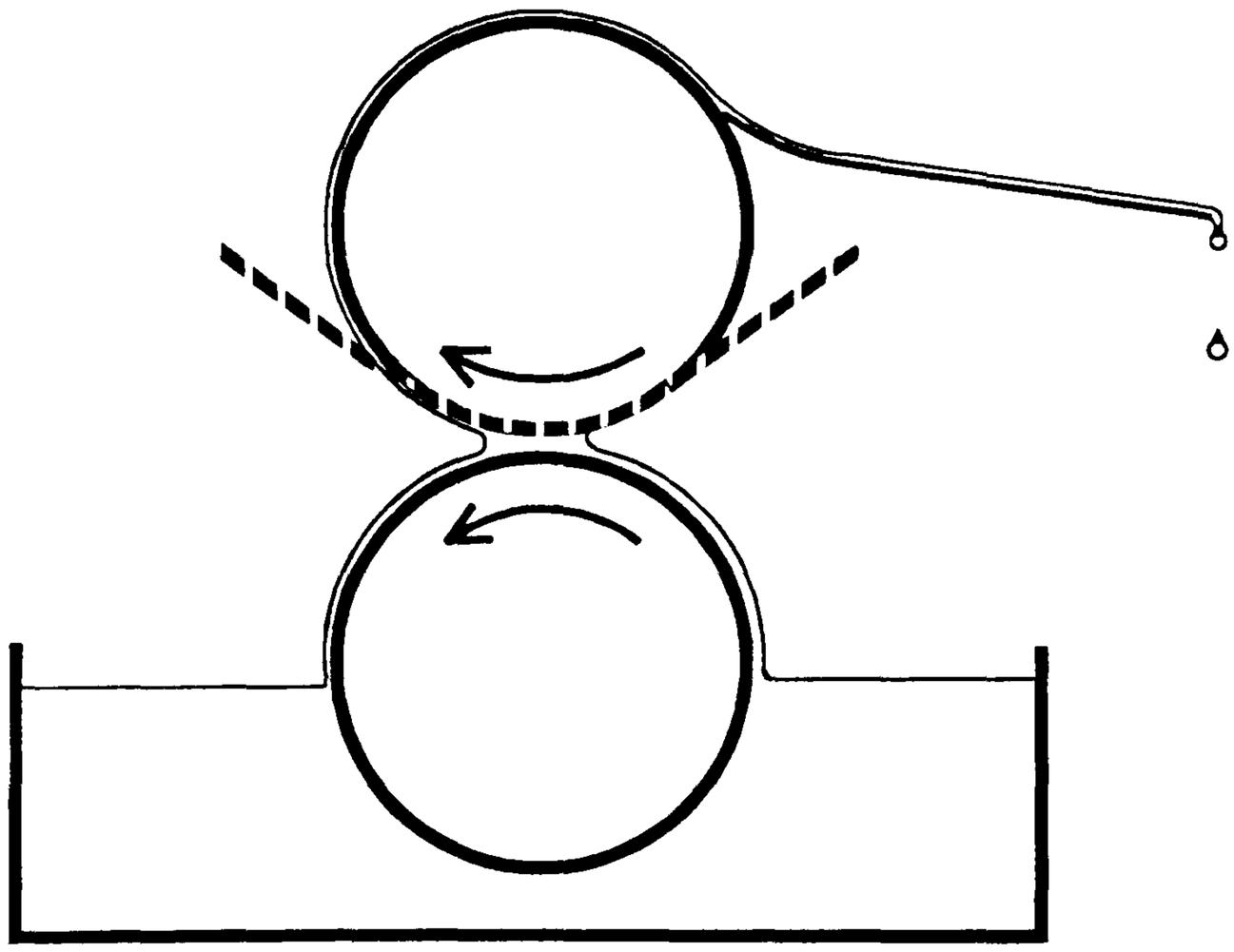

Figure 2.4: Introduction of a scraper to simulate a web

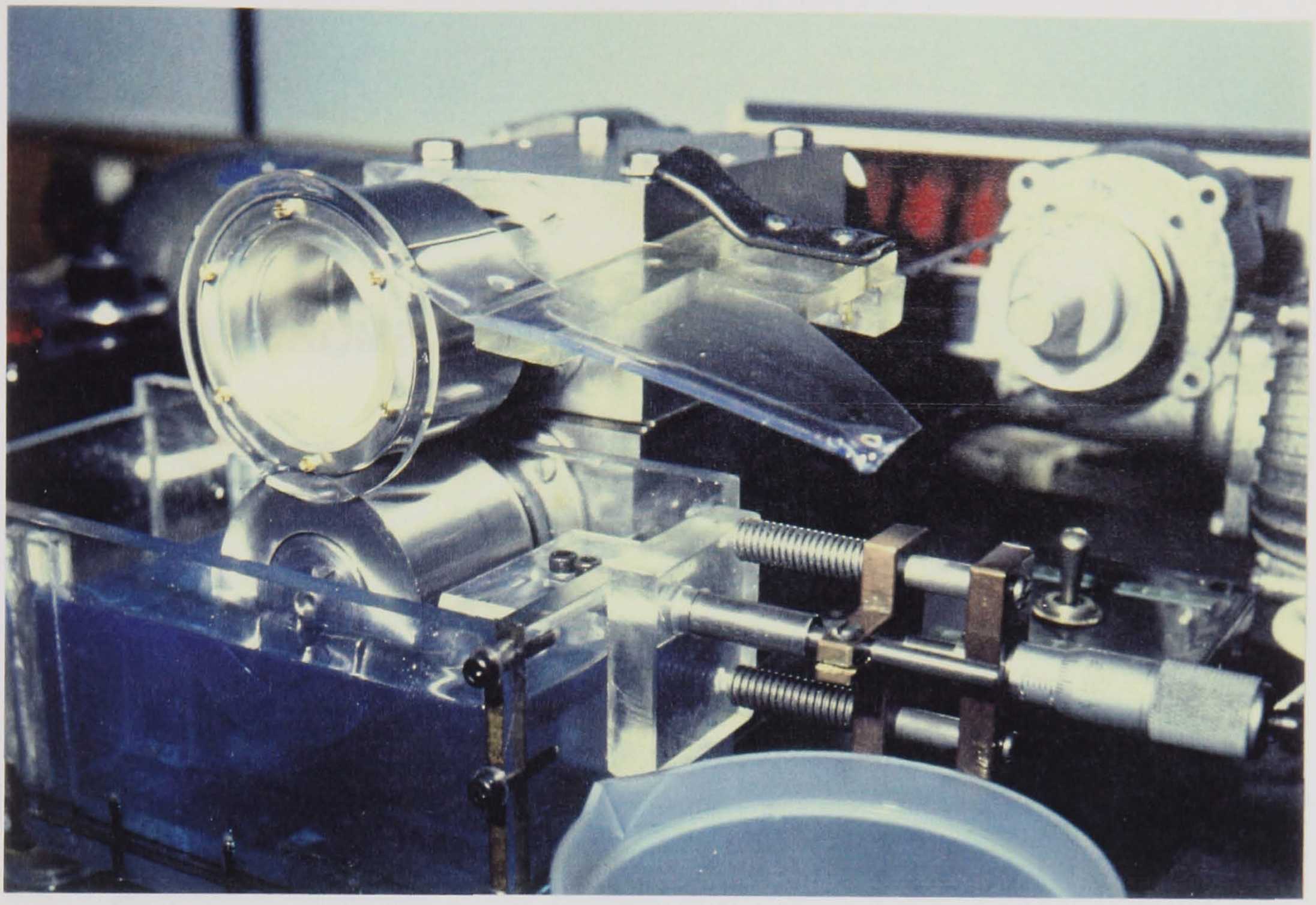

Figure 2.5: Operation of scraper

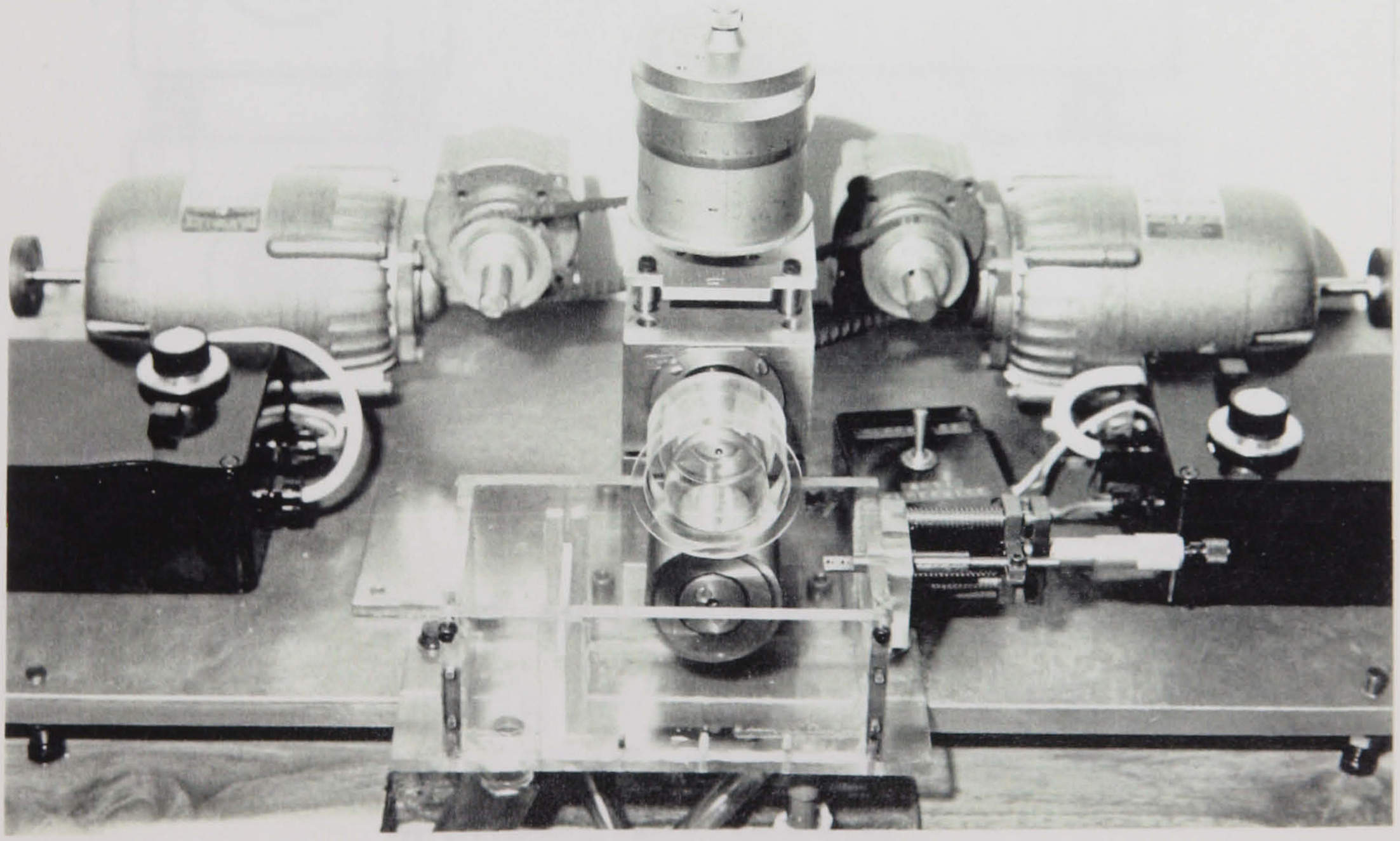

Figure 2.6: Layout of general experimental apparatus

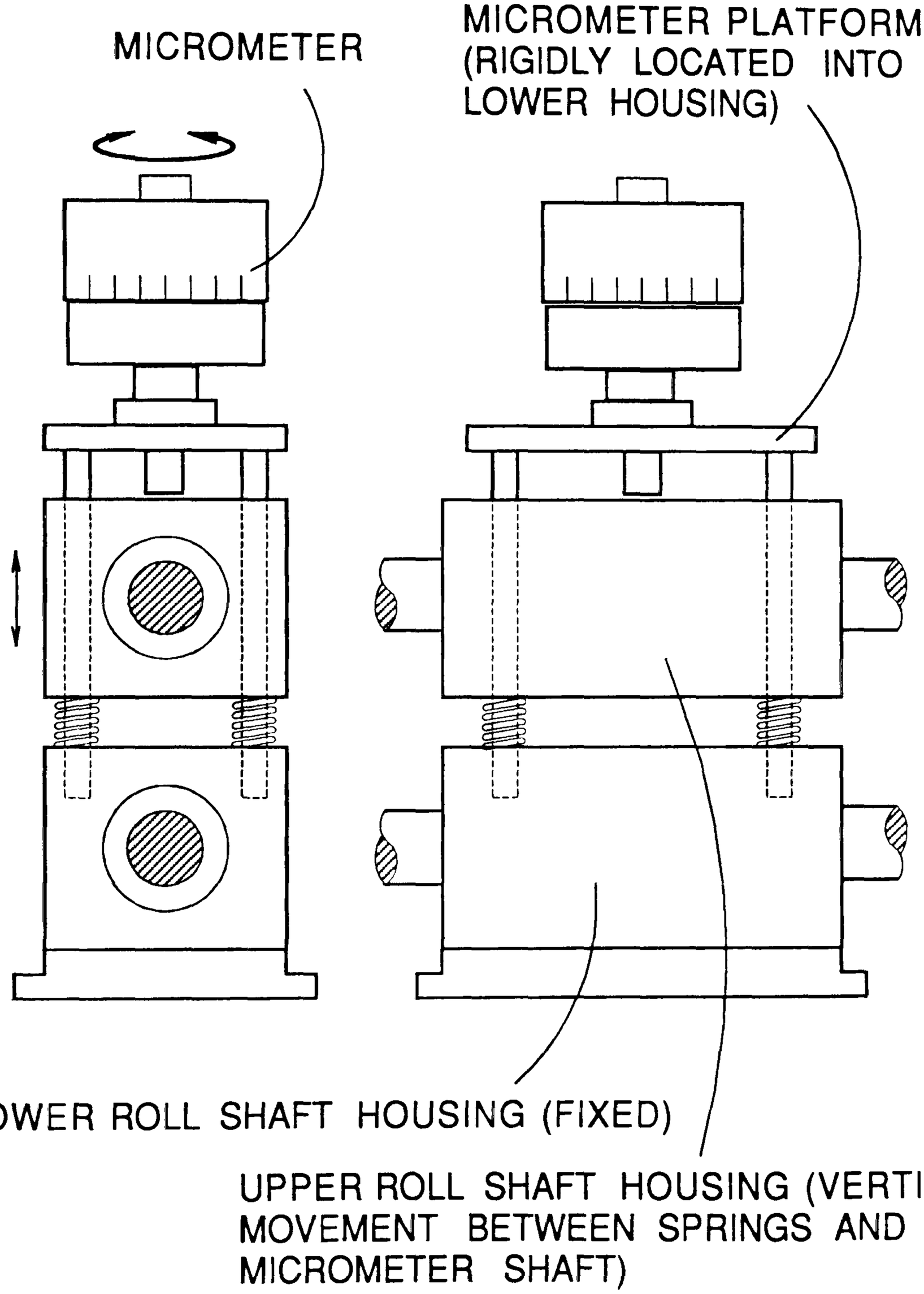

Figure 2.7: Illustration of micrometer gap adjustment mechanism

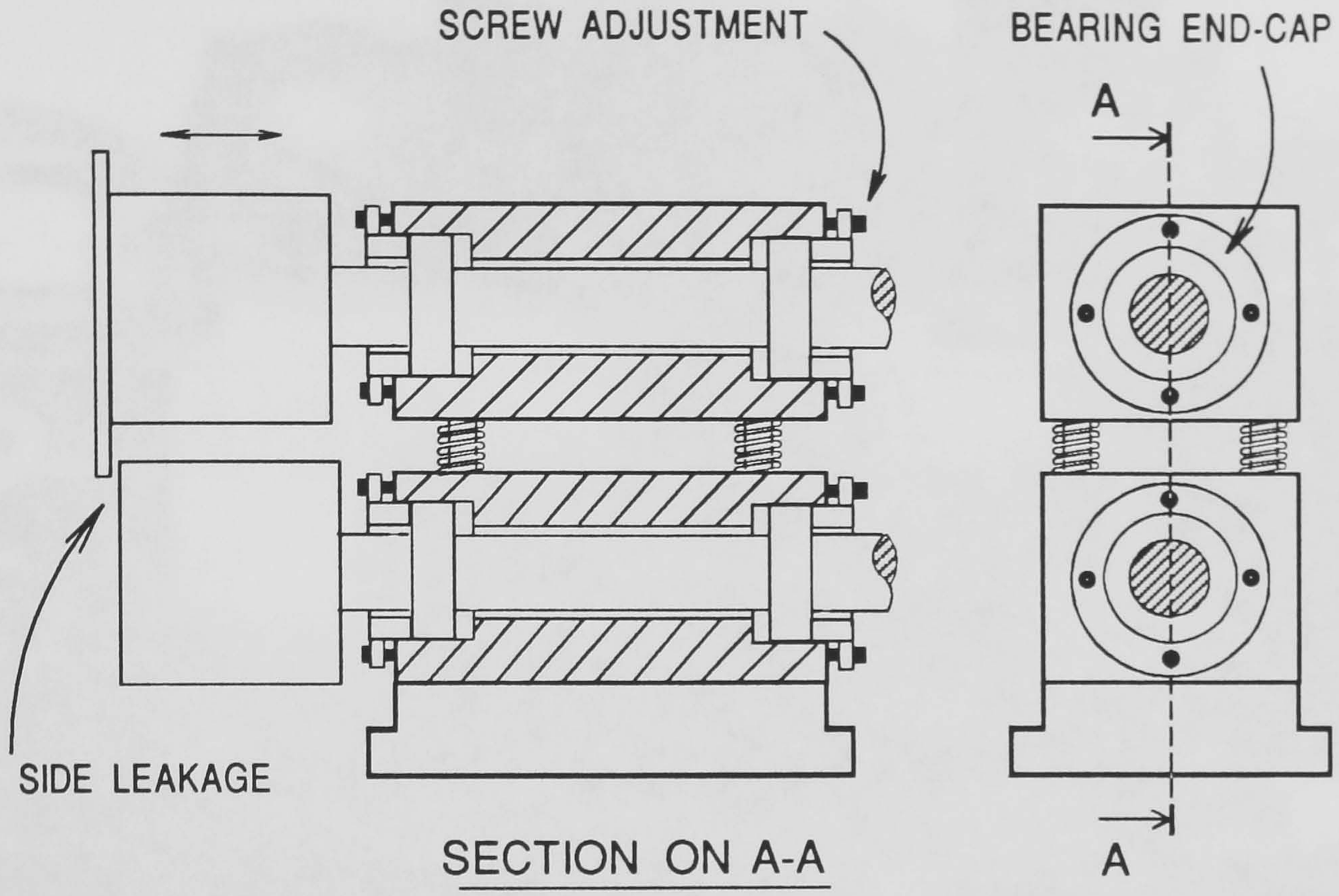

Figure 2.8: Illustration of roll shaft design and adjustment

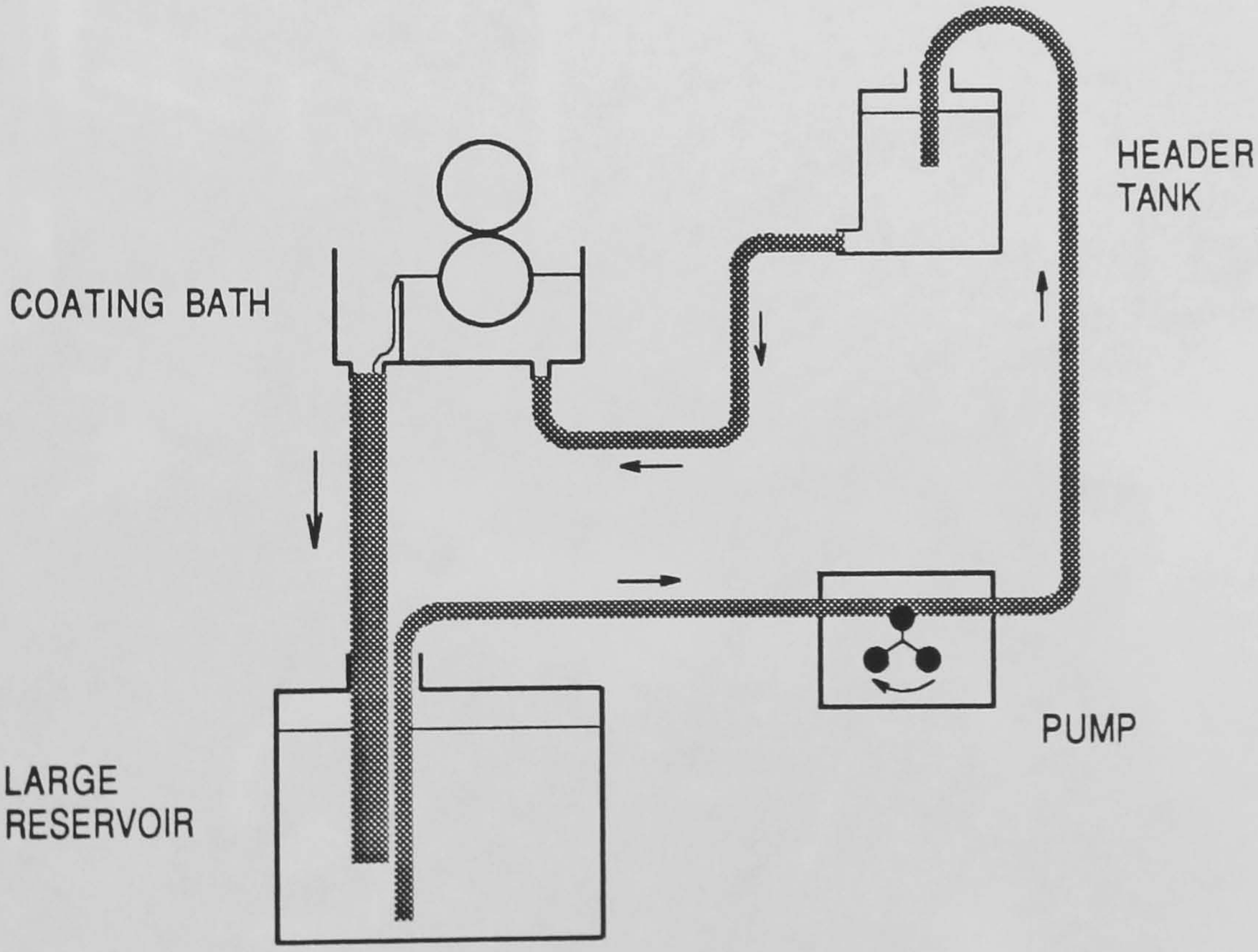

Figure 2.9: Fluid bath feed system

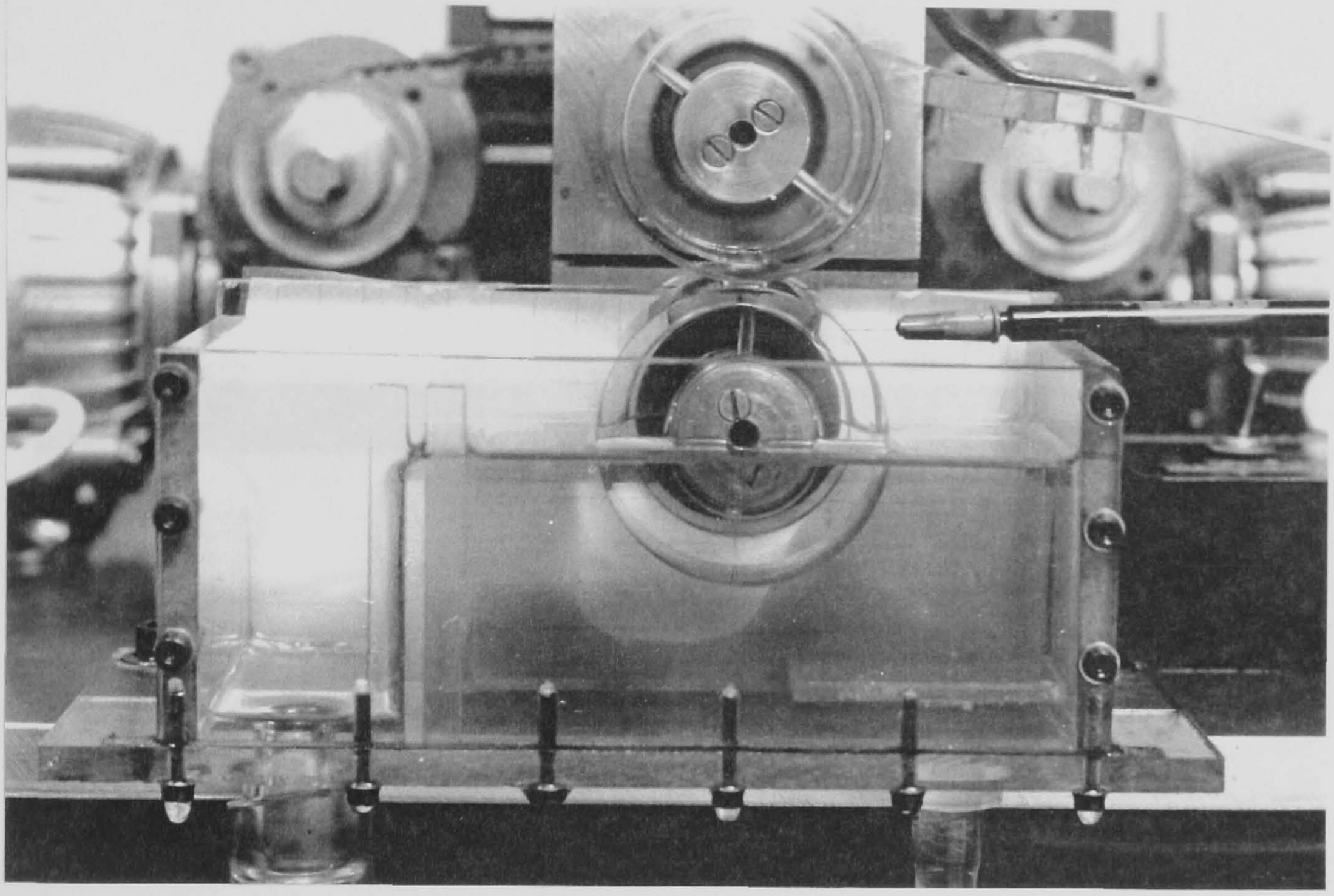

Figure 2.10: Fluid Bath

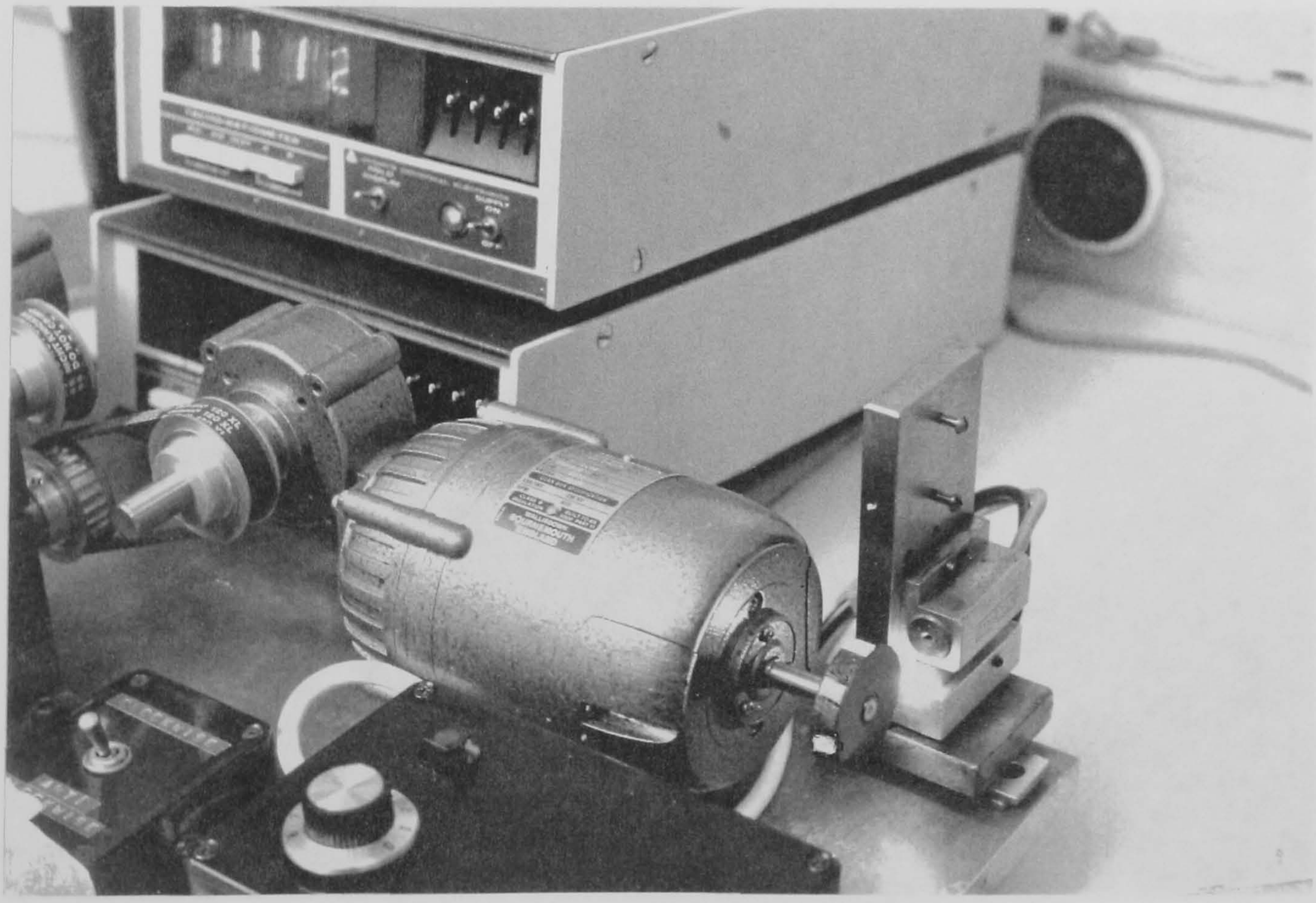

Figure 2.11: Motor/roll speed measurement using optical tachometer

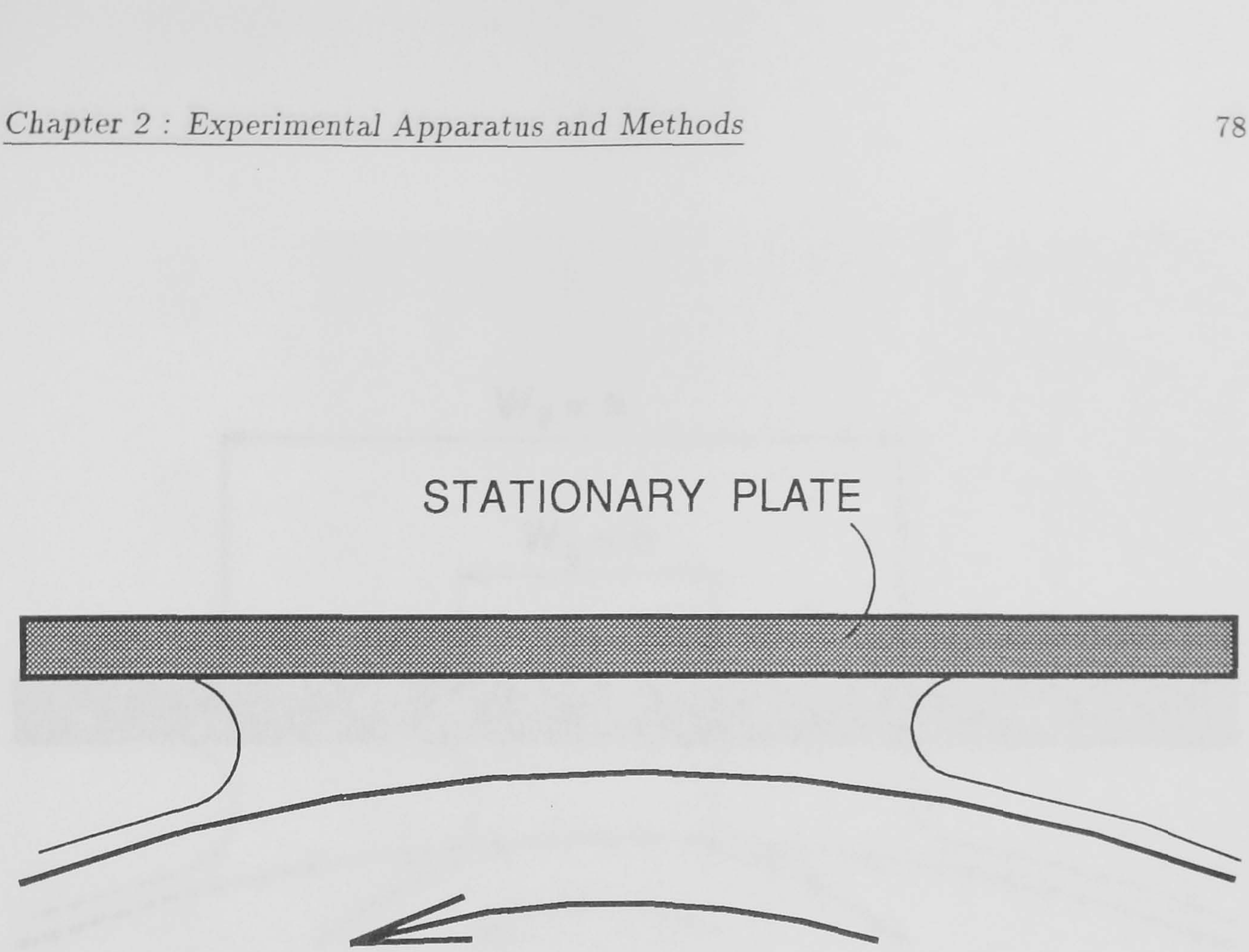

Figure 2.12: Plate-roll geometry

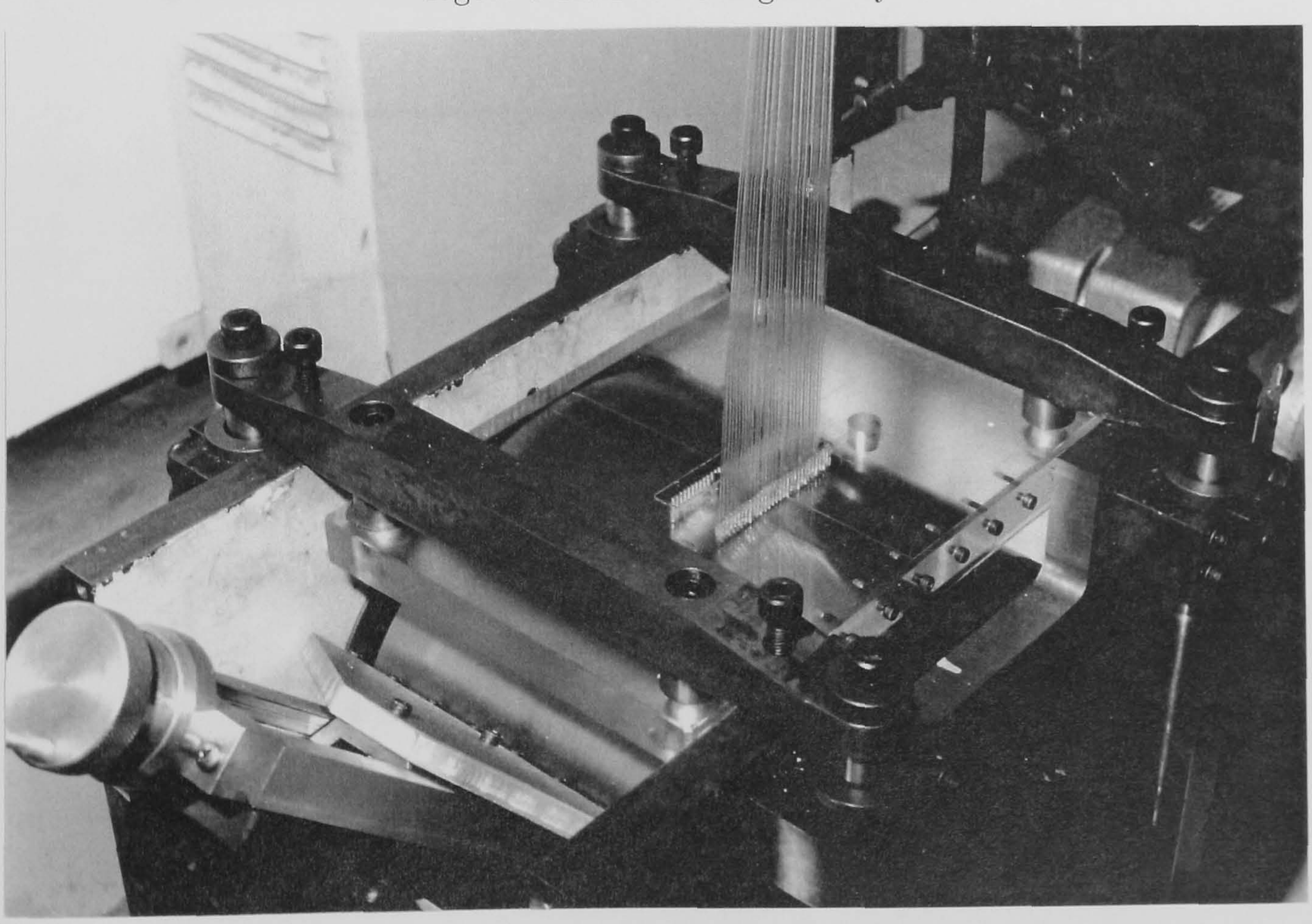

Figure 2.13: Layout of pressure measurement apparatus

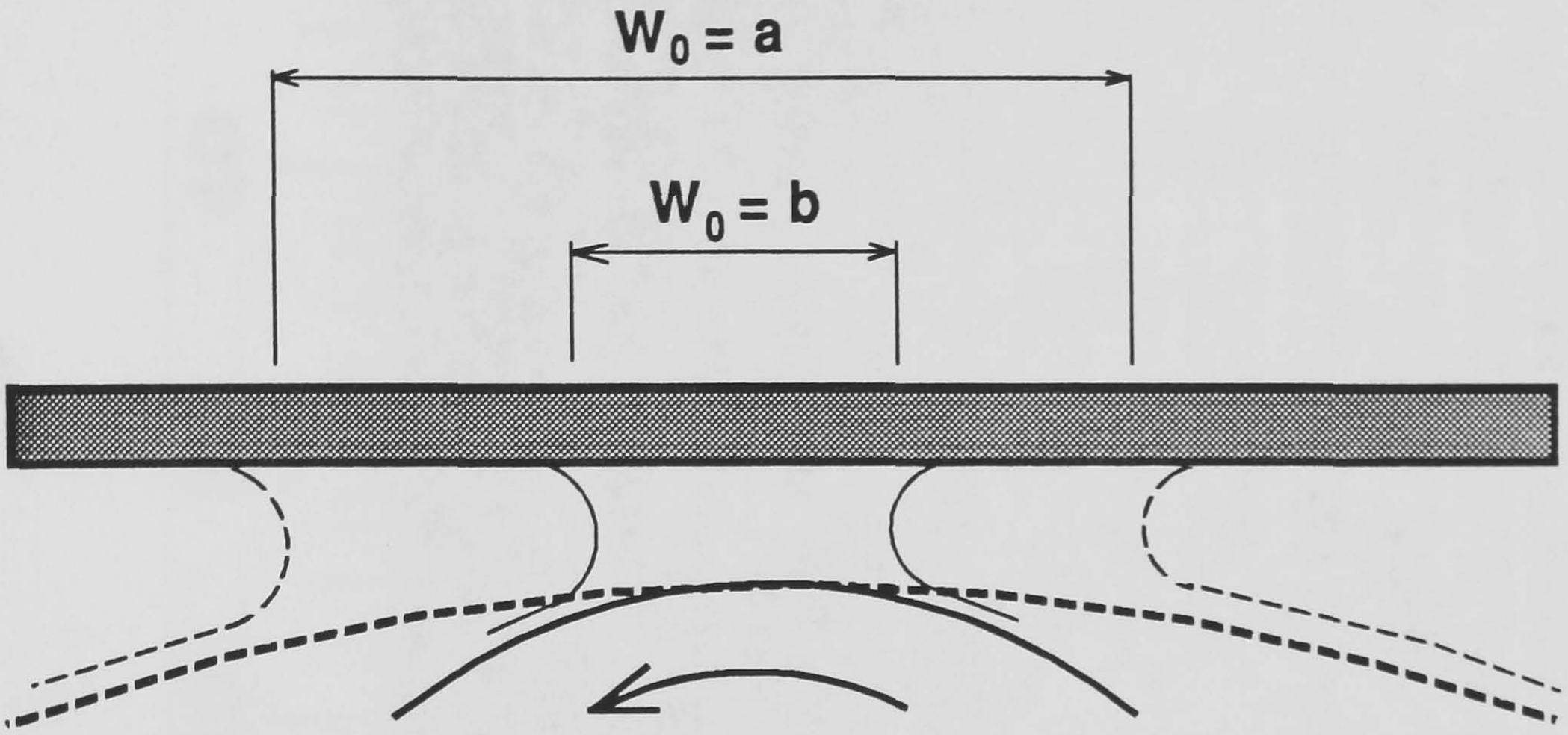

Figure 2.14: Illustration of effect of roll radius on fluid bead width, W_0

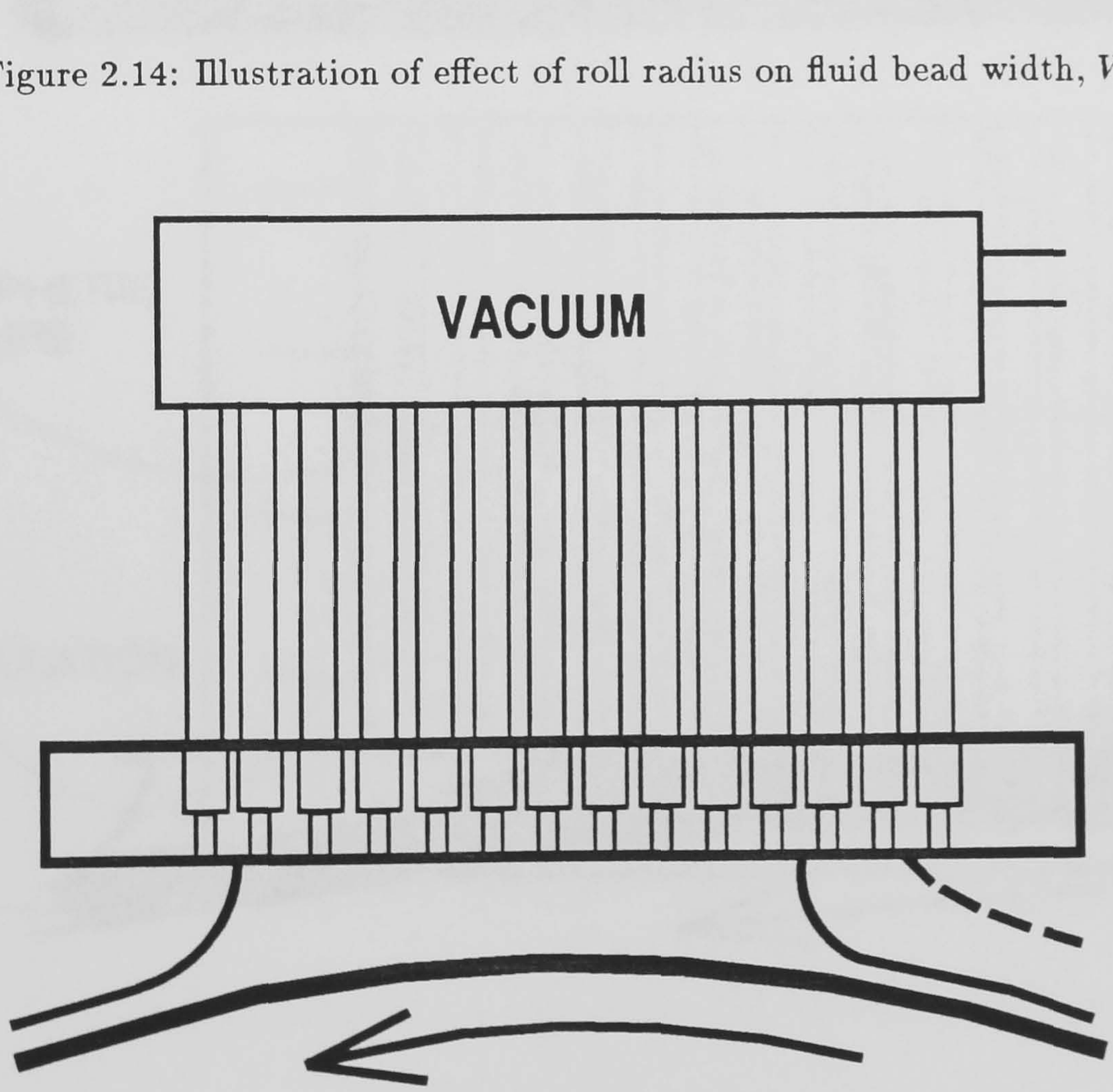

Figure 2.15: Manometer tube arrangement for pressure measurement

(a)

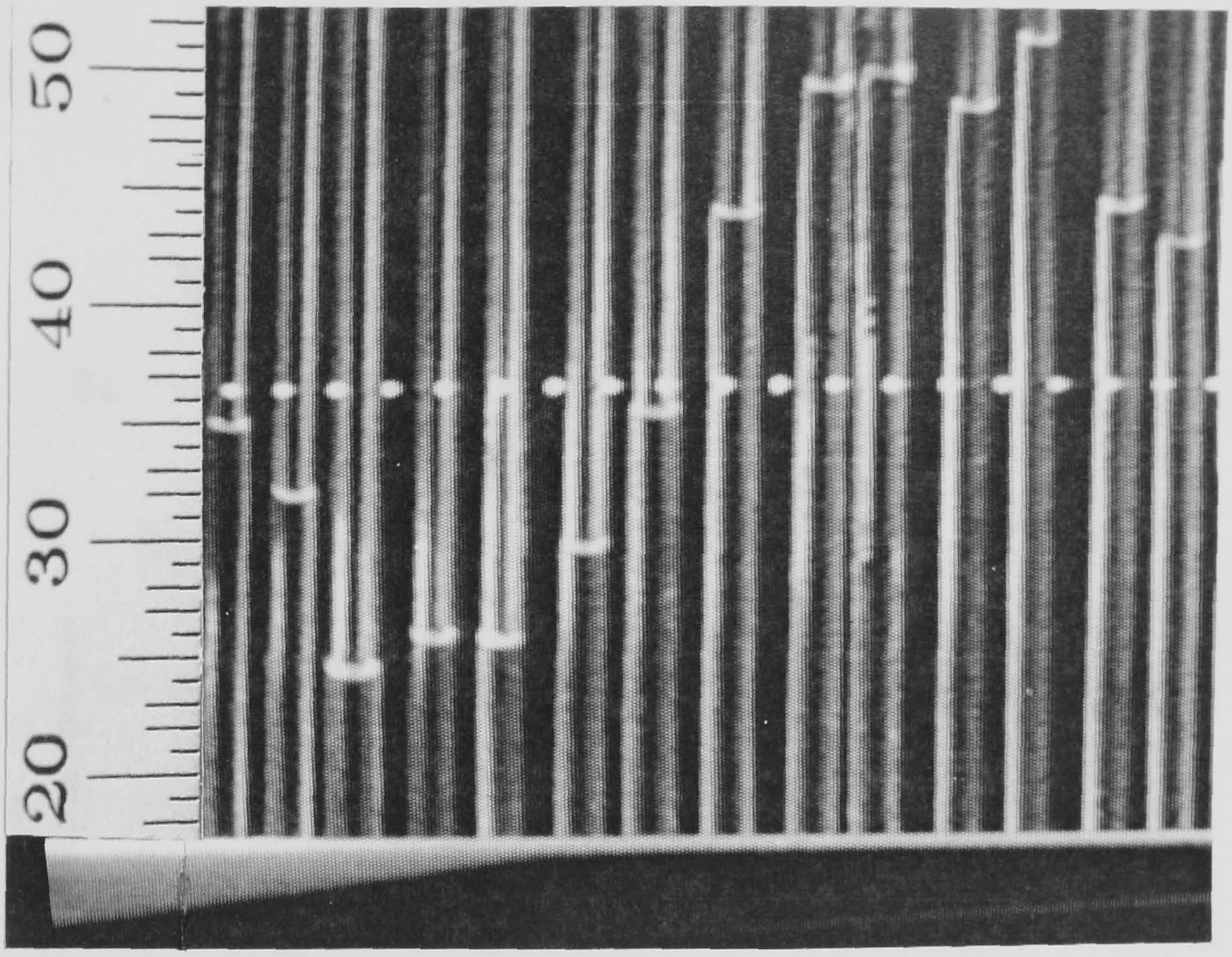

(b)

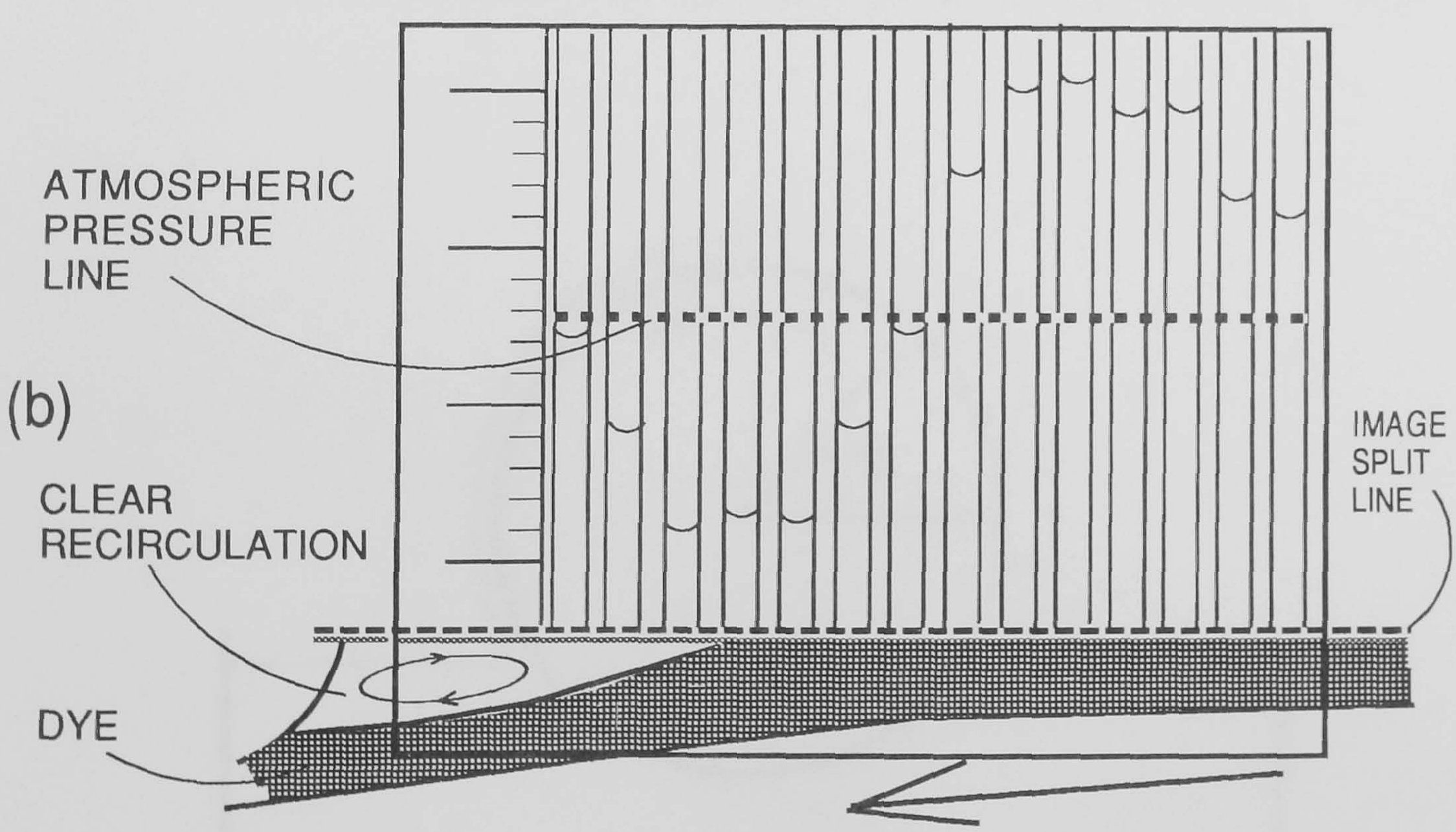

Figure 2.16: Combined image of pressure and flow field (a) video image, (b) schematic representation

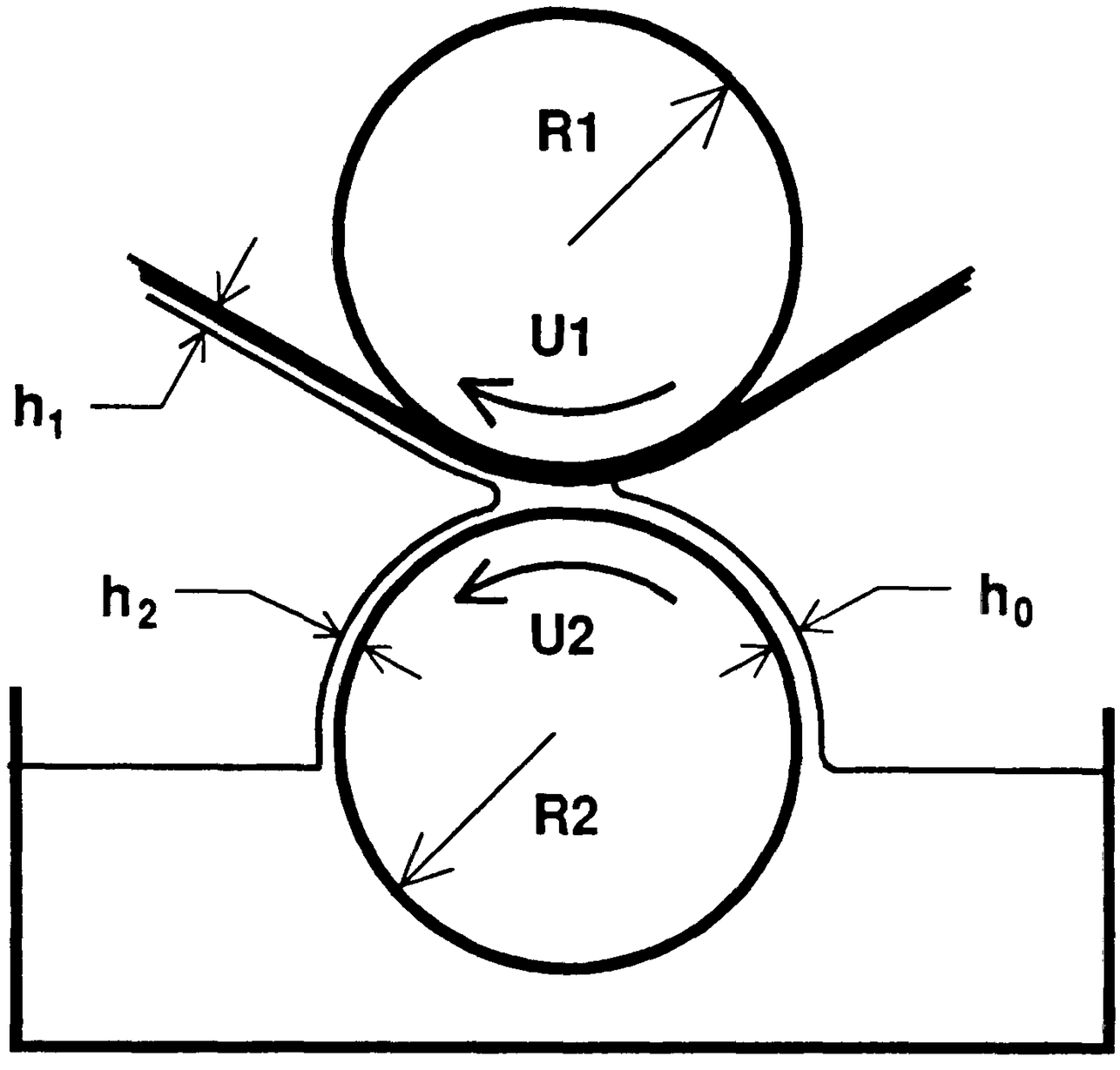

Figure 2.17: Definition of film thicknesses in forward roll coating

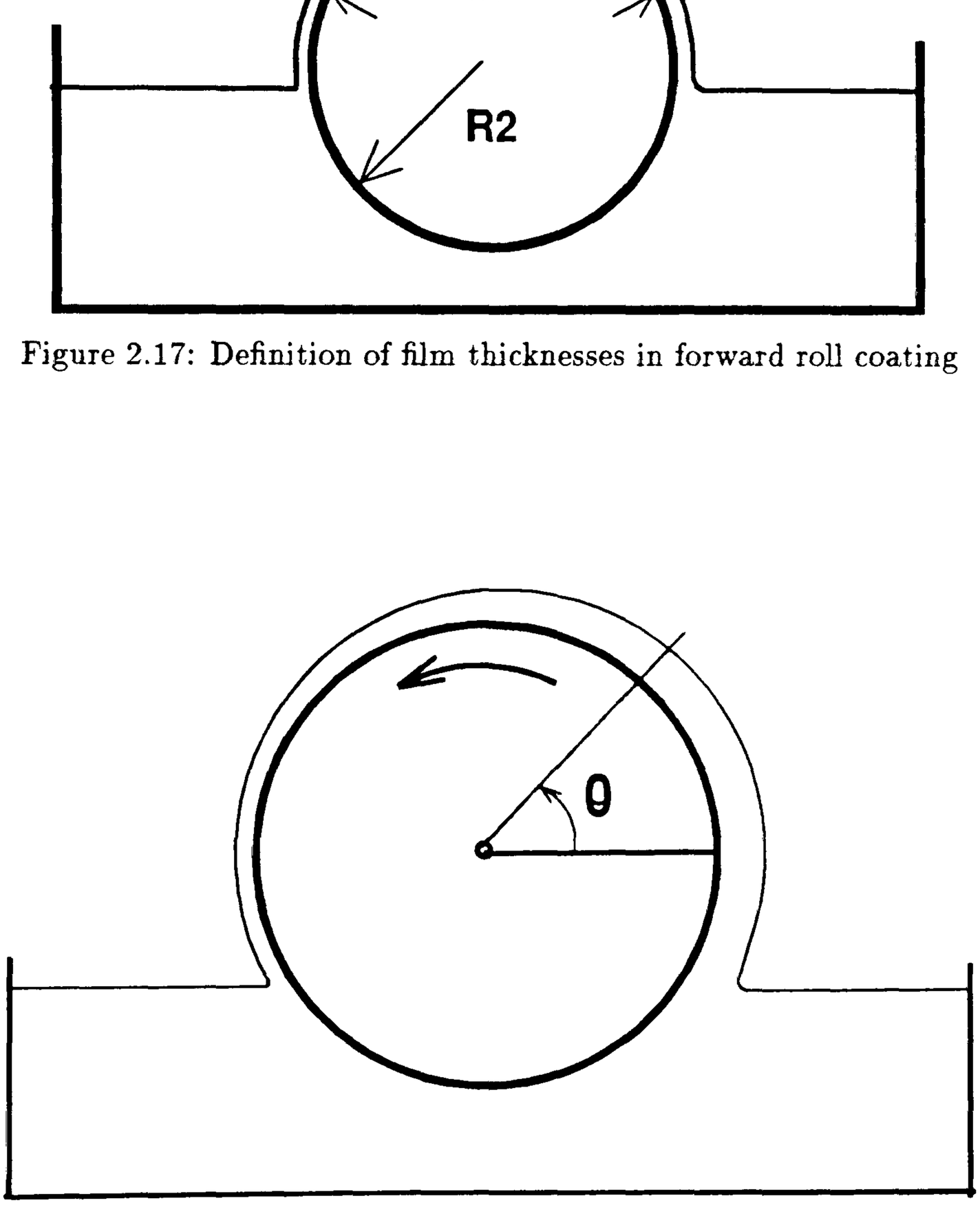

Figure 2.18: Fluid flow around a partially submerged rotating roll

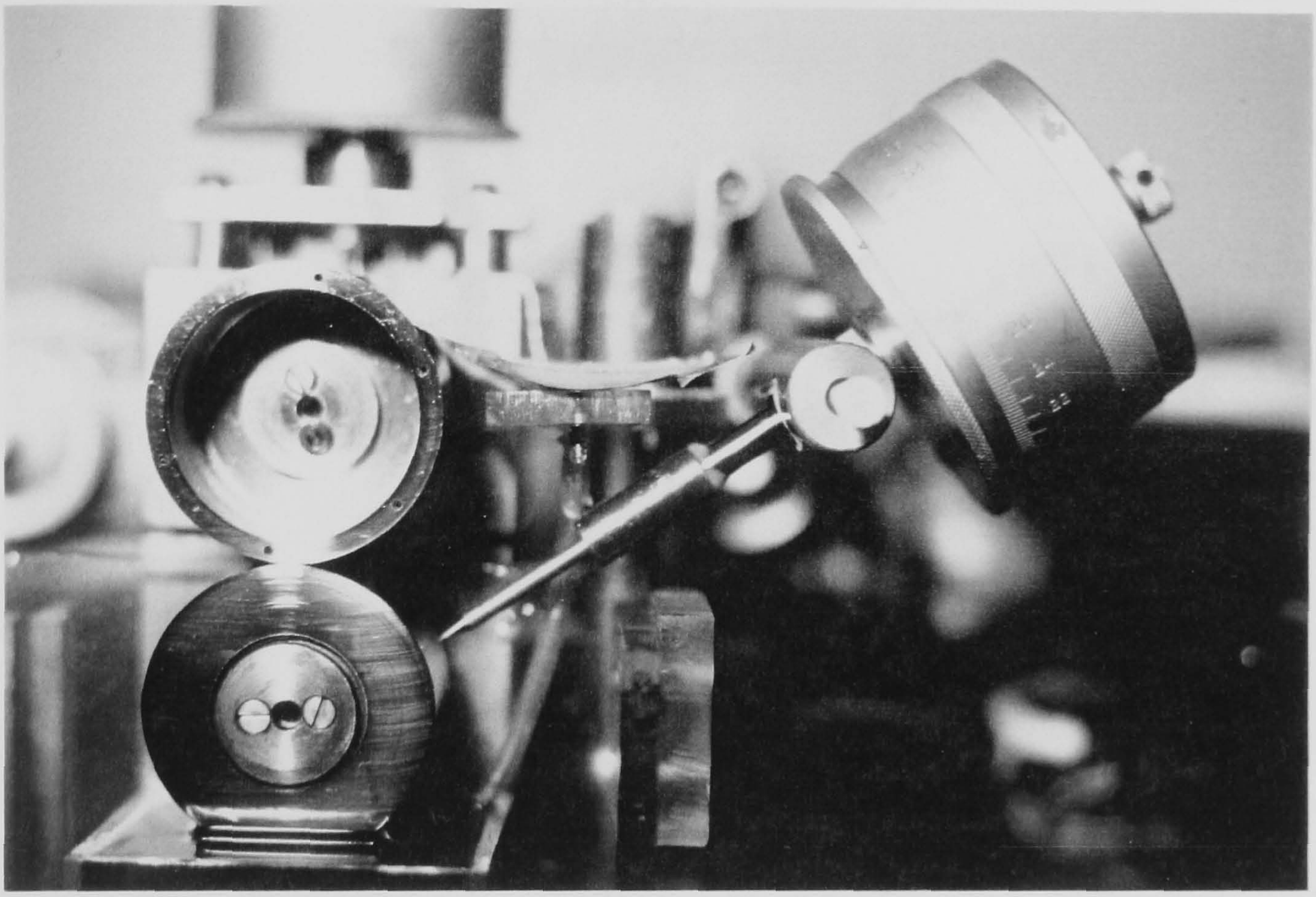

Figure 2.19: Operation of the micrometer-needle film thickness measurement device

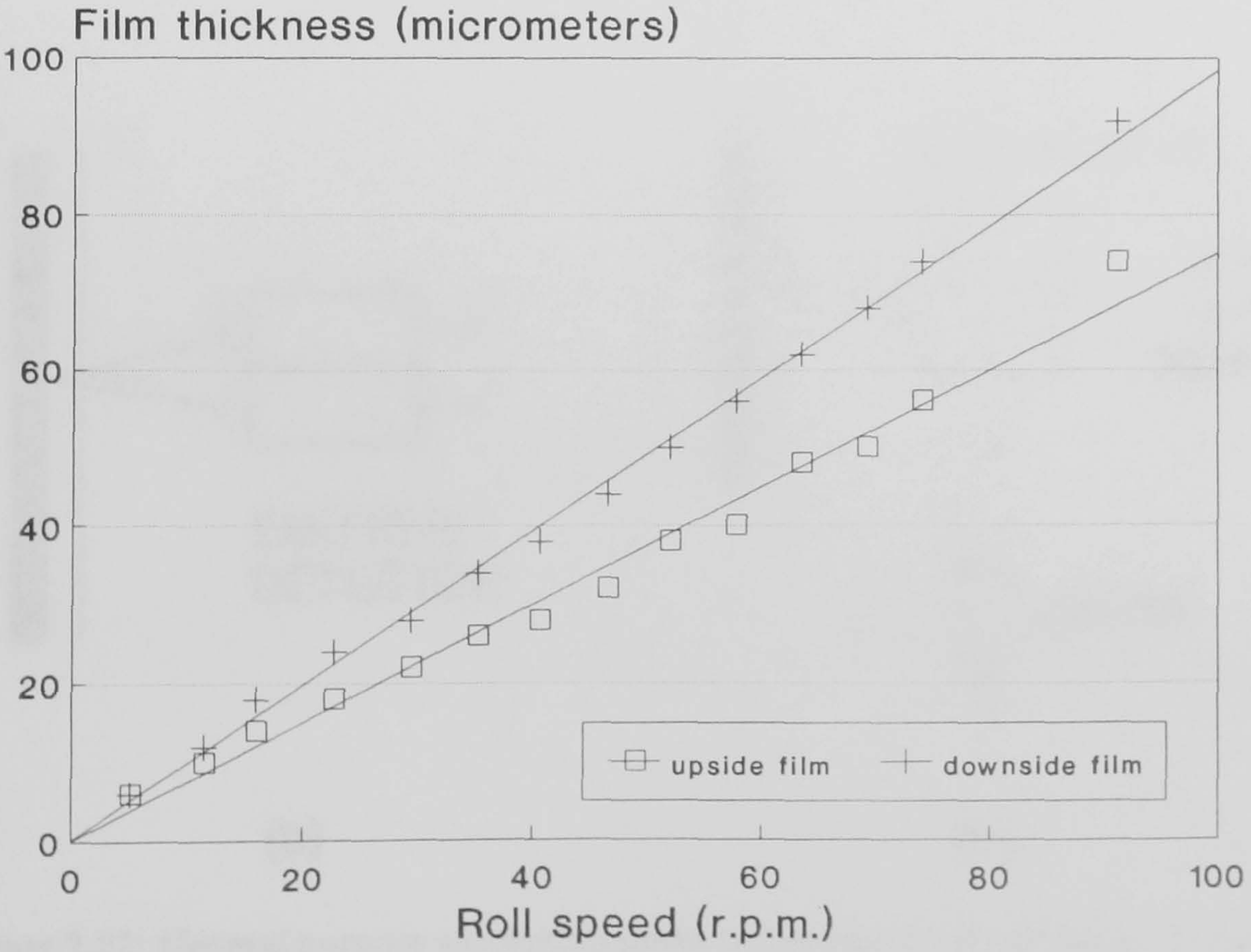

Figure 2.20: Comparison of film thicknesses on the up and down-side of a rotating roll

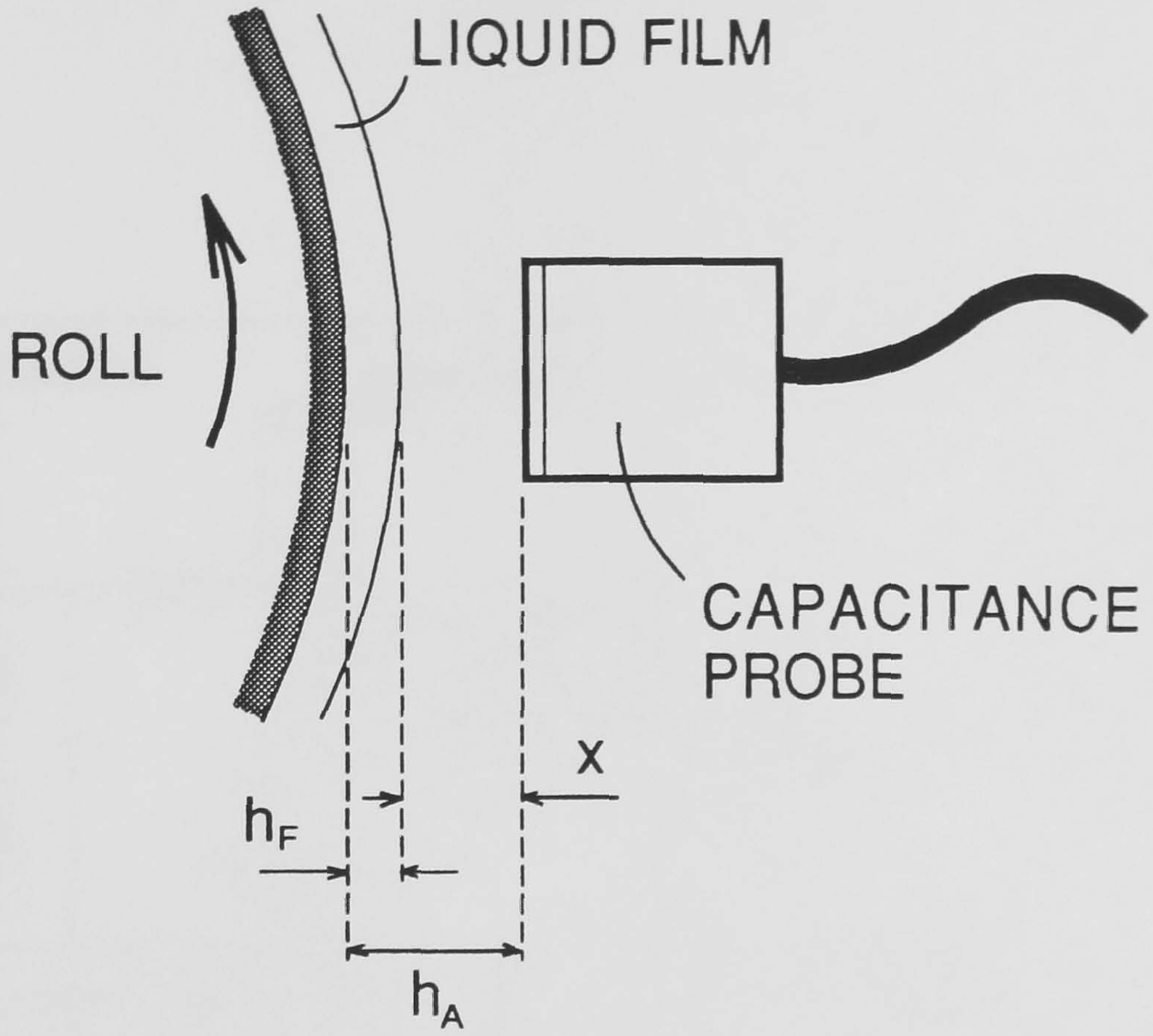

Figure 2.21: Capacitance film thickness detector - principle of operation

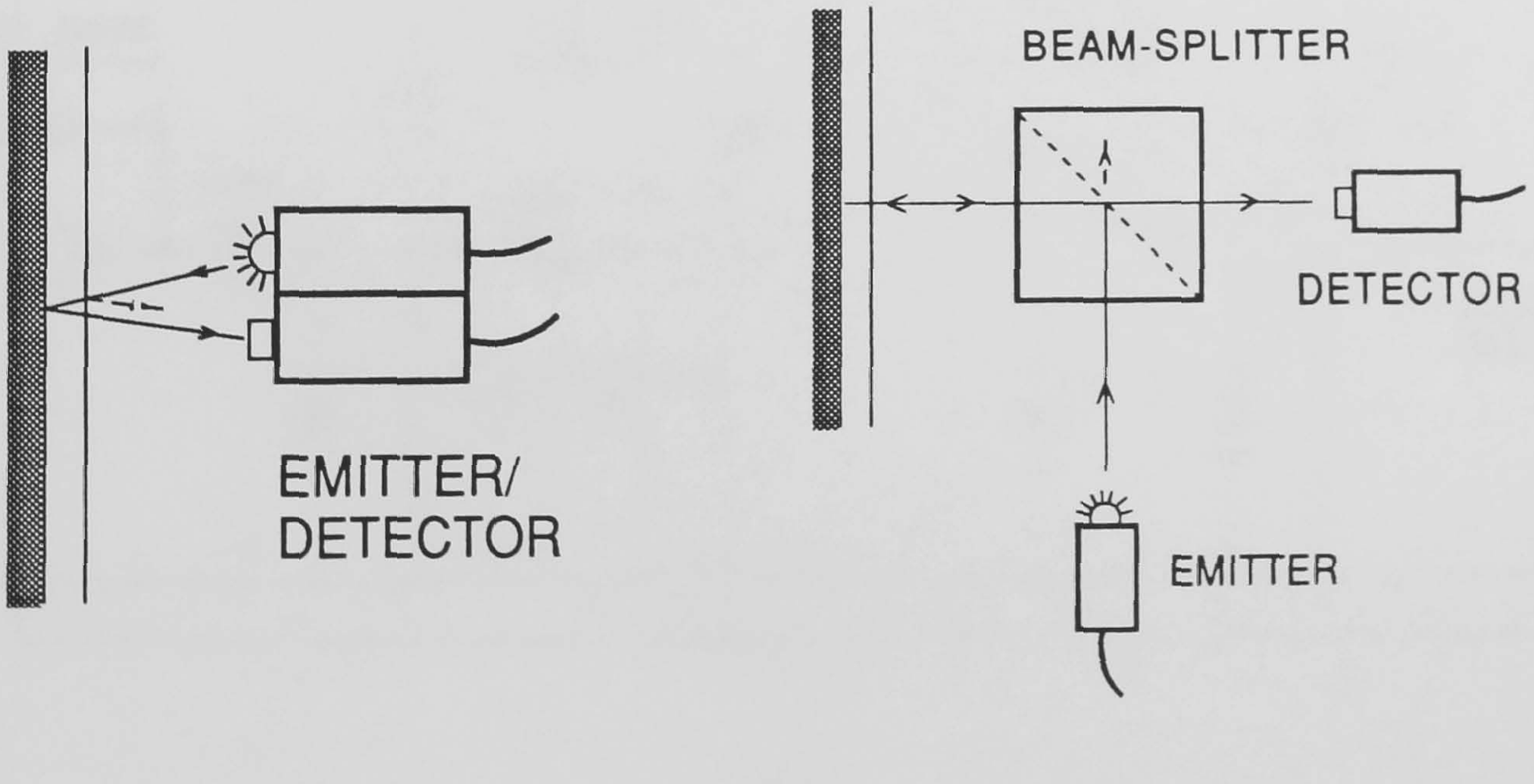

Figure 2.22: General purpose absorption probe (a) standard configuration (b) operation 'normal' to fluid film surface using a beam-splitter

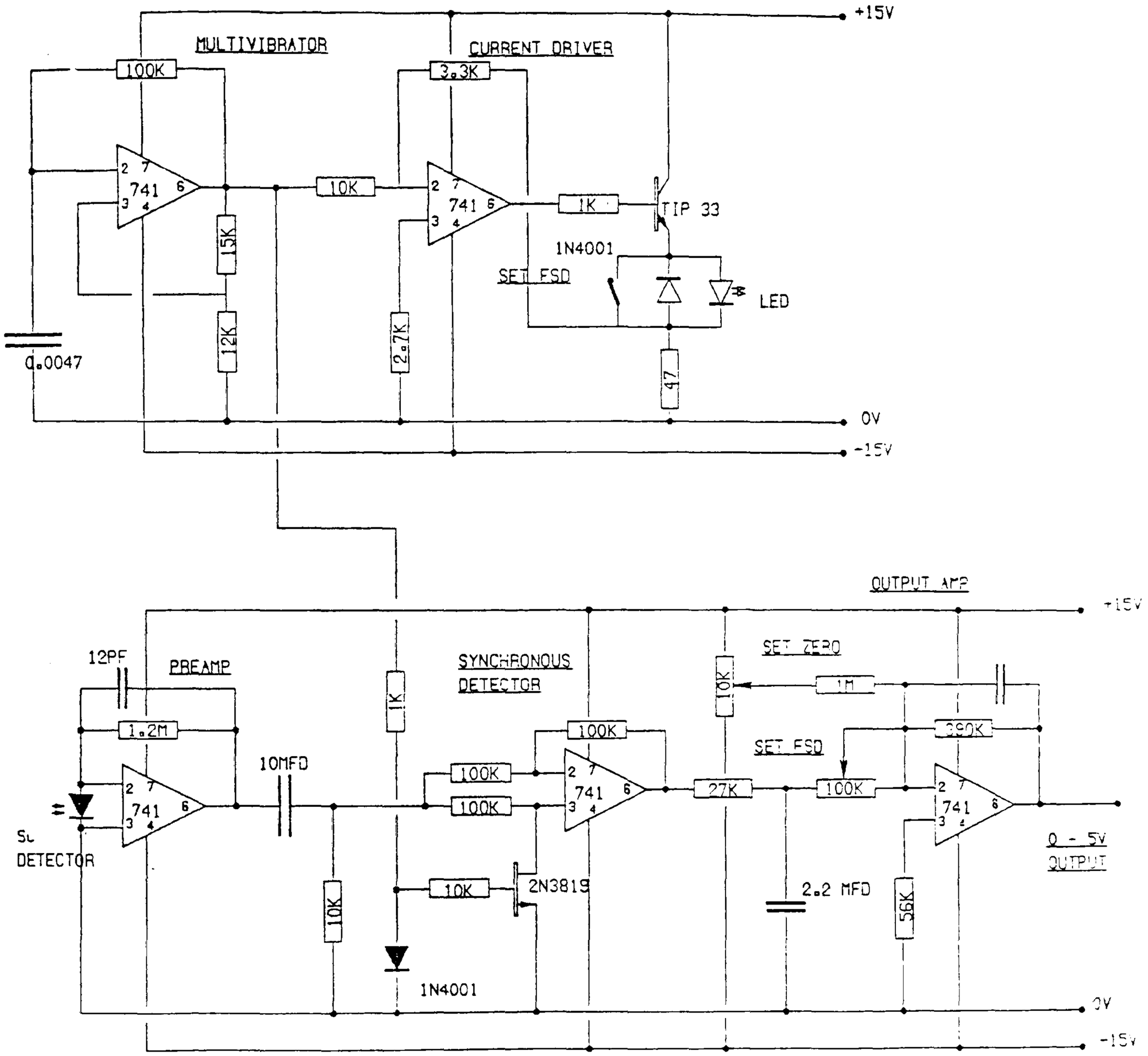

Figure 2.23: Absorption probe - synchronous emitter/detector electronic circuit

Figure 2.24: Absorption probe - control unit and emitter/detector head

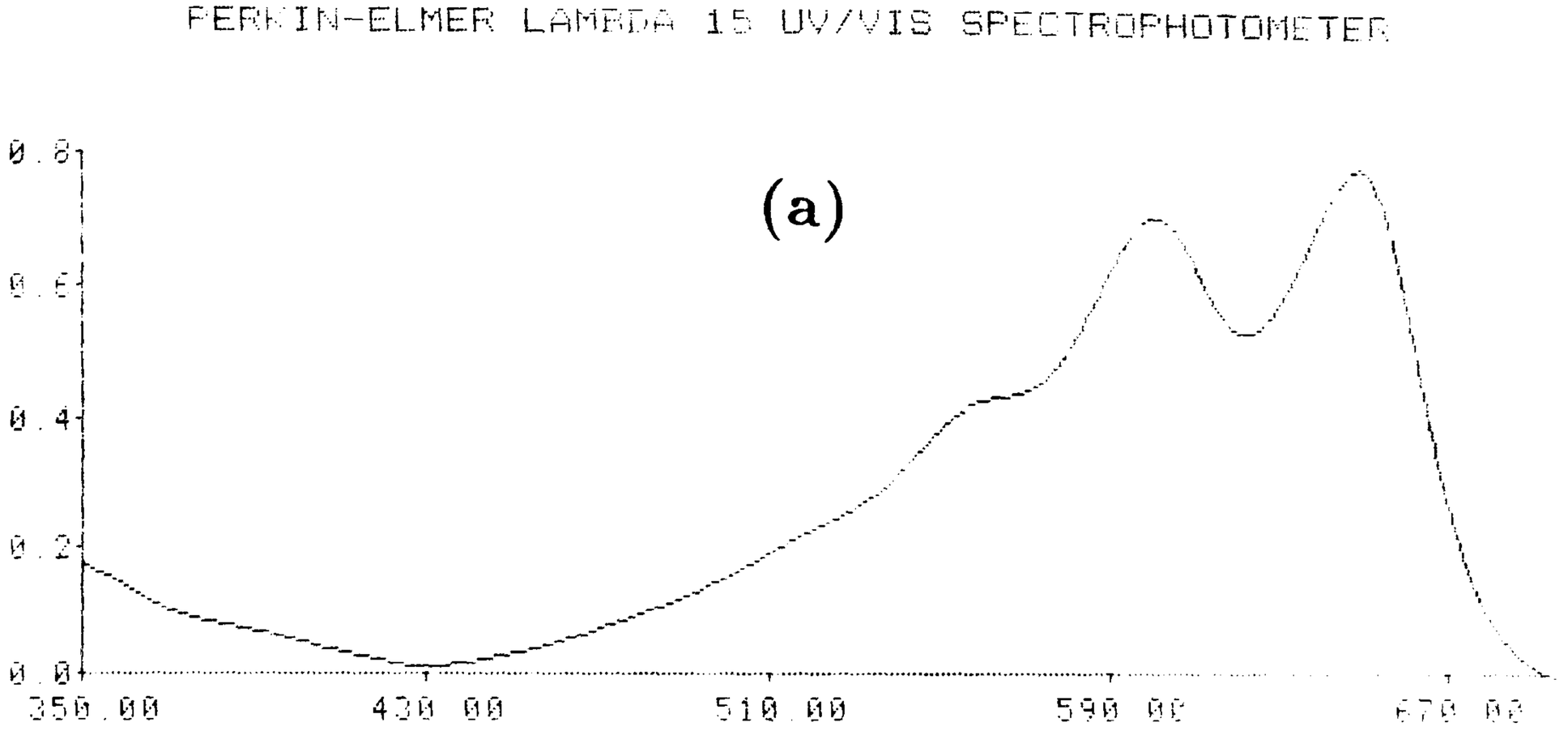

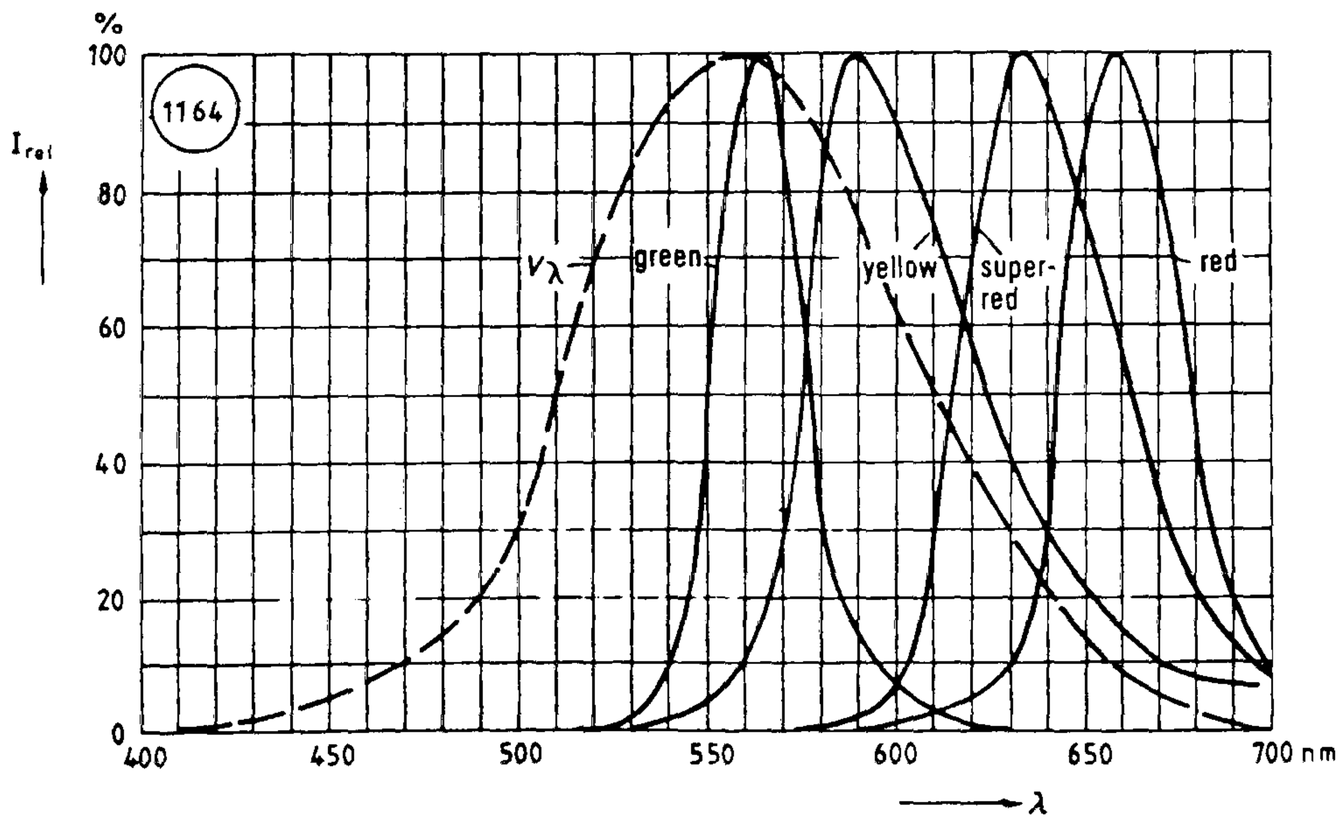

Figure 2.25: Absorption spectrum for (a) Anthraquinone Blue (b) Ariavit Blue FCF (c) Emmission spectrum for Stanley Super-red LED

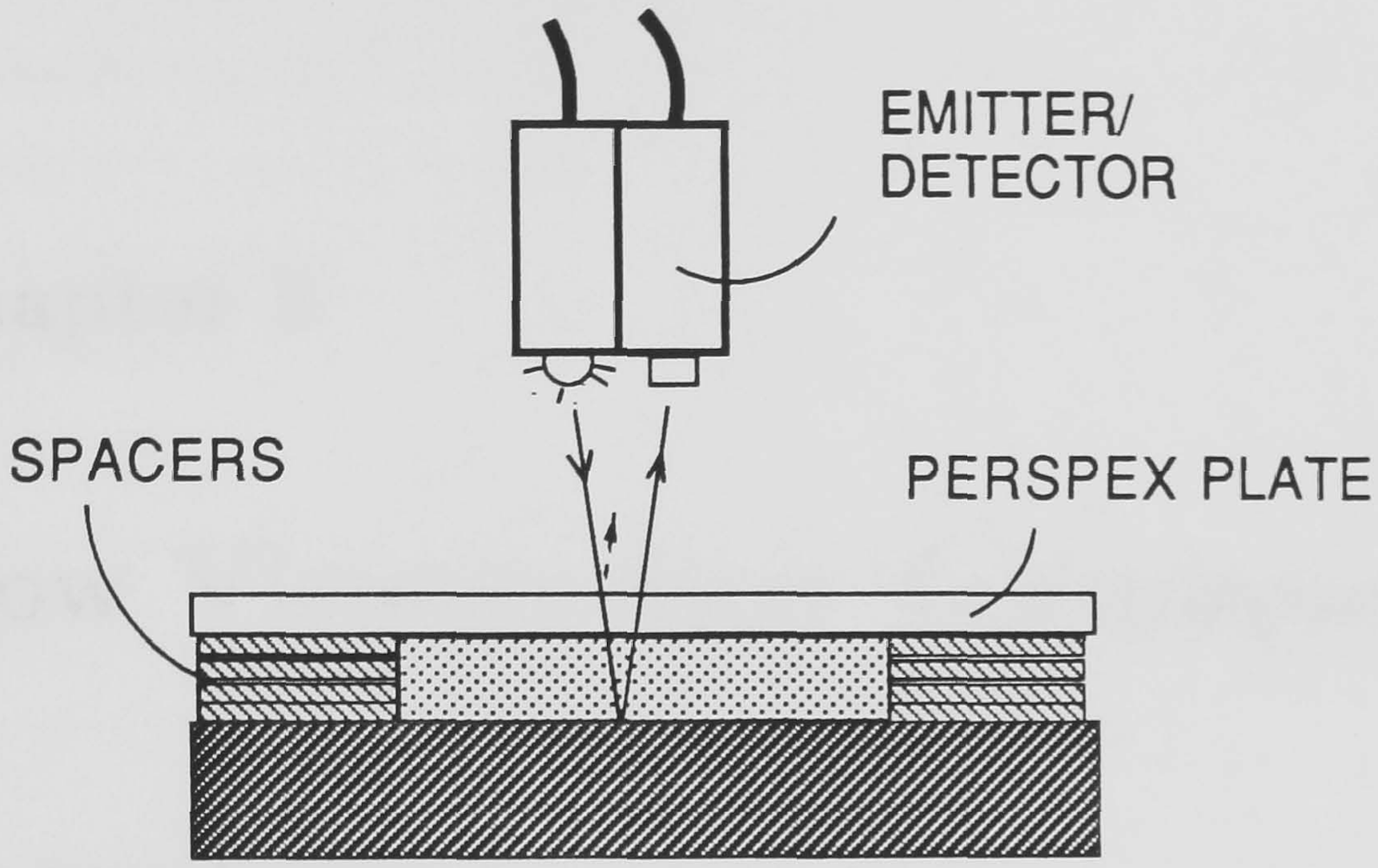

Figure 2.26: Calibration cell technique for film thickness measurement calibration

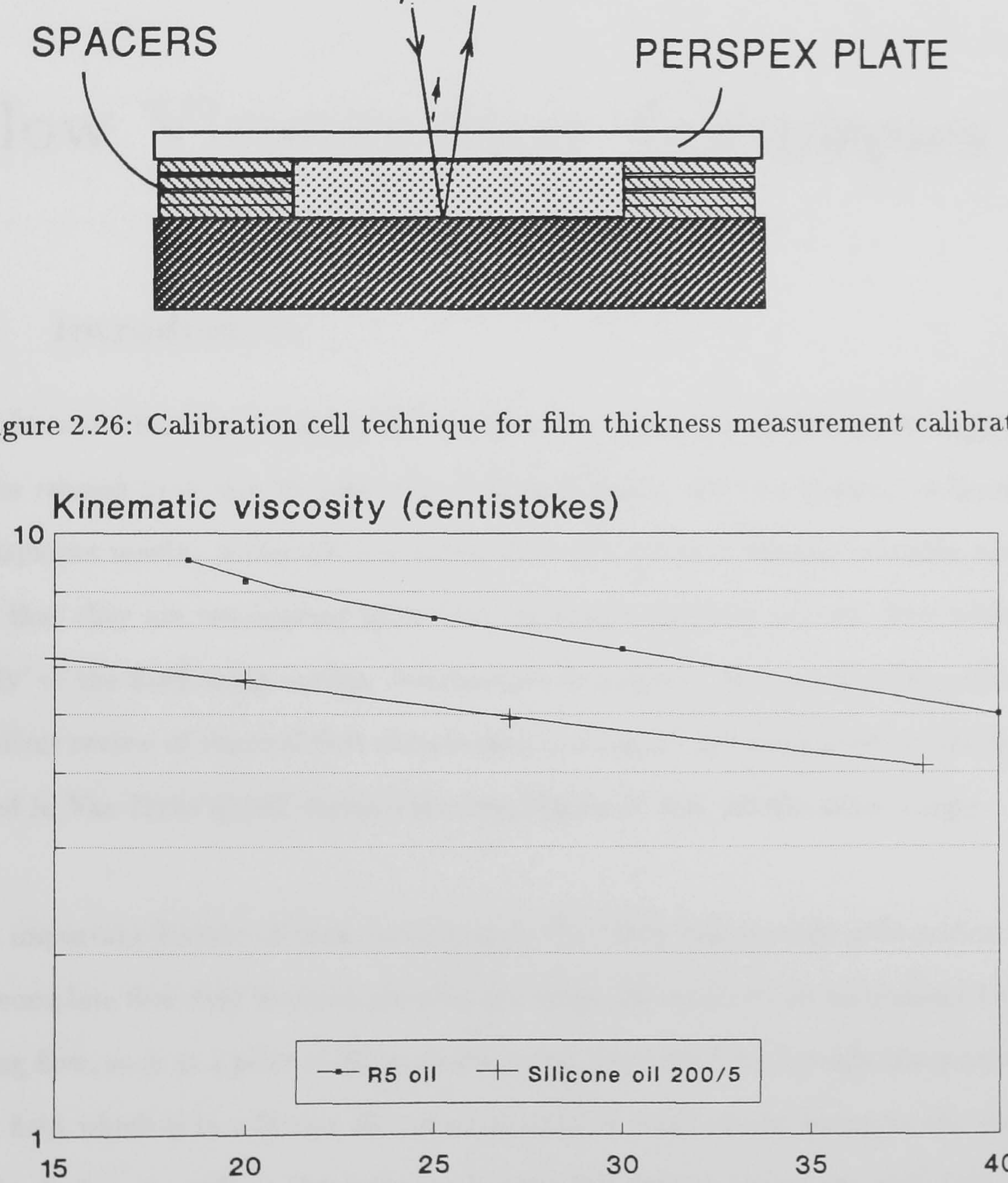

Figure 2.27: Viscosity-Temperature results for Shell Tellus R5 and Dow Corning 200/5 oils

Chapter 3

Flow Visualisation Techniques

3.1 Introduction

Insight into a fluid-mechanical process is greatly improved if the flow pattern produced by, or related to it, can be observed. Generally fluids, whether gaseous or liquid, are transparent media. Although this means that their motion remains invisible, the very fact that they are transparent allows the investigator to illustrate the flow within the 'body' of the fluid using various visualisation techniques. Merzkirch[1974] presents an excellent review of classical flow visualisation techniques and their power is vividly conveyed in Van Dyke's[1982] formidable compilation of flow visualisation images.

The important feature of such techniques is that they can provide information about the complete flow field without physical intrusion. In contrast, an instrument for measuring flow, such as a pitot static pressure probe, provides data for only one point in the flow field which is in addition disturbed/altered to some extent owing to the presence of the device. As well as obtaining qualitative information about the flow field, which reveals the broad features of the fluid-mechanical system, flow visualisation techniques often provide quantitative data, which can be derived from recorded images of the flow.

Roll coating flow fields can be highly two-dimensional. They are characterised by free surfaces, static and dynamic wetting lines and the geometry of such flows is very small. The last factor is the major hurdle in visualising such flow fields (a typical characteristic dimension, the gap size between the rolls, can be as small as 100 micrometres). The flow visualisation methods adopted in this investigation involve the addition of a foreign material to the flowing fluid. This class of methods are the most effective for incompressible flow systems wherein density remains constant. In effect, the specific methods described below enable portions of the fluid to be dyed or seeded with a foreign material, from which conclusions about the structure of the flow field and the velocity of the fluid can be made by observing the motion of these 'tracers'.

A recent comprehensive visual study of a widely-used coating flow was carried out by Schweizer[1988]. He investigated a related coating process, that of slide coating (see chapter 1, Figure 1.1(c)). Schweizer emphasises the need for an experimental flow visualisation technique capable of displaying free surface profiles, wetting lines, and the subtle details of the two-dimemsional flow field, including recirculations and stagnation points. Such results can be used to produce more realistic boundary conditions for the analysis of such flows. Using a combination of hydrogen bubbles, dye injection, and optical sectioning, he was able to obtain detailed results of the flow field.

In many respects the slide coating process studied by Schweizer is particularly amenable to the implementation of such standard flow visualisation techniques. Aqueous fluids were used, which facilitated the use of the hydrogen bubble technique. The slide itself is stationary and thus flow visualisation equipment can be 'mounted' in situ, including the hydrogen bubble wire, and holes, for the release of dye, can be machined into the surface. The free surface is illustrated by introducing a dye trace from an injection point adjacent to and just touching it; revealing the form and position very well. Ikin[1992]

has successfully confirmed the form of the free surface shape using a contacting wire method, similar to that of the micrometer-needle film thickness device described in Chapter 2, §§ 2.5.2.

3.2 The Roll Coating Flow-Field

In comparing the slide coating system, described above, with that of the roll coater, it is clear that flow visualisation of the latter is more difficult to achieve. Firstly, all the solid boundaries in roll coating are in motion, therefore it is not practical to inject tracers from holes in these surfaces. Secondly, the hydrogen bubble technique is not practical in the present study; characteristic speeds and viscosities are very low, which would result in relatively large diameter bubbles, violating the ratio of buoyancy to drag force ($<< 1$) to achieve an accurate reproduction of the streamline pattern. In addition, non-aqueous fluids are used here which cannot facilitate the hydrogen bubble technique. The effective illustration of the free surface position in the slide coater is possible because it is relatively large and accessible whereas for the far smaller and less accessible roll coating downstream free surface, for example, it is not possible to physically place a tracer there without significantly affecting the flow field.

In order to observe the fluid flow in the very small nip between a plate and roll or two rotating rolls it is necessary to look along the axis (Figure 3.1(a)), at a cross-section of the flow pattern in the nip region (Figure 3.1(b)). Two methods are employed to illustrate the flow field:

- Dye injection, to reveal the major features of the flow field and the main fluid transfer path.
- Particle flow, to obtain quantitative data of specific velocities throughout the flow field and relate this to system parameters, as well as comparison of the results

with theoretical predictions of the velocity field.

The experimentation and analysis of particle flow is described fully in § 3.9.

3.2.1 End-meniscus distortion

The major difficulty to be overcome in viewing the nip region is the unacceptable level of distortion caused by the fluid meniscus which forms at the roll ends - the effect of this distortion is illustrated in Figure 3.2(a). Here a hyperdermic needle is used as a viewable test piece. The problem was resolved by placing a transparent plate at the end of the rolls sufficient to cover the gap; the fluid attaches itself to the back of this plate creating a 'viewing window' into the nip. Figure 3.2(b) shows the viewing plate in position revealing an undistorted image of the hyperdermic needle.

There is a limit to the viewing depth that can be achieved along the gap because the effect of the 'out of focus' roll edges, on the magnified image, increases axially. The optimum viewing depth was found to be around 5mm at which distance edge effects from the viewing plate were considered negligible (for a gap size of less than 0.5mm, the viewing plane is 10 'gaps lengths' from the plate). Capillary leakage between the roll ends and the plate also gives rise to a secondary flow in the nip, directed along the axis towards the viewing plate. This flow however is extremely slow-moving and is found to be negligible when compared to the through-nip flow. The viewing arrangement is illustrated in Figure 3.3.

3.3 Dye Injection

An oil-soluble, powder dye was used throughout this investigation because it dispenses with the problem of matching the properties of a liquid dye with those of the working fluid. If they were too dissimilar the presence of the dye might alter the flow.

An important requirement of the liquid dye is that it does not exhibit excessive diffusion/dilution properties once it is introduced into the flow field. This can result in a lack of clarity of the key features of the flow field as the dye quickly colours the whole of the region of interest. This diffusion/dilution rate, as well as being a function of the combination of the fundamental properties of the dye and the particular working fluid, is also dependent on the viscosity of the fluid; the higher the viscosity the more vivid the resulting images of the flow field. Here the liquid dye is produced by simply dissolving a small percentage of the dye powder in a quantity of the working fluid. The liquid dye is injected into the incoming fluid film, far downstream of the roll nip, using a hyperdermic needle. The injection pressure is gravity-controlled and the height of the reservoir of liquid dye can be adjusted to increase or decrease the pressure, depending on the speed of the fluid film as it passes the needle (see Figure 3.4(a)).

In practise the injection pressure is adjusted to produce a smooth filament of dye, which is transported, by the fluid film, into the nip region (see Figure 3.4(b)). Insertion of the hyperdermic needle into the incoming fluid film produces a local distortion of the fluid flow but this is sufficiently far downstream of the nip so as not to influence the flow there. Figure 3.5 vividly demonstrates the injection of dye and the subsequent splitting of the fluid film in the nip. A useful variant to continuous dye injection is to 'pulse' the injection sequence by intermittently opening and closing the injection control valve. This serves to elucidate the major features of the flow. Several sizes of hyperdermic needle bore are used to deliver varying amounts of dye, depending on the speed of the system and therefore the fluid throughput (a larger volume of dye is required to illustrate the flow for a high throughput condition, alternatively if the dye volume is too large it can obliterate the flow field).

The difficulty in lighting such a small and inaccessible area was overcome using a

combination of the acrylic rolls together with two slide projectors, one on either side of the nip, to produce two concentrated beams of light for effective and even illumination (see Figure 3.6).

3.3.1 Storage and Manipulation of Results

The results were recorded onto VHS video tape using a Panasonic F10 CCD video camera attached to a set of bellows and a 90mm macro lens, to give up to 30X magnification. Information about test conditions could also be recorded as an overlay on the actual flow images, or prior to each test run using a video character generator. Images of the flow were captured and analysed using the image processing system described in § 3.6.

3.4 Particle Seeding

The principle behind seeding a fluid flow with particles is to illustrate the streamline pattern. The assumption therefore, is that the seeding particle mimics the motion of a fluid 'particle'. One of the simplest techniques to achieve traces of particle motion is to illuminate a thin cross-section of the particle flow and photograph it over a long time exposure which results in streaking (the method is often referred to as streak photography). The problem with this method, in the present study, is the insensitivity of photographic film to the low levels of particle illumination and the relatively high velocities involved (resulting in relatively low exposure times).

It is desirable to suspend the particles in the flow indefinitely. One experimental problem is that the suspended particles will acquire an appreciable settling velocity if their density differs significantly from that of the surrounding fluid. The motion of a sphere of radius a, density ρ_p falling freely in a liquid with density ρ_f and viscosity μ is given

by Stokes formula (Batchelor[1967]) for small Reynolds Number:

$$\rho_p V_p g = \rho_f V_p g + 6\pi\eta U_t a \tag{3.1}$$

where V_p is the volume of the particle, and U_t is its terminal velocity. The estimated time taken for a particle to move across the bead varies from 1 second (at very low roll speeds) to 0.01 seconds (at high roll speeds), for a typical bead width, W_0, of 5mm. Assuming a typical gap size of 150 micrometers, the particle must not fall more than $\frac{1}{10}$th of this distance, during its' travel, to produce a representative velocity vector. Therefore the upper and lower bounds on an acceptable value of U_t are $15\text{x}10^{-6}$ m/s and $20\text{x}10^{-9}$ m/s respectively. By rearranging equation (3.1) to give:

$$\rho_p = \rho_f + \frac{1}{v_p g}(6\pi\eta u_t a) = \rho_f + \frac{9\eta u_t}{2a^2 g} \tag{3.2}$$

an order of magnitude estimate of the particle/fluid density tolerance for Shell Tellus R5 oil can be obtained in terms of the lower bound on U_t, for a typical particle of 5 micrometres in diameter (i.e. an order of magnitude smaller than the nip). Then:

$$\rho_p = \rho_f \ (\pm 5\%)$$

Which shows that the densities of the particles and the fluid must be matched very accurately in order that the particles follow the fluid flow to an acceptable degree.

Illumination of the nip

In order to view the roll coating flow field, it is necessary to look at a thin cross-section somewhere along the length of the nip. The dye injection technique (described in § 3.3), by its' very nature, illustrates a 'slice' of the flow only, since the rest of the fluid domain is transparent - therefore flooding the nip with light is acceptable. In contrast, the seeded flow contains particles throughout the flow domain. It is therefore necessary

to effectively illuminate a discrete cross-section of the flow to illustrate the particle flow in that region only (also referred to as optical sectioning). The fact that particles are present throughout the whole of the flow field also has implications for the acceptable viewing depth into the nip; the further into the nip one looks, the more particles there are flowing in front of the illuminated section. Although these particles are not illuminated, their presence degrades the quality of the image. This effect is minimised by first ensuring that the viewing depth is not too large, and secondly that as little light as possible is allowed to enter the flow domain in front of the region of interest (in practice this means the creation of a discrete light sheet which leaves the surrounding flow in darkness).

It is possible to produce a sheet of light using the optical system illustrated in Figure 3.7. The lens serves to 'expand' the beam, while the slit produces a parallel-sided light plane. To achieve an evenly illuminated cross-section of the flow requires a double optical system - one on either side of the nip. Unfortunately the intensity of the light sheet produced by an incoherent white light source is not sufficient to adequately illuminate the particles under typical operating conditions, i.e. reasonable roll speeds and thus similar fluid/particle velocities. In order to capture the motion of a number of particles over a finite distance within the fluid bead necessitates the use of a high recording frame rate, which in turn lowers the possible exposure time. This problem is discussed more fully in §§ 3.8.2.

By replacing the white light source with a suitably powerful coherent laser light source, particle illumination over the whole range of recording frame rates was found to be good. In practice two 10mW HeNe lasers produced adequate results. The method used to produce the laser sheet was identical to that for the white light source (Figure 3.7). Indeed, neither the slit nor the lens were required under certain conditions; for a typical

minimum gap size of the order of 250 micrometres the unmodified laser beam diameter (typically 0.5mm) is of a sufficient size to illuminate this area well (with near-parallel walls. However to adequately illuminate the particle flow in the converging and diverging regions of the nip geometry necessitated adjustments to the laser beam geometry. Because the light source meets a particle in a direction normal to the viewing plane, the light experiences excessive scattering, which in turn leads to less light being picked up by the imaging system. This manifests itself as depleted particle illumination and intermittent illumination for non-spherical particles (as the light is scattered in different directions by variations in a particles' surface topography). In addition, the two-sided illumination system can result in particles, which are in the mid-region of the fluid bead, giving two reflections; one from each source. A major advantage of the laser illlumination technique is that it is a 'cold' light source and therefore it does not heat the fluid. A white light source, on the other hand, can produce significant localised heating of the flow, particularly if it is sharply focused.

An alternative method of illumination, which overcomes the unpredictable scattering effect of the light sheet method, is to place a beam-splitter between the viewing window and the camera lens (see Figure 3.8). A focused light source is positioned on one side to allow reflected light to illuminate particles in the nip region head-on. With this system, particles in the nip reflect a much higher percentage of light because they are illuminated in the same plane as the viewing axis. The major drawback of this method is that it does not illuminate a discrete cross-section of the nip flow, but rather the region extending from the viewing plate and into the nip. This means that it is only possible to view the particle flow in close proximity to the viewing plate with any clarity, however it is in this region where the plate edge effects are present. It is therefore not possible to treat this flow as a typical cross-sectional bead-flow. In trying to look further into the nip the problem of particles in front of the focal plane, as discussed

earlier, is even more pronounced since these particles are now also illuminated, which reduces the clarity of the particle flow plane dramatically. In addition, the inner and outer surfaces of the viewing window reflect this light and further degrade the quality of the image.

Having tested the above methods of particle illumination fully, the laser sheet configuration was used, together with the High Speed Video system (described in §§ 3.8.3), being by far the most effective means of defining the flow.

3.4.1 Choice of Particles

Particles must be near-spherical, opaque and neutrally buoyant. Spherocity is important so that as particles move through the fluid and experience rotation, they give a constant illumination/reflection. Opacity is required so that they reflect light and are not invisible in the fluid. Neutral buoyancy is necessary to enable the particles to follow streamlines (as discussed in § 3.4). If they were too dense for example, a downward component of velocity would be added to the velocity field due to gravitational effects.

The importance of neutral buoyancy depends on the magnitude of the horizontal velocities compared to the settling velocity of particles in stagnant fluid. It is simple to get an estimate of the magnitude of average settling velocity for a particular type of particles by mixing them with fluid in a transparent beaker and measuring the time for the majority of the particles to settle on the bottom from a relatively stagnant start point. This can then be compared with an order of magnitude estimate for the horizontal velocity in the bead under rolling conditions (the average roll speed is a suitable velocity to use) – see § 3.4. If the particles satisfy the criteria of size, shape, and opacity as well as the settling velocity being an order of magnitude smaller than the average bead flow velocities then they will be suitable for use as fluid tracers. An additional requirement

is that the particles exhibit mono-dispersive behaviour in the fluid; if they coalesce, tracking becomes impossible. The following table compares a number of particle types tried, where a '√' indicates good performance, a 'o' indicates fair performance, and a '•' indicates poor performance: After having tested all the above substances, the only

Test material	Opacity/ reflectance	Relative velocity/ density	spherocity	size	mono-disperse
Aluminium flakes	√	√	•	√	√
Diakon(acrylic)	•	•	√	•	•
Titanium oxide	√	•	o	o	•
Fluon(PTFE)	√	•	o	√	•
Bentonite	o	•	o	o	•
Nylon	√	√	√	o	•
Glass spheres	•	•	√	•	√
Polysterene	√	√	√	√	o
Lycopodium	√	√	√	•	•
Sephasorb	√	√	√	√	√

Table 3.1: Comparison of seeding material properties

particle material to satisfy all the criteria was Sephasorb (Pharmacia Fine Chemicals Inc.), which is in fact a product used for gel filtration. Therefore, this material was used to seed the fluid flow, producing good results when suitably illuminated (see Figure 3.9)

An alternative approach to matching fluid and particle densities is to change the density of the fluid to suit the density of the particle material. The following example considers water as an option for the working fluid. The acrylic (Diakon) particles de-

tailed above have a specific density of 1.18. To achieve a brine solution with the same density requires adding sodium chloride to water in the ratio 25:75. In practice sodium bromide is more suitable; giving a clearer liquid. It is also advantageous to make the fluid slightly more dense than the particles, so that they tend to rise, over a long period, in the fluid bath, ensuring that the roll always has particles to pick up. Viscosity can also be altered for such a working fluid by the addition of varying quatities of low molecular weight PolyVinyl Alcohol (PVA), for example:

- 1% PVA gives 1.57 c/s viscosity
- 2% PVA gives 2.61 c/s viscosity
- 5% PVA gives 11.96 c/s viscosity

With the lower percentages of PVA (i.e. 1 & 2%) the liquids are optically clear. However the higher percentages (5% and up) produce 'murky' solutions. It is necessary to dissolve the PVA in brine by heating it above a critical temperature of 70^0 using a magnetic stirrer. These 'designer' working fluids are by no means ideal; the use of water requires the addition of surfactants to produce surface wetting in roll coating, the PVA is likely to produce non-Newtonian effects in the fluid (although this was not assessed here) and its' dissolution in water is reversible with time. Because of the uncertainty of these effects these fluids were not deemed suitable for the present study.

3.5 Free surface profiles

It is necessary to obtain free surface profiles in roll coating flows, under various operating conditions, for three reasons:

1. In order to estimate the surface tension forces
2. For use with Finite Element analysis as a good first approximation for the position and shape of the free surface

3. To verify that free surface results from FE solutions are seen in practice for a given condition (i.e. using the continuation method to move through parameter space from point 2.)

The method used here for obtaining and measuring free surface profiles is described in detail below.

3.5.1 Obtaining and analysing profiles

Using the Panasonic F10 video camera and bellows with the reference-grid viewing plate, described in §§ 3.8.4, a series of three images are required to calibrate and analyse each profile:

1. Image 1 (see Figure 3.10(a)) is at low magnification and encapsulates the minimum gap and free surface to be measured in order to obtain the distance of a characteristic point on the free surface from the minimum gap, as well as the reference grid to calibrate the image; the distance between grid points is known (separation of points was 0.5 & 1mm, machined to within an accuracy of 15 micrometres, i.e. $\pm 0.05\%$).

2. Image 2 (Figure 3.10(b)) is at much higher magnification to allow accurate measurement of the free surface profile. It includes at least two grid points in both the vertical and horizontal axes (generally those closest to the free surface profile) for scaling purposes. This image is sharply focused on the grid points, with the out-of-focus free surface behind this plane (because the grid points and the free surface profile to be measured are not in the same plane).

3. Image 3 (Figure 3.10(c)) focuses sharply on the free surface, with the grid points out of focus; the optical set-up for image 2 is simply moved forward, using the linear displacement mechanism of the optical bellows, until the required free surface plane is in focus, thus the scale for image 2 and 3 is identicle (this assumes

that there is no lateral movement of the viewing arrangement as it is moved from Image 2 to Image 3).

The three images described above are digitally captured using the image processing system described in § 3.4. Then, using the standard image processing software, cross hairs can be overlaid on each image and moved at two pixel increments (i.e. 256×256 points), while displaying the row and column number of the cross location. As described above, Image 1 provides the location of the free surface with regard to the roll geometry. Image 2 is used to assess the scale of the magnified image, and to calculate the extent of image distortion on capturing (this phenomenon is explained in § 3.8). Finally the pixel positions of the grid points obtained from Image 2 are used as 'zero-points' in Image 3. A number of sampling points are taken on the free surface, using the cross-hair system, to obtain the actual free surface profile. Results of free surface location and profile are presented in Figure 3.11.

One problem with placing a viewing window on the end of the roll gap is that it can affect the shape of the menisci; they can locally 'swell up' or 'neck' in the immediate vicinity of the plate. When using the window to view the meniscus shape and position, these local distortions can give misleading results. To overcome this problem an alternative method of obtaining accurate results of free surface profiles is to look along the nip at a small angle to the roll axes (see Figure 3.12). The free surface profile at any position along the length of the gap can be revealed using a very thin vertical light sheet to illuminate a cross-section. This image is then digitally captured and the procedure described above, to quantify the free surface shape and location, implemented. The offset angle from the axis can be incorporated in the scaling calculations to achieve an 'undisturbed' profile of the meniscus. However, to include a reference grid and assess the actual location of a particular free surface profile (with regard to the roll geometry)

requires an accurate horizontal swing mounting system for the camera arrangement (refer to Figure 3.12); to facilitate accurate measurement of the offset angle and ensure the camera arrangement travels through an exact arc. In general, distortion of the menisci only becomes inhibitive at excessive operating conditions (e.g. very high roll speeds, very small gaps); such conditions were beyond the scope of the experimental analysis of the present study.

3.6 Contact Lines and Stagnation Points

Contact lines and the problems of obtaining physical measurements of actual contact angles were discussed briefly in Chapter 1. Using an optical microscope arrangement, it is only possible to gain an appreciation of the 'macroscopic' flow field in the vicinity of a contact line. Therefore it is only possible to provide experimental results for *apparent* contact line position and angle. When viewing the contact line region through the end viewing plate, the task of obtaining an estimate for the apparent contant line angle and position at some appropriate distance from the viewing plate (where the contact line is not influenced by the edge effects) is made even more difficult by the out-of-focus roll edges and free surfaces, which tend to degrade the image resolution in the critical area of interest (i.e. where they effectively meet at the dynamic contact line).

Illustrating separating flow and stagnation points within the flow domain (i.e. away from solid or liquid surfaces), such as the film-splitting point in forward roll coating, is less of a problem. Dye is used to reveal the salient part of the flow. For example Figure 3.13(a) illustrates flow separation in a two-roll geometry (upper roll stationary) where the dye is only present in the near-rectilinear part of the flow. Contrast this with Figure 3.13(b) where dye has entered the recirculation. Therefore the illustration of such regions is, to a large extent, due to the 'design' of the experiment.

An alternative approach to that of looking into the nip end-on is to look down on the bead in plate-roll and two-roll system (using the upper hollow acrylic roll). With dye in the near-rectilinear part of the flow it is seen to be more dense at the separation point (see Figure 3.14), and the small axial flow caused by the end viewing plate serves to illustrate the axial separation line position more clearly. The dynamic contact line position is also illustrated using this method, although it is not possible to measure the contact angle. This method overcomes the problem of looking into the nip axially, using the viewing window where, under certain conditions, the upstream free surface can be dragged in locally to obliterate the view of the contact line position as well as the separation point.

Another possible method of obtaining more reliable measurements of apparent dynamic contact angle is, rather than looking directly along the axis of the rolls into the nip using the viewing window, looking at a small offset angle without the viewing window present, at the free surface from the air-side, as opposed to the fluid side, as described in §§ 3.5.1, when measuring free surface profiles. The offset viewing angle can be taken into account in subsequent measurements of the apparent contact angle. This method minimises the problem of image resolution due to the out-of-focus solid and free surfaces, and any edge effects caused by the viewing window are eliminated.

3.7 The Image Processing System

3.7.1 Hardware

The image processing system consisted of an Epson AX Personal Computer and EGA monitor incorporating a:

- Data Translation DT2862 Arithmetic Frame Grabber (AFG)
- Data Translation DT2858 Auxiliary Frame Processor (AFP)
- Microvitec HL series High Definition Multisync RGB Monitor

The AFG is capable of the digitisation, manipulation and display of images at a real-time rate of 30 frames per second. It consists of four on-board frame stores for 512 lines × 512 pixels × 8-bit images, digitising and display hardware, 8 programmable input look-up tables, 8 programmable output look-up tables, 4 programmable resultant look-up tables, an 8-bit Arithmetic Logic Unit (ALU), a frame-store memory access mask, and multiple feedback paths. The 8-bit ALU and input look-up tables allow the board to process any images stored on-board in real time, as well as processing images actively being digitised. Some of the features of the AFG include real-time zoom, pan and scroll, frame addition/subtraction/multiplication by a constant, logic operations, contrast and brightness enhancement, false colour output, and graphic overlays.

The AFP is a frame processor board designed for high speed image processing with the AFG. Each board plugs into one slot of the Epson PC, with external ports connecting the AFG and AFP through a ribbon cable providing a very high speed communication path. The AFP greatly reduces the time required to accomplish arithmetic-intensive operations on the 512 × 512 image frames. Figure 3.15 shows a schematic of the hardware set-up, with the source image being captured via a standard video input cable,

either as a live image from a video camera or a recorded image from a video recorder. The AFP is connected to the AFG only and effectively increases its' operating speed. Any of the images stored in the frame-stores can be displayed on the Microvitec multisync monitor which is directly connected to the AFG. It is possible to load images stored in the frame-stores down to the hard disk of the PC, which acts as an off-line storage facility. However an image must be restored to the AFG board to undergo any manipulation or display.

3.7.2 Software

A comprehensive DT-IRIS subroutine library is supplied with the hardware system, together with a general purpose software package called IRISTUTOR, which allows the user to implement all of the standard processing operations (e.g. frame capture, storage, addition etc.). To perform more complex operations, original programs are required (tailored to the users specific needs) from which the Data Translation subroutine library is accessed. The subroutine library is supplied in Fortran, Pascal, and C programming languages. A Microsoft Fortran compiler was used for program development in the present study.

DT-IRIS's analytic functions can be placed into three categories; arithmetic, logical, and statistical operations. Arithmetic operations include image subtraction/addition and multiplication/division by a constant. The logical operations are useful in comparing pixel values (intensities) with a constant (e.g. a threshold value in the case of the particle recognition procedure, described in §§ 3.8.4). Statistical operations include a histogram facility, which displays the brightness distribution of the image.

It is possible to perform convolutions on images; DT-IRIS provides a number of predefined convolution filters as well as allowing user-defined filters. An interactive colour

palette capable of displaying a combination of 256(red level)×256(green level)×256(blue level) colours (effectively giving 256^3 colours) is incorporated in the package. DT-IRIS also provides the ability to overlay computer generated graphics on to frame buffer images. The three fundamental operations are drawing lines, arcs or circles, and text, where the pixel locations are used as cartesian coordinates. The graphic overlay facility is used extensively in the particle recognition and tracking system described in §§ 3.8.4 Another useful facility available within IRISTUTOR is the LEARN mode, whereby a series of commands can be remembered, stored in a macro buffer, and 'played back' using the EXECUTE command, as a means of repeating a sequence of operations (e.g. two consecutive images are captured into frame buffers 0 and 1, filtered, added together, and the resulting image saved onto the hard disk). A macro buffer can be saved as a file on the hard disk, for future use.

Greatly accelerated signal and image processing is achieved using DT-CONNECT. This is an interface specification, based on external input/output data ports and software protocols, which permits the direct connection of standalone data acquisition and frame grabber boards for rapid processing. The system supports Read/Write operations from/to the ports for high speed synchronous image transfers between the AFG and AFP boards.

3.7.3 Image Capture

Real time images from the input source (video tape playback or live video image) can be displayed continuously on the image monitor by putting the AFG into what is termed the 'Passthru' operating mode. In this condition, the actual images which the frame board 'sees' can be viewed for selective capture. It is not possible to capture a specified frame using this type of video recording (this applies to standard VHS recording as well). The problem is that when the video tape is paused to view a single frame the

synchronisation signal, which the tape would normally send before each 'picture' , is lost. The reason for this is to do with the way in which the tape is used to record and playback material. Information is stored on the video tape in oblique strips (see Figure 3.16) which are 'laid down' on the tape at standard running speed. In playback mode each strip is read by the rotating video head, which is angled to coincide with the orientation of the strips. When a picture is paused, this stops the tape, but the head continues to rotate to read the image information for the still frame. Now the recorded strips are at a slightly different angle to the video head because the relative motion between head and tape is lost, therefore some of the picture information is lost, including the synchronisation signal.

The frame grabber requires a synchronisation signal so that it knows where the start of an image is on the tape. In normal playback mode there is no problem, since the synchronisation signal is present and so running the program to capture an image means that the frame grabber will capture the next image. However, with the video outputting 25 frames per second it is not possible for an operator to capture a specific frame. This problem is discussed more fully in §§ 3.8.2, with regard to the requirement for the capture of a sequence of images.

3.7.4 False-Colour Image Enhancement

Using the image processing system described above, specific images can be captured and analysed. To elucidate certain features of the flow within these images, a method of false colour mapping was developed. When an image is captured, each picture element can be given any one of 256 grey level values depending on the signal intensity (i.e. a grey level value of 0 is equivalent to black and a value of 255 is equivalent to white). It is possible to alter the output look-up tables within the image processing software to replace the grey levels with a combination of red, green and blue levels. Each of

these primary colours can have one of 256 values. For example, red can be given any one of 256 'red' levels (i.e. a red level value of 0 is black and a value of 255 is red). In effect, by combining these three primary colours, each of which can have 256 levels, it is possible to create 256^3 different colours.

Several spectra are shown in Figure 3.17(a). The spectra can be tailored to suit a particular image and any important features to be highlighted. The data for a particular spectrum is calculated using a simple Fortran program, and transfered to the DT-IRIS output look-up tables by calling the appropriate subroutines. Hard copies of these images can be obtained by photographing the monitor or using a colour plotter (described below). Results of this colour mapping are illustrated in Figure 3.17(b), where a false colour image is shown with three sample spectra. Moving from Figure 3.17(b) (i) to (iii) demonstrates that key features of the flow can be reinforced by changing the spectra accordingly.

A more refined hard copy of the false colour image can be obtained using a Versatec colour plotter. The Versatec plotter is operated by Versaplot colour graphics software, which consists of a subroutine library to create user-defined colour plots, and the necessary software to drive the plotting device itself. The plotter is capable of producing 256 toned colours using the 'primary' colours of yellow, magenta, and cyan (which are the complementary colours to red, green, and blue. A standard Versaplot Fortran program was modified to incorporate the required spectra to produce continuous tone changes throughout each image. The raw grey-scale image data file, captured by the Data Translation image processing system, is used as the input data, and the method of false colour mapping is much the same as that described above for the Data Translation image display, but using the complementary colours. Figure 3.18 illustrates the quality of the plotted images. The drawback of this method is the time taken for the

plotting program to produce a plot; typically of the order of 20 minutes for a 512×512 image.

A third option for enhancing flow visualisation results was also available; Uniras is a very sophisticated interactive image processing package, which is capable of presenting data in a number of ways, including 3-D maps of an image. This system, which is installed on a Sun Sparcstation cluster, has the advantage that the time taken for the iterative procedure of refining a false-colour map for a particular image is much reduced. The mappings can be changed interactively, whereas the two methods described above require re-programming to achieve this. The 3-D colour mappings provide an impressive representation of the flow visualisation results obtained in this study (Figure 3.19 is a photograph of the workstation screen). The system simply plots the pixel value/intensity to create the third dimension, while still maintaining the pixel colour equivalent on the surface of the map (the original two-dimensional false colour image is shown to the left of the 3-D map). In a sense the 3-D representation of the image is totally misleading; the actual flow does not exist in such a form. However, with the correct image manipulation the untrained viewer is given *some* insight into the structure of the flow.

3.8 Computerised Particle Tracking

3.8.1 Introduction

Obtaining qualitative discrete measurements of velocities within complex flows presents a challenging and difficult problem. Traditional techniques cannot perform this function adequately. Point measurement devices such as Laser Doppler Velocimetry (LDV) and hot-wire anemometry measure the velocity at a single point in space. Using such techniques it is possible to take measurements at many locations in order to build up a picture of the velocity field. However this procedure is time-consuming and often unworkable in irregular flow geometries, or small scale flows such as those found in roll coating. Automated particle tracking techniques, on the other hand, have been used for many years to follow/measure the trajectories of individual particles and to provide a visualisation of the instantaneous velocity field. Their application has been limited due to difficulties in processing the large amounts of data which are produced. Recent improvements in the performance of computers and image processing equipment has enabled the use of such systems to be realised.

One such technique, Particle Image Velocimetry (PIV), combines the accuracy of LDV with the qualitative information of flow visualisation to provide quantitative results of velocity for an entire flow field. A double-pulsed laser technique is used to record the particle flow on film (i.e. each particles' position is recorded twice in one frame). The photograph is then analysed as a series of sub-regions (typically a 1mm square) using a laser and computer-controlled traverse mechanism. The image produced by each sub-domain is digitised and evaluated by an array processor. The drawbacks of such a system are the complicated techniques required to record and analyse the particle flow. In addition PIV is a relatively slow system; a typical commercial analysis system requires approximately 3.5 seconds to analyse and evaluate each velocity vector.

Therefore, to analyse one 35mm photograph with a relatively dense particle flow can take the order of ten minutes.

Schneider[1962] tracked the recorded motion of opaque particles in a roll coating nip by using a film viewer; projecting each frame on to a sheet of paper, successive particle positions were plotted and connected manually. The motivation for developing the present particle tracking system was to allow the rapid and efficient automated analysis of relatively dense particle flow images without the need for such sophisticated recording and evaluative techniques as double-pulsed laser photographs of the flow or complex laser/traverse equipment to analyse the photographs, as in the PIV system. Results of velocity fields under specific flow conditions are useful, in an empirical sense, in highlighting important features of the flow field (such as areas of sudden changes in flow direction), but more importantly they can be directly compared to finite element solutions for identical flow conditions and hopefully validate such a numerical approach. If the experimental and theoretical velocity fields are in good agreement then this implies that the pressure field generated by the finite element solution will be representative of the actual pressures in the coating system (experimental measurement of actual pressures are very difficult to achieve in coating flows, in all but the most simplified flow systems; see Chapter 6).

It is useful to carry out an interpolation routine on the irregular-placed velocity results of particle tracking techniques in order to obtain a 'regular' velocity field for comparison with results generated by other means. However, such procedures can create significant errors in the results and this technique is not addressed in this work (Agui & Jimenez[1987] discuss this problem with regard to the performance of particle tracking techniques).

The present technique has been developed in close collaboration with Dr. R.J. Perkins (Perkins & Hunt[1988]), Department of Applied Mathematics & Theoretical Physics, Cambridge. Their original motivation to develop such a system stemmed from the tracking of turbulent flows, and as such, the software lends itself very well to the rapidly changing two-dimensional flows under investigation here. The important difference between this work and that of Perkins & Hunt is that they were only able to achieve satisfactory results for well- defined particle flows recorded onto photographic film, whereas the present experimental technique has been developed to facilitate video recording, and high speed video in particular. The use of a video recording system automates the procedure further; in analysing a sequence of cine film images, each frame must be positioned under a camera and captured. The sequential capture from video tape playback or a live image is automated. It is the temporal resolution of video recording which limits its' application; however, the advent of High Speed Video systems no longer constrains such a flexible method of recording results. The present particle tracking technique, described below, is far quicker than the PIV technique. A typical flow can be analysed in less than 1 minute.

3.8.2 Recording And Analysing The Flow

Particle tracking techniques require some photographic record of the flow. There are two possible methods of recording a series of particle flow images at equal time intervals; cine film photography and video tape recording. High speed cine film has several advantages over the 'pulsed light' and streak photography methods used by many workers (e.g. Agui & Jimenez[1987], Imaichi & Ohmi[1983], Utami & Ueno[1984]), because the particles only appear as 'dots' in each frame which makes the images far less crowded and the particles are more easily identifiable. In addition, in pulsed light photography, any boundaries which do not move produce regions of overexposure on the film, which tend to 'burn in' with the result that trajectories close to these boundaries are

hard to distinguish. With cine film, and indeed video recording, all areas of the image receive equal exposure, so this is not a problem. These two methods also provide an absolute time base for the particle motion, so there is no ambiguity about the direction of motion (as there is in streak photography and indeed PIV, for example). Sato & Yamamoto[1987] describe a method for tracking particles in real time, but it requires expensive equipment and can only follow one particle at a time, so all the information about the structure of the velocity field as a whole is lost.

In general film is preferable to video because the spatial and temporal resolution of the video will not be adequate. However, in comparing the light sensitivity of film and video, the electronic CCD (charge-coupled device) 'chip' which records the image in a video system is far more sensitive than the 'chemical' device used to produce an image in the case of cine film (the section describing the High Speed Video system gives a comparison of the relative sensitivity of the two methods). For this investigation the light sensitivity of the system is of prime importance because of the difficulty encountered in illuminating a narrow plane in the constricted area of the nip between a plate-roll and two-roll coating system. To obtain consecutive images where the movement of each particle from one frame to the next is sufficiently small so as to be less than half the mean distance between particles distributed in the flow field requires a high recording frame rate; typically 250 to 1000 frames per second here.

The industrial Meniscus coating process runs at speeds of 20 metres/min (0.33 m/s). For a typical bead cross-sectional width, W_0, of 5mm (see Figure 2.3), the use of laser illumination, with cine film means that it is only possible to detect a reflection from a particle with an exposure of 1/500th of a second, force-processed to 3600 ASA; At these velocities a particle would travel 0.6mm in that exposure time and would therefore produce a 'streak' rather than a discrete 'dot'. In addition the above test was carried out

at an unacceptably low frame rate of 50 frames per second; increasing the frame rate decreases the exposure/sensitivity accordingly. The results from cine film, in terms of adequate particle exposure, and achievable frame rates were not acceptable.

Standard video systems run at 25 frames per second (PAL broadcasting system) and 30 frames per second (NTSC broadcasting standard). Although the particle exposure at these frame rates was more than acceptable the frame rate itself was totally inadequate. The answer was to use a specialised high speed video camera, which is described in detail in §§ 3.8.3. The drawback of such a video system is the spatial resolution, but it was found to be acceptable for the present application.

Another problem to be considered with regard to the resolution of particles in a video image is the way in which the video system records an image; it is not a continous image as in the case of a cine frame. In general an image is 'read' and recorded in an *interlaced* fashion. The video image is made up of a series of horizontal lines (see Figure 3.20), which are recorded in two 'fields' ; the first field consists of the even lines, and the second consists of the odd lines. The video system scans the first field and stores that information before scanning the second field. There is thus a time delay between 'acquiring' the two fields, which is due to the physical electronic constraints; the charge on the CCD's must have time to shift from the odd to the even rows. The implications of an interlaced image for particle tracking can be serious. Because there is a time delay (typically 20 milliseconds) between the capture of the even and odd lines, the particles will move during this period and therefore a particle captured in the first field will be slightly offset in the second field (Figure 3.21 illustrates this phenomenon). If the particle flow is so fast that the slices which make up the particle are totally disjointed, then it will not be possible for the tracking software to recognise this as a particle. Interlacing is the standard method of transmission and recording of video images and

it is the reason why a checked suit, for example, on a television screen can produce a flickering effect. However, the High Speed Video system, described below, is designed to record in a non-interlaced fashion to overcome this problem.

3.8.3 The Kodak Ektapro 1000 High Speed Video

The Kodak Ektapro 1000 Motion Analysis System is the fastest system of its kind on the market and the only machine which can achieve the required particle flow images at a sufficiently high frame rate to produce meaningful results from the particle tracking system. As pointed out earlier, a standard video camera records at a frame rate of 25 frames per second (PAL television standard) or 30 frames per second (NTSC television standard). The Kodak Ektapro High Speed Video (H.S.V.) can record images at rates of 30, 60, 125, 250, 500 and 1000 full frames per second. The operation of the system is menu-driven for ease of use. Figure 3.22 shows the components of the system which include the processing unit and tape transport system, a monitor, two Ektapro video cameras, and ancillary equipment which includes a VHS video recorder (for down-loading) and a video printer. The components of the system are described in some detail below.

Principles of operation

To understand the principles of the imaging system it is first necessary to understand how the image sensor works. The sensor is a "solid state imaging array". This array has thousands of photo capacitive cells which convert light focused by the lens into measurable electrical charges. The amount of charge in each cell varies according to the intensity of the light received by each cell. The electrical charge stored in each cell (referred to as a 'pixel') is an analog for the amount of light the cell has received. In the sensor, the charge that is stored by each cell is picked up once per frame by a scanning process which takes the charge consecutively from each cell in the array, one

after another. As each cell releases its charge, a new charge begins to accumulate for the next scan, based on the light that it then receives. The video signal is nothing more than a linear sequence of varying amounts of charge from each pixel scanned.

The pixel array is organised into a structure containing 240 columns and 192 rows. Following conventional television technology, the cell in the first row is read to obtain the first pixel, then the next cell in the same row is read and so on. This process continues until each pixel in the first row has been scanned. Then the second row of pixels is read in the same fashion and this process continues down the array until all 192 rows of 240 pixels per row have transferred their charges to the output of the sensor. Since each scanning cycle must read 46,080 pixels, scanning the sensor in this fashion limits frame rates to about 60 frames per second, due to the constraints of the speed of the electronics.

To obtain a frame rate of 1000 frames per second it is necessary to scan the array 16 times faster. This is achieved in the Ektapro H.S.V. by scanning sixteen rows of pixels simultaneously. The scanning sequence reads the first pixel in each of the first sixteen rows (refered to as a block) simultaneously, then it reads the next pixel in each of the same sixteen rows and so on until the block has been scanned from column 1 through to column 240 of the pixel array; the next block is then scanned, and so on until the whole image is input. Scanning sixteen pixels at a time requires a separate output from the sensor for each pixel. The sensor has sixteen output channels which are switched internally from one group of sixteen rows (referred to as a block) to the next group as the scanning of the array proceeds. It takes 12 blocks to make up a single frame of 192 pixel rows. The 16 output channels from the sensor are then amplified and transmitted to the processor unit via the imager cable. To deal with lesser frame rates the scanned block size is reduced accordingly (e.g. for a frame rate of 500, each

block contains 8 lines; for 250 f.p.s., 4 lines etc.).

The Kodak H.S.V. processor consists of a power unit for itself and the imaging equipment, an electronics card bin (which includes a microprocessor) to control the system and process the video, and a video tape transport system. A keypad is used to set operating parameters and configure the system for the desired mode of operation. The system operates in either the Live, Record or Play mode. Recording is carried out at the required frame rate (i.e. between 30 and 1000 frames per second). Playback however, is at the standard rate of 30 frames per second, which results in the slow motion effect of a sequence recorded at a higher frame rate. Additional video processing facilities include freeze frame and forward and reverse frame jog. The processor has the facility to accommodate two imager inputs which can be mixed to give, for example, two different views of a process.

The tape transport system accepts special cassettes, unique to the Kodak Ektapro H.S.V., which carry the 1/2 inch high-density magnetic tape, and it provides the mechanics and electronics to control tape speed and direction. These cassettes are specially conditioned in a conditioning unit each time they are used, in order to tension the magnetic tape correctly. The tape transport is a key component in producing slow motion video images. When the processor is making a recording at 1000 frames per second the tape is moving past the record head at 250 inches per second. During playback the tape is rewound to the beginning of the recording and then moved across the playback head at a relatively slow speed of 7.5 inches per second (equivalent to 30 frames per second). The recording time for a blank tape therefore varies from 16 minutes at a frame rate of 30 f.p.s. to 30 seconds at a frame rate of 1000 f.p.s.

A useful facility for documenting test runs with this system is the information bor-

der which is displayed around the actual video image. It contains useful information such as the recording frame rate, an absolute time counter and a session/test number.

Intensified Imager

The Kodak Ektapro Intensified Imager is far more sensitive than the standard Imager. To illustrate its' extreme sensitivity compared to photographic (cine) film and the standard Ektapro Imager, it is convenient to use the photographic Exposure Index (E.I.) ISO standard (i.e. known more familiarly on packaged film as the A.S.A. number). The sensitivity of the standard Imager is of the order of 150 A.S.A at a rate of 1000 frames per second. The Intensified Imager has 11 stops gain (i.e. each stop doubles the sensitivity), which gives this system a maximum equivalent A.S.A number of over 300,000.

The system is illustrated in Figure 3.23. The controller, which operates independent of the Ektapro processor, is used to alter the Gate and Gain functions. The Intensified Imager consists of a standard imager modified by the addition of an image intensifier assembly. The construction of the two-stage intensifier is shown in Figure 3.24(a). The photocathode is formed by a thin layer of photoemissive material on the inside surface of the first stage intensifier tube. The lens focuses the image onto the photocathode which emits an electron each time a photon strikes the surface. The electrons from the photocathode are drawn through and multiplied by the micro channel plate (MCP). The electrons leaving the MCP excite a phosphor screen recreating the image that was on the photocathode. Because of its' construction the MCP lends itself very well to being turned on or off very quickly. The gate generated by the controller, to act as an electronic shutter for the imager, is applied across the MCP.

The MCP is a secondary electron multiplier. It is constructed with millions of glass

channels. When an electron strikes the MCP channel wall, secondary electrons are emitted. These electrons are accelerated by the potential difference between the entrance and exit of the channel. As these electrons proceed down the channel they strike the MCP wall releasing further electrons. This continues until the electrons exit the channel. The process is illustrated in Figure 3.24(b). The image from the first intensifier stage is coupled to the second stage of the intensifier by a fibre optic plate. The light striking the photocathode of the second intensifier stage releases electrons from the photocathode. The electrons are accelerated and focused onto the phospher screen at the rear of the second stage. The rate at which the electrons are accelerated determines the gain of the intensifier. The gain adjustments made using the controller are used to control the speed of the electrons at this stage. The image created at the rear of the second stage is coupled to the image sensor by another fibre optic plate.

The Gate could be varied from 10 microseconds to 5 milliseconds and the Gain from 1 to 100. The great flexibility of these operational parameters facilitated the optimisation of required features in the image. As with the standard camera a universal lens mount allows the use of the optimum lens system. Because of the nature of the intensifier assembly it does in fact 'wear out'. It has an operational life of 500 million exposures, after which time a replacement is necessary . The definition of an exposure varies with gate and gain settings. For example, with the highest gate and gain settings and a frame rate of 1000 f.p.s. (i.e. the intensifier is working at maximum capacity), the exposure rate can be as much as 5 per second (the rate also depends on the level of illumination in the image).

Image Acquisition Software

As described in §§ 3.7.3 it is not possible to specify which images are captured. There is however a Data Translation subroutine which acquires sequential images (i.e. four

consecutive images with a four frame buffer system) in real time. Although there is always the problem of not being able to capture a specific sequence, the fact that a number of consecutive images can be acquired is sufficient as input data to the particle tracking system (i.e. the time between frames is similar and known).

The procedure involves the acquisition of a number of sets of consecutive images for a particular steady flow condition and calculation of the resultant velocity vectors in order to build up a comprehensive picture of the velocity field. It is necessary to adjust the particle flow recording rate so that the average distance travelled by particles from one frame to the next is not excessive (an obvious estimate of a suitable distance is something less than half the average particle separation within the flow). This procedure is not straightforward, since the object of developing the tracking system is to establish the velocity field for the flow, yet to record the flow at a suitable frame rate requires some knowledge of characteristic speeds; in practice the average roll speed is taken as a typical particle speed.

Once a particle flow has been recorded, there is also some flexibility in the sequential capture of frames. In addition to the predefined subroutine for sequential frame capture, it is possible to call the subroutine which captures a single frame four times by creating a macro program within IRISTUTOR (see §§ 3.7.2). This procedure is considerably slower than the sequential-acquire subroutine, because of the extra time taken in calling and initialising the single-acquire subroutine a number of times. There is still, however, a constant interval between frames since the time taken to recall the subroutine again and again remains consistent. The actual time base can be taken from the time counter displayed on the image border. A third option is that of manual capture; a program acquires an image each time the carriage return key on the computer keyboard is pressed. The time base is invariably inconsistent using this manual method,

but it is possible to modify the particle tracking software so that the individual frame separation times (calculated using the frame counter in the image border) could be entered. This method of capture is very slow, thus giving relatively large displacement vectors in the velocity field plot.

3.8.4 Method of identifying and tracking particles

The particle tracking software is effectively two separate programs. The first of these analyses a digitised image and identifies and locates all the particles, storing the information in a data file. The second program then uses the data file set to match particles from frame to frame.

Particle Identification

The digitisation process introduces noise into the signal and also a low frequency variation in the background intensity of the image, caused by uneven illumination. This makes it difficult to identify particles, because the threshold intensity for discriminating between background and particles does not remain constant over the image. These effects are overcome by dividing the image into small regions and estimating the average intensity for each region using a statistical model for the intensity distribution. The threshold intensity for the whole image is then obtained by area-weighted interpolation between the centres of these regions.

A particle is defined as a set of connected pixels, all having intensities greater than the threshold intensity. The program scans through the image, line by line, going from left to right, searching for such sets. Once one has been found, the program determines, from its area and ellipticity, whether it represents noise, a single particle or a cluster of overlapping particles. Clusters are resolved into their component particles using a model for the intensity profile for a single particle and a peak-fitting approach, together

with a maximum ellipticity factor, i.e. the program will attempt to break down a particle shape which is outside this stipulated ratio. A number of particles in a cluster are illustrated using different colours.

Figure 3.25(a) shows a typical image prior to processing. It is possible to analyse any region of interest within the frame by changing the size/position of the working window to work on a specific area (Figure 3.25(b)) or the full frame (Figure 3.25(c). Figure 3.25(d) shows the image after processing where recognised particles are coloured red. Clusters of particles are shown in a number of colours as illustrated in Figure 3.26(a) and 3.26(b) (where a cluster area has been magnified). When all particles in a frame have been located, their coordinates and areas are stored in a data file on the computer and the subsequent frame/frames are processed in the same way.

Particle Matching Technique

Once a set of consecutive frames have been processed, a second program analyses the data files, two at at time, and attempts to match each particle 'image' in the first frame with its corresponding 'image' in the second frame. This allows the user to build up results for the velocity field; the principle behind this process is illustrated in Figure 3.27. Consecutive image pairs are analysed independently (i.e. 1 & 2, 2 & 3, 3 & 4). For convenience, the accumulated matching results are shown for the consecutive images (1-4) to demonstrate how this system is used construct a 'picture' of the flow .

The algorithm for analysing particle motion between image pairs is entirely general; it makes no assumptions about the velocity field, and it requires no information about the previous motion of the particles. It also allows for particles which have left the image between frames, either at the edges, or because they have passed through the illuminated cross-section of the flow. It is assumed that, although the particles do

not follow the flow exactly, their displacements remain somewhat correlated over small times and distances.

Taking two adjacent images, Frame 1 and Frame 2, to illustrate the procedure; each particle in Frame 1 is matched with a particle in Frame 2 so as to minimise the difference in areas and the difference between the trajectory of that particle and the trajectories of its neighbours. The algorithm is iterative and continues until there is no change in the matching (4 iterations are normally sufficient). The procedures for matching are described more fully below:

1. *Initial matching:* The program matches each particle in Frame 1 (coordinates $X1, Y1$, say) with a particle in Frame 2 (coordinates $X2, Y2$) so as to maximise the correlation between the displacement of each particle and the displacements of its neighbouring ('satellite') particles (see Figure 3.28).

2. *Transformation:* A model displacement is calculated for each particle in Frame 1, based on the current matchings for that particle and its satellite particles. The coordinates of the transformed positions of the particles are XT, YT (these model trajectories are shown in green in Figure 3.29).

3. *Matching:* Each particle in Frame 1 is matched either to a particle in Frame 2 or to an empty space, so as to minimise the distance between the transformed coordinates (XT, YT) and the particle coordinates in Frame 2 $(X2, Y2)$. Multiple matchings are eliminated.

4. *Iteration:* The program iterates over 2 and 3 until the matchings do not change.

The program then updates the data file for Frame 1, assigning to each particle the index number of the particle in Frame 2 with which it has been matched. Using this approach there is no limit to the number of frames which can be processed, and the

effects of any incorrect matching are confined entirely to that particular match (i.e. the matching process for two particle frames is entirely independent of matchings made in the previous or subsequent frames).

There are a number of parameters which can be input by the program operator to achieve the best possible results for different sets of images (under different operating conditions, for example). These are:

1. *Maximum number of iterations* - this is the maximum number of times the iteration described above will be carried out.

2. *Factor for area weighting* - this determines the importance given to matching the particle areas.

3. *Maximum particle displacement* - this is an estimate of the maximum distance travelled by a particle between Frame 1 and Frame 2. If the estimate is too large, the program will run slower than optimum; if the estimate is too small, some matchings may be lost. The average roll velocity, U, is used as a first guess.

4. *Satellite radius* - the program will search for satellite particles within this distance from each main particle. Essentially it is a function of the length scale of the flow. If it is too large, the program will include the displacements of uncorrelated particles in its model for the motion of a main particle, and if it is too small, the program will not get the benefit of the correlations.

5. *Satellite search radius* - this determines the area around each satellite particle which will be searched for matching particles.

6. *Error radius* - provides an initial estimate for the acceptable error between a predicted location (XT, YT) and a particle position in Frame 2 ($X2$, $Y2$). The program updates this estimate as it progresses.

7. *Standard deviation* - this is used to update estimates for the acceptable error in matching transformed coordinates (XT, YT) onto particles in Frame 2 $(X2, Y2)$.

In addition, there are several utilities available for viewing and altering matchings:

1. *Plot results* - If this is selected, the matchings are plotted on the screen and it is possible to adjust them (i.e. cancel or match particles interactively) using the screen cursor. The particles in Frame 1 are illustrated in blue and the particles in Frame 2 are in red (see Figure 3.28).

2. *View matchings* - This option is only available if the previous option is selected. If selected, the program will display the current matchings (in black) at the end of each matching step, and the predicted displacements (in green) at the end of each transformation step (see Figure 3.29).

3. *Cursor operation* - If selected, a set of green cross hairs appear on screen, the position of which can be moved using the arrow keys on the keyboard. A particle nearest to the cursor can be 'selected' by typing either 1 or 2, corresponding to Frame 1 or a Frame 2 particle. If this particle is matched with another, the match can be cancelled by simply typing 'C'. If this particle has not been matched, then by 'selecting' another particle from the other frame, a match can be made by typing 'M'. The automatic matching system is not fullproof and the cursor option allows erroneous matchings to be cancelled and more obvious matchings to be made. Mis-matches account for less than 5% of total matchings.

4. *Viewing of data sets* - In order to build up a comprehensive flow field for a particular flow condition, it is necessary to merge a number of 4-frame sequences. This option facilitates viewing of one or more 4-frame data sets. Figure 3.30(a) illustrates a plot of a single data set and Figure 3.30(c) shows a plot of three combined data sets (shown in black, yellow and green). In practice it is not always

possible to obtain consecutive traces of all particles (i.e. 3 joined velocity vectors) because of the problems associated with intermittent particle illumination etc. discussed earlier.

5. *Choice of plotted particles* - This is a useful option, which allows the user to vary the size of the plotted particles as well as to plot only matched particles. Particles can be represented by circles which are either proportional to each identified particle, or all one size (which is variable), or alternatively all set to zero. This facility is available within the options for viewing single and multiple data set matchings, as described above. The last zero-particle-size option is very useful, particularly when viewing multiple data set matchings, because the screen can become very 'crowded' and it is difficult to appreciate the flow of particles (Figure 3.30(b) shows a plot with non-matched particles plotted, compared to the much clearer image, Figure 3.30(c), where unmatched particles are not plotted).

Image Calibration/Reference Grid

During the process of filming and digitising of a particle flow image, the object plane becomes distorted due to the discrepancy between the size of the 'pixel matrix' (CCD) of the video recording image (542×486 pixels for the Panasonic F10 video camera and 240×192 pixels for the Kodak Ektapro H.S.V.) and the digital framestore (512×512 pixels), which results in the vertical scale of an image being 'stretched' (Figure 3.31 illustrates the exaggerated result of this procedure). This is corrected by locating static reference points, of known separation, in the image during filming and the transformation necessary to map the image plane back onto the object plane is subsequently computed during the analysis of a digitised image, using a user-definable calibration routine, enabling the calculation of actual velocity vectors.

The experimental technique for including calibration points in an image involved the use of a stationary 'viewing plate' rather than the integral flange-type arrangement described in §§ 2.3.2. A grid of equispaced points were formed on the surface of the plate using an NC machine, with a ground silver steel pin, to achieve the required accuracy. The grid was designed to be symmetrical in order that it could be centralised with respect to the minimum roll separation position. The position of the grid can be adjusted using a centralised, symmetric fluid bead suspended between stationary rolls – in particular the location of the free surfaces are used as reference points. By polishing the side edges of the plate and directing a light source towards them, the principle of total internal reflection causes any imperfections on the plate surface to allow light to 'leak out', resulting in the machined points showing up as 'pinheads' of light. This technique produces an excellent illuminated grid (see Figure 3.32).

Velocity field results are presented in Chapters 4, 5 & 6. In each case a velocity vector is represented by an arrow, where the length of the arrow and the size of the arrow-head are directly proportional to the magnitude of the velocity.

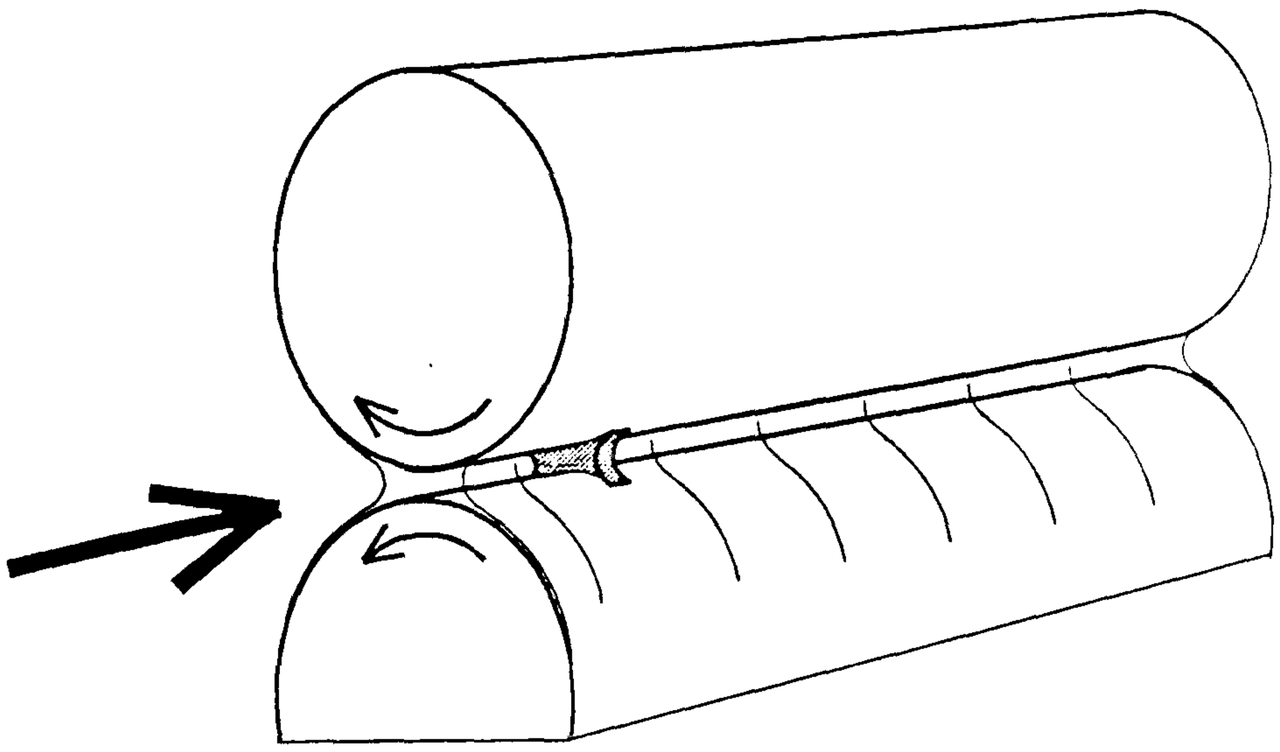

(a)

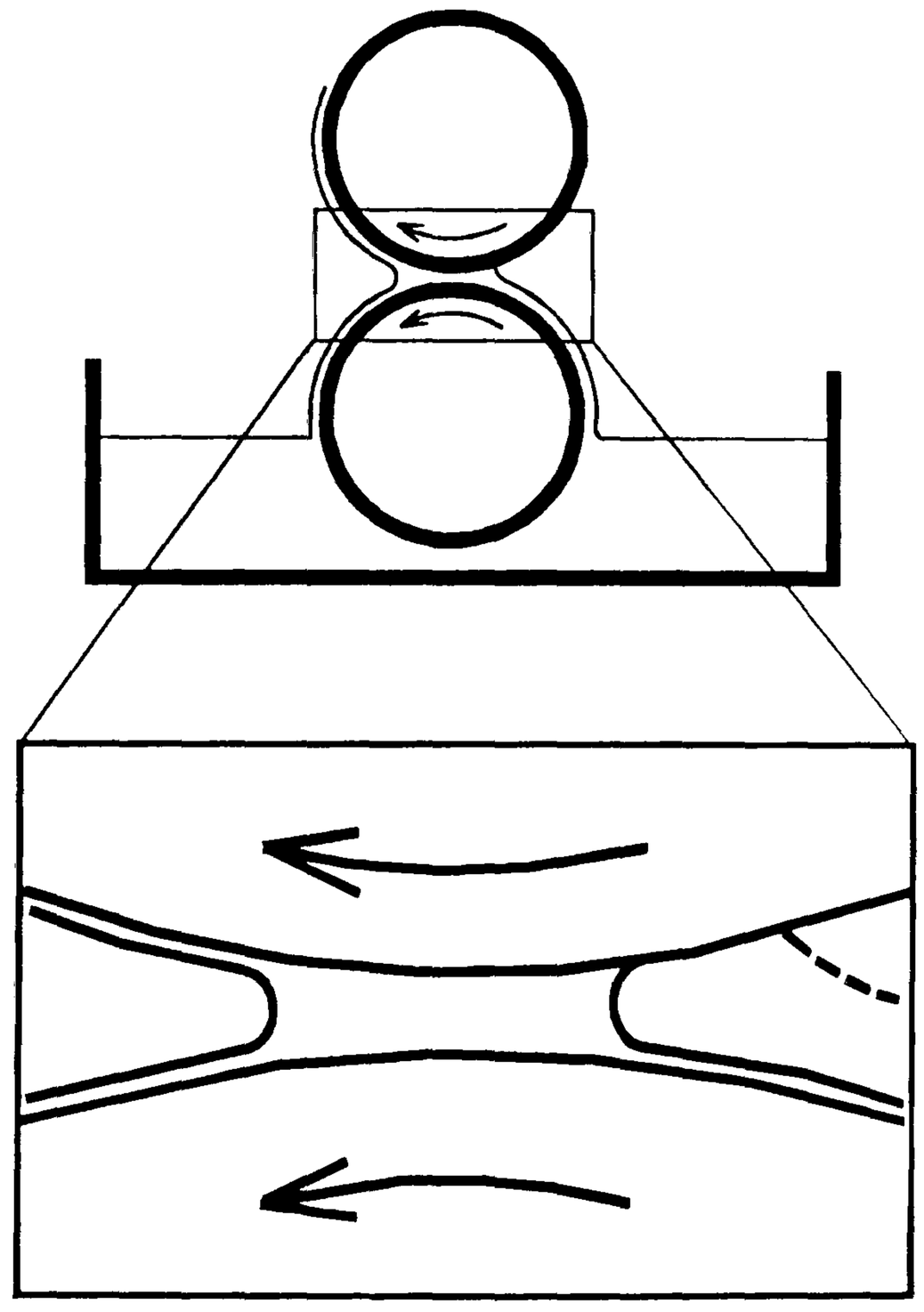

(b)

Figure 3.1: (a) The region of interest in the nip of a two-roll coater. (b) Exploded view

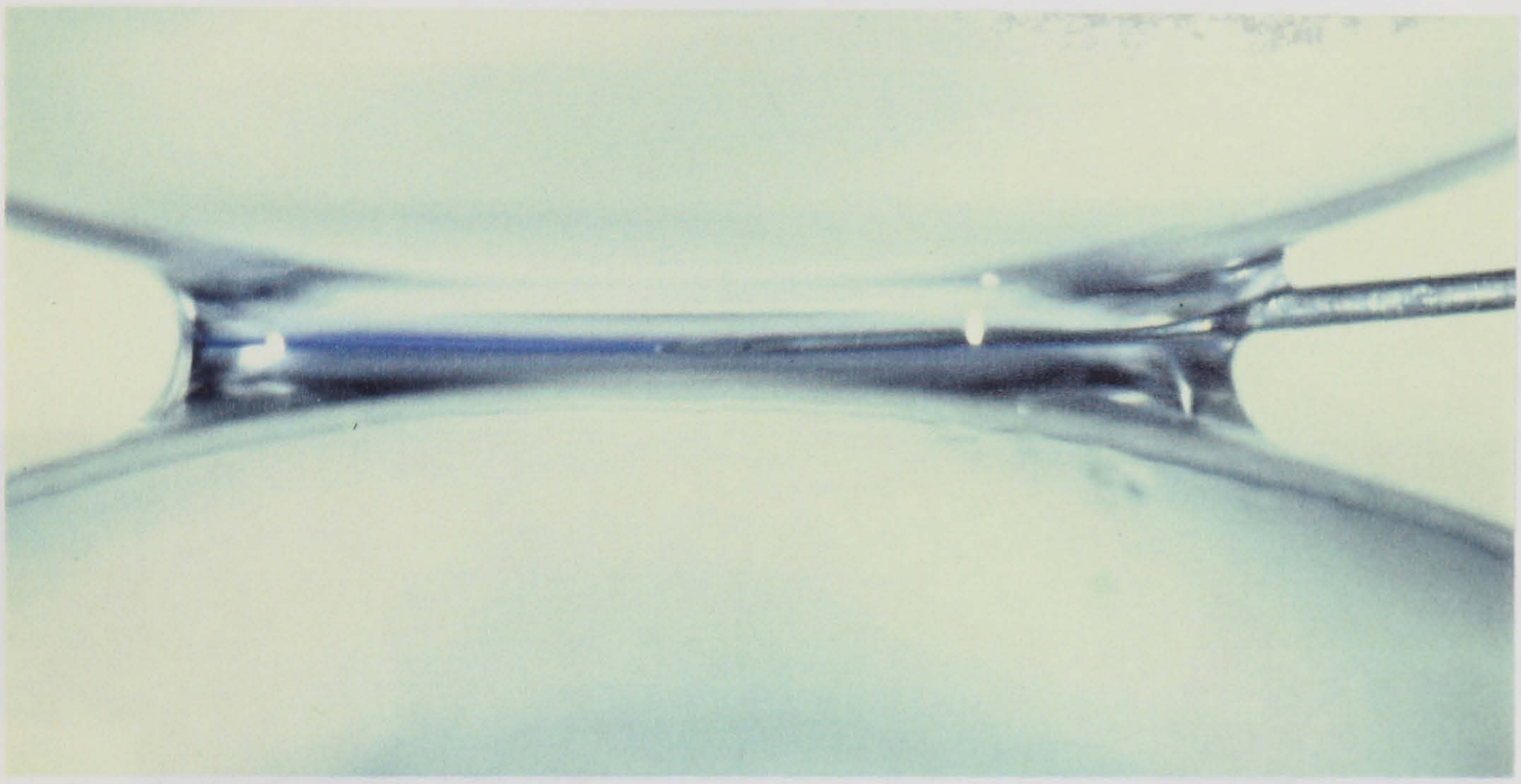

(a)

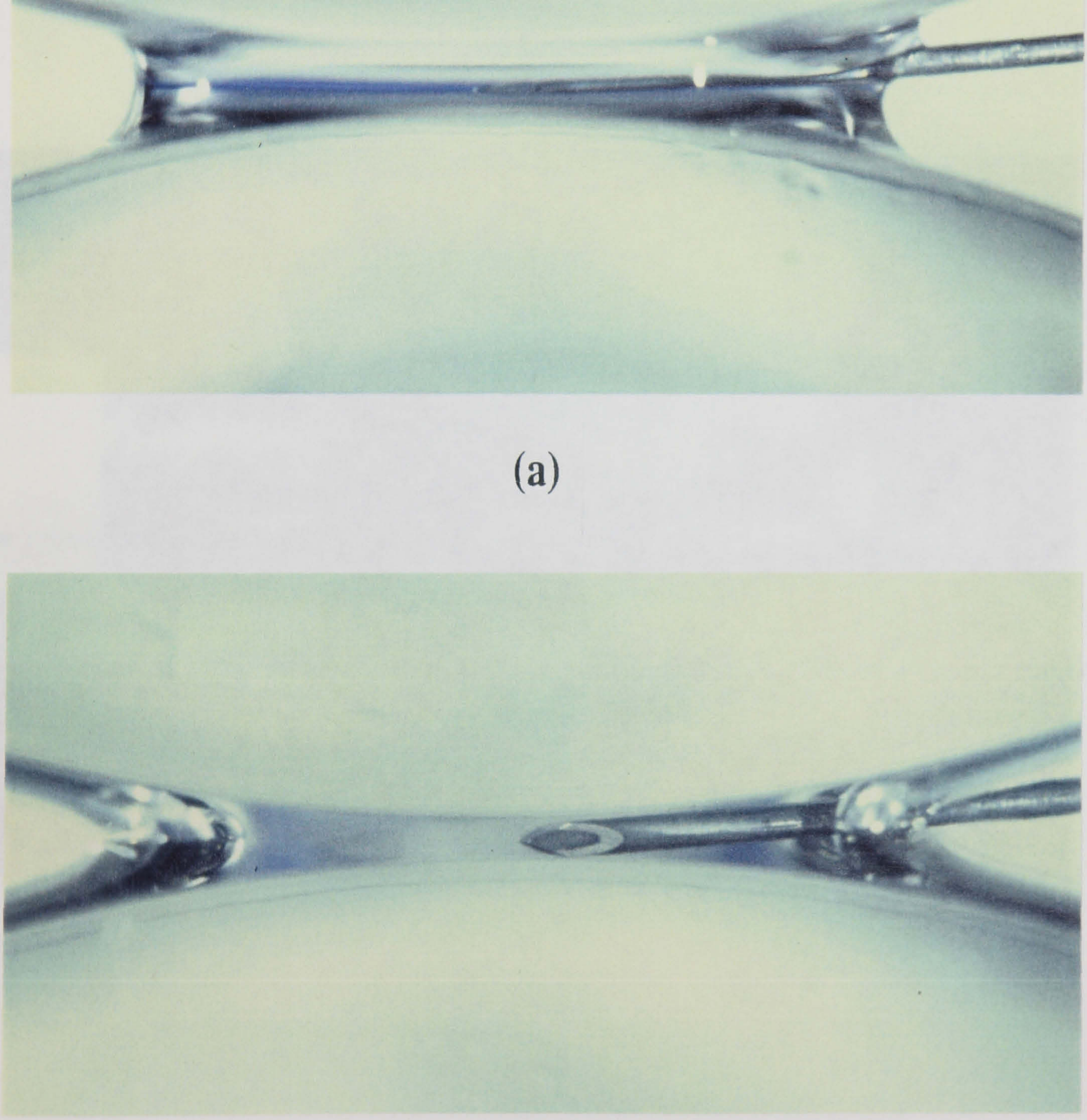

(b)

Figure 3.2: Effect of roll end-meniscus distortion (a) No viewing window, (b) Viewing window in position

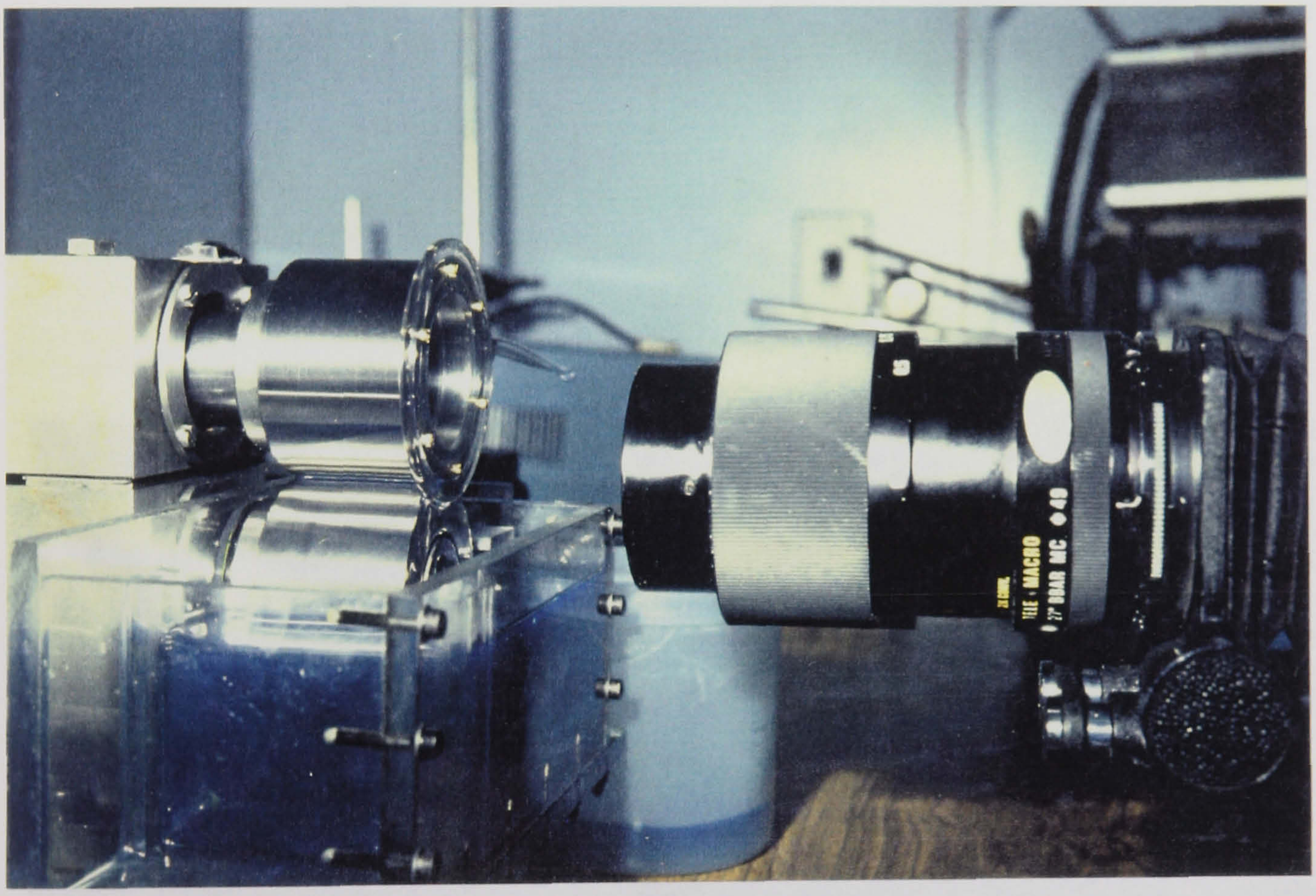

Figure 3.3: Illustration of axial observation of the nip

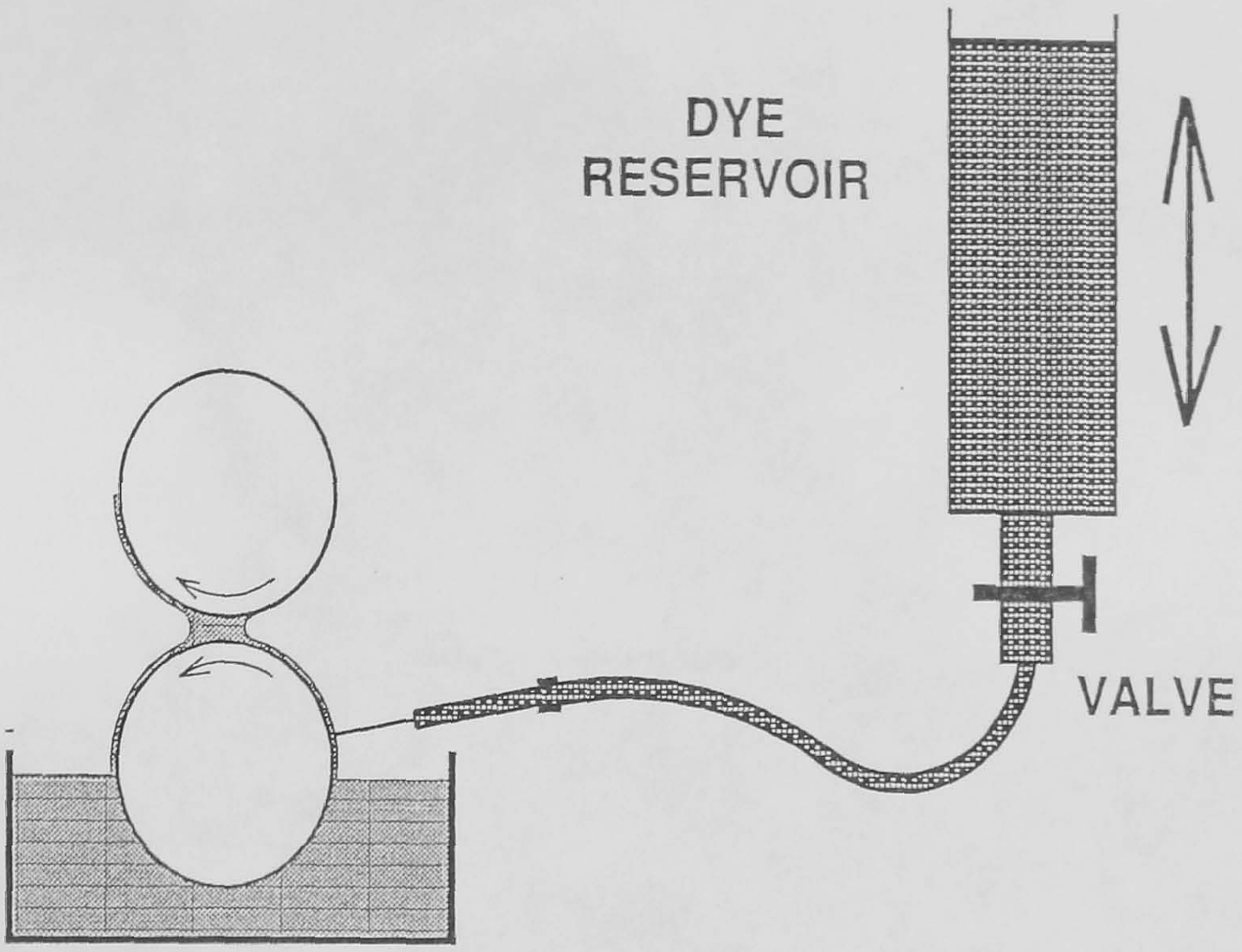

(a)

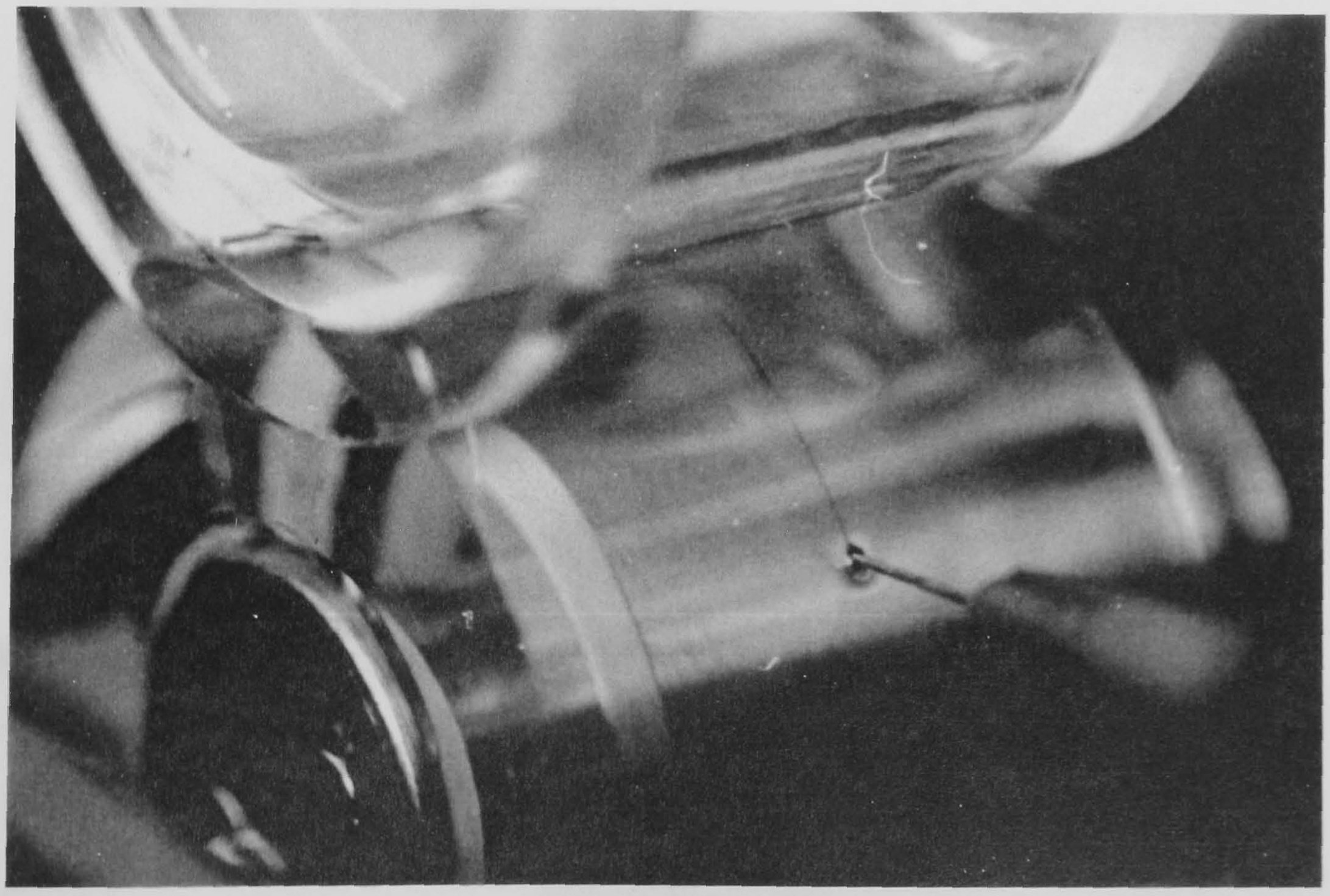

(b)

Figure 3.4: (a) Dye injection system, (b) Illustration of a filament of dye being transported into the nip

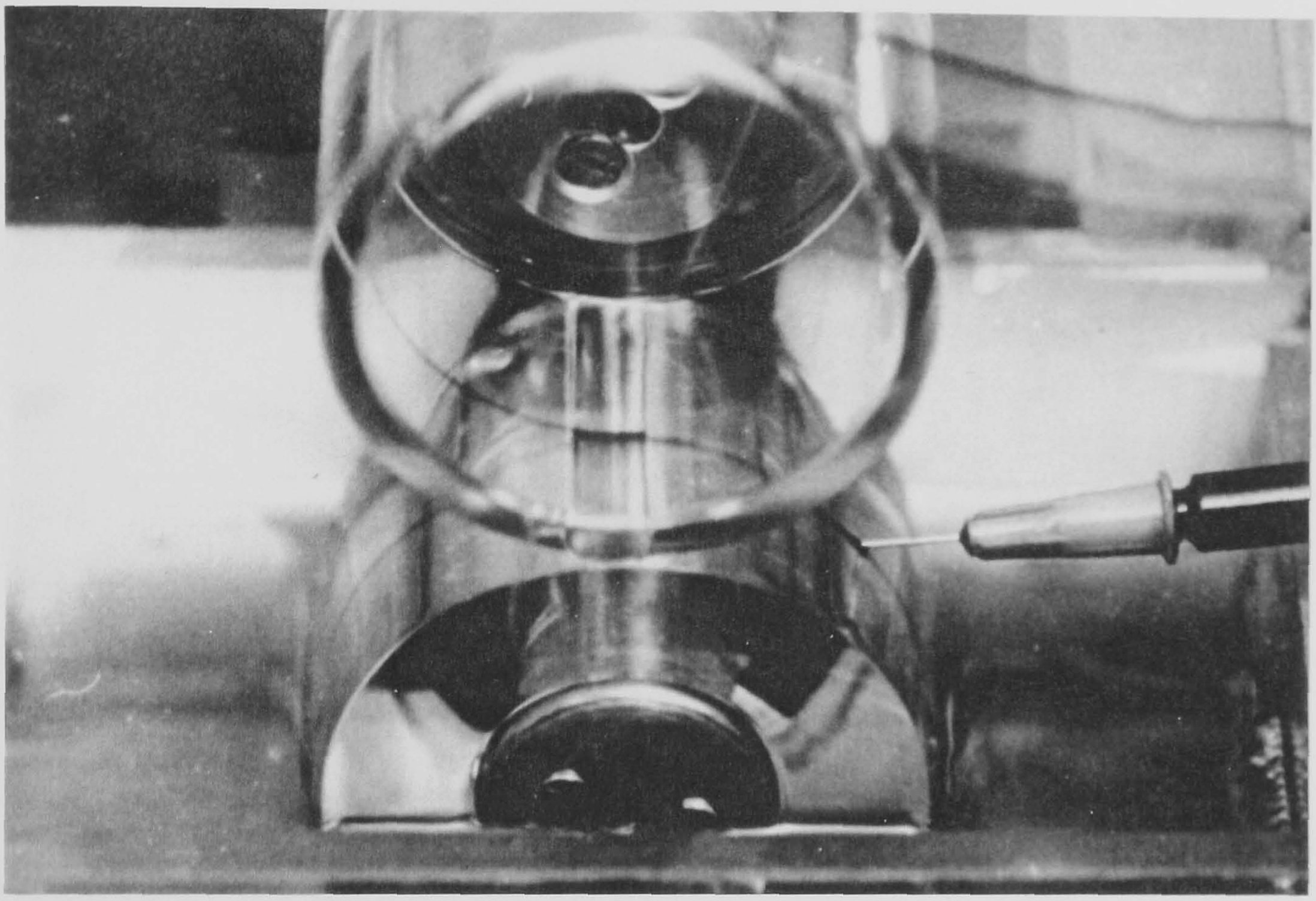

Figure 3.5: Dye injection demonstrating film splitting onto upper and lower rolls

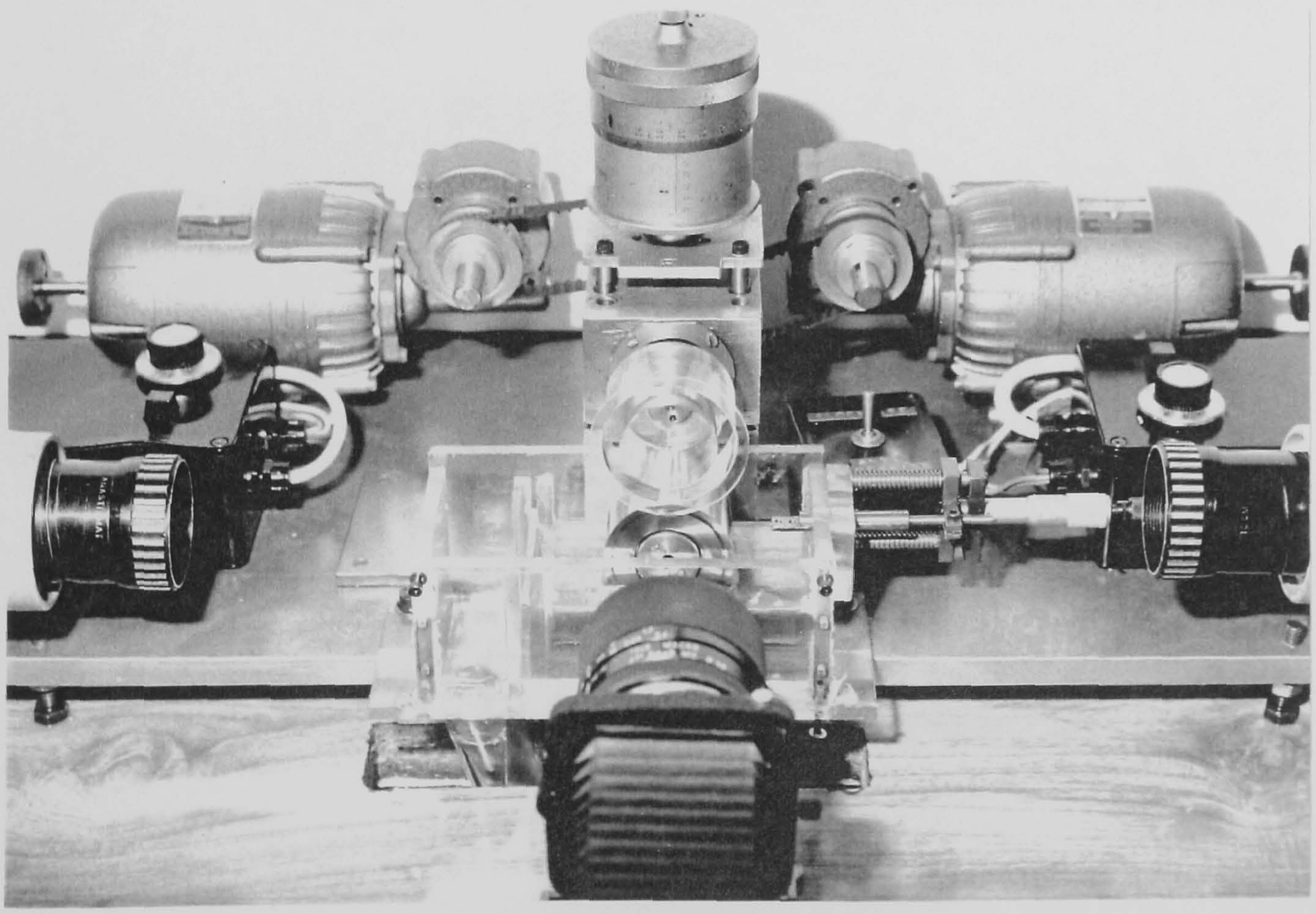

Figure 3.6: General viewing/illumination system

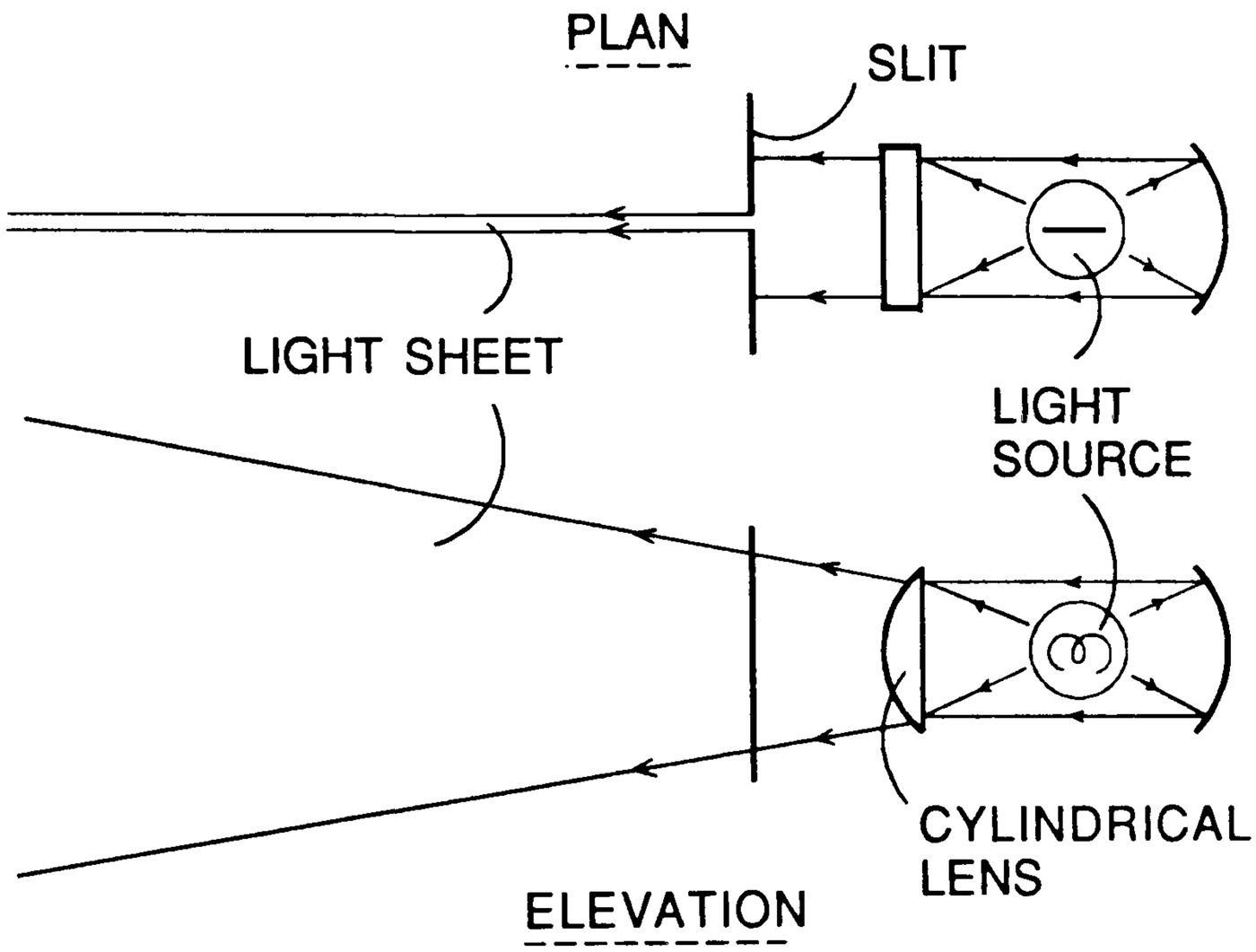

Figure 3.7: Method of producing a light sheet

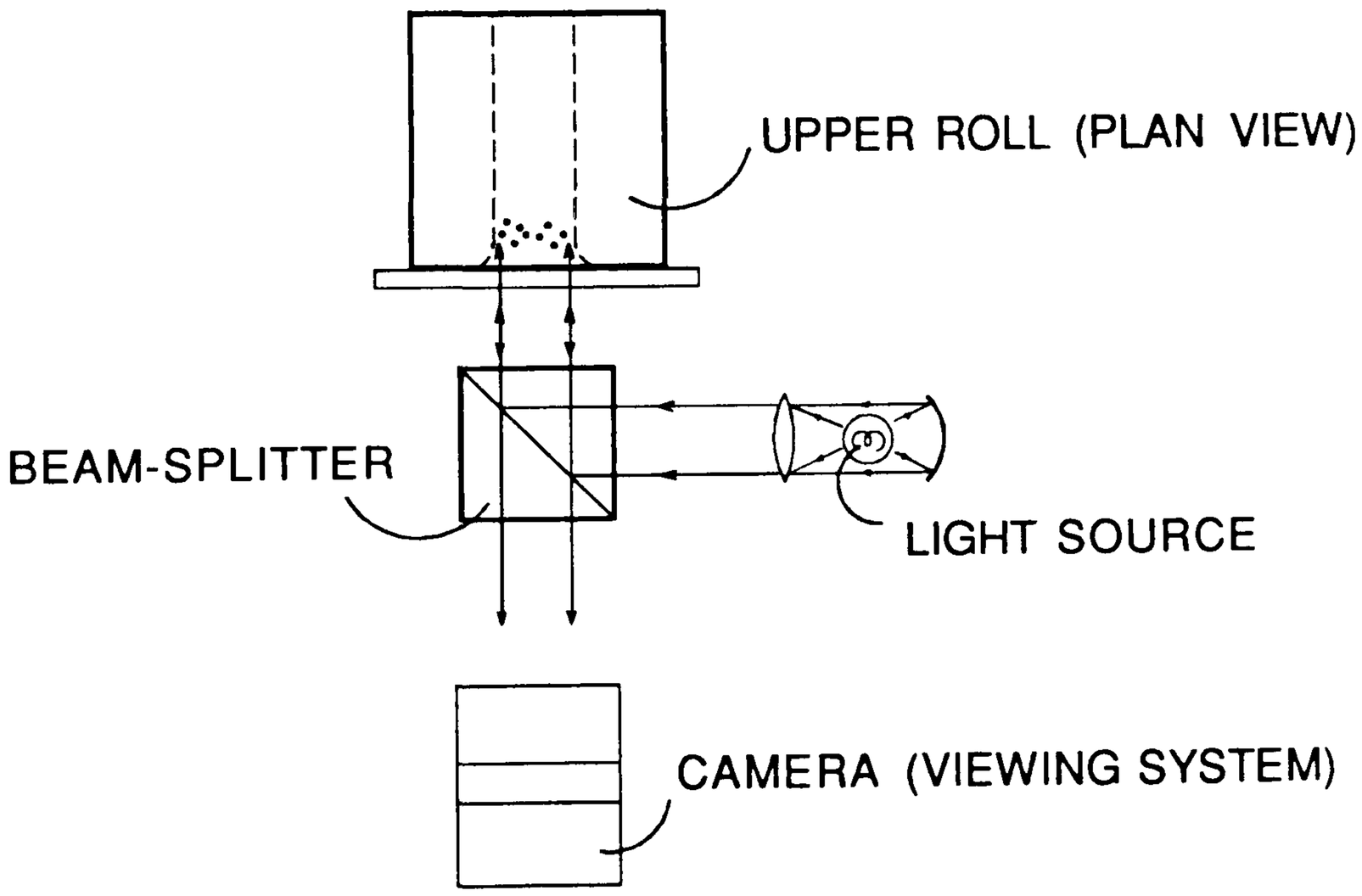

Figure 3.8: An alternative illumination system

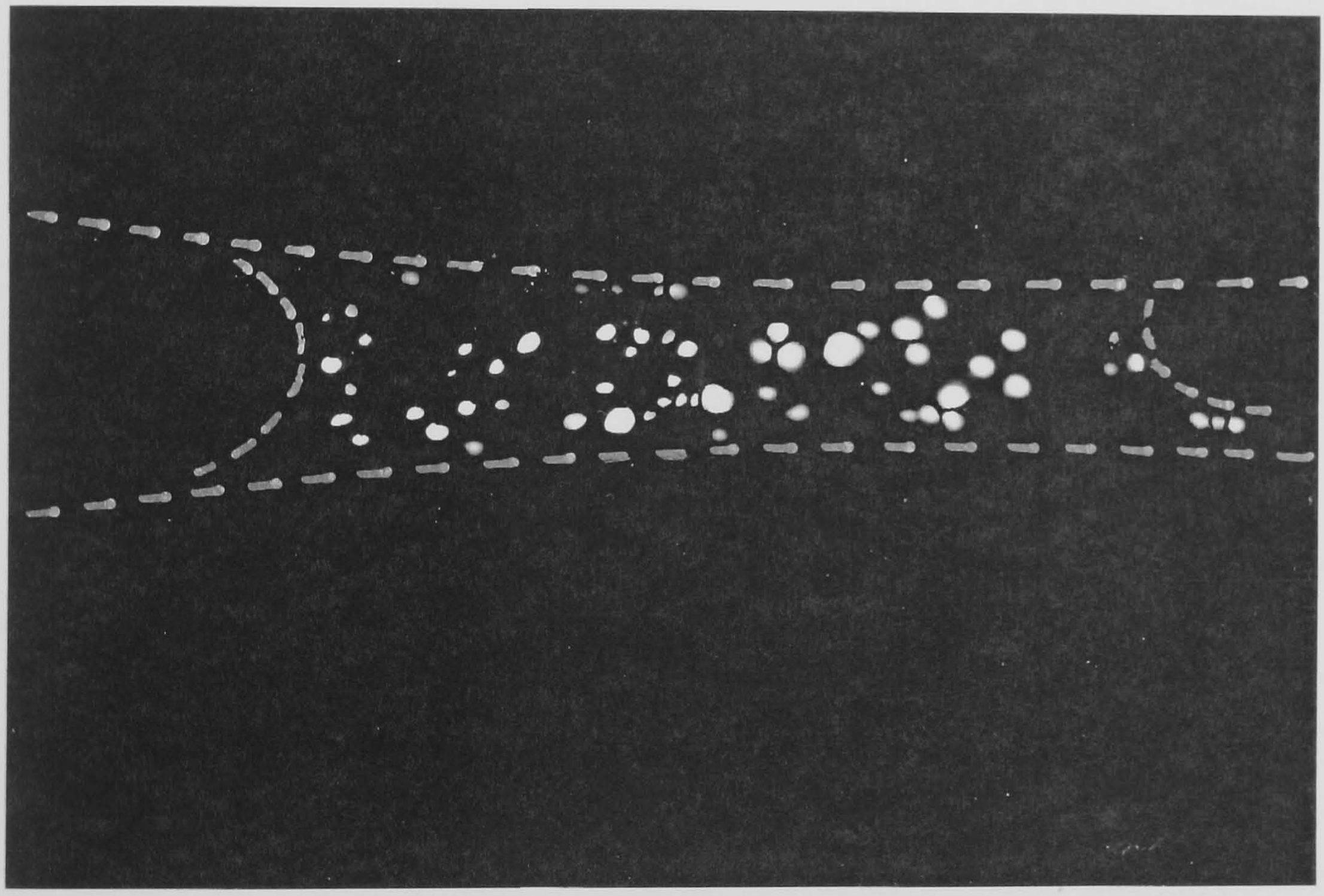

Figure 3.9: An example of laser-illuminated particle flow

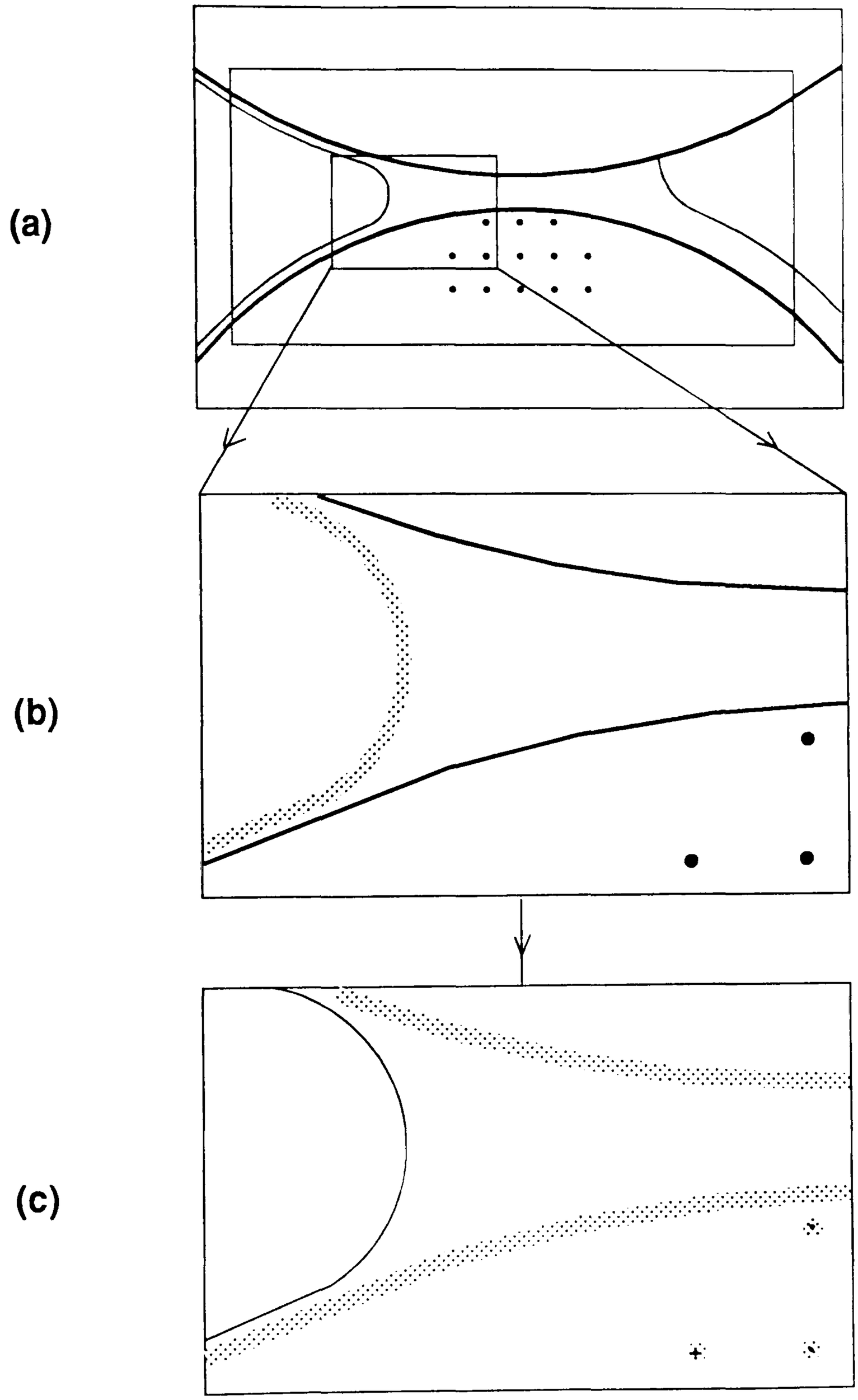

Figure 3.10: Technique for measuring free surface profiles/locations

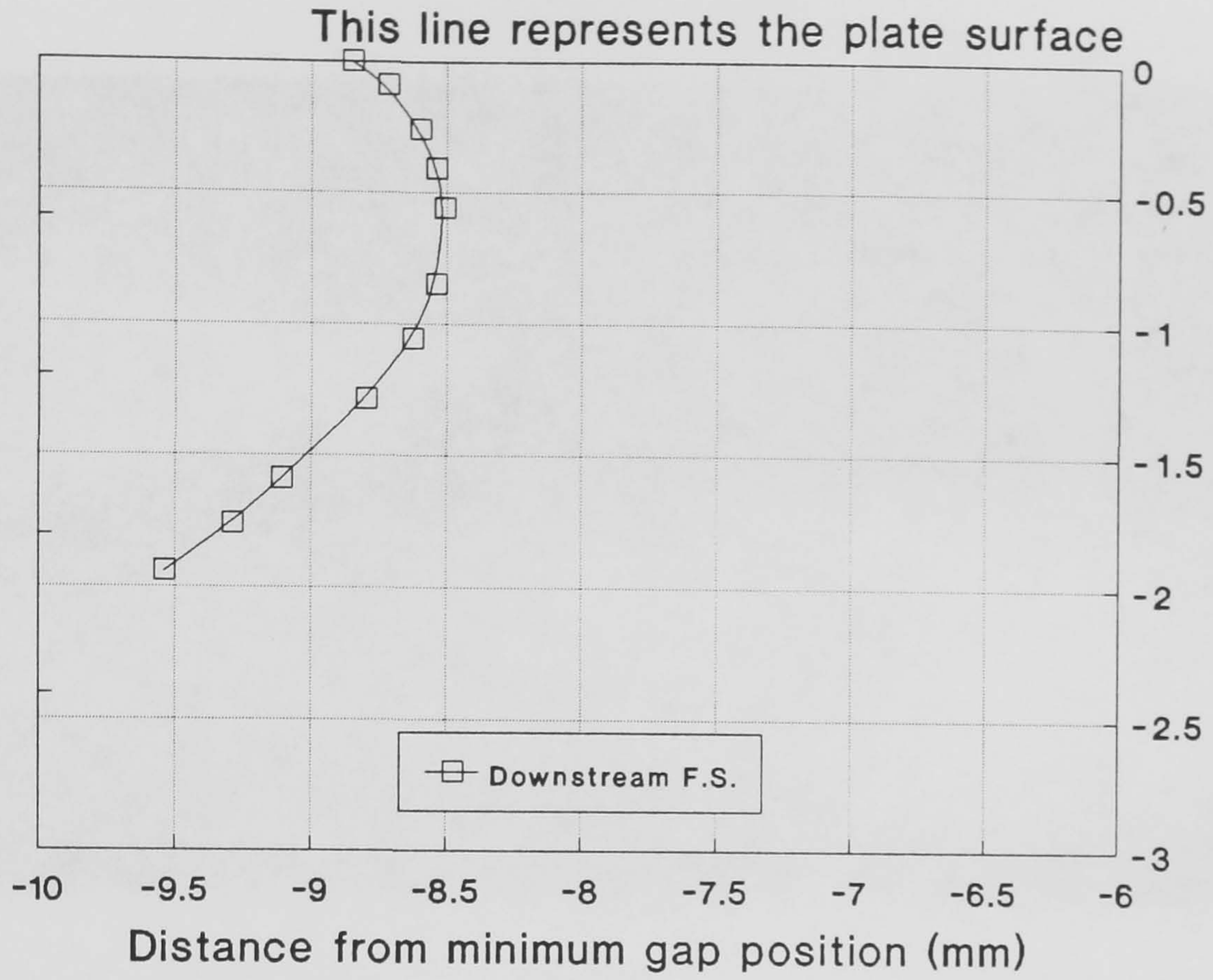

Figure 3.11: A typical donstream free surface profile for Classical roll coating

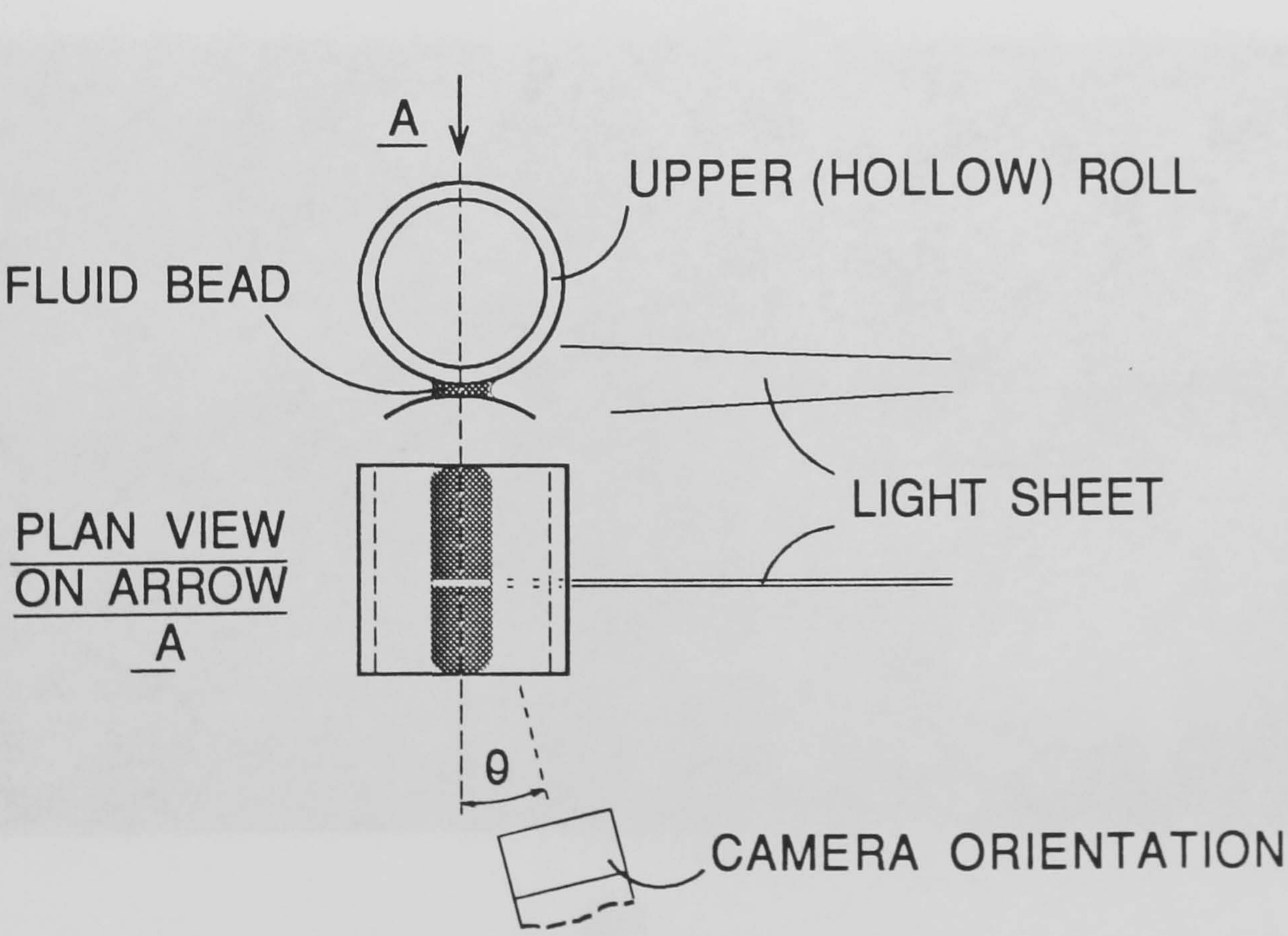

Figure 3.12: An alternative method of measuring free surface profiles/locations

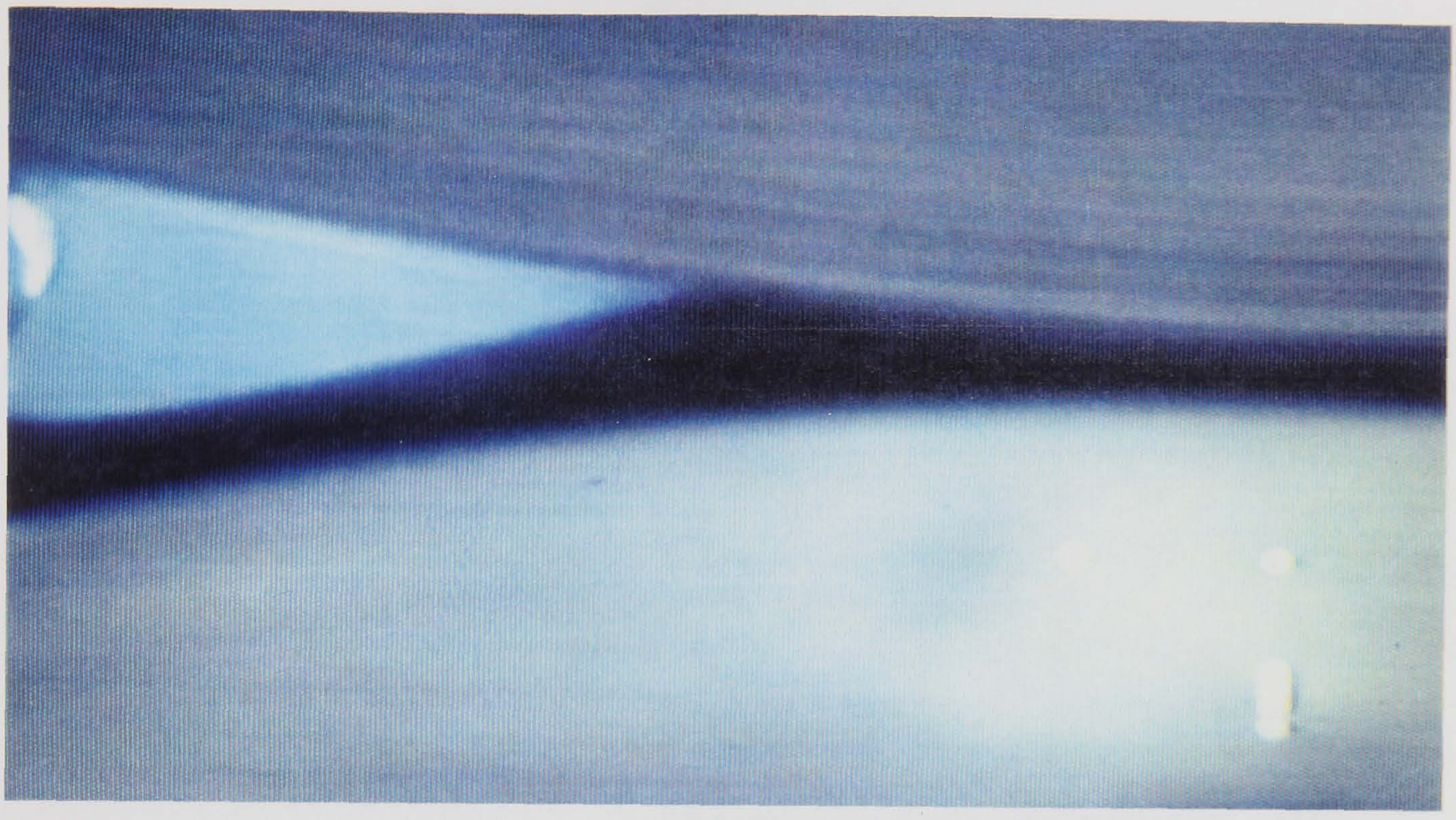

(a)

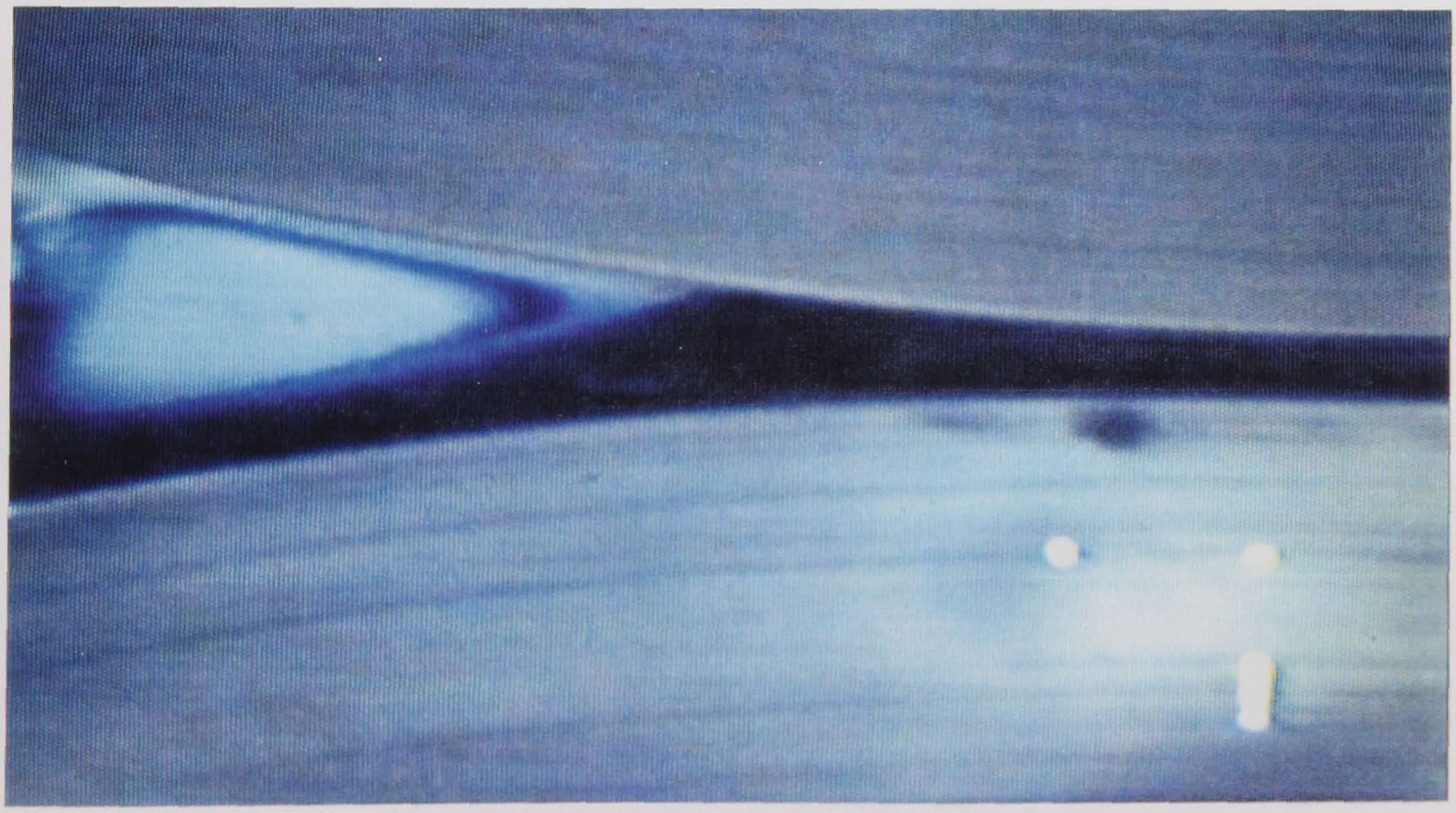

(b)

Figure 3.13: Two-roll coater (lower roll only moving) showing (a) dye in through-flow only, and (b) dye in through-flow plus recirculation

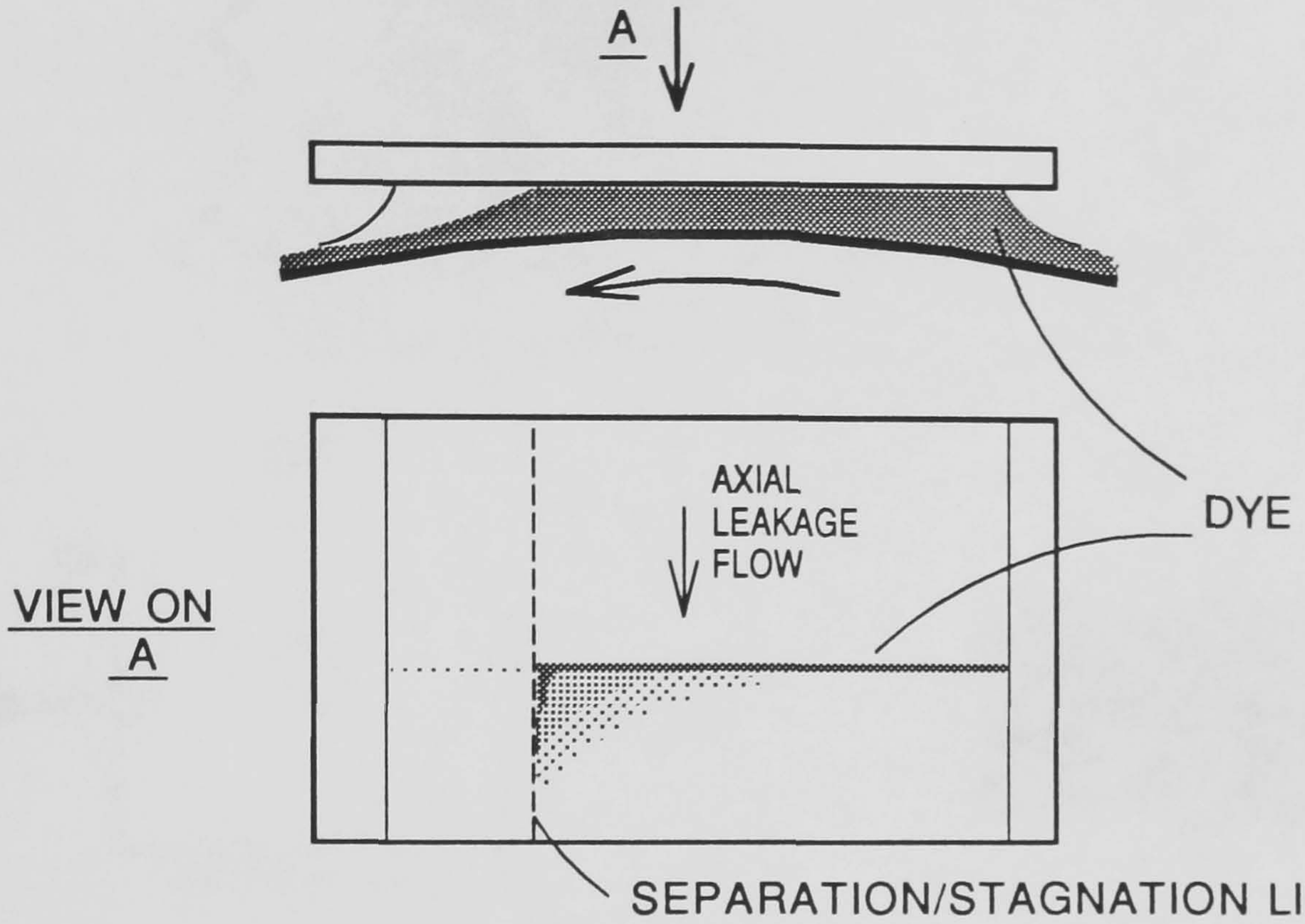

Figure 3.14: Illustration of axial leakage flow revealing the separation line in a plateroll geometry

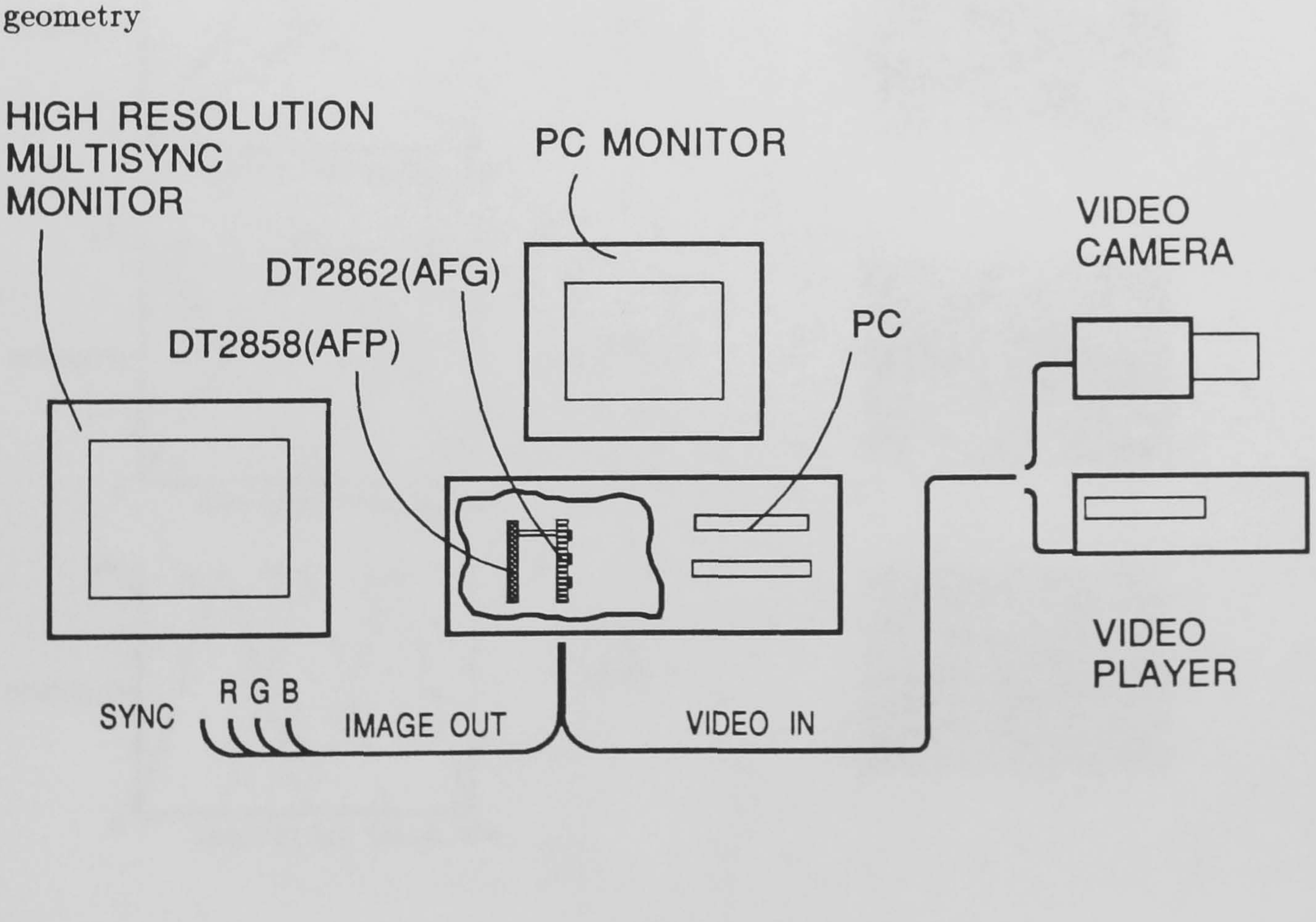

Figure 3.15: Image processing hardware system

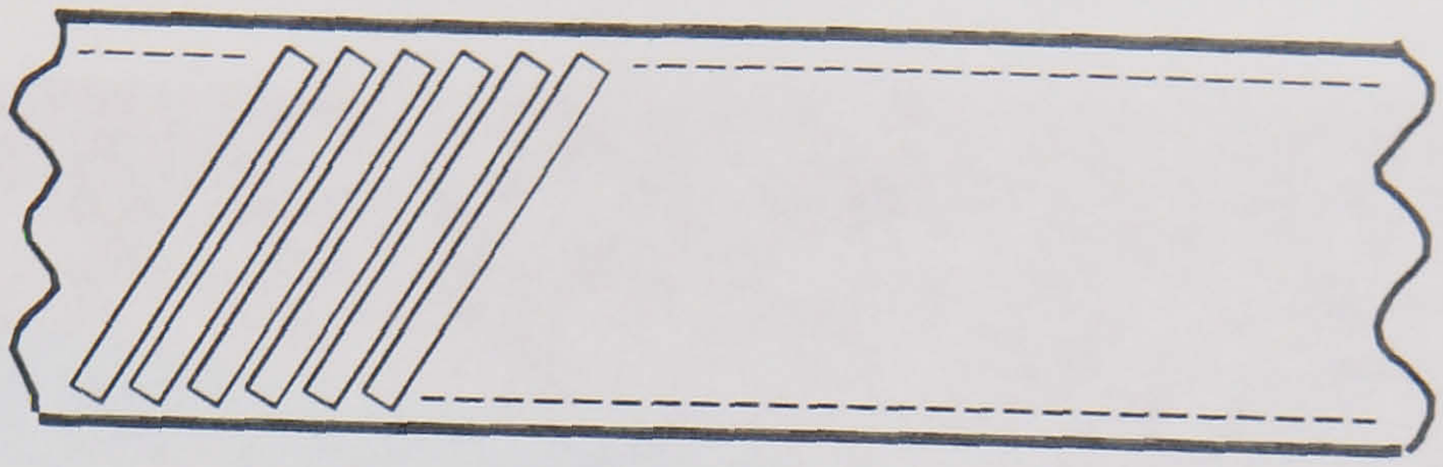

Figure 3.16: Recording of image onto video tape

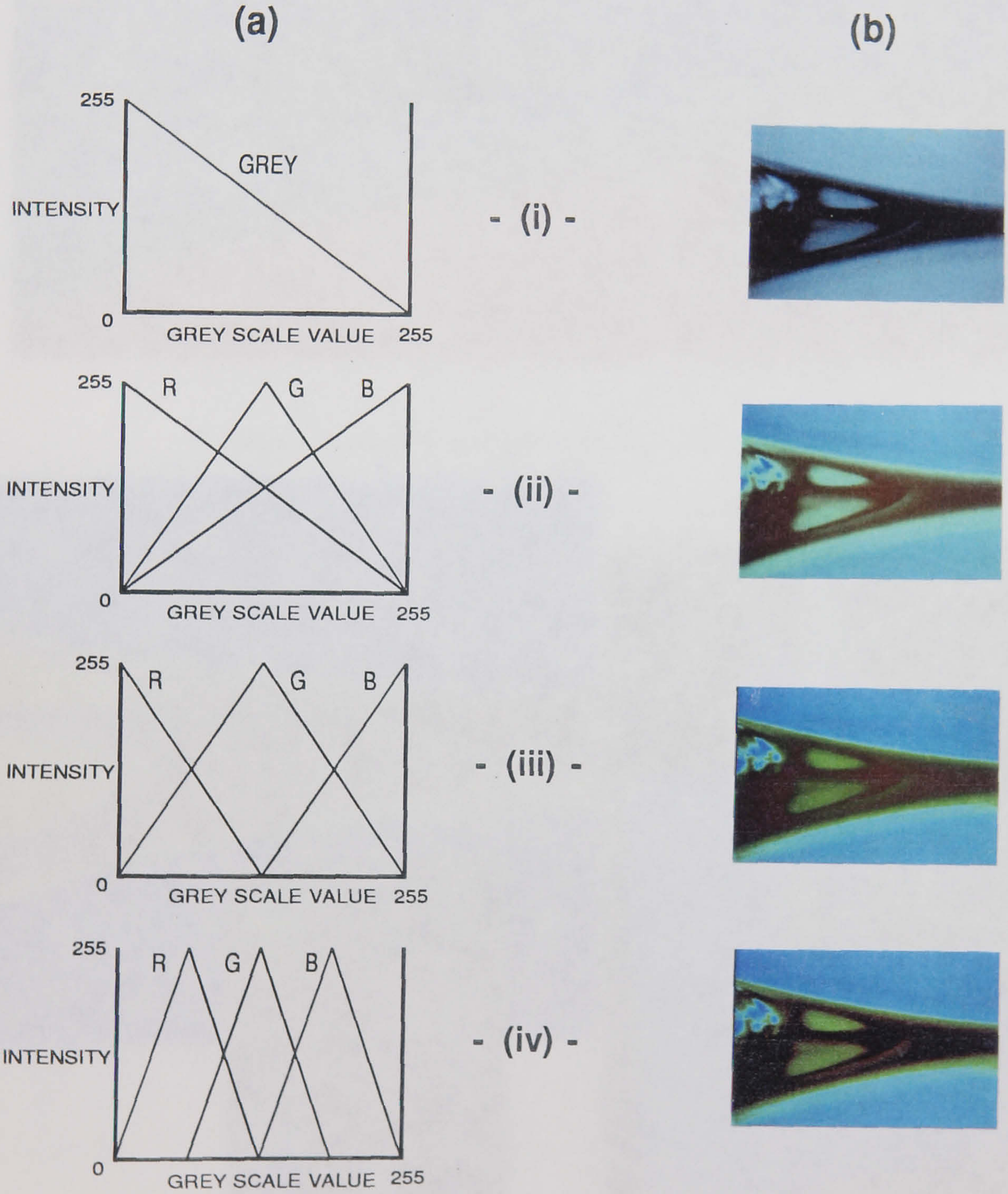

Figure 3.17: Examples of false colour image enhancement showing various (a) spectra, and (b) corresponding effect on a test image

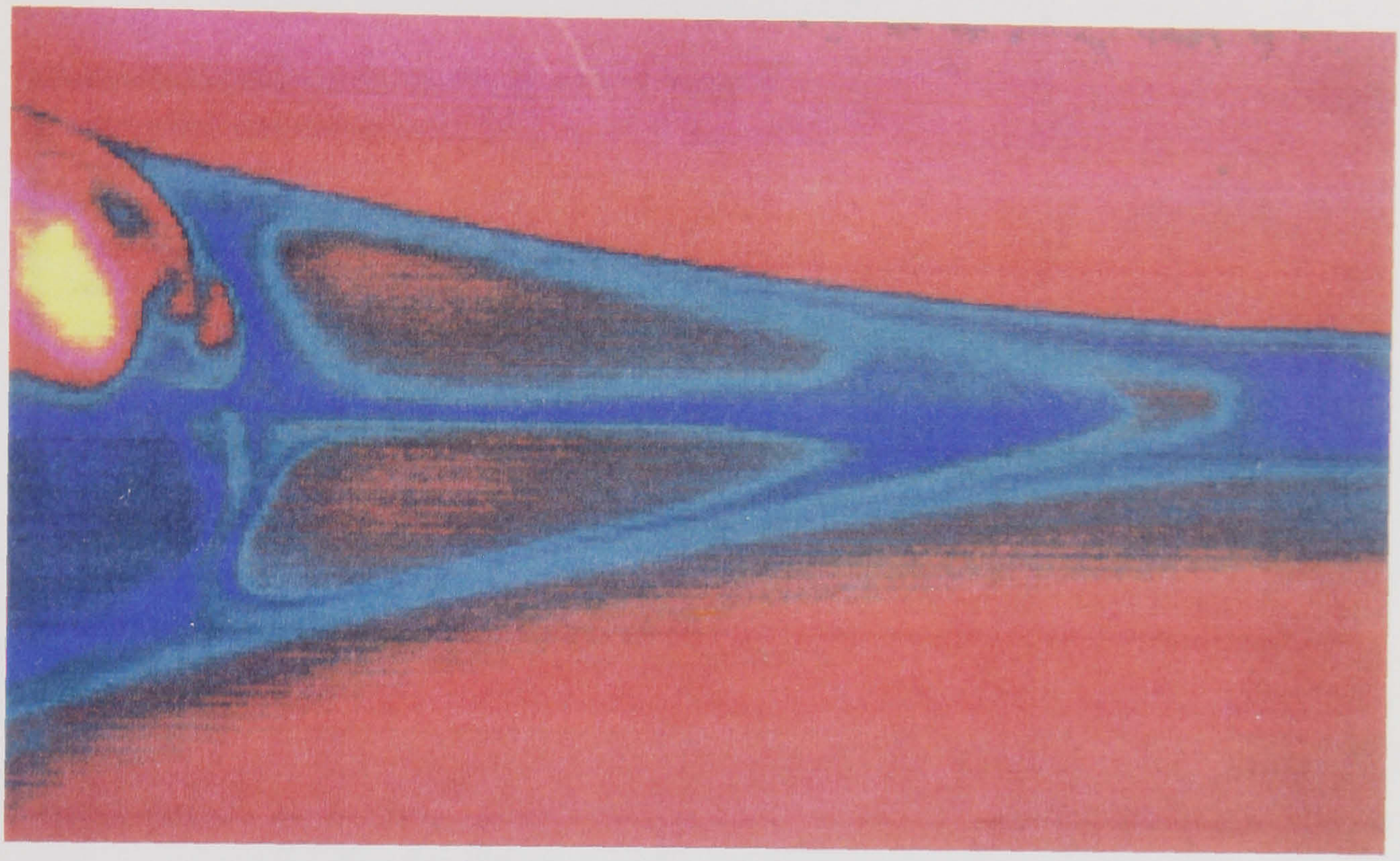

Figure 3.18: An example of a Versatec colour plot

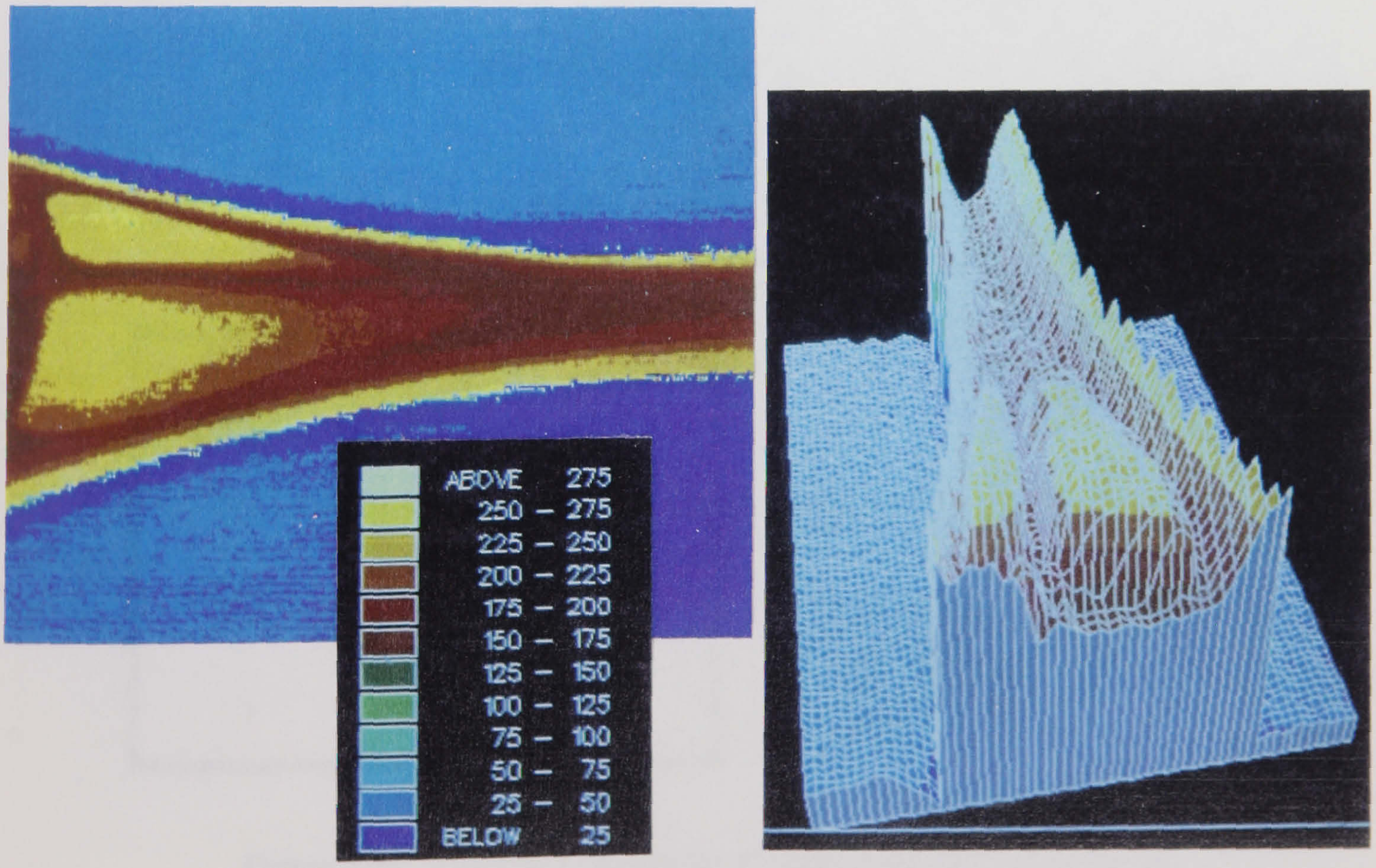

Figure 3.19: An example of a Uniras 3-D colour plot

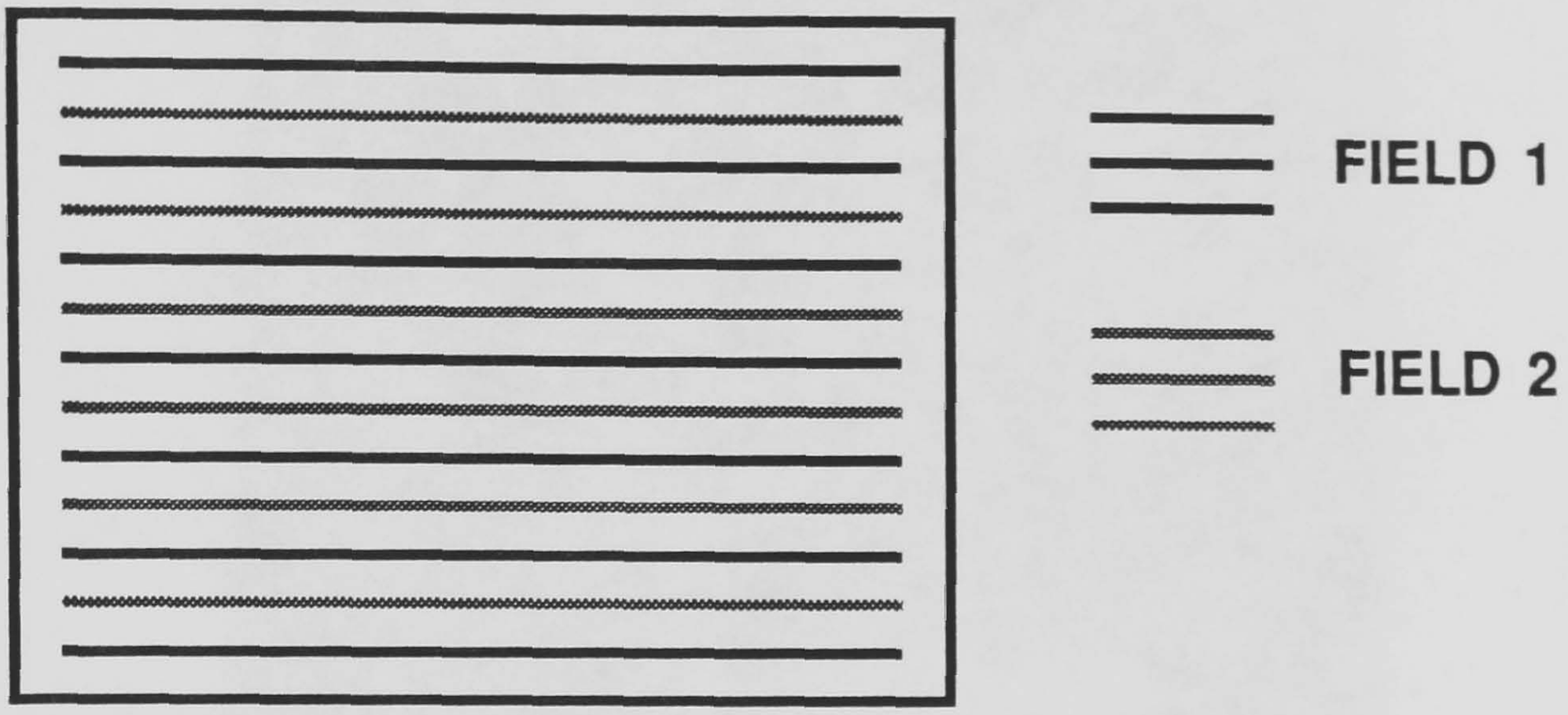

Figure 3.20: Standard video image composition

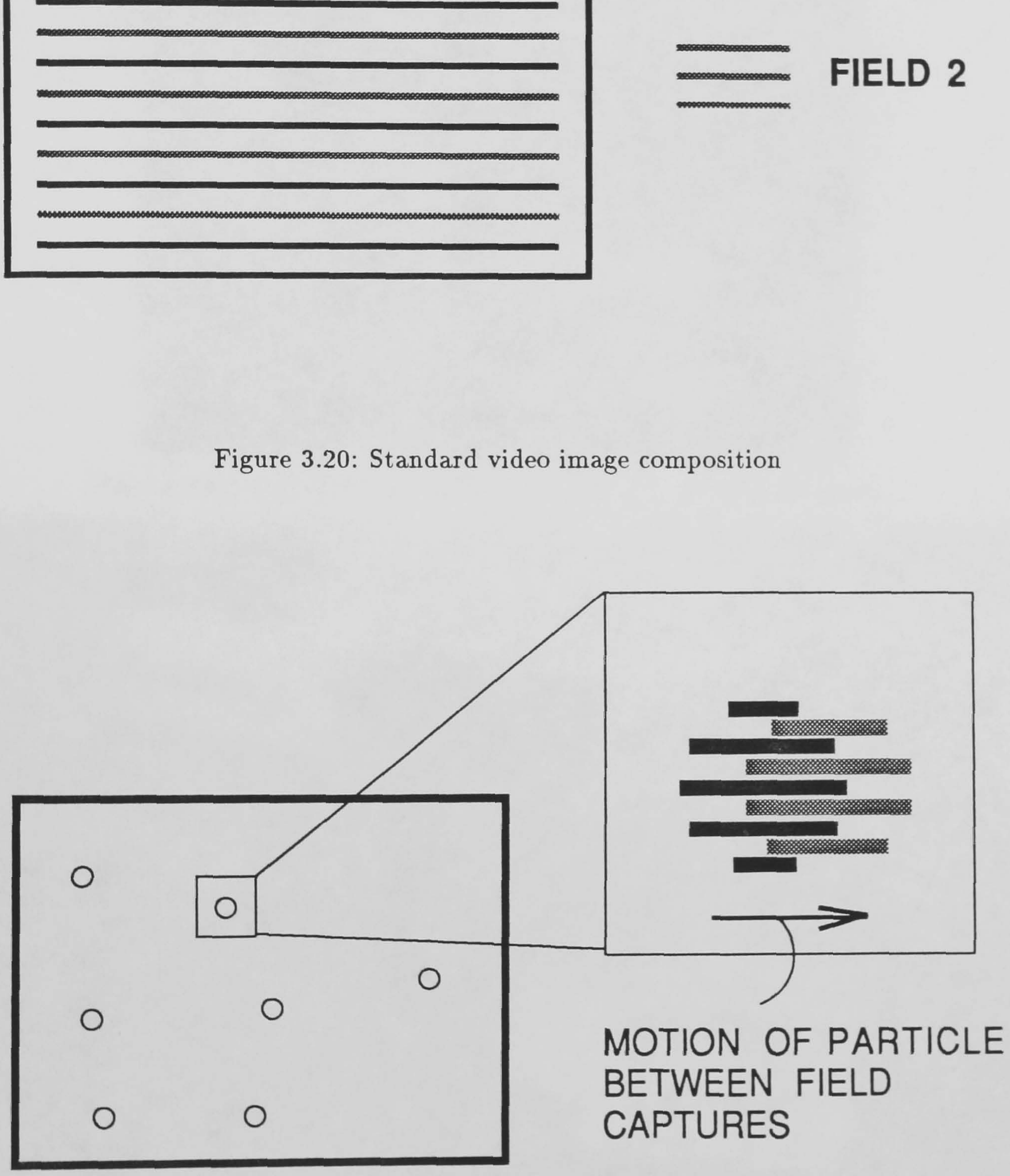

Figure 3.21: The effect of interlaced capture on object movement

Figure 3.22: Kodak Ektapro High Speed Video - Standard System

Figure 3.23: Kodak Ektapro Image Intensified Camera System

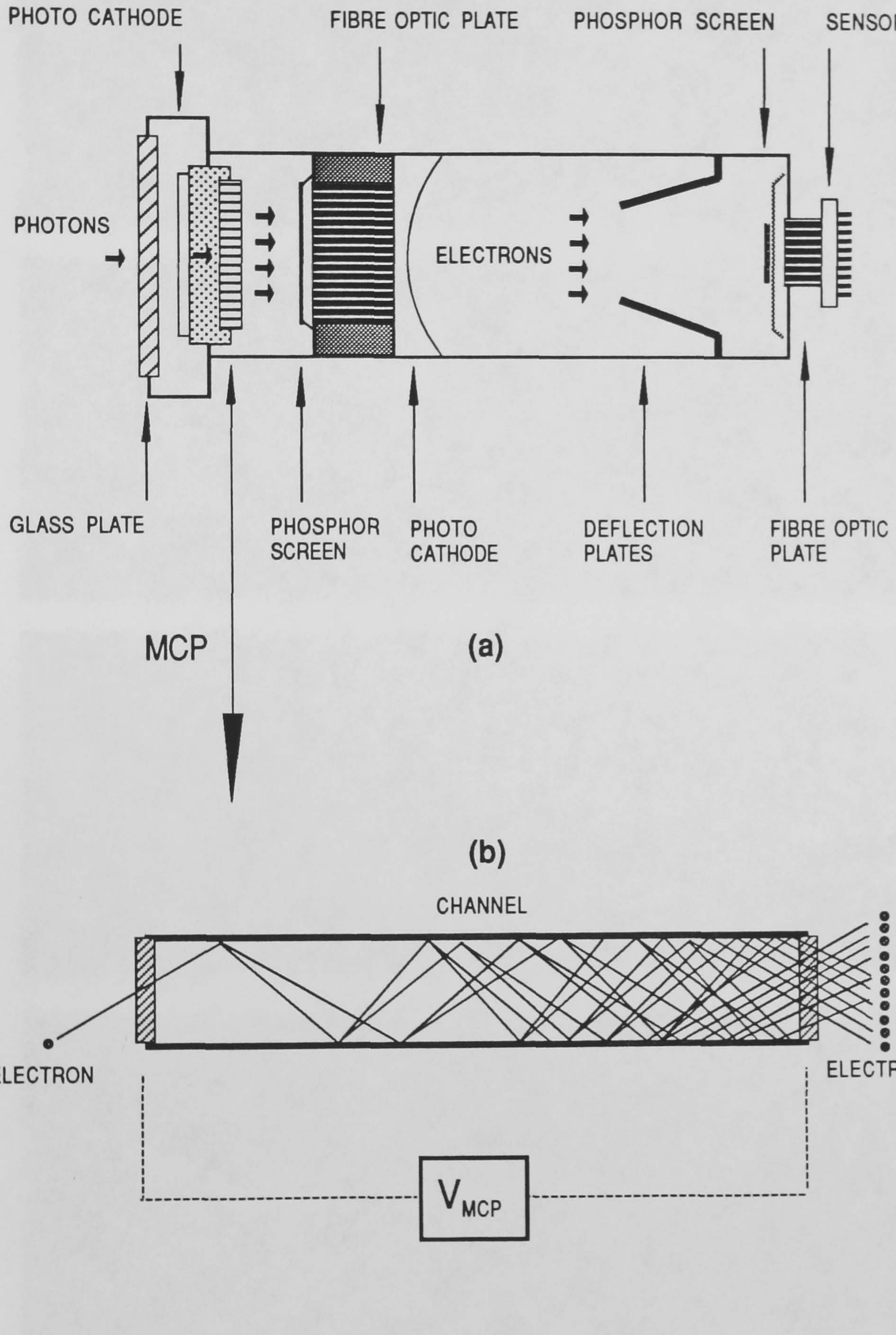

Figure 3.24: Kodak Image Intensifier Unit showing (a) general view, and (b) Micro Channel Plate Capillary

(a)

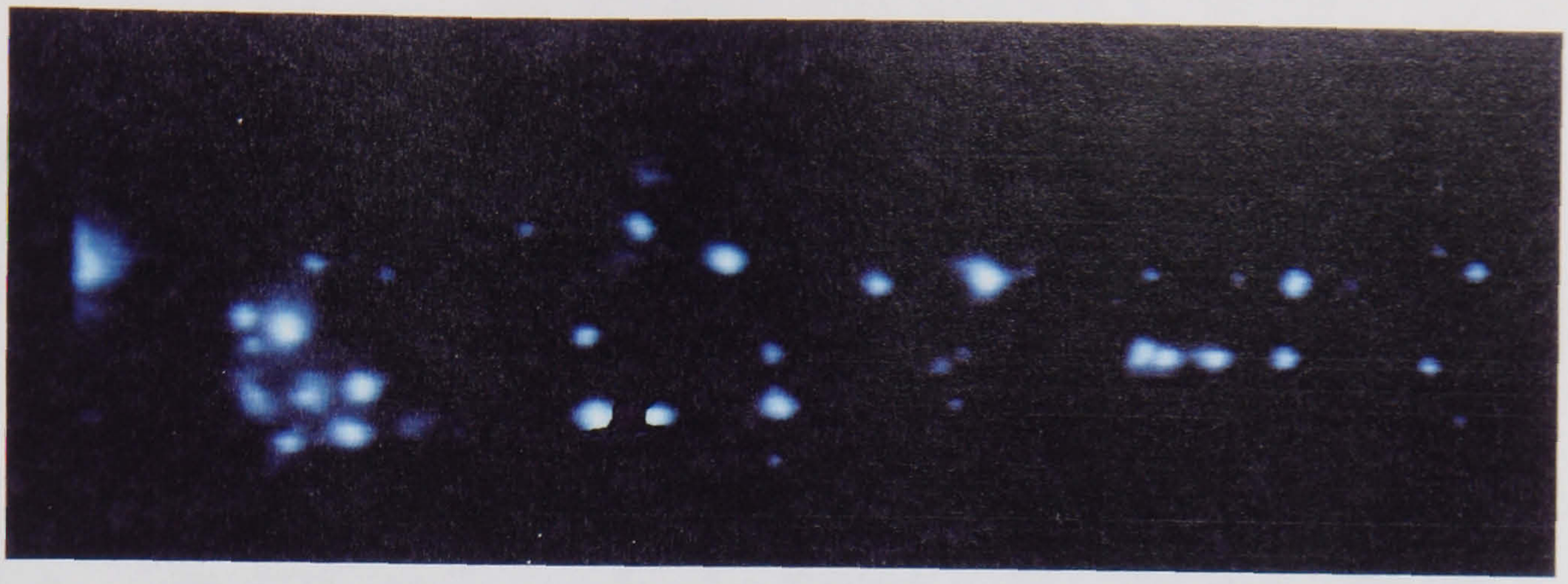

(b)

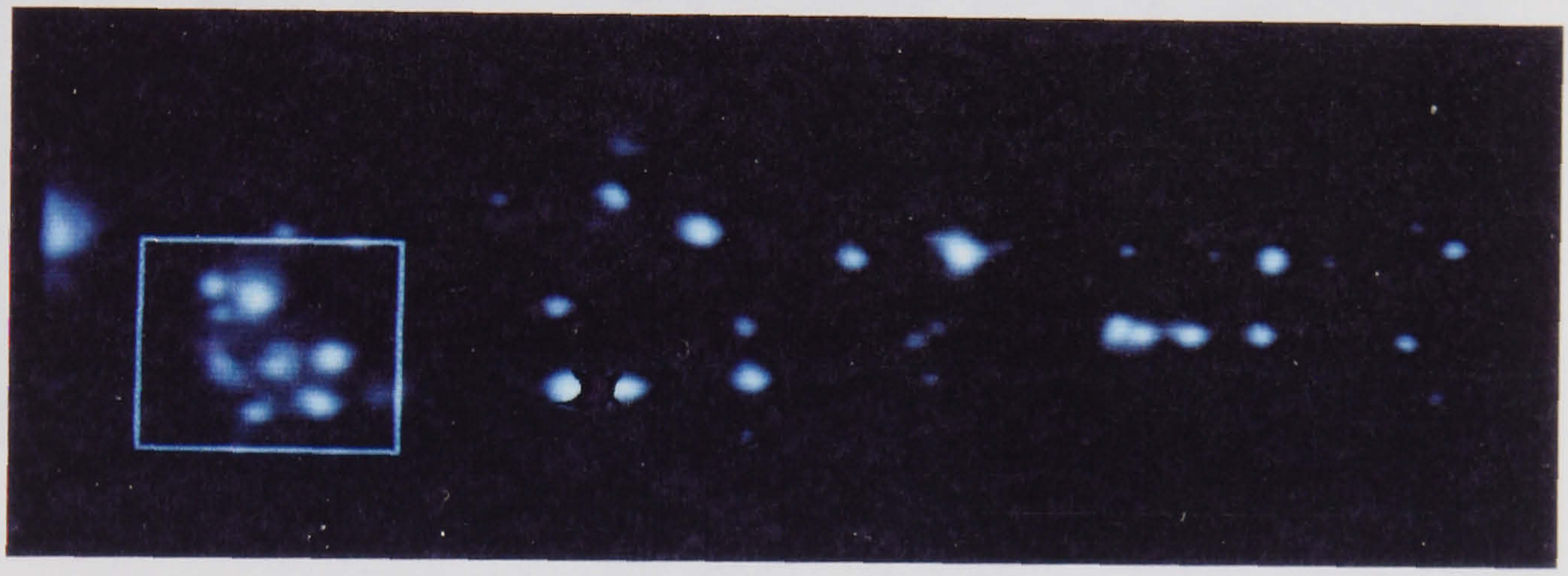

(c)

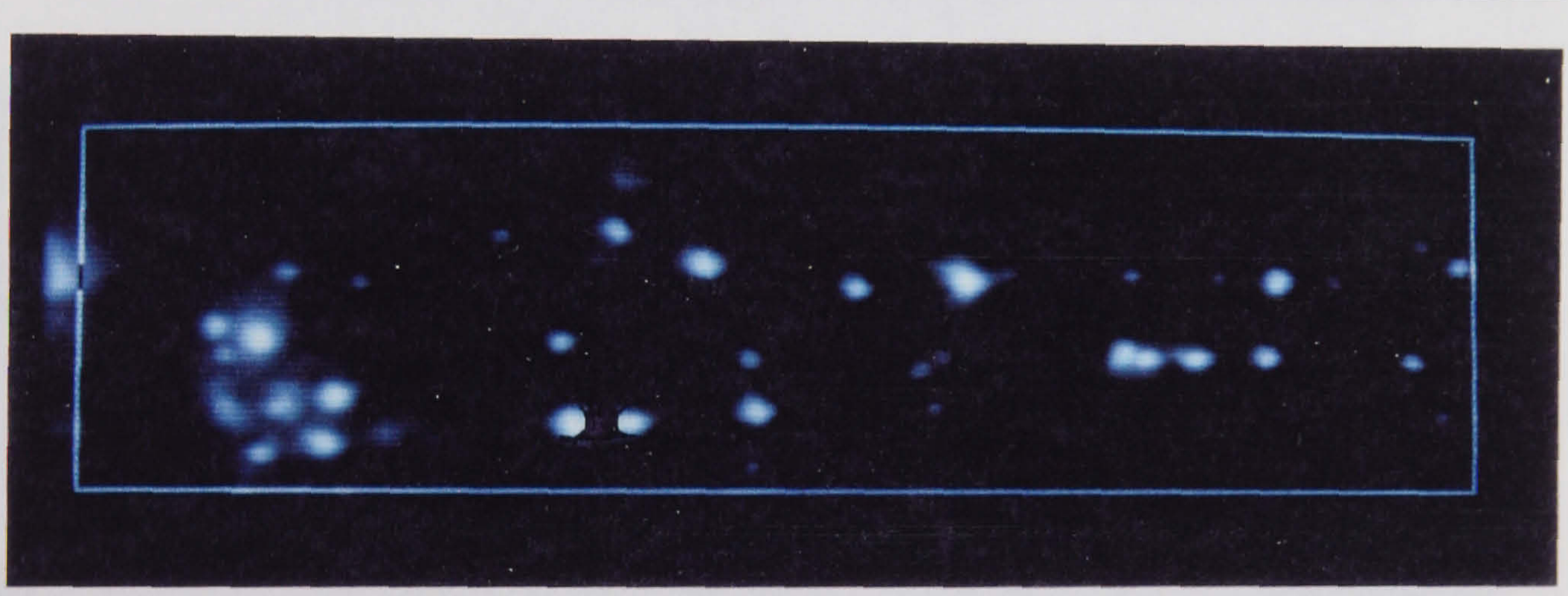

(d)

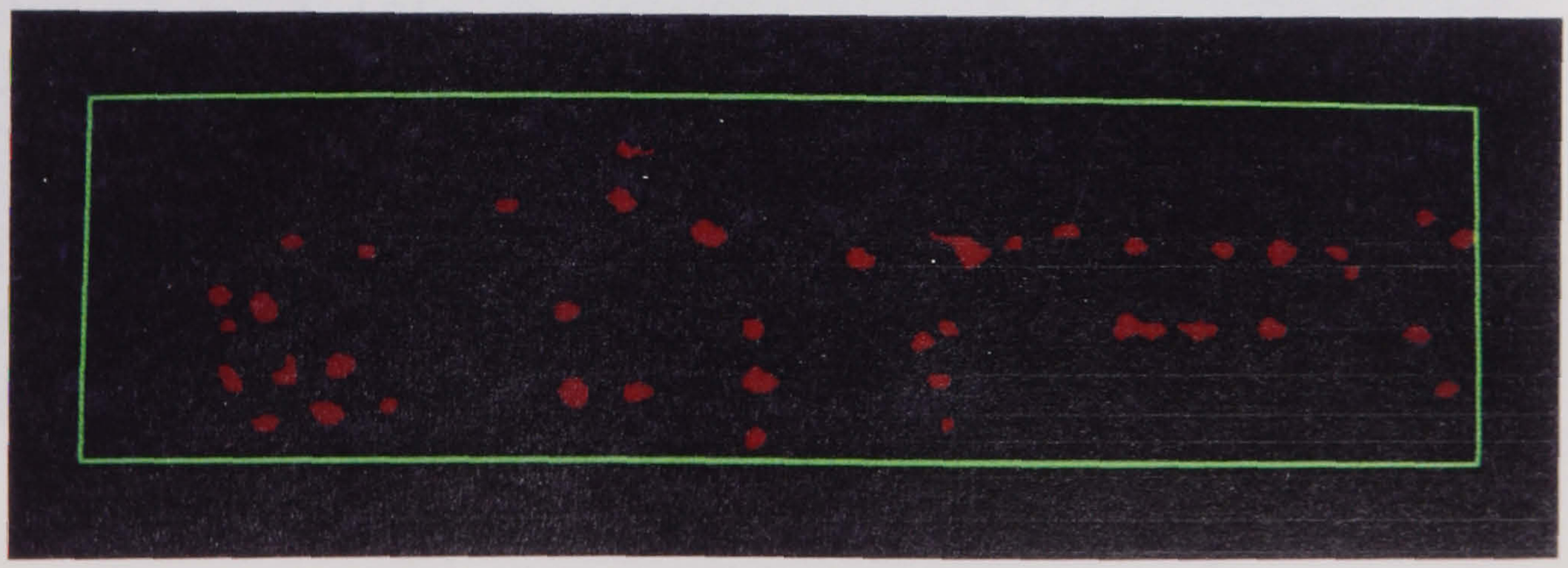

Figure 3.25: Particle recognition procedure (a) Raw image, (b) Small working window, (c) Full-region window, (d) Recognised particles (shown in red)

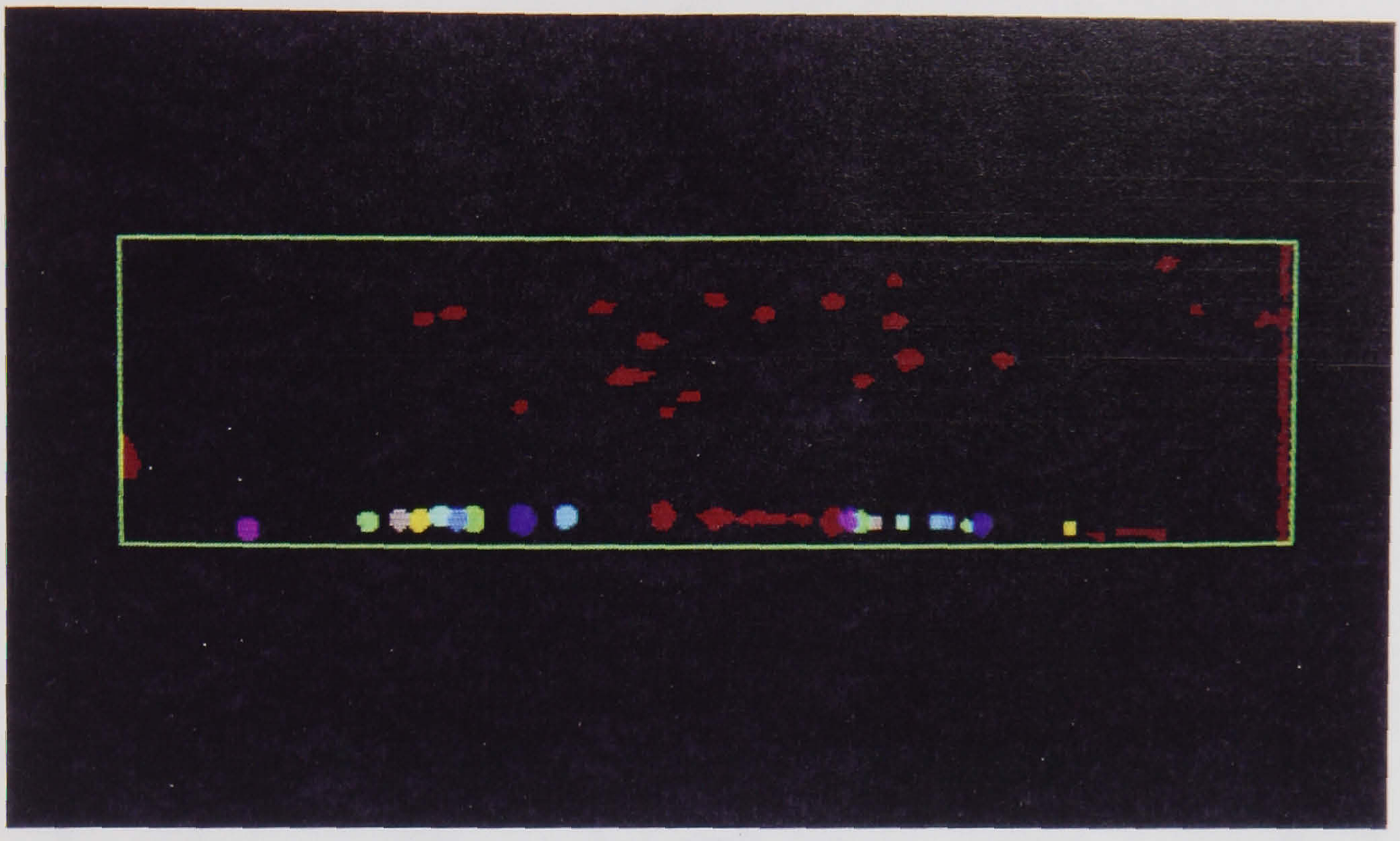

(a)

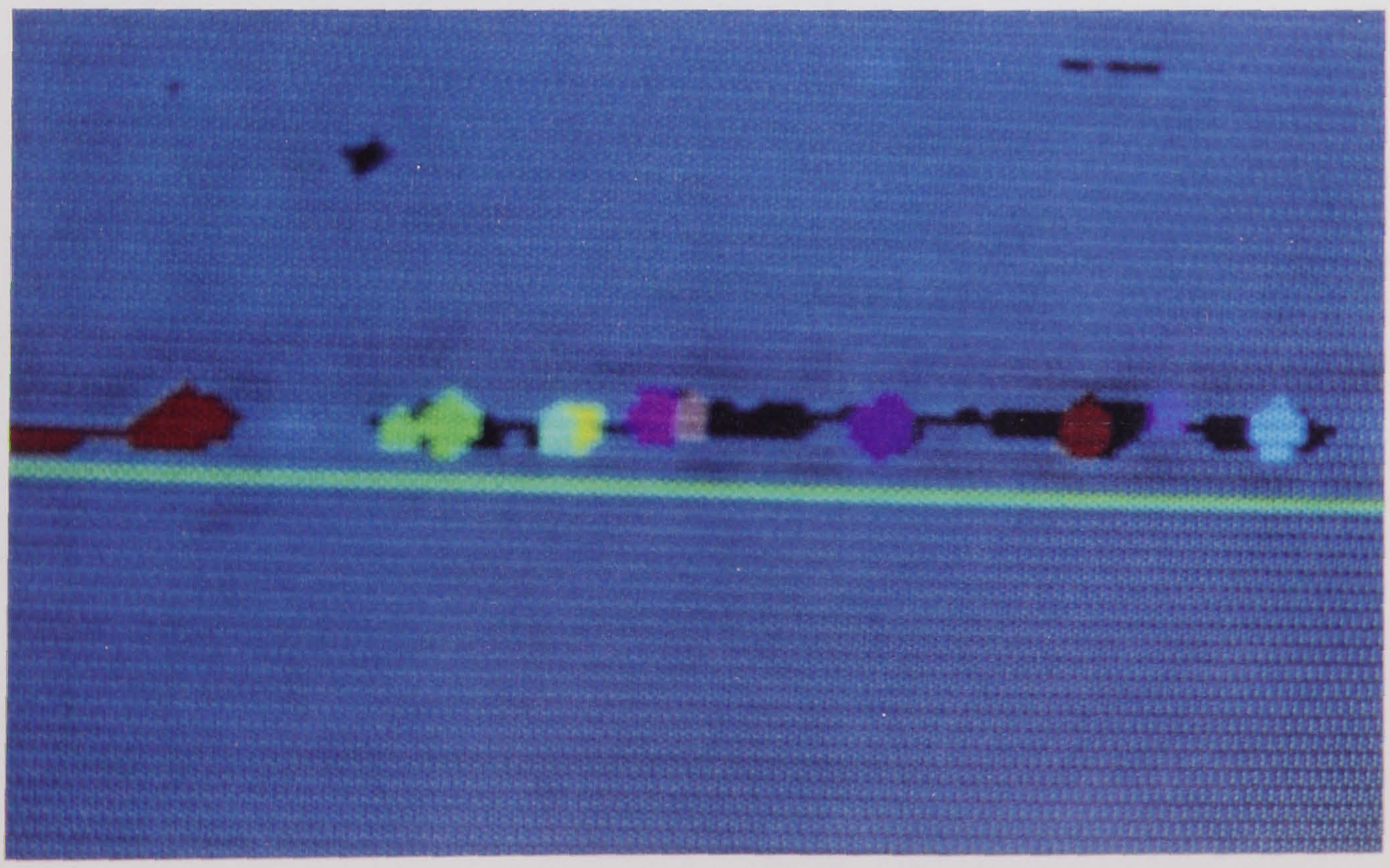

(b)

Figure 3.26: A typical particle flow image which has been analysed by the Particle Recognition software (a) full frame (b) magnified view of a cluster of particles

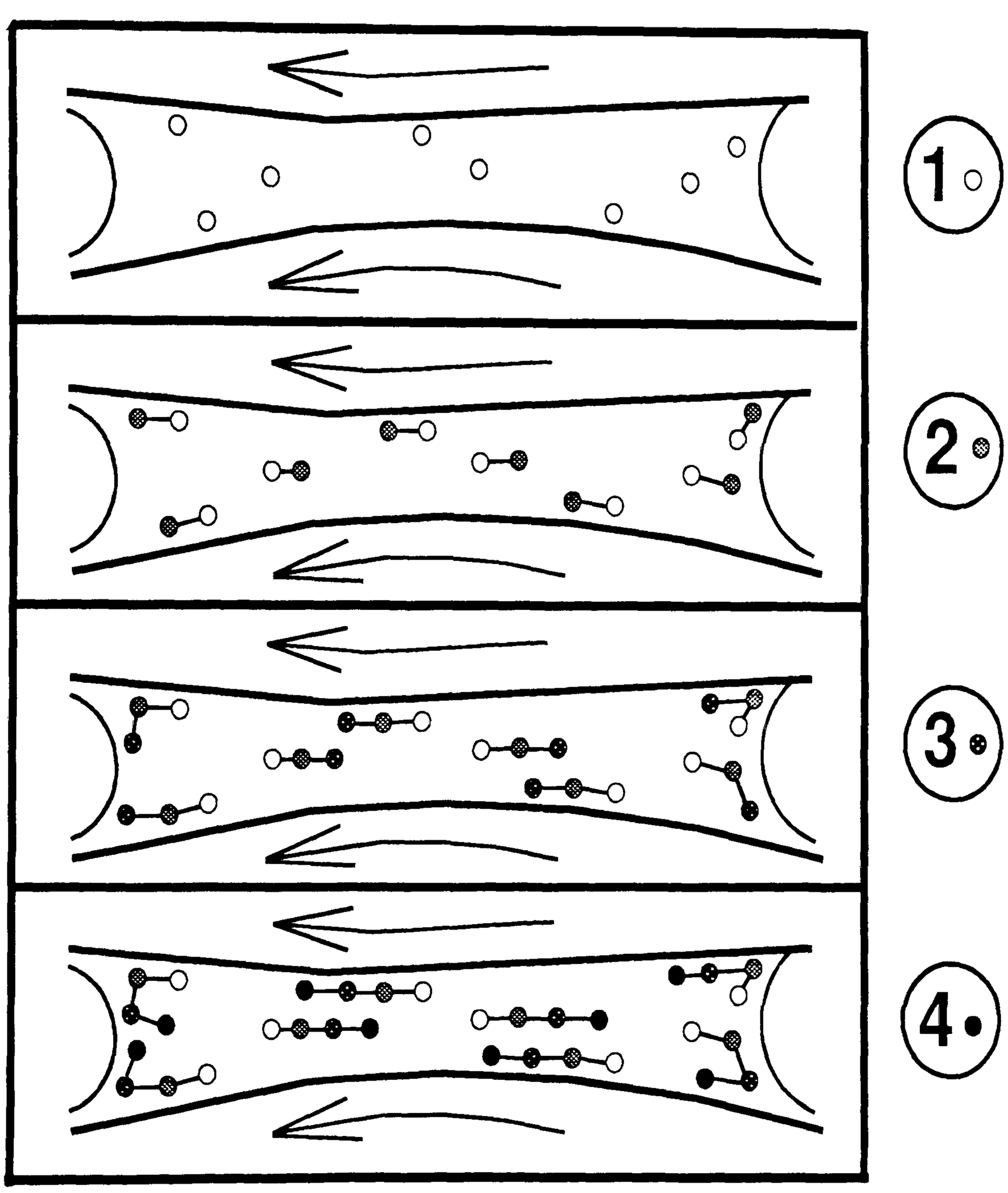

Figure 3.27: Illustration of consecutive-image particle flow analysis

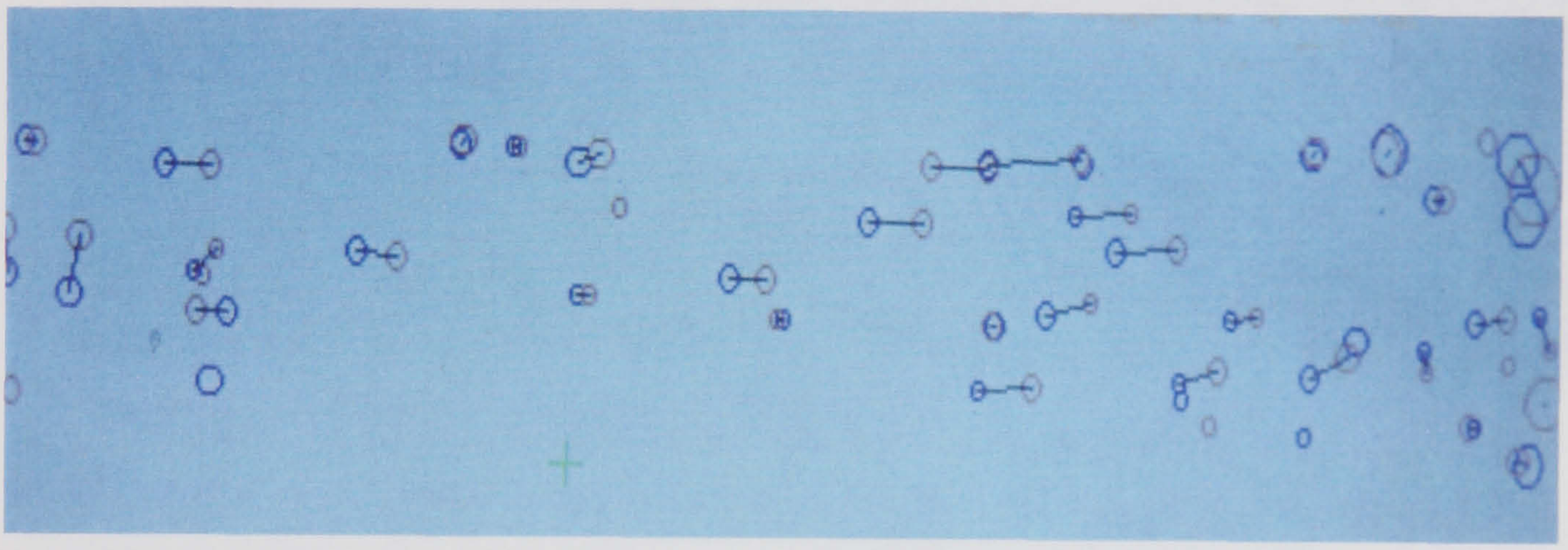

Figure 3.28: A two-frame particle flow analysis plot

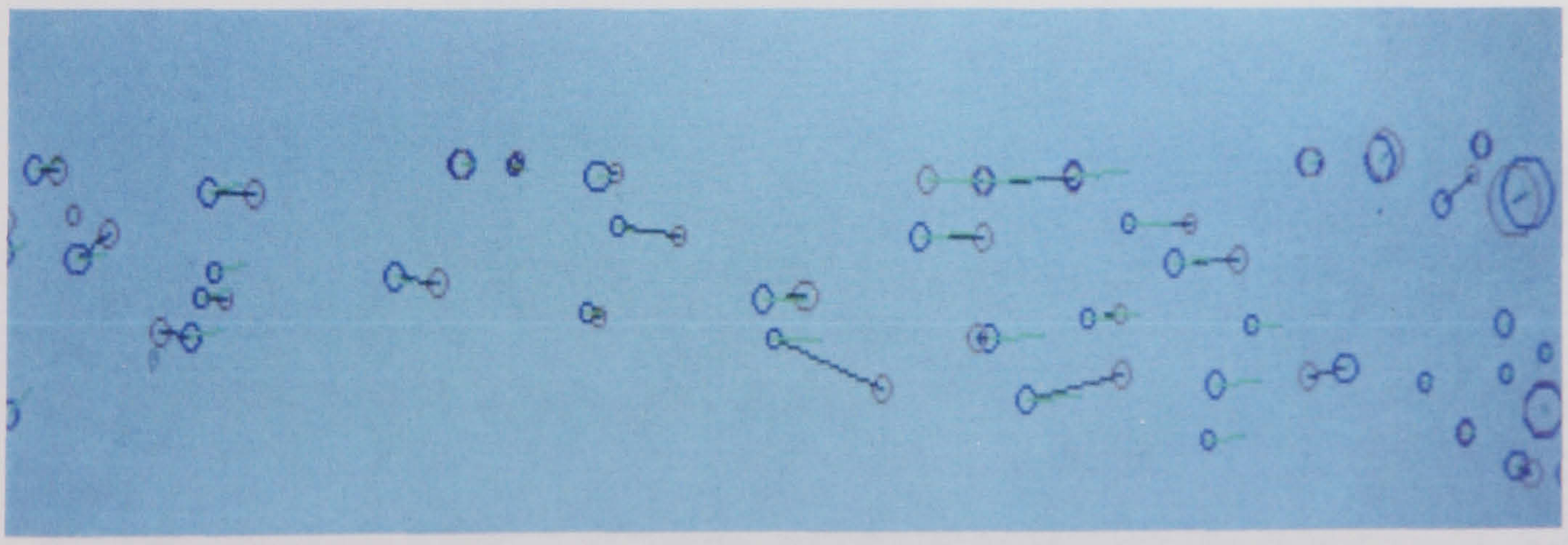

Figure 3.29: Predicted displacements between iterations (shown in green)

(a)

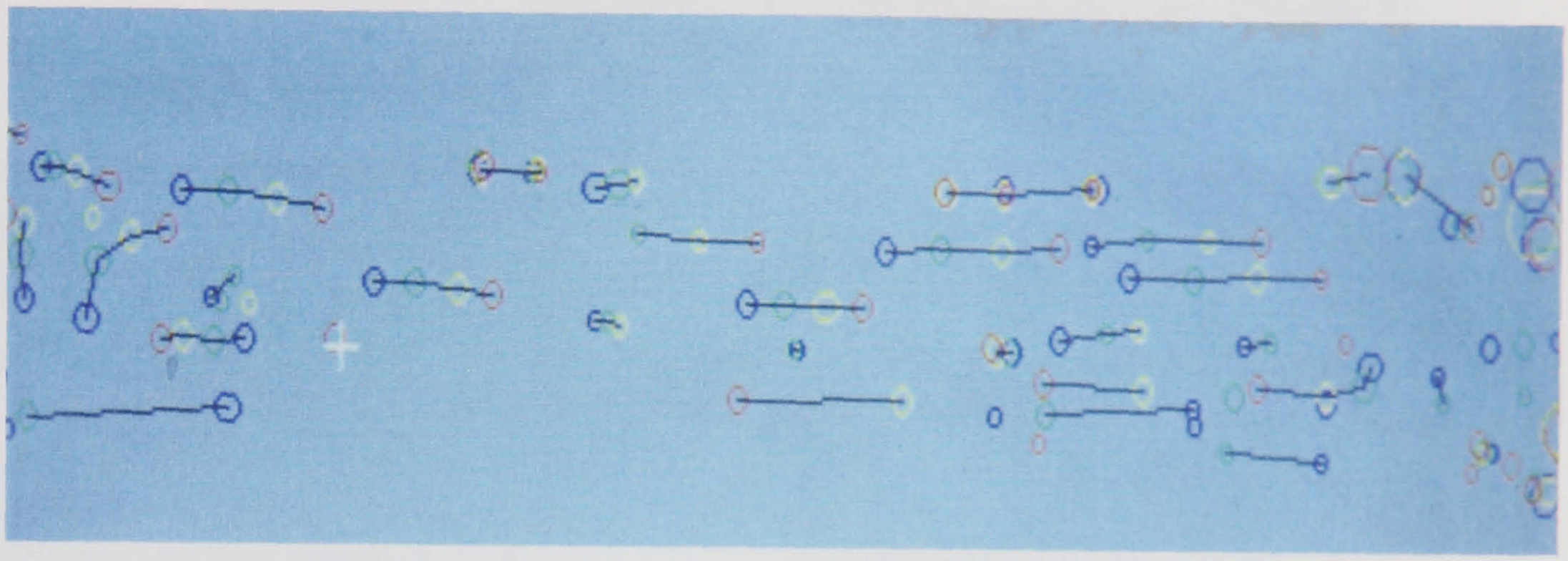

(b)

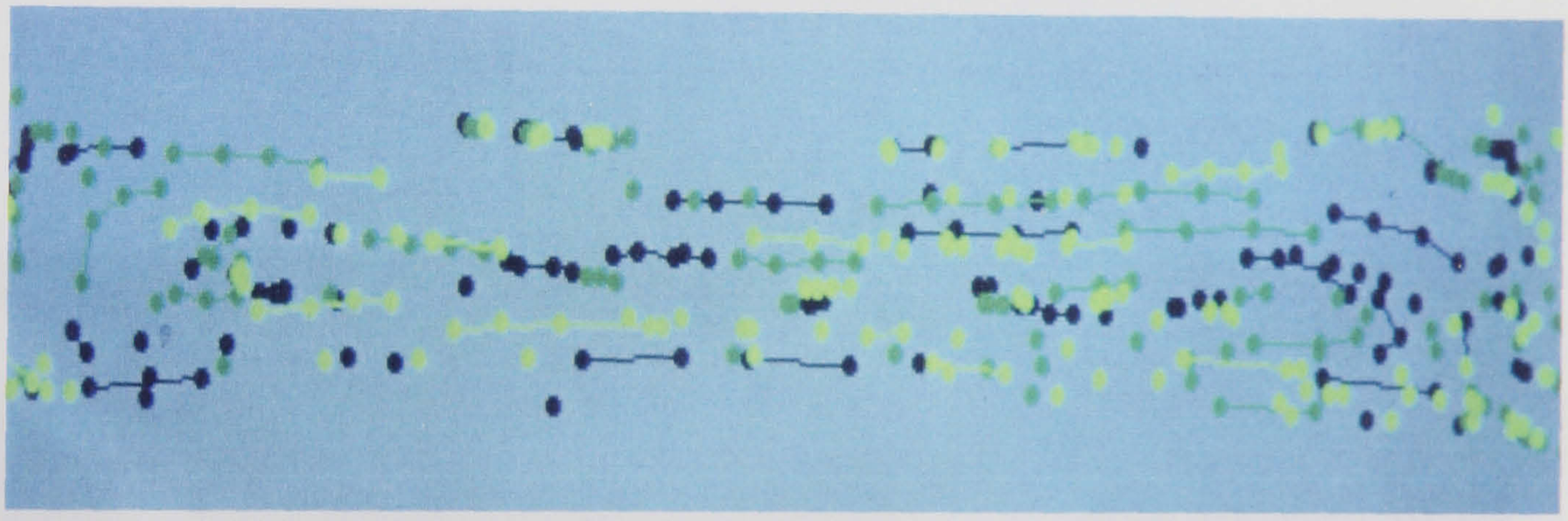

(c)

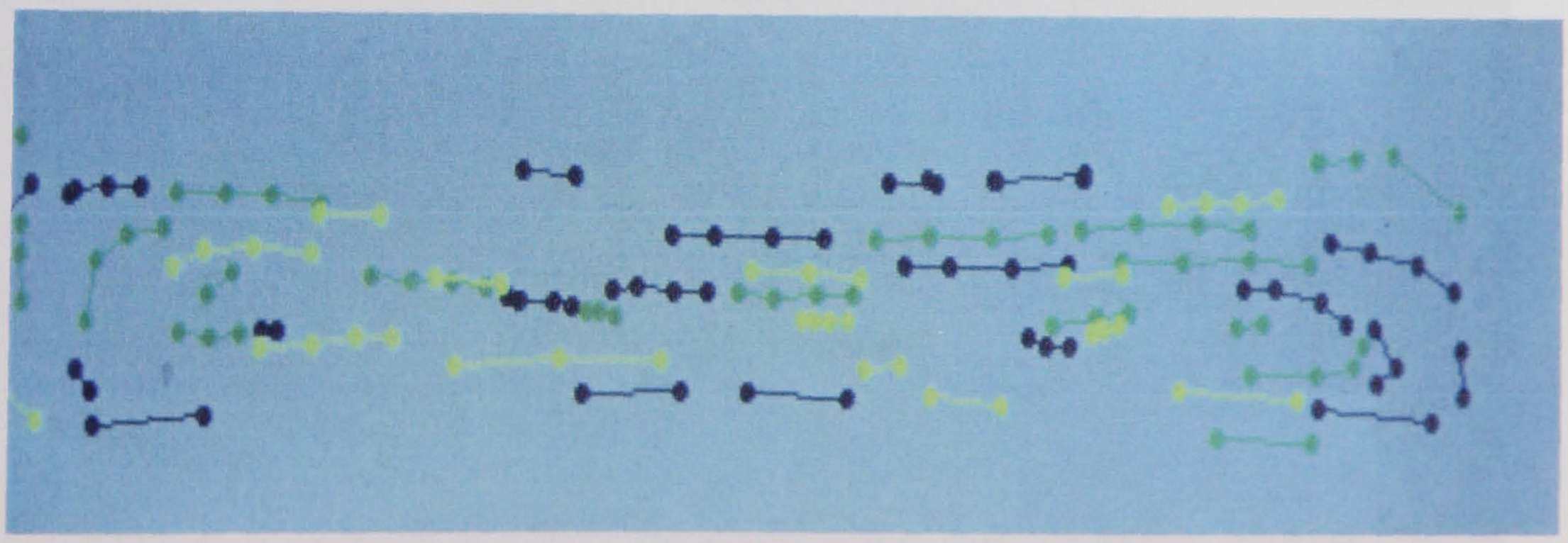

Figure 3.30: Particle tracking plots, (a) 1 four frame set, (b) 3 combined four frame sets, (c) 3 combined four frame sets with matched particles only plotted

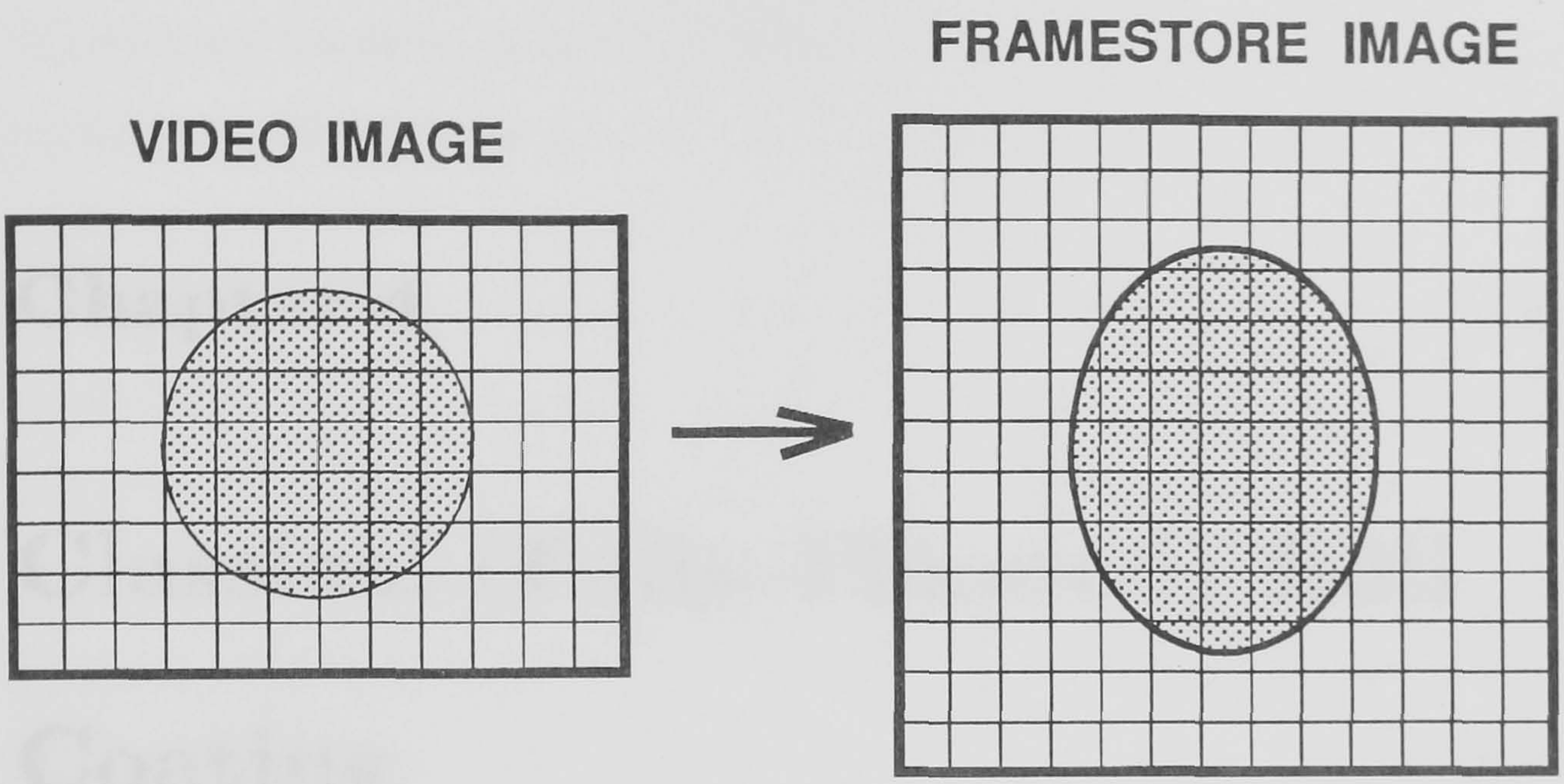

Figure 3.31: Image distortion due to capture system

Figure 3.32: Reference/Calibration Grid

Chapter 4

Classical (Fully-Flooded) Roll Coating

4.1 Introduction

The purpose of this chapter is firstly to document the entire flow field within the nip region of a fully-flooded two-roll coater. Although it appears from the open literature that such a detailed experimental investigation has not been undertaken before, it is perhaps more likely that such results have not been published for one reason or another. Secondly this flow field is presented in order to contrast it with Meniscus roll coating flow described in the next chapter. It is important to emphasise that the full flow field (including the upstream bank) is elucidated, and key features are discussed. A simple experimental investigation of the effect of gravity on film-splitting is also presented. The importance of experimentally verifying theoretical predictions is illustrated by the observation of a 'start-up jump' in the downstream stagnation point as predicted by Savages'[1992] refined roll coating film-splting model (described below). Film thickness measurements are also presented and compared with the predictions of the model. Velocity field results of the upstream bank and downstream

two-dimensional flow, obtained from the computerised particle tracking system, are discussed and the downstream two- dimensional flow results are compared to the FE predictions of Thompson[1992].

The literature associated with the experimental, analytical, and computational investigation of fully-flooded roll coating is extensive. Detailed accounts of this work are given in Chapter 1 and by Coyle[1991] and Savage et al [1992]. The motivation for such wide-ranging investigations has been the need for coating specialists to explain and predict various key features of the flow. These include the non-dimensional flux, ϵ, the film thicknesses, h_1 and h_2, deposited on the rolls, the pressure distribution $p(x)$, the velocity field $q = (u, w)$, the location of the fluid-air meniscus (at $x = c$), and the onset of the recirculation region (at $x = s$) – see Figure 4.1(b).

The presence of a recirculation region immediately upstream of the fluid-air interface in a roll nip was first reported by Pitts & Greiller [1961] and substantiated by Van den Bergh [1975]. For rolls rotating at equal speed several authors have measured flow rate: Pitts & Greiller[1961], Hintermaier & White[1965], Greener & Middlema[1975]. Benkreira et al [1981] obtained a non-dimensional flow rate of $\epsilon = 1.31$ which showed little variation with capillary number $Ca = \eta U/T$. In contrast, the position and shape of the fluid-air meniscus is highly dependent on capillary number, being closest to the nip when $Ca = \infty$ and moving away from the nip as capillary number decreases.

As briefly discussed in Chapter 1, §§1.3.1, Greener & Middleman[1975,1979] formulated a mathematical model for flow between equal speed rolls based on lubrication theory which gave rise to Reynolds equation for pressure $p(x)$. They considered a semi-infinite domain upstream of the nip, terminated at a downstream stagnation point where velocity is zero and velocity gradient is set to zero from symmetry considerations. These

conditions $u = \partial u/\partial z = 0$ (the Prandtl-Hopkins/Separation conditions) apply not only to symmetric flows, but also when one roll is at rest; they locate the point at which the flow separates from the stationary surface. Consequently Savage[1984] extended the model to the general case of unequal speed rolls by postulating that the Prandtl-Hopkins conditions specify the termination of the lubrication domain. This is referred to as the 'Separation Hypothesis' which locates the onset of the recirculation region as a stagnation point and a point of flow separation. A prediction for the film thicknesses h_1 and h_2 in terms of the roll speed ratio $S = U_1/U_2$ emerged from this separation model:

$$\left[\frac{h_1}{h_2}\right] = S^{\frac{1}{2}} \tag{4.1}$$

As Taylor[1963] pointed out, these flows can be divided into two distinct regions. Throughout the minimum gap region, flow is essentially unidirectional and lubrication theory is valid. Downstream of this region, as the geometry of the nip diverges, a two-dimensional flow is present ahead of the fluid-air meniscus. Ruschak[1982] translated these observations into analysis by means of the method of matched asymptotic expansions for the symmetric case. Essentially the inner problem required a two-dimensional solution of the Navier-Stokes equations in the vicinity of the meniscus which was matched onto an outer lubrication solution. Calculations revealed the importance of the Capillary number in locating the position of the meniscus and the ratio $h_1/h(c)$ of the film thickness to half-gap width at the meniscus.

This latter parameter arises from matching the pressure gradients of the inner and outer solutions. In fact its significance in specifying pressure gradient at the meniscus was first appreciated by Coyne & Elrod[1970] who performed an approximate analysis of the free surface flow from the meniscus to infinity by assuming that velocity tangential to the surface is a quadratic function of y, the normal coordinate. The agreement

between Coyne & Elrods approximate results and those of Ruschak's far more rigorous analysis is remarkable.

With regard to the development of computational work in the field of roll coating, Coyle et al [1986] generalised Ruschak's matched asymptotic analysis to the asymmetric case of unequal roll speeds, using the finite element method for the inner solution. Subsequently the finite element method was developed further to provide solutions to the Navier-Stokes equations for the full velocity and pressure fields, of the entire flow domain, subject to appropriate boundary conditions (Coyle, Macosko & Scriven[1982], Kistler & Scriven[1983]). Problems still remain with dynamic wetting lines where specifying the real boundary conditions is a matter of some dispute. Coyle et al [1986] found that their computational results for film thickness ratio as a function of speed ratio could be fit by a power law:

$$\left[\frac{h_1}{h_2}\right] = S^{0.65} \tag{4.2}$$

for $0.1 < S < 10$. The exponent 0.65 is identical to that found by Benkreira et al [1981] over the same range of speed ratio:

$$\left[\frac{h_1}{h_2}\right] = 0.875\ S^{0.65} \tag{4.3}$$

Furthermore it has been suggested that gravity may well account for the factor 0.87 in the sense that one might expect the upper roll film thickness to be less than that on the lower roll for equal speed rolling. Therefore experimental and computational results appear to be in accord and it would appear that it is the analytical Separation model which is lacking. This casts considerable doubt on the Separation model, and in particular the validity of the Prandtl-Hopkins boundary conditions. In light of this, Savage [1992] in a re-assessment of his earlier work (Savage[1982]) recognised that although these conditions hold in several special cases, there is no physical basis for imposing

the condition $\partial u/\partial z = 0$ for non-zero, unequal roll speeds to determine the position of the leading edge stagnation point. The problem therefore was to specify one extra condition. One alternative is to locate this stagnation point by imposing conditions on both components of velocity: $q = (u, w) = (0, 0)$, and this forms the basis of the refined lubrication model. Predictions from this model are both interesting and surprising, and have prompted additional experimental investigations. A key result of the new theory is the prediction of a 'start-up jump' which is not predicted by any previous analysis. As the upper roll, for example, is slowly increased from zero, the stagnation line jumps from its location on the stationary roll surface by a distance of the order of $(RH_0)^{1/2}$. This phenomenon is explored experimentally using flow visualisation.

The majority of published work on the analytical and numerical modelling of film-splitting in forward roll coating has only considered the flow region downstream from the minimum gap, on the assumption that lubrication approximations are sufficient to adequately describe the upstream fully-flooded inlet flow. However, a common feature of forward roll coating is the bank of liquid which accumulates on the upstream side of the nip. A qualitative description of the flow in the bank has been given by Pearson[1985], confirmed experimentally by Agassant & Espy[1985], and is illustrated and discussed here (see §§ 4.3.1).

Chen & Higgins[1988] carried out a finite element analysis of the upstream flow in a roll-web configuration, studying the effect of Capillary number on free surface location and form. They concluded that for $Ca > 0.2$ lubrication theory is sufficient to derive the upstream boundary conditions and therefore the flow in the film-split region can be decoupled from the influence of the upstream bank. However, when $Ca << 0.2$ Chen & Higgins describe the free surface of the bank as beginning to invade the nip, which means that the application of the upstream boundary condition $p(-\infty) = 0$ in

a lubrication analysis is invalid and requires modification.

They report that the same is true when the specified flow rate, ϵ, approaches unity (i.e. the film entering the nip attached to the lower roll has a thickness comparable with the minimum gap, H_0). Indeed, the aforementioned investigation appears to have addressed the onset of starvation in roll coating, although no results were presented for such a condition. During the course of this investigation it soon became apparent that in order to model the fully-flooded process successfully it is essential to take full account of the upstream bank, since the upstream flow is at least as important as the downstream flow in determining film-splitting (see §§ 4.3.1).

4.2 Mathematical Modelling

The major difficulty in developing accurate theoretical models of coating flows lies in dealing with the complexities associated with the presence of highly curved liquid-air interfaces, the locations of which are unknown. Surface tension is often important in these free surface flows. The action of surface tension at a curved interface gives rise to the capillary pressure, a resultant force per unit area which is locally perpendicular to the interface. The effect can often be dramatic in the flow field produced by a coating geometry. In addition, coating flows have three-phase contact lines where the solid substrate, the coated fluid, and the displaced gas meet. These contact lines, the physics of which are poorly understood (see Chapter 1, §1.5 for a brief summary of past work), can also strongly influence the flow field. In many cases the phenomenon associated with contact lines and the nearby flow can determine whether or not a coating system is capable of producing a stable process. Further complications arise when, as in many industrial applications, the coated liquid is non-Newtonian, producing flows which are very different to those of Newtonian fluids. The non-Newtonian effects in such coating

systems are not considered in this work.

The underlying impression one receives from recent reviews of coating flow analysis (Coyle[1991], for example) is that the scope for using lubrication theory to model roll coating flow is exhausted with the inference that its' predictions are inaccurate with regard to practical coating requirements (e.g. film thickness predictions). This chapter hopefully illustrates that this perception is false and that simple mathematical modelling has a powerful role to play in the practical application of such processes. Indeed the 'iterative process' necessary to refine numerical and experimental techniques has an equally important role to play in improving mathematical models.

4.2.1 A Refined Film-splitting Model

The film thickness model proposed by Savage[1982] rested, to a certain degree, on intuition. The various boundary conditions used to terminate the lubrication regime are discussed in Chapter 1, together with their associated drawbacks.

By reassessing the boundary conditions applicable at film-splitting Savage[1992] has modified his earlier roll coating model to provide a far more rigorous model, which produces the key result that:

$$\frac{h_1}{h_2} = \frac{S(S+3)}{(1+3S)} \tag{4.4}$$

where S is the ratio of roll speeds, U_1/U_2. This is in good agreement with the experimental data presented here and that found elsewhere (Benkreira et al [1981]) and computational predictions (Coyle et al [1986]), over the attainable speed ratio range (i.e. $0.1 < S < 10$).

Figure 4.1(a) shows predictions of h_1/h_2 verses S for this new model over a far wider

range of roll speed ratio; the gradient of the curve in the range $0.1 < S < 10$ has a value of 0.62, which is in good agreement with the exponents of the functional data fits of the experimental results of Benkreira et al and the numerical predictions of Coyle et al. However, outside this range the model predicts a marked change in the slope of the curve (these predictions have been confirmed by Thompson[1992], using finite element simulation). It must be said that these extreme values of roll speed ratio are outside the operating bounds of practical roll coating processes and predictions are extremely difficult to verify experimentally (see §§ 4.3.2). Nevertheless this new lubrication model is adequate in predicting film-splitting in forward roll coating and it provides far more insight into the splitting mechanism than a statistical data fit.

Using the Separation condition ($\partial u/\partial z = 0$) for a plate-roll geometry, the Navier-Stokes equations of motion imply that at the point of separation on the stationary surface:

$$\frac{dp}{dx} = \frac{2\eta U}{h^2} \tag{4.5}$$

However, the new film-splitting model predicts that as the upper roll speed, for example, tends to zero, a different value for the pressure gradient is attained, that of:

$$\frac{dp}{dx} = \frac{4\eta U}{h^2} \tag{4.6}$$

Therefore the position of the stagnation point appears to experience a jump immediately after start-up. This anomaly prompted an experimental study to investigate this behaviour, since this would indeed provide a sure test of the validity of this new lubrication model.

Another important prediction from the refined model is the value of the pressure gradient for symmetric rolling, where:

$$\frac{dp}{dx} = \frac{8\eta U}{h^2} \tag{4.7}$$

This prediction is identical to that of Savages[1982] separation model which is valid for symmetric rolling. This result adds further credance to the new model.

In summary, when the upper roll, for example, is at rest (i.e. $S = 0$) the separation point is at some position $X_{S(0)}$ (condition (4.5)) downstream of the nip (see Figure 4.1(b)), which the refined model gives to be of the order $(RH_0)^{1/2}$. On starting the upper roll the separation point jumps to a position $X_{S'(0)}$ (condition (4.6)) which is of the order $1.7(RH_0)^{1/2}$. For $S \neq 0$ the stagnation point is predicted to be independent of Capillary number (i.e. roll speed/speed ratio), as predicted numerically by Coyle et al [1986].

4.3 Experimental Investigation

4.3.1 Flow Field

A number of authors have presented sparse, schematic results for typical experimental streamline patterns in a two-roll coater. In order to redress this lack of information, a comprehensive set of images is presented here using the flow visualisation techniques described in Chapter 3, together with schematic diagrams to clarify the flow. The measurement of discrete velocities within the nip has received little attention (Schneider[1962] being a notable exception). Several key velocity field results obtained using the high speed video and computerised particle tracking technique are presented. Finally, the 'start-up jump', predicted by the refined film-splitting model of Savage[1992], is confirmed experimentally.

Streamline Patterns

A typical dye injection image of the full flow field for symmetric rolling is shown in Figure 4.2; specific features are not particularly clear because of the high aspect ratio and

low magnification. However it is possible to see three distinct regions of the flow: (I) the 2-dimensional upstream bank recirculatory flow, (II) the one-dimensional flow through the nip, and (III) the downstream two-dimensional recirculation region. Focusing first on the nip-to-downstream part of the flow (which the majority of workers have considered, while neglecting the upstream flow) Figures 4.3(a) & (b) show the downstream recirculation region and corresponding schematic portrayal (showing streamlines and stagnation/separation points) respectively. Here, the one-dimensional flow leaving the nip splits into two at the stagnation/film-splitting point, X_S, and these 'films' go on to coat either the upper or lower roll. The classic 2-dimensional eddy-flow has the function of bridging the gap between this film-splitting point, X_S, and the downstream free surface (as the Capillary number is increased the eddy- flow region contracts because the free surface moves back towards the nip until it eventually disappears, whereupon the free surface becomes the boundary of the film-splitting flow). It was not possible to achieve such a flow condition in this work, because of the very low operational roll speed range and fluid viscosities.

It is important to consider the flow structure in the upstream bank (illustrated in Figures 4.4(a) & (b)) and in particular the path taken by the incoming fluid. A portion of the entering fluid travels with the roll and passes directly through the nip (see Figure 4.4(b)). The remaining portion must therefore reverse direction at an internal stagnation point, X_I, located near the nip and flow back to the free surface, winding its way between the two contra-rotating eddies. This upstream stagnation point, X_I, is positioned at an equal distance upstream to that of the downstream stagnation point, X_S. Another key feature of the upstream bank flow, which causes it to differ significantly from that of the two-dimensional downstream flow is the presence of the dynamic wetting line (for the situation when a dry web is present). It may be that the flow structure in the upstream bank is crucially important in determining dynamic

wetting.

If the inlet is excessively flooded, resulting in visible flowback down the roll, it is at the free surface where splitting occurs to allow the excess fluid to drain down over the incoming film, resulting in the extension and elongation of the lower vortex in this region, while the remainder of the fluid continues around the upper eddy to wet the moving upper roll/web before being carried through the nip (see Figure 4.4(c)). Moreover the upstream stagnation point, at which the upper and lower roll fluid films come together and whereupon one-dimensional flow is achieved, is the counterpart of the much- studied downstream film-splitting stagnation point and as such it is equally important in determining film-splitting behaviour. The snaking path taken by the fluid in the upstream bank is similar to the flow observed throughout the nip under ultra-starved inlet conditions (these results are presented in Chapter 5).

Finally, returning to the nip-to-downstream part of the flow Figure 4.5(a) shows the downstream similar-sized eddies in more detail for symmetric rolling. Contrast this with a non-symmetric rolling condition; Figure 4.5(b) shows the dye pattern for $S < 1$. Here the eddy associated with the lower, faster moving, roll is larger than its' counter-part.

A preliminary dye injection image for reverse fully-flooded roll coating is shown in Figure 4.6(a) and schematically in 4.6(b). Here a single vortex is maintained on either side of the nip with uni-directional flow through the nip itself. The fluid transfer path from inlet to upper roll is directed along the lower roll, around the downstream vortex and back along the upper roll. The structure and development of this flow is discussed more fully in Chapter 6.

Velocity Field

The velocity vector plot of the nip-to-downstream part of the flow is presented in Figure 4.7(a). Velocity vectors have been plotted so that length of arrow and size of arrow-head are proportional to the magnitude of the velocity. Although the initial particle tracking results, presented throughout this work, do not provide a fully comprehensive view of particular velocity fields, it is clear that in refining this technique a powerful experimental tool will emerge.

Nevertheless, Figure 4.7(a) does provide a significant insight into the structure of the flow. The one-dimensional flow through the nip is clear. The velocity of the flow approaches that of the roll surfaces as one moves closer to them, as would be expected. The most interesting part of the flow is that associated with the downstream recirculation region; large re-direction of the flow is observed (particularly adjacent to the free surface), velocities within the eddies are relatively small, and a reasonably stagnant region around the *implied* film-splitting point, X_S, is evident (see Figure 4.3 for clarification). A comparison of experimental results with Thompsons'[1992] finite element results, an example of which is given in Figure 4.7(b), shows good overall agreement.

The upstream bank velocity field results of Figure 4.8(a) clearly show the two eddies, the flow reversal down the centre of the flow field, and the eventual one-dimensional flow through the nip. Viewed in conjunction with the dye injection image under similar operating conditions (Figure 4.8(b)), the full value of having these two sets of experimental data to provide a better understanding of such a complex flow is clear.

Movement Of Separation/Filmsplitting Line

Consider a fully-flooded two roll system, with the upper roll stationary. The flow separates from the upper roll at the onset of the single recirculation (see Figure 4.9(a)). Once the upper roll is moving, this separation point becomes the film-splitting point, and a second recirculation, caused by the motion of the upper roll is formed (see Figure 4.9(b)).

The key observation is the significant jump experienced by the stagnation line in the x-direction, as the upper roll is started (its speed being negligible compared to the lower roll speed). Figure 4.10 shows the position of the stagnation point before (upper image) and immediately after (lower image) start-up. The minimum gap position is illustrated by the vertical white line (overlaid on the video image, using the character generator). The distance between the two white points is of the order of $(RH_0)^{1/2}$; this is used as a reference scale to illustrate the magnitude of the start-up jump. The movement of the stagnation point is indeed of the order $0.7(RH_0)^{1/2}$ as predicted by Savages'[1992] refined model.

Measurements of the downstream free surface profile, using the techniques described in Chapter 3, are in fair agreement with the finite element predictions of Thompson[1992] (see Figure 4.11).

4.3.2 Film Thickness Behaviour

Experimental results of film thickness ratio versus speed ratio, presented in Figure 4.12, are compared with the experimental results of Benkreira et al [1981] and the predictions of Savages'[1992] model. Agreement is good for 'moderate' speed ratio. However, for low speed ratio (and therefore relatively low characteristic speed) experimental results

are significantly lower than the theoretical predictions and the experimental data of Benkreira et al. This may be due to an exaggerated gravity affect (discussed below) as a result of the relatively low viscosity fluids used. Alternatively, evaporation of fluid from the measured layer on the upper roll, in particular (having a longer distance to travel prior to removal and collection - see Figure 2.4), may be a source of error (i.e. if an amount of fluid is lost from the liquid layer due to evaporation, it will constitute a larger proportion of the upper, relatively thin film, for $S < 1$, and therefore give an under-estimate of the film thickness ratio, h_1/h_2). The affect of fluid evaporation is not assessed here.

Coyle et al [1986], in referring to the work of Benkreira et al [1981], point out that it would appear that gravity has a significant effect on the film-splitting mechanism. This is indeed borne out in the present results of film thickness ratio versus roll speed ratio; measured results for $S < 2$ are consistently lower than those predicted by the film thickness model of Savage[1992] and numerical simulations (Coyle et al [1986], Thompson[1992]), in which gravity is ignored. Indeed with the relatively low viscosity fluids and low roll speeds used in the present investigation, this effect appears to be more dramatic, as the viscous force is low. Benkreira et al [1981] used a wide range of fluid viscosities, typically much greater than those employed here, which may account for the discrepancy in the two sets of experimental data presented in Figure 4.12.

The effect of gravity on film-splitting is illustrated by taking measurements of h_1 and h_2 under symmetric rolling conditions, beginning with very low roll speeds (implying low viscous forces in the nip compared to gravity forces) and successively increasing speeds (thus increasing the relative viscous forces). Figure 4.13 shows a typical set of results and it is clear that gravity has a significant effect on film-splitting; particularly at lower roll speeds.

4.3.3 Pressure Field (Plate-Roll Geometry)

The experimental method for obtaining pressures is described in Chapter 2, § 2.4. Figure 4.14 shows a typical set of results of manometer height (pressure) versus position across the nip, in a plate-roll geometry. The classical maximum/minimum pressure distribution, reported by many workers for a lightly loaded system (Dowson & Taylor[1979] review much of this work), is observed. Under fully-flooded conditions and low Capillary number the pressure builds up to a maximum on the upstream side of the nip and then turns to form a quasi-linear gradient through the nip, and a minimum downstream. The pressure is then allowed to recover to near-atmospheric pressure adjacent to the downstream free surface. However, as the Capillary number is increased the downstream free surface moves back in towards the nip and the recovery of the negative downstream pressure must take place over a shorter distance (see Figures 4.15(a) & (b)). If the magnitude of the pressure gradient at the downstream free surface becomes too large, then an unstable regime will ensue (i.e. ribbing - Carter & Savage[1984]).

These measured plate-roll pressures are characteristic of those in a two-roll system; Coyle et al [1986] present numerical predictions of pressure for a two-roll system which are not too dissimilar from those presented here and elsewhere for the plate-roll geometry.

4.4 Discussion of Results

The experimental results presented here are for low Capillary Number ($Ca < 1$) Classical roll coating flow . Under such conditions the downstream double-eddy formation is present and indeed it is relatively large (at higher Capillary numbers the downstream free surface moves back into the nip and the eddy structure disappears - see Coyle et al [1986]). With the aid of dye injection images and unique velocity field results, the flow in the nip of a fully-flooded two-roll coater can be clearly classified into three distinct regions: the upstream bank, the rectilinear flow through the nip, and the downstream recirculation region.

Although the majority of workers have dismissed the effect of the upstream bank, when focusing on lubrication analysis in the nip leading to film-splitting downstream, it is clear that this flow has an equally important role to play in determining the upstream pressure condition. At the upstream stagnation point just ahead of the nip, the fluid has attained rectilinear flow above and below this point and is therefore in its' film-split ratio long before moving through the nip to meet the downstream film-splitting point. Indeed these two stagnation points are at the same height and equidistant from the nip as predicted from theory.

It has been demonstrated that gravity does affect the way in which the fluid within the nip splits to form the films on the upper and lower rolls. These results are in accord with those of Benkreira et al [1981] who reported a film-splitting coefficient of 0.875. Only at extremely low roll speeds (and therefore Capillary number) does this value decrease.

Predictions of the refined film-splitting model of Savage[1992] are validated experi-

mentally, and in particular the start-up jump is observed in practice. This observation serves to dismiss the original Separation model as being inadequate for anything other than plate-roll flow or symmetric rolling, while adding credance to the new boundary conditions for the refined model.

The work of this Chapter demonstrates that the Classical roll coating flow system is far from well understood; the scope for future studies is considerable and in particular the affect of the upstream flow cannot be dismissed.

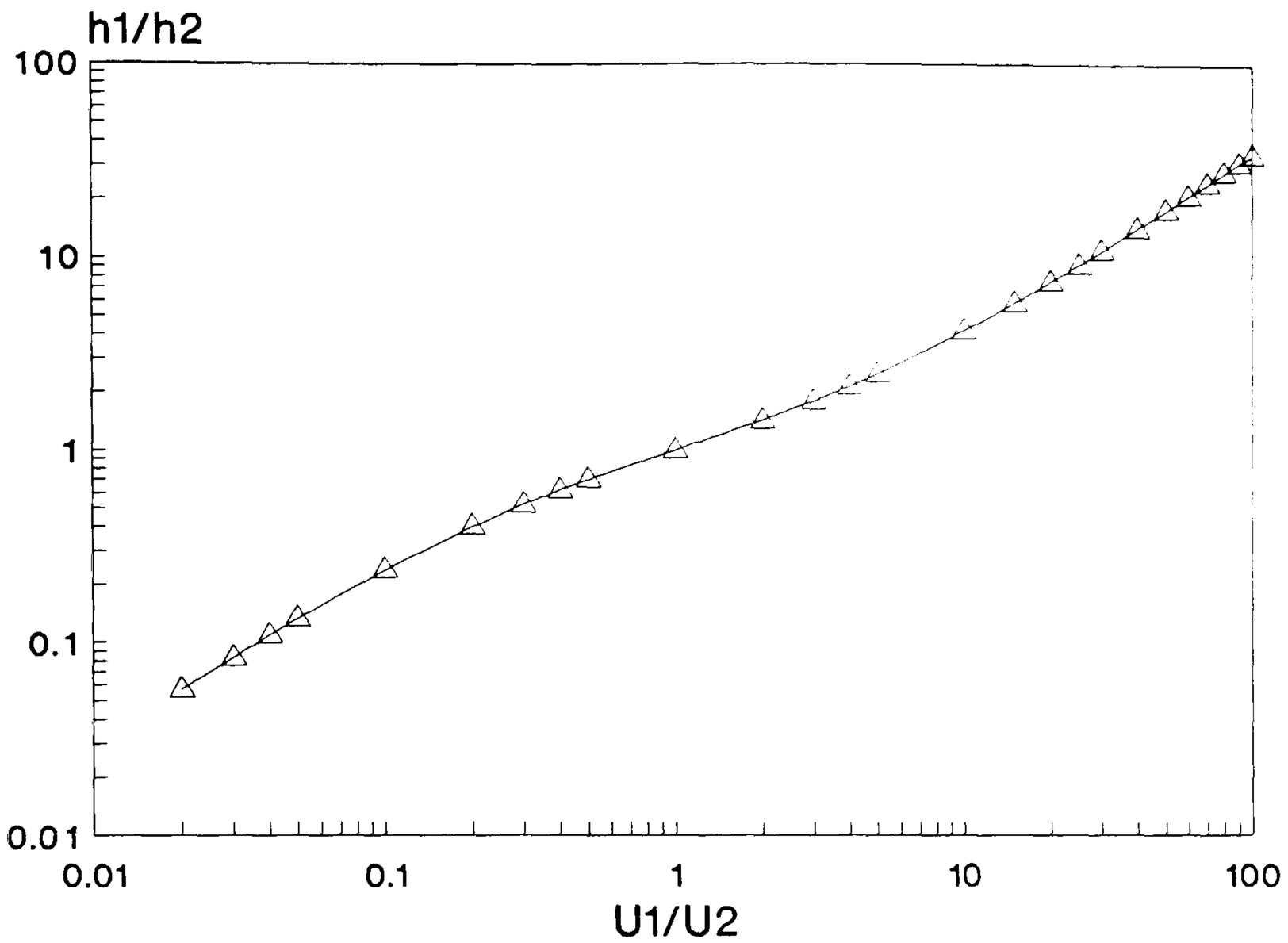

(a)

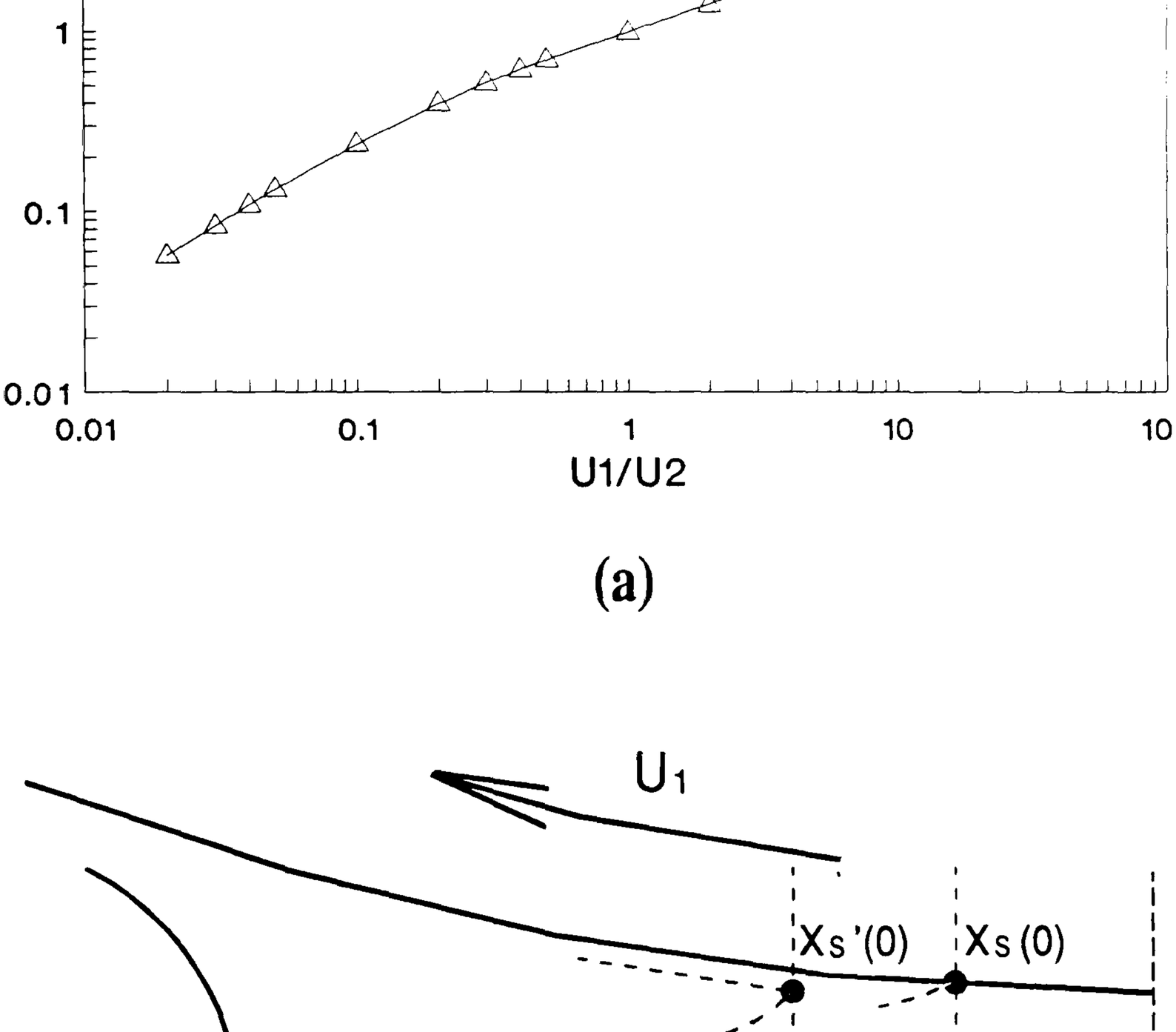

(b)

Figure 4.1: Predictions of Savages'[1992] refined film-splitting model (a) Film thickness ratio versus speed ratio, (b) Stagnation/film-splitting point movement

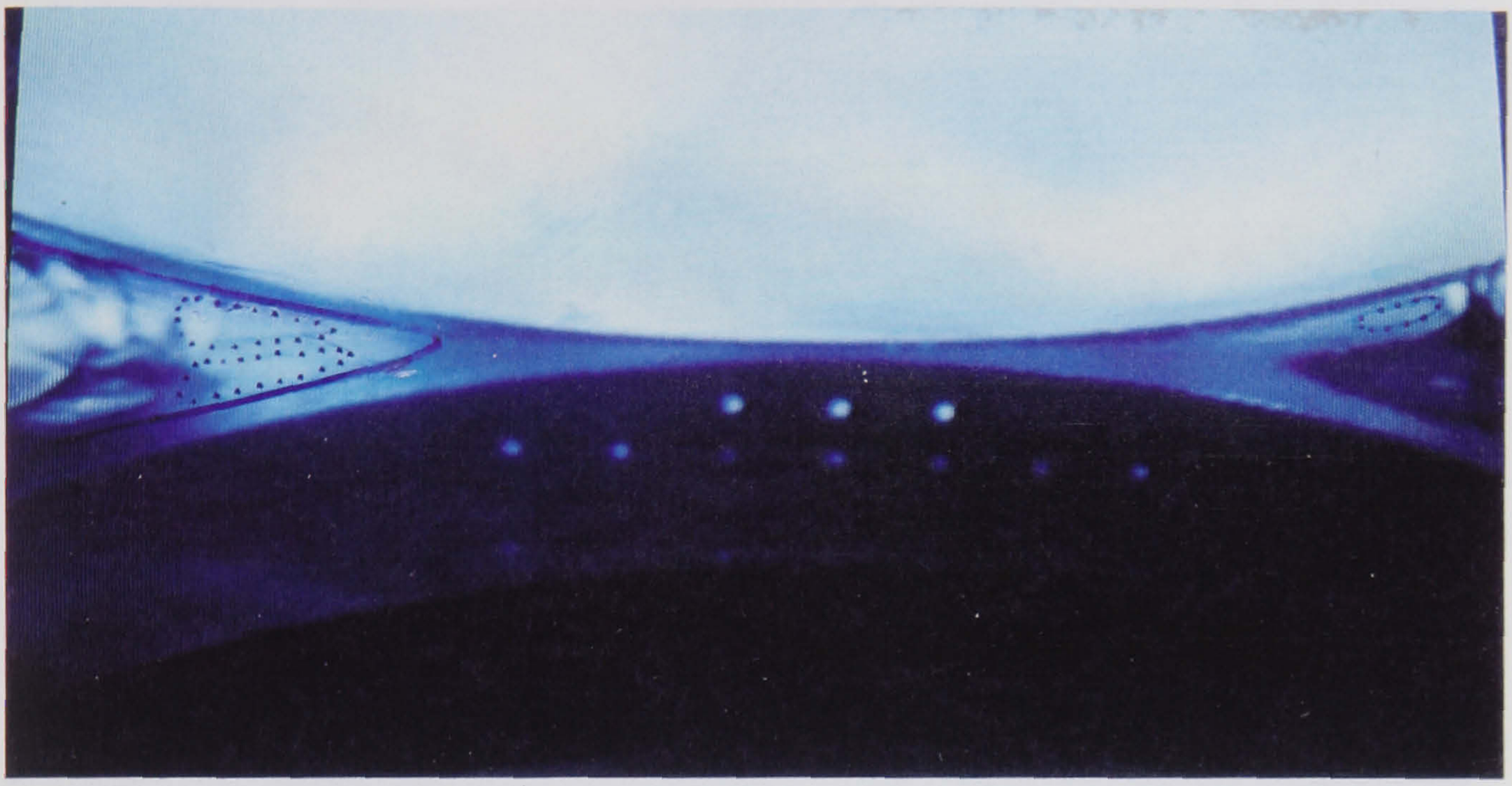

Figure 4.2: Classical roll coating flow, showing three distinct flow regions

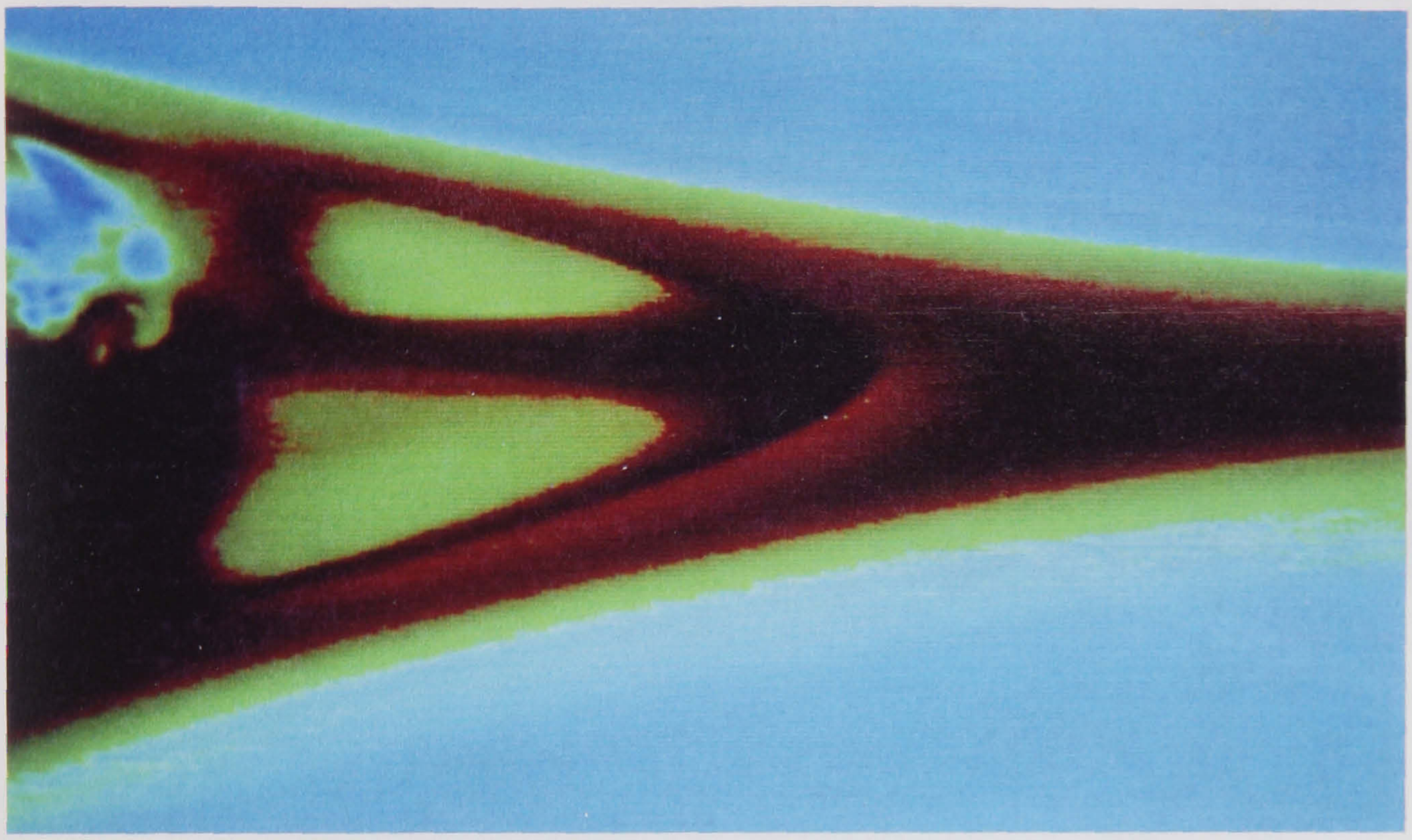

(a)

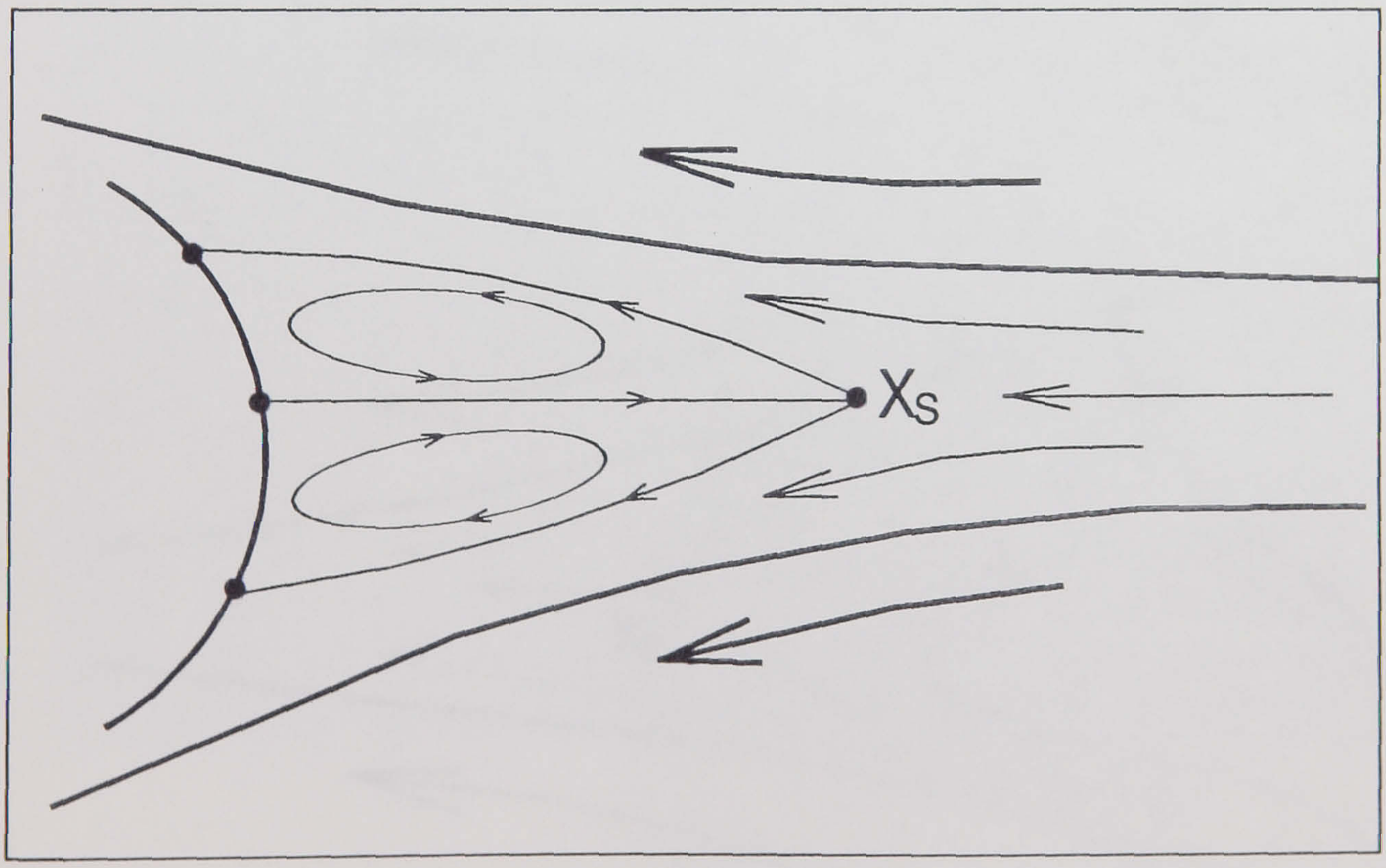

(b)

Figure 4.3: (a) Classical downstream eddy flow, (b) Schematic representation

(a)

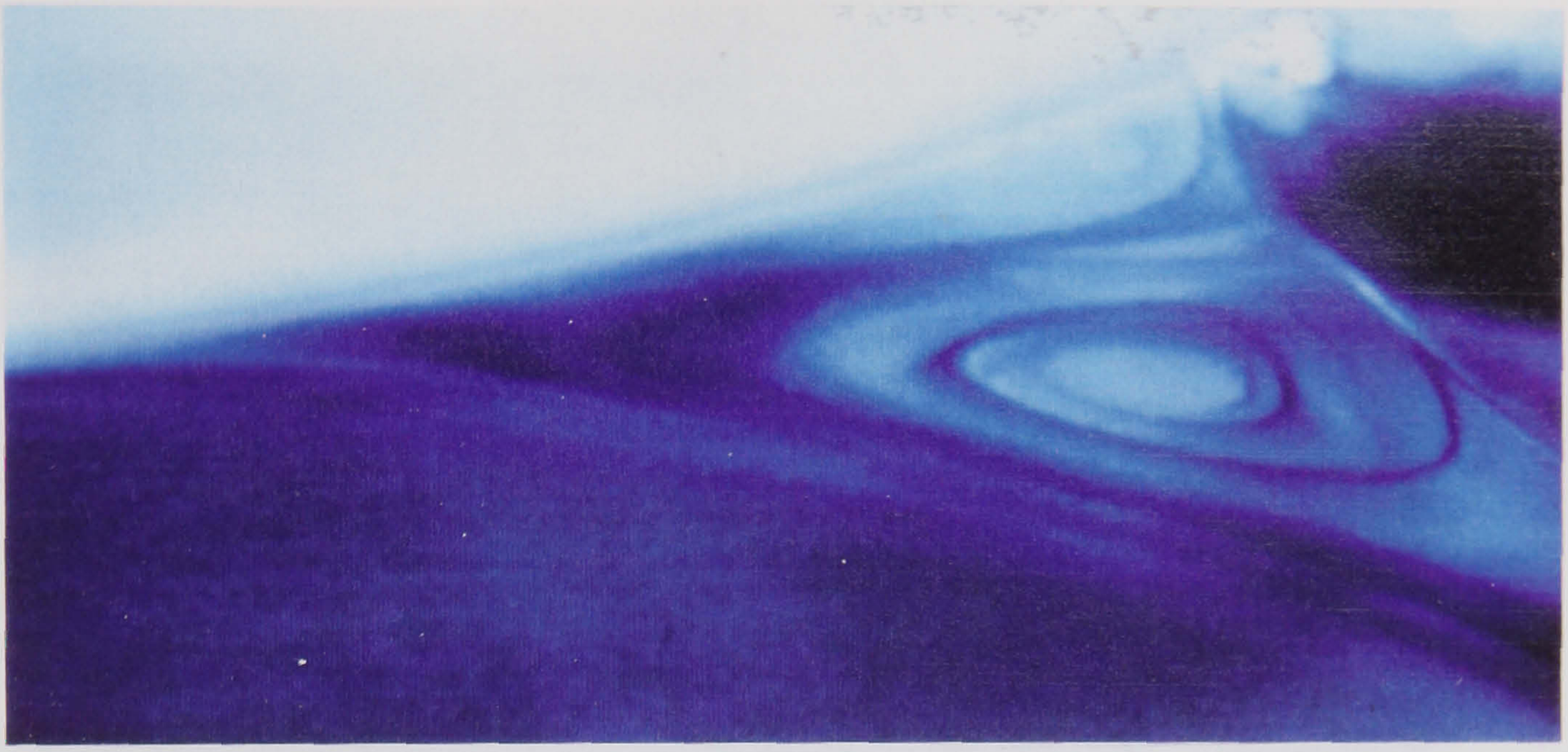

(b)

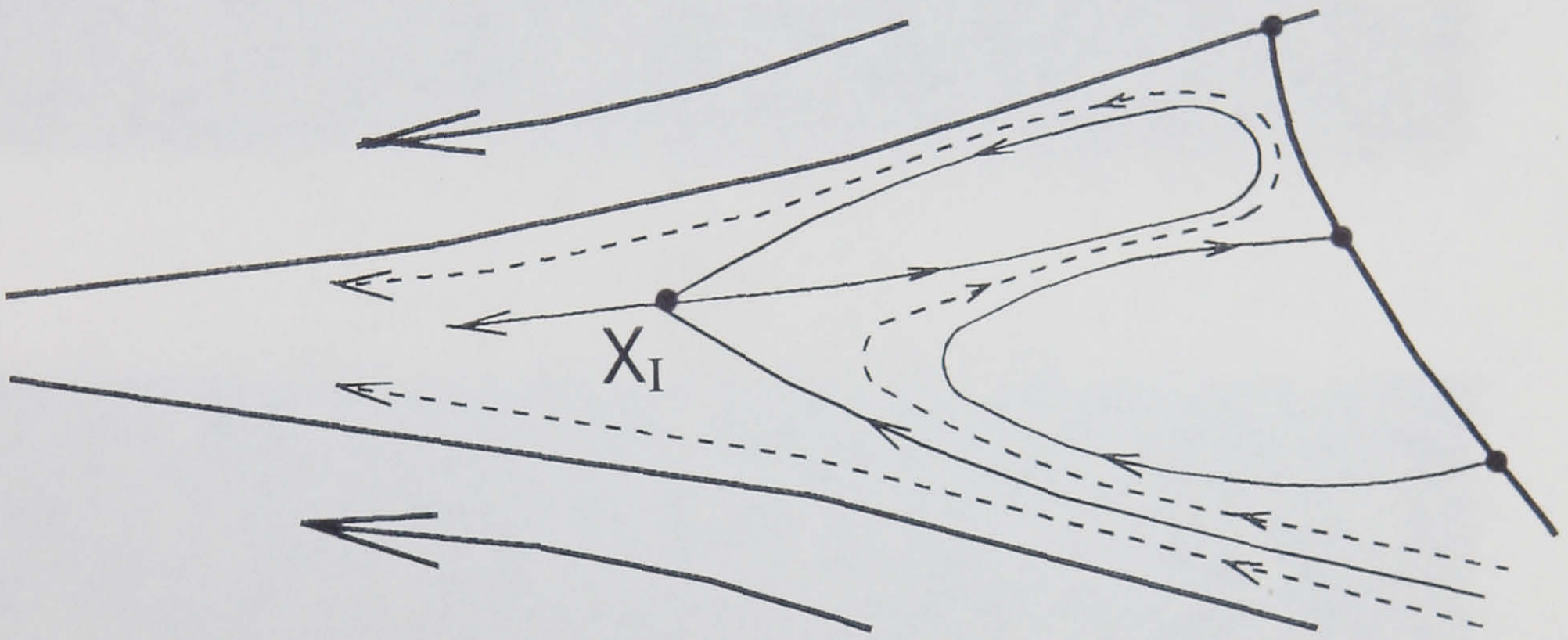

(c)

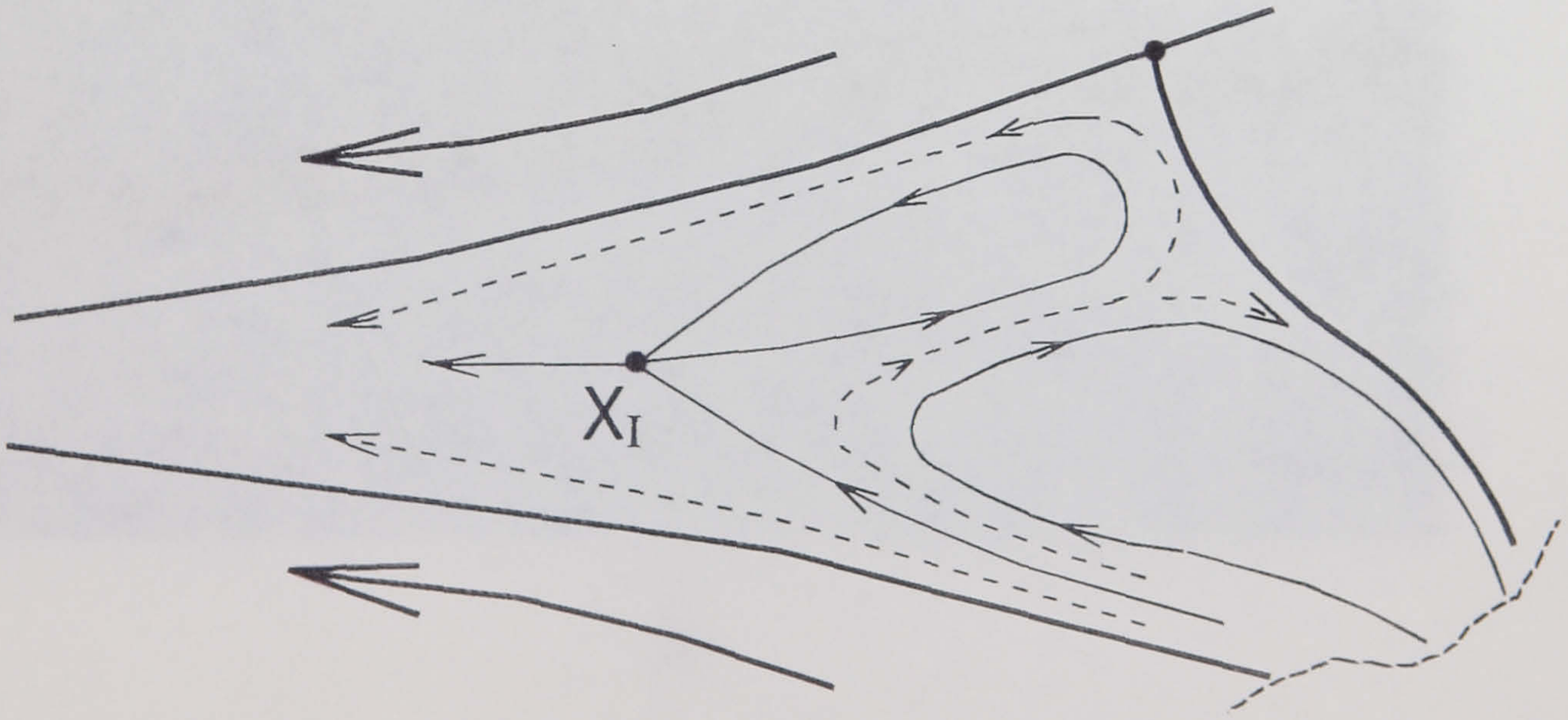

Figure 4.4: (a) Upstream bank flow, (b) Schematic representation, (c) Upstream bank with flow-back

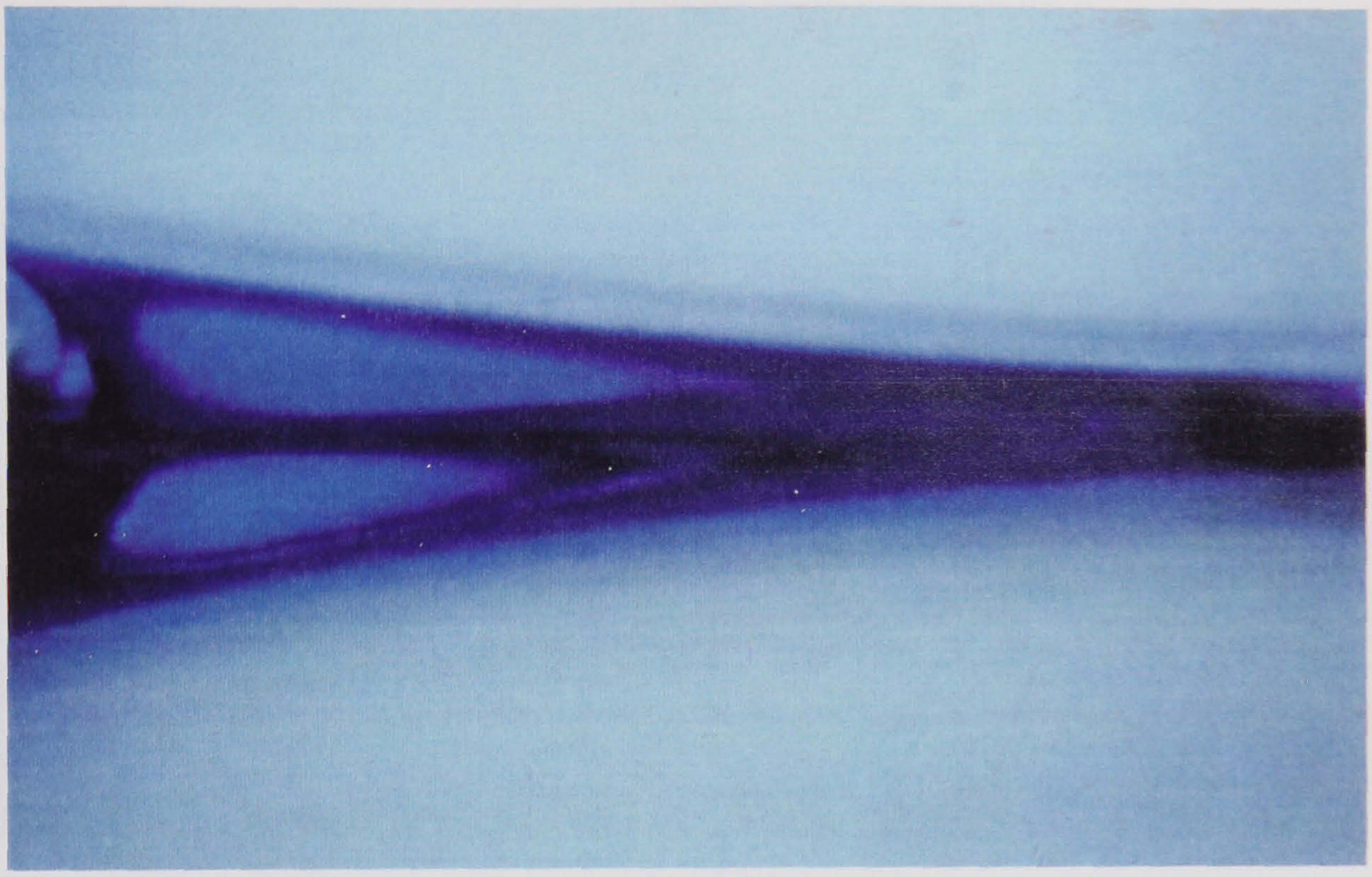

(a)

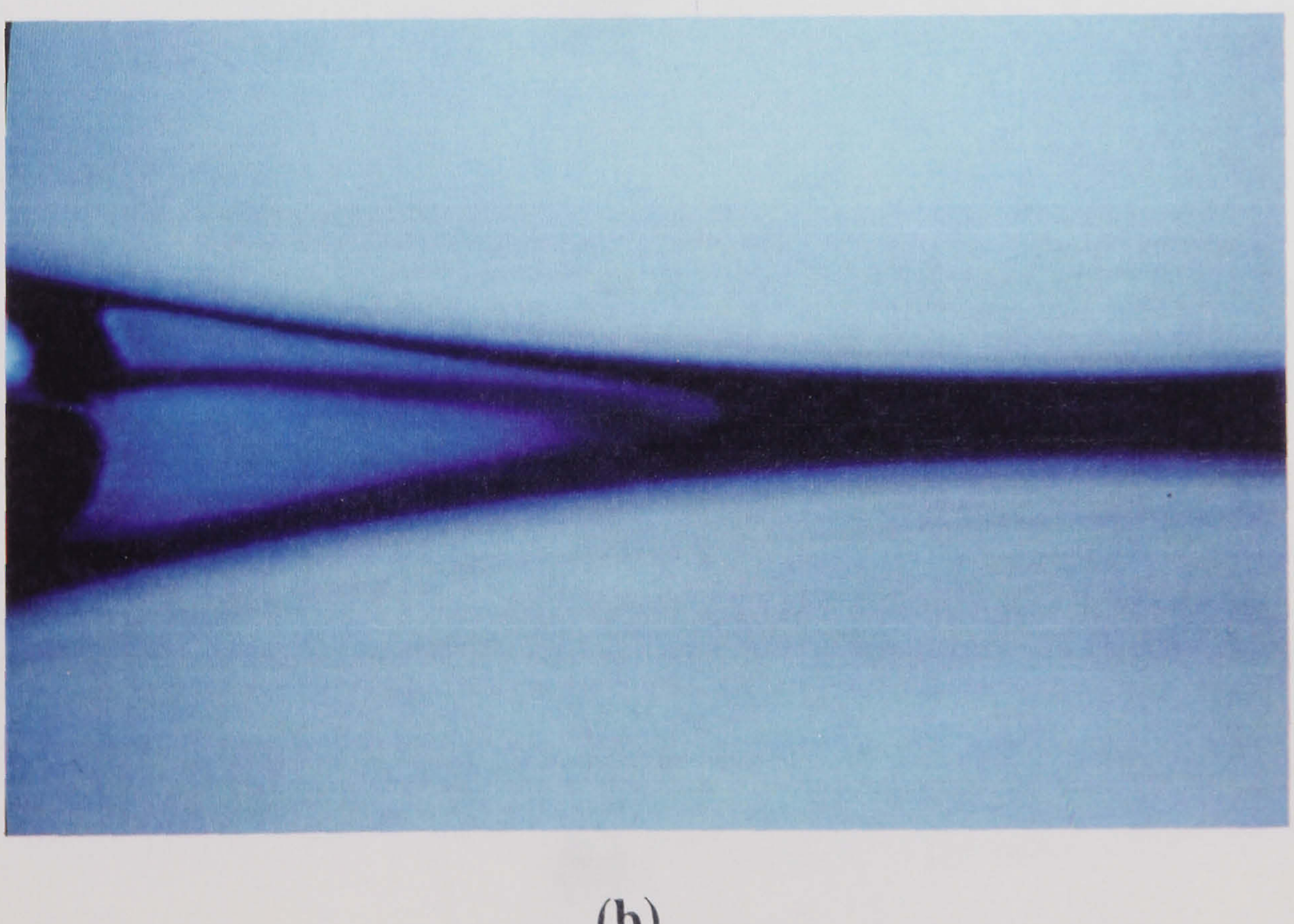

(b)

Figure 4.5: Effect of roll speed ratio on downstream eddy flow (a) equal speed ratio, (b) lower roll moving faster ($S < 1$)

(a)

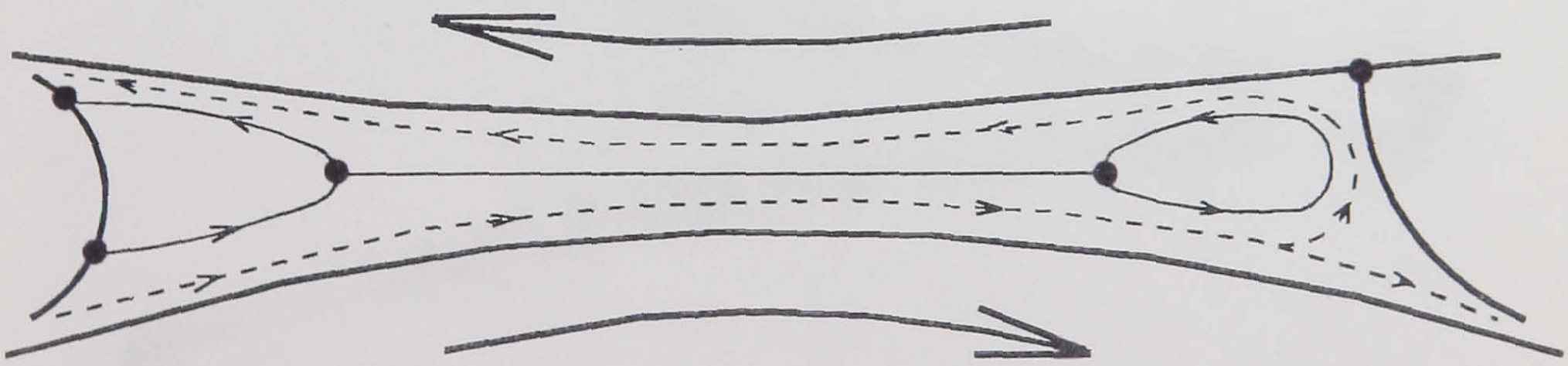

(b)

Figure 4.6: Reverse fully-flooded roll coating flow (a) Dye flow, (b) Schematic representation. Lower roll moving from left to right, upper roll moving from right to left

(a)

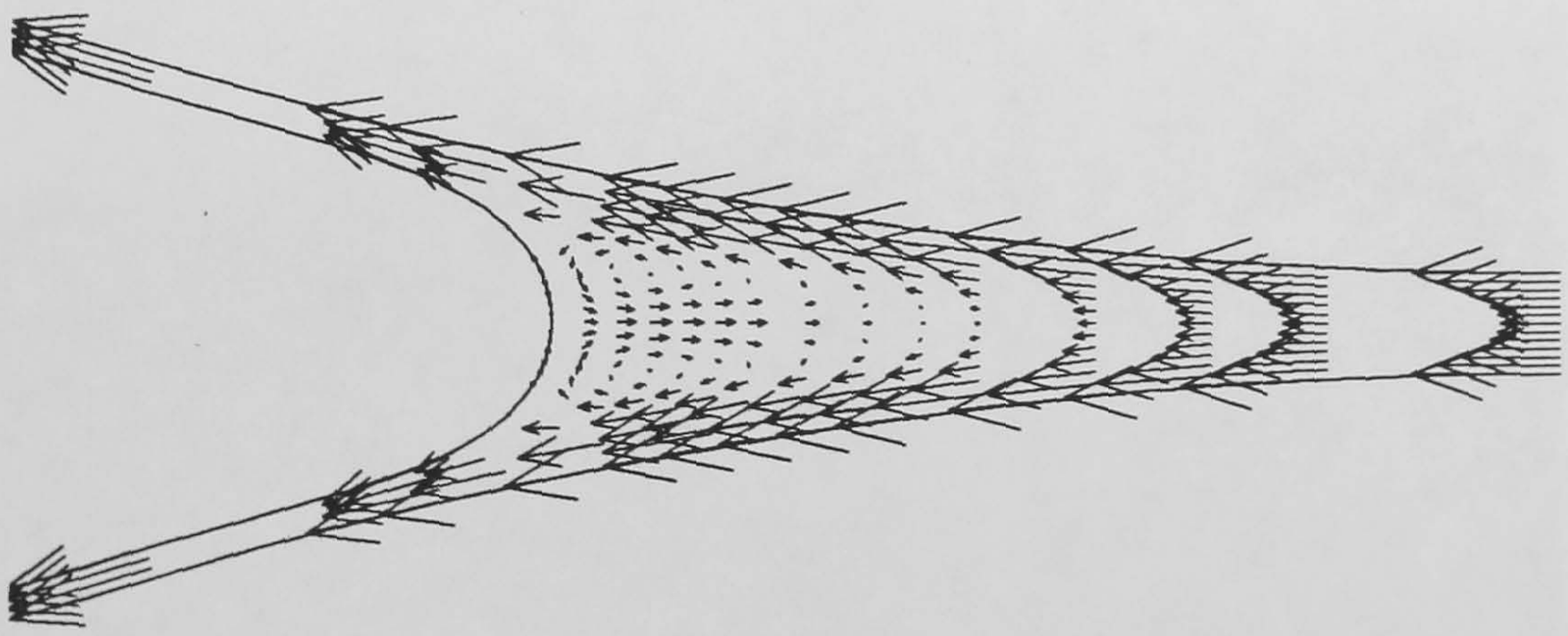

(b)

Figure 4.7: Downstream recirculation region (a) Computerised particle tracking velocity field results, (b) Thompsons[1992] finite element solution for comparison

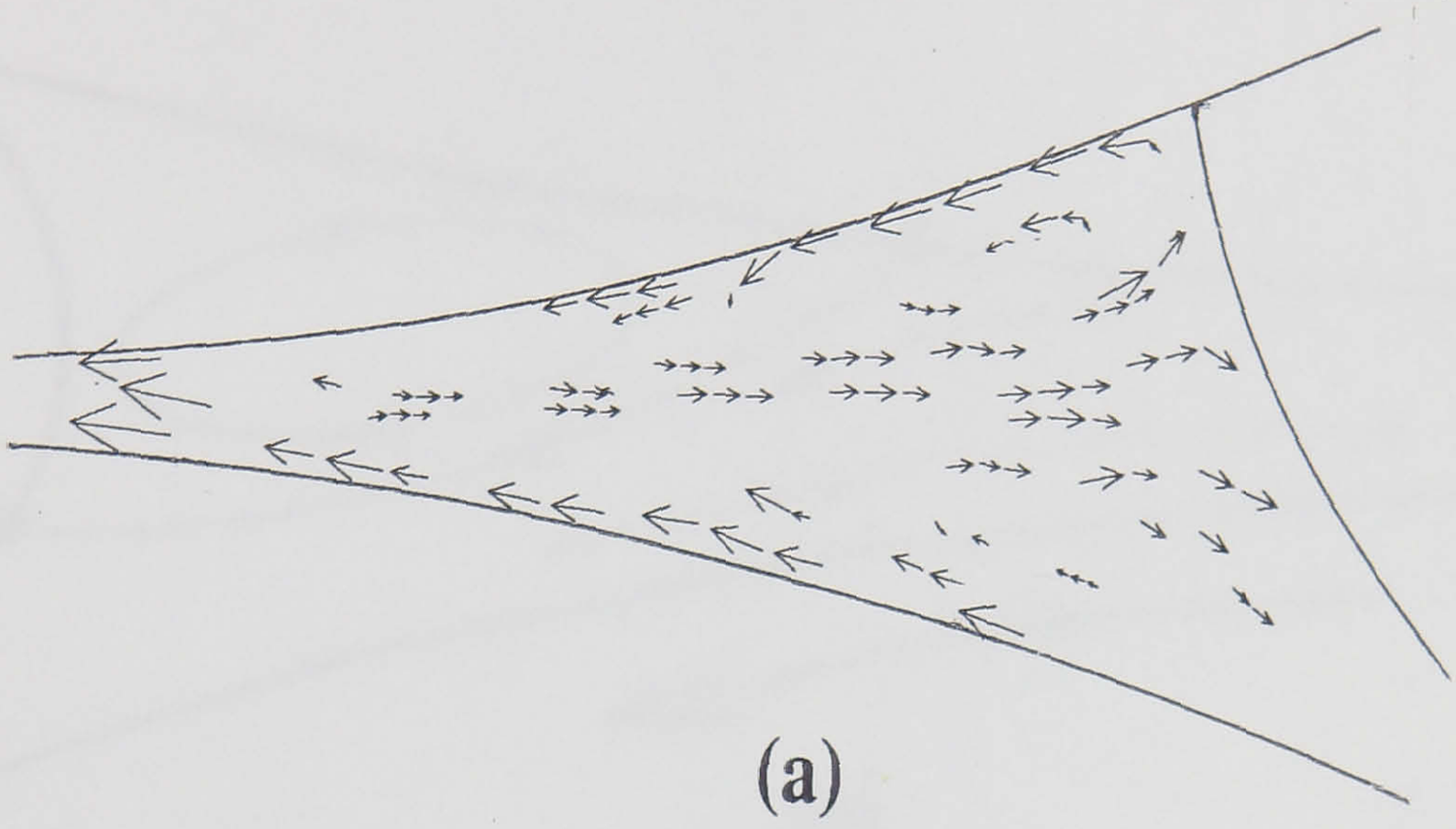

(a)

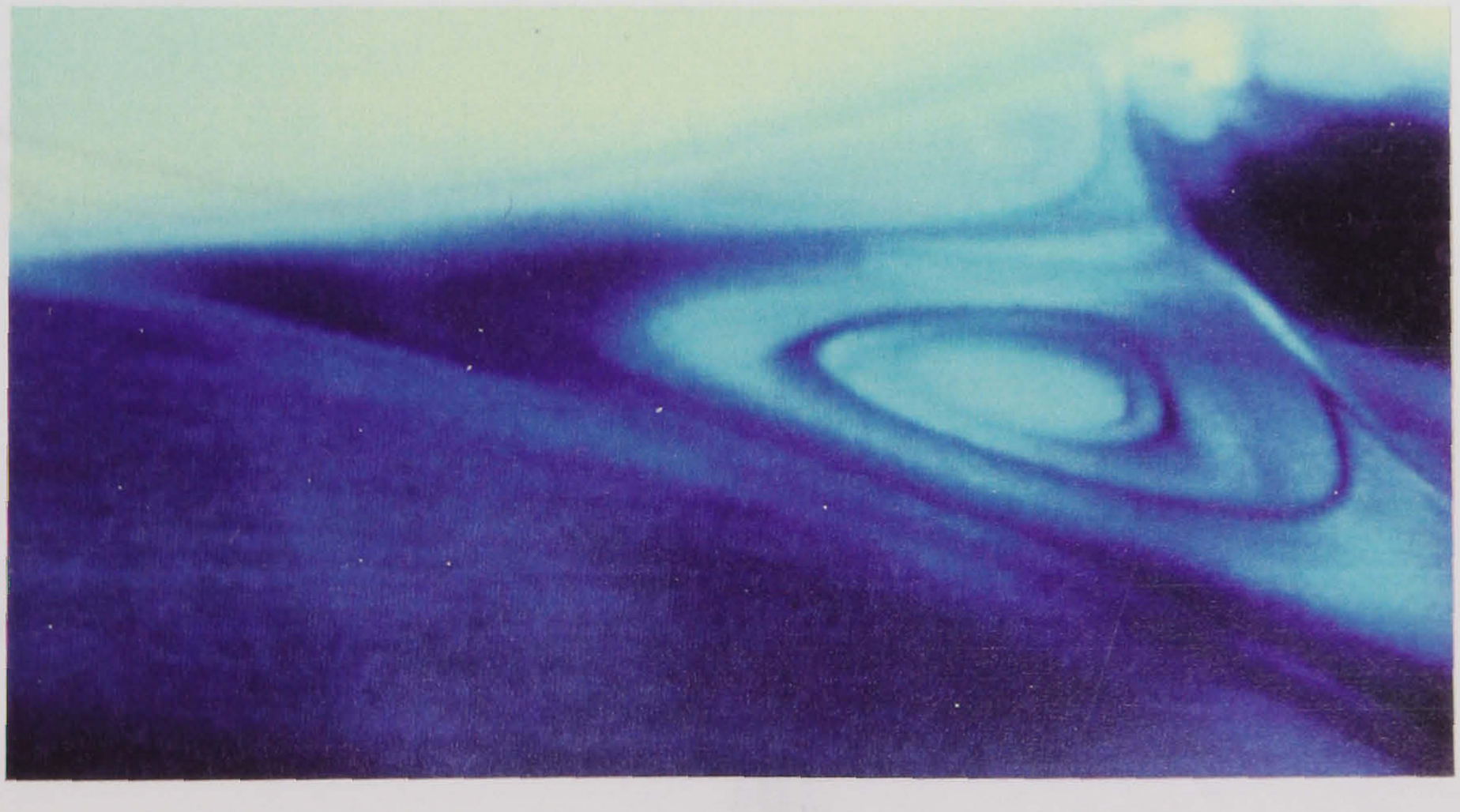

(b)

Figure 4.8: Upstream bank flow (a) Velocity field results, (b) Dye injection image

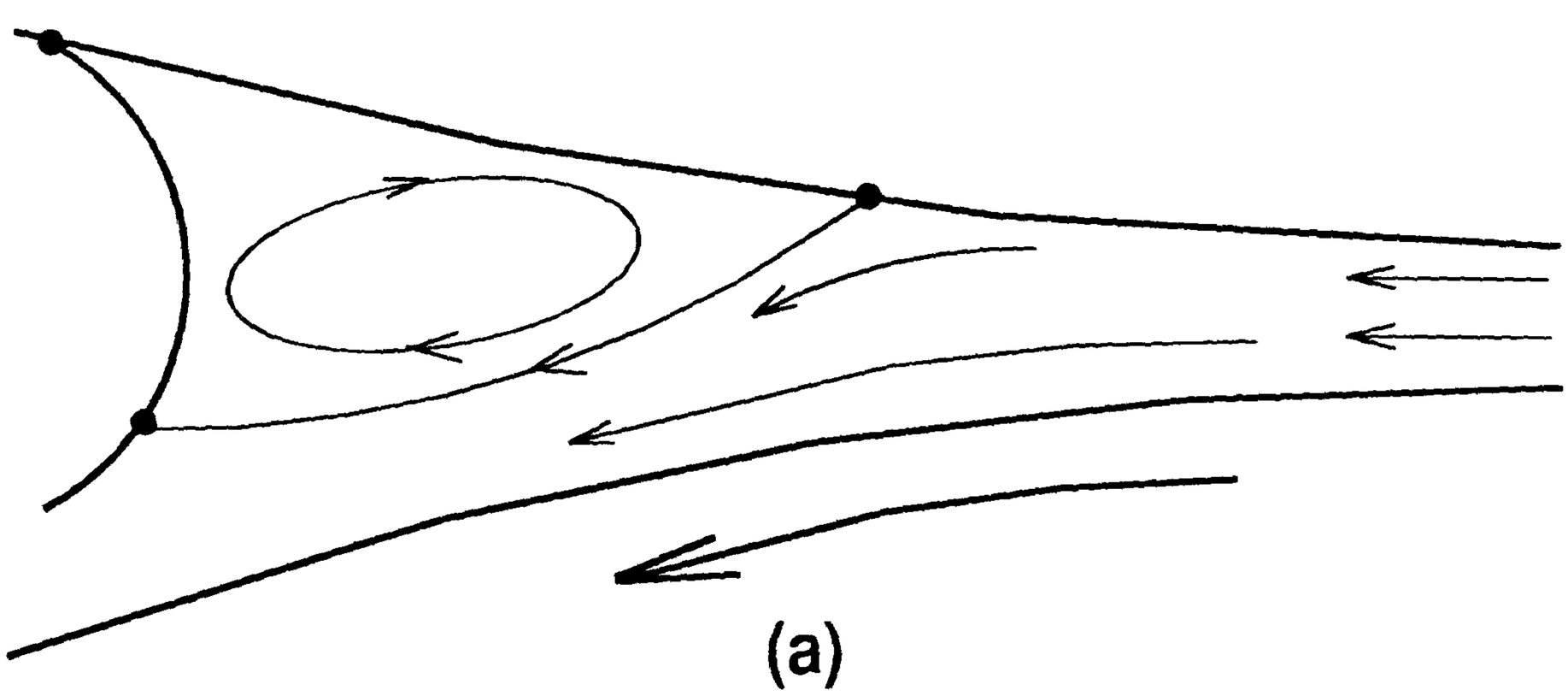

(a)

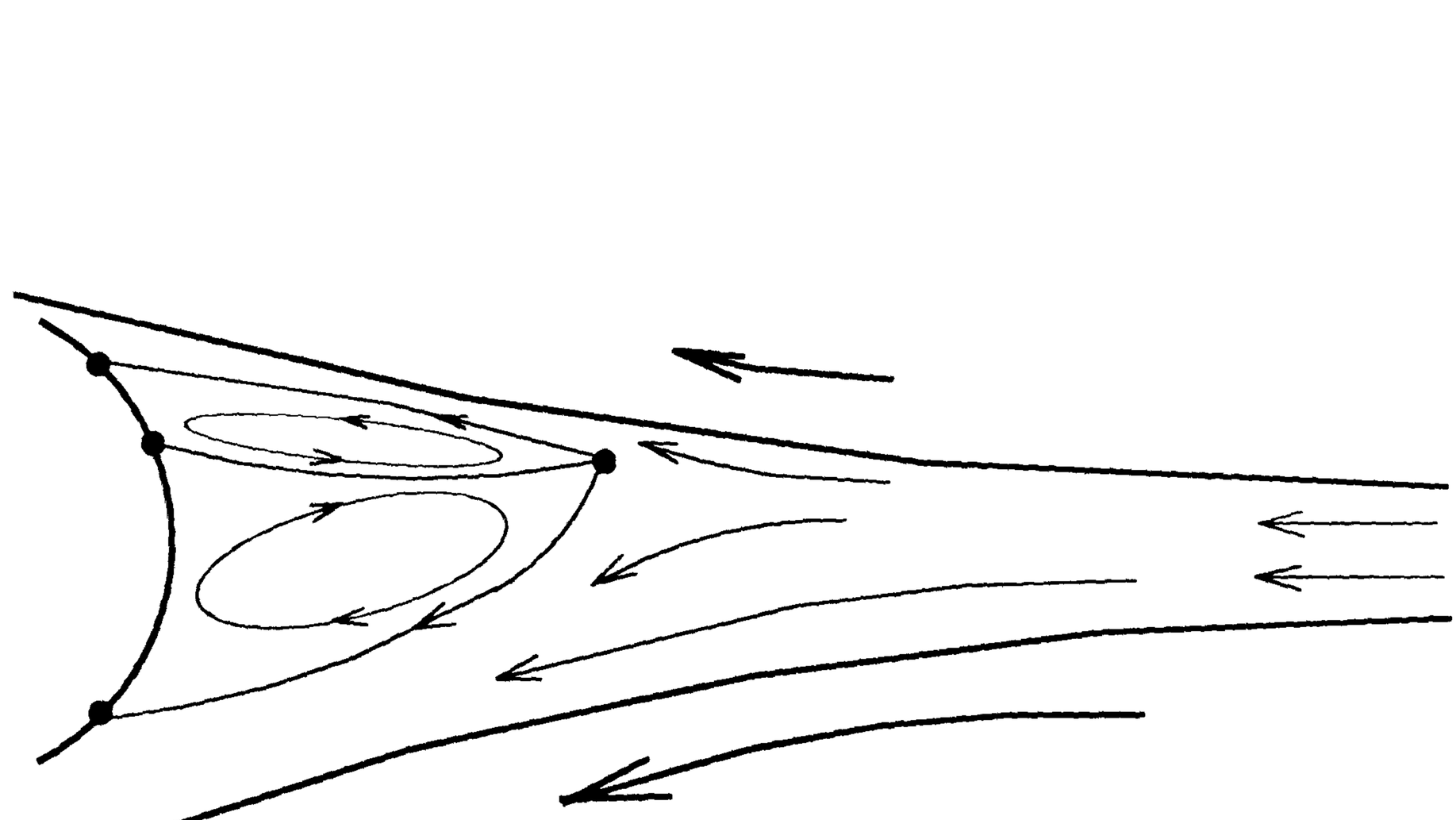

(b)

Figure 4.9: (a) Lower roll only moving; showing flow separation from upper roll, (b) Upper roll started slowly

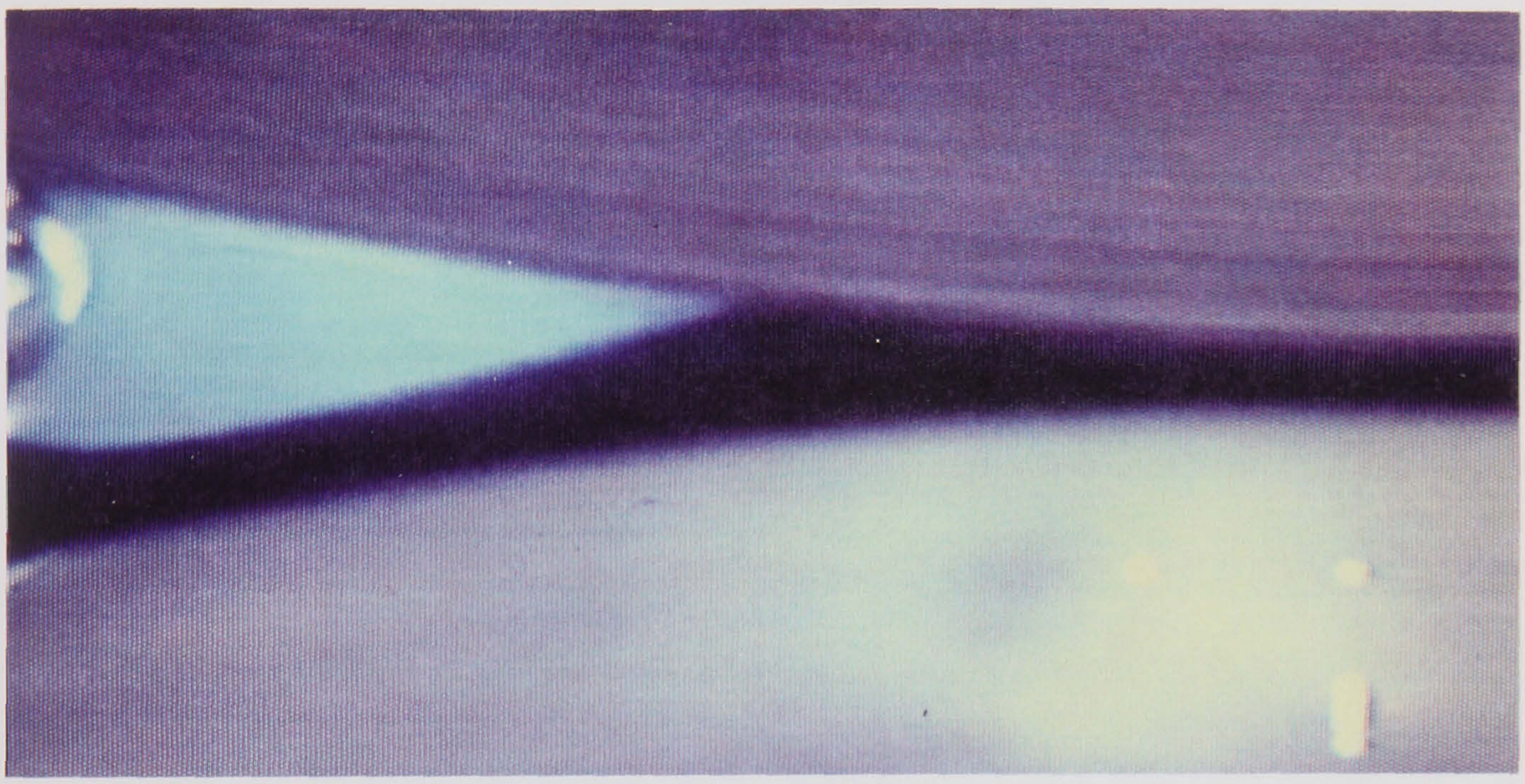

(a)

(b)

Figure 4.10: Dye injection images of start-up jump showing (a) Upper roll stationary, (b) Upper roll started

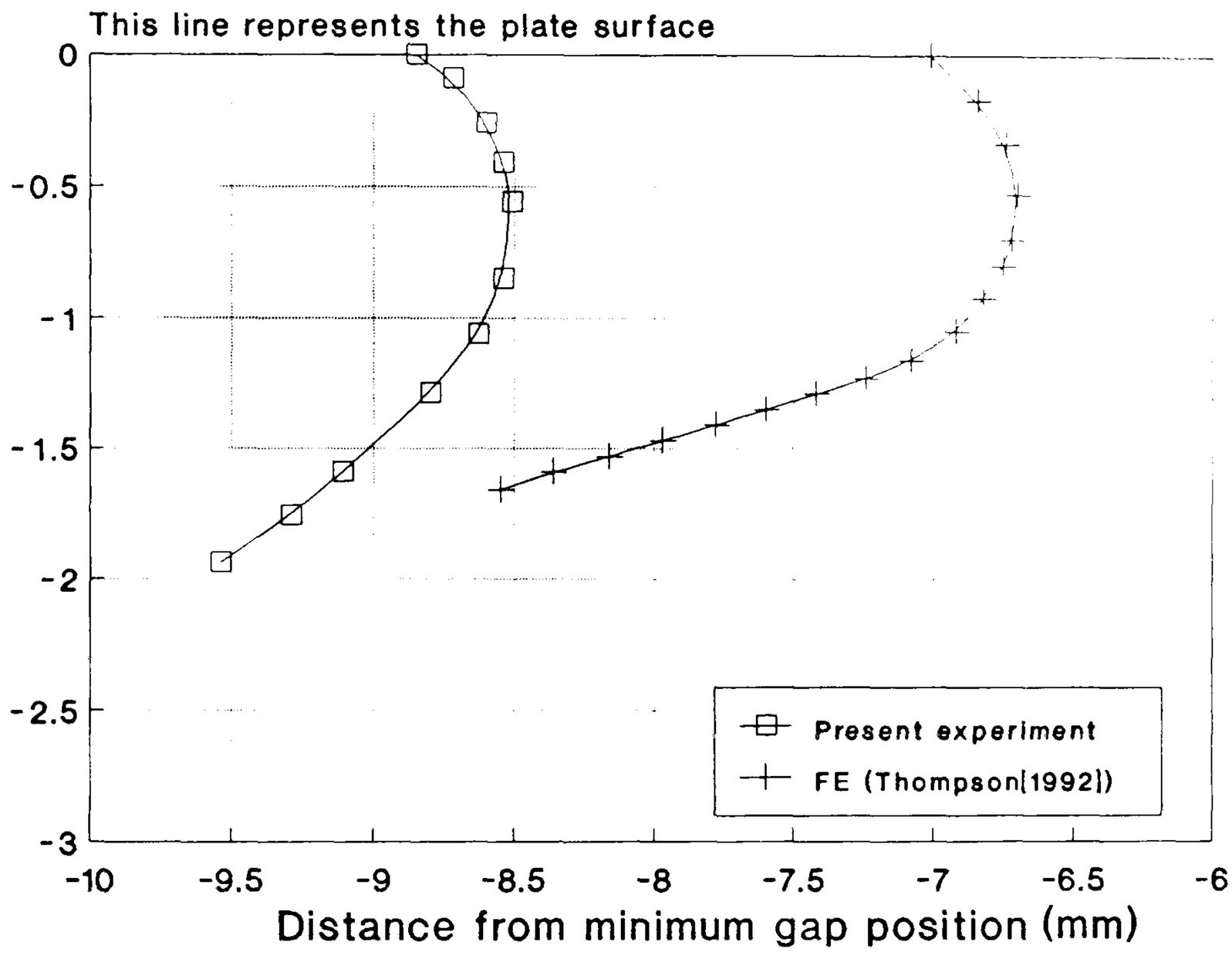

Figure 4.11: Downstream free surface profile: comparison of experimental results with Thompsons'[1992] finite element predictions

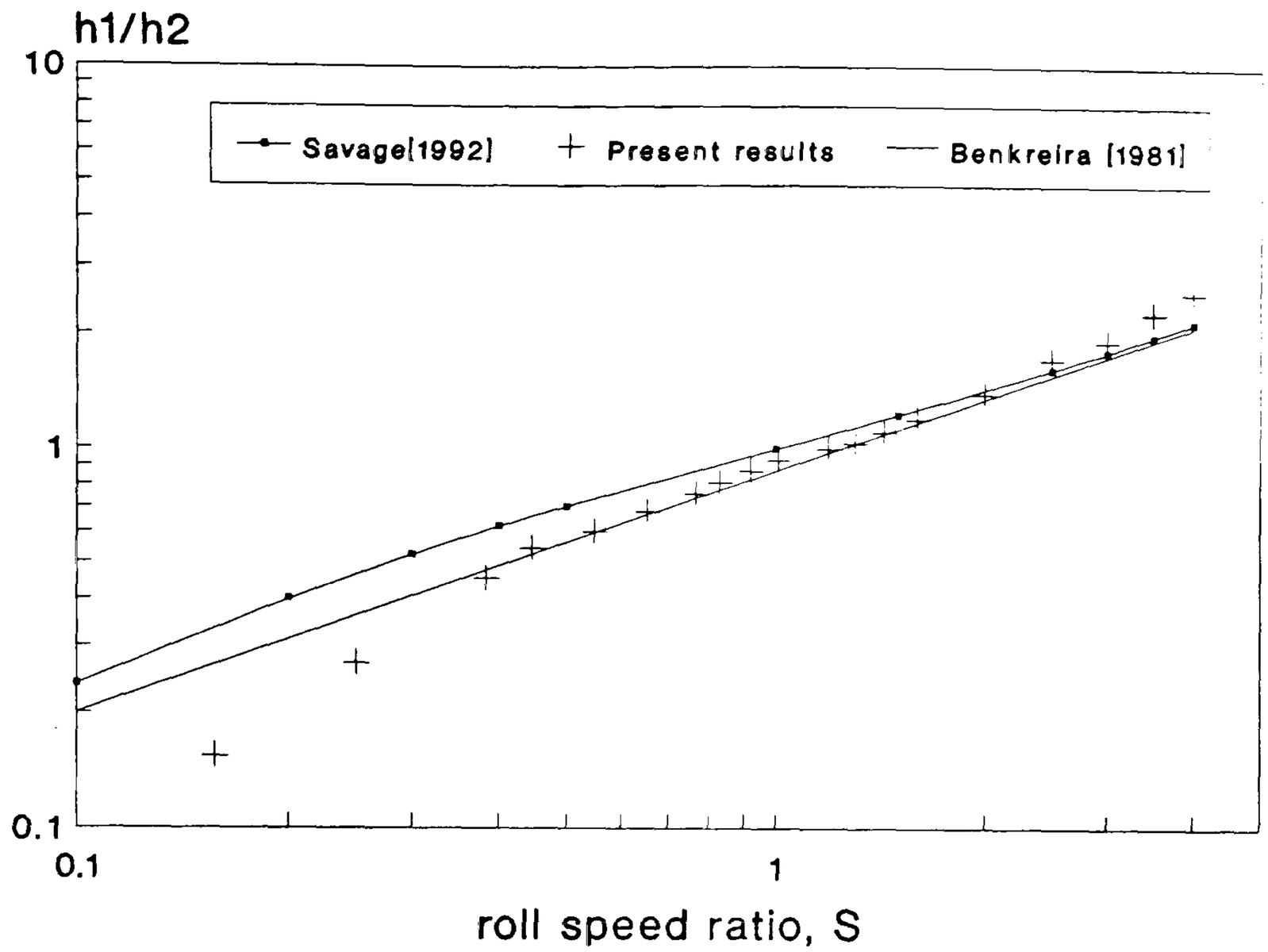

Figure 4.12: Comparison of present experimental film thickness results with those of Benkreira et al [1981] and predictions of Savages'[1992] refined model

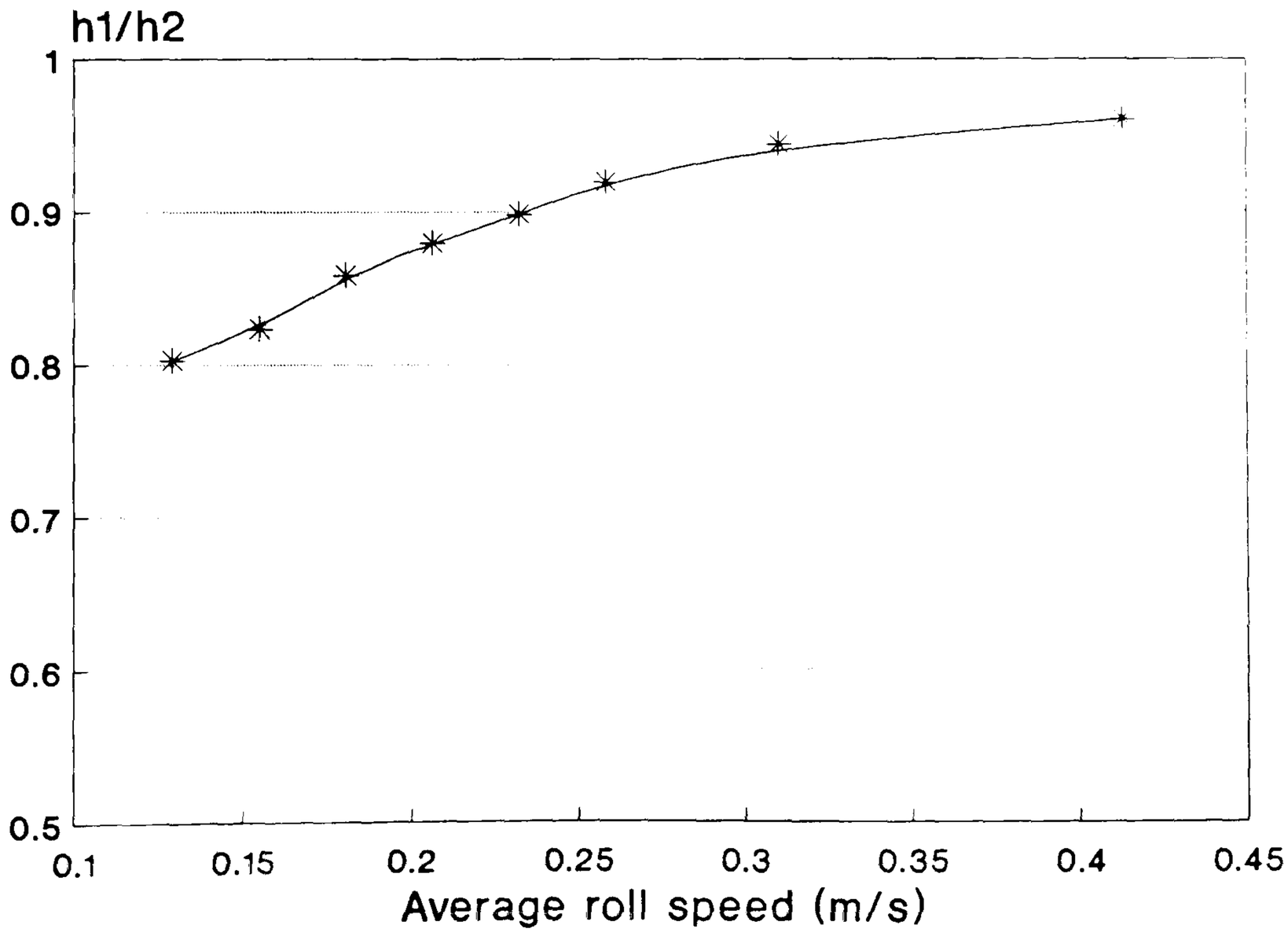

Figure 4.13: The effect of gravity on the film-split ratio

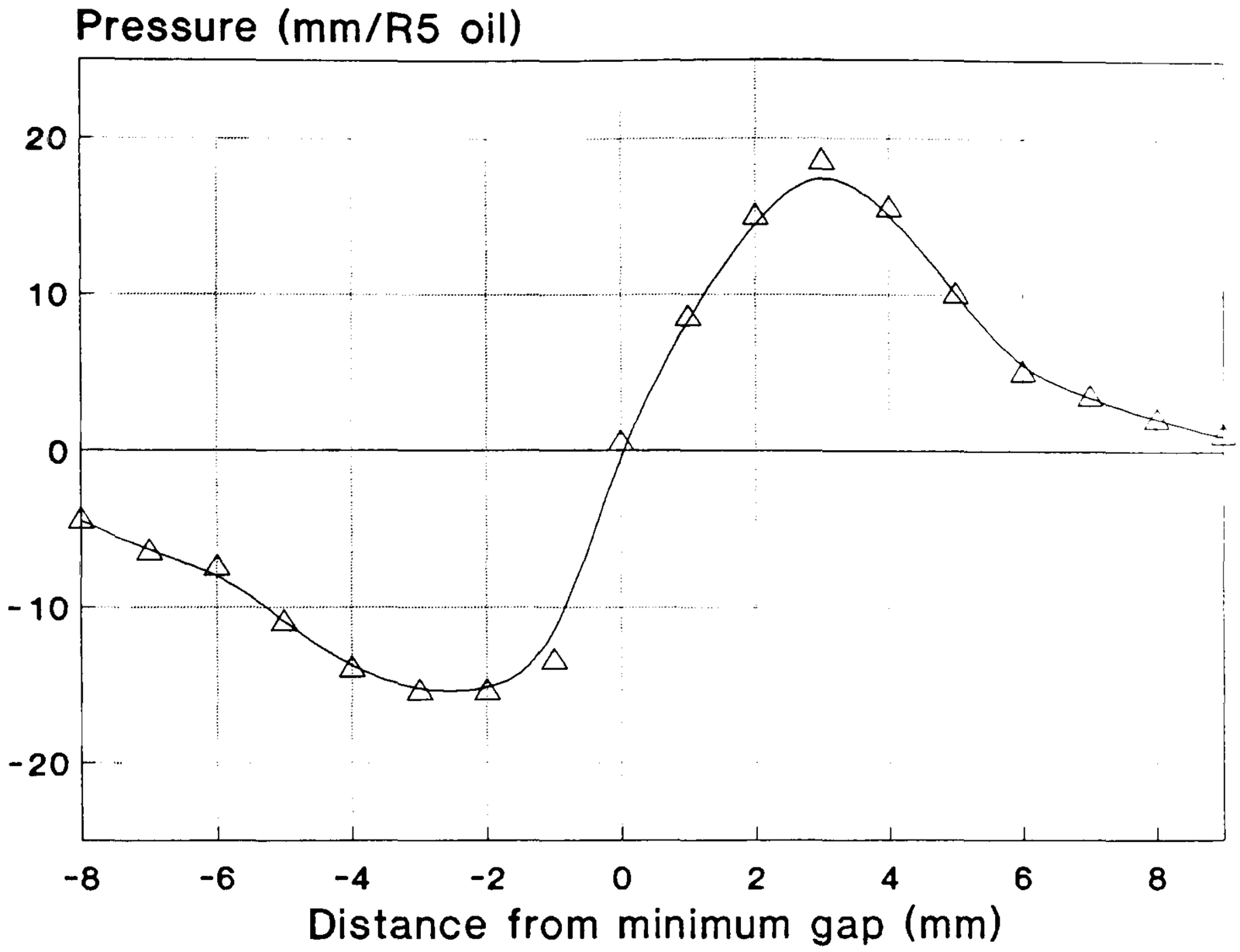

Figure 4.14: Classical roll coating pressure profile

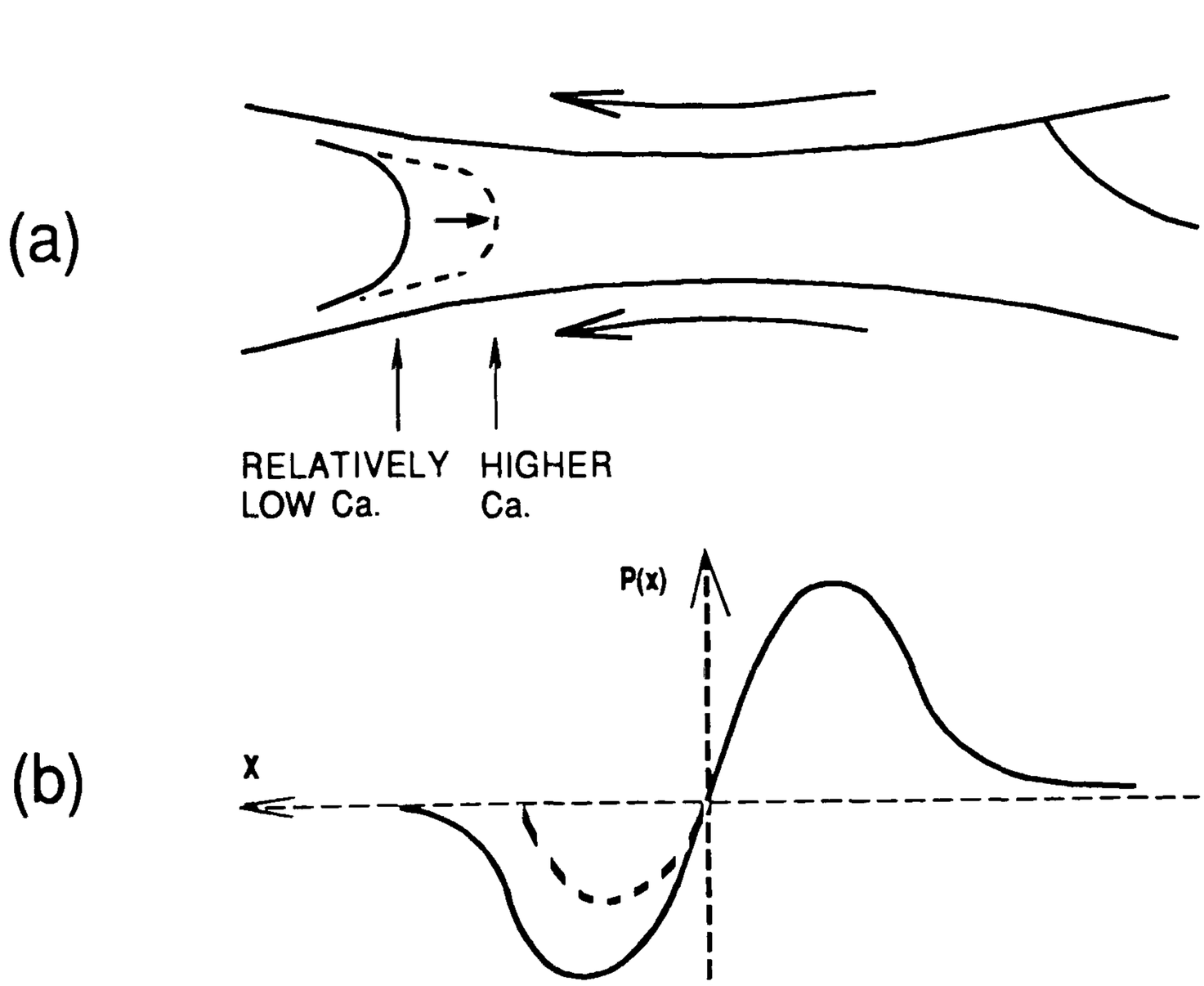

Figure 4.15: Effect of Capillary Number on (a) downstream free surface location, and (b) Subsequent pressure profile

Chapter 5

Meniscus (Ultra-Starved) Roll Coating

5.1 Introduction

The experimental techniques described in Chapter 2 are employed to investigate flow and behavioural characteristics of a hitherto unreported regime of roll coating. Results for this 'new' condition, in which the magnitude of the inlet film, to the nip, is much reduced (this phenomenon is introduced and discussed in Chapter 1, §1.4), are compared to those for the fully-flooded roll coating condition described in the previous chapter, and illustrate that the two cases exhibit quite different flow characteristics. Flow visualisation techniques used to study the very small nip region vividly demonstrate the large and unexpected differences in the flow patterns, while pressure measurements obtained using the simplified plate-roll apparatus (described in Chapter 2), with an ultra-starved inlet condition, demonstrate an equally surprising result for the pressure distribution in this new flow regime.

In roll coating processes it has been assumed, for modelling purposes, that the in-

let is fully flooded and that lubrication theory models the flow in the nip. Motivation for the present work arose when industrial coating specialists questioned the validity of the film thickness model for roll coating proposed by Savage[1982]. It was only at this point that a distinction between two possible operating modes for roll coating became apparent.

The process can be operated with the gap fully flooded on the inlet side (see Figure 5.1(a)), giving effectively only one meniscus downstream of the nip where the fluid splits into two layers, or under an ultra-starved condition (see Figure 5.1(b)), whereby the incoming film of fluid is considerably reduced, resulting in the upstream free surface becoming significant with regard to the nip flow. Previous work on modest starvation conditions is discussed in Chapter 1. In practice the ultra-starved regime appears to produce superior quality, ultra-thin wet coat films (in terms of uniformity) and it is less sensitive to factors such as roll run-out, for example. However, coating speeds tend to be significantly lower than for Classical roll coating, in order to maintain a stable operating condition.

In Classical roll coating the magnitude of the inlet film is taken to be at least of the same order as the minimum roll gap (although it may be significantly larger); since, under the assumption of a fully-flooded inlet, the nip effectively 'meters' the inlet film. In Meniscus roll coating, however, the magnitude of the inlet film cannot be predetermined. In general, fluid is transported into the bead from the fluid bath by the viscous lifting action of the lower roll (although there are alternative techniques for controlling the inlet film such as the use of a doctor blade or a slot-feed system whereby fluid is directed onto the lower roll via a slotted die prior to entering the bead - see Chapter 1). The size of the inlet film is therefore dependent on the mechanism of viscous lifting, for which properties such as roll speed, fluid viscosity and surface tension are important.

Previous work related to viscous lifting and fluid flow over rotating rolls is described in Chapter 2, §§ 2.3.1.

The important point to note is that, in addition to the problems of dealing with a second, upstream, free surface and a dynamic wetting line, the inlet film or flux, Q, passing through the bead is also unknown and must be determined either by the theory of free coating onto a roll (as described in Chapter 2, §§ 2.3.1), or by adding measurements of upper and lower roll outlet flux. The theory of coating a roll immersed in a fluid bath does not, however, take into account the presence of an upper roll, which is contacted by a dynamic wetting line, or a bead of fluid.

The experimental results described here enabled Thompson[1992] to formulate two simple mathematical models for Meniscus roll coating; the 'zero-flux' and 'finite-flux' models. Results from the models exhibit the experimentally observed flow characteristics, and in particular predict a linear pressure profile across the bead. The idealised 'zero-flux' model was extended further to

1. accommodate a small, non-zero flux and

2. predict asymptotic film thicknesses in Meniscus roll coating.

Free surface finite element techniques developed by Coyle, Macosko and Scriven[1982, 1986] for the fully-flooded case are employed by Thompson[1992] to obtain predictions of flow characteristics in Meniscus roll coating. Experimental data for free surface location or dynamic contact angle is required as a boundary condition for the finite element scheme. Experimental results for the velocity field obtained from the computerised particle tracking system (described in Chapter 2) are compared to numerical results. This tripartite (experimental, analytical, and numerical) approach to the Meniscus roll coating problem is seen to produce dividends, with the three areas complementing each

other well.

5.2 Experimental Investigation

The experimental techniques employed to investigate the flow field, film thickness behaviour, and velocity field are described in detail in Chapters 2 & 3. The measurement of the two outlet film thicknesses, h_1 and h_2, were added to give the inlet film thickness, h_0, and this was non-dimensionalised to provide a value for the non-dimensional flux, $\epsilon = h_0/H_0$. A value of ϵ in the region of 0.1/0.2 (i.e. an order of magnitude smaller than a fully-flooded condition) was considered to constitute an ultra-starved inlet.

5.2.1 Flow Field

Streamline Patterns

Figures 5.2(a) to (d) illustrate the main path taken by the injected dye as it progresses through the flow field (the rolls are moving from right to left). The dye enters on the lower roll (Figure 5.2(a)) and moves with the roll surface until it splits in the bottom left corner of the bead (Figure 5.2(b)); some of it continues along with the lower roll to form the outlet film thickness, while the rest makes a 'U-turn' to travel in the reverse direction through the flow field (Figure 5.2(c)). Once the fluid reaches the upstream free surface it experiences a second U-turn whereupon it wets the top roll and moves along with this surface (Figure 5.2(d)) only to leave the bead; forming the film on the upper roll.

The ultra-starved (Meniscus) case exhibits a complex flow regime whereby the transfer of fluid from lower to upper roll follows an S-shaped path (see Figure 5.3(a)), giving rise to a a fully 2-dimensional flow field. Important features of the flow include the two large recirculations associated with the upper and lower rolls extending across the

whole of the flow domain, and the fluid 'jet' travelling down the centre of the nip (for $S = 1$), between the eddies, in the opposite direction to that of the moving roll surfaces (Figure 5.3(b) illustrates the stagnation points and the boundaries of the eddy structure associated with this flow field). Furthermore, the fluid in the main transport path appears to undergo extremely sudden changes in direction at the meniscii - this implies that the fluid experiences sudden changes in momentum.

Comparing the flow pattern for the Classical and Meniscus coating cases in Figures 5.4(a) & (b) respectively, one can see a marked difference. In the flooded case the classic pattern of one-dimensional flow through the nip and two-dimensional flow just ahead of the meniscus is observed (as reported by Taylor[1963]). Although there are certain similarities if one considers the flow within the upstream bank in the Classical case; as discussed in Chapter 4, the fluid path from inlet on the lower roll to the upper roll takes an S-shaped path.

As the ratio S of the roll speeds is altered, the flow pattern also changes in a predictable manner. Figure 5.5 shows the flow field for $S > 1$. Here the vortex associated with the faster roll is significantly larger than that associated with the slower one. This figure also illustrates that as the speed ratio is increased for a constant gap, the aspect ratio (W_0/H_0) of the bead of fluid in the nip decreases as the meniscii move towards the minimum gap position. In industry the speed ratio is generally greater than 1, and therefore this low aspect ratio will be typical. The same result is achieved by increasing the gap for constant speed ratio.

In the case of reverse Meniscus roll coating, a single recirculation occupies the nip region (see Figure 5.6 - the lower roll is moving from left to right, while the upper roll is moving from right to left, produces an anti-clockwise recirculation).

There is evidence to suggest that each of the two large recirculations in the forward case and the single recirculation in the reverse case, which are the key features of the Meniscus roll coating flow field, themselves consist of two vortices joined by a stagnation point (see Figure 5.7(a) for forward case). It is useful to view the results presented here, in conjunction with the velocity plots in the next section to obtain a better understanding of the flow structure.

Under certain operating conditions the two vortices in a particular recirculation may become divorced as in Figure 5.7(b) where the lower right vortex has separated from the lower left vortex and becomes concentrated close to the right meniscus (this small vortex can only be inferred from the image by the high concentration of dye). Here $S > 1$ which results in the lower vortex decreasing in size, and it is effectively 'squashed' until a 'pinching' effect takes place somewhere in the centre of the bead, to cause the observed separation.

Velocity Field

Figure 5.8(a) is a velocity plot of a two-roll geometry with lower roll only moving. It is clear from this plot that there exist two vortices joined by an inferred stagnation point (illustrated by the highly stagnant flow region in the centre of the bead).

A typical Meniscus roll coating condition is illustrated in Figure 5.8(b). The figure clearly shows the reverse jet down the centre of the bead and large redirection of the flow adjacent to the free surfaces. The velocity of the reverse flow jet is measured to be approximately half that of the roll speeds (for symmetric rolling). This is in good agreement with Thompsons'[1992] Meniscus roll coating model.

The Meniscus roll coating velocity results are compared to Thompsons'[1992] F.E. predictions (see Figure 5.8(c)), and agreement is good (Thompson has only solved for the nip-downstream flow region). The basic principles of the F.E. technique are described in § 5.4.

5.2.2 Film thickness measurements

It is necessary to ascertain the relationship between the inlet film thickness h_0 and the two outlet film thicknesses h_1 and h_2 under various operating conditions. The measurement of dynamic fluid films is particularly difficult when the gradient of the substrate is always changing (in this case the rolls, to which the fluid is attached, are constantly rotating - this is discussed fully in Chapter 2). The techniques that can be used for measuring film thicknesses are described in Chapter 2.

As discussed in Chapter 4, gravity appears to significantly affect the film-splitting mechanism. This effect will be present and indeed may be more pronounced in the Meniscus coating regime, since the viscous forces tend to be lower (with reduced roll speeds and fluid viscosities, in general). Also, in considering the transport path of the fluid from the inlet to the upper roll, gravity has a relatively long time to act on this flow as the fluid travels around the vortices.

Results for film thicknesses have been plotted as ratios of h_2/h_0 (Figure 5.9) and h_1/h_0 (Figure 5.10), for comparison with the predictions of Savages film-splitting model for fully-flooded roll coating (these graphs also show the predictions of the Meniscus roll coating model developed by Thompson[1992] - described in §§ 5.3.4). The experimental film thickness results for the Meniscus case differ significantly from the predictions of Savages'[1982] model for the fully-flooded case. However, a surprising result emerges when comparing the film-splitting ratio, h_1/h_2; the results are in good agreement with

the predictions of the fully-flooded model (see Figure 5.11). Moreover, the Meniscus film-splitting model predicts h_1/h_2 against S identical to that of Savage[1992] for the fully-flooded case.

An important result to emerge from experimental observations and Thompsons[1992] mathematical model is that the net flux (and therefore the resulting outlet film thicknesses) passing through the nip is independent of the roll separation in Meniscus coating. Conversely, in Classical roll coating the net flux is a function of the gap size. In this respect the previous comparison of film thicknesses for the two regimes is not a direct one, since for the Meniscus case film thickness is non-dimensionalised with respect to inlet film thickness, and for the Classical condition with respect to the minimum gap size, H_0.

5.2.3 Free Surface Profile/Location Measurement

It is necessary to obtain a good estimate of the free surface profile and position from experimental observations to use as input to the finite element scheme, described below, in order to be confident of achieving a converged solution. Equally, experimental data can be used to verify numerical predictions obtained by the continuation method – see Thompson[1992].

The free surfaces are quite clearly defined when looking axially into the nip through the viewing window. A reference point grid (described in Chapter 3, § 3.5) is included in each image in order to calculate the form of the free surface and its position relative to the minimum gap. The experimental method used to obtain and analyse the free surface profiles is described in Chapter 3. Figure 5.12(a) & (b) show examples of upstream and downstream free surface profiles, and the downstream experimental result is compared with the numerical prediction of Thompson[1992]. Agreement is reasonable

for the shape of the profile, however the downstream position is not consistent. This discrepancy may be attributed to Thompson's limited solution, in which the upstream flow and free surface are not considered.

5.2.4 Pressure Field (Plate-Roll Geometry)

The pressure apparatus described in Chapter 2 is used to obtain an estimate of the characteristic pressure distribution in Meniscus roll coating. This experimental investigation was motivated by the predictions of the Meniscus roll coating model developed by Thompson[1992] (described briefly in § 5.3). In particular, this model predicts a linear pressure gradient across the coating bead. However, the position of this pressure gradient, in relation to the ambient pressure, cannot be predicted by the model.

Figure 5.13 shows a typical set of results of manometer pressure versus position across the nip; the roll is travelling from right to left. A sudden, dramatic pressure drop occurs across the upstream free surface and then recovers linearly through the nip to arrive at the downstream free surface at near-atmospheric pressure. Thus a linear pressure gradient, predicted by Thompson's simple model is verified. Moreover, experimental results provide the position of this pressure gradient with respect to ambient (atmospheric) pressure. Under an ultra-starved condition, the fluid pressure in the nip is everywhere sub-ambient. In addition, a simple analysis of the upstream and downstream free surface profile obtained experimentally shows the assymmetry (refer to Figure 5.12(a) & (b)) and thus the difference in the surface tension pressure term (T/r, where r is an estimate of the radius of curvature of the surface) at each free surface (see Figure 5.14).

The pressure predictions of Thompson's film thickness model for a two roll coater are in agreement with the experimental results presented here for the simplified plate-roll geometry, thus the initial assumption that this geometry would serve to provide

characteristic pressure profiles applicable to the two-roll process appears to be borne out, as indeed was the case for the widely studied fully-flooded plate/two-roll system.

5.3 Mathematical Modelling

5.3.1 Introduction

Previous models for fully-flooded roll coating, based on classical boundary conditions are not valid for the ultra-starved regime. The underlying deficiency of using lubrication theory to model roll coating flow has always been that the approximation breaks down in the region near a meniscus because the assumption of near-rectilinear flow fails there. The experimental observations presented above show that an assumption of rectilinear flow everywhere in the case of Meniscus roll coating would be incorrect. The problem of modelling this 'new' flow using established lubrication theory can also be illustrated from a consideration of the reduction in the magnitude of the inlet flux alone; following Greener and Middleman[1975] this theory is applied to the flow in the centre of the nip far away from the meniscus:

Denoting the $x - component$ of fluid velocity by $u(x,z)$ (refer to Figure 1.4(b) in Chapter 1), and introducing the usual lubrication assumptions that both gravity and inertial effects are negligible and $\frac{\partial}{\partial z} \gg \frac{\partial}{\partial x}$ (i.e. flow is uni-directional), then the Navier-Stokes equations in the x and z directions reduce to:

$$\frac{\partial p}{\partial x} = \eta \frac{\partial^2 u}{\partial z^2} \tag{5.1}$$

$$\frac{\partial p}{\partial z} = 0 \tag{5.2}$$

where p represents the fluid pressure.

These equations are subject to boundary conditions derived from no-slip on the roll

surfaces:

$$u = U_1 \text{ on } z = h(x),\ u = U_2 \text{ on } z = 0$$

(the gap thickness is approximated by $h(x) = H_0 + \left[\frac{x^2}{2R_1} + \frac{x^2}{2R_2}\right]$

The solution subject to the boundary conditions is:

$$u(x,z) = U_2 + (U_1 - U_2)\frac{z}{h} + \frac{1}{2\eta}\frac{\partial p}{\partial x}(z^2 - zh) \tag{5.3}$$

For steady flow in which axial leakage is ignored, the flux Q of fluid passing any point x is constant; hence for continuity of flow:

$$Q = \int_0^h u\partial x = const = U_1 h_1 + U_2 h_2 \tag{5.4}$$

$$Q = U_2 h + (U_1 - U_2)\frac{h}{2} + \frac{1}{2\eta}\frac{\partial p}{\partial x}(z^2 - zh)h \tag{5.5}$$

At the point of maximum pressure in the fluid,

$$h(x) = h_m,\ \frac{\partial p}{\partial x} = 0$$

Therefore from the previous equation for flux:

$$Q = U_2 h_m + (U_1 - U_2)\frac{h_m}{2} \tag{5.6}$$

and since

$$Q = U_2 h_0 \tag{5.7}$$

then

$$h_0 = [S + 1]\frac{h_m}{2} \tag{5.8}$$

For $S = 1$, then $h_0 = h_m$, but $h_m \backsimeq H_0$, therefore:

$$h_0 \geq H_0 \tag{5.9}$$

This is contradictory to experimental observations where h_0 can be much less than H_0 for Meniscus roll coating. If this analysis leads to erroneous results for Meniscus roll coating, then an assumption must be false; there are three obvious possibilities:

1. The assumption that $dp/dx = 0$ at $h = h_m$ is incorrect.

2. The flow field is very different.

3. A classical lubrication-type analysis is not valid.

The question is which of the above statements true. The experimental pressure results presented in §§ 5.4.2 suggest that there is no location where $\partial p/\partial x = 0$ and hence (1) is true. Moreover, the experimental observations of Meniscus roll coating (see §§ 5.2.1) reveal a flow field which is very different to that of Classical roll coating. The new regime is characterised by extensive recirculatory flow and as such (2) is also true. However, (3) is false – Thompson[1992] has shown that lubrication theory can be used to describe the flow in the 'core' of the fluid bead of a Meniscus roll coater (see §§ 5.3.3).

The equations governing coating flows are always made non-linear by the conditions applicable at the free surfaces, and in some cases by the inertia of the liquid. The experimental observations described above illustrate that the fluid mechanics of roll coating depend critically on the inlet condition, namely, whether the nip between the rolls is fully flooded or starved of fluid at inlet.

With regard to modelling roll coating flow, the fully-flooded (Figure 5.1(a)) and ultra-starved (Figure 5.1(b)) cases are seen to have important differences. For example, the dynamic wetting line, where the fluid meets the top roll at inlet, can be ignored in the modelling of Classical roll coating where it is assumed to lie far upstream of the nip flow (only the flow region extending from the nip to downstream is generally considered). The influence of this wetting line cannot be ignored in Meniscus roll coating since it is a primary component of the flow in the nip region. This complicates analysis because very little is known about the physical mechanisms by which one fluid displaces another at such a location, either from a molecular or continuum point of view. This

problem has received attention from numerous researchers and is discussed more fully in Chapter 1, § 1.4. In Meniscus roll coating note also the presence of a free surface at the inlet side of the nip which means that the combined effects of two curved meniscii must be considered. This is a problem because highly curved meniscii defy traditional mathematical analysis due to the nonlinear boundary conditions that have to be satisfied at the unknown meniscus location.

This has led to the finite element technique being applied to the free surface flow problems encountered in coating applications with great success, most notably in the work of Ruschak[1982], Coyle et al [1982,1986] and Kistler & Scriven[1984]. The techniques for the numerical solution of free surface flows, including the effects of dynamic wetting lines, have been thoroughly reviewed by Kistler & Scriven[1983].

A simple model for Meniscus roll coating has been developed by Thompson[1992], motivated by the observation that the influx, Q, is small compared to the influx in the fully-flooded case. In the first instance the flux is set to zero and the flow is modelled as a cavity-driven flow generated by moving upper and lower lids. Cavity driven flows arise in a wide variety of situations and have been extensively studied due to their practical importance as examples of flows with closed streamlines. Thompson[1992] gives a full review of previous work in this area

The work of Thompson[1992] in modelling Meniscus roll coating is covered in some detail below in order to provide an appreciation of the concepts involved and also the interplay between analytical, experimental, and numerical results in developing such a model.

5.3.2 Zero-flux model

Figure 5.15(a) illustrates the modelling situation for the zero flux case in which the following assumptions are made:

(a) The flow is steady, isothermal, two-dimensional and creeping.

(b) The curvature of the rolls can be neglected

(c) The fluid is Newtonian and of constant density ρ and viscosity μ.

(d) Free surfaces are modelled as lines of zero shear stress.

(e) The fluid domain is closed - no influx into fluid bead.

In (a) the effects of fluid inertia are neglected, which is valid for flows of practical interest. This means that the fluid mechanical equations reduce to the biharmonic equation, $\nabla^4\psi = 0$, for the streamfunction ψ. The effect of assumption (d) is to ignore the curvature of each meniscus and hence the surface tension pressure. Therefore the normal stress balance at each meniscus cannot be satisfied. These assumptions allow the flow to be modelled as a cavity-driven flow with one important modification: the usual no-slip condition on the side walls is replaced by a zero shear stress condition. In the following analysis the aspect ratio, A, the ratio of (half) cavity width to cavity depth and the velocity ratio, S, are used.

In (e) it is assumed that no fluid crosses the cavity boundaries so that the streamfunction ψ is constant on the boundaries. This constant is set to the value zero hence

(i) $\psi(x,1) = \psi(x,0) = \psi(A,z) = \psi(-A,z) = 0$

The velocities of the lids are given in terms of derivatives of the streamfunction and are:

(ii) $\frac{\partial\psi}{\partial z}(x,1) = S; \quad \frac{\partial\psi}{\partial z}(x,0) = 1$

Finally, the free surfaces are modelled as lines of zero shear stress so that

(iii) $\sigma_{xz} = -\nabla^2\psi = 0$ at $x = A, -A$

However $\psi = 0$ at $x = A, -A$ so that

$$\frac{\partial^2 \psi}{\partial z^2} = 0 \text{ at } x = A, -A$$

and (iii) reduces to

(iv) $\frac{\partial^2 \psi}{\partial x^2} = 0$ at $x = A, -A$

The boundary value problem is symmetric so that one need only consider the flow in one half of the fluid domain. The streamfunction ψ is obtained in the form of an infinite series of orthogonal eigenfunctions (see Thompson[1992] for the full solution).

The horizontal pressure gradient, $\frac{\partial p}{\partial x}$, is very important in coating flow analysis and may be readily obtained from the Navier-Stokes equations for creeping flow:

$$\frac{\partial p}{\partial x} = \nabla^2 u = \frac{\partial^3 \psi}{\partial x^2 \partial z} + \frac{\partial^3 \psi}{\partial z^3} \tag{5.10}$$

where u is the horizontal component of fluid velocity.

An example of a streamline plots obtained analytically by truncation of the solution after 20 terms is presented in Figure 5.15(b) for a cavity with an aspect ratio of $A = 4$. A number of key results follow:

1. For $S = 0$ (top lid stationary), the flow has a single vortex structure and the streamlines are similar to those observed experimentally in a plate-roll geometry.

2. For $S = 1$ (forward case) the flow separates completely into upper and lower vortices of equal size. This is in qualitative agreement with the experimentally observed flow structure - see Figures 5.16(a) & (b) (although there is obviously no through-flow in the idealised zero-flux model.

3. For $S = 2$ (forward case) the upper vortex is twice the size of the lower vortex (see Figures 5.17(a) & (b)).

4. When $S = -1$ (reverse case) a perfectly symmetrical, single vortex is predicted, and this is confirmed experimentally (see Figures 5.18(a) & (b)).

The model predicts a horizontal pressure gradient with little vertical variation – pressures on the centreline are therefore representative of pressures throughout the bead. The value of the horizontal pressure gradient, $\partial p/\partial x$, is found to be constant in the central core (sufficiently far from the meniscii). It was this surprising result which prompted the experimental investigation of pressures, presented earlier in this chapter. In addition, the magnitude of the pressure gradient is proportional to the magnitude of $(1 + S)$. This implies that for the reverse flow case of $S = -1$ the pressure gradient effectively disappears. This is an important result, the implications of which are discussed in Chapter 7, §§ 7.2.4.

5.3.3 Finite-Flux Model

Although the idealised zero-flux model was a first attempt at modelling Meniscus roll coating flow, it is not representative of the physical process where there is a small, but non-zero flux through the bead. The prediction of a constant pressure gradient in the central core of the bead led Thompson[1992] to question whether the flow in the central core could be simplified.

He proceeded to model the flow in the bead core as a combination of Poiseuille plus Couette flow with a constant pressure gradient (private communication, Richardson[1988]). This leads to a velocity profile of the form:

$$u = \overbrace{\frac{1}{2}\frac{\partial p}{\partial z} z(z - H)}^{Poiseuille} + \overbrace{(S-1)\frac{z}{H} + 1}^{Couette} \tag{5.11}$$

where u is the velocity across the bead, S is the speed ratio of the upper and lower lids, H is the distance between the lids, and

$$\frac{\partial p}{\partial x} = \frac{6}{H^2}((S+1) - 2\epsilon) \tag{5.12}$$

is the dimensionless pressure gradient in the interior where ϵ is the total dimensionless net flux through the bead. From the Poiseiulle plus Couette expressions it is possible to obtain $(\partial p/\partial x)_0$ and u_0, i.e. the pressure gradient and velocity profile in the limit as $\epsilon \rightarrow 0$. By setting $\epsilon = 0$ in the above expressions gives:

$$\left(\frac{\partial p}{\partial x}\right)_0 = \frac{6(1+S)}{H^2} \tag{5.13}$$

and

$$u_0 = \frac{3}{H^2}(S+1)z(z-H) + (S-1)\frac{z}{H} + 1 \tag{5.14}$$

There are thus two independent predictions for the velocity profiles and pressure gradient in the bead in the idealised case of zero net flux, namely, those obtainable from the zero-flux model and those from the small flux limit of the Poisieulle plus Couette model. These two predictions are found to be in excellent agreement for all S and in particular the earlier prediction that pressure gradients are proportional to $(1+S)$ is borne out in expression (5.13).

These results suggested that the Poisieulle plus Couette model was valid for the core flow and this prompted Thompson to use this in the prediction of film thicknesses on upper and lower rolls for the forward Meniscus coating case.

5.3.4 A Predictive Model For Film Thicknesses

In §§ 5.2.1 of this chapter experimental observation of streamlines in forward Meniscus roll coating showed that the fluid in the bead is composed of upper and lower vortices

with the inlet fluid entering the bead and moving along with the lower roll before splitting into two layers, one of which proceeds to coat the lower roll and the other which forms a jet of fluid that snakes between the two vortices before coating the upper one. The flux splitting actually occurs near the downstream free surface where the flow is fully two-dimensional and as a result cannot be modelled by the simple models described above.

Nevertheless, it is possible to predict film thicknesses without analysing the flow near the film-split point. By hypothesis, and with reference to Figure 5.19, the flux in the jet between the upper and lower vortices, i.e. in $Z_L \leq z \leq Z_U$, equals the flux that flows out on the upper roll. In order to determine the flux in this jet, Q_{jet} say, it is necessary to locate Z_L and Z_U; Q_{jet} is then obtained by integrating the expression for the velocity profile obtained from the zero-flux model between Z_L and Z_U.

As for the zero-flux model, the assumptions of steady, two-dimensional, creeping flow of a Newtonian, incompressible fluid in which the rolls are modelled as flat surfaces are valid for the finite-flux model. In contrast however the non-dimensional flux, ϵ $(= Q_0/U_2H_0)$ is small, but non-zero, in the sense that $\epsilon \ll 1$. If the fluxes out on the upper and lower lids are $\epsilon_1(S,\epsilon)$ and $\epsilon_2(S,\epsilon)$ respectively then continuity of flux yields

$$\epsilon \;=\; \epsilon_1 \;+\; \epsilon_2 \tag{5.15}$$

Determination of Z_L

The location of Z_L is obtained by observing that the flux under Z_L equals the total net flux ϵ, hence

$$\int_0^{Z_L} \frac{u}{H}\, dz \;=\; \epsilon \tag{5.16}$$

which yields a cubic equation for Z_L, the relevant solution of which is

$$Z_L(S,\epsilon) \;=\; H\left(\frac{1}{(1+S)} \;-\; \frac{S(S+3)}{(1+S)^2}\epsilon\right) \;+\; O(\epsilon^2) \tag{5.17}$$

The other solutions for Z_L are (i) $Z_L = \epsilon$ corresponding to the top of the inlet film and (ii) $Z_L = H$ corresponding to the top lid.

Determination of Z_U

This is far more difficult. In the idealised case of zero net flux, there is no fluid jet between the vortices so Z_U and Z_L coincide. If $Z_S = Z_U = Z_L$ denotes the position of the dividing streamline separating flow in the upper vortex from flow in the lower one in this idealised case, its location is given by the solution of

$$\int_0^{Z_S} u_0 \, dz \;=\; 0 \tag{5.18}$$

giving $Z_S = 0,\ H/(1+S)$ and H. As before the relevant solution is in the interior of the bead, namely

$$Z_S \;=\; \frac{H}{(1+S)} \tag{5.19}$$

This enables (5.17) to be reinterpreted. When a small, non-zero flux flows through the bead, the locations $Z_U,\ Z_L$ are displaced to allow the fluid jet to flow between the vortices. Hence from (5.17), Z_L is displaced downwards by an $O(\epsilon)$ amount given by $HS(S+3)\epsilon/(1+S)^2$. Moreover the problem of determining Z_U reduces to finding the displacement $\delta(S,\epsilon)$ by which Z_U is displaced when a non-zero flux ϵ flows through the bead, i.e.

$$Z_U(S,\epsilon) \;=\; \frac{H}{(1+S)} \;+\; \delta(S,\epsilon) \tag{5.20}$$

Now any model must, in the absence of gravity, satisfy the symmetric film splitting condition

$$\text{(i)}\ \epsilon_1(1,\epsilon) \;=\; \epsilon_2(1,\epsilon) \;=\; \epsilon/2$$

and in the asymptotic limits

(ii) $\epsilon_1 \rightarrow \epsilon$ as $S \rightarrow \infty$

(iii) $\epsilon_2 \rightarrow \epsilon$ as $S \rightarrow 0$

Since both Z_U and Z_L are displaced from $Z_S = H/(1+S)$ by an $O(\epsilon)$ amount, the thickness of the fluid jet, $Z_U - Z_L$, is also $O(\epsilon)$. By hypothesis

$$\epsilon_1 = \frac{\int_{Z_L}^{Z_U} u dz}{H} \tag{5.21}$$

So by a simple order of magnitude argument ϵ_1, which is also $O(\epsilon)$, is determined by considering only the $O(1)$ fluid velocity in the jet at the location Z_S; expression (5.11) gives,

$$u_{jet} = -\frac{S}{(S+1)} \tag{5.22}$$

It can be shown that condition (i) gives $\delta(1,\epsilon) = 0$; and conditions (ii), (iii) yield $\delta(S,\epsilon) \rightarrow 0$ as $S \rightarrow \infty$, 0 respectively. These results motivate the key assumption of this model: postulate that $\delta(S,\epsilon) = 0$ for all S and ϵ. Under this hypothesis

$$Z_U(S,\epsilon) = \frac{H}{(1+S)} \text{ for all } S \text{ and } \epsilon \tag{5.23}$$

i.e. when a small flux flows through the bead Z_U remains at the same position and Z_L drops by an amount $HS(S+3)\epsilon/(1+H)^2$ to accomodate the jet.

Predictions of the Film Thickness Model

Using equations (5.15), (5.17), (5.22) and (5.23) yields:

$$\epsilon_1 = \frac{S^2(S+3)}{(1+S)^3}\epsilon \ , \quad \epsilon_2 = \frac{(1+3S)}{(1+S)^3}\epsilon \tag{5.24}$$

If Q_1, Q_2 are the *actual* fluxes on the upper and lower rolls respectively, (5.17) is easily rewritten in terms of, Q_0, the *actual* flux through the bead:

$$Q_1 = \frac{S^2(S+3)}{(1+S)^3}Q_0 \ , \quad Q_2 = \frac{(1+3S)}{(1+S)^3}Q_0 \tag{5.25}$$

Now in roll coating theory it is usual to assume that the fluid films on the upper and lower rolls are 'fully-developed' sufficiently far downstream, i.e. flow is uniform

'plug' flow. Theoretical analyses of relaxation to uniform flow have been performed by Wilkinson[1978], Higgins[1982] and Carter[1985]. The problems of attaining 'plug' flow on a rotating roll in practice have been discussed in Chapter 2. Fortunately these effects are reduced for Meniscus roll coating (where film thicknesses are 'ultra-thin') and therefore it is possible to calculate the film thicknesses h_1, h_2, namely

$$Q_1 = U_1 h_1 \ , \ Q_2 = U_2 h_2 \tag{5.26}$$

Equations (5.25), (5.26) combine to predict

$$\frac{h_1}{h_2} = \frac{S(S+3)}{(1+3S)} \tag{5.27}$$

This result is very interesting because it is the same as Savage's[1992] prediction for the fully-flooded case. In Figure 5.11 this film thickness ratio prediction is compared with data for both the Meniscus and Classical forward roll coating cases. The experimental data provides strong evidence for the validity of the film thickness model developed here. It also shows that the film thickness ratios are very similar in the fully-flooded and ultra-starved cases – a surprising result given the major differences in their flow structures. On reflection it is perhaps not so surprising in view of the similarity of the flow structure in Figure 5.19 and that in the upstream bank for the fully-flooded case (see Chapter 4, Figure 4.4).

Although the film thickness ratios h_1/h_2 are the same, these models predict many differences between fully-flooded and ultra-starved roll coating. For example, in Menis-cus coating the amount of fluid passing into the bead depends on the lower roll speed due to viscous lifting action, as discussed earlier. When the lower roll speed is increased the thickness, h_0, of the inlet also increases. This means that h_1 and h_2 depend not only on the *ratio* of the roll speeds, but also on the *magnitude* of the lower roll speed, U_2, through this viscous lifting action. This stands in contrast to the fully-flooded case

where the inlet is already flooded so the extra fluid picked up when U_2 is increased further cannot pass through the nip. Instead this excess fluid forms a 'rolling bank' upstream of the nip - see Chapter 4, Figure 4.4(a). Therefore, in the fully-flooded case, h_1 and h_2 depend only on the ratio of the roll speeds, not on their magnitudes.

A second difference lies in the dependence of the individual film thicknesses on the minimum roll separation H_0 ($\equiv H$ in the previous analysis). In the fully-flooded case the amount of fluid passing through the nip is limited by the roll separation so h_1, h_2 are directly proportional to H_0. In Meniscus coating, however, the inlet film thickness $h_0 \ll H_0$ so this limitation does not exist; consequently h_1, h_2 are *independent* of H_0. This has been confirmed experimentally.

The flux-splitting results, (5.26), can be rearranged to yield ratios of outlet film thicknesses on upper and lower rolls respectively to the inlet film thickness h_0, namely

$$\frac{h_1}{h_0} = \frac{S(S+3)}{(1+S)^3} \quad , \quad \frac{h_2}{h_0} = \frac{(1+3S)}{(1+S)^3} \tag{5.28}$$

In order to test these predictions experimentally, the roll speed ratio is varied by changing the upper roll speed only. Therefore the total flux through the bead (which is dependent on the lower roll speed) remains constant. Figure 5.9 shows the graph of h_2/h_0 versus S. Experimental results compare well with the predictions of the Meniscus film-splitting model, and as expected the marked difference in the predictions of Savages[1982] fully-flooded model is observed.

In roll coating h_1 is the important parameter as it is generally this film which coats the final product. The graph of h_1/h_0 predicted by (5.28) is shown in Figure 5.10; this is very useful since it predicts that h_1 should be relatively insensitive to small variations in S for a process operating at $S \geq 3$. This is a typical value of roll speed ratio used in

industry, which it seems has only been arrived at by trial and error. Therefore Meniscus coating predictions and experimental data are in good agreement over the attainable range of velocity ratio.

5.4 Numerical (F.E.) Free Surface Scheme

5.4.1 Introduction

The simple models for Meniscus roll coating developed by Thompson[1992] and described above are only valid in the central 'core' region, sufficiently far from the free surfaces which exist on either side of the fluid bead. A fuller treatment of free surfaces is needed to model Meniscus coating realistically. Modelling a free surface, or meniscus, requires satisfaction of the following three nonlinear conditions at the curved, unknown free surface location:

1. zero normal velocity,

2. zero tangential stress, and

3. normal stress balanced

Coyle, Macosko & Scriven[1982] developed a generally applicable finite element analysis of fully-flooded roll coating which has been applied to (i) Symmetric[1982], (ii) Asymmetric[1986] forward roll coating of Newtonian liquids; (iii) a shear-thinning rheology; (iv) stability analysis of forward roll coating[1991]. This section gives a brief overview of the work of Thompson[1992] in extending the techniques described by Coyle et al [1986] to model the effects of inlet fluid starvation on the forward roll coating of a Newtonian liquid.

5.4.2 Free Surface Representation

For a number of years the principle hurdle in modelling free surface coating flows was how to represent the location of a free surface. The breakthrough came with the development of the 'Spine Method' by Kistler[1983]; its practical implementation is discussed at length by Kistler & Scriven[1983]. In essence, the free surface is located at the termination of a number of 'spines' with fixed origins and direction (see Figure 5.20); only the height of the spines can vary, and these values $h_A, h_B, ..$ are determined as part of the full finite element solution.

Following Coyle et al [1986], Thompson[1992] has addressed the flow from the nip to the downstream free surface only in a first attempt to model Meniscus roll coating flow. In the fully-flooded forward roll coater the dimensionless flow rate ,Q, is determined as part of the solution, see Coyle et al [1986]. However when the coater is starved of fluid, the assumption that $p(-\infty) = 0$, which leads to the pressure condition at the nip, is no longer valid due to the appearance of an inlet meniscus. The effects of fluid starvation were therefore simulated by imposing the dimensionless flow rate Q to be smaller than its fully-flooded value. Consequently it is no longer possible to impose the condition on the pressure at the nip, so the nip pressures are free to be determined as part of the solution. This is appropriate since experiments suggest that Meniscus coating is surface tension controlled, i.e. the (sub-ambient) pressures in the fluid bead depend on the location of the free surfaces. Therefore it is not possible to determine the pressures by considering only one (the downstream) free surface.

The Navier-Stokes equations are solved by the Galerkin finite element method allied to Kistler's 'Spine Method' for free surface representaion, as described in Kistler & Scriven[1983]. The algebraic equations resulting from the finite element method are

solved iteratively using Newton's method. Results for the velocity and pressure fields and free surface location are calculated simultaneously.

5.4.3 Numerical Results

Figure 5.21 shows a comparison between (a) fully-flooded and (b) ultra-starved forward roll coating for a flow with $Re = 0.01, Ca = 0.1$. In the fully-flooded case, the dimensionless flow rate, ϵ, is equal to 1.33, whereas in the starved case $\epsilon = 0.3$. In particular, the reverse flow down the centre of the bead is readily observed. The structure of the Meniscus coating flow field is in good agreement with that observed experimentally, and the velocities obtained using the computerised particle tracking technique are comparable to those of the numerical simulation (see Figures 5.8(b) & (c)). Numerical film thickness predictions are also in good agreement with experimental results (see Thompson[1992]).

5.5 Conclusions

This study has revealed the presence of a 'new' roll coating regime, using experimental flow visualisation techniques. The key features of this flow include a fully two-dimensional flow field, consisting of two primary recirculation regions for the forward rolling case, and one for the reverse rolling case.Of particular interest is the snaking transfer path of fluid onto the upper roll. Although this flow appears complex, it can be described by simple mathematical models which capture important features of the flow. Alongside the experimental and analytical approaches, a more realistic free surface finite element scheme has been developed by Thompson[1992] to investigate this phenomenon.

In the first model, which is for the idealised situation of zero flux, the problem re-

duces to the solution of a biharmonic boundary value problem for the streamfunction whose solution exhibits some important characteristics of Meniscus roll coating, i.e. separation of the flow into two vortices in the forward case and a single vortical structure for reverse flow are predicted. The pressure profiles for Meniscus roll coating are also markedly different from those in Classical roll coating in that there is no longer a pressure peak in the fluid bead, instead there is a constant pressure gradient in the central core. Experimental results have confirmed the predictions of the model of a linear pressure gradient and have provided the location of the pressure distribution with respect to atmospheric pressure. The key result of a sub-ambient pressure distribution throughout the fluid bead is both interesting and surprising.

In the finite-flux model (Thompson[1992]), the flow in the central core of the bead is modelled by the assumptions of Poiseuille plus Couette flow with a constant pressure gradient. This simplified profile has been used to predict film thicknesses using the observation that the predictions of any model must tend uniformly to the zero flux case as the flux, Q, tends to zero. Preliminary results from this Meniscus roll coating film thickness model are most encouraging.

Experimental results of film thickness versus roll speed ratio for the Meniscus regime are in good agreement with predictions of the above model, which in turn are in marked contrast to those for the Classical case. In particular, the independence of film thickness on roll gap size (and therefore roll eccentricities, for example) for Meniscus coating may partly explain why this system produces superior quality coatings (in terms of uniformity). In addition the identical behaviour of h_1/h_2 versus S in both the Classical and Meniscus regimes is surprising but not remarkable when one begins to compare the flow field in the fully-flooded upstream bank with that in the ultra-starved bead. In addition, the predictions of Thompsons'[1992] finite element simulation are in good

agreement with the observed flow field and film thickness measurements.

Having now obtained experimental evidence of the marked differences in the two 'extremes' of roll coating flow; those of fully-flooded and ultra-starved conditions, the key question is how does the flow transform from one regime to the other. This is addressed in the next chapter.

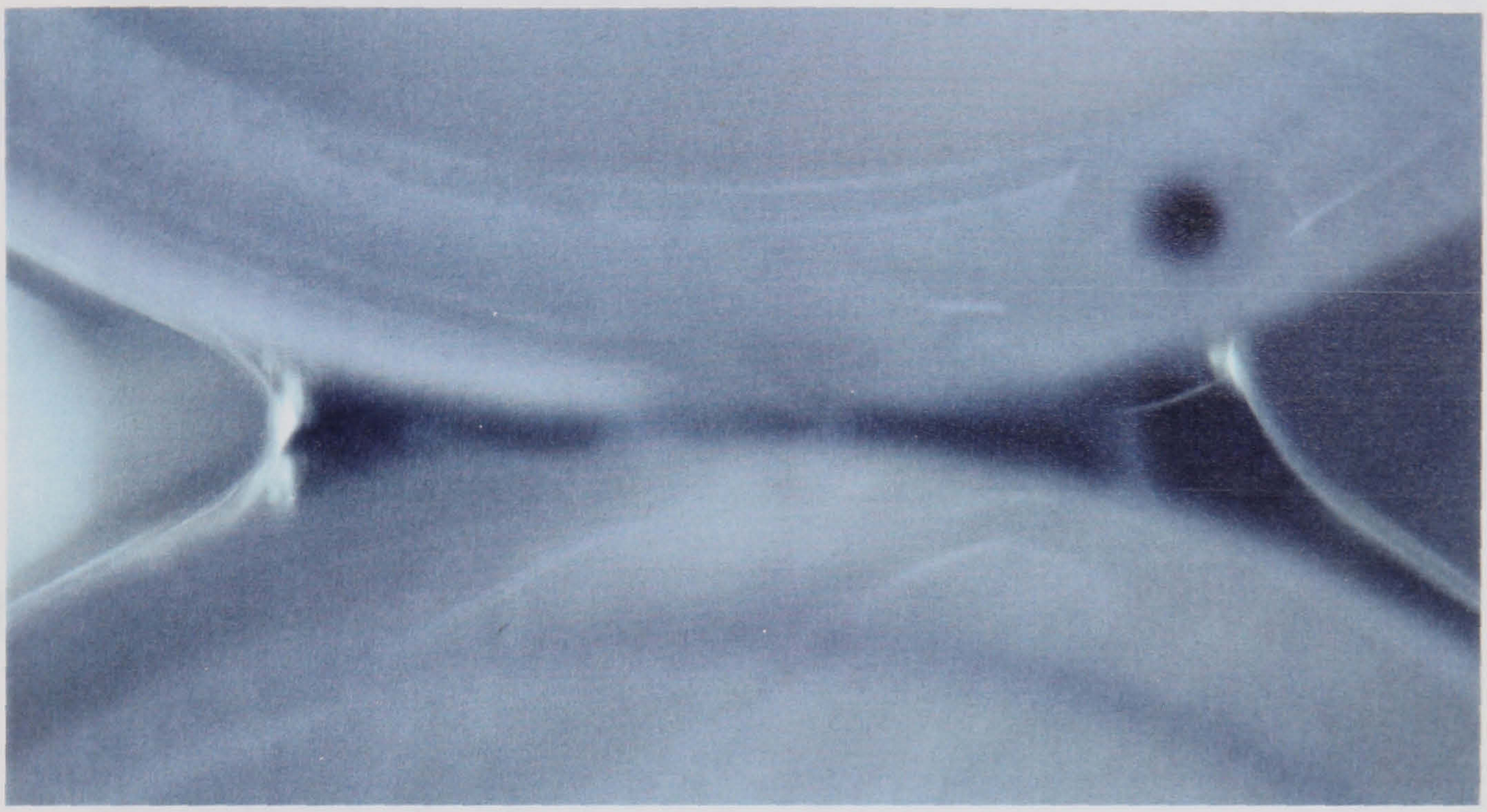

(a)

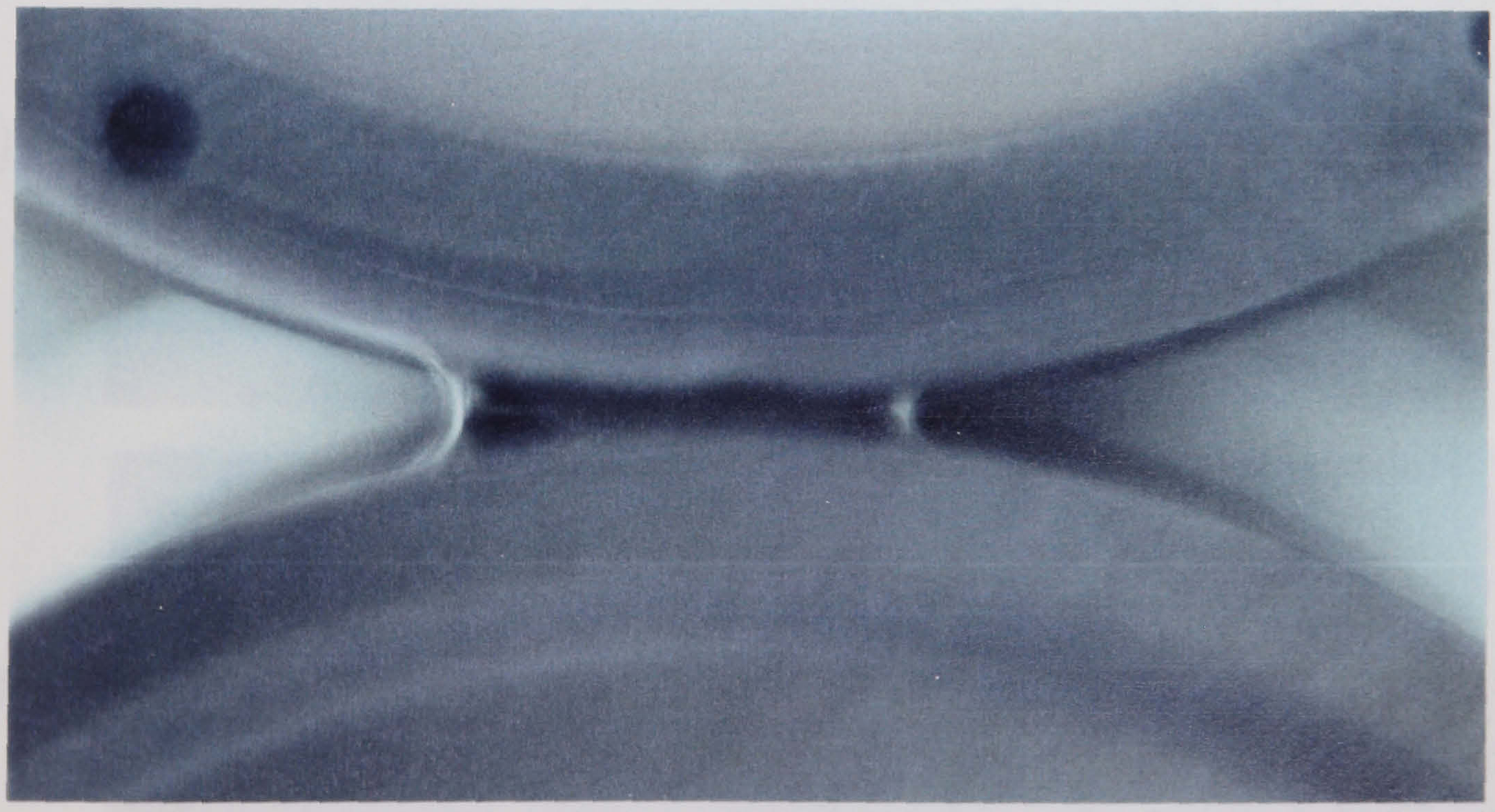

(b)

Figure 5.1: (a) Fully-flooded roll coating 'profile', (b) Ultra-starved roll coating 'profile'

(a)

(b)

(c)

(d)

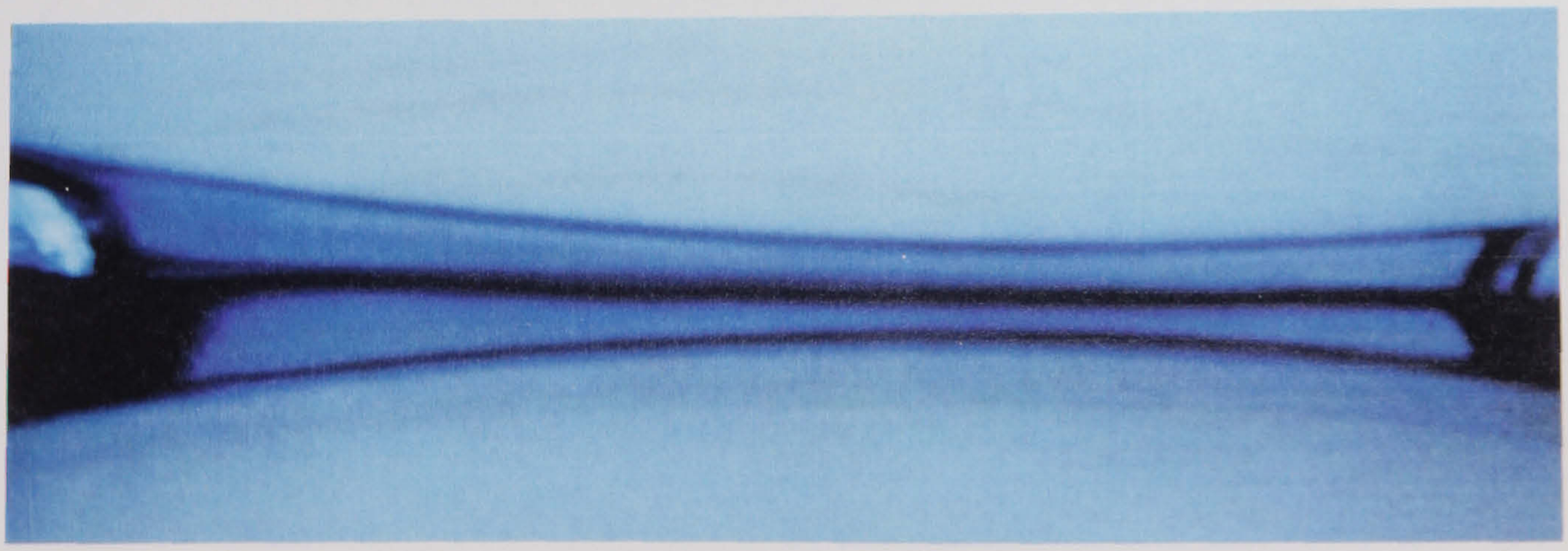

Figure 5.2: Dye injection sequence for Meniscus (ultra-starved) roll coating

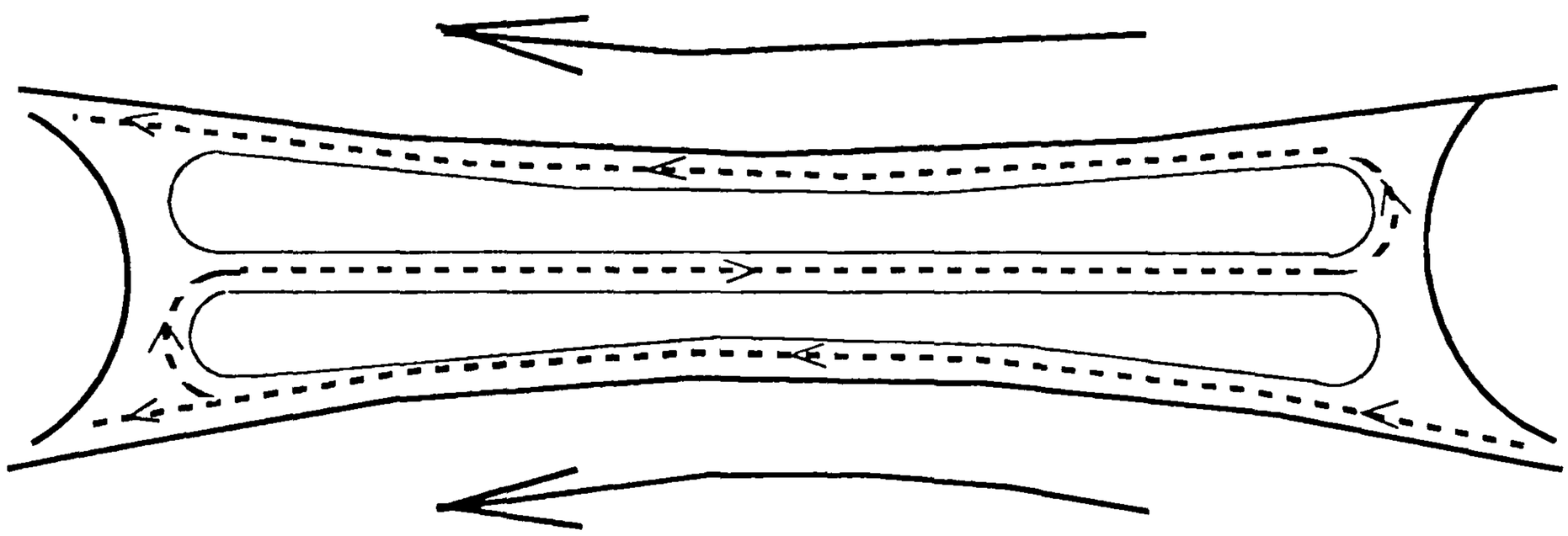

(a)

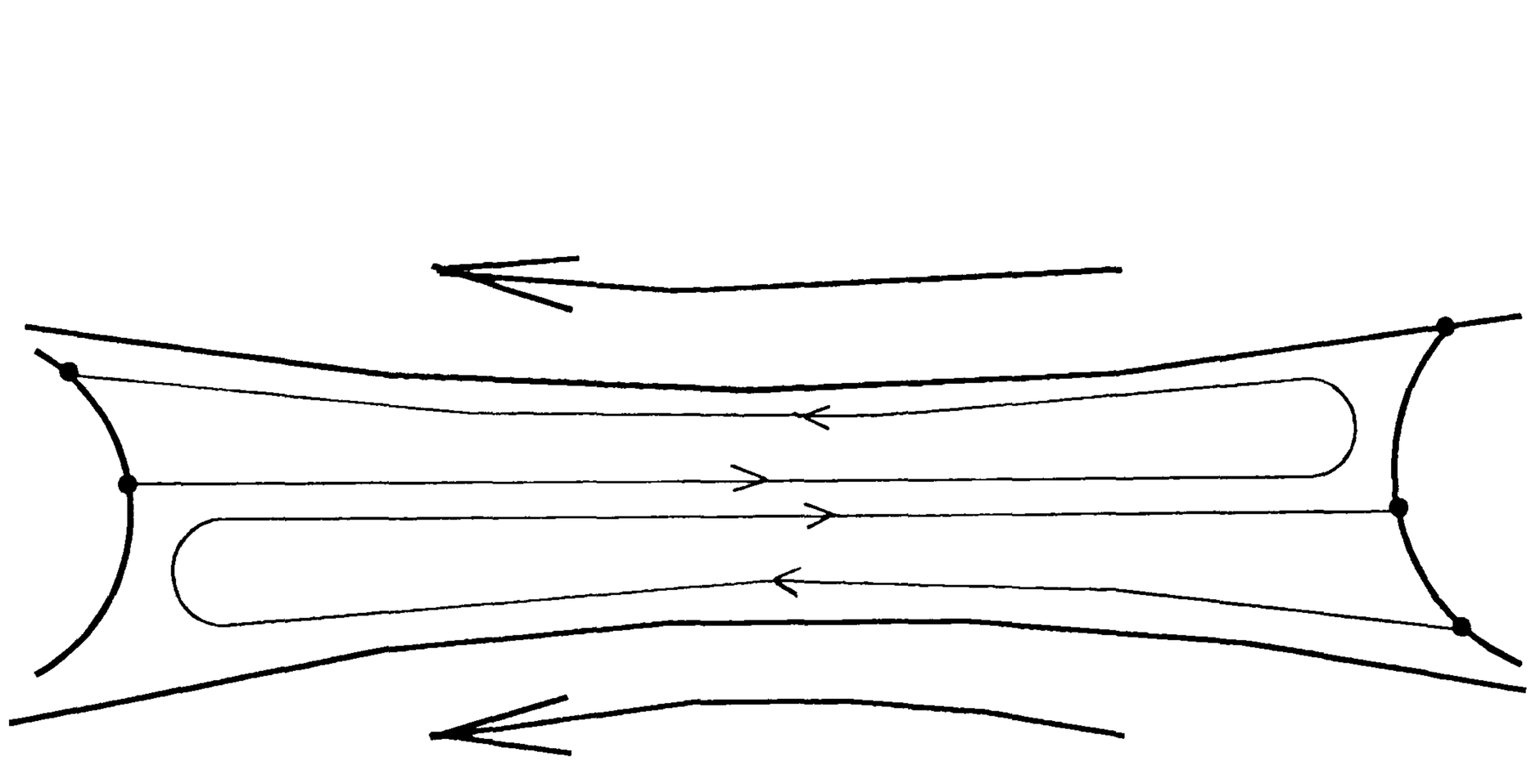

(b)

Figure 5.3: Schematic diagrams showing (a) Fluid transfer path from inlet to upper roll, (b) Eddy structure and stagnation points

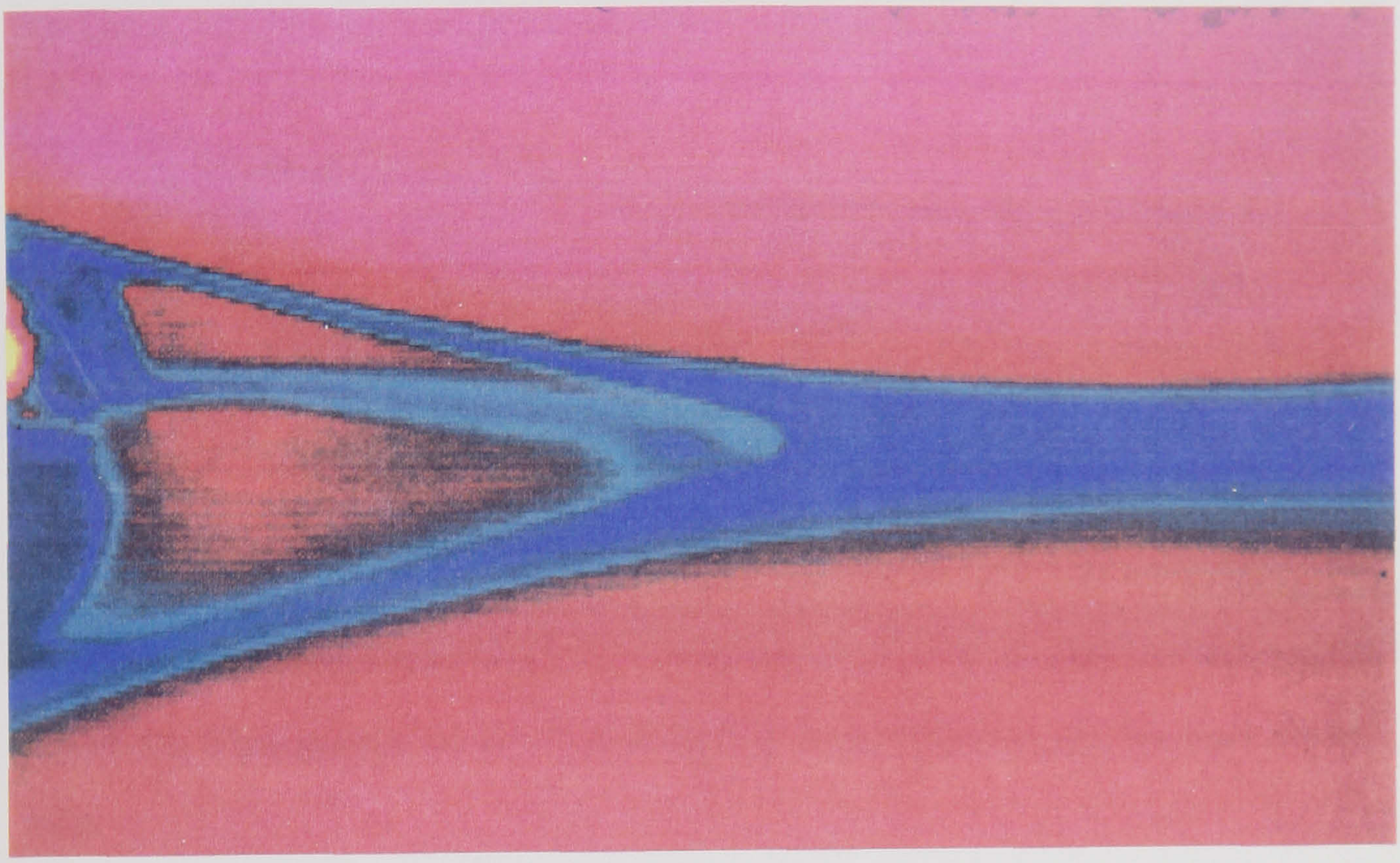

(a)

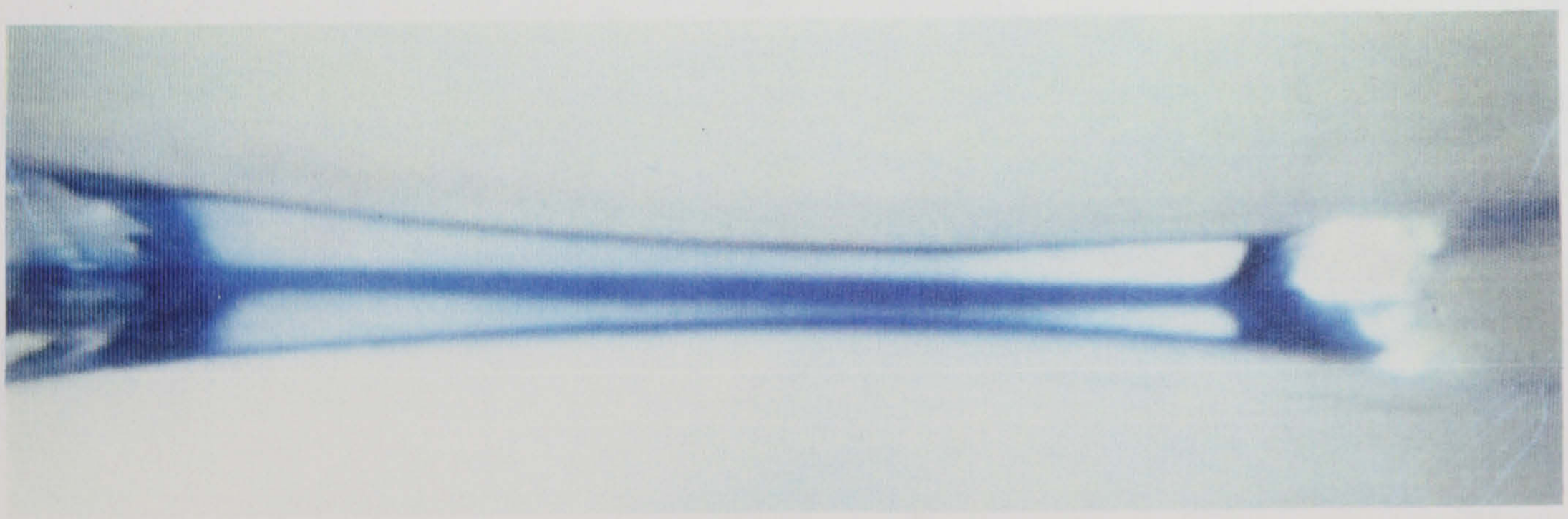

(b)

Figure 5.4: Comparison of (a) Classical roll coating nip flow, and (b) Meniscus roll coating nip flow

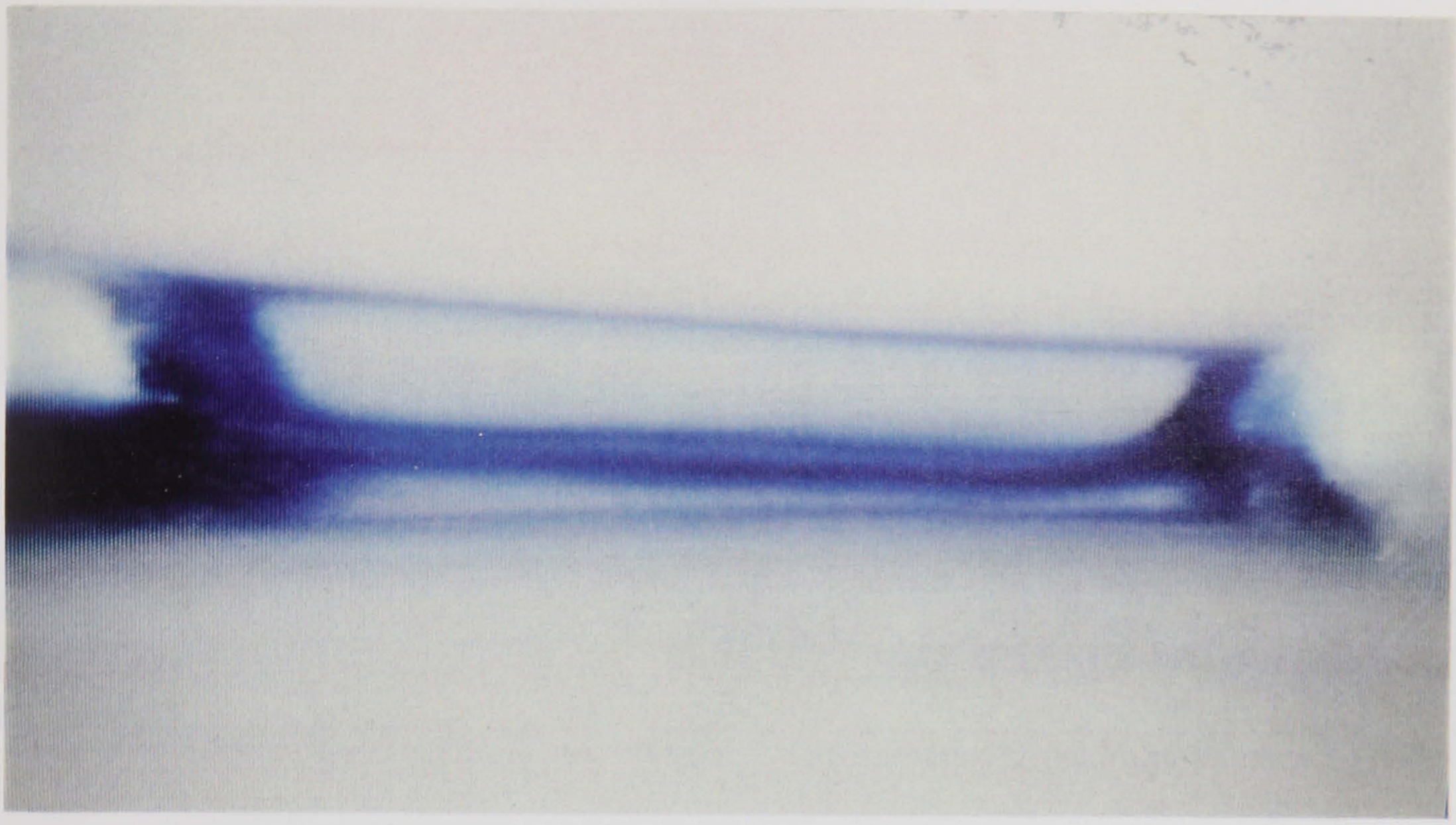

Figure 5.5: Flow pattern for $S = 2$ showing differential eddy size and low bead aspect ratio

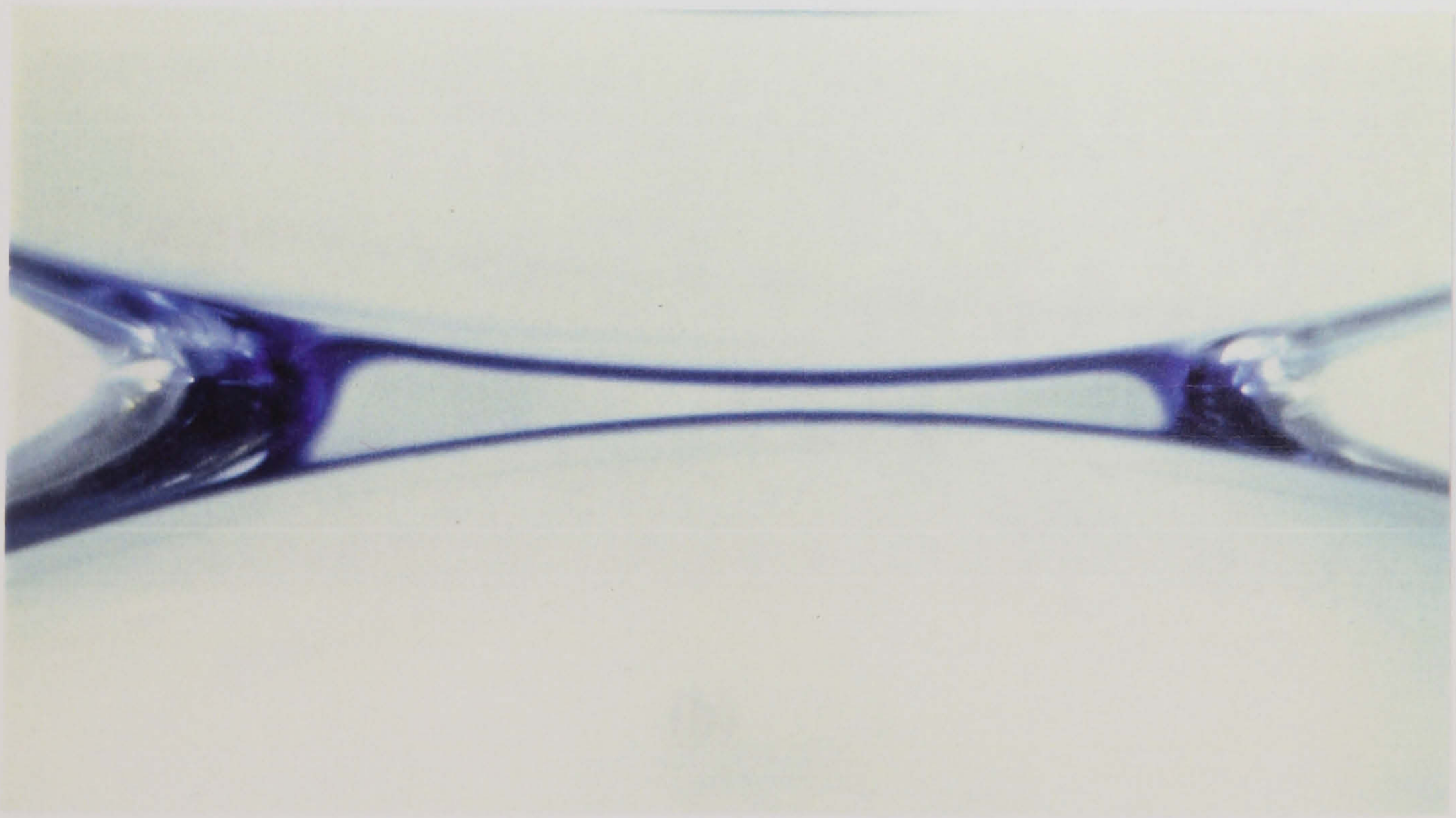

Figure 5.6: Reverse Meniscus roll coating flow (lower roll moving from left to right, upper roll from right to left

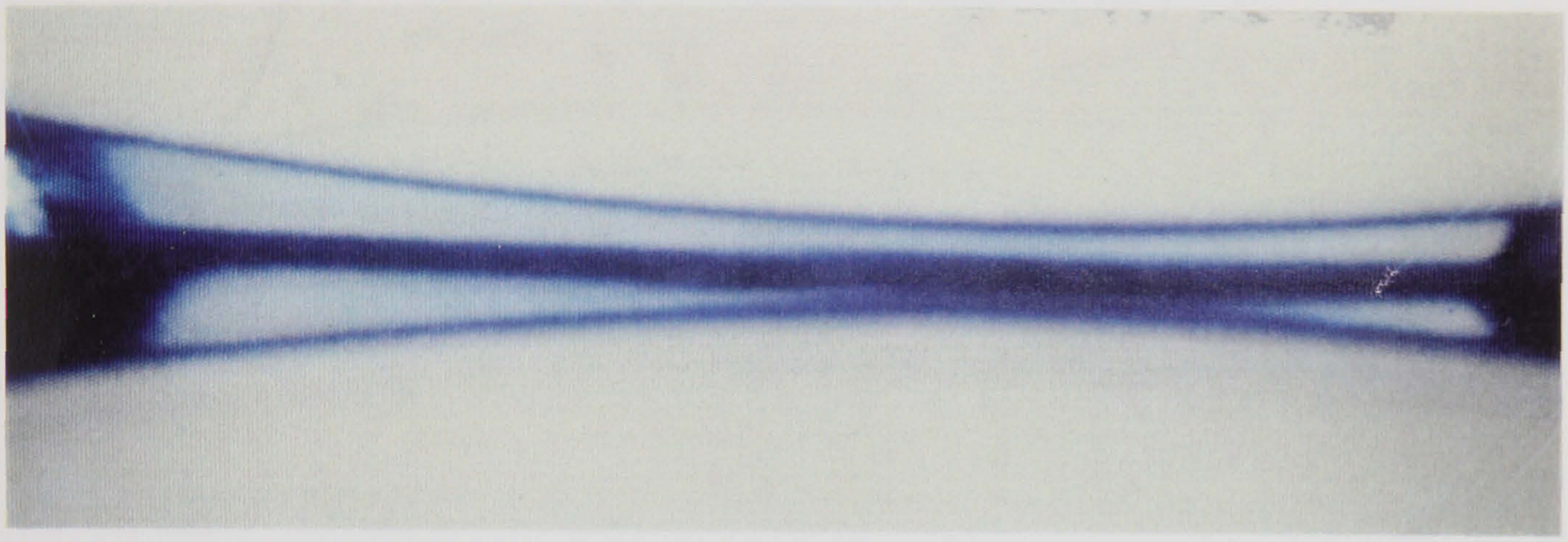

(a)

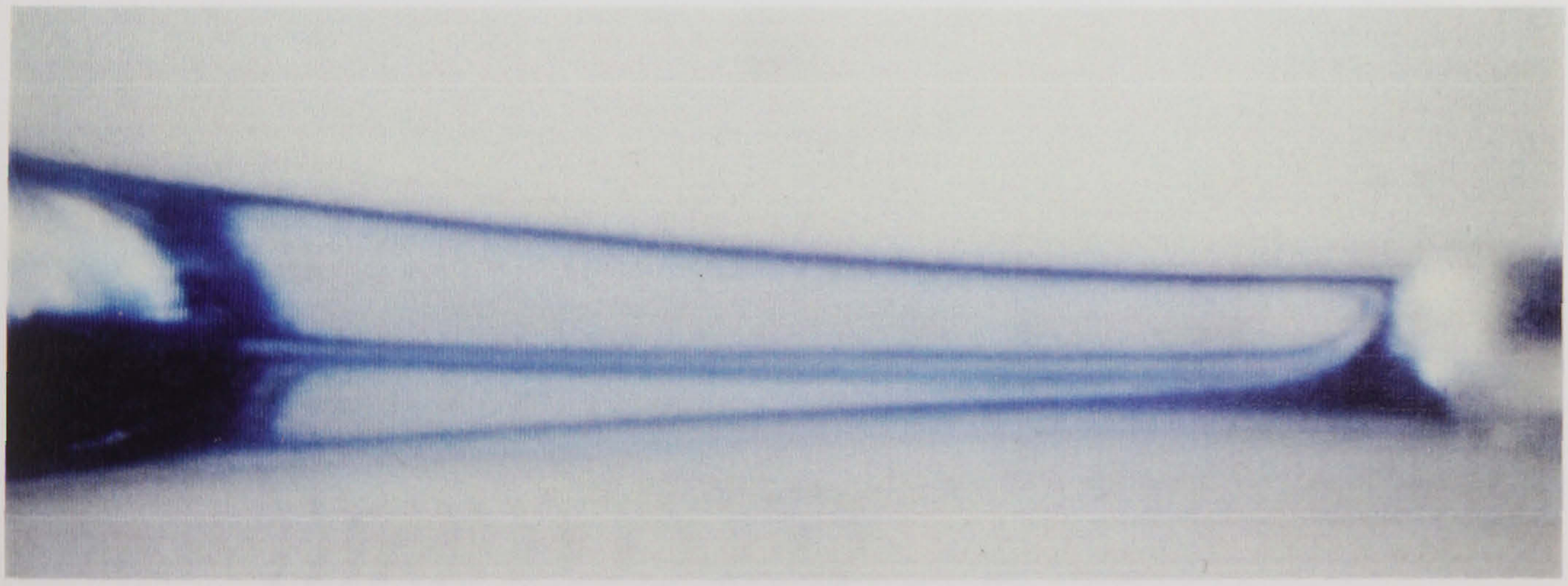

(b)

Figure 5.7: Flow pattern showing (a) 'nipping' effect within lower recirculation, (b) separation of small vortex (concentrated in lower right corner of the fluid bead

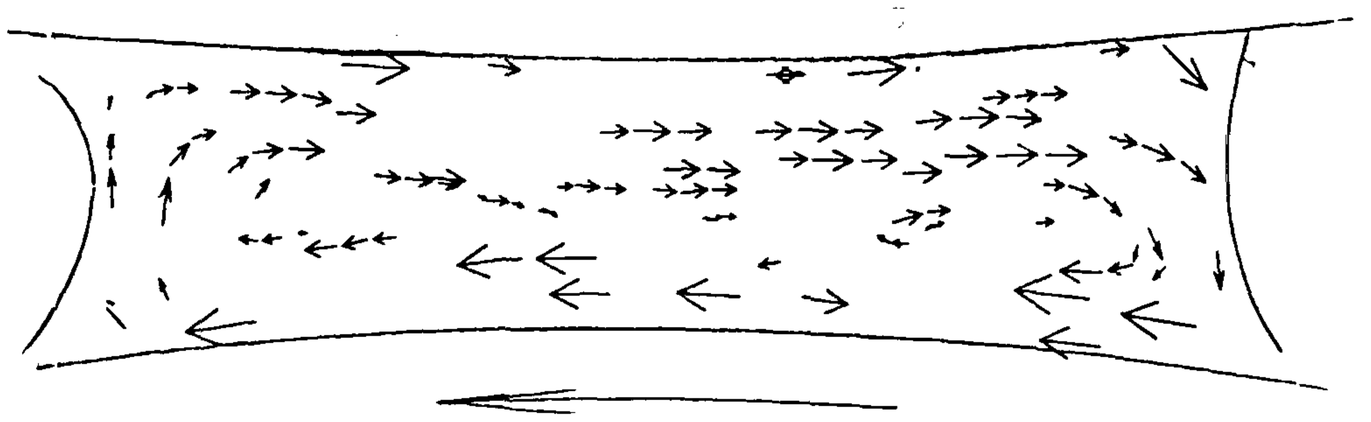

(a)

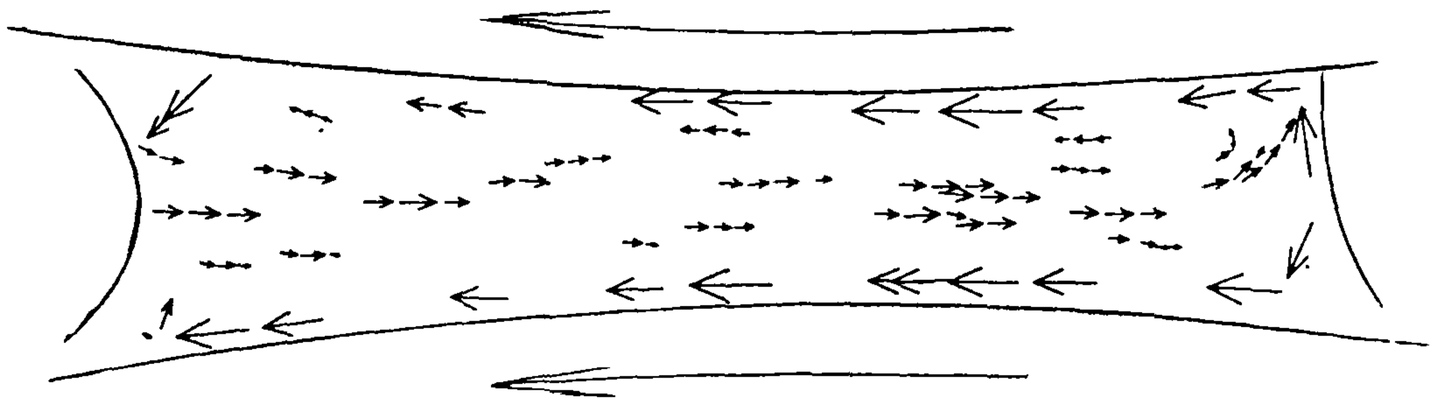

(b)

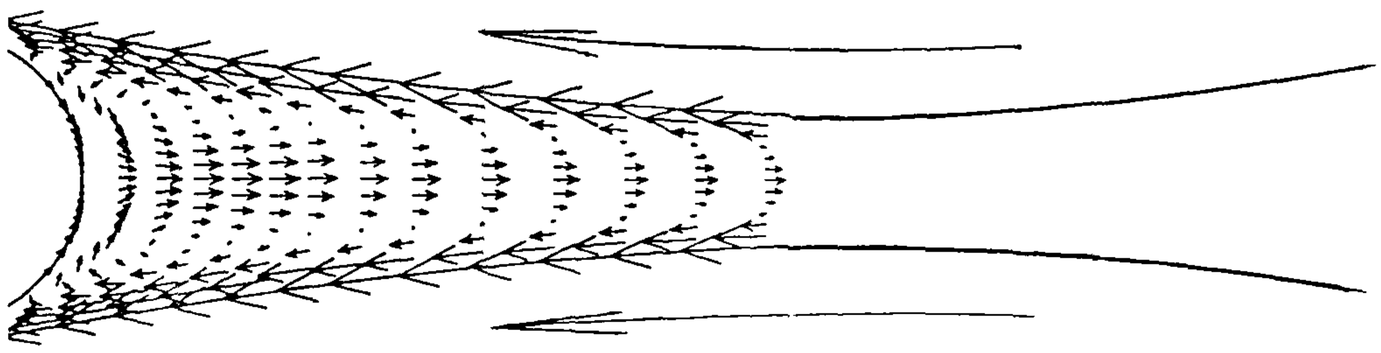

(c)

Figure 5.8: Computerised particle tracking velocity plots (a) Reverse Meniscus roll coating, (b) Forward Meniscus roll coating, (c) Finite element prediction (Thompson[1992])

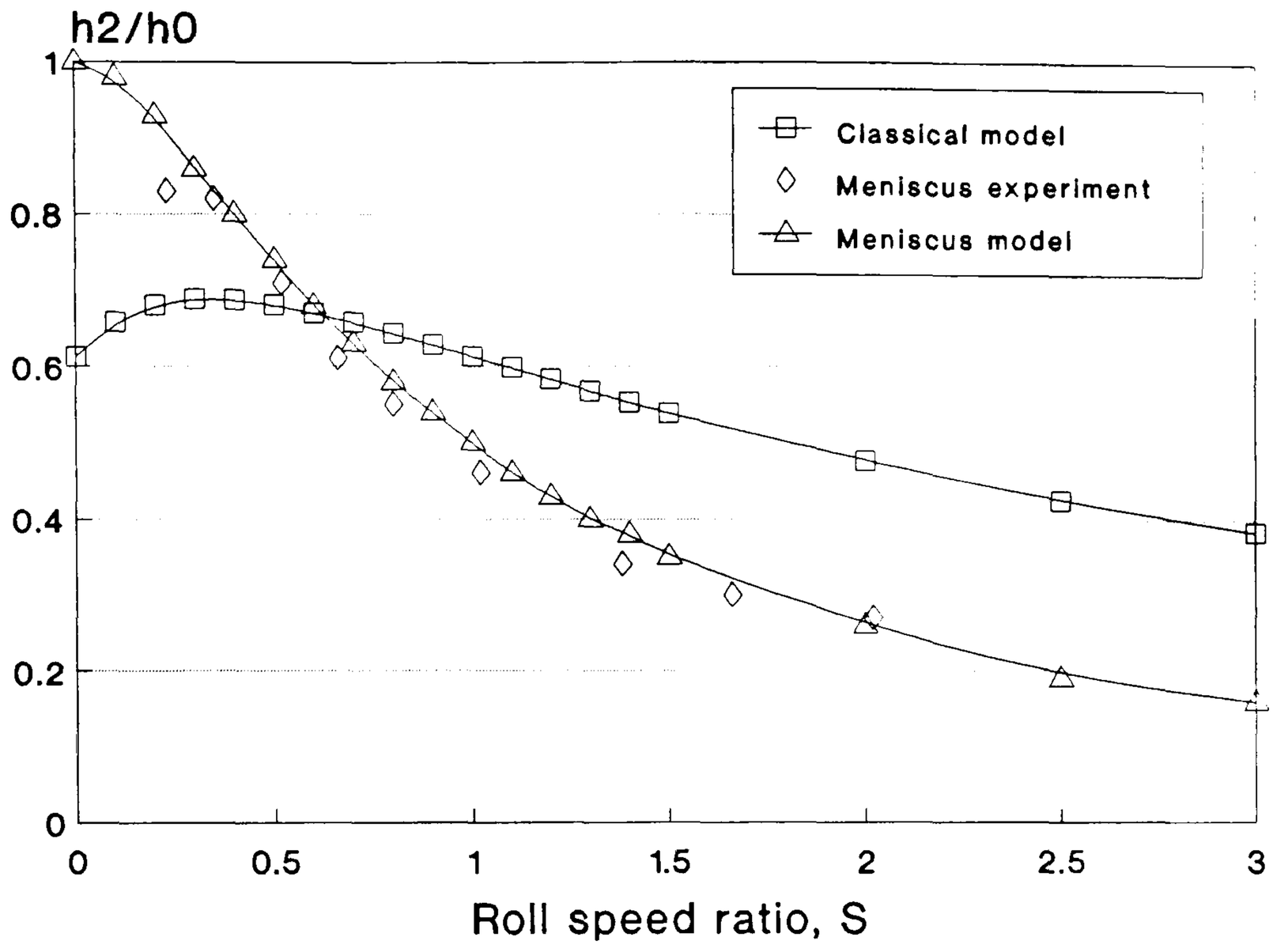

Figure 5.9: Comparison of inlet/outlet film thickness ratio versus speed ratio results of Meniscus roll coating with Classical roll coating predictions: h_2/h_0.

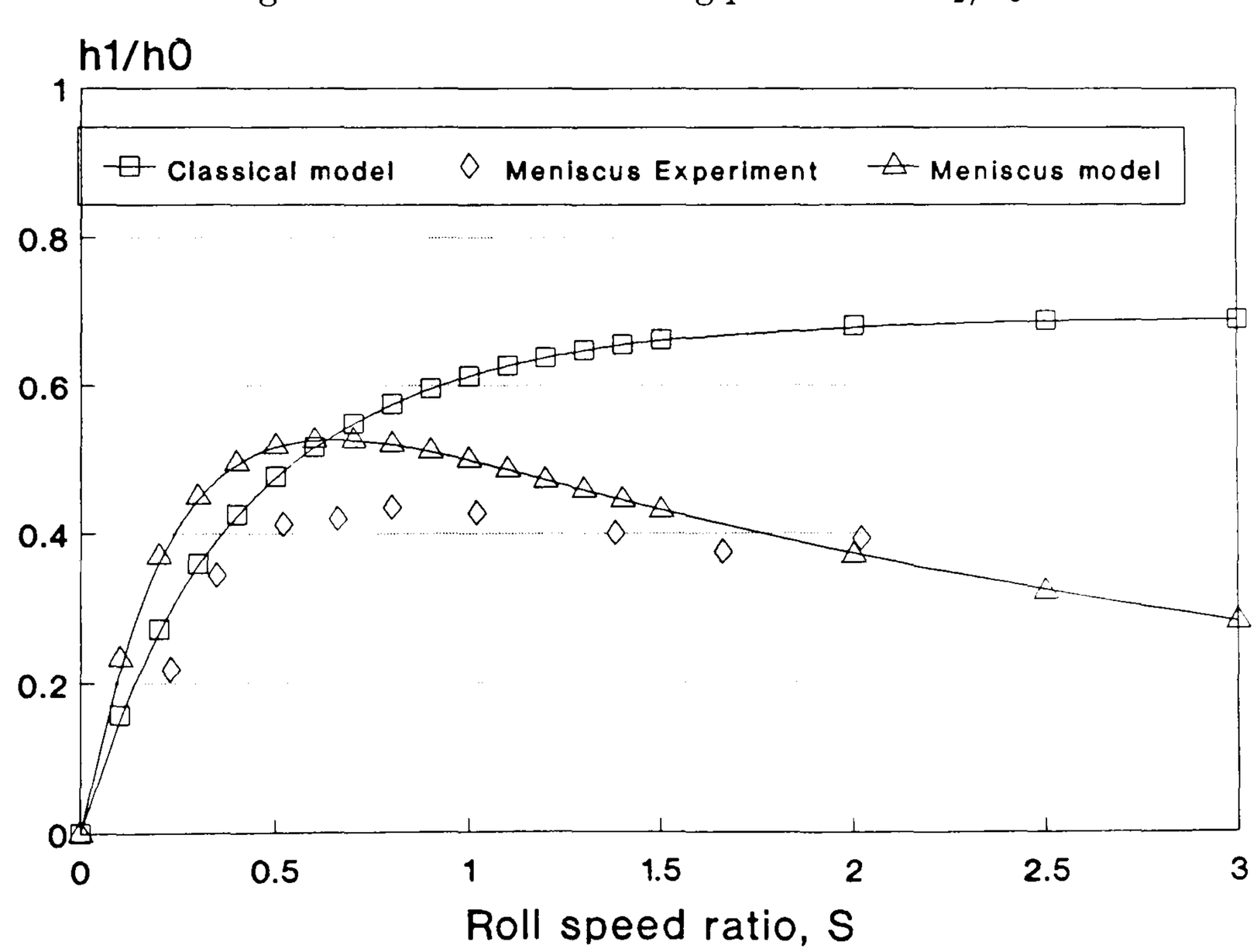

Figure 5.10: Comparison of inlet/outlet film thickness ratio versus speed ratio results of Meniscus roll coating with Classical roll coating predictions: h_1/h_0.

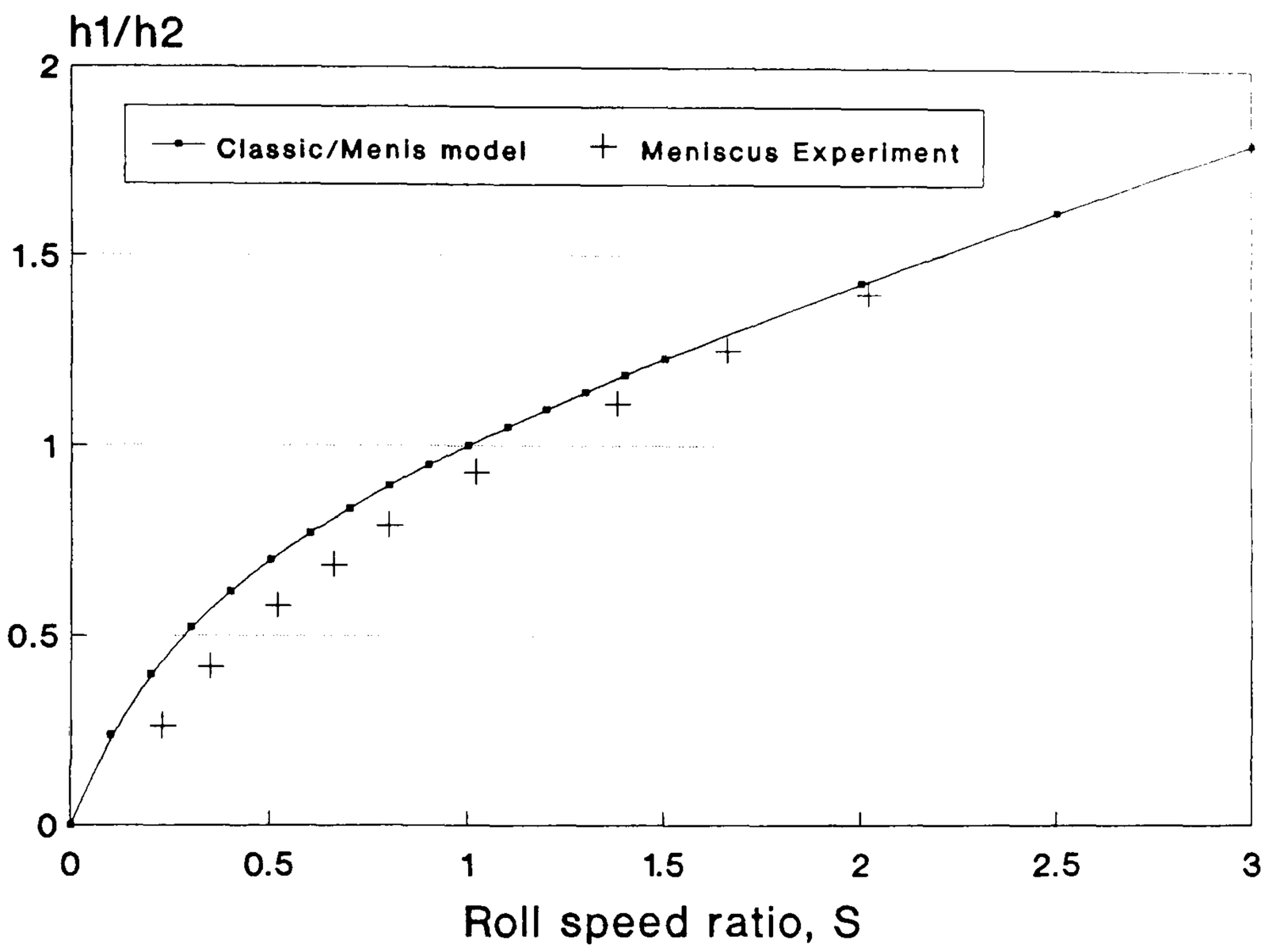

Figure 5.11: Outlet film thickness ratio, h_1/h_2, versus roll speed ratio: Experimental/theoretical comparison

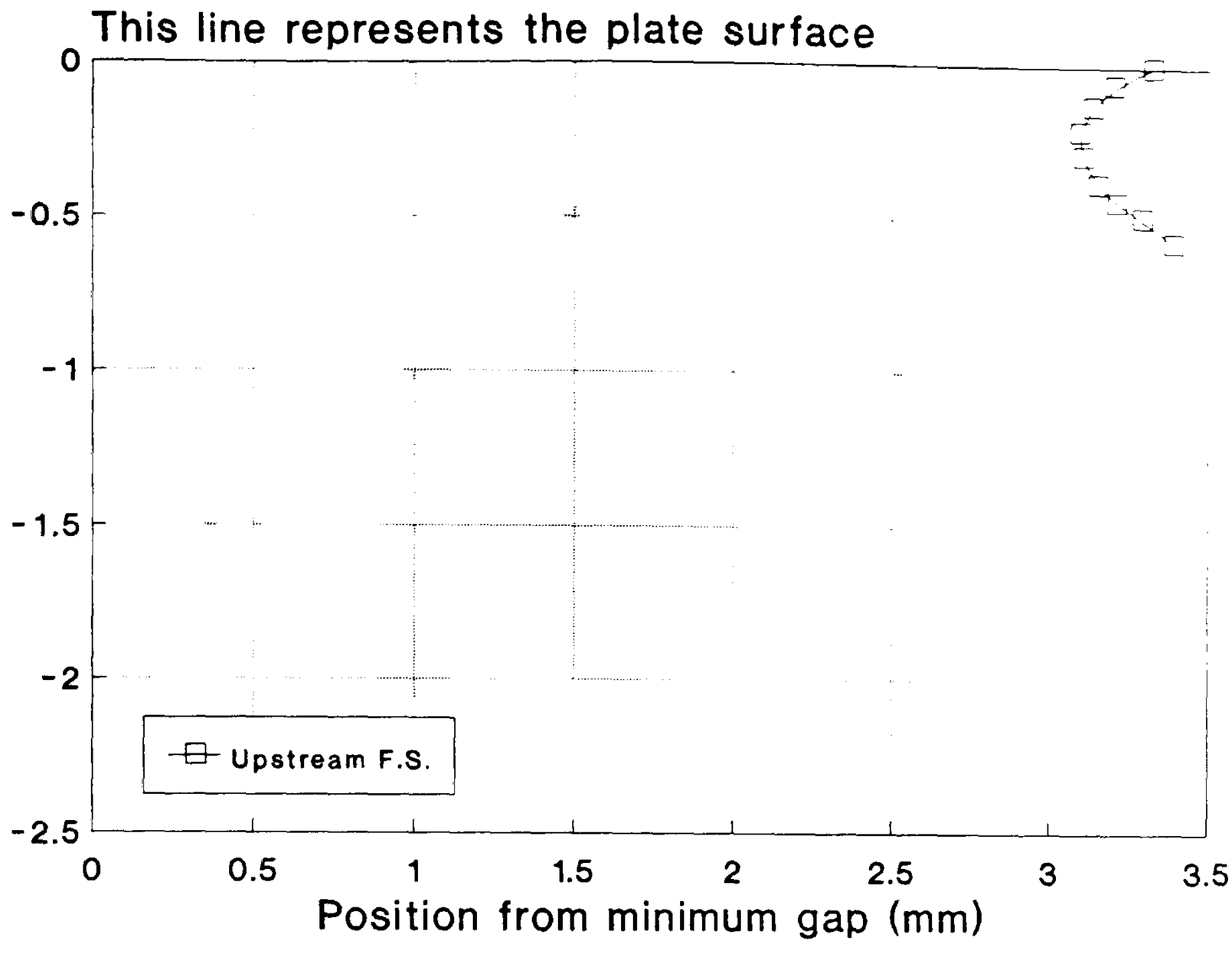

(a)

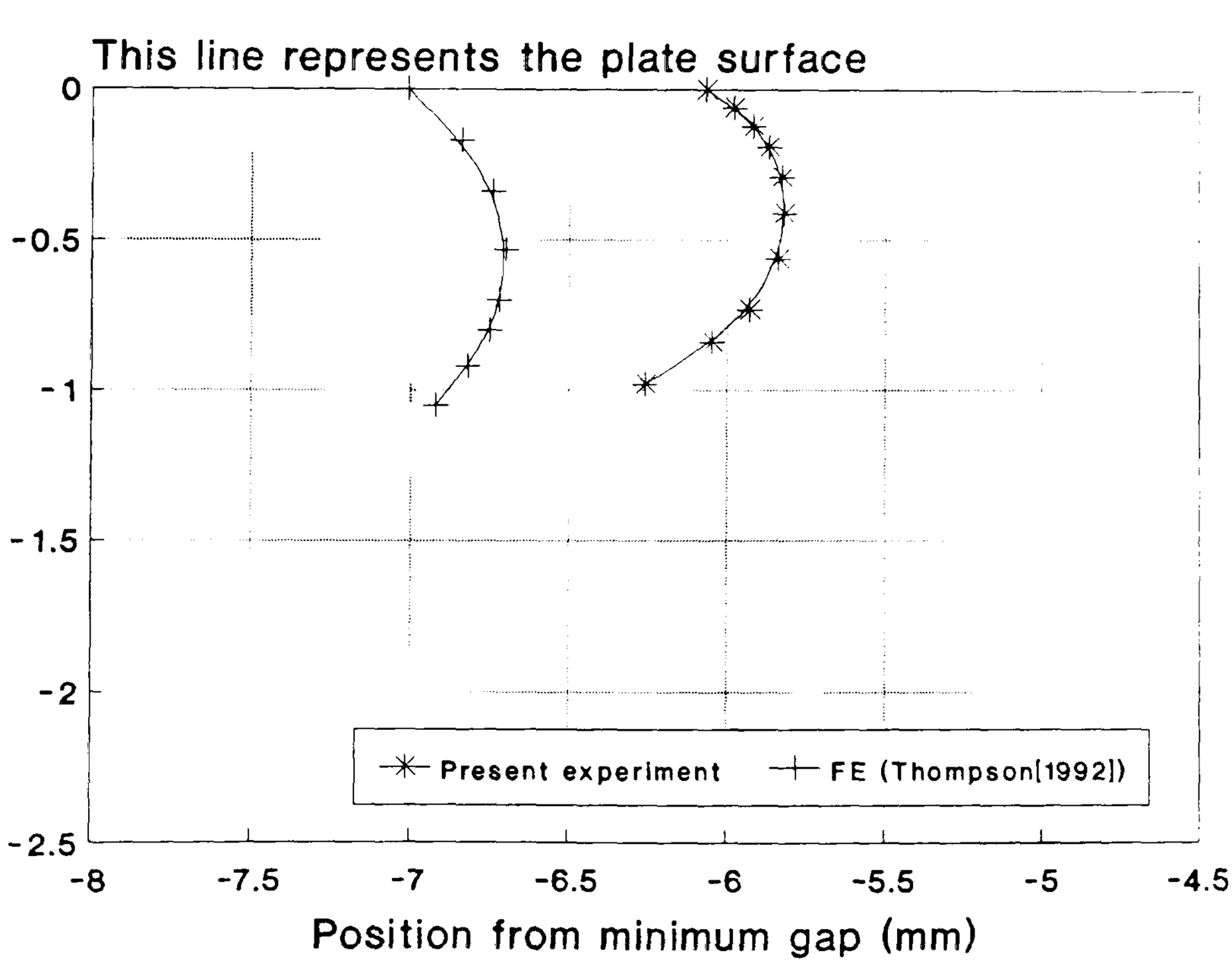

(b)

Figure 5.12: Free surface profile and position (a) upstream, (b) downstream. Comparison with finite element predictions (Thompson[1992]); $R/H_0 = 110$, $Ca = 0.01$, $\epsilon = 0.13$

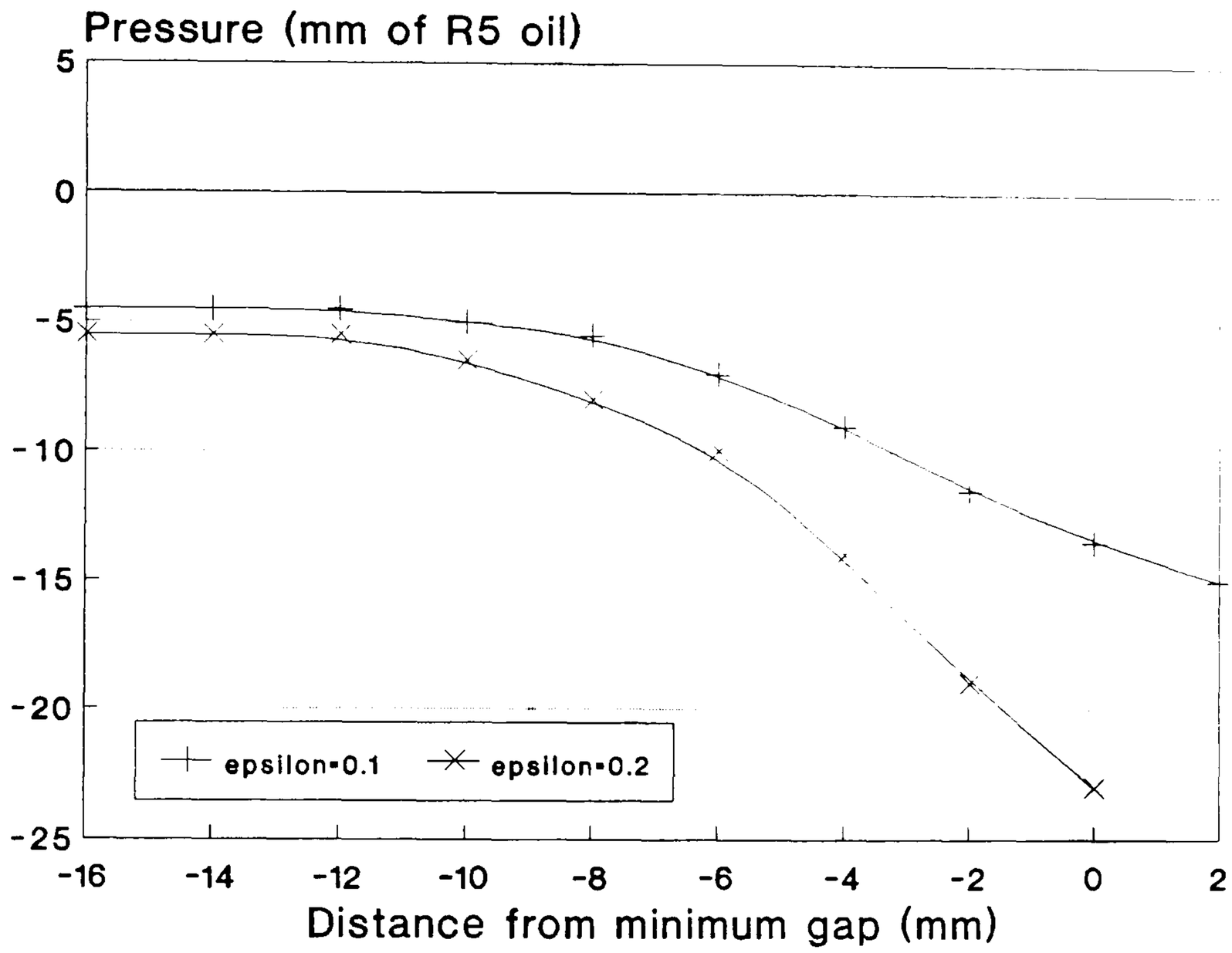

Figure 5.13: Experimental pressure results for Meniscus roll coating

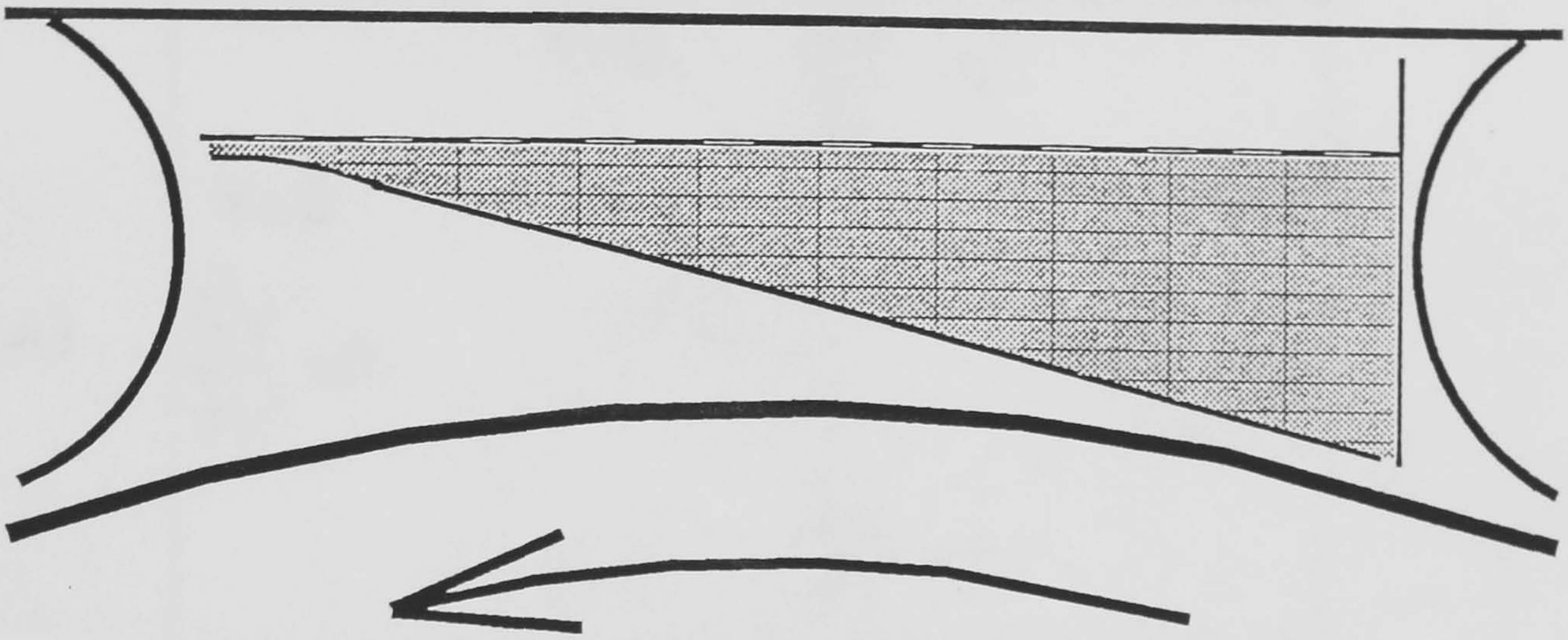

(a)

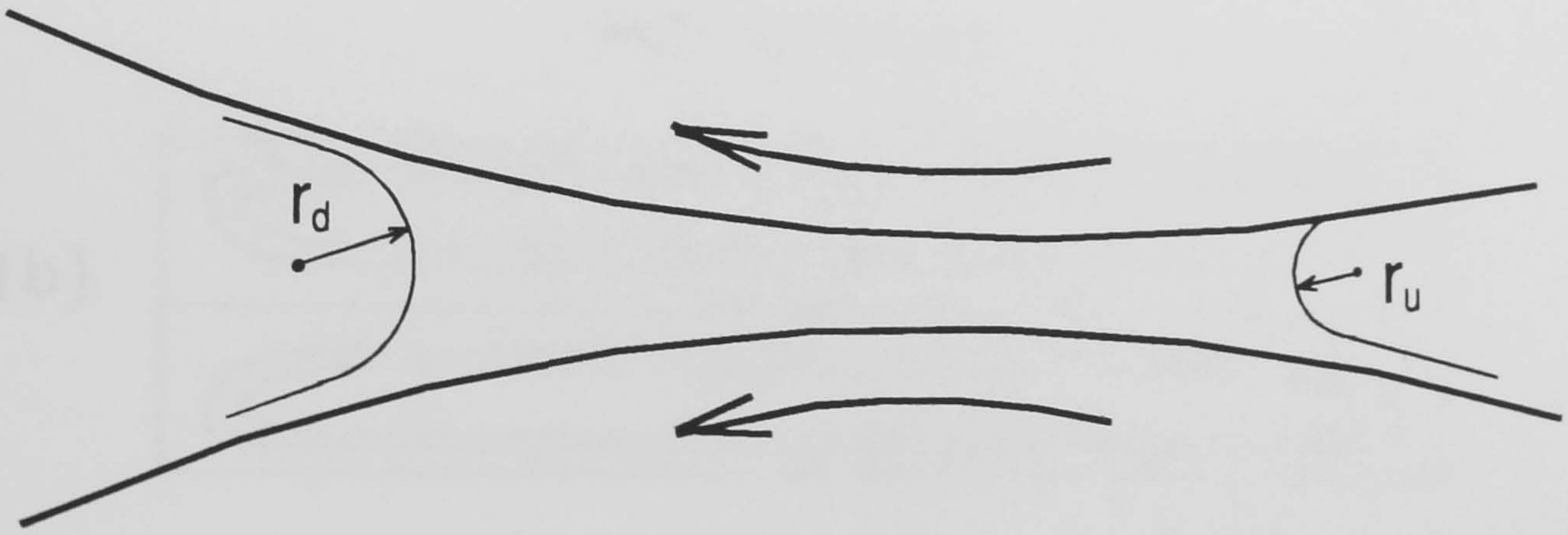

(b)

Figure 5.14: Schematic view of (a) pressure distribution across the fluid bead, (b) Upstream and downstream differences in radii of curvature

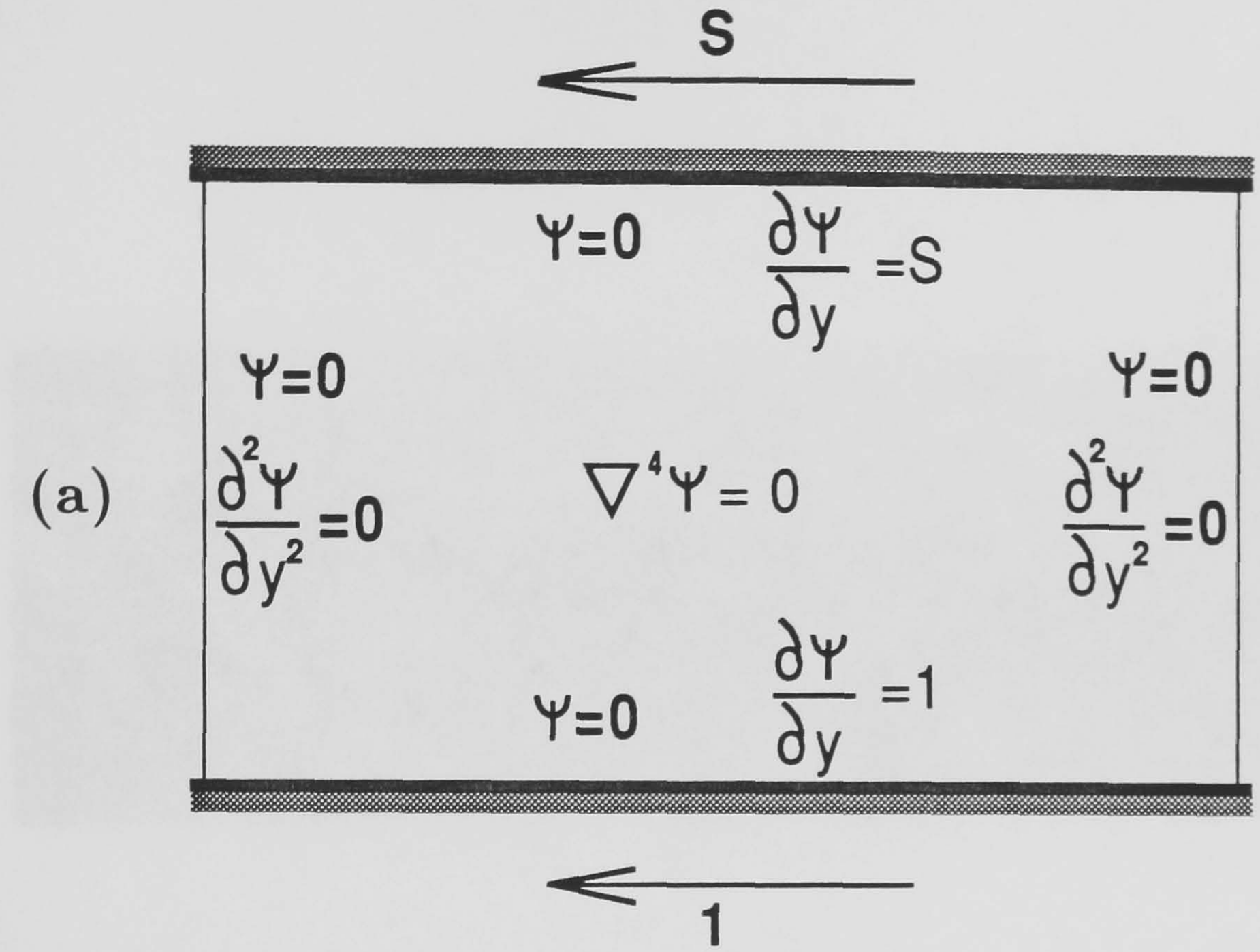

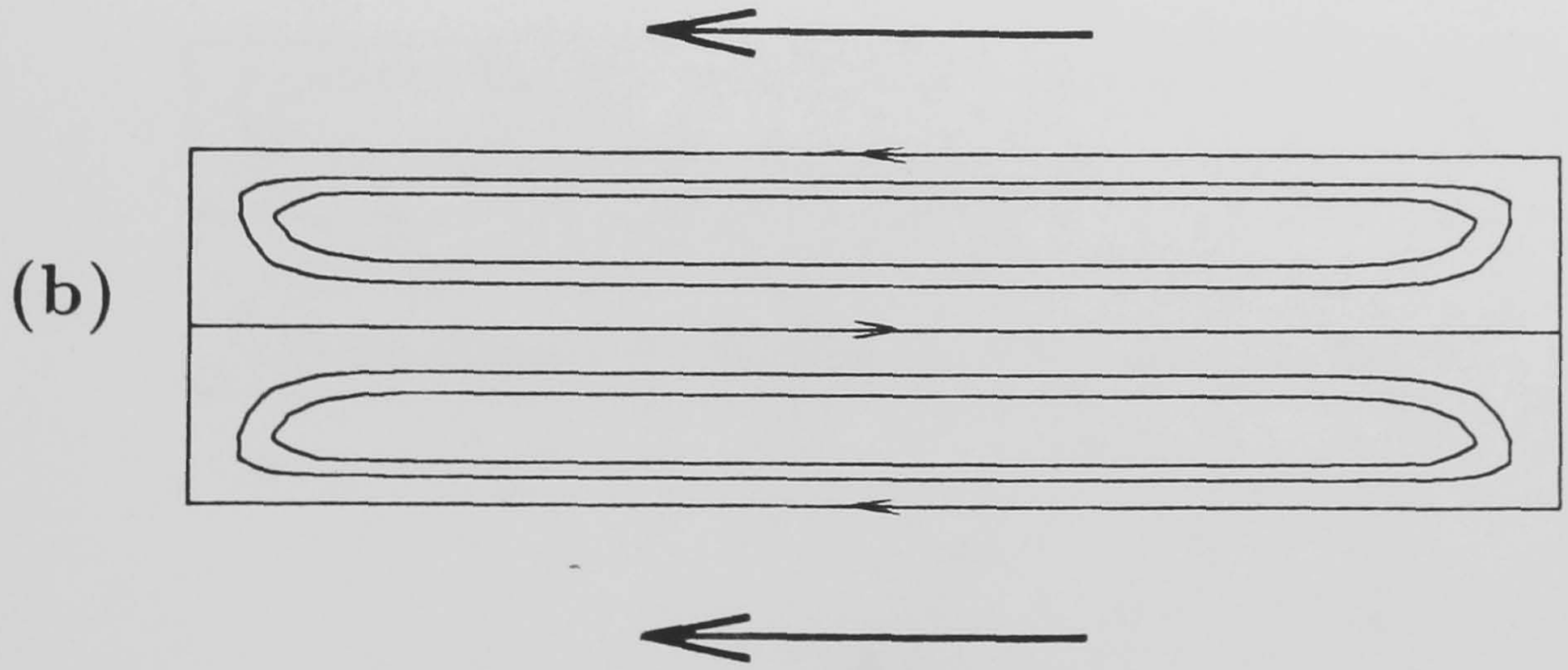

Figure 5.15: (a) Formulation of the zero-flux model (Thompson[1992]), (b) Streamline predictions for equal upper and lower lid speed

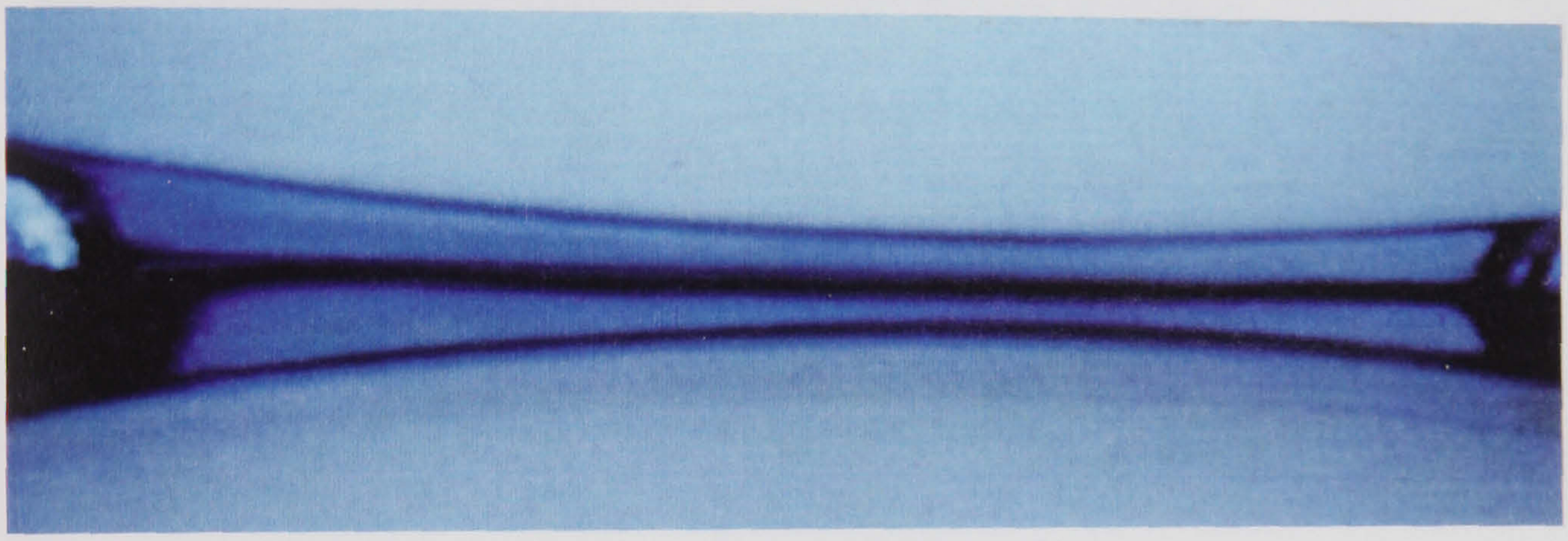

(a)

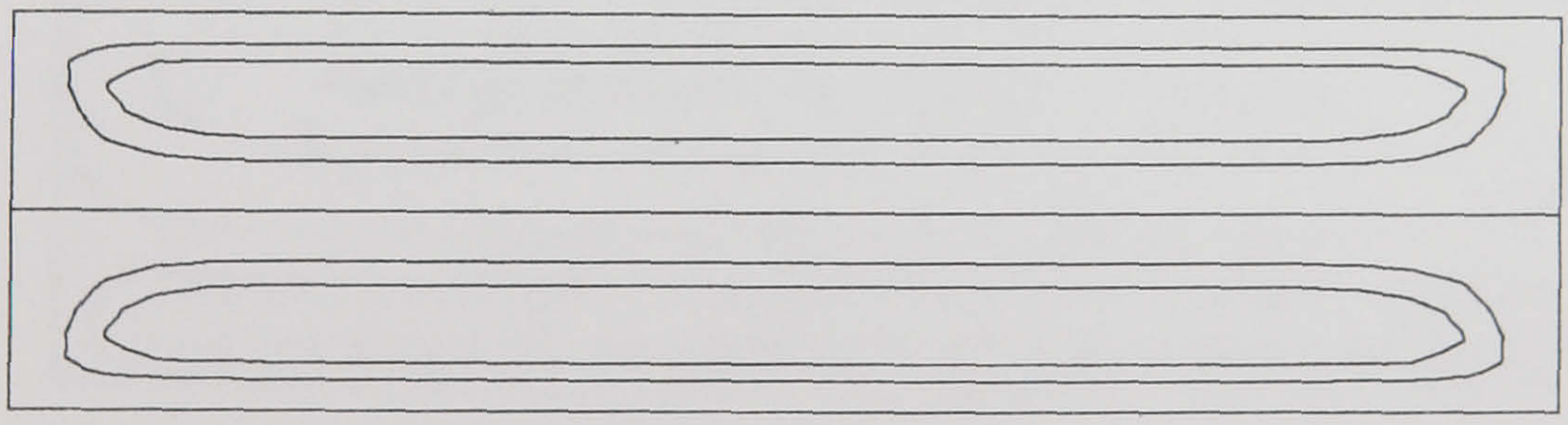

(b)

Figure 5.16: Comparison of (a) dye injection flow image with (b) zero-flux model prediction, for $S = 1$.

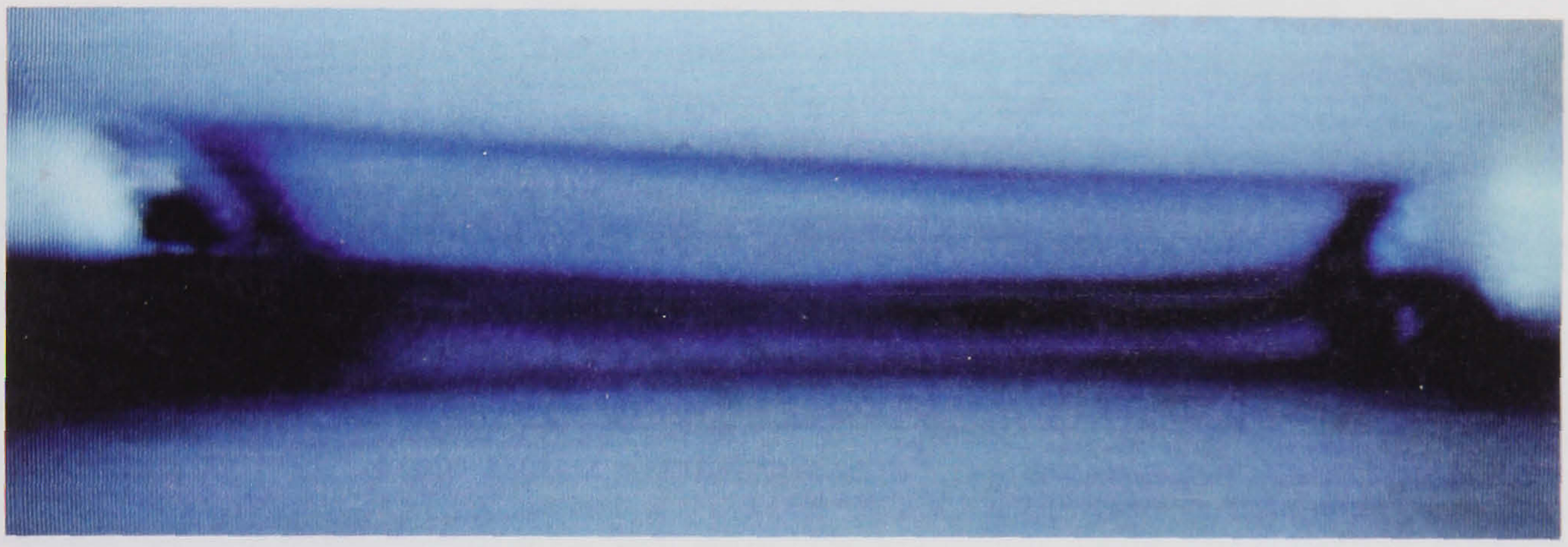

(a)

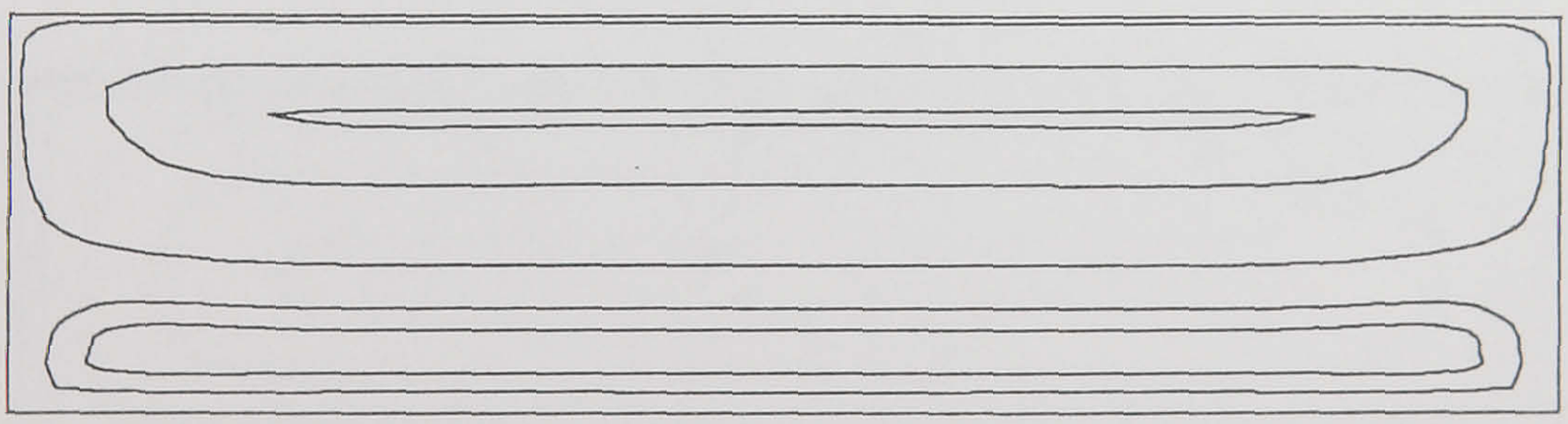

(b)

Figure 5.17: Comparison of (a) dye injection results and (b) zero-flux model predictions, for $S = 2$

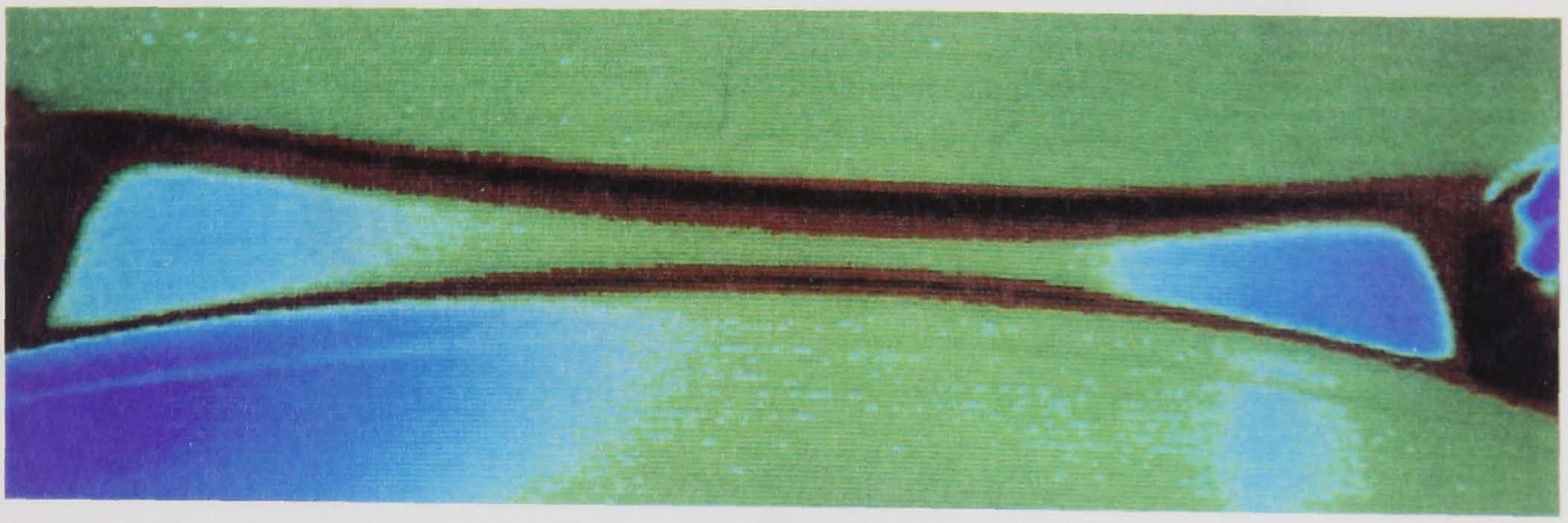

(a)

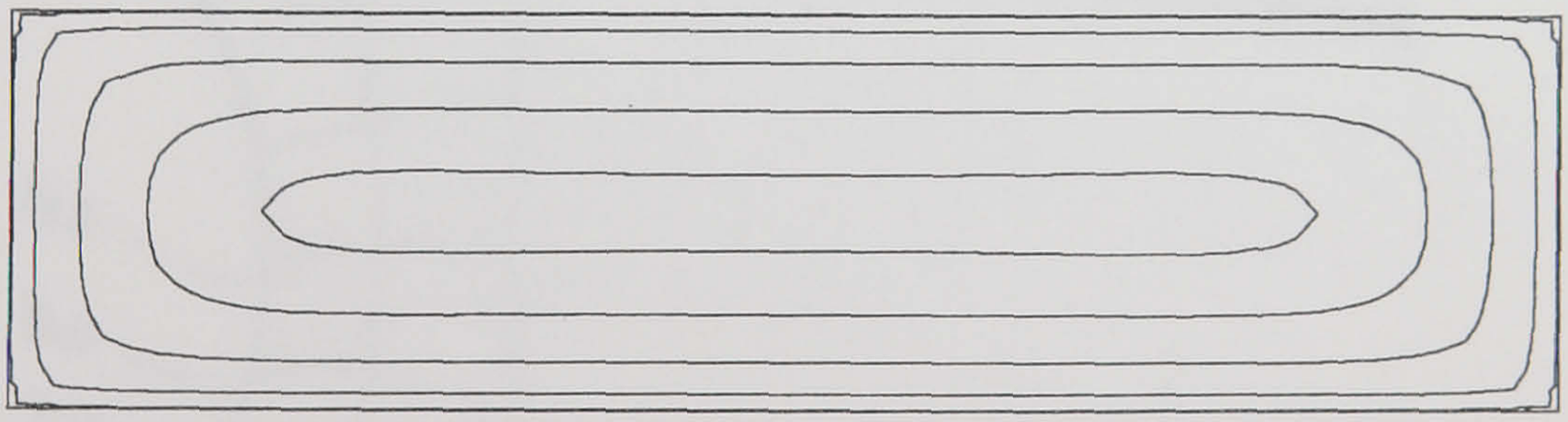

(b)

Figure 5.18: Comparison of (a) dye injection results and (b) zero-flux model predictions, for $S = -1$ (i.e. reverse Meniscus roll coating)

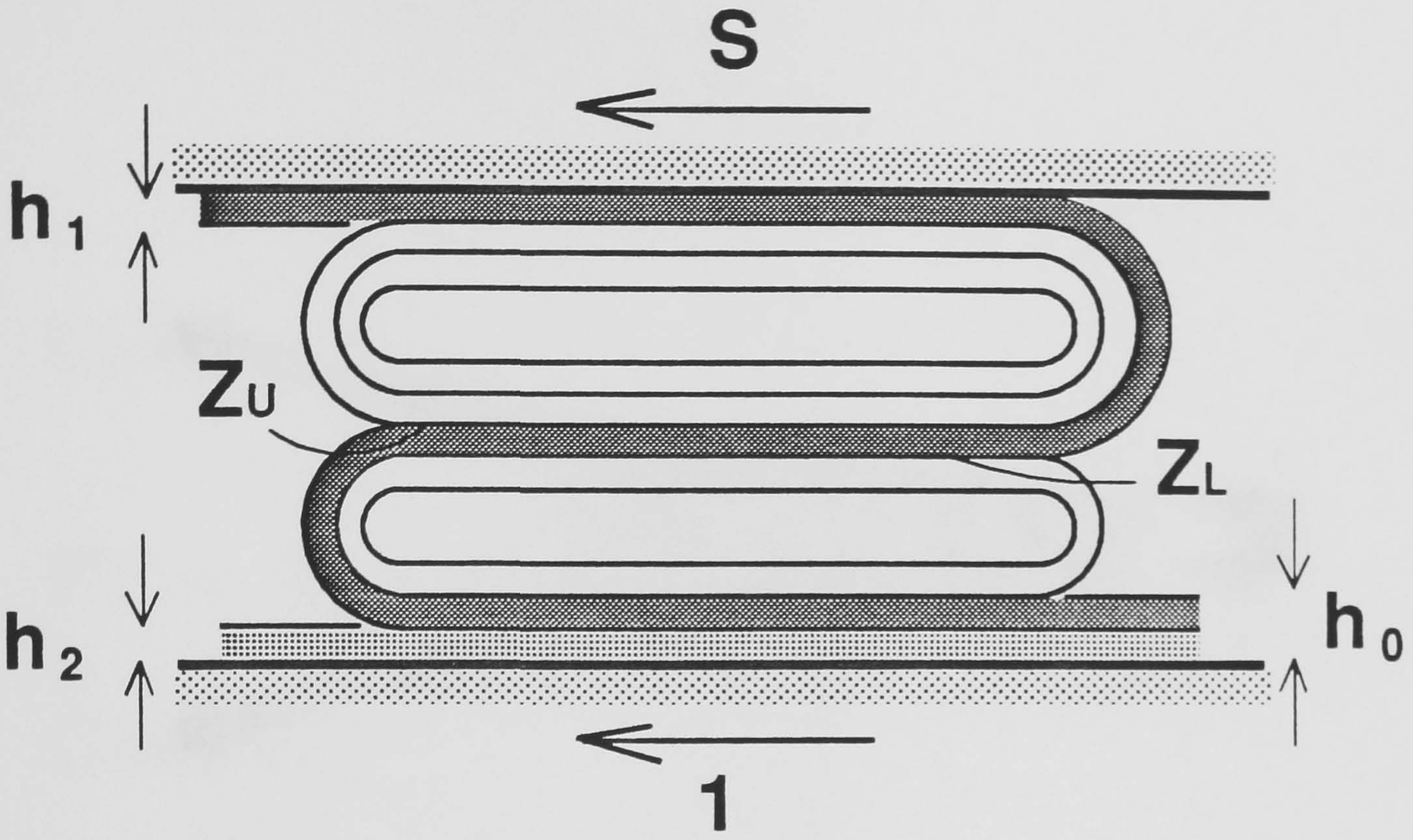

Figure 5.19: Analysis of fluid transfer path for finite-flux model formulation

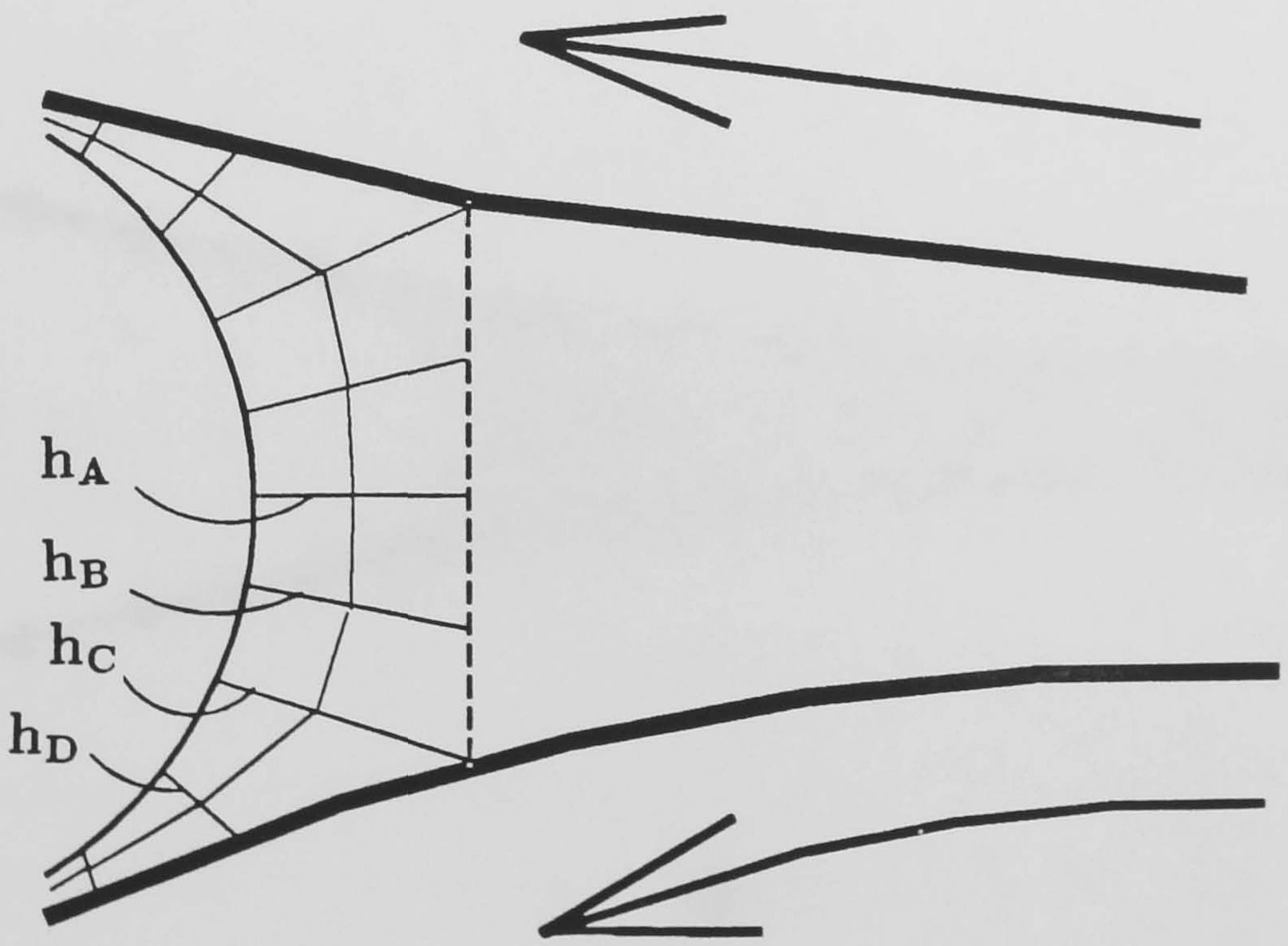

Figure 5.20: Spine method for locating a free surface in FE formulation

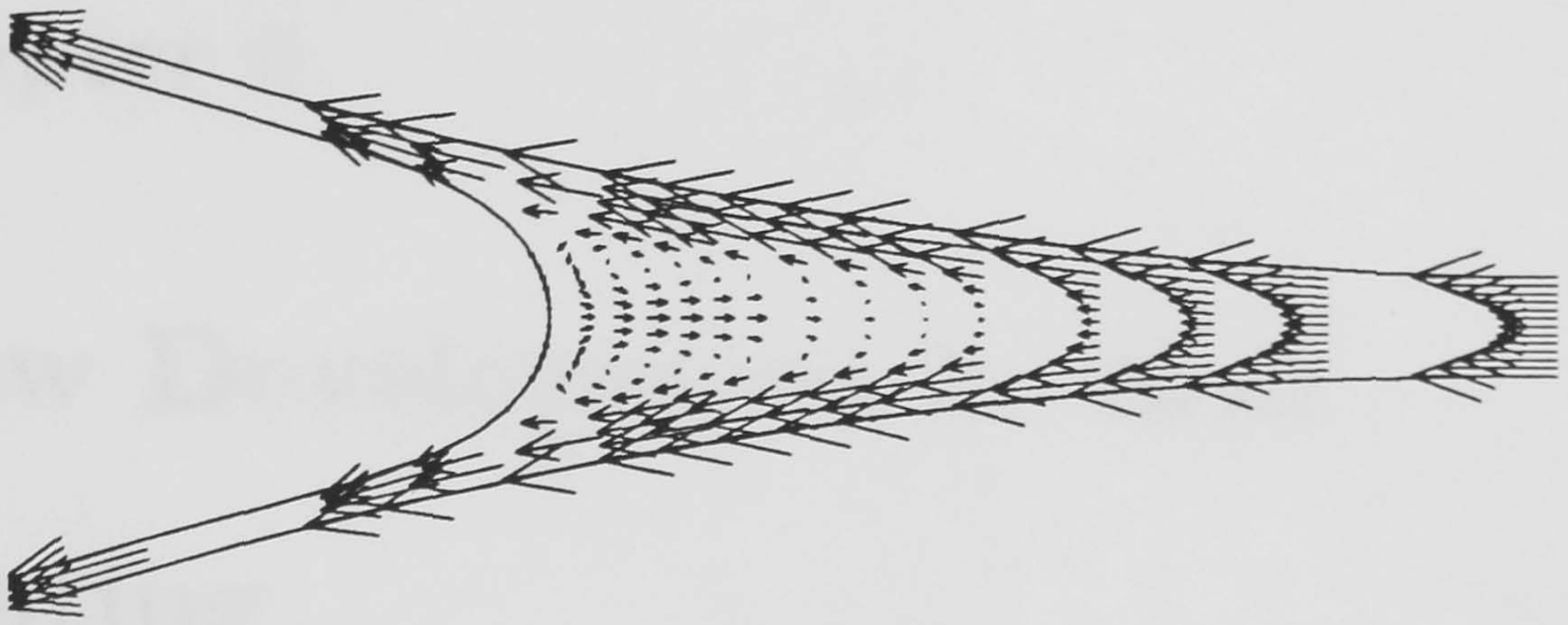

(a)

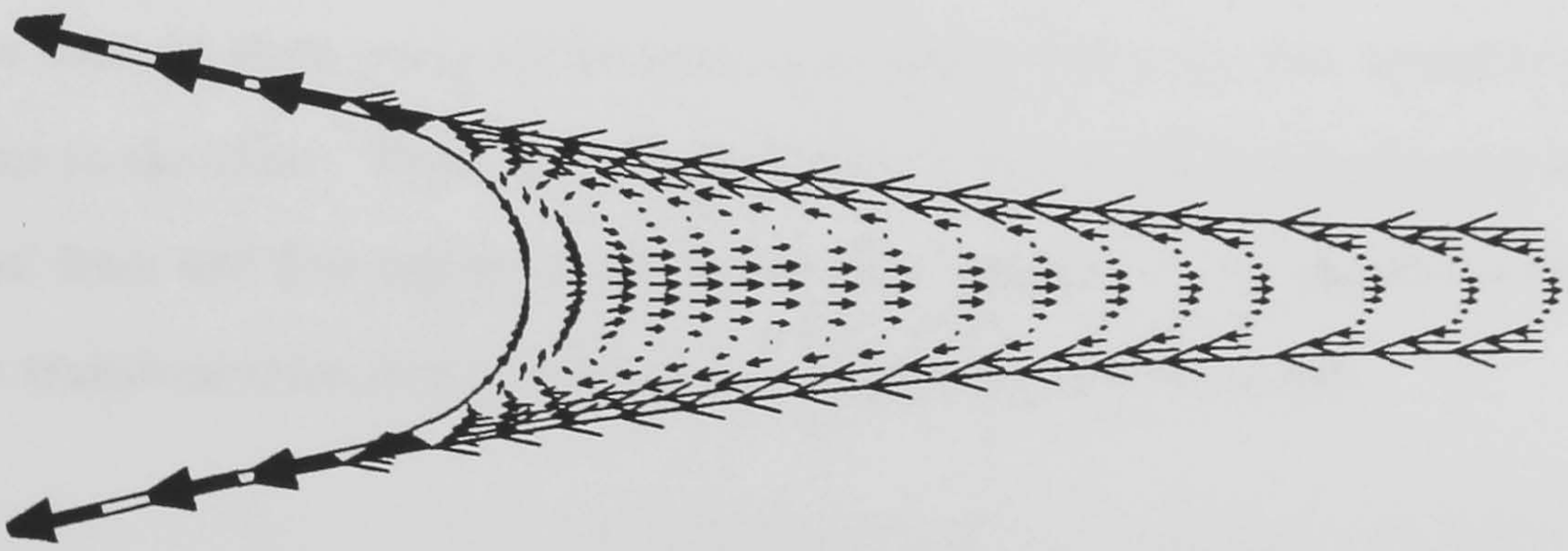

(b)

Figure 5.21: Comparison of (a) fully-flooded ($\epsilon = 1.3$) and (b) ultra-starved ($\epsilon = 0.3$), for a flow with $Re = 0.01$, $Ca = 0.1$.

PAGE

MISSING

IN

ORIGINAL

Chapter 6

Flow Development In Roll Coating

6.1 Introduction

Having observed the flow and obtained measurements of the pressure distribution for both fully-flooded (Chapter 4) and ultra-starved (Chapter 5) roll coating, the marked difference between them poses the interesting question of how the flow transforms from one regime to the other. There are two possibilities - either the development is smooth or it 'flips' from one flow regime to the other. The purpose of this chapter is to document the transformation and to explore the 'transforming mechanism'.

It is extremely difficult to obtain realistic, discrete measurements of pressure in the nip of a two-roll coater and therefore the simplified plate-roll system, the apparatus of which is described in Chapter 2, is employed. The flat plate and roll geometry (Figure 6.1) can be thought of as a two roll system with the upper roll stationary and of infinite radius. In fact this configuration does have practical application for a flooded inlet: the plate meters and spreads the fluid picked up on the roll as it passes through the

nip (it is often referred to as a spreader bar). Other features of this simplified flow include two *static* wetting lines instead of the single *dynamic* wetting line present in the two-roll system. Despite these differences, the plate-roll system retains the salient features of roll coating flow and moreover this geometry may be regarded as the link between both modes of roll coating (i.e. forward and reverse), therefore the pressure distribution results, for example, should be characteristic of both cases as the upper roll speed tends to zero.

In order to relate the plate-roll pressure transformation to that of the flow field, a flow visualisation study was also performed using this geometry. Indeed, the plate-roll system is more ameanable to visualisation of the flow than the equivalent two-roll system; the single vortex structure is simpler than the double vortex structure in the two-roll case, and in particular the vertical scale is effectively enlarged in the former situation (Figure 6.2(a) & (b) illustrate the two conditions).

In considering the flow transformation it is necessary to understand how varying the non-dimensional flux, ϵ, relates to the flow pattern in the bead (i.e. eddy formation and position of contact lines). Lubrication theory is applied to fluid flow in a plate-roll geometry in order to predict the pressure distribution and its dependence on volume flux.

Finally, tentative explanations are put forward for flow transformation in the far more complex *two-roll* forward and reverse cases, based on knowledge gained from the plate-roll transformation and flow visualisation images of the two-roll systems.

6.2 Lubrication Theory (Separation model)

The Separation model has been discredited for $S > 0$ and more generally for $S \neq 1$ (Savage[1992]). However it is valid for $S = 0$ (plate-roll geometry) and $S = 1$ (symmetric rolling). Consider the flow in the plate-roll geometry in Figure 6.3 where R is the radius of the roll, U its speed and the origin of the (x, z) coordinate system lies on the roll surface such that x is the horizontal coordinate measured from the minimum gap position; $h(x)$ is the plate-roll separation at a general position x.

Introducing the usual lubrication assumptions that both gravity and fluid inertia effects are negligible and that $\frac{\partial}{\partial z} >> \frac{\partial}{\partial x}$, the Navier Stokes equations reduce to:

$$\frac{\partial p}{\partial x} = \eta \frac{\partial^2 u}{\partial z^2} \; ; \; \frac{\partial p}{\partial z} = 0 \tag{6.1}$$

where η is the fluid viscosity and p and u represent the fluid pressure and horizontal velocity respectively. The solution to (6.1) is subject to the boundary conditions:

$$u = 0 \text{ on } y = h(x), \; u = U \text{ on } y = 0$$

giving:

$$u = \frac{1}{2\eta} \frac{\partial p}{\partial x}(z^2 - hz) + U(1 - \frac{z}{h}) \tag{6.2}$$

For steady flow, with no axial leakage the flux Q past a point x must be constant, hence integration of equation (6.2) yields:

$$\frac{dp}{dx} = \frac{6\eta}{h^3(x)}[Uh(x) - 2Q] \tag{6.3}$$

The solution to this flow problem requires the determination of the flux Q, the location $x = s$ marking the termination of the lubrication regime, and a constant resulting from the integration of equation (6.3).

In the region of interest, the roll surface can be approximated by a parabola giving the plate-roll separation to be:

$$h(x) = H_0 \left[1 + \frac{x^2}{2RH_0} \right] \tag{6.4}$$

Introducing the dimensionless coordinate $X = x/(2RH_0)^{\frac{1}{2}}$ and defining $P = (H_0^2/6\eta U)(p/(2RH_0)^{\frac{1}{2}})$, equation (6.3) simplifies to give:

$$\frac{dP}{dX} = \frac{1}{(1+X)^2} - \frac{2Q}{UH_0(1+X)^3} \tag{6.5}$$

Making the substitution $X = \tan\phi$:

$$\frac{dP}{d\phi} = \cos^2\phi - \frac{2Q}{UH_0}\cos^4\phi \tag{6.6}$$

which can be readily integrated to give:

$$P = \frac{\phi}{2} + \frac{\sin 2\phi}{4} - \frac{2Q}{UH_0}\left(\frac{3\phi}{8} + \frac{\sin 2\phi}{4} + \frac{\sin 4\phi}{32}\right) + const \tag{6.7}$$

The constant of integration , the location, $x = s$, of the termination of the lubrication regime and the flux Q are determined by specifying three boundary conditions. The separation boundary conditions, often refered to as the Prandtl-Hopkins conditions, are used.

The key assumption in the separation model (Savage (1982)) is that the lubrication regime terminates where fluid separates from the plate, i.e. at $x = s$ where

$$u = \frac{\partial u}{\partial z} = 0 \tag{6.8}$$

which in turn yields a condition on the pressure gradient at separation, namely:

$$\frac{\partial p}{\partial x}(s) = \frac{2\eta U}{h^2(s)} \tag{6.9}$$

Evaluating the volume flux at $x = s$ gives:

$$Q = \frac{Uh(s)}{3} \tag{6.10}$$

The fluid pressure at rupture is given by:

$$p(s) \approx p(c) = -\frac{T}{r} \tag{6.11}$$

where T is the surface tension of the fluid and r the radius of curvature of the fluid-air interface. From Figure 6.3 an approximate radius of curvature is given by: $r = h(c) - h^{\infty}$ where h^{∞} is the asymptotic film thickness on the roll. Since $Q = Uh(c)/3 = Uh^{\infty}$ then $r = 2h(c)/3$ and (6.11) becomes

$$p(c) = \frac{-3T}{2h(c)} \tag{6.12}$$

Finally the pressure distribution is assumed to begin at a (variable) location $x = x_i$ $(X = X_I)$ such that:

$$p(x_i) = 0 \tag{6.13}$$

The solution of equation (6.7) subject to the above conditions yields the following non-linear equation for the dimensionless separation point $X = S$:

$$\begin{aligned} 0 = \frac{\beta}{4\sqrt{2}(1+S^2)} &+ \frac{\phi}{2} + \frac{\sin 2\phi}{4} - \frac{2}{3}(1+S^2)(\frac{3\phi}{8} + \frac{\sin 2\phi}{4} + \frac{\sin 4\phi}{32}) \\ &- \frac{\phi_i}{2} - \frac{\sin 2\phi_i}{4} + \frac{2}{3}(1+C^2)(\frac{3\phi_i}{8} + \frac{\sin 2\phi_i}{4} + \frac{\sin 4\phi_i}{32}) \end{aligned} \tag{6.14}$$

where $\beta = \frac{T}{\eta U}(\frac{H_0}{R})^{\frac{1}{2}}$ is a modified capillary number for the flow and $\phi_i = \tan^{-1}(X_i)$

This equation is conveniently solved by Newton's method (Savage[1992]) for various inlet locations $X_I(= \tan\phi_i)$ beginning with a fully flooded inlet $\phi_i = -\frac{\pi}{2}$ $(X_I = -\infty)$ and gradually increasing ϕ_i so that the inlet position approaches the minimum gap.

6.2.1 Implications of the plate-roll separation model

In Figure 6.4 it is seen that as the inlet approaches the nip the magnitude of the pressure maximum is gradually reduced yet the subatmospheric pressure distribution

(downstream of the nip) remains almost unaffected by the inlet location. The dimensionless flux $\epsilon = Q/(UH_0)$ takes its maximum value of 0.63 when the inlet is fully flooded. As the inlet moves towards the nip, the flux is gradually reduced and $\epsilon \rightarrow 0.5$. Indeed it is readily shown that $\epsilon > 0.5$ is a neccesary condition for generating pressure profiles with the characteristic maximum and minimum. Equation (6.5) gives:

$$\frac{dP}{dX} = \frac{1}{(1+X)^3}\left((1+X^2) - 2\epsilon\right) \tag{6.15}$$

and when $dP/dX = 0$ this gives:

$$X^2 = 2\epsilon - 1 \tag{6.16}$$

clearly there can be no stationary points once ϵ falls below 0.5. In fact this argument holds regardless of the boundary conditons used to terminate the lubrication region.

In addition the pressure gradient in this geometry is given by equation (6.3) and can be written as:

$$\frac{dp}{dx} = \frac{6\eta U}{h^2}(1 - \frac{2Q}{Uh}) \tag{6.17}$$

The Separation model predicts that at the point of separation:

$$\frac{dp}{dx} = \frac{2\eta U}{h^2} \tag{6.18}$$

therefore:

$$1 - \frac{2Q}{Uh} = \frac{1}{3} \tag{6.19}$$

where

$$h = H_0(1 + x^2) \tag{6.20}$$

giving

$$\left[\frac{Q}{UH_0}\right] = \epsilon = \frac{1}{3}(1 + x^2) \tag{6.21}$$

therefore

$$x^2 = 3\epsilon - 1 \tag{6.22}$$

It follows via (6.22) that the upstream and downstream stagnation points (X_I & X_S - see Figure 6.5) remain equidistant from the minimum gap position such that $X_{I,S} = \sqrt{3\epsilon - 1}$, and that the minimum value of non-dimensional flux, ϵ_{min}, occurs when the stagnation points reach $x = 0$:

$$\epsilon_{min} = \frac{1}{3} \tag{6.23}$$

There are thus two critical values of ϵ in the flow transformation:

At $\epsilon = \frac{1}{2}$ The maximum/minimum pressures disappear

At $\epsilon = \frac{1}{3}$ the stagnation points are at the minimum gap position

In summary, there are a number of conditions worthy of note as the non- dimensional inlet flux, ϵ, is reduced (refer to Figure 6.5):

- $P(\pm\infty) = 0, \quad \epsilon = 0.63$

  This represents a submerged plate-roll system, with X_I effectively at ∞ and an asymmetric maximum/minimum pressure profile.

- $P(\pm X_I) = 0, \quad \epsilon < 0.63$ - As the flux is gradually reduced (e.g. $X_I = 2.5$ when $\epsilon = 0.62$).

- $P(\pm X_S) = 0$ (i.e. $X_I = X_S \approx 1.0$ - Samans criterion for a starved inlet - see Chapter 1, § 1.3).

  At this point $\epsilon = 0.59$.

- $0.5 < \epsilon < 0.59$. Lubrication theory still predicts turning points in the pressure profile over this region.

- $\epsilon \leq 0.5$. There is no pressure maximum/minimum predicted.

- $\epsilon = 0.33$. The stagnation point is at the minimum gap position.

Therefore, if the definition of the transformation is the development of the system from one-dimensional to two-dimensional flow through the nip, then theory predicts that

the true transformation from a fully-flooded to an ultra-starved condition occurs at the second critical point; $\epsilon = 1/3$.

The above result permits the degree of fluid starvation to be classified in a more satisfactory manner, namely that flows with $\epsilon < 0.33$ are ultra-starved flows. These notable predictions of pressure profile characteristics as a function of volume flux are used to guide the experimental investigation.

6.3 Experimental Procedure

It is important to realise that the transformation from a Classical to a Meniscus regime can only be achieved if the magnitudes of the surface tension and viscous pressures are comparable at the point of transformation; otherwise the fluid bead cannot be maintained and will disintegrate. The more viscous the fluid, the less resilient the flow system is in maintaining a bead over a wide speed range. In attempting to achieve the transition with a particular fluid, it is a balance between needing a relatively viscous fluid to produce a flooded inlet at moderate roll speed and being able to maintain the bead during transition (as well as having a useful gap size to visualise the flow transition). Keeping all other parameters constant, the transition can be achieved with varying degrees of success using three methods:

1. Varying roll speed and therefore varying the amount of fluid picked up by viscous lifting: this is the best and most controllable method of achieving the transformation and maintaining intermediate conditions. However, because the roll speed is altered to achieve the change, the characteristic speed of the system is changed. In particular the Capillary number, Ca, does not remain constant and the magnitude of the pressures generated within the bead are roll speed (viscous force) dependant. Therefore this method will not produce a 'pure' transition, whereby

only the critical parameter is changed (i.e. the flux, ϵ).

2. Varying the minimum gap size to change the value of the non-dimensional flux (i.e. $\epsilon = Q/UH_0$). This method can be successful in obtaining the transformation, however by changing the gap size, the aspect ratio of the flow field is changed and hence it is difficult to relate the inlet, outlet and stagnation point movements throughout the transition.

3. Varying the inlet flux using a doctor blade. This is difficult to achieve; for a given constant speed, which produces a flooded inlet, and using a doctor blade to reduce this inlet film to an ultra-starved condition has the result that the bead cannot be maintained because the magnitude of the speed (and therefore the viscous force) is too great. In addition the velocity profile of the inlet film may be extensively altered by the scraper (i.e. the fluid layer may be extensively sheared on passing the scraper edge).

Indeed, the major difficulty with this investigation is the complex dependence of the system parameters on one another. In adopting any of the above methods, more than one of the system parameters will be affected. It is therefore necessary to 'extract' the salient information from any results, rather than take them 'as read'. For example, using speed as a means of reducing the inlet flux, it is obvious that the pressures in the classical maximum/minimum pressure distribution for roll coating, illustrated in Chapter 4, Figure 4.14, will decrease; there is no justification for assuming that this reduction in pressure is part of a flow transformation to a linear pressure distribution. The only information which can be used with any confidence is the point at which the 'nature' of the pressure profile changes – see §§ 6.4.3 .

In order to understand the interaction of the salient parameters in this system it is necessary to obtain simultaneous results for pressure profile, flow field, flux, free sur-

face and stagnation point locations.

6.3.1 Recording Results

Figure 6.6 illustrates the initial experimental apparatus for obtaining simultaneous results of the required parameters (described in Chapter 2). The recording system consisted of two Panasonic F10 video cameras mounted one above the other. In the early stages of this study the lower camera was used to view the flow field, using the dye tracer method described in Chapter 3, as well as to monitor the positions of the free surfaces and stagnation points.

In order to obtain a detailed pressure profile it is necessary to increase the aspect ratio of the fluid bead significantly, by decreasing the curvature of the roll so that the bead covers more pressure 'tappings'. In so doing, visualisation of the flow field becomes more difficult; it is possible to appreciate characteristics of the flow field (i.e. whether the flow through the nip is one or two-dimensional), but accurate measurements of the free surface and stagnation point locations, in particular, are made even more difficult by the edge effect of the viewing plate on the bead. The necessity for a high aspect ratio bead means that a detailed analysis of the development of the flow is not possible using this apparatus, because of the poor resolution in the subsequent 'squashed' flow system.

In addition the video viewing system image could not accommodate the whole of this excessive bead width, without the need to lower the magnification factor considerably, which in turn affected the definition of the flow. Therefore the smaller scale general experimental apparatus, described in Chapter 2, was modified by replacing the top roll with an acrylic plate to visualise the flow transformation in this geometry. The two sets of results, i.e. pressure distribution from the large scale plate-roll apparatus and flow field development from the small-scale general apparatus, were equated by measuring

the non-dimensional flux through the nip in both cases.

It soon became apparent that it was possible to obtain most of the required observations using the upper camera only. The free surface locations (but not the profiles) and stagnation point locations can be tracked quite accurately using a precision glass block beam-splitter placed on the perspex top plate and in front of the pressure tappings. The upper camera therefore sees the pressure profile with an image of the free surface and stagnation line locations superimposed over it (see Figure 6.7). The scaling is achieved by having horizontal and vertical rulers in the recorded image and the stagnation/contact lines are clearly visible running along the bead, when dye is injected. In fact the secondary axial flow (which is set up when the viewing end-plate is put in place and the system experiences side- leakage due to capillary action) is used to illustrate these lines.

In having a double image of pressure tappings and free surface locations, it is clear which tappings are in the fluid and which are not, as the transformation progresses (see Figure 6.7). Flux is measured using a scraper (as described in Chapter 2) and its' value can be superimposed on the final image using a character generator allowing all the required information to be recorded at once.

6.4 Transformation From Classical To Meniscus Roll Coating

6.4.1 Flow field

Streamline Patterns

The development of the flow field from the fully-flooded to ultra-starved condition is illustrated in Figures 6.8(a) to (e) (false-colour images). Here the minimum gap size is steadily increased in order to decrease the non-dimensional flux, ϵ. Figure 6.8(a) shows the familiar fully-flooded case ($\epsilon \approx 0.5$) with one-dimensional flow through the nip (dye shown in deep red) and downstream separation from the plate. In order to increase resolution, the 'full picture' is not captured (i.e. that shown schematically in Figure 6.5). It is possible to see the front of the downstream recirculation in Figure 6.8(a), as well as the downstream separation point X_S; unfortunately the upstream flow, including the point X_I, and the downstream free surface is not shown. Nevertheless, it is possible to appreciate the development of the flow from fully-flooded (figure 6.8(a) to ultra-starved (figure 6.8(e) conditions.

As ϵ is slowly reduced the point X_S clearly moves back into the nip. while the point X_I (which is now the dynamic contact line) moves forward into the nip, and Figure 6.8(b) shows $X_I \approx X_S$ (the minimum gap position is illustrated by the three grid points) As ϵ is further reduced, the two points X_I and X_S meet (Figure 6.8(c)); this is the condition at which the transformation is predicted to occur. Taking ϵ below this value results in the stagnation point travelling down the upstream free surface (Figure 6.8(d)) to produce the now familiar fully two-dimensional flow field (Figure 6.8(e) shows a recirculating filament of dye).

Hence, the flow appears to undergo a smooth transition from one regime to the other. Therefore, although the flows have been classified here, they are in fact extreme cases of a continuous flow regime, and are simply highlighted to illustrate the complex change which is undertaken. Measured values of ϵ are, however, consistently lower than those predicted by theory for a given flow condition. In addition the points X_I and X_S did not appear to meet at the minimum gap position, but at a position some distance upstream. This could be attributed to the fact that a fluid cannot come to rest instantaneously at a given point, but in fact it 'banks up' ahead of this area. Nevertheless the experimental observations are in qualitative agreement with the theoretical predictions.

6.4.2 Variation in Free Surface Location, Stagnation/Wetting lines

Figure 6.9 shows the movement of (a) the upstream free surface using the conventional end-viewing technique and (b) the upstream and downstream free surfaces using the plan-view technique, as the non-dimensional flux is varied. The method used for illustrating stagnation/wetting lines is described in §§ 6.3.1 and Chapter 2. These particular results were obtained using the roll speed as a means of controlling the inlet flux, and a surprising result has emerged; while the downstream free surface exhibits a very small change in position throughout the transformation, the upstream free surface is seen to move into the nip prior to transformation (at $\epsilon \approx 0.33$) whereupon it moves back out again. The movement of this free surface is smooth, i.e. there is no 'jump' as the flow transforms.

Thus for certain upstream free surface positions it is possible to have more than one value of flux associated with it (e.g. at $x = -7mm$, $\epsilon = 0.1,\ 0.44$); therefore this problem is not single-valued and further research is required.

6.4.3 Pressure field

The method used to obtain measurements of pressure is described in Chapter 2, § 2.4. As seen in Chapter 4 the fully-flooded condition exhibits the characteristic assymetric pressure profile with a peak upstream of the minimum gap position and a trough downstream. The pressure distribution for the ultra-starved case (see Chapter 5, §§ 5.2.4) bears no resemblance to that of the fully-flooded case, experiencing a very sharp reduction in pressure over the upstream free surface followed by a reasonably linear pressure gradient throughout. Figure 6.10(a) & (b) shows the graph of measured pressure v's position, relative to minimum gap, for a wide range of values of non-dimensional flux, ϵ, beginning with a fully-flooded condition (Figure 6.10(a)) and moving to an ultra-starved condition (Figure 6.10(b)). Both graphs are part of a continuous series of measurements; they have been split up in this way for clarity.

As the system is starved of fluid the upstream free surface moves in towards the nip, as described in the previous section, and therefore the number of pressure tappings in the fluid decreases which explains the 'shortening' of the pressure profile results as the non-dimensional flux is reduced. The characteristic pressure maximum decreases significantly, for an extremely small change in ϵ. The pressure profile becomes sub-ambient throughout the fluid bead, however, there is still a clear maximum and minimum. As ϵ is reduced further, the sub-ambient maximum disappears and the overall pressure profile takes on a linear form. Figure 6.10(b) shows that the gradient of this linear profile decreases as ϵ is continually reduced.

The key features of these results include the smooth pressure profile transformation and the presence of a sub-ambient pressure loop only, prior to the full transformation to a linear sub-ambient pressure profile in the ultra-starved case. Reducing the inlet

film further serves to maintain this linear pressure distribution (although the magnitude of the pressure profile is reduced as roll speed is decreased).

An order of magnitude comparison of theoretical and experimental viscous and surface tension pressures in Classical and Meniscus roll coating illustrates the balance of forces under each regime. Values for characteristic experimental pressure, P_{ex} can be calculated directly from Figure 6.10:

$$P_{ex} = \rho g h_p \tag{6.24}$$

where h_p is a manometer height. Taking $dp/dx = (\eta U)/(H_0)^2$ as the expression for pressure gradient and taking $(RH_0)^{1/2}$ as a characteristic length scale, the theoretical viscous pressure, P_η, is given by:

$$P_\eta = \left[\frac{\eta U}{H_0}\right]\left[\frac{R}{H_0}\right]^{\frac{1}{2}} \tag{6.25}$$

where $R = 0.13$m for the large-roll pressure apparatus. An estimate of surface tension pressure, P_T, is given by:

$$P_T = \frac{T}{r} \tag{6.26}$$

where r is the radius of curvature of the free surface. Typical radii of curvature can be estimated from observations of the free surface profiles (e.g. Figure 5.12(a) gives $r \approx H_0$).

Under fully-flooded conditions $P_{ex} \approx 160\ Pa$ (peak pressure from Figure 6.10(a)), compared to $P_\eta = 221 Pa$ [H_0 =250 micrometres, U=0.55 m/s]. For the ultra-starved condition, the measured pressure adjacent to the upstream free surface is $P_{ex} \approx 180\ Pa$ compared to a calculated surface tension pressure of $P_T = 172$ (from Figure 5.12(a)). Therefore it appears that the viscous and surface tension forces are in balance for the ultra-starved roll coating regime, whereas viscous forces dominate in the fully-flooded

case.

A surprising result to emerge from a comparison of pressure measurements for fully-flooded and ultra-starved conditions is that the *magnitude* of the minimum pressures are similar, in spite of the fact that the roll speed (and thus the relative viscous force) has been reduced four fold (i.e. 0.55 m/s $\rightarrow$ 0.16 m/s). Common sense would have dictated a reduction in the characteristic pressure if it were wholly viscosity-generated. The fact that the magnitude of the fully-flooded sub-ambient pressure loop is similar to the ultra-starved linear pressure profile poses the interesting question of whether the Classical sub-ambient pressure minimum is generated by surface tension pressure. It would indeed appear that pressures in the reverse flow region lie in the range: $\frac{T}{h(c)} < |P| < \frac{T}{h(s)}$ Further work is required to confirm this hypothesis.

Measured values of ϵ are lower than predictions for certain key stagnation point locations. Although this may be due to errors in flux measurement, there may also be a hysteresis effect which is dependent on which direction the transformation is approached (i.e. fully-flooded $\rightarrow$ ultra-starved, or vice versa). Further investigations are required to clarify this effect.

In a sense this 'new' pressure profile is not surprising; by comparing the flow patterns in the Classical and Meniscus systems, the downstream eddy flow (and it's associated pressure distribution) in the Classical case simply extends back through the nip to meet the upstream free surface in the Meniscus case (see Figure 6.11).

6.5 Two-Roll Coater Flow Transformation

6.5.1 Forward Roll Coating

Figure 6.12(a) to (d) is a schematic illustration of the flow transformation (ultra-starved → fully-flooded) in the forward two-roll coater; note the 'jump' in the position of the film-splitting point, which is facilitated by the separation of the two lower vortices (moving from (b) to (c)). This appears to be the point of transformation; the two large vortices are effectively enclosed, with the fluid splitting around them. They then decrease in size and move downstream through the nip to form the classical fully-flooded flow structure (Figure 6.12(d)), while the small upstream vortex disappears. Increasing the inlet flux further brings about the formation of the upstream bank (see Chapter 4).

Observations of the switch in the film-splitting point are shown in Figures 6.13(a) & (b) by taking selected images of initial dye injection in order to follow the splitting behaviour. Figure 6.13(a) clearly illustrates the separation of the lower recirculation into two vortices (images (i) & (ii)); the film-splitting point, however, remains in the lower left region of the fluid bead and the large 'snaking' fluid transfer to the upper roll is evident (image (ii)). By increasing ϵ the splitting point jumps to the lower right region of the bead (Figure 6.13(b)), and the small upstream recirculation becomes more concentrated (illustrated by the dense area of dye). The 'symmetric' splitting of the flow is shown by the position of the upper and lower dye streams; they remain 'neck and neck ' throughout the fluid bead. In addition the large scale snaking action of the transfer is no longer present. However, a much smaller scale snaking action is taking place around the lower concentrated vortex, before the film splits around the two large vortices. This flow structure only becomes clear by looking at the experimental velocity plot in Figure 6.14(b) (6.14(a) is the equivalent dye flow image). The concentrated vortex adjacent to the inlet region is clearly visible, as is the film-splitting point.

Increasing ϵ further serves to eliminate the small vortex at inlet and film-splitting takes place almost adjacent to the upstream free surface (see Figure 6.15(a) - this image is taken after initial dye injection, and the clear region between the two dye streams has a flow structure much the same as Figure 6.15(b)). The Classical roll coating flow structure of Figure 6.15(b) is achieved by increasing ϵ further, and is a result of the film- splitting point moving downstream through the nip.

The above explanation of flow transformation in a forward two-roll coater is very much a qualitative description; further work is required to systematically analyse this mechanism.

6.5.2 Reverse Roll Coating

The transformation of the reverse two-roll coater, from fully-flooded to ultra-starved conditions, appears simpler than the forward case and is illustrated schematically in Figure 6.16(a) to (d). The stagnation points, joined by a stagnation line, gradually come together as the inlet flux is reduced, meeting at the minimum gap position. Thereafter the flow field is fully two-dimensional throughout. Figures 6.17(a) to (d) are experimentally observed images of this transformation; note that the aspect ratio of the fluid bead is dramatically reduced in moving to an ultra-starved flow condition. There is evidence to suggest that film-splitting does not take place solely in the lower right region of the fluid bead under fully-flooded conditions; as roll speed ratio is increased ($S > 1$), the inlet film appears to split earlier at some point between the two vortices (Figure 6.18(a) to (d) shows a dye injection sequence). There is no question that further work is required to clarify this flow.

The result obtained from the zero and finite-flux models, presented in Chapter 5, of

the dependence of the pressure gradient on $(1 + S)$ implies that the pressure profile is zero when $S = -1$, i.e. reverse roll coating (classical analysis for the fully-flooded condition also produces the same prediction). Figure 6.19 shows the graph of location of free surfaces v's roll speed ratio. It is possible to make a qualitative comparison of the pressures upstream, and downstream of the nip, by considering the position of the upstream and downstream free surfaces. For $S < 1$ the upstream free surface postion, X_U, is greater than the downstream free surface position, X_D, which implies that the upstream pressure is greater than that downstream. When $S = 1$, $X_U \approx X_D$, which implies that there is a negligible pressure gradient across the fluid bead. For $S > 1$, $X_D > X_U$; therefore the pressure differential has reversed. Experimental observations are therefore in good agreement with theoretical predictions.

6.6 Discussion of Results

These results graphically demonstrate the development of the flow from Classical to Meniscus roll coating case and indeed that the transformation is smooth and continuous. It is clear that viscous forces dominate the Classical condition (the measured pressures are generated within the 'body' of the flow; returning to near-atmospheric both upstream and downstream). However, in the Meniscus coating case the viscous pressure generated within the bead is sustained and balanced by the surface tension pressure at the upstream free surface. Therefore a fundamental shift in the parameters which control the flow takes place as the transformation occurs. The delicate balance between viscous and surface tension forces during the transformation is readily apparent by the fragility of the fluid bead; only under limited conditions will it be maintained. The most important conclusion to draw from these results is that the surface tension of a fluid being coated under ultra-starved conditions is a key factor in the control of the fluid-mechanical process.

Agreement between the predictions of simple lubrication theory in locating the movement of the separation/stagnation point and those observed in practice are reasonable. Indeed the location and tracking of stagnation points is the key to understanding the development of complex flows such as these. The theoretical predictions of the stagnation point positions (for particular values of non- dimensional flux) provided invaluable information on which to base the investigation. This illustrates that such classical analysis can still make a significant contribution in previously 'uncharted' regimes.

The ultra-starved case is considered to be one in which the dimensionless flux, ϵ, is small. In considering the expression for pressure gradient presented earlier (equation 6.3) this would suggest that an approximation to the pressure gradient in the ultra-starved case is:

$$\left[\frac{\partial p}{\partial x}\right]_0 = \frac{6\eta U}{h^2(x)} \tag{6.27}$$

This estimate is found to be in exact agreement with pressure gradients obtained from Thompsons[1992] idealised ultra-starved model in which ϵ is actually set to zero. In addition comparison with the present experimental pressure profile results proves to be consistent.

A comparison of actual pressures and pressure gradients taken from the graph and theoretical results are in good agreement. The Finite Element pressure profile predictions of Thompson(1992) for the simplified and two-roll geometry are consistent (see Thompson[1992]), which adds credance to the use of the plate-roll geometry to obtain estimates of the pressures for the two-roll case.

The present results, together with measurements of film thickness behaviour in Chapters 4 & 5 for the fully-flooded and ultra-starved cases, respectively, demonstrate that

the film-splitting mechanism is the same in the two cases. This strengthens the argument that the two flows are basically the same and the only difference is the prominance of surface tension in the Meniscus condition, which essentially helps to maintain the fluid bead.

It is clear that a comprehensive, structured programme of work is now required in order to fully appreciate the complex nature of the transformation, both in the forward and reverse roll coating cases.

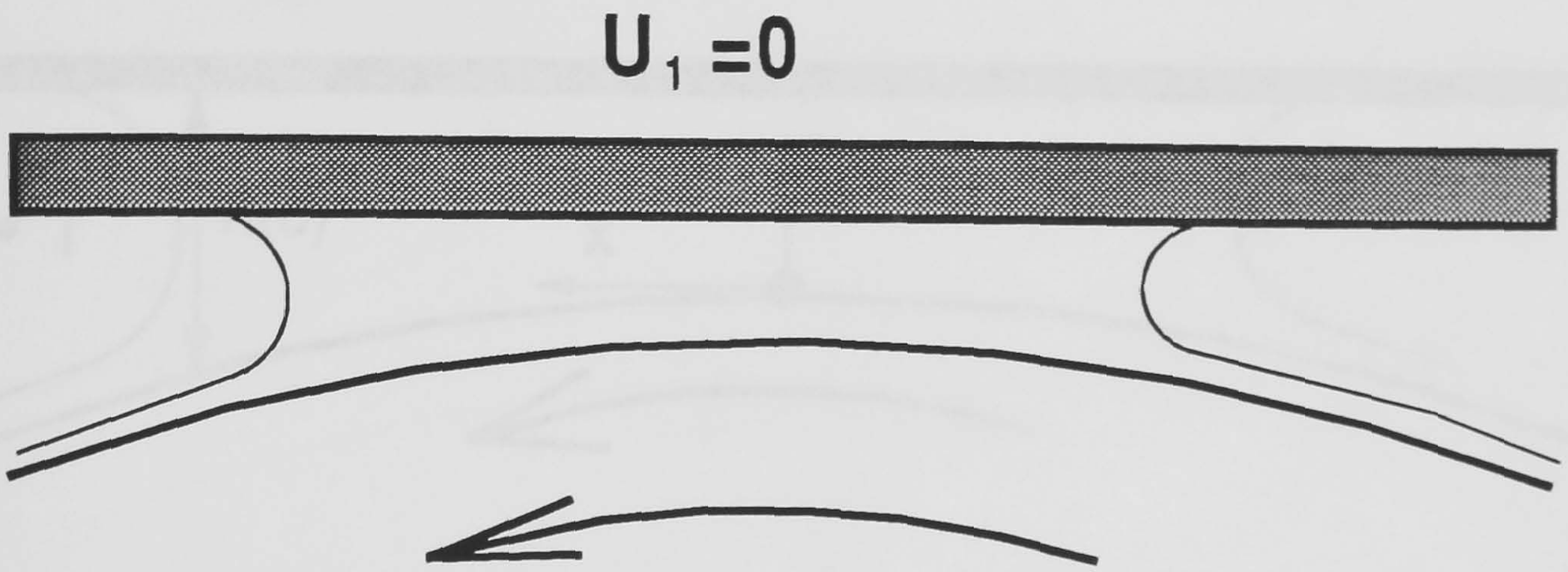

Figure 6.1: Plate-roll geometry

Figure 6.2: Illustration of flow distortion in a high aspect ratio fluid bead (a) two-roll system, (b) plate-roll system

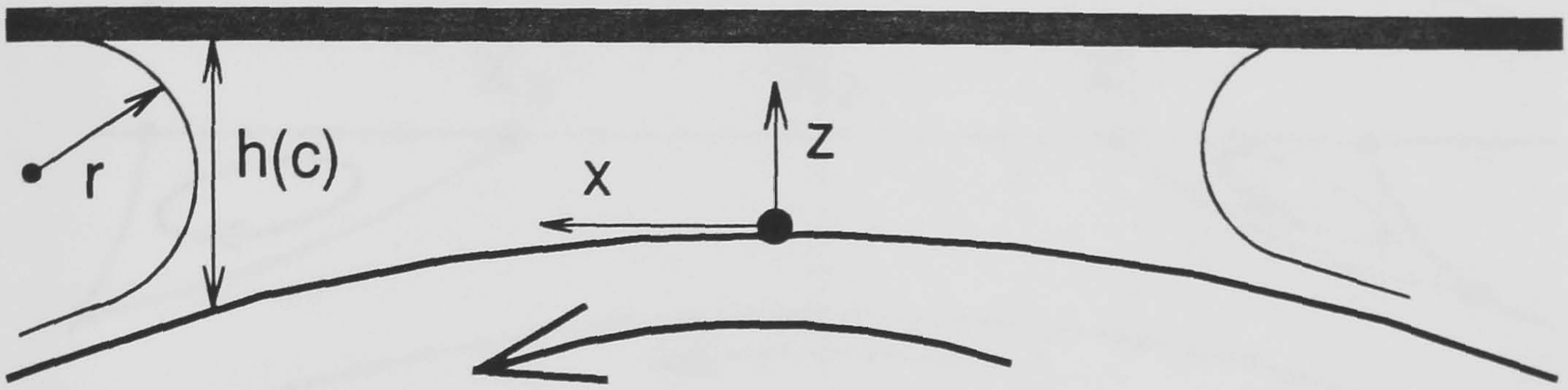

Figure 6.3: Plate-roll flow coordinate system

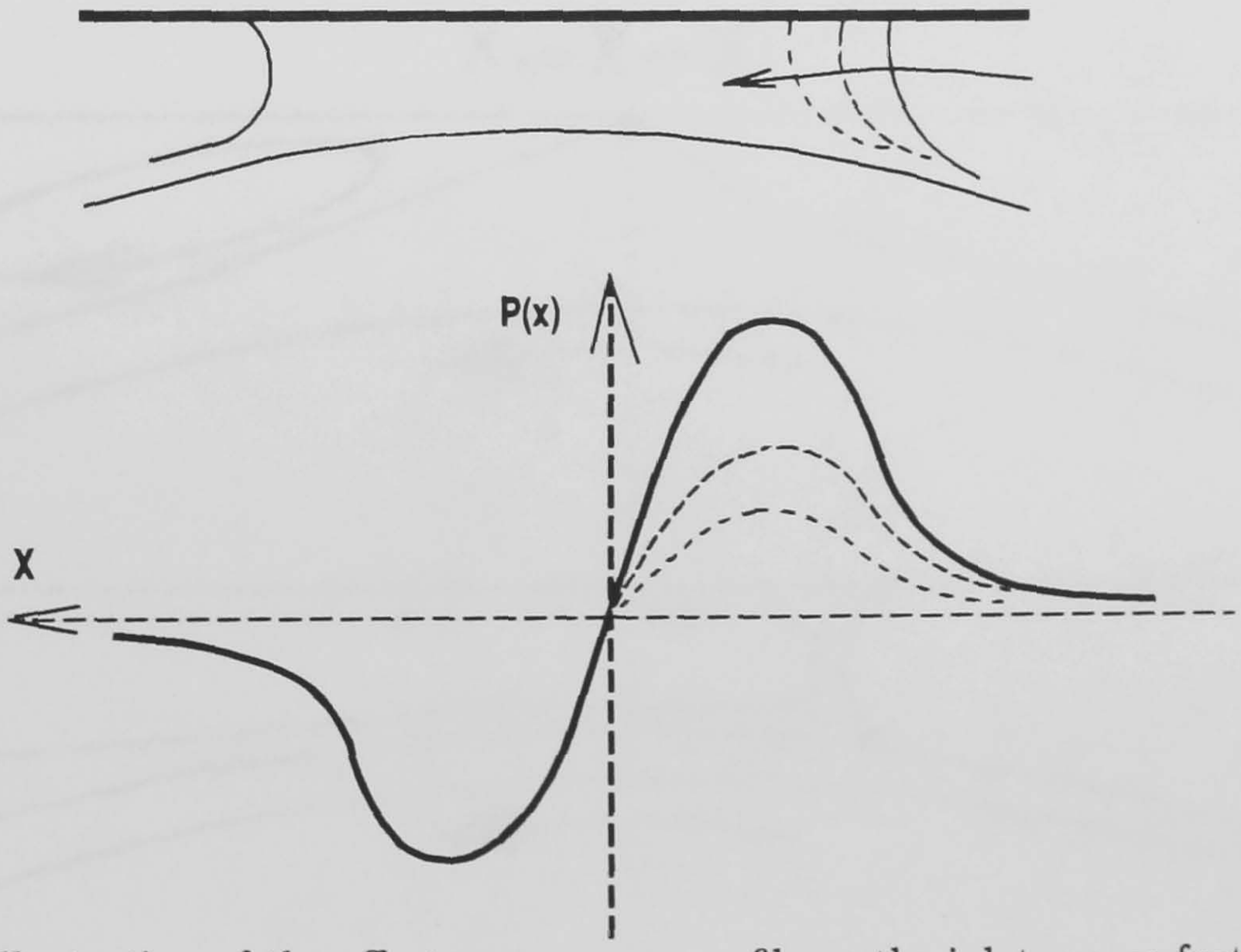

Figure 6.4: Illustration of the effect on pressure profile as the inlet moves further into the nip

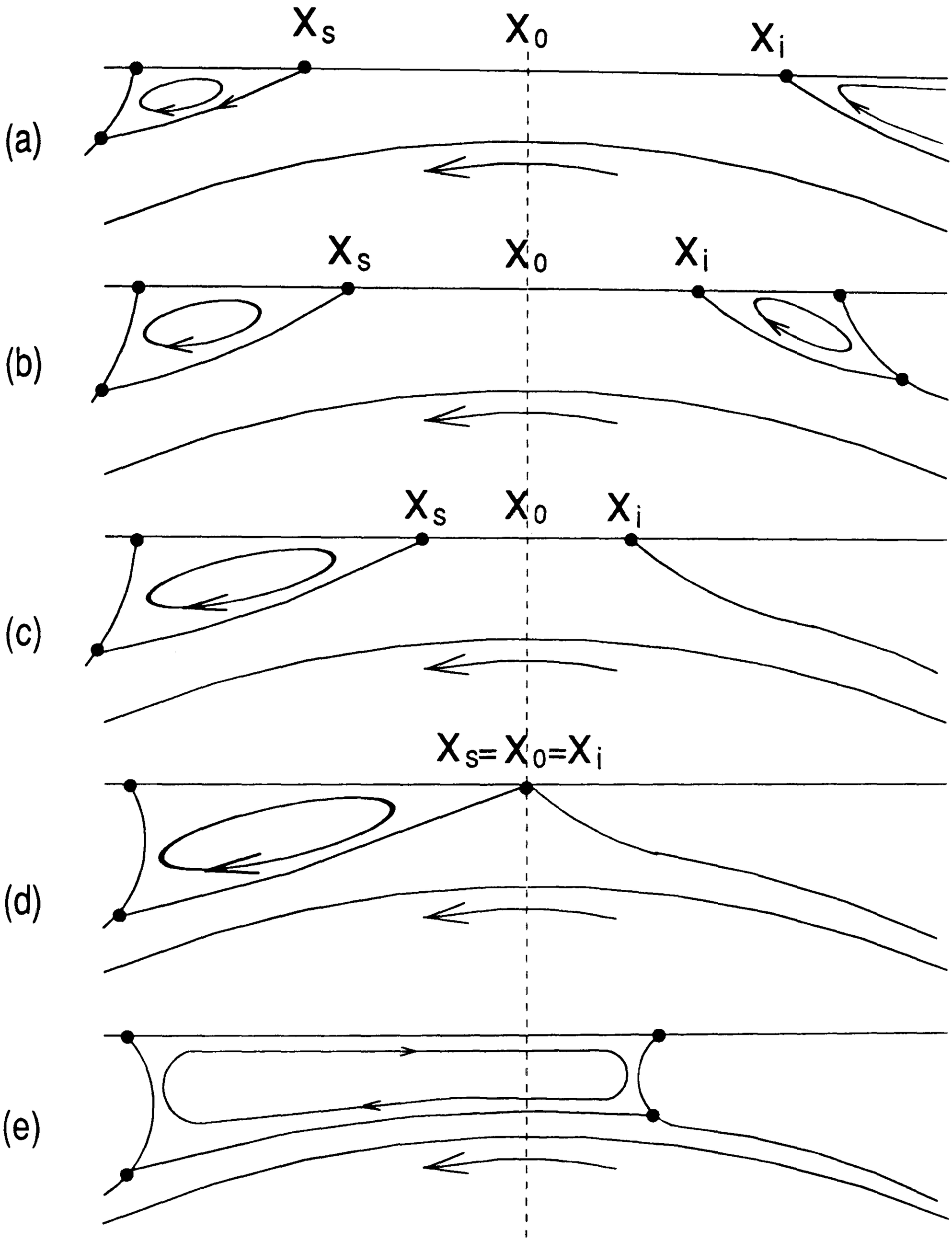

Figure 6.5: Predictions of flow development/stagnation point movement as dimensionless flux, ϵ, is reduced (a) $\epsilon = 0.63$, (b) $\epsilon = 0.59$, (c) $\epsilon = 0.5$, (d) $\epsilon = 0.33$, (e) $\epsilon < 0.3$

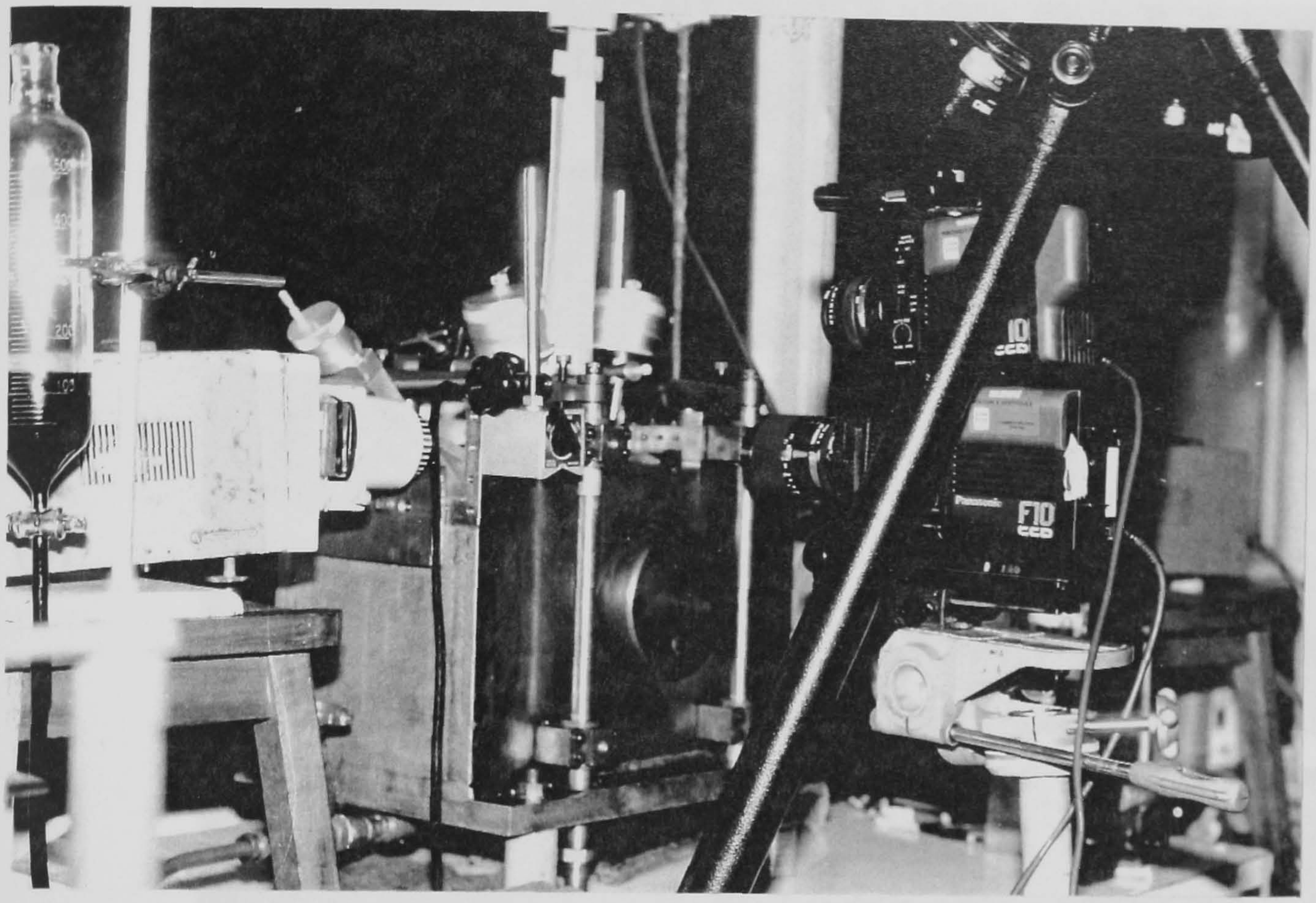

Figure 6.6: View of experimental pressure measurement apparatus and video system

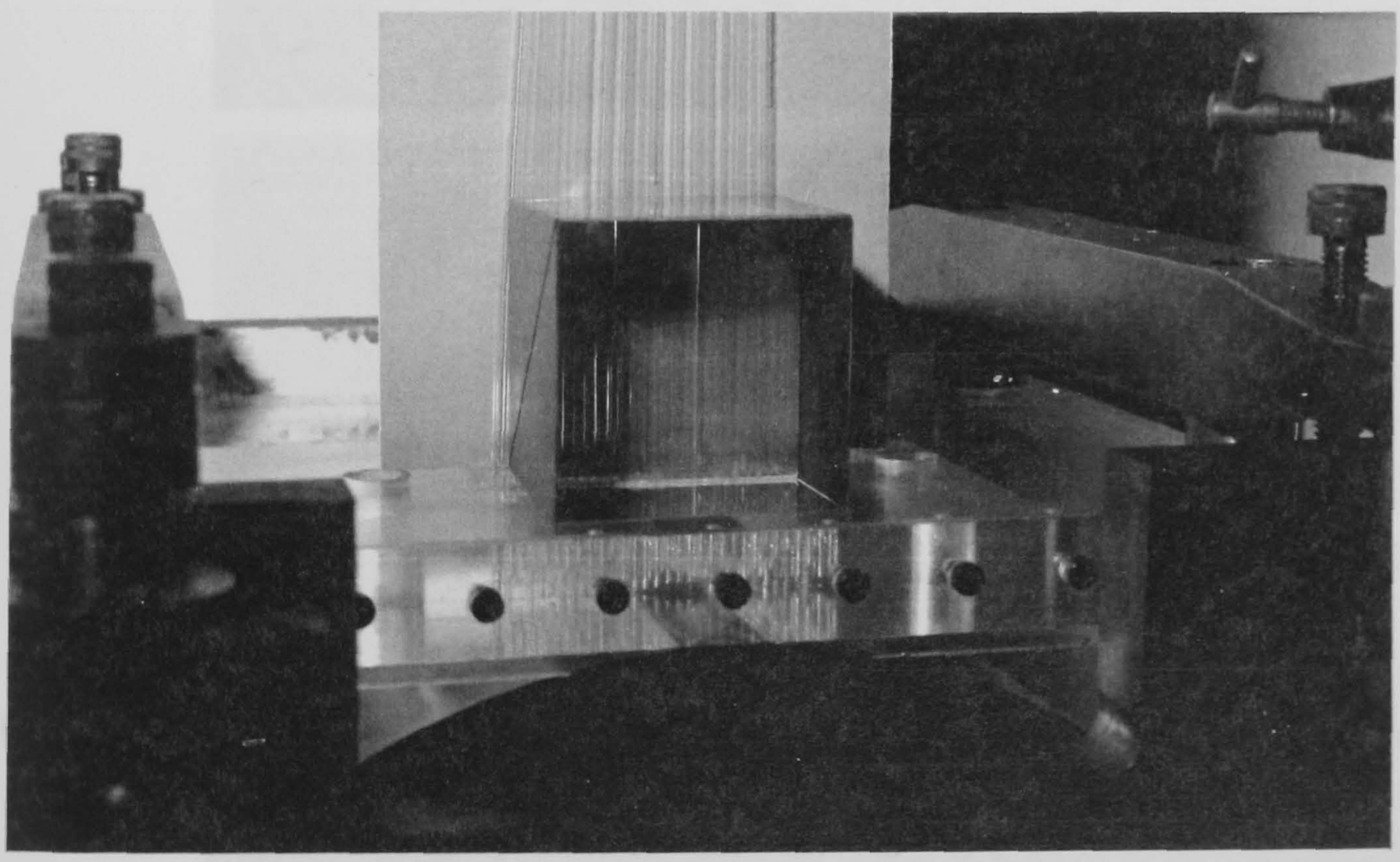

Figure 6.7: Close-up view of beam-splitter block in front of manometer tube, showing free surface locations super-imposed on tube image

(a)

(b)

(c)

(d)

(e)

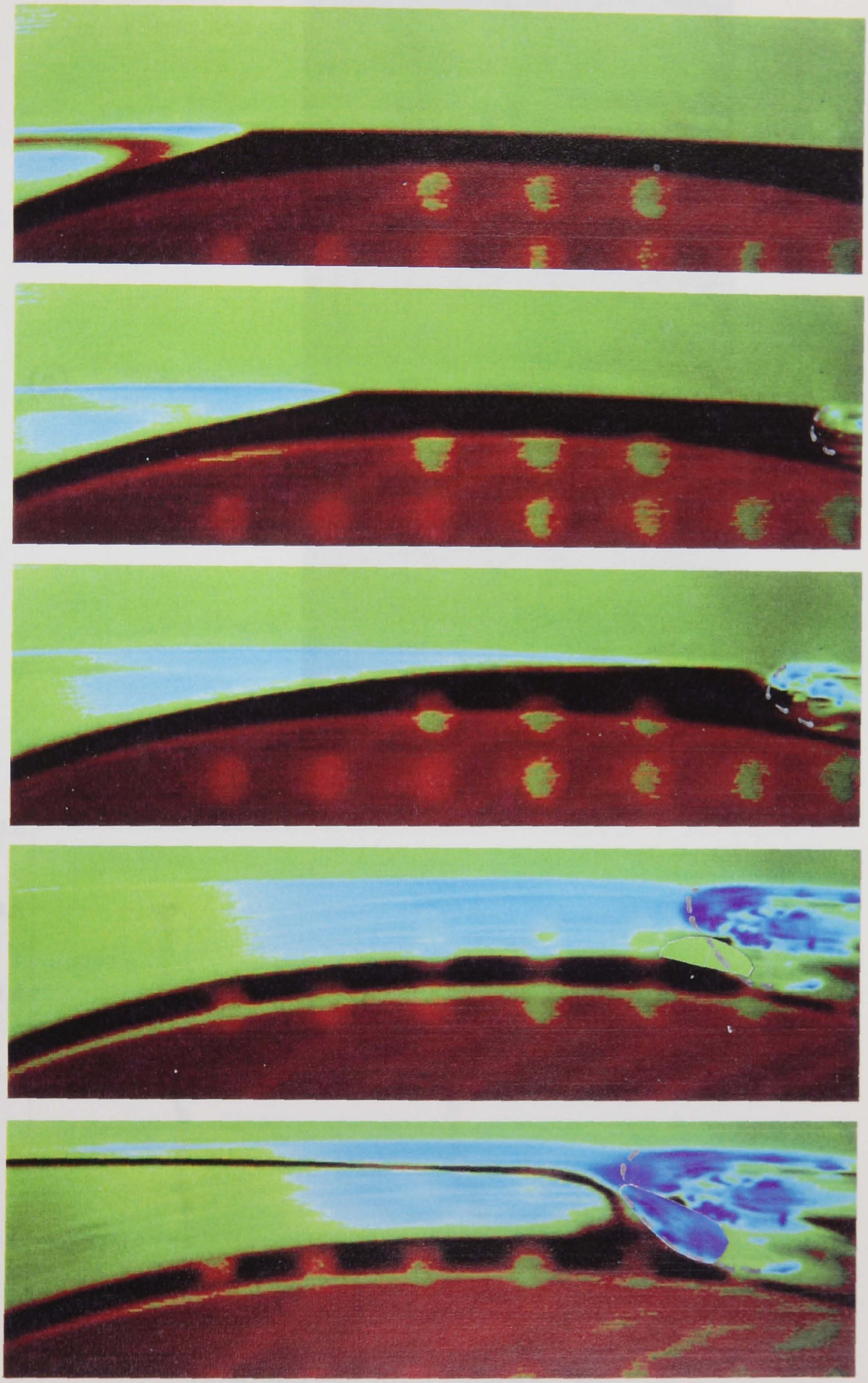

Figure 6.8: Plate-roll flow transformation, (a) $\epsilon = 0.51$, (b) $\epsilon = 0.4$, (c) $\epsilon = 0.29$, (d) $\epsilon = 0.21$, (e) $\epsilon = 0.16$

(a)

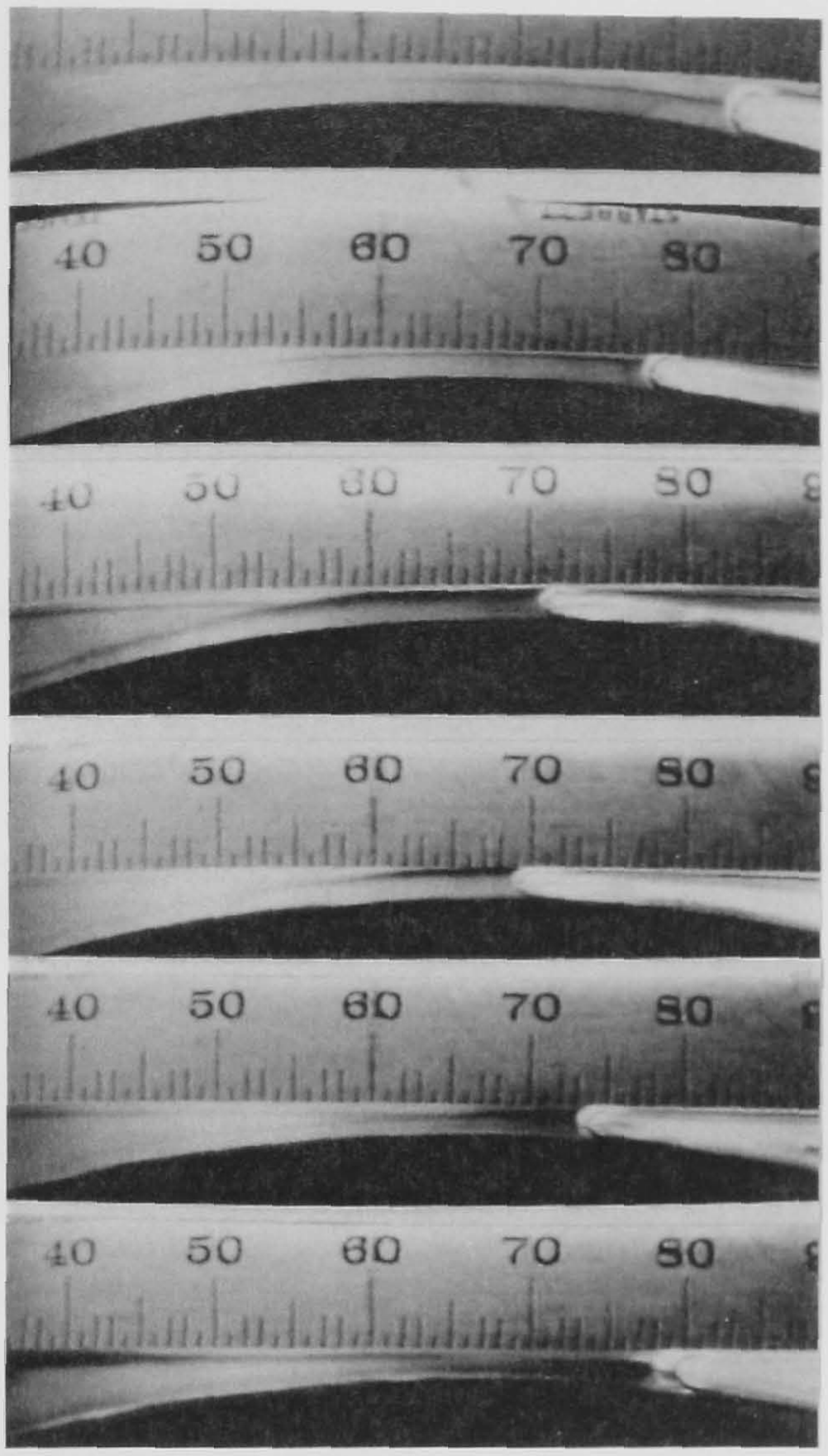

(b)

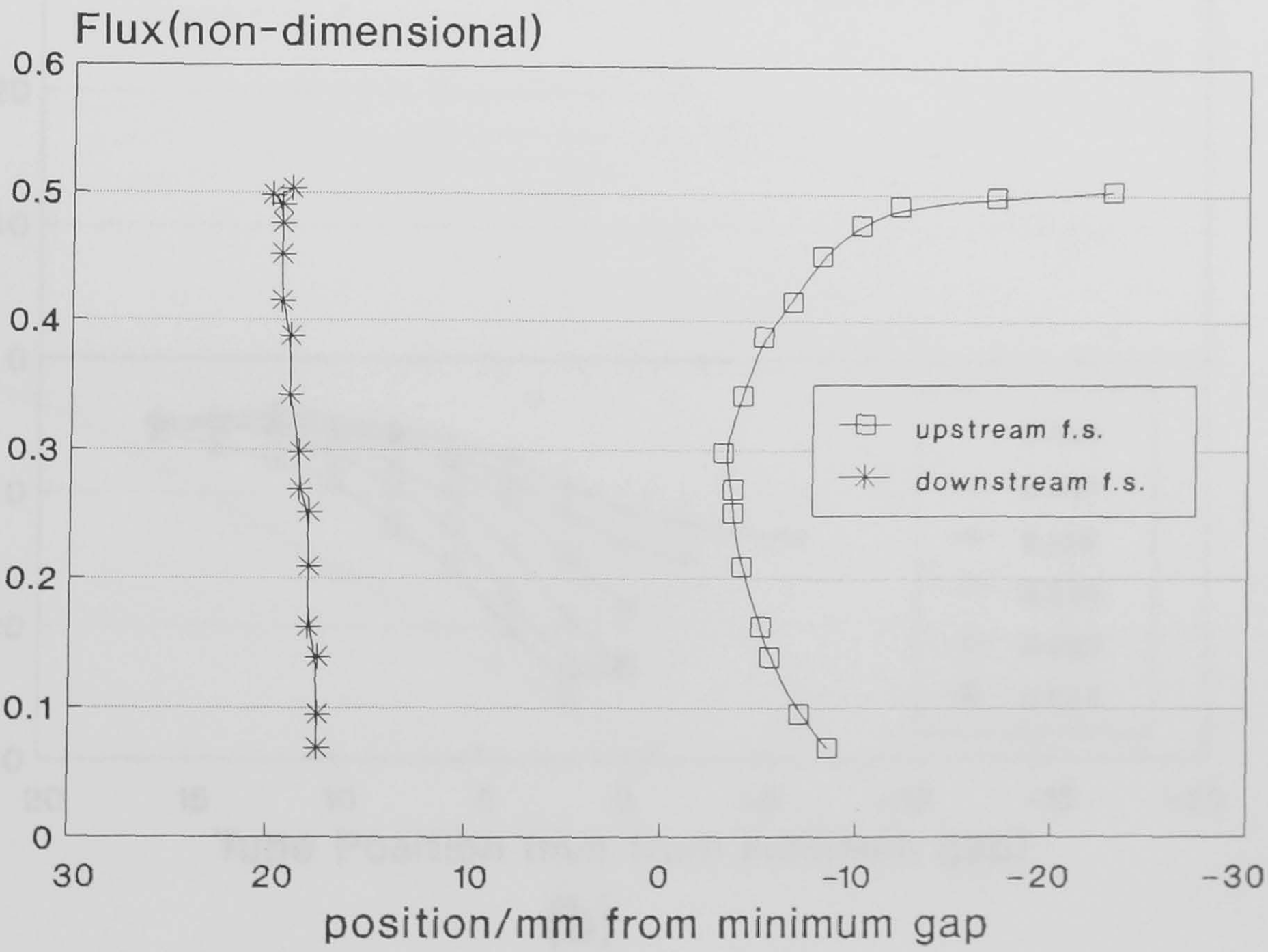

Figure 6.9: Movement of free surface positions during flow transformation (a) pictorial view of upstream free surface, (b) graph of upstream and downstream free surface position versus ϵ.

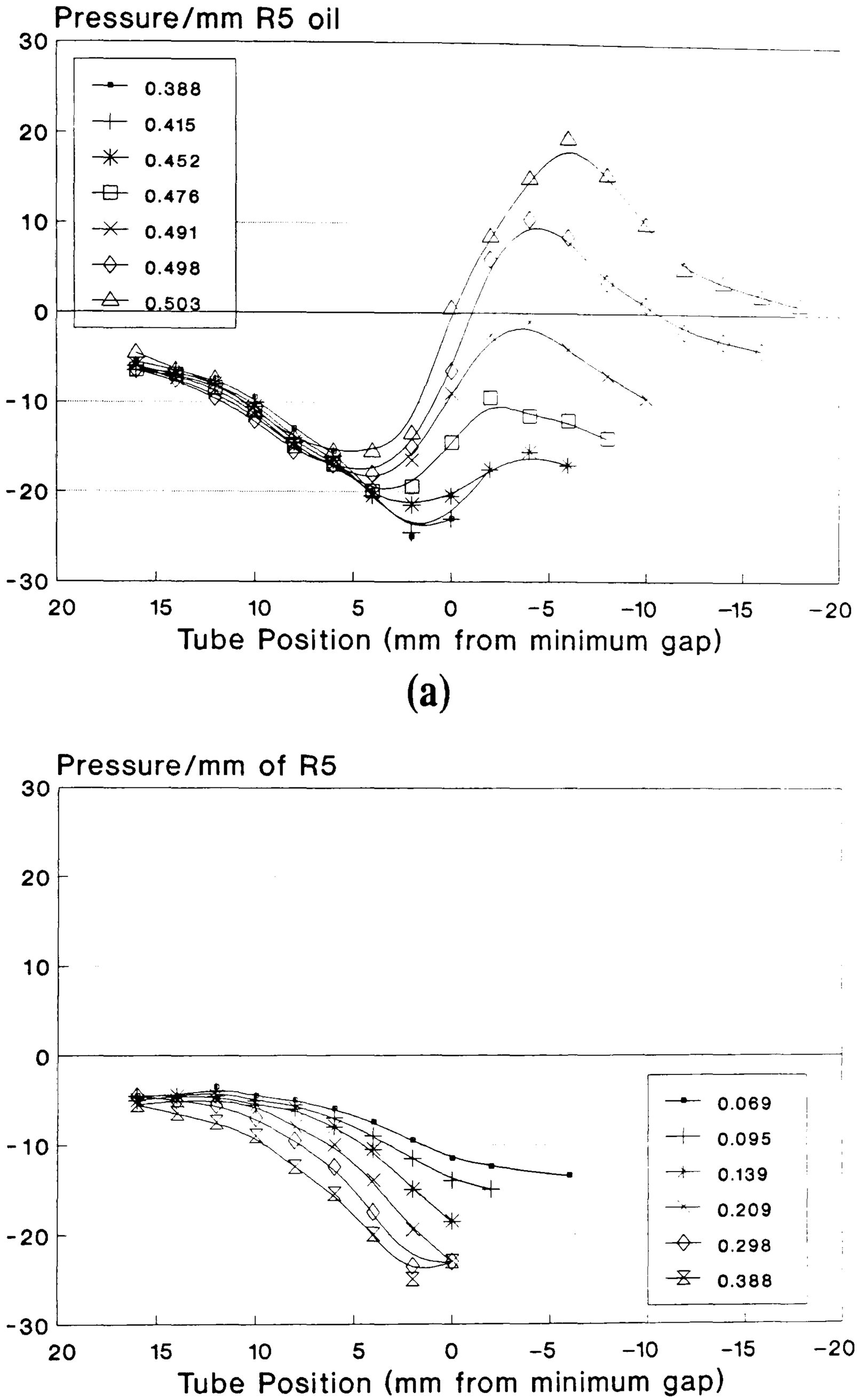

Figure 6.10: Pressure profile transformation ((a) & (b) are part of the same set of results, but have been separated for clarity)

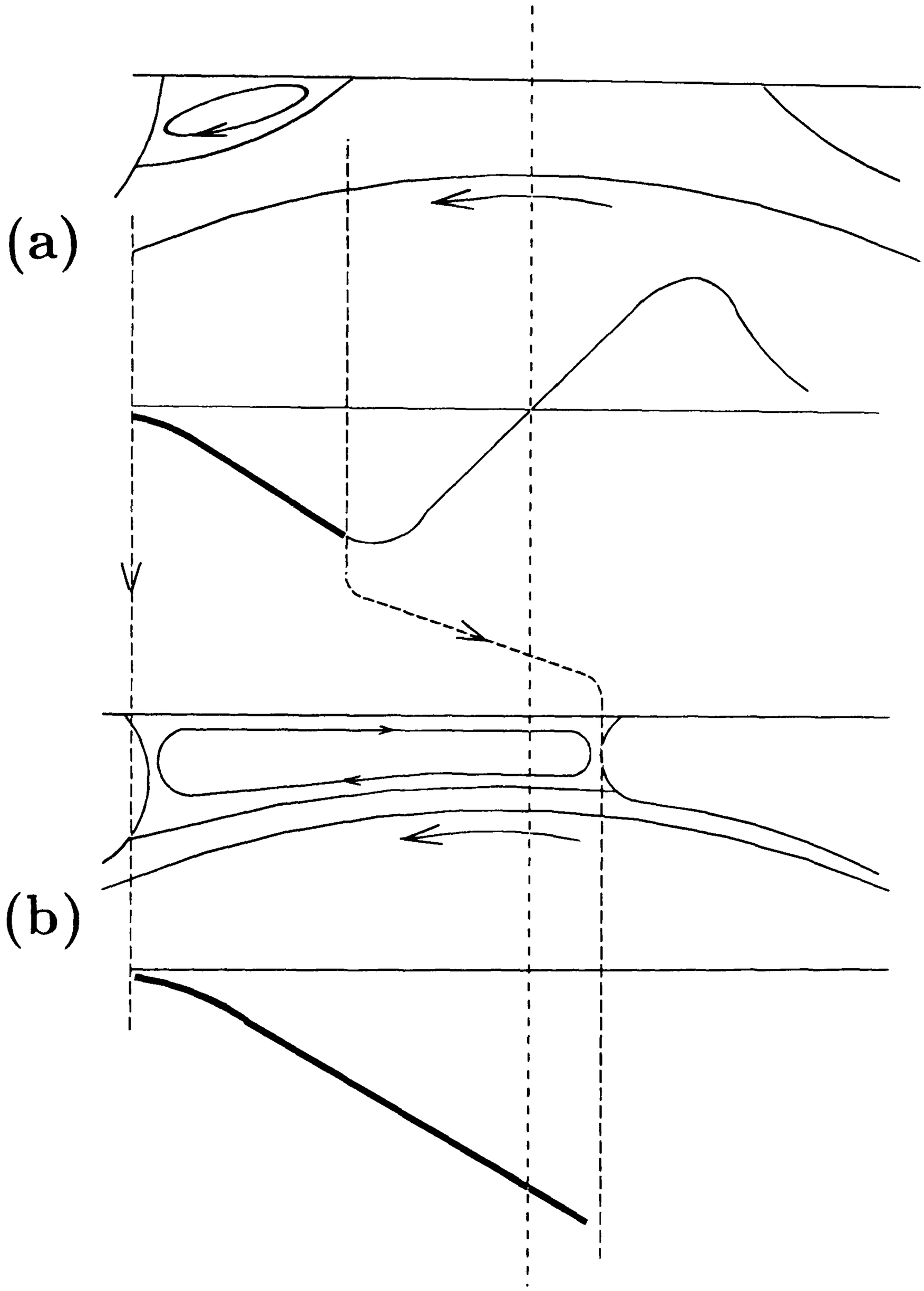

Figure 6.11: Proposed development of the plate-roll flow and associated pressure profile from (a) fully-flooded to (b) ultra-starved conditions

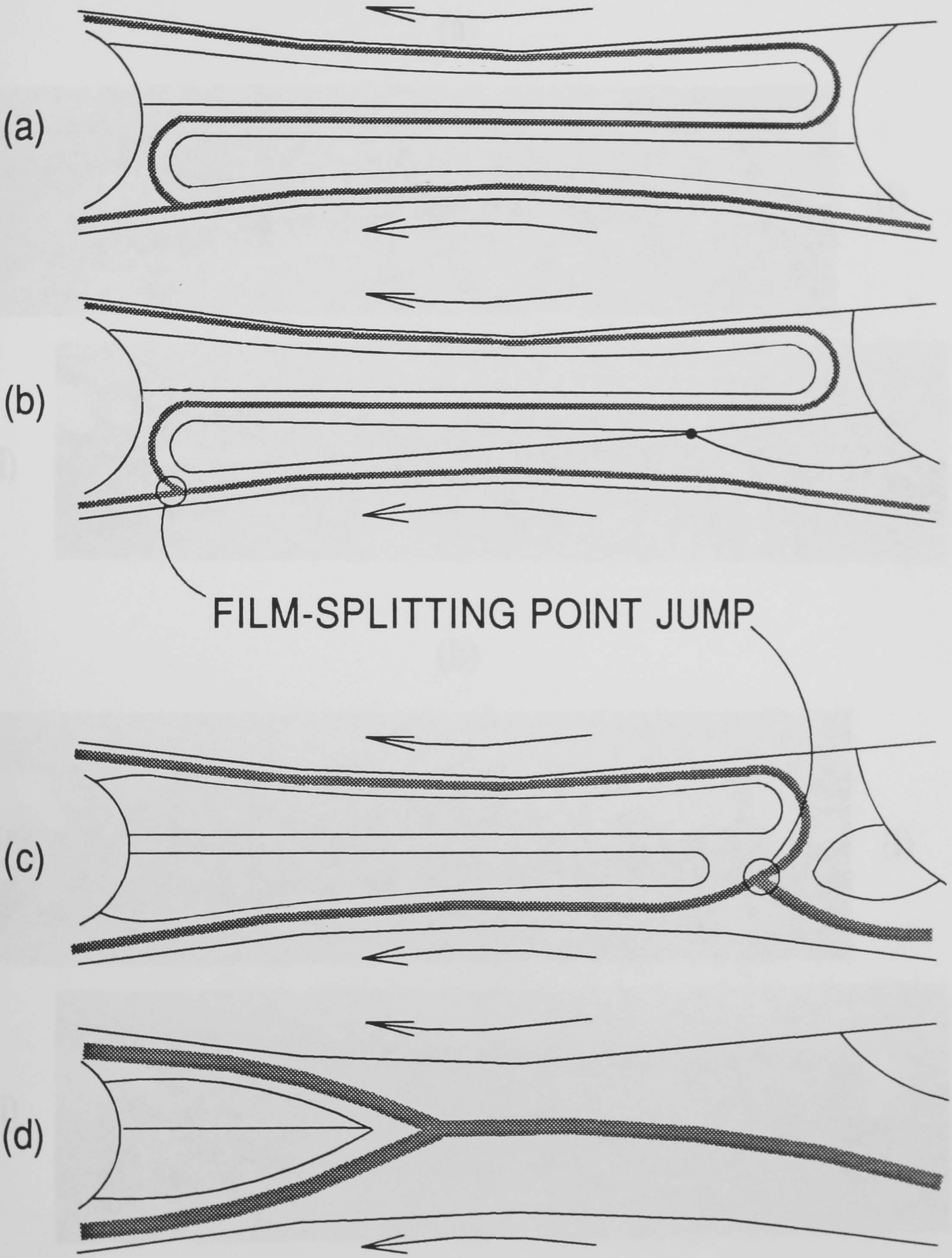

Figure 6.12: Schematic illustration of the forward two-roll coater flow transformation

(a)

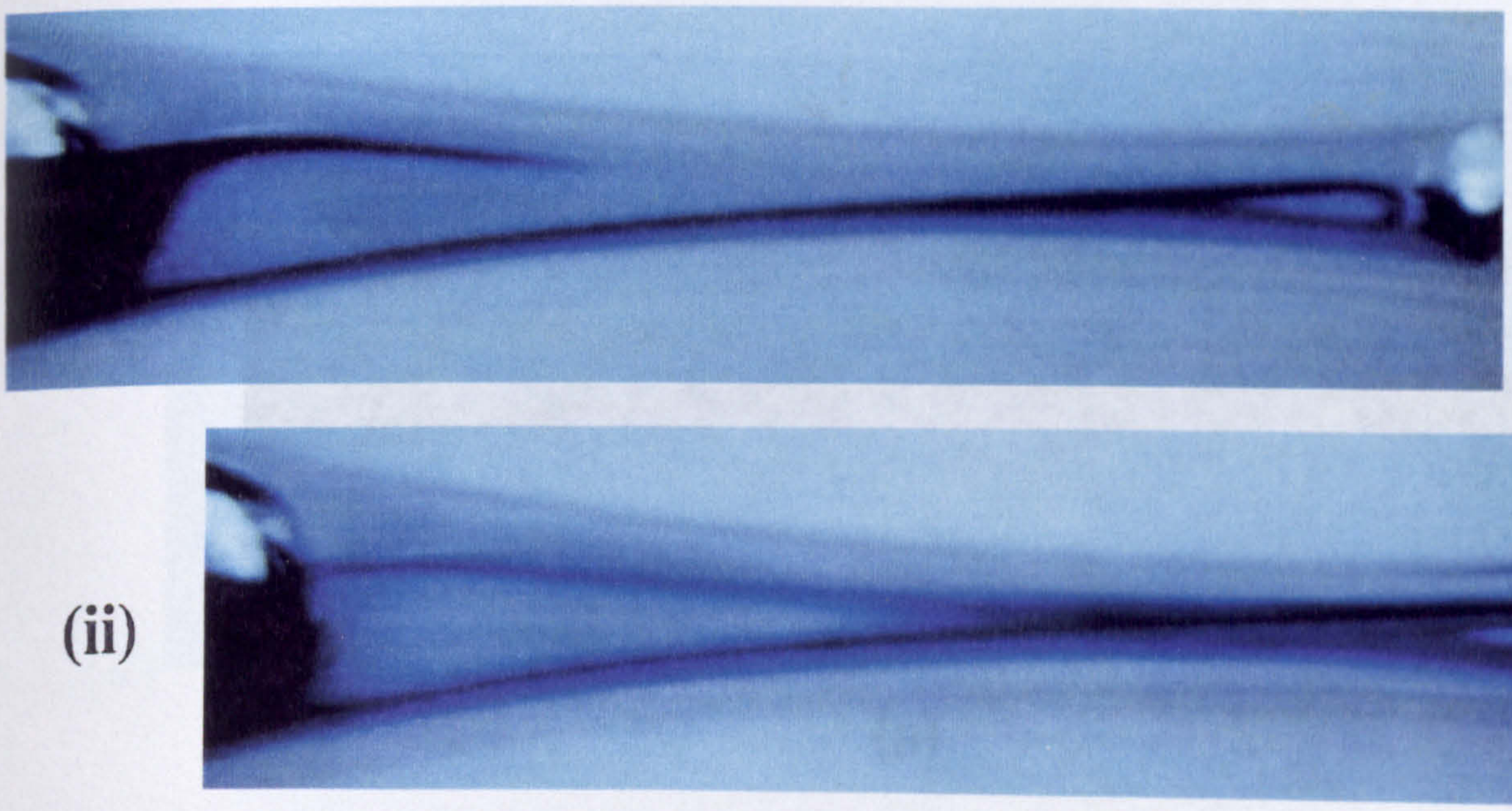

(i)

(ii)

(b)

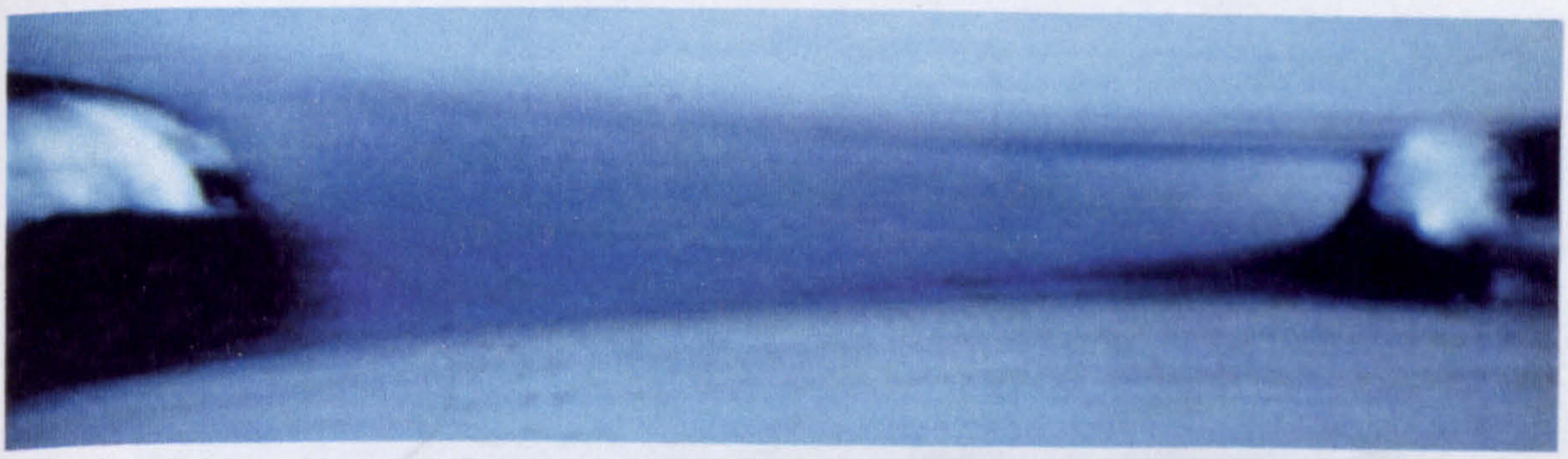

(i)

(ii)

Figure 6.13: Dye images of (a) ultra-starved flow with characteristic S-shaped transfer path and reversed central 'jet'(the effective film-splitting point is in the lower right of the bead), and (b) flooded flow with two- dimensional 'downstream' eddy flow (here the film-splitting point has moved to the lower right of the fluid bead)

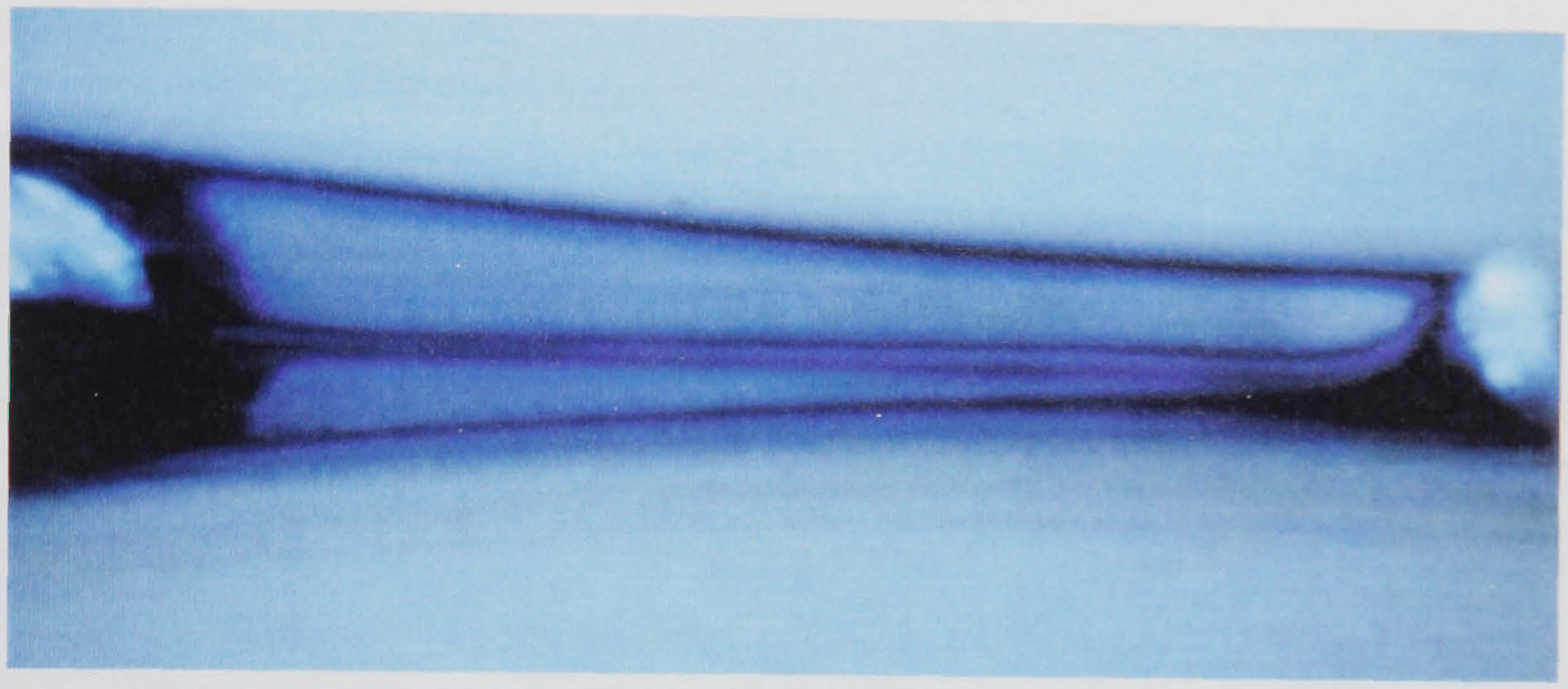

(a)

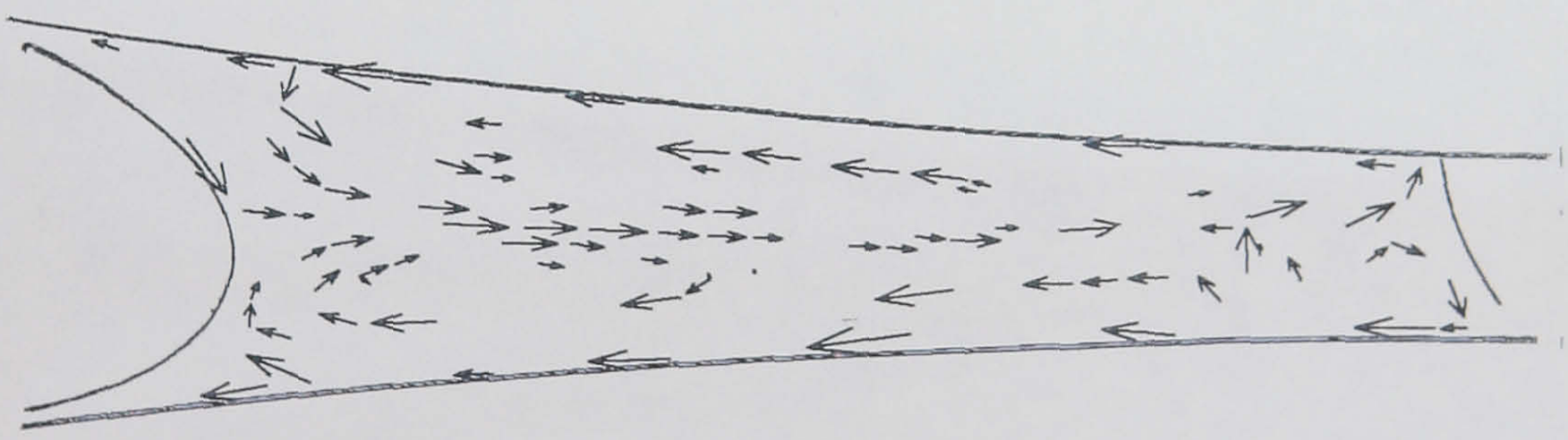

(b)

Figure 6.14: Comparison of (a) Dye image and (b) Velocity plot at the point of transformation

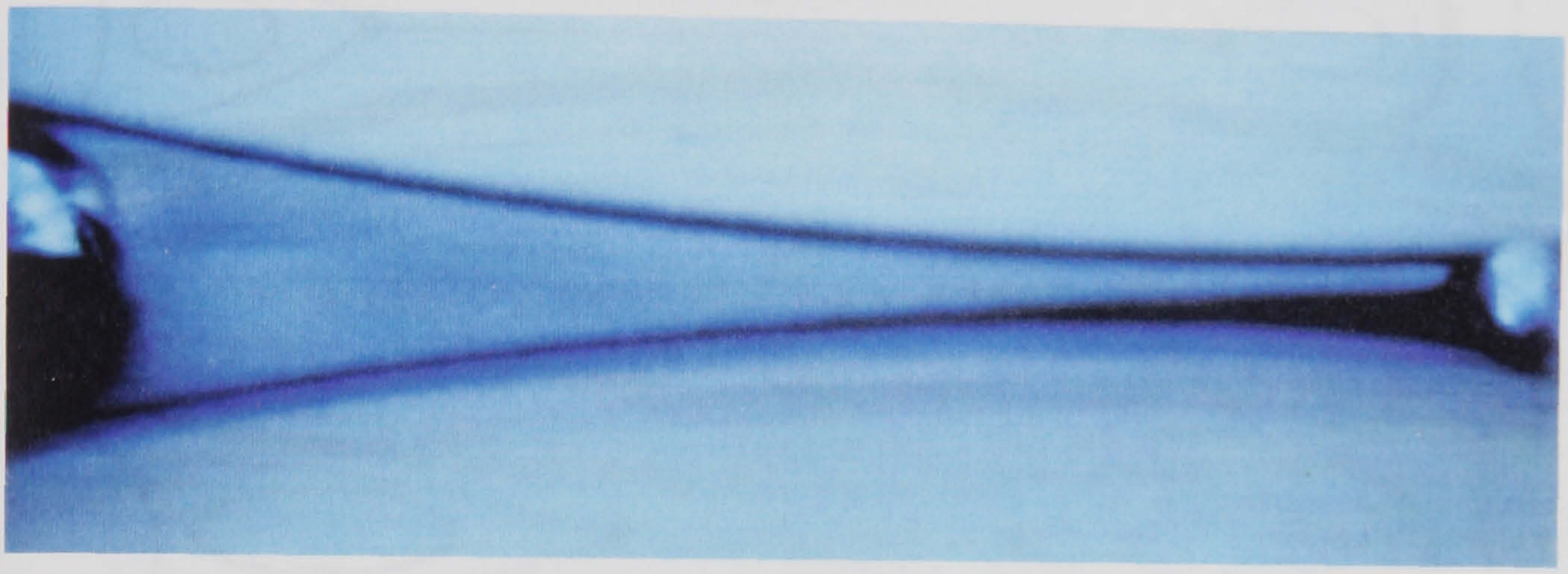

(a)

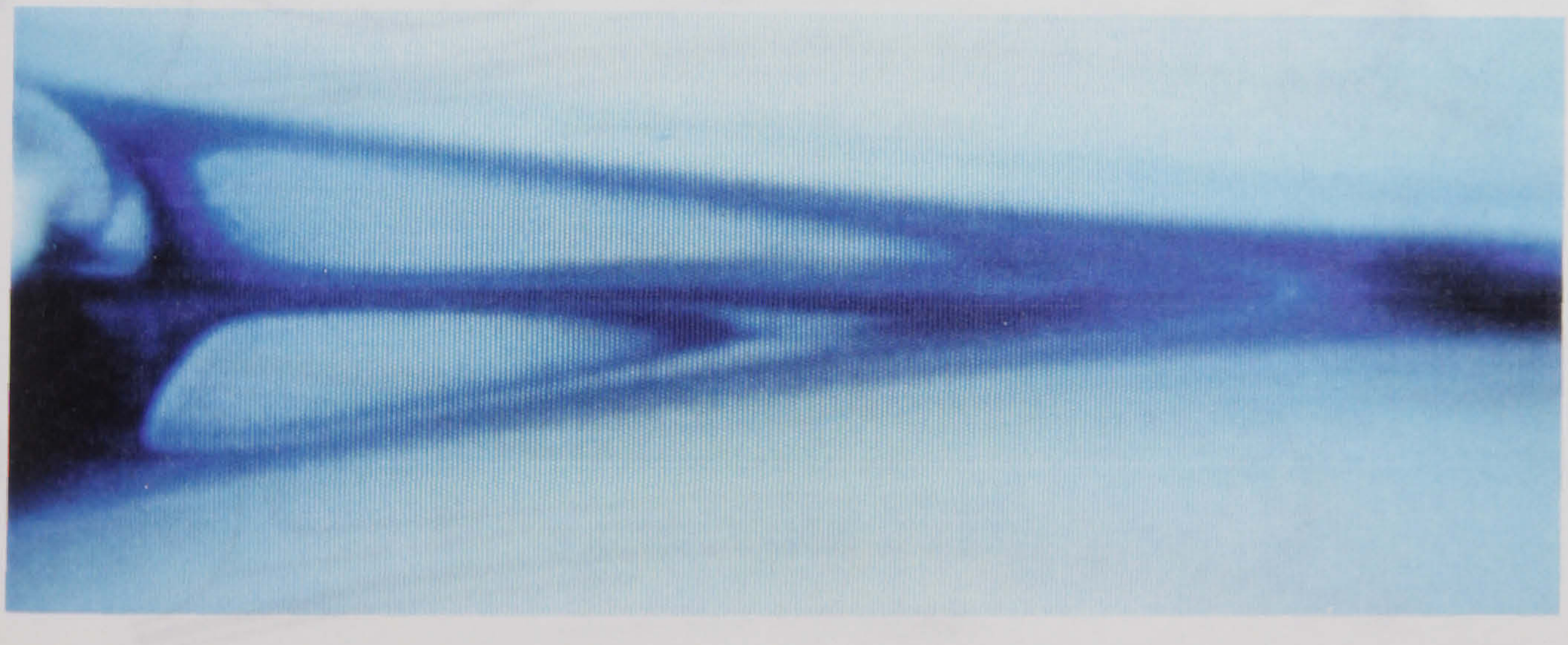

(b)

Figure 6.15: Illustration of (a) film-splitting occurring adjacent to the upstream free surface and (b) the downstream eddy flow

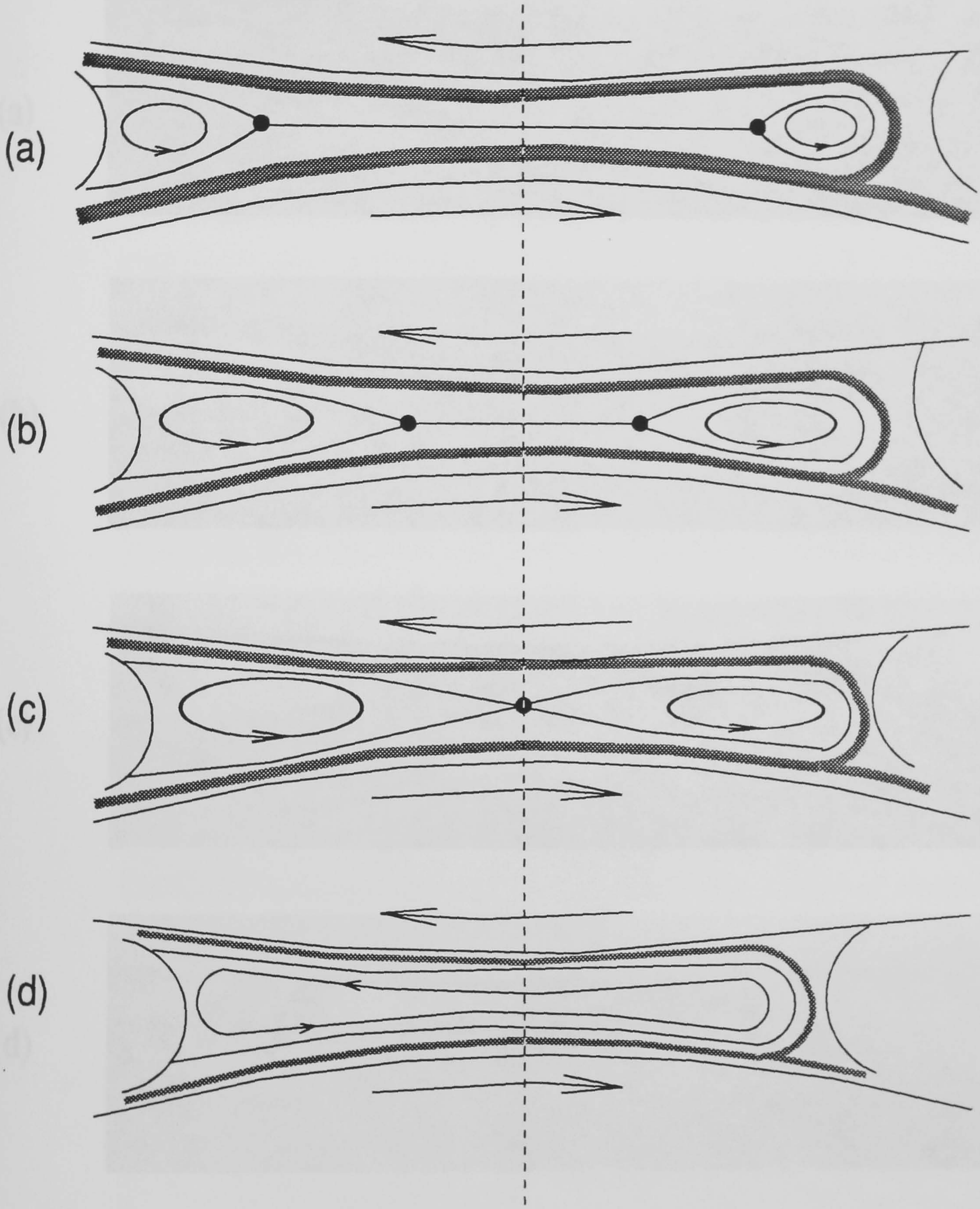

Figure 6.16: Schematic illustration of the reverse roll coating transformation, moving from (a) fully-flooded to (d) ultra-starved inlet

(a)

(b)

(c)

(d)

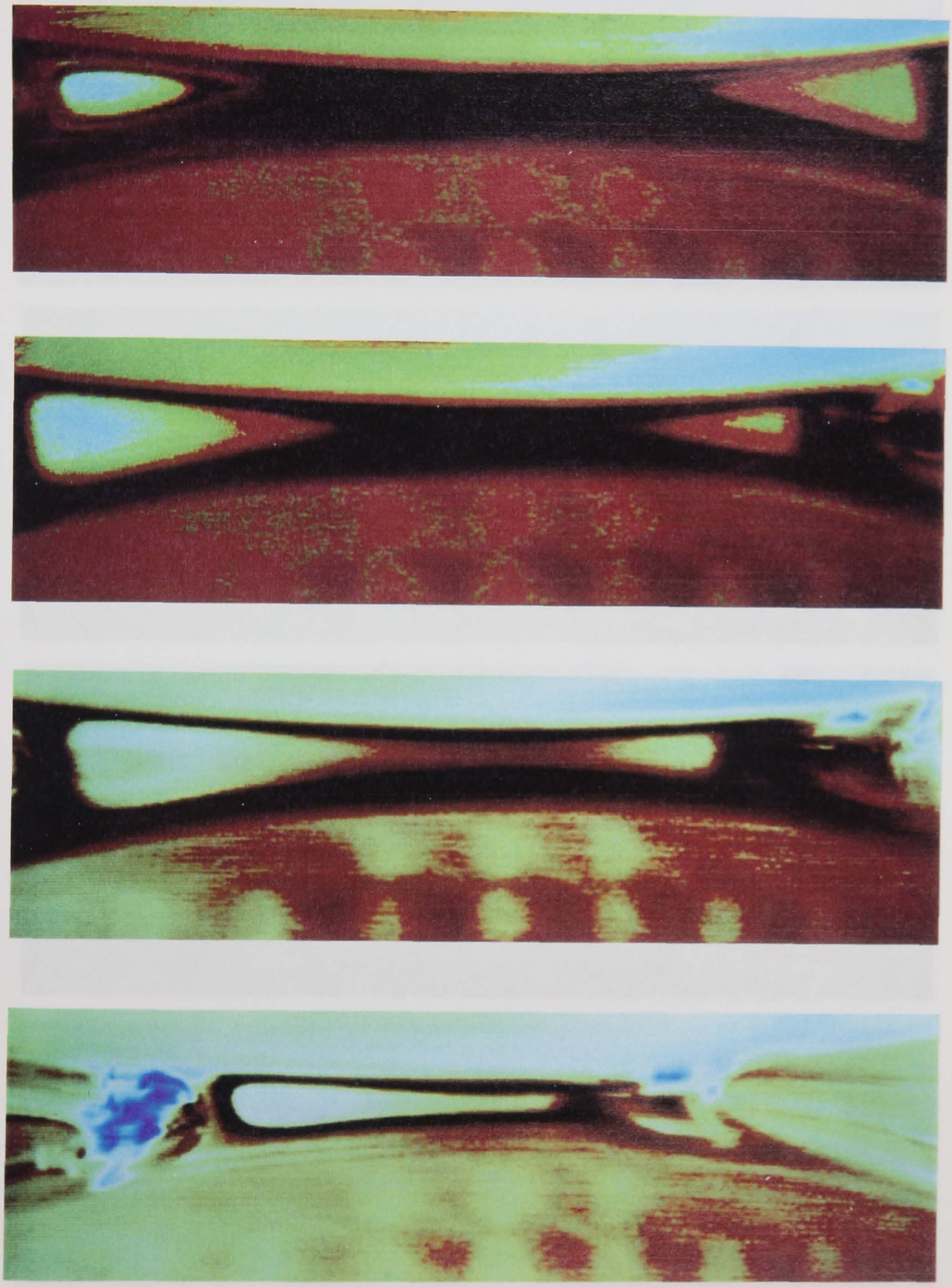

Figure 6.17: Equivalent dye images (false colour) of reverse roll coating transformation

(a)

(b)

(c)

(d)

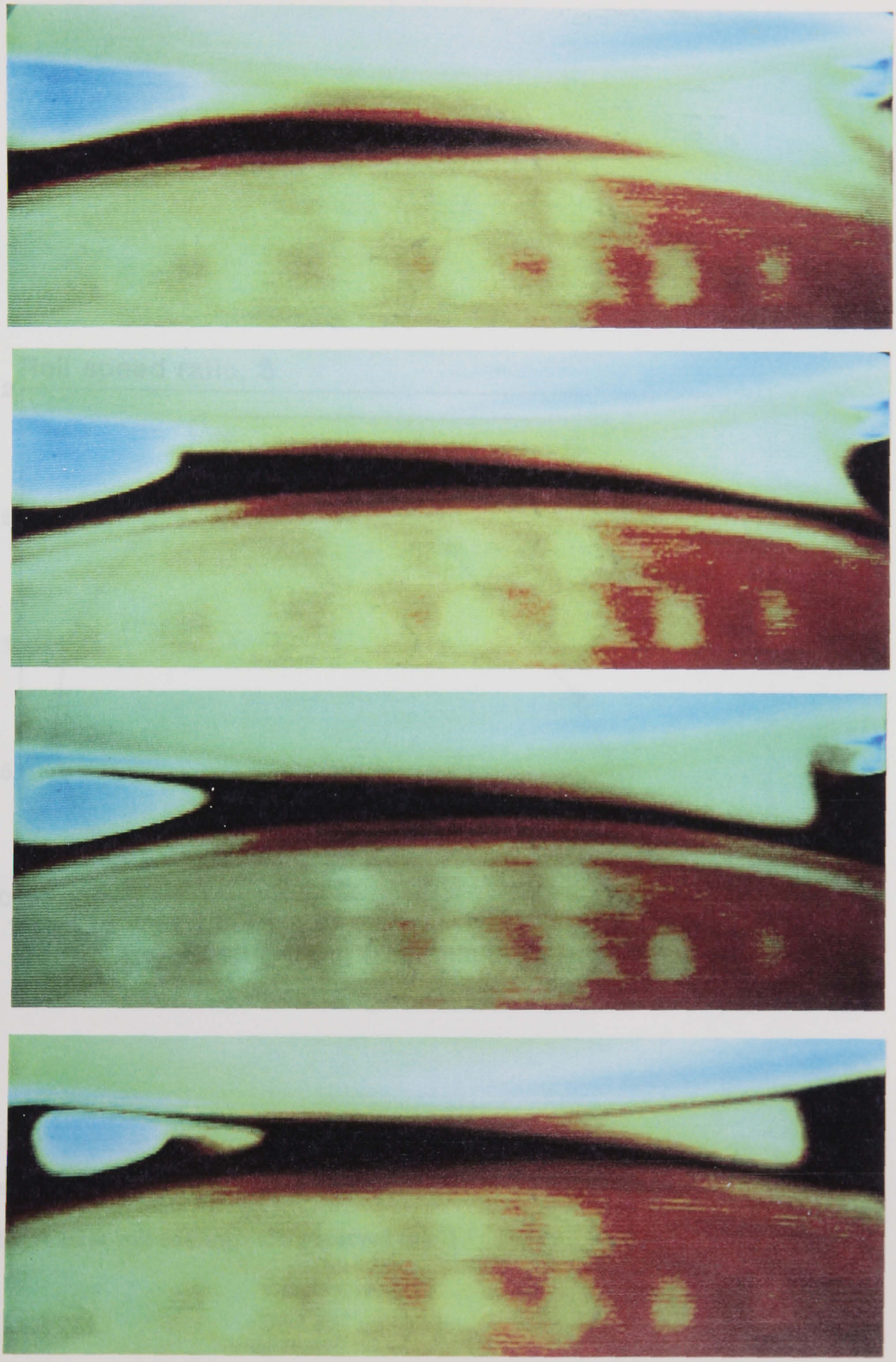

Figure 6.18: Dye injection sequence – fully-flooded reverse roll coating

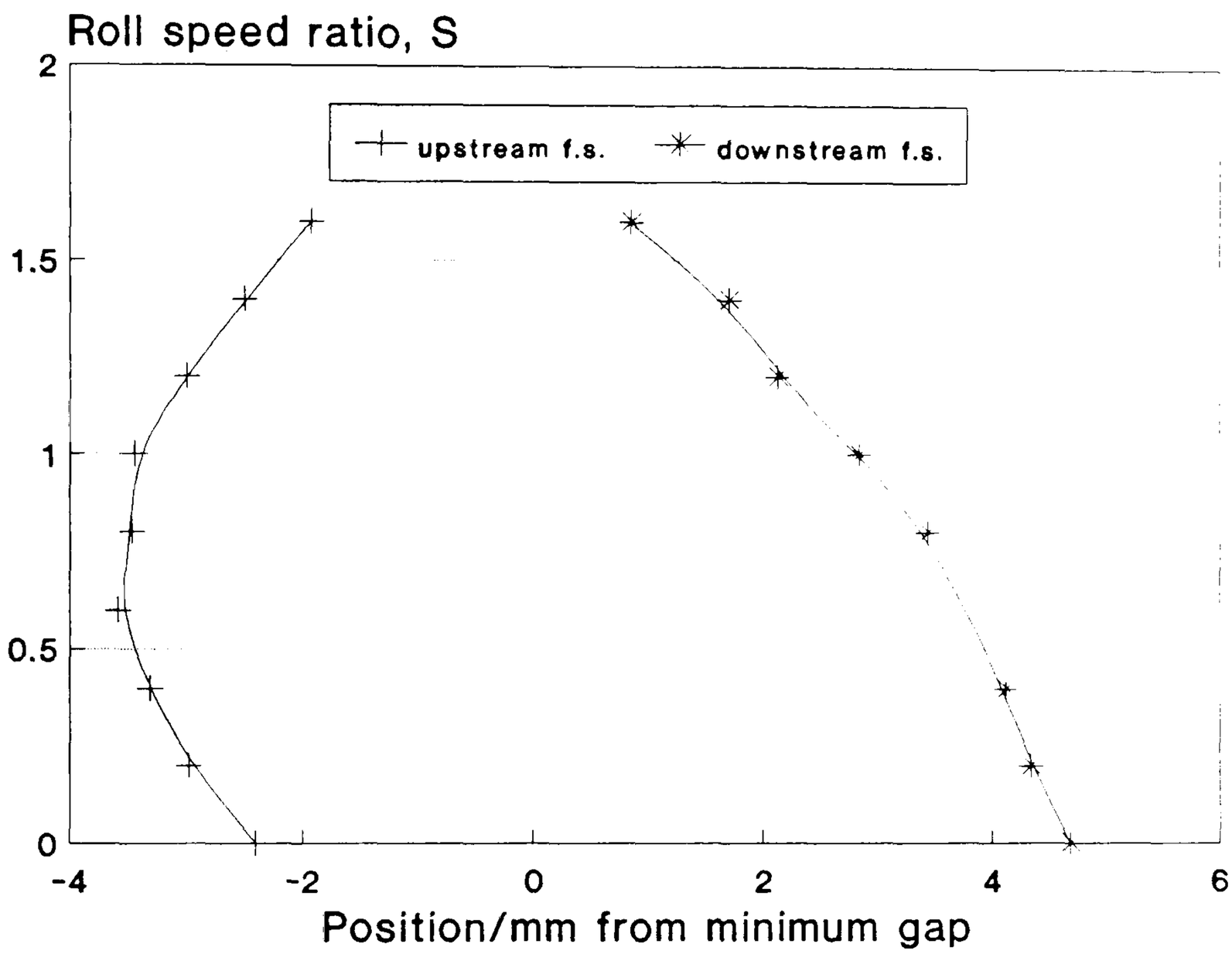

Figure 6.19: Graph of upstream and downstream free surface position versus roll speed ratio for reverse roll coating (ultra-starved inlet)

Chapter 7

Preliminary Investigation of Instabilities, Conclusions, and Future Work

7.1 Introduction

The main objective of this chapter is to discuss several previously reported instabilities in Classical roll coating and to provide in addition qualitative experimental observations of a number of Meniscus roll coating instabilities. A mechanism for the cause of these new instabilities is proposed, based on the knowledge gained in previous chapters.

The reverse roll coating regime is discussed briefly with regard to the work of Coyle et al [1990b], which raises several interesting questions about the behaviour of the flow in the nip of a reverse roll coater. In attempting to validate their numerical predictions here, attention is drawn to the influence of the crucially important dynamic wetting line.

Finally, the significance of this work is discussed, and suggestions are made for fu-

ture experimental studies in the area of roll coating flows.

7.2 Instabilities In Roll Coating

A successful coating operation is one which results in a liquid layer which is uniform in both time and space, i.e. a coat that does not suffer from either down-web or cross-web irregularities. The challenges in this area are not simply of a theoretical nature. Experimental difficulties arise from the small-scale structure of these flows. For example, rapidly rotating rolls, with a very small clearance between their surfaces, are employed in most industrial roll coating processes, which make it difficult to observe or probe the flow extensively and to make accurate measurements. In general instabilities occur in a system when one or more of the operating parameters become 'excessive' (e.g. in Classical roll coating, excessively high roll speeds lead to ribbing). As a result, experimental analysis of instabilities is made increasingly difficult, because the investigator must work at the 'extremes' of a particular flow system in order to make observations.

In industry it is very difficult to compare the quality of films produced by alternative coating techniques (e.g. forward and reverse roll coating, and indeed Classical and Meniscus conditions) immediately after coating (i.e. when the coating is still wet), because of the poor performance and response of wet film thickness monitoring equipment (see Chapter 2, § 2.5). In general, the coated liquid will contain a small percentage of solids. Therefore, when dried, the layer will only be a fraction of its' wet coat thickness. The difference in coat quality for two systems only becomes apparent when, for example, a dye layer (as used in the photographic industry), which is required to perform under very stringent conditions, is exposed and reveals an inhomogenity in the layer, be it regular or random. In addition, finished film products tend to be coated with a number of layers, each performing a different function (e.g. a base coat, two dye layers,

and an anti-abrasion layer). This makes it far more difficult to focus on the offending layer and/or coating process once a functional defect arises.

There are three categories of instabilities which arise in roll coating systems; the first is associated with fluid wetting a dry surface, the second is caused by the nip flow, and the third is related to the 'motion' of the thin fluid films themselves (be they on the inlet or outlet side of the coating system). An example of the first category is that of air entrainment during roll coating which can result in bubbling/foaming of the coated film. Ribbing falls into the second category; it is a consequence of the nature of the flow between the two rolls. An example of the third category is the way in which the inlet fluid film, for example, is 'manipulated' – a common method of feeding a roll nip is to dip the lower roll in a pan of fluid. A layer of fluid then attaches itself to the ascending roll surface by the action of viscosity (see Chapter 1, Figure 1.3). It is often the case that only a very shallow pan is used, and the fluid film is picked up from well below the centre-line of the roll. Therefore the film on the surface spends quite some time at an inverted angle (see Figure 7.1); in this position the fluid layer is gravitationally unstable and any small perturbations may cause the fluid to form drips in the layer which, when coupled with the motion of the roll surface, result in streaking as the fluid layer enters the nip. In addition, the size and shape of the pan can affect the quality of the lifted film; in an extreme case, where the side wall of the pan is in close proximity to the fluid pick-up region, a geometry similar to a plate-roll system is set up.

7.2.1 Experimental Apparatus

In using a cylindrical cantilevered upper roll, manufactured from acrylic, it is a simple matter to observe a number of the instabilities which may occur on the free surfaces along the axis of the nip between the two rolls and indeed within the fluid which fills this region. The experimental apparatus is shown in Figure 7.2. A mirror is suspended

inside the upper hollow roll, at an angle of 45^0 to allow horizontal viewing of the fluid bead. In the present work the internal features of the bead flow were not investigated under unstable conditions.

The curvature of the upper roll wall, through which these instabilities are observed, is effectively negligible over the width of the fluid bead formed in the nip. Instabilities which create 'steady' flow patterns can be observed with a standard video system. However, to observe high speed 'unsteady' instabilities required the use of the Kodak Ektapro High Speed Video system (see Chapter 3).

7.2.2 Classical Roll Coating Regime

Ribbing

Ribbing is a common feature of many of the methods which involve the spreading or rolling of a liquid. Figure 7.3 illustrates this phenomenon for a roll coater - regularly-spaced streaks are present running in the down-web direction. Hoare[1937] reported some early results of ribs formed when direct rolling is used to coat metal sheets with a layer of tin and offered the first crude attempt to explain this phenomena. Pearson[1960] makes a number of references to examples of ribbing as observed in the printing (e.g. Sjodahl[1951]), photographic, leathercloth and paint industries. In fact he discusses perhaps the most familiar example of ribbing – that which occurs when thick paint is applied to a flat surface using a brush or roller. Pearson was the first to undertake a theoretical investigation of this problem by applying the lubrication approximation and linear stability theory to the flow associated with a wedge spreader. He showed the Capillary number ($\eta U/T$) to be the critical parameter governing stability - viscous forces are de-stabilising while surface tension is stabilising. Lacking a set of boundary conditions for the film-splitting region, he was unable to derive a specific criterion for

the onset of ribbing.

Pitts & Greiller[1961] took this analysis one step further by investigating the symmetric film-splitting flow between counter-rotating rollers (i.e. forward roll coating). Adopting the creeping flow approximation they solved the biharmonic equation for the flow behind the meniscus; the result was the flow rate as a function of the Capillary number. From experimental observations the free surface was assumed to be parabolic (sinusoidal in the transverse direction) in the calculation of the curvature terms. This led to the following condition for the onset of ribbing, involving the Capillary number and the geometric parameter, H_0/R:

$$\frac{\eta U}{T} \simeq A\left(\frac{H_0}{2R}\right)^B \tag{7.1}$$

Where $B = 1$ and $A = 28$. This is a crude approach, which rests on many approximations; in solving the biharmonic equation, the traction boundary conditions on the free surface were satisfied only very close to the symmetry plane, while the no-slip boundary conditions on the roll surfaces were not satisfied. Theoretical predictions were found to be in poor agreement with experimental data to which they fitted a curve giving $A = 31$. Further experimental data has been reported with equal speed rollers; Mill & South[1967] found A and B to have the values 17.3 and 0.75, respectively. Greener et al [1980], on the other hand, reported values for A and B of 1875 and 2, respectively.

Savage[1977] used the basic ideas of Pearson and Pitts & Greiller, but instead applied the Separation boundary conditions (see Chapter 1, §§1.2.1) adopted by Coyne & Elrod[1971] to solve the problem of film-splitting between a roll and a flat plate, and using a simple force balance between the pressure and surface tension forces acting on the perturbed meniscus produced the following stability criterion for the onset of

ribbing:

$$\frac{d}{dx}\left\{P + \frac{T}{r}\right\} < 0 \tag{7.2}$$

where P is the fluid pressure immediately upstream of the interface and r is the radius of curvature of the interface. Lubrication theory was used to give an expression for dP/dx (as a function of flow rate, which was calculated as a function of the Capillary number).

Greener & Middleman[1979] adapted Savage's calculations for the case of symmetric film-splitting between rollers. Savage[1984] noting the widely differing theoretical predictions also observed that the reported experimental data fell into separate regions of the $(\eta U/T,\ H_0/R)$ plane. He performed a linear stability analysis for both the plate-roller and equal speed two-roll coater geometries using the Separation boundary conditions. The analysis yields a criterion for ribbing involving the two dimensional parameters $(T/\eta U)(H_0/R)$ and $(T/\eta U)(H_0/R)^{1/2}$. The theoretical predictions for the equal speed two roll coater were found to exhibit remarkably close agreement with the experimental data of Pitts and Greiller, Mill and South and Greener et al for $0 < Ca < 1$.

Coyle[1985] pointed out the major difficulty with the experimental studies of the onset of ribbing carried out by the above workers; each used the naked eye to detect the onset of instability. Considering the subjective nature of the discrimination between uniformity and non-uniformity, their results are discordant. He devised two different measurement schemes to detect and quantify the onset and behaviour of ribbing. Both systems rely on the effect of the meniscus on a focused light sheet. In one case the light sheet travels through the nip and onto a plate of opal glass (the viewing screen); in the other case the light sheet is reflected off a length of the meniscus, at a glancing angle, onto a similar viewing screen.

When the process is stable the projected light appears as a uniform rectangular patch. As ribs form on the meniscus, the light sheet is focused into alternating bright and dark bands by the curvature associated with the ribs. This detection system has the advantage that it exaggerates the behaviour of the meniscus and is thus far more sensitive. Coyle reports that the critical Capillary numbers for the onset of ribbing are as small as one-tenth of the previously published values. It would appear that further experimental and analytical studies are required to clarify these results.

Coyle carried out a finite element stability analysis on the two roll coater, with the obvious advantage that gross simplifications of the flow field near the meniscus are not necessary, in contrast to the analytical models described above. He concludes that, although the lubrication-type model proposed by Savage[1977] underestimates the wave number at criticality (because it uses an inaccurate critical capillary number), if the wave number is calculated by the Savage model using the Capillary number predicted by the finite element analysis, the agreement is excellent. In comparing the finite element-based linear stability analysis and light-sheet reflection experiments, Coyle reports poor agreement, with theory predicting the flow to be much more stable than is observed in practice. He proposes that the end effects of the rolls serve to destabilise the flow by creating 'escape' routes for fluid, which causes the position of the downstream free surface to move back into the nip. It is true to say that this effect is significantly reduced in an industrial two-roll coater, with one roll mounted vertically above the other, the body of liquid in the nip tends to remain suspended, thus minimising end leakage.

Chatter

'Chatter' is the appearance of cross-web lines, bands, or bars of fairly uniform width and period, indicating small down-web mechanical vibrations which can show up as web

speed variations and/or pulsations in the coating bead. The source of these vibrations can include the roll drives and/or the web handling system. Resonant frequencies in the drives, supports and the web itself can cause severe problems. This instability is generally present on all coatings, to some degree, due to the vibration of the coating machinery being transmitted to the coat, but under most circumstances it can be tolerated. For new applications where the coating tolerances are more stringent, this type of instability is a real problem.

This vibration has a major effect in the nip of a fully-flooded roll coater; here the outlet film thicknesses are directly proportional to roll separation and thus any change (cyclical or otherwise) in this parameter. It is generally considered that Meniscus roll coating produces exceptionally uniform films and is more tolerant of roll vibration and runout (Howe[1991]). This may be due, in part, to the fact that the outlet film thicknesses are independent of roll gap (Thompson[1992]), which has been verified experimentally here. Indeed it is intuitive to think of the vortices acting as 'dampers' within the fluid bead - 'protecting' the film-splitting flow.

Air Entrainment

Air entrainment is a common feature in coating flows when certain operational parameters are reached - in particular roll speeds and fluid properties - see Chapter 1, § 1.4. Figure 7.4 shows an example of air entrainment in roll coating with the characteristic 'Vee' shaped contact line and bubbles which have broken off from the apex (see Burley & Kennedy[1976], for example). O'Connell[1989] gives a comprehensive review of air entrainment and the mechanisms involved.

7.2.3 Meniscus Roll Coating Regime

With reference to the pressure results inside the nip for the Meniscus roll coating condition (i.e. sub-ambient throughout, with the largest negative pressure immediately downstream of the upstream free surface), the possibility of a small perturbation in the flow will tend to 'upset' the equilibrium of the surface tension force exerted by the free surface and the viscous force within the fluid, resulting in the free surface being locally 'sucked' into the nip. From the results of the Meniscus roll coating film thickness model, described in Chapter 5, it is clear that important parameters such as the coated film thickness are independent of the gap between the rolls.

Therefore, under stable operating conditions, problems such as the eccentricity of the rolls, which produce a cyclical variation in the gap size can be accommodated without detriment to the outlet film. When considering the causes of instabilities it is clear that the position of the upstream free surface is of paramount importance in determining its' shape and thus the surface tension force resulting from it. Therefore any operating parameters which influence the movement or change in shape of this free surface, such as increasing roll speeds or the speed ratio (tending to move the 'body' of the bead further through the nip) together with the effect of the eccentricity of the rollers (tending to cyclically perturb the flow) may result in a 'necking' instability (see below).

Upstream Wave

As the upstream free surface is forced to approach the minimum gap position under a condition of transformation from fully-flooded to ultra-starved flow (e.g. by increasing roll speed ratio), a travelling wave is observed on the upstream free surface (see Figures 7.5(a), (b) and (c)). This is in fact an 'air wave' invading the fluid bead. By increasing the speed ratio still further, the crest of the travelling wave becomes elongated and this

can result in entrainment of an air bubble into the fluid bead (see Figures 7.6(a), (b) and (c)). Multiple bubbles can also be entrained (see Figures 7.7(a) & (b)). Waves travel in both directions along the upstream free surface (see Figure 7.8(a)) and collisions occur periodically (see Figure 7.8(b)) resulting in entrainment of a far larger volume of air.

Bead Break

If speed ratio is increased under ultra-starved conditions the flow moves from a stable operating regime to one in which the fluid bead exhibits localised upstream necking (see Figures 7.9(a) & (b)) which can lead to bead break in a random (Figure 7.10(a)) or regular (Figure 7.10(b)) fashion producing a cellular array of beads. It would appear that the surface tension pressure cannot balance the increased viscosity-generated negative pressure in the bead and therefore the free surface is sucked in when perturbed. As the upper roll speed, U_1, is increased further, increased local neckings can occur until a quasi-stable regime is reached with equi-spaced beads of fluid along the nip, producing a regular striped coating pattern on the roll. This instability is unlike ribbing in that it's origin stems from the upstream free surface, and it produces alternate wet and dry stripes on the upper roll (which would be the web in practice). In Classical roll coating the ribbing instability stems from the downstream free surface and the stripes are alternately of high/low coat weight.

The flow in these regular beads cannot be treated as two-dimensional since the axial length is similar to the bead width. In industry random coating 'misses' are observed on the web - they are sometimes referred to as 'cigar misses' due to their characteristic shape on the web. It would be logical to assume that they are caused by the bead breaking and then reforming very quickly (i.e. alternating between Figure 7.9(b) and 7.10(a)) - this could be thought of as a perturbation which is overcome and not allowed to propagate.

Alternatively as S is increased by reducing U_2 (i.e. the nip experiences excessive starvation), a break in the bead will occur somewhere along it's length and this will be followed by the rest of the bead disintegrating, leaving a layer of fluid on the lower roll only, or contraction of the bead longitudinally away from one or both of the roll ends can occur. This is very dependent on gap size; the smaller the gap, the more stable the bead is to this effect.

Thus it appears that there is a 'coating window' (the bounds of which have yet to be determined) below which the bead cannot be sustained as fluid starvation reaches a critical level and above which a stable, but totally unacceptable cellular bead instability is present. In addition, the higher the fluid viscosity, the earlier the onset of bead break etc. - this is understandable because there is a higher negative viscous pressure to balance. Conversely, the lower the viscosity the faster the possible running speed/speed ratio.

Bubble Generation

A common observation in Meniscus coating is the appearance of bubbles/bubble lines on the coated web or in the bead itself (Howe[1991]). In practice this undesirable behaviour is eliminated by:

1. Decreasing roll speed (therefore decreasing viscous forces and thus the magnitude of the negative pressure).
2. Increasing coolant flow rate on a chilled roll system (thereby lowering the temperature of the fluid).
3. Increasing the roll gap slightly (thereby increasing the curvature of the free surfaces which will decrease surface tension (T/r) pressures).

This suggests that vapourous cavitation is occurring within the fluid bead, which is consistent with the sub-ambient pressure results presented in this work. However the measured pressures (see Chapter 5, §§5.2.4) appear to be an order of magnitude smaller than those required for vapourisation (for example, the vapour pressure of a typical industrial fluid, toluene, is –23 mmHg which is equivalent to –3000 Pa). This could be explained by the lower roll speeds used in the present work to clarify the flow/pressure field. In addition, the pressures measured here are average values only, taken over relatively large areas of the flow; when considering the small-scale, sudden changes in the velocity/momentum of the fluid (particularly adjacent to the free surfaces) the pressures could be significantly lower in localised regions. There is also evidence that increasing fluid viscosity causes the onset of bubble formation at more moderate roll speeds/speed ratios. This is understandable since the negative viscous pressures generated in the bead will be larger in magnitude.

An alternative cause of bubbles is degassing; dissolved gases can come out of solution. This phenomenon is dependent on temperature, pressure and the degree of agitation of the fluid (a bottle of 'fizzy' lemonade is a good example of how these factors affect degassing). Careful, controlled handling of the fluid, prior to coating, can help to minimise this problem.

Bubbles can remain in the bead and wander axially along the nip, tending to grow and produce localised low coat weight, down-web lines which could be caused by the bubble lodging on the downstream side of the nip, up against the free surface, giving the effect that the free surface locally moves into the nip - the upstream bubble interface is treated as the bead free surface (see Figure 7.11).

7.2.4 Reverse roll coating

Classical reverse roll coating is probably the most versatile coating method in use today (Booth[1990]; this technique is more stable than the forward case over a wide range of operating parameters (i.e. it can apply defect-free wet coatings of 12 – 1200 μm thickness at roll speeds of 0.02 – 8 m/s, and can handle coatings of 0.05 – 500 Pa s viscosity).

It appears that the ribbing instability is 'the norm' in reverse rolling and only disappears close to U1/U2=1 (i.e. when there is no pressure gradient dp/dx in the nip; $dp/dx \leq \partial/\partial r\{T/r\}$ for stability).

The interesting numerical reverse roll coating results of Coyle et al [1990b], whereby the flow can be entirely upstream of the nip (upstream being classed as the origin of the inlet film) above a certain roll speed ratio, prompted an attempt to experimentally verify these findings. The numerical theory predicts that for $S > 1$ the downstream meniscus is pulled back through the nip, and the flow is maintained entirely upstream (apart from the outlet film, which travels through the nip). A steady flow is maintained until the height of the outlet film thickness travelling through the nip becomes of the same order as the roll separation, whereupon the film attempts to re-attach itself to the upper roll, and an oscillatory motion occurs (see Figure 7.12), which Coyle describes as the mechanism causing an instability referred to as 'Cascade'.

In tests carried out on the general-purpose experimental apparatus, described in Chapter 2, it was only possible to achieve a condition whereby the downstream free surface was maintained at the minimum gap even for $S > 2$ (i.e. the downstream free surface was not observed to move back through the nip). This inconsistency may be explained by the fact that the nip flow is not trying to wet a dry boundary in the present appara-

tus – the surface is already wetted by virtue of using a scraper. This condition appears to be all-important in controlling the dynamic wetting line. Further investigations are required using experimental apparatus which can accommodate a web, to facilitate a true dry boundary condition.

Reverse Meniscus roll coating generally experiences similar instability phenomena to that of the forward case, although it appears to be more resilient to such effects (Howe[1991]). From the work presented here, for the pressure distribution in a plate-roll geometry, for Meniscus roll coating and the mathematical model for plate-roll and two-roll coating flow, there exists a linear pressure distribution which tends to atmospheric pressure at $U_1/U_2 = 1$, before 'flipping' the other way. This suggests that running a reverse Meniscus roll coater at a speed ratio of unity is guaranteed to produce no defects arising from the nip flow.

7.3 Conclusions

The complexity and small-scale nature of roll coating flows has required the development of specialised experimental apparatus and techniques in order to gain an understanding of such systems. A novel cantilevered roll-coating rig was designed to permit optimum access to the nip region, for flow visualisation in particular. Flow visualisation techniques were developed to firstly reveal the general structure of the nip flow (dye injection) and secondly to quantify this flow (particle seeding and tracking). The second area consumed a considerable amount of time and effort in overcoming a number of hurdles; firstly a long selection process to find suitable particles, then a means of effective illumination (laser sheet) and capture of particle flow images (Kodak H.S.V. system), and finally the development of the computerised particle tracking system. Simple, yet effective, methods of measuring film thickness and pressures in roll coating were also

assessed and developed. These experimental systems are now firmly in place and the way is open to develop the techniques further in order to study roll coating flow in far more depth.

The Classical roll coating flow field has been extensively documented and serves to strengthen the body of knowledge in this area. The flow field can be conveniently split into three distinct regions: the upstream bank, the rectilinear flow through the nip, and the downstream two-dimensional flow region (see Figure 4.2, Chapter 4). The upstream bank, which has often been omitted in analyses of this flow, is at least as important as the downstream flow in determining film-splitting, and thus it cannot be ignored. The characteristic flow in the upstream bank also provides a clue as to the similarity in the film-splitting ratio,h_1/h_2, for the fully-flooded and ultra-starved systems; the snaking flow path observed in the upstream bank associated with the fully-flooded regime is identical to that found throughout the ultra-starved flow. The effect of gravity on the film-splitting ratio is in addition shown to be significant for this class of flow, particularly at low Capillary Numbers.

A 'new' Meniscus roll coating regime has been revealed using specialist flow visualisation techniques. It's structure is very different to that of the Classical regime. but although it appears complex it can be described by simple mathematical models which capture important features of the flow (Thompson[1992]). The most surprising result to come out of this investigation is the presence of a constant pressure gradient in the Meniscus roll coating fluid bead, where pressures are sub-ambient throughout. This is in marked contrast to that of the Classical case (with its' characteristic maximum/minimum). The largest sub-ambient pressure in the bead is maintained adjacent to the upstream free surface, which implies that it is the surface tension pressure here which balances this viscosity-generated internal pressure. Thus, there has been a fun-

damental shift in the parameters which control the coating flow; in the Classical case viscosity is the dominant property and surface tension effects are minimal, whereas for Meniscus roll coating, surface tension becomes equally important. This finding has major implications for industrial Meniscus roll coating; the surface tension of a coating fluid must be considered in the 'design' of the coating process.

A comprehensive comparison of the Classical and the Meniscus roll coating regime is given, and the transformation from one regime to the other has been explored. It has been shown that these conditions form part of a continuous flow system, at opposite ends of the flow 'spectrum'. This is confirmed by the agreement of the film thickness models in each case and the very simple physical explanation as to how the two-dimensional downstream eddy flow in the Classical case progresses back through the nip to form the fully two-dimensional flow of the Meniscus coating case. Indeed the pressure profile largely follows this trend, with the gradient of the pressure curve associated with the downstream eddy pattern in the Classical case being expanded back through the nip, together with the associated eddy flow, and recovering over the upstream free surface in the Meniscus coating condition.

It is clear from this work that there is still a great deal to learn about roll coating flows and, in particular, Meniscus roll coating. This 'new' process, although allowing only limited coating speeds, can provide far thinner, more uniform films than the Classical roll coating process. It is far more robust than the Classical system in that roll run-out, roll eccentricity, and machine vibration do not significantly affect coat quality.

7.4 Suggestions for future work

In order to fully simulate the industrial roll coating process, the incorporation of a web is essential – it is only then that the effects of a 'true' dry boundary condition can be explored.

In terms of improving flow visualisation results, a superior optical viewing system, such as a trinocular zoom microscope, would be more versatile and provide clearer, highly-magnified images of discrete regions of the flow field. In addition, the simultaneous injection of several colours of dye could also provide a more comprehensive image of the flow.

The computerised particle tracking technique works well; however, to take full advantage of this system requires the development of interpolation techniques to map the experimental data onto the same plane as the finite element results in order to provide a comprehensive quantitative comparison with predictions. Also, improved particle properties and High Speed Video system image resolution will provide more accurate results.

More film thickness/flux measurements are required to explore these low Capillary number flows; results reported elsewhere (e.g. Benkreira et al [1981]) appear to be consistently higher than those presented in this work.

There is much scope for a structured investigation of the transformation from the Classical to Meniscus roll coating regimes, in order to 'tie up' the *actual* point of transition in terms of dimensionless flux, ϵ, flow structure, and pressure profile. It is feasible to measure pressures in a two-roll coater by incorporating a pressure transducer into the surface of one of the rolls to register a reading as it travels through the nip flow.

Problems with this method may include the response of the transducer (it may be too slow to give an accurate measurement) and also the physical size of the transducer will limit the measurement of 'discrete' pressures as it travels through the bead; the pressure will be an integrated reading across the probe surface, which may not be much less than the bead width.

Forward roll coating flow is clearly not fully understood and there is need for further investigation. In addition, the reverse roll coating regime, which is more widely used in industry, has received even less attention and is therefore ripe for future study.

The problem of roll coating flow instabilities, particularly with regard to the Meniscus regime, merits further investigation. Instabilities such as bubble formation appear to be caused by a number of factors, e.g. differential temperatures between the web and fluid (i.e. the web might be at 30^0 and fluid at 5^0), increased fluid viscosity and roll speeds etc..

Finally, it is useful to bear in mind that although experimentation is the major driving force in any investigation of a physical process, such as roll coating, analytical modelling and numerical simulation have important roles to play. It is clear that combining these three approaches in a structured manner will provide a rapid, comprehensive understanding of such complex systems.

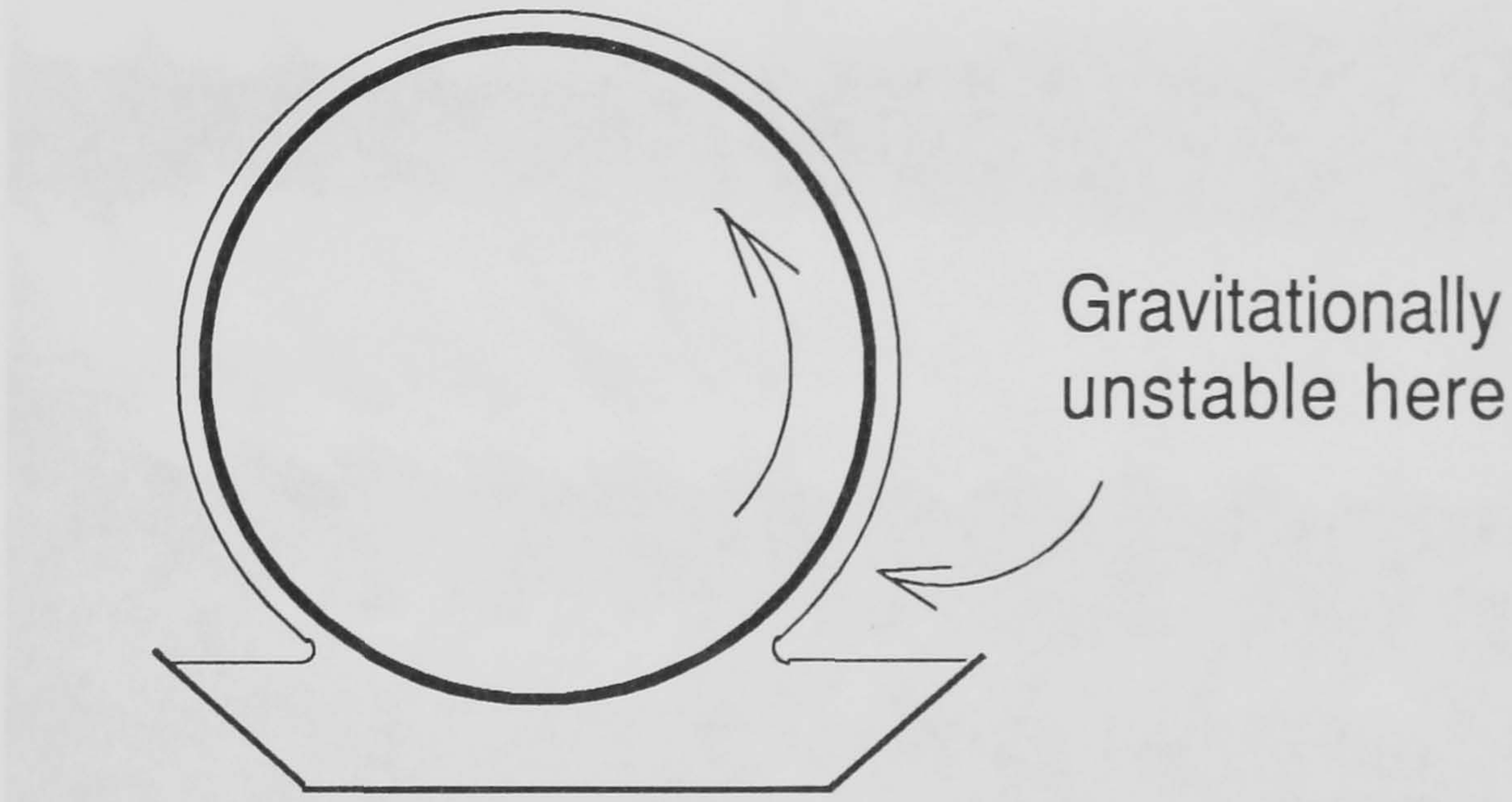

Figure 7.1: The effect of gravity on a thin fluid film attached to a rotating roll

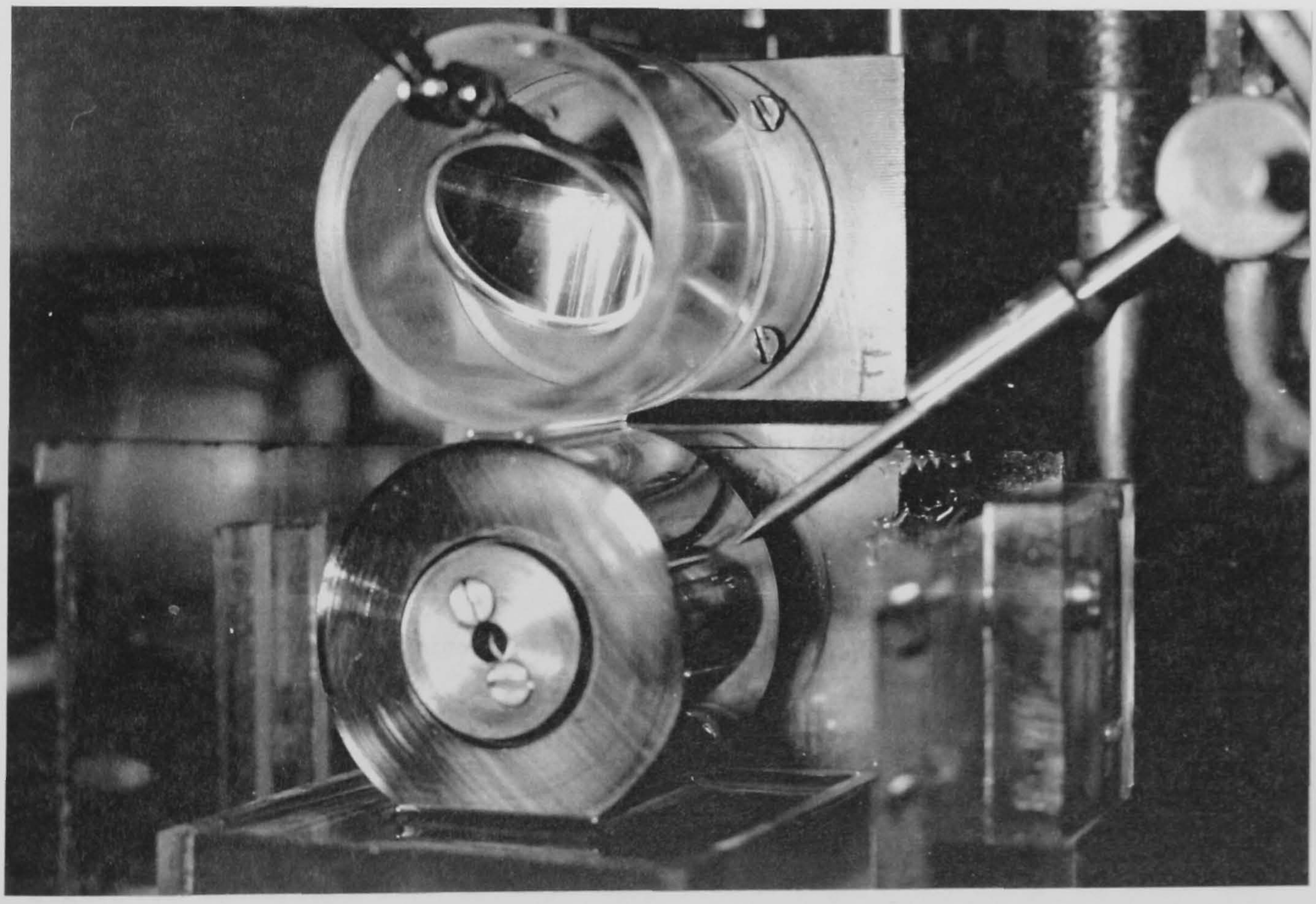

Figure 7.2: Experimental apparatus for observing flow instabilities in roll coating

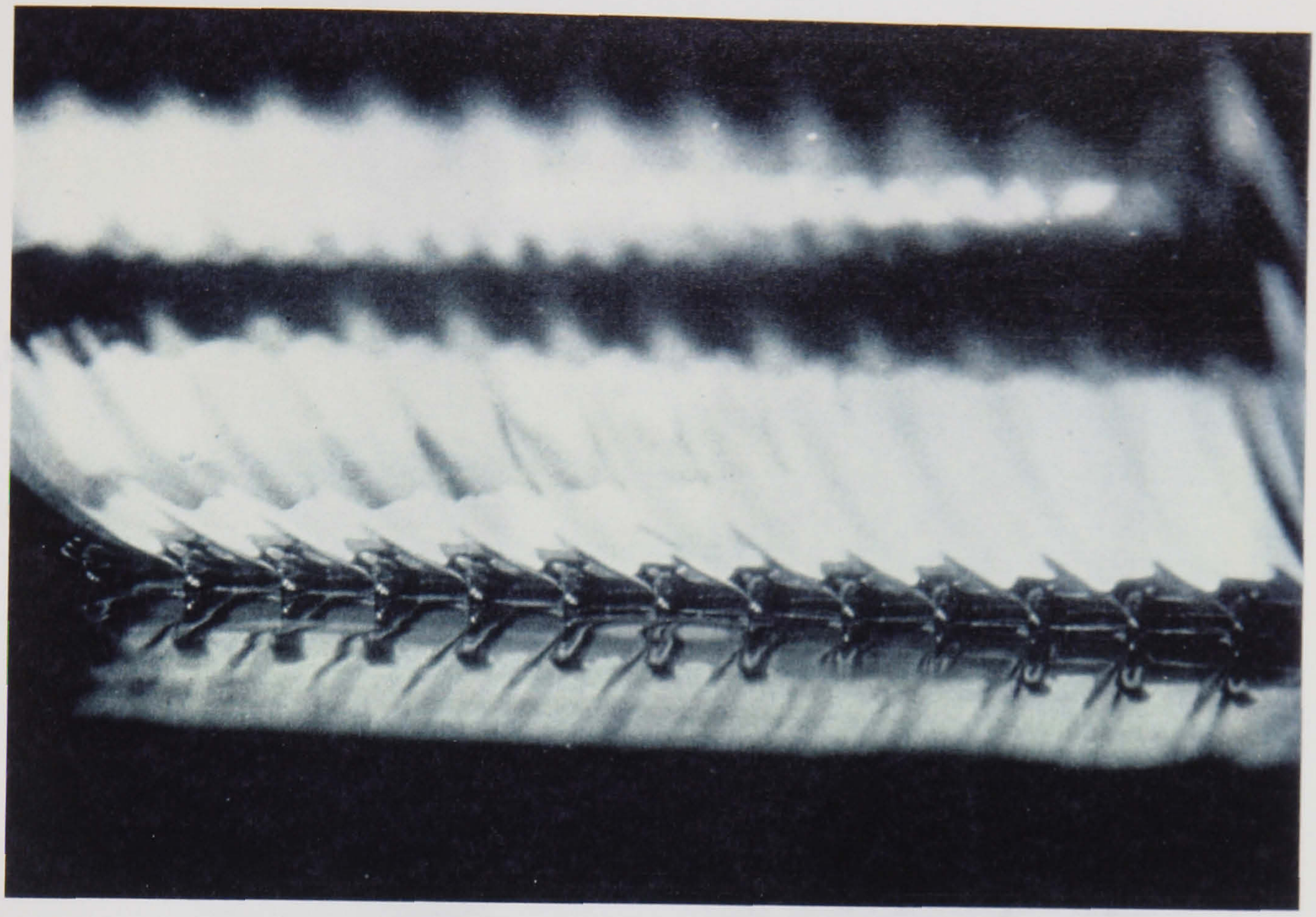

Figure 7.3: Classical ribbing in fully-flooded roll coating

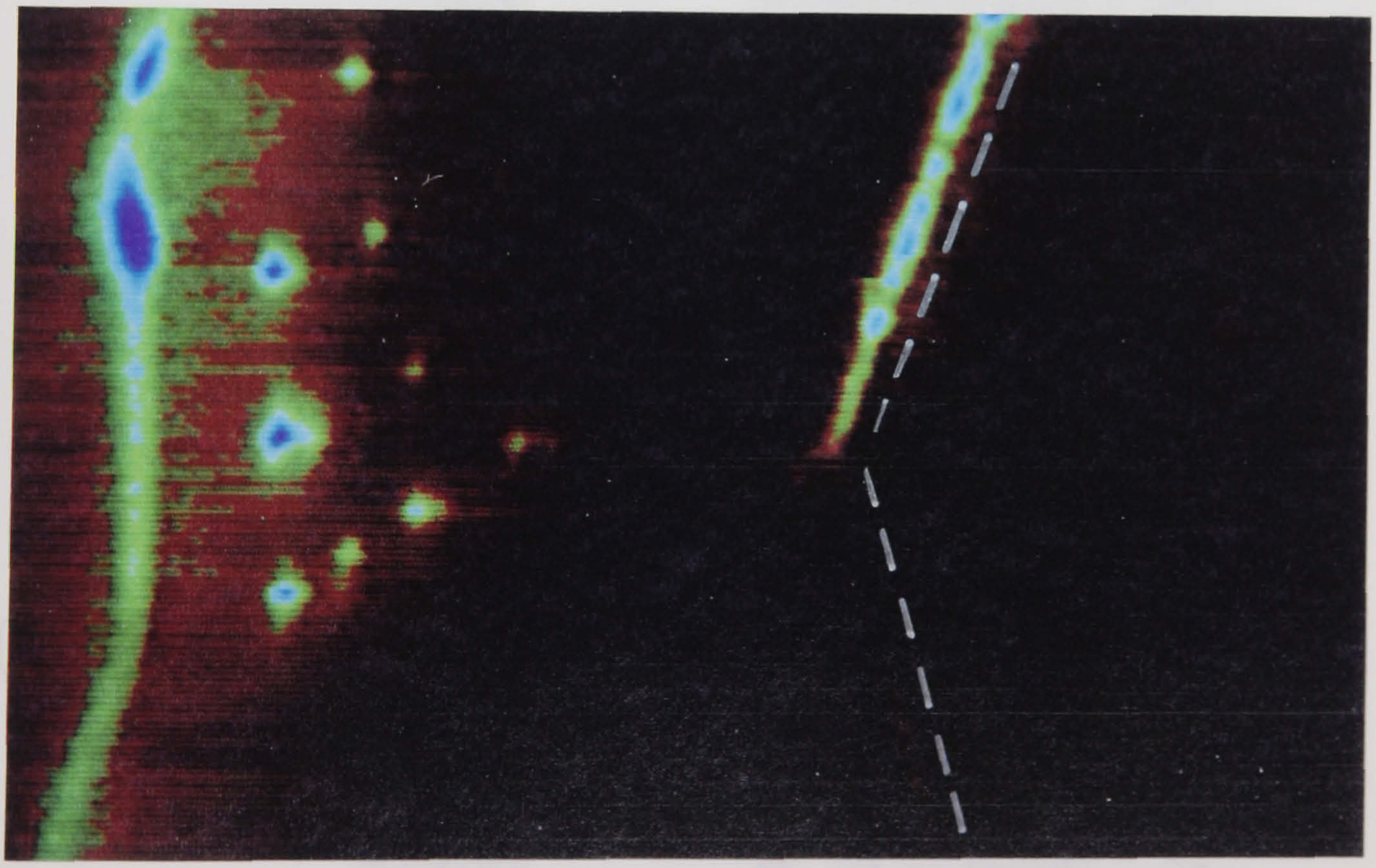

Figure 7.4: Illustration of air entrainment in roll coating (upstream free surface on right of image, downstream free surface on left)

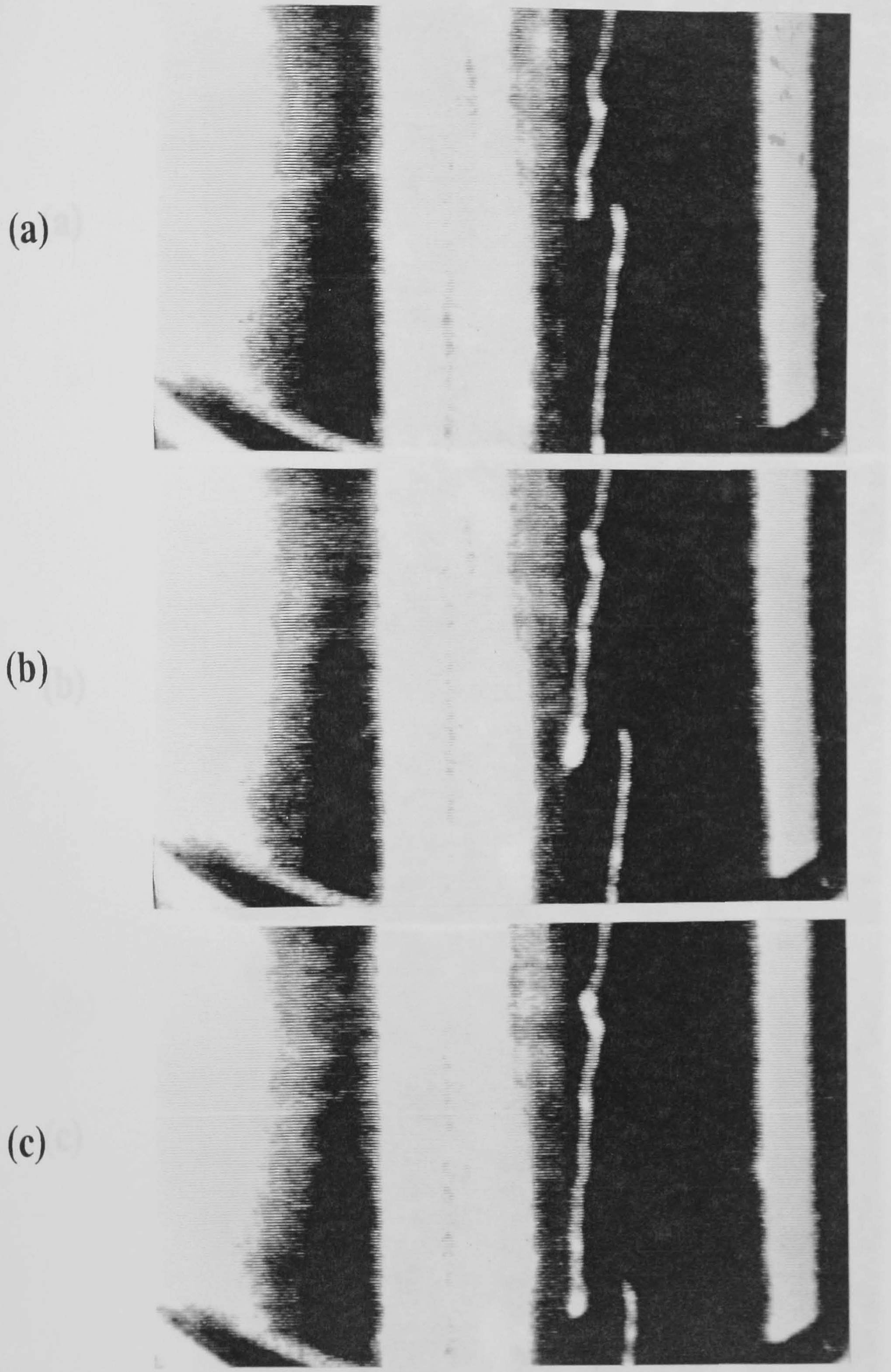

Figure 7.5: Illustration of a travelling wave on the upstream free surface in Meniscus roll coating

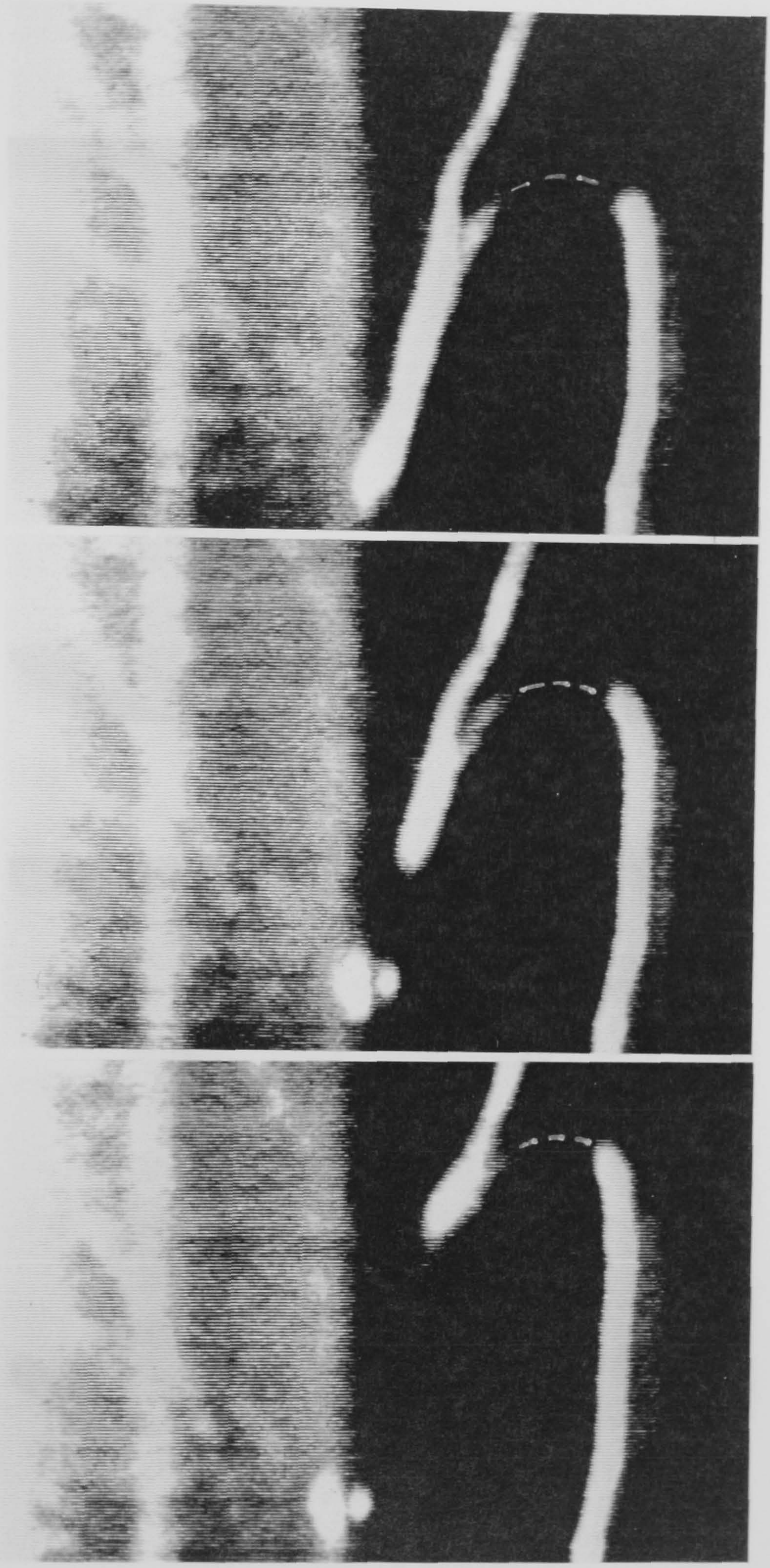

Figure 7.6: Illustration of an elongated travelling wave, resulting in the detachment of an air bubble into the fluid bead

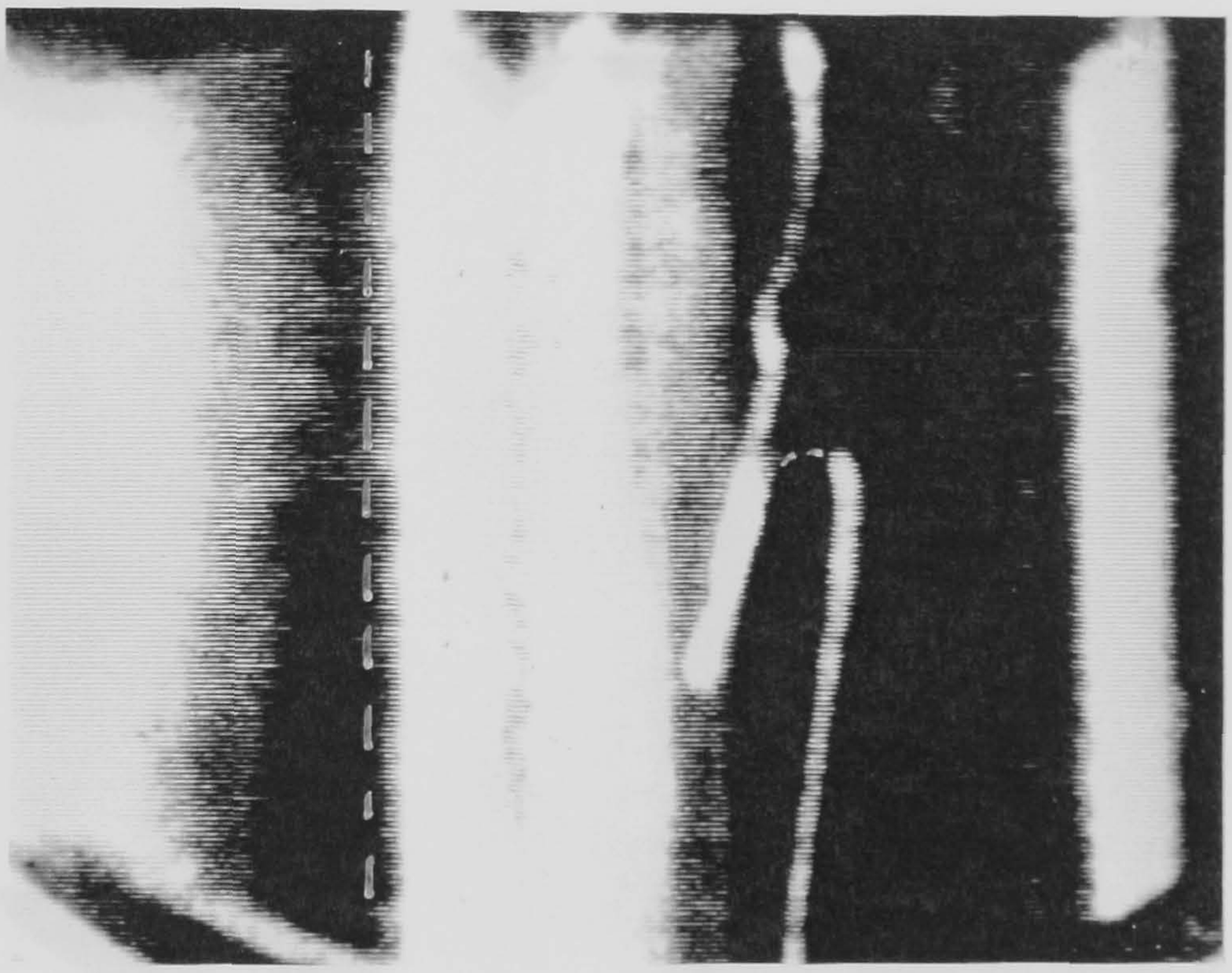

Figure 7.7: Illustration of an elongated travelling wave, resulting in the detachment of multiple air bubbles into the fluid bead

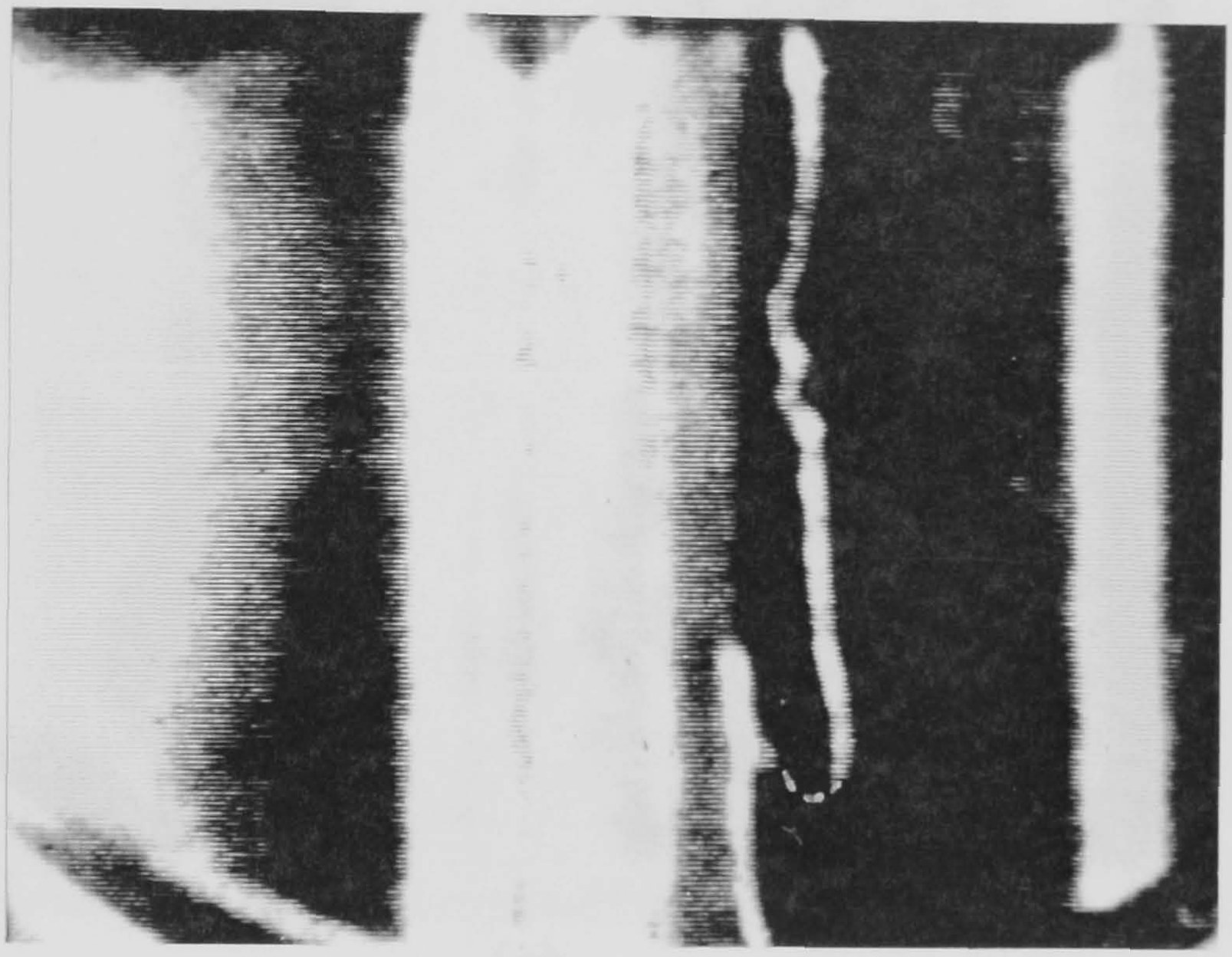

(a)

(b)

Figure 7.8: Illustration of (a) travelling wave in the opposite direction to that shown previously, and (b) a 'collision' of two waves travelling in opposite directions, producing an anvil-shaped air bubble in the fluid bead

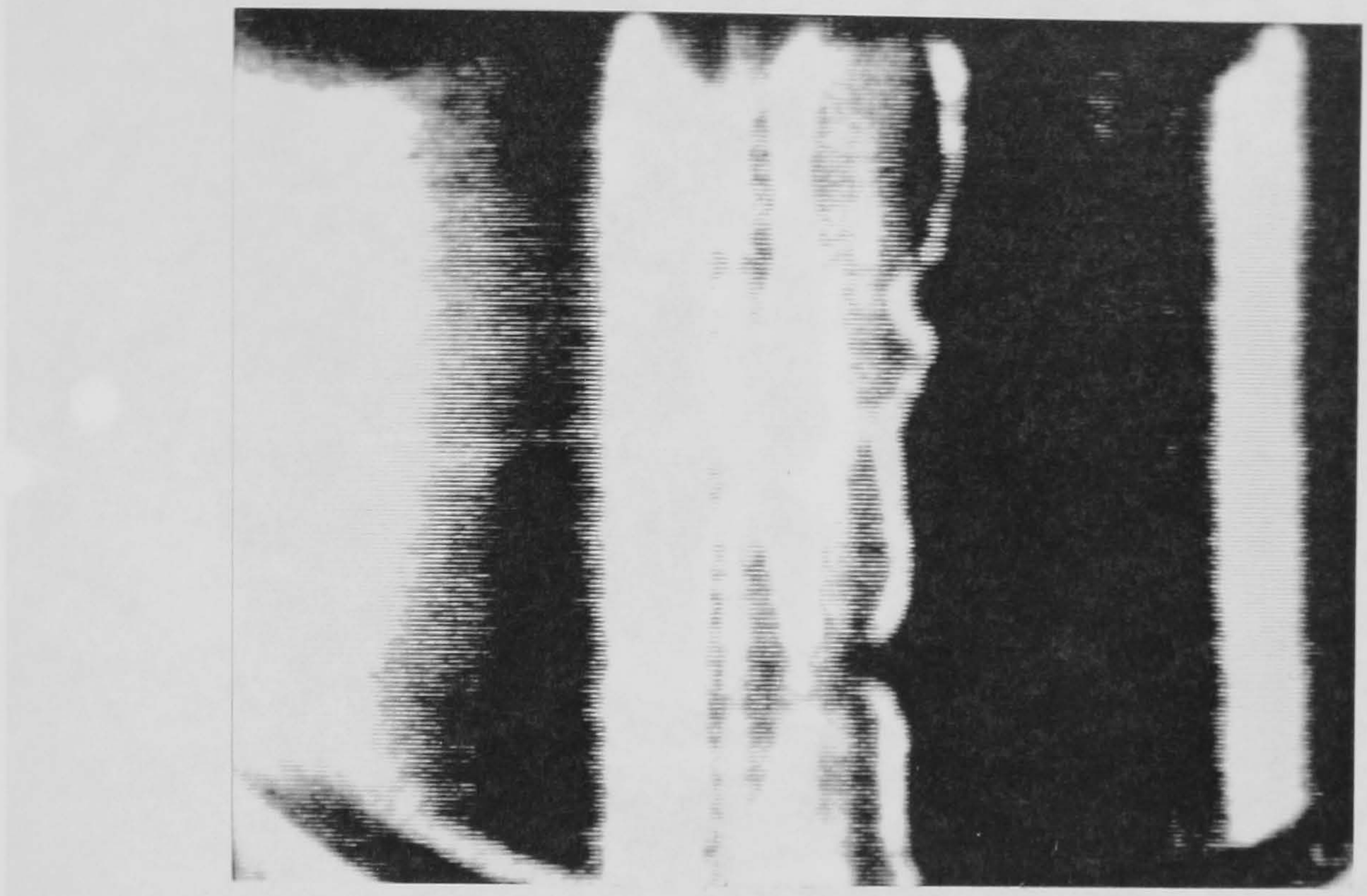

(a)

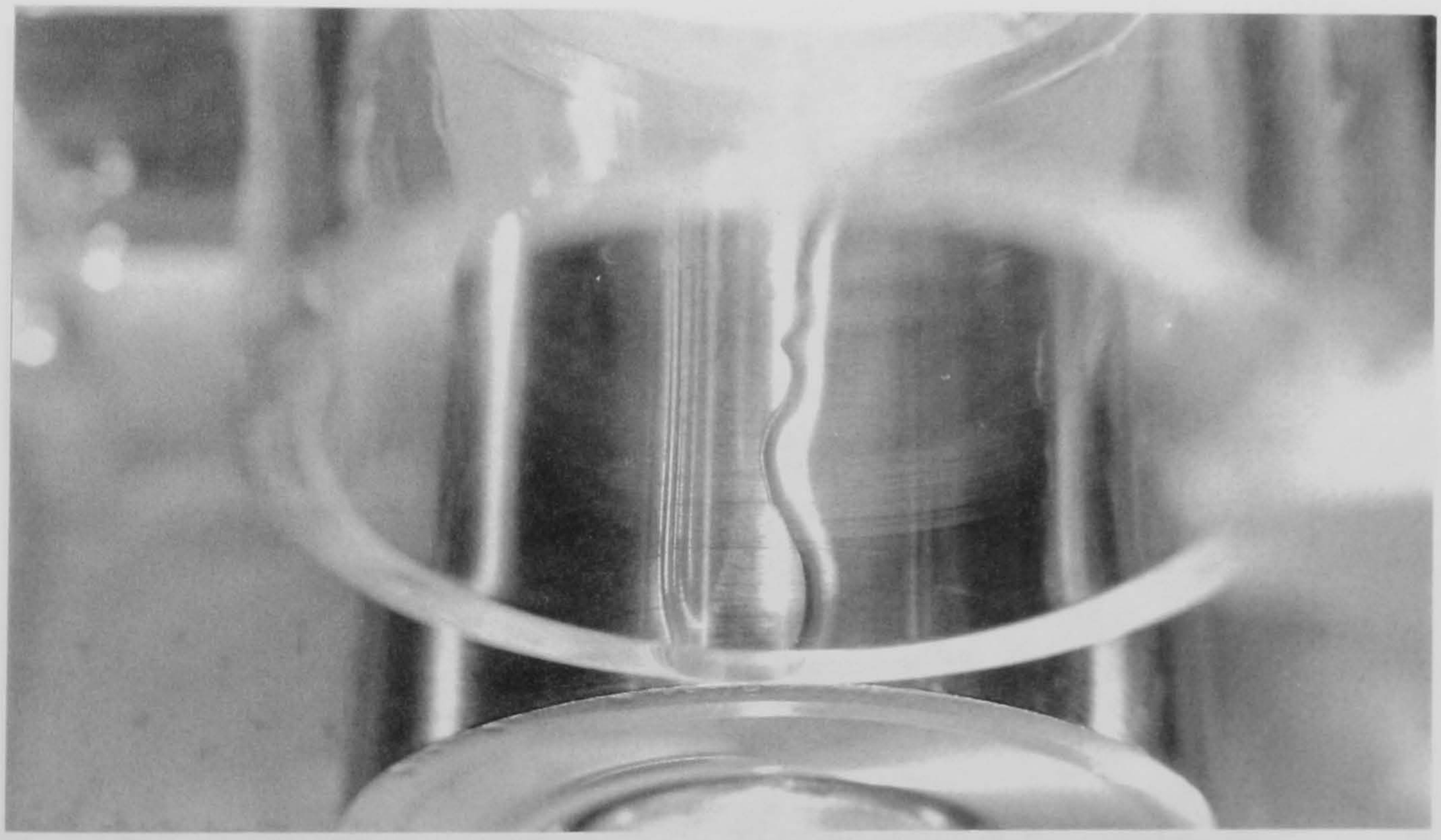

(b)

Figure 7.9: Illustration of the upstream free surface necking phenomenon in Meniscus roll coating

(a)

(b)

Figure 7.10: Illustration of (a) a single bead break, (b) a regular array of bead breaks, producing a cellular pattern

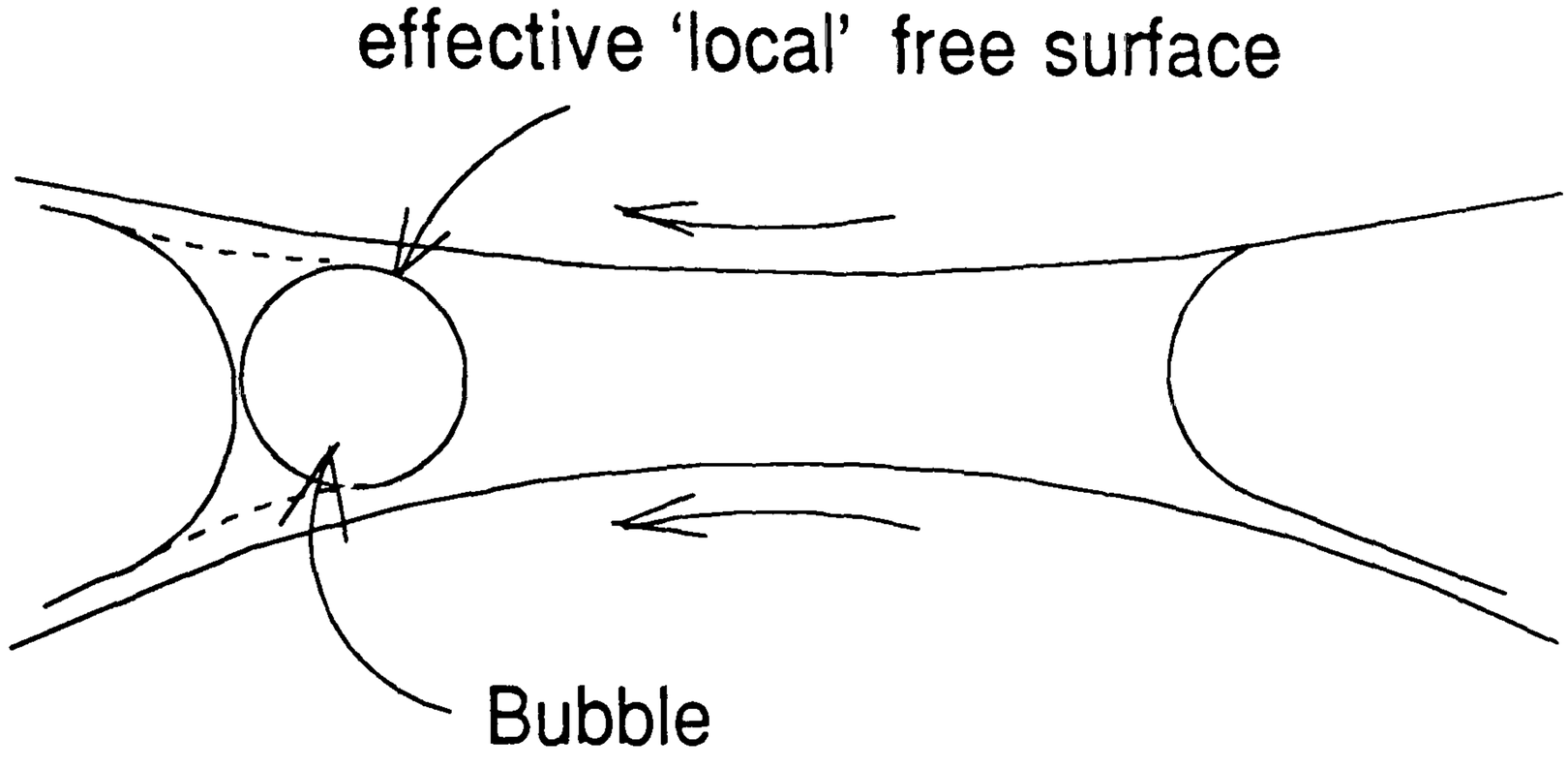

Figure 7.11: The effect of a trapped bubble in the fluid bead

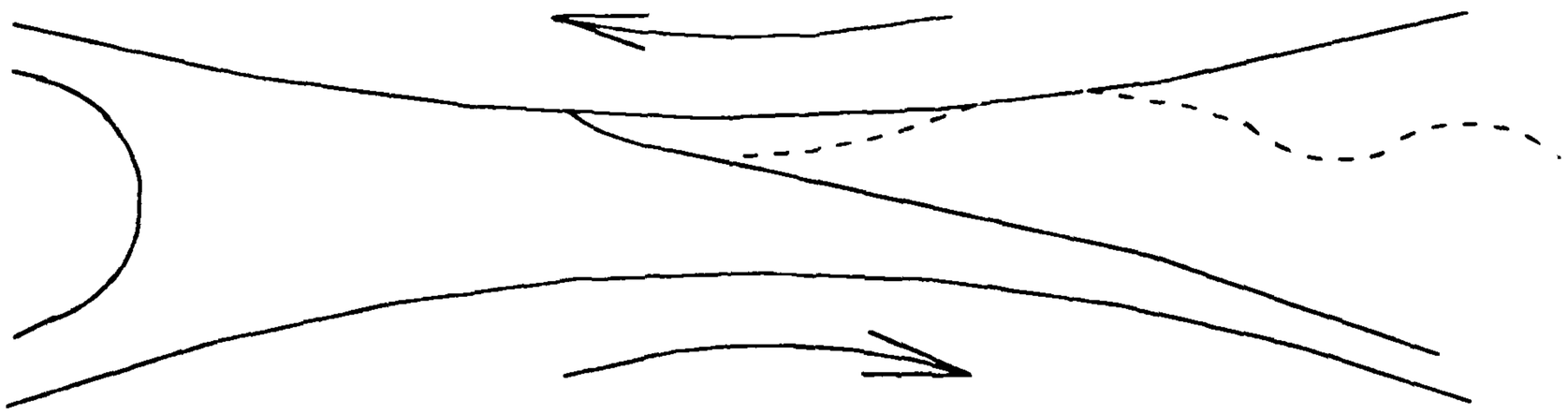

Figure 7.12: Reverse roll coating – illustration of the cause of the 'Cascade' instability

PAGE

MISSING

IN

ORIGINAL

Chapter 8

Bibliography

Agassant, J.F., Espy, M. [1985] *"Theoretical and Experimental study of the molten polymer flow in the calender bank"* Polym. Eng. S. 25(2), pp 118-121

Banks, W.H., Mill, C.C. [1954] *"Some observations on the behaviour of liquids between rotating rollers"* Proc. Roy. Soc. London ser. A, 223, pp 414-419.

Benkreira, H., Edwards, M.F., Wilkinson, W.L. [1981b] *"Roll Coating of Purely Viscous Liquids"* Chem. Eng. Sci. 36, pp 429-434.

Birkhoff, G., Hays, D.P. [1963] *"Free boundaries in partial lubrication"* J. Math. Phys. (M.I.T.), 42(2).

Booth, G.L. [1970] *"Coating Equipment and Processes"* Lockwood Publishing Company, New York.

Booth, G.L. [1990] *"Coating converting processes: Traditional methods and new uses"* 21st Annual IGC Coating Systems Conference, Boston, M.A.

Burley, R., Kennedy, B.S. [1976] *"An experimental study of air entrainment at a solid/liquid/gas interface"* Chem. Eng. Sci., 31, pp 901-911.

Cameron [1976] *"Basic Lubrication Theory"* Wiley, New York.

Carter, G.C., Savage, M.D. [1987] *"Ribbing in a varaible speed two-roll coater"* Math. Eng. Ind., 1(1), pp 83-95.

Chalmers, B., Hoare, W.E. [1937] *"Variation in thickness of the Tin Coating of Tinplate and its effect on Porosity"* J. Iron. Steel Inst., 136, p 99.

Chen S.A., Higgins B.G., [1988] *"Study of the flow in the upstream bank of liquid in a Forward Roll Coater by the Finite Element Method"* Chem. Eng. Sci., 43, pp 2867-2875.

Chen, S.A. [1991] PhD. Thesis, University of Leeds.

Cox, R.G. [1986] *"The dynamics of the spreading of liquids on a solid surface Part I: Viscous flow"* J. Fluid Mech., 168, pp 169-194.

Coyle, D.J. [1984] *"The Fluid Dynamics of Coating Flows: Steady Flows, Stability, and Rheology"* Ph.D. Thesis, University of Minnesota.

Coyle, D.J. [1988a] *"Experimental studies of the flow between deformable rolls"* Paper no. 3D, A.I.Ch.E. Spring National Meeting, New Orleans.

Coyle, D.J. [1988b] *"Forward roll coating with deformable rolls: A simple one-dimensional elastrohydrodynamic model"* Chem. Eng. Sci., 43(10), pp 2673-2684.

Coyle, D.J., [1990] *"Nonlinear theory of squeeze roll coating"* Paper no. 35h, A.I.Ch.E. Spring National Meeting, Orlando.

Coyle, D.J., [1991] *"An introduction to coating and drying technology"* Chapter 3, VCH Publishers, New York.

Coyle, D.J., Macosko, C.W., Scriven, L.E. [1982] *"Computer simulation of nip flow in roll coating"* A.C.S. Symp. Series 197.

Coyle, D.J., Macosko, C.W., Scriven, L.E. [1986] *"Film- splitting flows in forward roll coating"* J. Fluid Mech., 171, pp 183-207.

Coyle, D.J., Macosko, C.W., Scriven, L.E. [1987] *"Film- splitting flows of shear-thinning liquids in forward roll coating"* A.I.Ch.E. J., 33(5), pp 741-746.

Coyle, D.J., Macosko, C.W., Scriven, L.E. [1990a] *"Stability of symmetric film-splitting between counter-rotating cylinders"* J. Fluid Mech., 216, pp 437-458.

Coyle, D.J., Macosko, C.W., Scriven, L.E. [1990b] *"The fluid dynamics of re-*

verse roll coating" A.I.Ch.E. J., 36(2), pp 161-174.

Coyle, D.J., Macosko, C.W., Scriven, L.E. [1990c] "*A simple model of reverse roll coating*" Ind. Eng. Chem. Res., 29, pp 1416-1419.

Coyle, D.J., Macosko, C.W., Scriven, L.E. [1990d] "*Reverse roll coating of non-Newtonian liquids*" J. Rheol., 34(5), pp 615-636.

Coyne, J.C., Elrod, H.G. [1970] "*Conditions for the rupture of a lubricating film. Part I: Theoretical model. Part II New boundary conditions for Reynolds equations*" A.S.M.E. Paper Nos. 69-Lub-3 and 70-Lub-3.

Dowson, D., Taylor, C.M. [1979] "*Cavitation in Bearings*" Ann. Rev. Fluid. Mech., 11, pp 35-66.

Dowson, D., Smith, E.H. [1980] "*An Experimental Study of Hydrodynamic Film Rupture in Steadily-loaded, Non-conformal Contact*" J. Mech. Eng. Sci., 22(2), pp 71-78.

Dussan V, E.B. [1976] "*The moving contact line: the slip boundary condition*" J. Fluid Mech., 77(4), pp 665-684.

Dussan V, E.B. [1979] "*On the spreading of liquidson solid surfaces: static and dynamic contact angles*" Ann. Rev. Fluid Mech., 11, pp 371-400.

Esmail, M.N., Hummel, R.L. [1975] "*Nonlinear theory of free coating onto a vertical surface*" A.I.Ch.E. J., 21(5), p 958.

Floberg, L. [1965] "*On hydrodynamic lubrication with special reference to sub-cavity pressures and numbers of streamers in cavitation regions*" Acta. Polytech. Scad., ME19.

Gatcombe, E.K. [1945] "*Lubrication Characteristics of Involute Spur Gears - A Theoretical Investigation*" Trans. A.S.M.E., 67, pp 177-188.

Greener, J., Middleman, S. [1975] "*A theory of roll coating of viscous anf viscoelastic fluids*" Polymer Eng. Sci., 15(1), pp 1-10.

Greener, J., Middlman, S. [1979] "*Theoretical and experimental studies of the*

fluid dynamics of a two-roll coater" Ind. Eng. Chem. Fundam., 18, pp 35-41.

Greener, J. [1979] "*Bounded Coating Flows of Viscous and Viscoelastic Fluids* " Ph.D. Thesis, University of Massachusetts.

Greener, J., Sullivan, T., Turner, B. and Middleman, S. [1980] "*Instability of a Two-Roll Coater: Newtonian Fluids*" Chem. Eng. Commun., 5, pp 73-83.

Hansen, R.J., Toong T.Y.,[1971] "*Dynamic contact angle and its relationship to forces of hydrodynamic origin*" J. Colloid Interface Sci., 37, pp 196-207

Hayashi, H., Taylor, C.M. [1980] "*A determination of cavitation interfaces in fluid film bearings using finite element analysis*" J. Mech. Eng. Sci., 22, No. 6, pp 277-285.

Hintermaier, J.C., White, R.E. [1965] "*The splitting of a water film between rotating rolls*" Tappi, 48(11), 617-625.

Hoare, W.E. [1937] "*Variation in thickness of the tin coating of tinplate and its effect on porosity*" J. Iron. Steel Inst., 136, p 99.

Hocking, L.M. [1977] "*A moving fluid interface Part II: The removal of the force singularity by a slip flow*" J. Fluid Mech., 79(2), pp 209-229.

Hoffman, R.D., Myers, R.R. [1962] "*The splitting of thin liquid films*" Trans. Soc. Rheol., 6, pp 197-207.

Hopkins, M.R. [1957] "*Viscous flow between rotating cylinders and a sheet moving between them*" Brit. J. Appl. Phys., 8, p 442.

Howe, S. [1991] Private Communication, ICI Imagedata.

Huebner K.H. [1975] "*The Finite Element Method for Engineers*" Wiley.

Huh, C., Scriven, L.E. [1971] "*Hydrodynamic model of steady movement of a solid/liquid/fluid contact line*" J. Colloid Interface Sci., 35, pp 85-101.

Ikegawa M., Wasizu K. [1973] "*Finite element method applied to analysis of flow over a spillway crest*" Int. J. Num. Meth. In Engng. 6, pp 179-189.

Ikin, B. [1992] Private Communication. Ilford Ltd., Mobberley, Cheshire.

Jeffrey, G.B. [1922] "*The Rotation of Two Circular Cylinders in a Viscous Fluid*" Phil. Roy. Soc. London Ser. A. 101, p 169.

Kelmanson, M.E. [1983] *"Boundary Integral equation solution of viscous flows with free surfaces"* J. Eng. Math., 17, pp 329-343.

Kistler [1983] *"The fluid mechanics of curtain coating and related viscous free surface flows with contact lines"* PhD Thesis, University of Minnesota.

Kistler, S.F., Scriven, L.E. [1983] *"Coating flows"* Computational Analysis of Polymers, Chapter 8, p 343.

Landau, L., Levich, B. [1942] *"Dragging of a liquid by a moving plate"* Acta Physicochimica U.R.S.S., XVII(1-2), p 42.

Lauder, W. [1966] *"Hydrodynamic lubrication of proximate cylindrical surfaces of large relative curvature"* Proc. Inst. Mech. Engrs. Elastohydrodyn. Lubr., 180(Pt.3B), pp 101-106.

Lothian, G.F. [1949] *"Absorption Spectrophotometry"* Adam Hilger Ltd., London.

Martin, H.M. [1916] *"The Lubrication of Gear Teeth"* Engineering(London), 102, pp 119-121.

McCorquodale J.A., Li C.Y. [1971] *"Finite element analysis of sluice gate flow "* Trans. Eng. Inst. Can., 14, No. C-2.

Mill C.C., South G.R. [1967] *"Formation of Ribs on Rotating Rollers"* J. Fluid Mech., 28, p 523.

Miller, J.C., Myers, R.R. [1958] *"A photographic study of liquid flow in a roll nip"* Trans. Soc. Rheol., 2, pp 77-93.

Moffat H.K., [1977] *"Behaviour of a Viscous Film on the Outer Surface of a Rotating Roll"* Journal de Mecanique, 18(5), p 651.

Myers, R.R., Hoffman, R.D. [1961] *"The distribution of pressures in the roll application of Newtonian fluids"* Transacs. Soc. Rheol., V, pp317-328.

Myers, R.R., Miller, J.C., Zettlemoyer, A.C. [1959] *"The splitting of thin liquid films - kinematics"* J. Colloid Sci., 14, pp 287-299.

O'Connell, A. [1989] *"Observations of air entrainment and the limits of coatability"*

PhD thesis, Heriot-Watt University.

Oteri, B.I. [1972] PhD Thesis, University of Leeds.

Patel, R. [1989] PhD Thesis, University of Bradford.

Pearson J.R.A. [1960] *"The instability of uniform viscous flow under rollers and spreaders"* J. Fluid Mech., 7, p481.

Perkins R.J., Hunt J.C.R. *"Particle Tracking in Turbulent Flows"* Department of Applied Mathematics and Theoretical Physics, University of Cambridge.

Pitts E., Greiller J. [1961] *"The Flow of Thin Liquid Films Between Rollers "* J. Fluid Mech., 11, p 33.

Prandtl, L. [1904] *"Motion of fluids with very little viscosity"* Tech. Memor. Nat. Adv. Comm. Aero. Wash., no.452.

Reynolds; O. [1886] *"On the theory of lubrication and its application to Mr Beauchamp Towers experiments, including an experimental determination of the viscosity of olive oil"* Philos. Trans. Roy. Soc. London Ser. A, 177, pp 157-234.

Roache, P.J. [1972] *"Computational Fluid Dynamics"* Hermosa Press, Alburquerque.

Ruckenstein, E., Dunn, C.S. [1977] *"Slip velocity during wetting of solids"* J. Colloid. Int. Sci., 59(1), p 135.

Ruckenstein, E., Rajora, P. [1983] *"On the no-slip boundary condition of hydrodynamics"* J. Colloid Int. Sci., 96(2), p 488.

Ruschak, K.J. [1980] *"A method for incorporating free boundaries with surface tension in Finite Element fluid flow simulators"* Int. J. Num. Meth. Engng., 15, pp 639-648.

Ruschak, K.J., [1982] *"Boundary conditions at a liquid/air interface in lubrication flow"* J. Fluid Mech., 119, pp 107-120.

Sato Y., Yamamoto K. [1987] *"Lagrangian measurement of fluid particle motion in an isotropic turbulent field"* J. Fluid Mech., 175, pp 183-199.

Saito, H., Scriven, L.E. [1980] *"Study of coating flow by the finite element method"*

J. Comp. Phys., 42, pp 53-76.

Saman, W.Y. [1974] *"A study of starved elastohydrodynamic lubrication with particular reference to gyroscopic bearings"* PhD thesis, University of Leeds.

Savage M.D. [1977] *"Cavitation in lubrication. [a] Part I. On boundary conditions and cavity-fluid interfaces; [b] Part 2. Analysis of wavy interfaces"* J. Fluid Mech. 80, p743.

Savage, M.D. [1982] *"Mathematical models for coating proceses"* J. Fluid Mech., 117, pp 443-455

Savage, M.D. [1984] *"Mathematical Model for the Onset of Ribbing"* A.I.Ch.E. J., 30, no. 6, pp 999-1002.

Savage [1992] *"A refined lubrication model for roll coating"* Private communication, University of Leeds.

Schneider, G.B. [1962] *"Analysis of forces causing flow in roll coaters"* Trans. Soc. Rheol., 6, pp 209-221.

Schweizer, P.M. [1988] *"Visualisation of coating flows"* J. Fluid Mech., 193, pp 285-302.

Sjodahl L.H. [1951] *"Ink Flow On Rotating Rollers"* Amer. Ink Mkr., 29, pp 31-33 and p 57.

Soroka, A.J., Tallmadge, J.A. [1972] *"Velocity profiles for plate withdrawal at high speeds"* Appl. Sci. Res., 25, p 413.

Steiber, W. [1933] *"Das scwimmlager, hydrodynamische theorie des gleitlagers"* Berlin V.D.I.

Swift, H.W. [1931] *"The stability analysis of lubricating films in journal bearings"* Proc. Inst. Civ. Engrs., 233, p267.

Taylor, C.M. [1974a] *"Separation cavitation in lightly loaded fluid film bearings with both roll surfaces in motion. Part 1: Theoretical considerations"* J. Mech. Eng. Sci.,

16(4), pp 147-150.

Taylor, C.M. [1974b] *"Separation cavitation in lightly loaded fluid film bearings with both surfaces in motion. Part 2: Analysis of the cylinder plane and journal bearing configurations"* J. Mech. Eng. Sci., 16(4), pp 150-155.

Taylor, C.M. [1974c] *"Film rupture for a lubricated film lightly loaded against a plane"* J. Mech. Eng. Sci., 16(4), pp 225-231.

Taylor, G.I. [1963] *"Cavitation of a viscous fluid in narrow passages"* J. Fluid Mech., 16, pp 595-619.

Tekic, Jovanovic, [1982] *"Liquid Coating onto a Rotating Roll"* Chem. Eng. Sci. Vol 37, No. 12, pp 1815-1817.

Teletzke, G.F., Davis, H.T., Scriven, L.E. [1984] *"Wetting Hydrodynamics"* Unpublished.

Tharmalingam S. Wilkinson W.L., [1978] *"The Coating of Newtonian Liquids onto a Roll Rotating at Low Speeds"* Polymer Engineering and Science, Vol. 18, No. 15, p 1155.

Thompson, H.M. [1992] *"A theoretical investigation of roll coating phenomena"* PhD thesis, University of Leeds (*to be submitted*).

Van de Bergh [1974] "A study of cavitation for a cylinder sliding against a plane" MSc project, University of Leeds.

Van Dyke, M. [1982] *"An Album of Fluid Motion"* Parabolic Press, Stanford, California.

White, D.A., Tallmadge, J.A. [1965] *"Theory of drag out of liquids on flat plates"* Chem. Eng. Sci., 20, pp 33-37.

Williamson, A.S. [1972] *"The tearing of an adhesive layer between flexible tapes pulled apart"* J. Fluid Mech., 52, pp639-656.

Wilson, S.D.R. [1982] *"The drag-out problem in file coating theory"* J. Engg. Math., 16, pp209-221.

Wolveridge, P.E., Baglin, K.P., Archard, J.F. [1971] *"The starved lubrication of cylinders in line contact"* Proc. Inst. Mech. Eng., 185, pp 1159-1169.

Wu C-Y. Weng C-I. Chen C-K., [1985] *"Analysis of Free Coating on a Rotating Roll"* Chem. Eng. Commun. Vol 33, pp 245-254.

Yih C-S., [1960 *"Instability of a Rotating Liquid Film with a Free Surface "* Proc. Roy. Soc., Vol. A258, pp 63-89.

Zienkiewicz O.C. [1977] *"The Finite Element Method"* McGraw Hill.